Electrokinetic Flow and Transport in Porous Media:

Experimental Methods, Numerical Analysis, and Applications

Habilitationsschrift

von Dr. rer. nat. Ulrich Tallarek

geb. am 23. Juli 1967 in Hannover

zur Verleihung des akademischen Grades

Doktor rerum naturalium habilitatus

(Dr. rer. nat. habil.)

genehmigt von der Fakultät für Verfahrens- und Systemtechnik

der Otto-von-Guericke-Universität Magdeburg am 7. Dezember 2004

Gutachter:

Prof. Dr. Andreas Seidel-Morgenstern

Institut für Verfahrenstechnik, Otto-von-Guericke-Universität Magdeburg

Prof. Dr. Hans-Joachim Warnecke

Department für Chemie und Chemietechnik, Universität Paderborn

Prof. Dr. Andreas Manz

Institut für Spektrochemie und Angewandte Spektroskopie an der Universität Dortmund

Dankwort

Die in der vorliegenden Habilitationsschrift einfließenden Ergebnisse resultieren aus meiner Zeit als Marie-Curie-Stipendiat (1998-2000) an der Wageningen University and Research Centre, Niederlande, und als wissenschaftlicher Assistent bzw. später Juniorprofessor (2000-2004) an der Otto-von-Guericke-Universität Magdeburg.
Ich möchte daher allen Personen aus beiden Umfeldern danken, die mich während dieser Zeit tatkräftig unterstützt und zum Gelingen dieser Arbeiten maßgeblich beigetragen haben.

Zunächst möchte ich mich sehr herzlich bei Prof. Dr. Andreas Seidel-Morgenstern (Universität und MPI Magdeburg) für seine großzügige Unterstützung, die eingeräumten Freiheiten, Rat und das ständige Interesse an meinen Arbeiten bedanken, die es mir ermöglicht haben, in kurzer Zeit eine Arbeitsgruppe mit eigenem Forschungsprofil aufzubauen.
Weiterhin danke ich sehr herzlich Prof. Dr. Henk Van As (Wageningen) für das große Interesse an meiner Arbeit, stete Diskussionsbereitschaft und die geförderte Eigenständigkeit während meiner Zeit in den Niederlanden.

Außerdem möchte ich Kollegen und Gruppenmitgliedern für die gute Zusammenarbeit und angenehme Arbeitsatmosphäre der letzten Jahre danken. Bei der Magdeburger Arbeitsgruppe handelt es sich um Felix Leinweber, Erdmann Rapp, Ivo Nischang, Dima Hlushkou, Martin Pačes und Dr. Guofang Chen. Aus meiner Zeit in den Niederlanden sind es Dr. Tom Scheenen, Frank Vergeldt, Adrie de Jager (Wageningen), sowie Dr. Drona Kandhai, Dr. Alfons Hoekstra und Prof. Dr. Pieter Sloot (University of Amsterdam).

Darüberhinaus danke ich den folgenden Personen vor Ort in Magdeburg für die Unterstützung auf wichtigen Arbeitsgebieten: Dr. Heiner Sann und Prof. Dr. Udo Reichl (MPI Magdeburg) beim Einsatz der konfokalen Lasermikroskopie für die Untersuchung von Transportvorgängen in porösen Materialien, sowie Bernd Ebenau und Prof. Dr. Jürgen Tomas (Universität Magdeburg) bei der elektrokinetischen Oberflächencharakterisierung von Mikropartikeln.

Dr. Dietmar Schmid und Prof. Dr. Günther Jung (Universität Tübingen) danke ich für die äußerst effektive, erfolgreiche Arbeit zur Kopplung von kapillarmonolithischen Trennphasen mit der Fourier-Transform Ionenzyklotronresonanz-Massenspektrometrie.

Dieter Lubda und Dr. Karin Cabrera (Merck KGaA, Darmstadt) danke ich für die fruchtbaren gemeinsamen Arbeiten zu monolithischen Kieselgelmaterialien. Ihnen, sowie Dr. Gerard Rozing (Agilent Technologies, Waldbronn) gebührt darüberhinaus mein tiefer Dank für mehrere wertvolle, sehr hilfreiche Geräteleihgaben.

Am Ende möchte ich nicht versäumen, meinen Mentoren Prof. Dr. Ernst Bayer (1927-2002; Universität Tübingen) und Prof. Dr. Georges Guiochon (University of Tennessee, Knoxville, TN, USA), die meinen wissenschaftlichen Werdegang wesentlich beeinflußt haben, meinen Dank auszusprechen.

Zusammenfassung

Die vorliegende Habilitationsschrift beschäftigt sich mit analytisch- und physikalisch-chemischen experimentellen, aber auch theoretischen und numerischen Aspekten der Elektrokinetik in porösen Materialien. Im Hinblick auf diese Arbeit zählen dazu insbesondere offene, einfachere Kanalstrukturen (die z.B. als Sensoren oder Bauteile in Lab-on-a-Chip-Technologien Einsatz finden), sowie kapillare Festbetten und Kapillarmonolithen für Elektrochromatographie und auch kapillare HPLC. Ergebnisse der Untersuchungen sind darüberhinaus für elektrokinetische Prozesse in deutlich größeren Säulen (z.B. mit dem Ziel präparativer Chromatographie) und Membranen (z.B. für Elektrodialyse oder potentialgesteuerte Reaktionsführung) von Bedeutung. Es wurde versucht, miteinander eng verknüpfte Themen in einer durch stark zunehmende Komplexität geprägten Chronologie zu bearbeiten, um letztlich zu einem abgerundeten globalen Verständnis relevanter Stofftransportphänomene in den untersuchten Materialien zu gelangen. Dies beinhaltete die elektrokinetische Charakterisierung der involvierten Oberflächen, transiente und stationäre Dynamik des elektroosmotischen Flußfeldes, Kopplung der Adsorption von geladenen Spezies mit der lokalen (quasi-)Gleichgewichtselektrostatik, Elektrophorese, axiale und radiale Dispersion, Eigenschaften der Elektrolytlösung (insbesondere ihre Ionenstärke) und Analyten (Ladung, Adsorption, Diffusion), Struktur der Materialien (hierarchischer Aufbau, Porendimensionen, Oberflächenheterogenität), sowie entstehende Konzentrationspolarisation und mögliche Nichtgleichgewichtseffekte in starken elektrischen Feldern.

Ein Ziel dieser Arbeit ist es, moderne und im Hinblick auf die bearbeiteten Themen kaum oder noch nicht genutzte experimentelle Methoden (chromatographische Verfahren und direkte Bildgebungstechniken wie dynamische NMR-Mikroskopie und konfokale Lasermikroskopie) mit einerseits anspruchsvollen, aber andererseits auch kompakten, sehr effizienten numerischen Verfahren zu verknüpfen, um auf mikroskopischen Strukturdetails und mesoskopischen Zusammenhängen aufbauend Elektrokinetik und den Stofftransport auf makroskopischer Ebene besser zu analysieren, verstehen und optimieren.

Wie bereits erwähnt zählen zu den adaptierten und intensiv eingesetzten Bildgebungsmethoden die Kernspintomographie und die konfokale Lasermikroskopie. Beide Mikroskopietechniken ergänzen sich in einzigartiger Weise. Während mithilfe der dynamischen NMR-Mikroskopie die Flußfelddynamik in einem sehr attraktiven örtlichen und zeitlichen Fenster direkt in dem porösen Material untersucht wird, kann durch die empfindlichere konfokale Lasermikroskopie der Transport in geringer Konzentration vorliegender Tracermoleküle erfaßt werden. Somit sind die Dynamik der fluiden Phase, aber auch die Transportcharakteristik eines in ihr gelösten Analyten mit (leicht zu realisierender) Adsorption und/oder Reaktion an der Oberfläche komplementär zugänglich. Mit diesen beiden Mikroskopietechniken konnte quantitative Information zum Massentransport (Diffusion, Dispersion, Elektrophorese, Elektroosmose, Adsorption) in porösen Materialien sowohl orts- (im unteren Mikrometer- bis in den Submikrometerbereich), als auch zeitaufgelöst (im Millisekundenbereich) erhalten und der Übergang zu makroskopischem Verhalten dokumentiert werden. Damit stellen diese experimentellen Untersuchungsmethoden eine sehr dringend benötigte Ergänzung zu den vielfältigen chromatographischen Verfahren dar, die lediglich Informationen über örtlich und zeitlich gemitteltes (makroskopisches) Verhalten geben können.

Bezüglich der Hydrodynamik von elektroosmotischem Fluß und einhergehender Dispersion in porösen Materialien, sowie der erzielbaren Trenneffizienzen in der Flüssigchromatographie wird gewöhnlich der Vergleich zu dem bereits ausgiebig charakterisierten und gut verstandenen Transportverhalten für hydraulischen Fluß gewählt (und gewünscht). Daher beginnt auch diese Arbeit mit neuartigen Untersuchungen (sowohl Experiment, als auch Modellierung betreffend) zur Hydrodynamik in Festbettstrukturen wie Kugelpackungen und Monolithen, die insbesondere die Schlüsselstellung stagnanter Zonen in den porösen Materialien für die resultierenden Dispersionseffekte verdeutlichen und unmittelbar auf das große Potential elektrokinetischen Transports zuarbeiten [1-3]. Mithilfe der dynamischen NMR-Mikroskopie gelang es, direkt in den porösen Materialien die in stagnanten Zonen verbleibende Flüssigkeit (auf einer Zeitskala von wenigen Millisekunden) zu visualisieren und die Massentransferkinetik zwischen der stagnanten (diffusiven) und konvektiven fluiden Phase zu quantifizieren.

Dieser neue experimentelle Zugang zur Charakterisierung der Hydrodynamik hat es ermöglicht, direkt in porösen Partikeln einer Kugelpackung Diffusionskoeffizienten unter statischen und dynamischen Bedingungen zu bestimmen, für verschiedene chromatographische Materialien zu vergleichen und bezüglich ihrer Porenmorphologie zu diskutieren [1]. Darüberhinaus konnte der unmittelbare Einfluß der stagnanten Zonen auf die transiente und asymptotische (axiale) Dispersion in den Kugelpackungen verfolgt und im Vergleich zu nichtporösen Partikeln klar herausgearbeitet werden. Diese experimentellen Ergebnisse wurden durch sehr anspruchsvolle numerische Simulationen in recht guter Einstimmung komplementiert [2, 3]. Die Modellierung der hydrodynamischen Dispersion erfolgte in dreidimensionalen Kugelschüttungen, die die reale Packungsstruktur relativ gut abzubilden vermochten. Für die Diskretisierung des Flußfeldes wurde der lattice-Boltzmann Formalismus verwendet, eine vielversprechende Alternative (basierend auf einem von Natur aus parallelen Algorithmus) für Modellierung rechenintensiver Hydrodynamik, insbesondere in sehr komplexen Geometrien. In guter Übereinstimmung zeigten Experiment und Modellierung, daß poröse Partikel zwar eine deutlich größere und für viele Anwendungen in der Tat erforderliche (spezifische) Oberfläche anbieten können als nichtporöse Partikel, daß aber dadurch mit hydraulischem Fluß stagnante Zonen generiert werden, die zu unerwünschten Dispersionseffekten führen.

Einen vielversprechenden Ausweg aus diesem Engpaß (hierarchischer Aufbau des Materials im Hinblick auf spezifische Oberfläche, Permeabilität und Dispersion) könnte der Einsatz von neuartigen Kieselmonolithen mit bimodaler Porenstruktur weisen. Ein direkter Vergleich aber mit konventionellen Festbetten aus porösen, partiell porösen oder nichtporösen Partikeln erweist sich durch grundsätzliche Unterschiede (kontinuierliche vs. diskontinuierliche Struktur) zunächst als schwierig. Mithilfe eines recht einfach gehaltenen, aber verhältnismäßig weitreichenden phänomenologischen Ansatzes wurden die hydraulische Permeabilität und hydrodynamische Dispersion in monolithischen und partikulären Festbettstrukturen gemessen und durch dimensionslose Skalierung der gewonnenen Daten universell analysierbar [4, 5]. Damit wurde es möglich, die für Permeabilität und Dispersion maßgebliche Hydrodynamik in Monolithen durch äquivalente Teilchendimensionen (in den Kugelpackungen) auszudrücken und die beiden Typen von Festbettstrukturen in dieser Hinsicht zu vergleichen. Diese ausführlichen Arbeiten haben gezeigt [5], daß gerade die Kieselgelmonolithen aufgrund ihrer bimodalen Porenstruktur und Gesamtporosität eine Kombination aus hydraulischer Permeabilität, hydrodynamischer Dispersion und Adsorptionskapazität realisieren, die mit den partikulären Festbetten nicht erzielt werden kann.

Mit diesen einführenden Arbeiten zur Hydrodynamik in porösen Materialien (z.B. partikuläre und monolithische Festbetten) sind bereits wesentliche Themen erkannt und behandelt worden (stagnante Zonen, diffusionslimitierter Transport, axiale Dispersion), die bei der Untersuchung der Elektrokinetik in diesen Strukturen wiederkehren und dann eine neue Bedeutung im Hinblick auf die erreichbare Dimension des Stofftransports erlangen können.

Die Untersuchungen zur Elektrokinetik in porösen Materialien beginnen mit elektroosmotischem Fluß durch einfache Kanalstrukturen mit homogener Oberfläche (z.B. zylindrisch geformte Kapillaren) [6, 7], gewinnen aber schon bald an Komplexität, indem allgemein Oberflächen mit heterogener Verteilung ihres elektrokinetischen Potentials betrachtet werden, z.B. durch die Adsorption geladener Analyten an der Oberfläche während der Stofftrennung [8]. Es resultiert ein komplexes Wechselspiel zwischen lösungsseitiger Dynamik (Fluß, Elektromigration, Diffusion) und lokalen Grenzflächeneffekten (Adsorption, quasi-Gleichgewichtselektrostatik). Während für ideale Bedingungen (z.B. homogene Oberfläche und Elektrolytzusammensetzung) mittels dynamischer NMR-Mikroskopie und einem eigens dafür gebauten NMR-Meßstand [6] ein oft postuliertes, pfropfenförmiges (plug-flow) Flußprofil für elektroosmotischen Fluß tatsächlich auch gemessen werden konnte, sind aufgrund von Oberflächenheterogenitäten (durch Adsorption oder fehlerhafte Fertigung) unter praxisnäheren Bedingungen Abweichungen von diesem Flußprofil zu erwarten, die wegen der Kontinuität der fluiden Phase auf induzierte Druckkomponenten zurückzuführen sind. Das verursacht hydrodynamische Dispersionsbeiträge ähnlich wie beim Poiseuille-Flußprofil [6-8].

Der allgemeine Fall heterogener Verteilung des elektrischen Oberflächenpotentials erfordert die (in der Regel dreidimensionale) numerische Lösung der folgenden gekoppelten Gleichungen. Navier-Stokes-Gleichung für Konvektion der flüssigen Phase (die Wechselwirkung des externen elektrischen Feldes mit der lösungsseitigen elektrischen Doppelschicht wird dabei durch einen separaten Term für die resultierende Volumenkraft berücksichtigt), Poisson-Gleichung für Verteilung des elektrischen Potentials, und Nernst-Planck-Gleichung für die Verteilung ionischer Spezies [7]. Das hydrodynamische Problem wurde durch Code-Parallelisierung mithilfe der lattice-Boltzmann-Methode analysiert. Die Stärke des präsentierten Modellierungsansatzes liegt in seiner großen Reichweite. Insbesondere die Fluiddynamik in noch komplexeren Materialien wie partikulären und monolithischen Festbettstrukturen mit beliebiger Porenarchitektur und Oberflächenpotentialverteilung läßt sich damit sehr vorteilhaft numerisch-effektiv behandeln. Die Ergebnisse verdeutlichen, daß die elektrische Doppelschicht an (fest-flüssig-)Phasengrenzen allgemein besser als Nichtgleichgewichtssystem behandelt wird. Zentrale Fragestellungen beinhalten den Einfluß physikalischer und chemischer Heterogenität (Oberflächenrauhigkeit und Fraktalität, Kanalmorphologie, Inhomogenität des Zeta-Potentials durch lokale Adsorption oder uneinheitliche Oberflächenmodifizierung), sowie einsetzender Konvektion auf die lokale Elektrostatik und resultierende Elektrokinetik. Deshalb müssen inherent gekoppelte Parameter entflochten werden, um den dynamischen Einfluß der Oberflächen und lokalen, wie globalen Stofftransport in mikrofluidischen Systemen systematisch zu analysieren (und auch optimieren).

Aufbauend auf den bisherigen Arbeiten vollzieht sich der Übergang zu elektroosmotischem Fluß und seiner (spatio-temporalen) Dynamik in Festbetten aus porösen Partikeln. Als ein erstes Merkmal fällt der Einfluß der Säuleninnenwand auf das resultierende makroskopische Flußprofil auf. Da die involvierten Oberflächen (Säuleninnenwand, Adsorbensoberfläche) allgemein unterschiedliche physikalisch-chemische Eigenschaften aufweisen ist zu erwarten, daß lokal

generierter elektroosmotischer Fluß wegen verschiedener Oberflächenladungen unterschiedlich stark ausfällt. Dies führt, wie mithilfe dynamischer NMR-Mikroskopie deutlich gezeigt werden konnte [9], zur Ausbildung makroskopischer Flußheterogenität, die laterale Äquilibrierung über den gesamten Säulenquerschnitt benötigt. Abhängig vom Unterschied elektrokinetischer Potentiale (Wand-Partikel) und dem Verhältnis Säulen-/Partikeldurchmesser kann das Flußprofil eine ansonsten gute Dispersionscharakteristik des elektroosmotischen Flußes in der Packung völlig überdecken [10]. Diese Arbeiten setzen damit bei Festbettstrukturen die bereits für Kanalstrukturen gemachten Anmerkungen und Untersuchungen zur allgemeinen Heterogenität des elektrokinetischen Potentials in porösen Materialien fort. Sie weisen auf einen wichtigen Aspekt, dem bei Verständnis und Optimierung der Elektrokinetik große Bedeutung zukommt, da elektroosmotischer Fluß lokal an der Oberfläche generiert wird. Somit leistet die direkte Charakterisierung von Grenzflächeneffekten, z.B. mit der Kernspintomographie oder konfokalen Lasermikroskopie, auf (transienter und asymptotischer) hydrodynamischer Ebene eine fast unentbehrliche Ergänzung zu herkömmlichen chromatographischen Untersuchungsmethoden.

Von einer makroskopischen Flußheterogenität über den gesamten Säulenquerschnitt kommend steht dann als wesentlicher Schwerpunkt der vorliegenden Arbeit die elektroosmotische Permeabilität von einzelnen porösen Partikeln des Festbettes im Vordergrund. Die zentrale Fragestellung in diesem Zusammenhang war, ob (und in welchem Ausmaß) ein intrapartikulärer elektroosmotischer Fluß existiert, wie er sich auf die globale Dispersionscharakteristik auswirkt und gezielt in miniaturisierten Trennverfahren genutzt werden kann. Ein erstes Indiz für die elektroosmotische Perfusion war die Beobachtung, daß im Vergleich zu hydraulischem Fluß um bis zu eine Dekade verbesserte hydrodynamische Dispersionskoeffizienten für Elektroosmose in einer (mit makroporösen kugelförmigen Partikeln) gepackten Kapillarsäule gemessen werden konnten [11]. Während es nahe liegt, eine derartige Effizienzsteigerung auf signifikanten intrapartikulären elektroosmotischen Fluß zurückzuführen (im Hinblick auf die vorangegangenen Arbeiten sei daran erinnert, daß intrapartikuläre Porenflüssigkeit bei hydraulischem Fluß als stagnante Region mit diffusionslimitiertem Massentransfer verbleibt), sind makroskopisch effektive Dispersionskoeffizienten nur schwer bezüglich einzelner Beiträge zu analysieren, die auf intra- und interpartikulärer Flüssigkeit beruhen. Daher wurden mit der NMR-Mikroskopie komplementäre (transiente) Messungen durchgeführt, die es erlaubt haben, die intrapartikuläre Flüssigkeit zu visualisieren und hinsichtlich der intrapartikulären Geschwindigkeiten zu analysieren [10]. Mithilfe eines für diese Untersuchungen konzipierten Setups konnte direkt gemessen werden, daß intrapartikulärer elektroosmotischer Fluß von der angelegten Feldstärke (auf die elektrische Doppelschicht wirkende Kraft) und Ionenstärke der Elektrolytlösung (durch die Dicke der elektrischen Doppelschicht bezüglich Porendurchmesser) abhängt. Es war gelungen, in porösen Partikeln des Materials Geschwindigkeiten für elektroosmotischen Fluß zu messen und den Beweis für eine signifikante elektroosmotische Perfusion direkt zu erbringen. Auf makroskopischer Ebene konnte dieses Verhalten (Abhängigkeit des intrapartikulären elektroosmotischen Flußes von Porengröße und Ionenstärke) systematisch durch die Dynamik des mittleren elektroosmotischen Flußes in den kapillaren Festbetten (verglichen mit Festbetten aus nichtporösen, d.h. nichtleitenden und impermeablen Partikeln) dokumentiert werden [12]. Weiterhin konnte der bei abnehmender elektrischer Doppelschichtwechselwirkung in den porösen Partikeln zunehmende intrapartikuläre elektroosmotische Volumenstrom deutlich mit einer parallel erfolgenden Steigerung der Trenneffizienzen für neutrale Analytmoleküle korreliert werden [13], so daß ein mikroskopisch und makroskopisch konsistentes Bild von Fluß und Dispersion resultierte, das nachhaltig zum Verständnis elektroosmotischer Perfusion beiträgt.

Während mit der dynamischen NMR-Mikroskopie und dem für die Untersuchungen in Kapillaren entwickelten Setup bereits wesentliche Beiträge zur relevanten Hydrodynamik in porösen Materialien geleistet werden konnten, wurde an dieser Stelle die konfokale Lasermikroskopie (wegen des im Vergleich größeren räumlichen Auflösungsvermögens und der deutlich besseren Empfindlichkeit) benutzt, um auf der Ebene eines einzelnen porösen Partikels in den Festbetten Analytkonzentrationsprofile von fluoreszierenden Tracermolekülen sowohl örtlich, als auch zeitlich aufgelöst im Hinblick auf die elektrokinetischen Tansportphänomene zu untersuchen und analysieren (single bead analysis). Zwar erlaubt auch die NMR-Mikroskopie auf ihre eigene elegante Weise die Visualisierung der intrapartikulären Flüssigkeit, aber erreicht dies durch die Bewegungskodierung (auf einer im Millisekundenbereich liegenden Zeitskala) sämtlicher Flüssigkeitsmoleküle, die sich im aktiven Messvolumen befinden (welches selbst viele poröse Partikel enthält). Aufgrund schneller Bildaufnahme und Ortsauflösung im Submikrometerbereich ist mit der konfokalen Lasermikroskopie hingegen die spatio-temporale Transportcharakteristik eines Tracers in einem einzelnen Partikel zugänglich.

Um mit der konfokalen Lasermikroskopie quantitative Daten zu erhalten und in jeder Tiefe eines porösen Partikels die Analytkonzentration bestimmen zu können, wurde im ersten Schritt ein mikrofluidischer Versuchsstand präpariert und der Brechungsindex der flüssigen Phase dem der porösen festen Phase angeglichen um sphärische Abberation durch die kugelförmigen Partikel zu minimieren [14]. Die im darauffolgenden unter wohldefinierten Bedingungen erhaltenen Zeitserien für intrapartikuläre Analytprofile haben eindrucksvoll (und komplementär zu den mit NMR-Mikroskopie direkt gemessenen Geschwindigkeiten) den Einfluß von intrapartikulärem Fluß auf die Symmetrie dieser Profile und eine Einzelbead-Massentransferkinetik demonstriert. Es konnte visualisiert werden, daß der gerichtete elektroosmotische Fluß (im Vergleich zu diffusionslimitiertem Transport) die intrapartikulären Analytprofile axial in Feldrichtung deformiert [14, 15]. Das auf Partikelebene beobachtete Phänomen ist für mehrere elektrische Feldstärken herausgearbeitet und mit einem mathematischen Modell, das intrapartikuläre Diffusion und elektroosmotische Konvektion elektroneutraler Analyten berücksichtigt, analysiert worden [15]. Diese Studie hat ergeben, daß bereits unter Bedingungen, die als moderat einzustufen sind (hinsichtlich einer elektrischen Doppelschichtwechselwirkung im Partikel, benötigter Feldstärken und Ionenstärken im Elektrolyten, sowie thermischer Effekte), die realisierte Elektrokinetik den intrapartikulären Transport in das konvektionsdominierte Regime verlagert, d.h. daß der Massentransfer durch elektroosmotischen Fluß bereits viel schneller erfolgt als durch Diffusion. Damit wird das bereits zuvor sowohl in makroskopischen Dispersionskoeffizienten [11], als auch in den NMR-mikroskopischen Untersuchungen [10] erkannte, enorme Ausmaß einer elektroosmotischen Perfusion auf der Ebene eines einzelnen porösen Partikels eindrucksvoll bestätigt und die Untersuchung dieses Transportmechanismus abgerundet. Somit ist schließlich erreicht, auf Basis mikroskopischer Strukturdetails (poröses Material) und mesoskopischer Zusammenhänge (Stofftransport) makroskopische Elektrokinetik und Hydrodynamik besser zu analysieren, verstehen und optimieren.

Während für elektroneutrale Analytmoleküle im Hinblick auf hydrodynamischen Transport und Dispersionseffekte die elektroosmotische Perfusion eine große Rolle spielt, kommt für geladene Spezies ein Aspekt hinzu, der ihre Transportcharakteristik noch weitaus komplexer gestaltet. Es handelt sich dabei wiederum (wie schon bei der Perfusion) um den Einfluß der gewöhnlich mesoporösen oder makroporösen Porenräume in den Partikeln oder dem Gerüst (Skelett) eines Monolithen. Die Dicke der elektrischen Doppelschicht ist gewöhnlich sehr klein verglichen mit

Porendimensionen in Festbettstrukturen, welche außerhalb der porösen Partikel selbst bzw. des porösen Monolithskeletts angetroffen werden. Deshalb kann die Elektrolytlösung in diesen Porenräumen als praktisch elektroneutral betrachtet werden. Anders sieht es in den kleineren Poren der Partikel (bzw. des Monolithskeletts) aus. Die Dicke der elektrischen Doppelschicht ist hier vergleichbar mit der Porengröße, so daß die innere Oberflächenladung durch die den Porenraum sättigende Lösung nicht vollständig abgeschirmt werden kann. Es werden Koionen aus diesem Porenraum ausgeschlossen und Gegenionen angereichert. Im (elektrochemischen) Gleichgewicht kann diese Situation durch die Donnan-Potentiale beschrieben werden.

Wie mit quantitativer konfokaler Lasermikroskopie gezeigt und analysiert werden konnte, kommt es bei Überlagerung eines elektrischen Feldes zur Ausbildung von Konzentrationspolarisation im angrenzenden Elektrolyten [16]. Die sich formierende Diffusionsgrenzschicht bedingt lösungsseitigen diffusionslimitierten Transport zwischen dem elektroneutralen (interpartikulären) und intrapartikulären (Ionen-permselektiven) Porenraum. Für ideale Permselektivität werden Koionen komplett aus letzterem ausgeschlossen, während Gegenionen durch gleichgerichtete Elektrophorese und Elektroosmose beschleunigt transportiert werden. Mit zunehmender Feldstärke wird schließlich intrapartikulärer Transport der Gegenionen den (diffusionslimitierten) Transport durch die Diffusionsgrenzschicht überschreiten und die porösen Partikel verlieren deutlich an effektiver Adsorptionskapazität (die Gegenionen betreffend) [16]. Zugleich kann es in der Elektrolytlösung unter diesen Bedingungen (Konzentrationspolarisation in starken elektrischen Feldern) zur Abweichung lokaler Elektroneutralität kommen. Die dadurch induzierte Raumladung wechselwirkt mit dem elektrischen Feld und generiert elektroosmotischen Fluß, der in seiner Intensität sehr stark sein kann und, da die Raumladung (im Gegensatz zu permanent vorhandener Oberflächenladung der Partikel) induziert werden muß, eine in erster Näherung quadratische Abhängigkeit von der elektrischen Feldstärke zeigt. Dies steht im klaren Gegensatz zur klassischen Elektroosmose, die linear von der Feldstärke abhängt. Ein weiteres Merkmal ist, daß die induzierte Elektroosmose entlang gekrümmter Oberflächen eine nicht einheitliche Intensität aufweist und die Ausbildung lokaler Druckkomponenten bedingt. Je nach Geometrie und Intensität können sich hydrodynamische Strukturen formieren, die zu verstärkter lateraler Durchmischung in der Lösung und reduzierter axialer Dispersion führen. Für die Entwicklung dieser Phänomene ist neben der Morphologie des Porenraums die Anwesenheit genügend starker elektrischer Felder entscheidend.

Diese äußerst komplexen Zusammenhänge konnten in Festbetten aus porösen Partikeln und Monolithen visualisiert, makroskopisch charakterisiert und konsistent analysiert werden [16, 17]. Da in der Praxis viele Analyten geladen sind (kleinere pharmazeutisch-relevante Moleküle, größere in der Proteomforschung) besitzen die aufgezeigten Phänomene und Folgen für den Transport, sowie Dispersionseffekte eine enorme Bedeutung. Obwohl die Phänomene zunächst kurios anmuten mögen und z.B. in der Elektrochromatographie bisher nicht berücksichtigt worden sind, haben sie andererseits in der Grenzflächenchemie und -Physik, insbesondere im Zusammenhang mit Membrantransportprozessen wie Elektrodialyse und Überschreiten von Diffusionsgrenzströmen, über Jahrzehnte theoretische, verfeinerte numerische und zahlreiche experimentelle Untersuchungen nach sich gezogen. Daher rundet diese komplexe Thematik die vorliegende Arbeit nicht ab, sondern hat vielmehr den Charakter eines Ausblicks, indem sie auf ein anspruchsvolles und gerade im Hinblick auf elektrokinetische Transportphänomene in (hierarchisch-strukturierten) porösen Materialien wenig untersuchtes Gebiet mit gundlegend physikalisch-chemischem Hintergrund weist.

Die vorangegangene Beschreibung und Einschätzung der in die vorliegende Habilitationsschrift einfließenden Ergebnisse verdeutlicht, daß ein substanzieller Beitrag zum Verständnis von elektrokinetischen Transportvorgängen in ausgewählten porösen Materialien geleistet werden konnte, insbesondere im Hinblick auf miniaturisierte Trennverfahren. Die erhaltenen Ergebnisse dokumentieren nicht nur den Weg zu bisher dafür kaum eingesetzten numerischen und experimentellen Ansätzen, sondern besitzen auch universellen Charakter im Hinblick auf die zukünftige Bearbeitung weitreichender Fragestellungen.

Zitierte Arbeiten

[1] U. Tallarek, F. J. Vergeldt, and H. Van As, *J. Phys. Chem. B* **1999**, *103*, 7654.

[2] D. Kandhai, U. Tallarek, D. Hlushkou, A. G. Hoekstra, P. M. A. Sloot, and H. Van As, *Philos. Trans. R. Soc. Lond. A* **2002**, *360*, 521.

[3] D. Kandhai, D. Hlushkou, A. G. Hoekstra, P. M. A. Sloot, H. Van As, and U. Tallarek, *Phys. Rev. Lett.* **2002**, *88*, art. no. 234501.

[4] U. Tallarek, F. C. Leinweber, and A. Seidel-Morgenstern, *Chem. Eng. Technol.* **2002**, *25*, 1177.

[5] F. C. Leinweber and U. Tallarek, *J. Chromatogr. A* **2003**, *1006*, 207.

[6] U. Tallarek, E. Rapp, T. Scheenen, E. Bayer, and H. Van As, *Anal. Chem.* **2000**, *72*, 2292.

[7] D. Hlushkou, D. Kandhai, and U. Tallarek, *Int. J. Numer. Meth. Fluids* **2004**, *46*, 507.

[8] M. Pačes, J. Kosek, M. Marek, U. Tallarek, and A. Seidel-Morgenstern, *Electrophoresis* **2003**, *24*, 380.

[9] U. Tallarek, T. W. J. Scheenen, and H. Van As, *J. Phys. Chem. B* **2001**, *105*, 8591.

[10] U. Tallarek, E. Rapp, A. Seidel-Morgenstern, and H. Van As, *J. Phys. Chem. B* **2002**, *106*, 12709.

[11] U. Tallarek, E. Rapp, H. Van As, and E. Bayer, *Angew. Chem. Int. Ed.* **2001**, *40*, 1684.

[12] G. Chen and U. Tallarek, *Langmuir* **2003**, *19*, 10901.

[13] G. Chen, M. Pačes, M. Marek, Y. Zhang, A. Seidel-Morgenstern, and U. Tallarek, *Chem. Eng. Technol.* **2004**, *27*, 417.

[14] U. Tallarek, E. Rapp, H. Sann, U. Reichl, and A. Seidel-Morgenstern, *Langmuir* **2003**, *19*, 4527.

[15] U. Tallarek, M. Pačes, and E. Rapp, *Electrophoresis* **2003**, *24*, 4241.

[16] F. C. Leinweber and U. Tallarek, *Langmuir* **2004**, *20*, 11637.

[17] I. Nischang and U. Tallarek, *Electrophoresis* **2004**, *25*, 2935.

Table of Contents

Part 1: Introduction

Part 2: Contributed Articles

G. Chen, M. Pačes, M. Marek, Y. Zhang, A. Seidel-Morgenstern, and U. Tallarek
Chemical Engineering and Technology **2004**, *27*, 417-428.

U. Tallarek, E. Rapp, T. Scheenen, E. Bayer, and H. Van As
Analytical Chemistry **2000**, *72*, 2292-2301.

U. Tallarek, T. W. J. Scheenen, P. A. de Jager, and H. Van As
Magnetic Resonance Imaging **2001**, *19*, 453-456.

U. Tallarek, T. W. J. Scheenen, and H. Van As
Journal of Physical Chemistry B **2001**, *105*, 8591-8599.

M. Pačes, J. Kosek, M. Marek, U. Tallarek, and A. Seidel-Morgenstern
Electrophoresis **2003**, *24*, 380-389.

D. Hlushkou, D. Kandhai, and U. Tallarek
International Journal for Numerical Methods in Fluids **2004**, *46*, 507-532.

U. Tallarek, E. Rapp, H. Van As, and E. Bayer
Angewandte Chemie International Edition **2001**, *40*, 1684-1687.

U. Tallarek, E. Rapp, A. Seidel-Morgenstern, and H. Van As
Journal of Physical Chemistry B **2002**, *106*, 12709-12721.

G. Chen and U. Tallarek
Langmuir **2003**, *19*, 10901-10908.

U. Tallarek, E. Rapp, H. Sann, U. Reichl, and A. Seidel-Morgenstern
Langmuir **2003**, *19*, 4527-4531.

U. Tallarek, M. Pačes, and E. Rapp
Electrophoresis **2003**, *24*, 4241-4253.

F. C. Leinweber and U. Tallarek
Langmuir **2004**, *20*, 11637-11648.

I. Nischang and U. Tallarek
Electrophoresis **2004**, *25*, 2935-2945.

Part 1:

Introduction

1 Why miniaturization in liquid chromatography?

The miniaturization in high performance liquid chromatography (HPLC) concerning the column inner diameter (i.d.) and associated volumetric flow rates has been initiated more than 25 years ago [1-5]. It is an ongoing development, mainly because of the need for handling small amount of complex samples. While the typical dimensions in analytical and narrow-bore HPLC include 2.1-4.6 mm i.d. columns, bed lengths of less than 250 mm and random sphere packings prepared with 3-10 µm average diameter (d_p) particles, further miniaturization towards nano-LC (see Table 1) can offer significant advantages [6-11] including the

i) reduced consumption of adsorbent phase, solvents and chemicals, facilitating the use of expensive stationary phases, exotic mobile phases and minute samples in the environmental and biomedical sciences,
ii) increased mass sensitivity due to reduced chromatographic dilution,
iii) use of smaller, but still porous particles which leads to higher column efficiencies by a significantly reduced contribution to the overall dispersion due to intraparticle stagnant zones,
iv) compatibility with the flow rate requirements of nano-ESI (electrospray ionization) interfaces in view of an on-line coupling to mass spectrometry, and
v) possible application of strong electrical fields for additional or exclusive transport of bulk liquid and solute through porous media like sphere packings or monolithic structures by electroosmosis and electrophoresis.

Table 1. Nomenclature for HPLC regimes [11].

Category	Column diameter (cross-sectional area)	Vol. flow rates	Typical loading
Analytical HPLC	5.0-3.9 mm (20-12 mm^2)	5-1.5 ml/min	2-10 mg
Narrow-bore HPLC	3.9-2.1 mm (12-3.5 mm^2)	1.5-0.2 ml/min	0.5-2 mg
Micro HPLC	2.1-0.5 mm (3.5-0.2 mm^2)	300-10 µl/min	50-500 µg
Capillary HPLC	0.5-0.15 mm (0.2-0.02 mm^2)	15-1 µl/min	1-50 µg
Nano(scale) LC	< 0.15 mm (< 0.02 mm^2)	< 1 µl/min	< 1 µg

Related to the perspective of the last aspect, in general, the devised transport of mobile phase and complex samples through (high and low surface area) materials being induced by externally applied electrical fields plays a central role in many analytical, technological, and environmental processes, including dewatering of waste sludges and soil remediation, capillary electrophoresis

or electrochromatographic separations in various particulate and monolithic fixed beds, as well as on micro-chip devices [12-45]. The transport is primarily achieved via electromigration of ions (background electrolyte), electrophoresis (charged analyte molecules), and electroosmosis (bulk liquid) driven by the shear stress concentrated in the electrical double layer (EDL) at solid-liquid interfaces [46]. Both a local and macroscopic transient behaviour, as well as long-time average magnitude, stability, and uniformity of electroosmotic flow (EOF) in porous media are inherently related to the physico-chemical nature of the surface and its dynamics, pore space morphology, and properties of saturating liquid electrolyte [47-58]. The detailed analysis of these parameters on the relevant spatio-temporal scales consequently has fundamental importance, as it critically guides the performance and design strategies of a particular electrokinetic process with respect to alternative diffusive-convective transport schemes. This becomes amplified by the significant role of non-continuum effects, interfacial contributions and surface forces, as well as multi-scale (and multi-physics) effects in the low-Reynolds number fluid dynamics on micro- and nanometer dimensions [59-71].

In the present work we are concerned with the dynamics of EOF and solute transport in packed bed capillary electrochromatography (CEC) and related systems, e.g., open-tubular geometries. While column efficiency in HPLC may be increased by a reduction of the particle size this option is limited via the maximum operating pressure with conventional instrumentation. A significantly improved performance in view of the dispersion and permeability is achieved in CEC by utilizing EOF the for transport of mobile phase.

2 Historical aspects of electrochromatography

CEC is a relatively new separation technique which is commonly carried out in capillary columns packed with conventional HPLC adsorbent materials by utilizing an electroosmotically driven mobile phase at high electrical field strength (50-100 kV/m) in an apparatus similar to that used in capillary zone electrophoresis (CZE). Consequently, CEC combines the great variety of retention mechanisms and stationary phase selectivities popular in HPLC with a miniaturization potential of CZE. Tsuda [72] has described electrochromatography as basically electrophoretic analysis where sorptive interactions with the stationary (retentive) phase of the support material are a major contribution; the separation is achieved by the differential partitioning and migration. Although origins of CEC trace back to 1974 when Pretorius et al. [73] have reported successful electrokinetic transport of eluent through a comparatively large chromatographic column, it have been Jorgenson and Lukacs [74] who demonstrated the feasibility of CEC for the separation of neutral analytes by applying an electrical potential gradient along a packed column of capillary dimension, before Knox and Grant [75-77] examined a number of fundamental aspects and the advantages of CEC with respect to capillary HPLC, including the influence of mobile phase ionic strength and thermal effects on separation efficiency.

3 Advantages of CEC compared to capillary HPLC

CEC is usually performed in a 50-150 µm i.d. fused-silica capillary column configuration which is composed of a packed bed and open tubular segment, as well as a detection window immediately behind the outlet frit of the fixed beds. Compared to pressure-driven flow a superior performance of EOF through a single, straight and open capillary originates from the fact that in the limit of a thin EDL the velocity apparently slips at the inner wall of the capillary and, thus, the fluid moves as in plug-flow (assuming isothermal conditions) [78-81]. Further, for fixed pressure and potential gradients, the ratio of volumetric EOF to hydraulic flow is inversely proportional to the square of the capillary radius [46]. The flat pore-level velocity profile of EOF observed for the single-pore geometry (as in CZE) [82, 83] and permeability criterion have important implications for the fluid dynamics (and the improved dispersion behaviour, in particular) in CEC where many pores are actually interconnected, as in a fixed particulate or monolithic bed, including the

i) use of micron- and submicron-sized particles as the packing material [84, 85] for reduction of band spreading toward the diffusion-limited regime,
ii) operation of relatively long packed columns (if needed) or, vice versa, the use of very short chromatographic beds [86],
iii) further reduction of column diameter toward chip format [24, 40, 87-89],
iv) generation of substantial EOF in the porous particles (electroosmotic perfusion) which strongly reduces the intraparticle mass transfer resistance and associated holdup dispersion [90-95],
v) better separation efficiency due to the hydrodynamic dispersion characteristics in the interstitial pore space of the sphere packings (between particles) over a wide range of moderate experimental conditions [77], and
vi) the enhancement of intraparticle transport of charged species by migration and surface (electro)diffusion [96, 97].

Thus, CEC offers a potential for implementation into miniaturized systems, allowing high sample throughput, resolution, speed and sensitivity. Compared to liquid chromatography CEC offers a better permeability and efficiency, as well as selectivity (in the case of charged analytes), and concerning CZE it operates in systems with far higher surface-to-volume ratio in view of sample capacity and sensitivity against dynamic changes of surface properties. As in capillary HPLC the actual flow rates are inherently compatible with a direct mass spectrometric detection. As shown in Figure 1 for a representative case, the separation efficiency in CEC is twice as high as that in HPLC when using particles with pore size ($d_{pore} \approx 10$ nm) of about the EDL thickness of typically 1-10 nm. We see below how this improvement can still be substantially increased by optimizing intraparticle EOF with macroporous particles ($d_{pore} > 30$ nm).

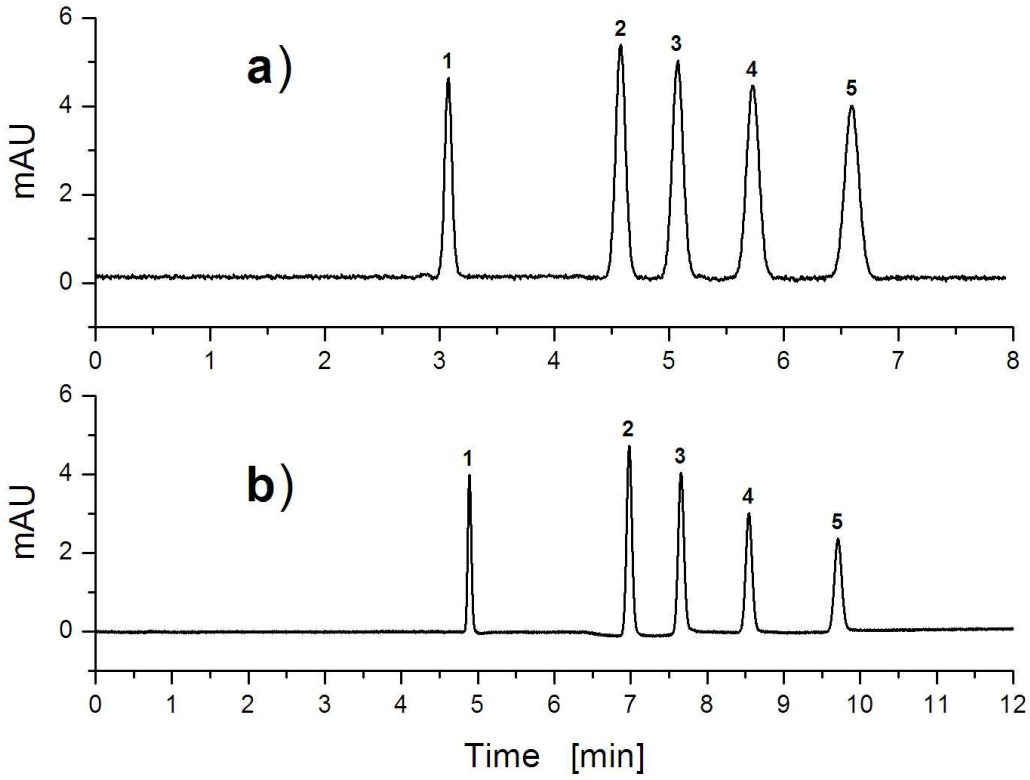

Figure 1. Comparison of separation efficiencies at a similar mobile phase average velocity. a) Capillary HPLC, packed bed of 150 mm length in a 100 µm i.d. capillary (in-column detection at 215 nm). Analytes: (1) thiourea, (2) methylbenzoate, (3) ethylbenzoate, (4) propylbenzoate, (5) butylbenzoate. b) CEC with a 325 mm long capillary setup (effective packed bed length: 240 mm) x 100 µm i.d., applied voltage: 20 kV. Stationary phase: porous C18-silica particles (d_p = 2.45 µm, d_{pore} = 14 nm). The mobile phase is a 5 mM aqueous Tris (pH-8.3)/acetonitrile 20:80 (v/v) buffer solution and the separation efficiency realized in CEC is about 2 x 10^4 N/m (plates per meter).

These considerations leave longitudinal molecular diffusion as the only limitation to performance in CEC, like in CE, but in porous media with much higher surface-to-volume ratio. On the other hand, returning to the benefits of a miniaturization in HPLC, the electrokinetic transport of liquid and solutes through packed capillaries or monolithic structures increases separation efficiencies and mass sensitivity further towards a new dimension. Despite these clear advantages CEC still awaits comprehensive validation including the interfacial electrokinetics [98] and, in this respect, especially the influence of samples on the matrix, and it is far from being an alternative to HPLC and/or CE on routine basis. Among other problems, including a preparation of chromatographic beds with sufficient long-term stability, the minimization of system dead-volumes and fast mixing of small amounts of liquid for gradient elution, a very important issue in CEC and capillary HPLC practice is related to needed improvement in generation and control of micro- and nanoliter flow rates, thus, to the actual hardware development [11].

4 Background: EOF in a microfluidic channel

Before we analyze the relatively complex dynamics of EOF in random-close packings of (non)porous, (im)permeable spherical particles, it is instructive to realize the simpler behaviour of EOF in a single, open (unpacked) channel.

For this purpose, Figure 2 illustrates (at different length scales) basic aspects of electroosmosis in microfluidic channels with a locally flat, smooth surface. When a dielectric solid (e.g., a fused-silica capillary) is contacted with liquid electrolyte (e.g., a dilute aqueous NaCl solution) an EDL develops at the solid-liquid interface due to the ionizable groups of the material (dissociation of silanol groups in the above example: $\equiv Si–OH + H_2O \Leftrightarrow \equiv Si–O^- + H_3O^+$) or by ions adsorbing on its surface. The resulting negative charge density of the capillary (channel) inner wall affects the distribution of the hydrated sodium counter-ions in the solution. In an immediate proximity to the surface there exists a layer of ions which are relatively strongly fixed by electrostatic forces. It forms the inner or compact part of the fluid-side domain of the EDL and its typical thickness is of the order of only one ion diameter (about 0.5 nm). The outer Helmholtz plane (OHP, Figure 2c) separates inner and diffusive layers which, together, constitute the EDL. While the ionic species in the diffusive layer undergo Brownian motion they are also influenced by the local electrostatic potential. At the equilibrium their accumulation in this region can be described by the Boltzmann equation. The spatial dimension (thickness) of the developed diffuse layer is typically between a few and hundred nanometers.

EOF sets in when an external electrical field ($\mathbf{E}_{ext}$) is applied which interacts with the EDL field to create an electrokinetic body force on the liquid. Consequently, the bulk of liquid is driven by the viscous drag via shear stresses concentrated in the relatively thin EDL (compared to a capillary radius r_c of micrometer dimension). The electrical potential (ψ) at the shear plane separating the mobile and immobile phases is the electrokinetic (ζ) potential. For the situation considered here (smooth surface, simple ions) ζ must be close to, if not coincident with the diffusive double layer potential ψ_{OHP} (see Figure 2c). The fluid velocity rises from zero at the shear plane to a limiting value $\mathbf{v}_{max}$ beyond the EDL at the slipping plane where, from a macroscopic point of view, liquid seems to slip past the surface (Figure 2b) [39]

$$\mathbf{v}_{max} = \mu_{eo}\mathbf{E}_{ext} = -\varepsilon_0\varepsilon_r\left(\frac{\zeta}{\eta_f}\right)\mathbf{E}_{ext}\ , \tag{1}$$

where μ_{eo} denotes the electroosmotic mobility and η_f the dynamic viscosity of the fluid. ε_0 is the permittivity of vacuum and ε_r the relative permittivity of the electrolyte solution. The minus sign in Eq. 1 means that $\mathbf{v}_{max}$ and $\mathbf{E}_{ext}$ point in the same direction when ζ is negative. Without externally

applied pressure forces and uniform distribution of ζ along the channel wall the liquid moves as in plug-flow because the gradient in ζ beyond the EDL is negligible. The thickness of the EDL is characterized by [39]

$$\lambda_D = \left(\frac{\varepsilon_0 \varepsilon_r RT}{F^2 \sum_i z_i^2 c_{i,\infty}} \right)^{1/2} , \qquad (2)$$

where R is the gas constant, T absolute temperature and F Faraday's constant, z_i is the valency of ionic species i and $c_{i,\infty}$ its molar concentration in the (electroneutral) solution. λ_D is the Debye screening length and ca. 10 nm for 10^{-3} M 1:1 aqueous electrolyte. In this case the EDL is much smaller than the radius of the micrometer channels ($r_c/\lambda_D > 100$), and the volumetric EOF rate is approximately given by $Q = v_{max}A$, where A is the cross-sectional area of the channel. However, as the channel diameter approaches submicrometer dimension and/or as λ_D increases the EDL cannot be regarded as thin any longer (e.g., $r_c/\lambda_D \approx 10$) and plug-like velocity profiles deteriorate towards a parabola, as known for Poiseuille flow ($r_c/\lambda_D = 2$), with an accompanying increase in hydrodynamic dispersion evidenced by Figure 3 [78, 99].

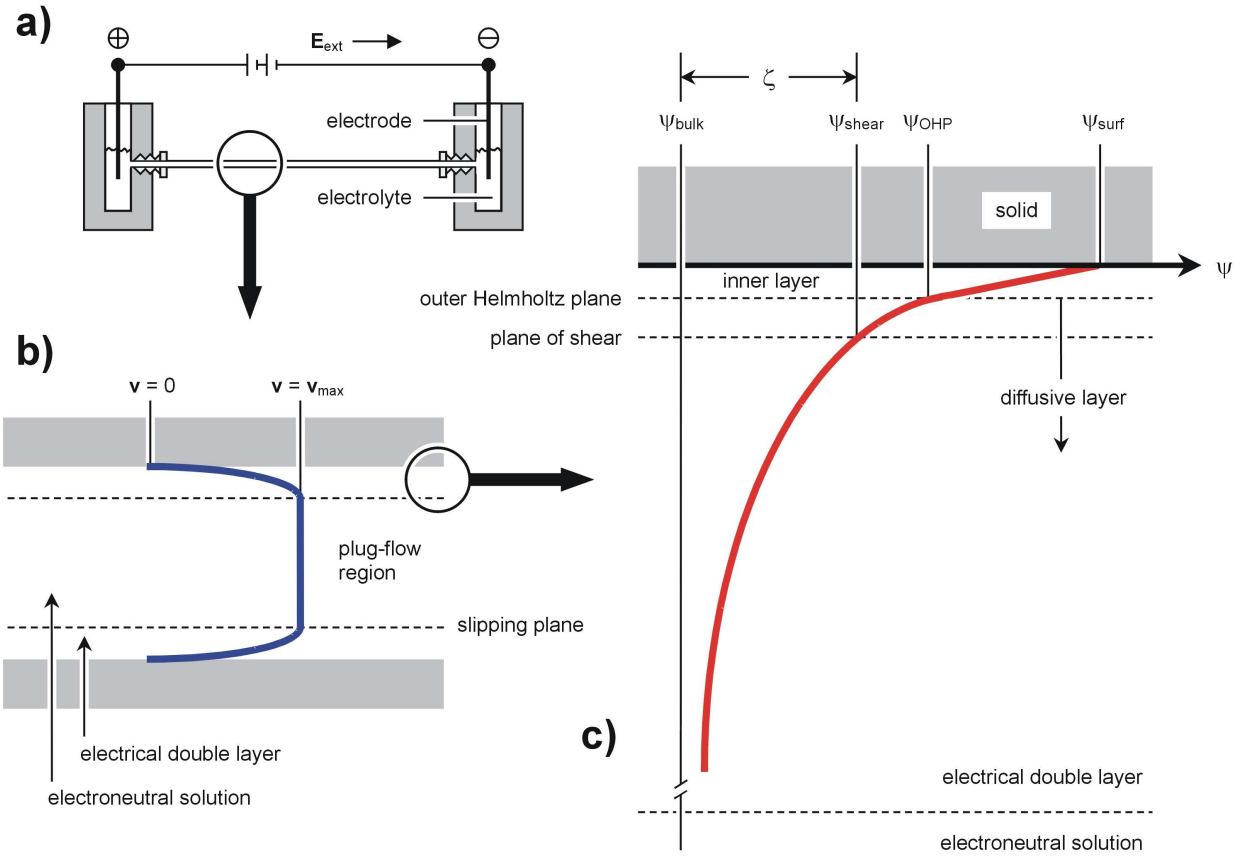

Figure 2. Electrokinetic flow through a straight cylindrical capillary (ζ < 0). a) Device , b) the pore-scale EOF **velocity profile**, c) distribution of **electrical potential** in the quasi-equilibrium EDL.

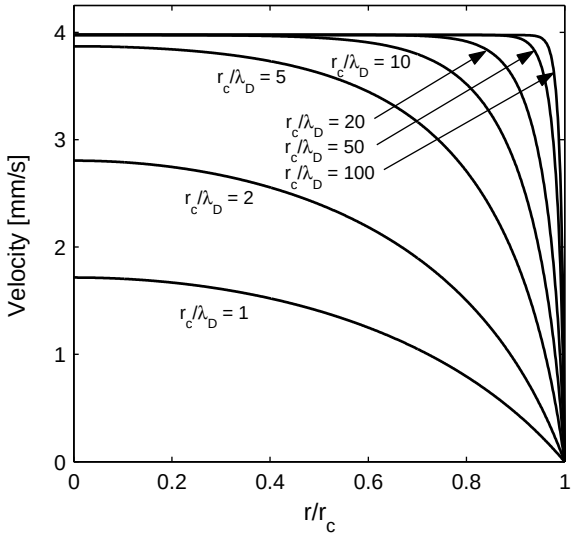

Figure 3. EOF velocity profiles with different values of r_c/λ_D in a straight and open cylindrical capillary obtained by solution of the momentum balance equation [99].

The applied (external) electrical field strength is 5×10^4 V/m, $\zeta = -0.1$ V, and $\varepsilon_r = 80$; the liquids density and viscosity at T = 298 K are 10^6 g/m and 0.89 g/(m·s), respectively, while the Debye screening length (λ_D) is taken as 10 nm.

Stimulated by the enormous potential (and accompanying need for detailed characterization) of electrokinetically driven mass transport in microfabricated devices, numerical simulation of EOF in microfluidic channels has received increased attention over the past few years [100-114]. The investigations have revealed that, in good agreement with the available experimental data, flow and transport characteristics in these microchannels clearly depend on properties of the working fluid and geometrical, as well as physico-chemical parameters of the surfaces. Severe deviation from the ideal plug-flow picture in single microfluidic channels can develop by the introduction of a heterogeneous surface charge distribution in porous media under more general conditions. In fact, the spatial scale of locally varying electrical potential can be often significant with respect to the EDL thickness (for a number of reasons). For example, it may be introduced by the inherent material manufacturing process, specific aging, the storage conditions, chemical reaction, or the eventually irreversible adsorption of molecular or colloidal species on surfaces, with concomitant changes of local roughness and electrokinetic properties [99, 115-120]. As a consequence, the favourable, i.e, plug-like EOF velocity profile becomes disturbed by induced pressure gradients resulting from an axial variation of the surface charge at the inner walls of a microfluidic channel [119-121] which leads to additional hydrodynamic dispersion. The problem is especially severe for the transport of sample mixtures containing large biomolecules such as proteins, peptides or DNA [122] which are charged and, thus, can interact strongly with the (in most cases) oppositely charged surfaces by hydrophobic and electrostatic mechanisms. As their adsorption progresses in time, it continues to cause unreproducible local, as well as average EOF velocities and a loss of resolution by an increased axial dispersion coefficient and strong tailing in the residence-time distributions. In general, local variations in electrical potential produce nonuniform electrokinetic driving forces that require local positive or negative pore pressures for compensating associated momentum in the fluid assumed incompressible [58, 119-121].

The importance and complex interplay of parameters like the ζ-potential, adsorption isotherms, surface-to-volume ratio, pH and electrolyte concentration with respect to an elution of adsorbing charged analytes is demonstrated in Figure 4. It shows the results of a numerical simulation for open-tubular capillary electrochromatography which takes into account the coupling of nonlinear adsorption with the local electrokinetics, the continuity of volumetric incompressible flow, as well as the continuity of charge transport [58].

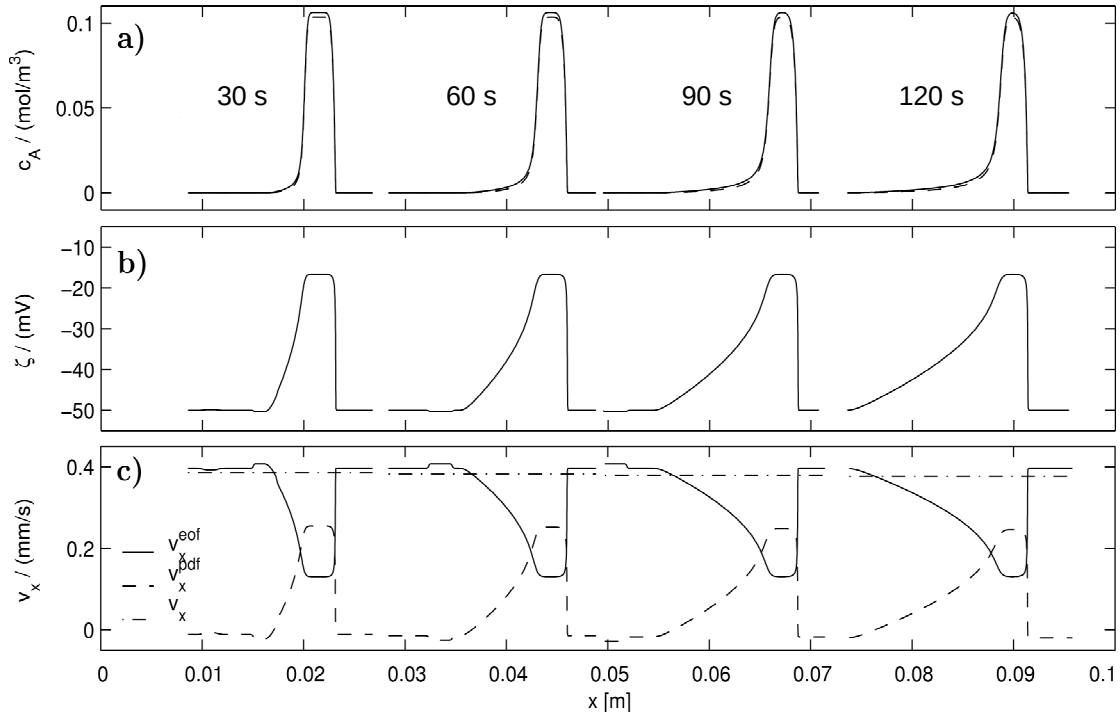

Figure 4. Elution of a sample plug which contains charged analyte molecules electrostatically attracted by (and adsorbing at) the inner surface of a cylindrical capillary [58].

Figure 4a shows elution profiles after 30, 60, 90 and 120 s for an overloaded sample plug which was injected for 4 s into a 100 µm i.d. capillary. The sample contains positively charged analyte molecules which are electrostatically attracted by the negatively charged surface. The nonlinear adsorption of charged analyte molecules has significant consequences for the distribution of the electrokinetic potential, hydrostatic pressure and electrical potential gradients, velocity, and pH along the column. As the ζ-potential varies with the concentration of charged analyte the actual profiles in Figure 4b are the natural result of the adsorption phenomenon. This inhomogeneous distribution of ζ along a capillary axis, together with a local perturbation of the electrical potential gradient, leads to an accompanying change in EOF velocities (Figure 4c, solid line). It requires a compensating hydraulic flow component (Figure 4c, dashed line) in order to conserve volumetric flow rates (Figure 4c, dash-dotted line). (N.B. No pressure differences between both ends of this capillary are applied.)

The foregoing discussion and analysis could suggest that the observation and maintenance of a plug-flow profile for EOF in a single cylindrical capillary represents a situation with special rather than general appearance. It is a limiting (ideal) case which, however, has important implications for ultimate gains in performance when comparing EOF to pressure-driven flow (PDF) in porous media from a general point of view.

As shown by Figure 5 for EOF and PDF through a straight-cylindrical open capillary the carefully conducted pulsed field gradient nuclear magnetic resonance (PFG-NMR) experiments operating over discrete temporal and spatial domains indeed reveal averaged propagator distributions for fluid molecules in EOF representative of plug-flow with a single, apparent EOF velocity ($\mathbf{v}_{eo}$) and broadening only due to axial molecular diffusion resulting in a perfect Gaussian [83]. In contrast, the measured displacement probability distribution for PDF basically shows box-car shape (with its edges smoothed by diffusion over the observation time) as expected for a parabolic or nearly so velocity profile under the laminar flow conditions. The consequences for axial dispersion due to the underlying velocity distributions should be recalled which, for EOF, leave axial diffusion as limitation to performance, while for PDF Taylor-Aris dispersion occurs.

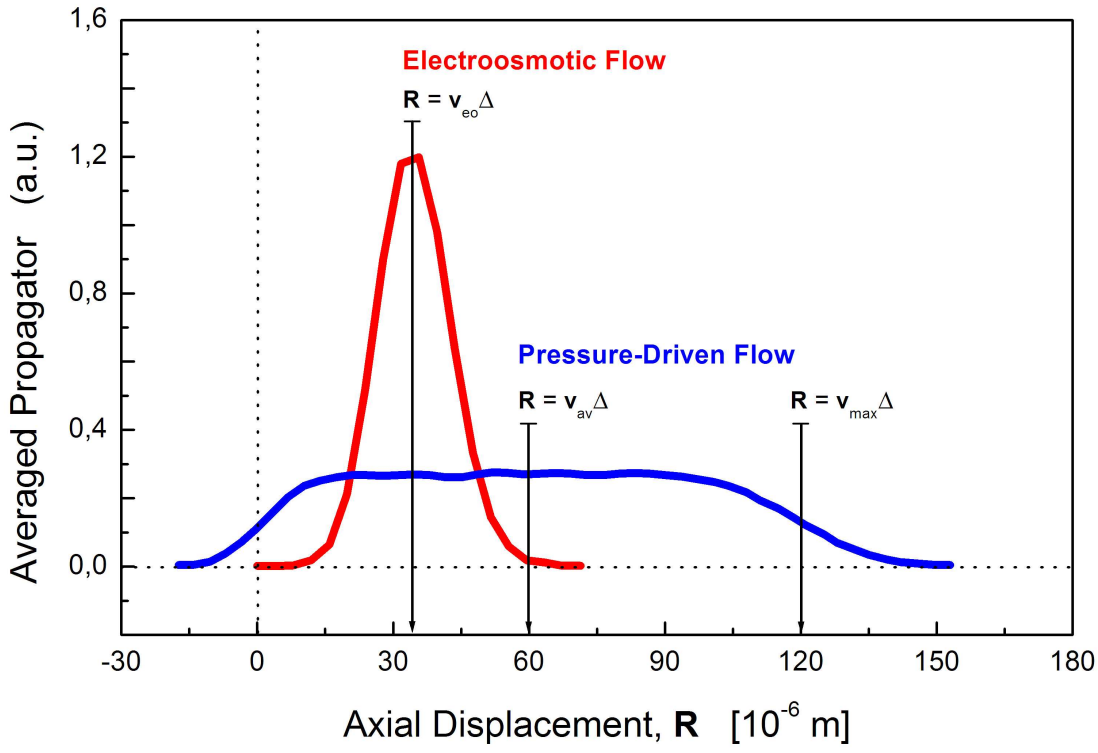

Figure 5. Axial displacement probability distribution of the fluid molecules (H_2O) for electroosmotic flow and pressure-driven flow through a (0.65 m x 250 µm i.d.) fused-silica capillary column. The mobile phase is a 2 x 10^{-3} M sodium tetraborate buffer solution at pH 9.0 (thus, $r_c/\lambda_D > 10^4$) and the observation time (Δ) in the PFG-NMR measurements is 14.2 ms [83].

5 Background: Dispersion in chromatographic beds

We have mentioned earlier the significant hydrodynamic performance advantages of the EOF in electrochromatography as compared to hydraulic flow in capillary HPLC. In this chapter a brief introduction is given into the hydrodynamics encountered with hydraulic flow in a random sphere packing consisting of porous spherical adsorbent particles. This is done in anticipation of a strikingly different dynamics realized with EOF (in the same porous medium) and prepares for the analysis of transport by perfusive electroosmosis.

A detailed understanding of the fluid flow field, diffusion-limited mass transfer and hydrodynamic dispersion in porous media over intrinsic temporal and spatial domains is actually important in a number of processes, including enhanced oil recovery, the subterranean transport of hazardous waste, filtration, or the fixed-bed operations in catalysis and separation science [123, 124]. Most natural and industrial porous media contain low-permeability and stagnant regions, where time and length scales associated with exchange of fluid molecules moving in velocity extremes may cover orders of magnitude depending on the material. For example, columns packed with totally porous particles are used in liquid chromatography and many engineering applications. In these cases the pore space consists of a (relatively discrete) bimodal distribution of the pore sizes due to inter- and intraparticle sets of pores. One consequence is that solute transport also occurs on different scales, the particle and flow field scale, and is governed by different mechanisms [125]. While the fluid phase driven with a pressure gradient actually flows between particles diffusion is practically the only transport mechanism which operates inside particles because their pores are usually too small compared to the interparticle channels to allow a significant intraparticle forced convection. Indeed most fixed-bed operations employ porous particles with spherical shape and narrow size distribution. Then, stagnant mobile phase mass transfer is characterized by the well defined time and length scales corresponding to the particle radius and the effective intraparticle diffusion coefficient.

Figure 6 shows how it is possible using PFG-NMR to resolve directly (and on quantitative basis) the stagnant and flowing fluid molecules in packed beds of porous particles, and thus study their exchange between the intra- and interparticle pore space [126]. This approach was successfully implemented for a detailed study of topological effects like pore size and distributions, or particle shape and size on the effective intraparticle diffusion coefficient and tortuosity factor, as well as on diffusion-limited mass transfer and resulting hydrodynamic dispersion [127]. The relevance of stagnant zones stems from their tremendous influence on dispersion. Fluid molecules entrained in the deep diffusive pools of a particle cause substantial liquid holdup and affect the time scale of (transient) dispersion and value of the (asymptotic) dispersion coefficient [127-130]. Thus, the associated kinetics of mass transfer between fluid percolating through the medium and stagnant fluid becomes rate-limiting in a number of dynamic processes including the separation efficiency of chromatographic columns.

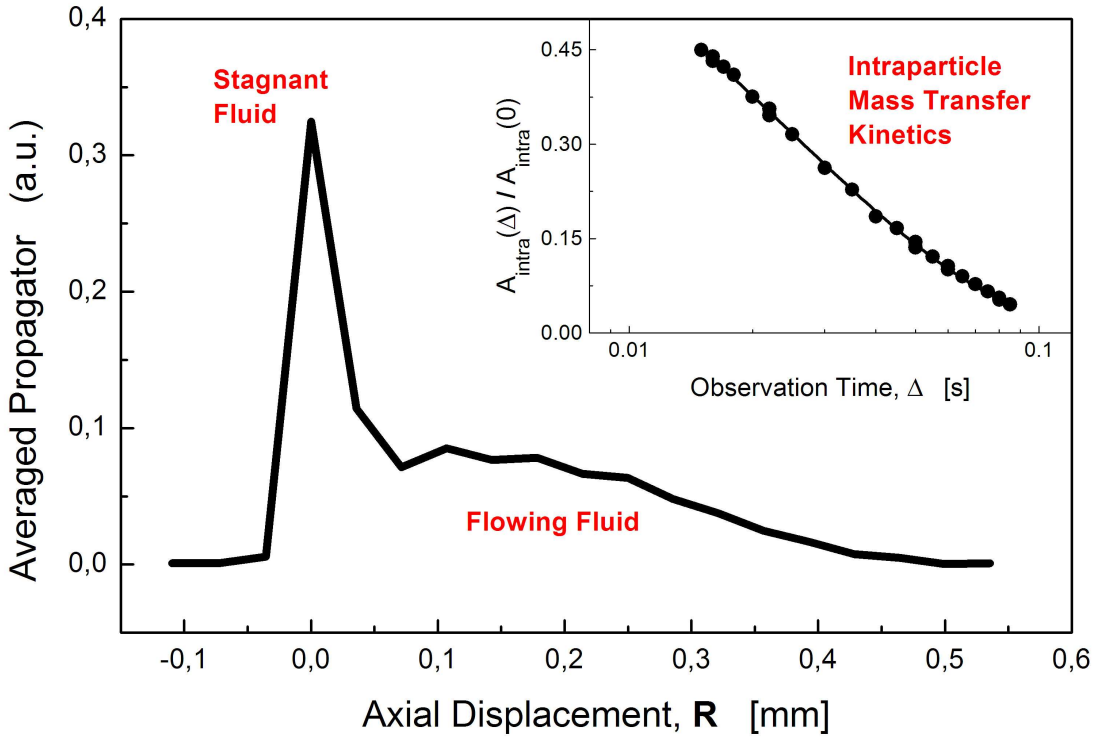

Figure 6. Axial displacement probability distribution of water molecules in pressure-driven flow through a bed of spherical porous particles (d_p = 41 µm, Δ = 20 ms), and intraparticle mass transfer kinetics based on the time-dependence of the stagnant fluid fraction around zero net displacement. From this kinetics an intraparticle diffusion coefficient and tortuosity factor can be obtained [95, 126].

Hydrodynamic dispersion with single-phase incompressible fluid flow through a bed of spherical porous particles has been studied over a range of mobile phase velocities and contrasted to the fluid dynamics in a bed of nonporous, impermeable spheres (Figure 7). Experimental data were acquired in the laminar flow regime with PFG-NMR and complemented by numerical simulations employing a hierarchical transport model (in computer-generated sphere packings) with discrete lattice-Boltzmann interparticle flow field [127, 131]. As demonstated by Figure 7, the intraparticle liquid holdup contribution dominates axial dispersion at higher average velocities v_{av} (and Peclet numbers, $Pe = v_{av}d_p/D_m$) as convective times $t_C = v_{av}t/d_p$ significantly exceed the dimensionless time for diffusion, $t_D = D_m t/d_p^2$ with d_p, the average particle diameter and D_m, molecular diffusivity [125]. The behaviour is in sharp contrast with that of the nonporous and relatively monodisperse particles (cf. Figure 7) [132] or also materials containing particles with a bimodal size distribution and sintered beds [133, 134]. In these cases, the (long-time) axial dispersion coefficient may be dominated by the boundary-layer contribution or medium and large-scale velocity fluctuations in the flow fields, respectively, which depends on the actual disorder of a material and investigated range of Peclet numbers.

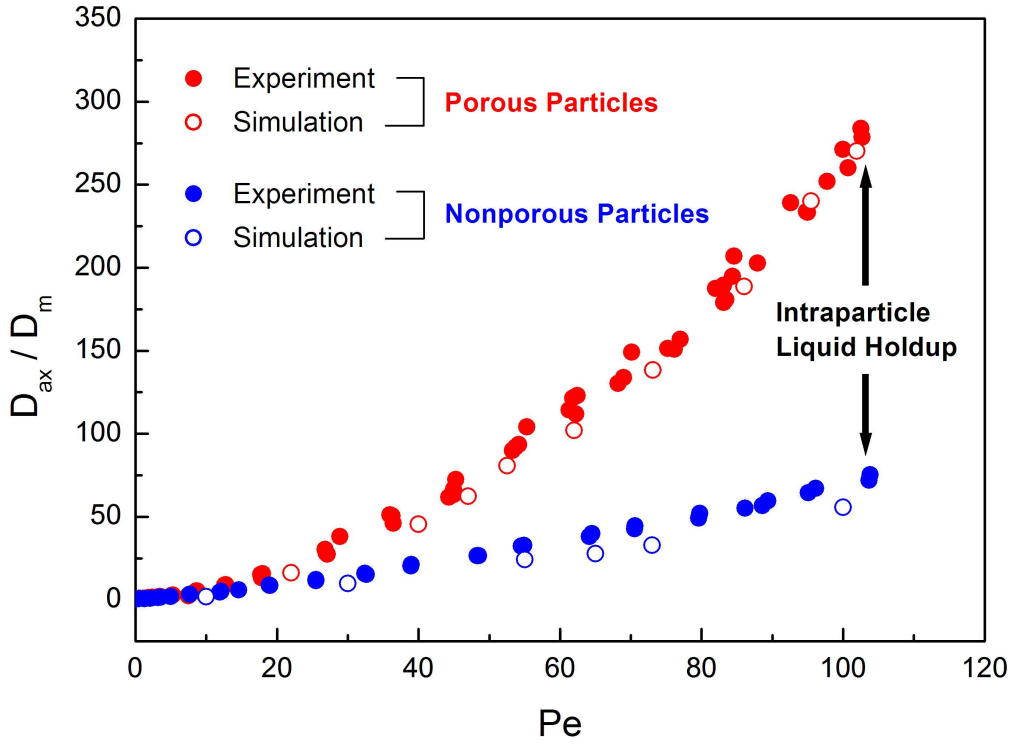

Figure 7. Dependence of the asymptotic axial dispersion coefficient normalized by molecular diffusivity on the particle Peclet number in random-close packings of porous and nonporous, spherical-shaped silica particles (with d_p = 34 µm and a column inner diameter, d_c, of 4.6 mm). Liquid phase: water. Intraparticle pores have a mean diameter of 12 nm.

One promising alternative to the use of discontinuous fixed beds of discrete particles concerning hydraulic permeability, hydrodynamic dispersion and dynamic adsorption capacity are monoliths with continuous solid skeletons. However, due to their complex (and often sponge-like) structure it is difficult to define an appropriate constituent unit that characterizes the hydrodynamics in this material, and to determine relevant shape and size distribution factors like for spherical particles in fixed beds (Figure 8). Based on a phenomenological analysis of the friction factor – Reynolds number relation and longitudinal dispersivity – Peclet number dependence for particulate beds it was possible to derive characteristic lengths (i.e., "equivalent" particle dimensions) for monoliths concerning hydraulic permeability and the dispersion originating in stagnant zones. Equivalence to hydrodynamic behavior in sphere packings has been established via dimensionless scaling of the respective data for monolithic structures [135]. This phenomenological approach, just based on liquid flow and stagnation in a porous medium, successfully relates hydrodynamic properties of the monolith to that of particulate beds. These comparative studies have shown that, e.g., the bimodal pore size distribution of silica-based monoliths (with large macropores and a thin, highly porous skeleton) is the basis for the unique combination of high bed permeability, short diffusion

path lengths, and high adsorption capacity which cannot be achieved with a bed of any diffusive particle type. While this material provides relatively large flow-through pores, it only needs short diffusion lengths to combine high permeability with a large surface area [136]. Since, up to date, only silica-based monoliths show a distinct bimodal pore size distribution, this material is clearly favored for use in chromatographic applications, especially in those for which the combination of a high bed permeability, short diffusion path lengths and high surface area is stringently needed as in high-throughput routine analysis, process-scale chromatography based on, e.g., simulated moving bed technology, and a sensitive determination of targets in complex samples (like library screening) by liquid chromatography coupled on-line to mass spectrometry.

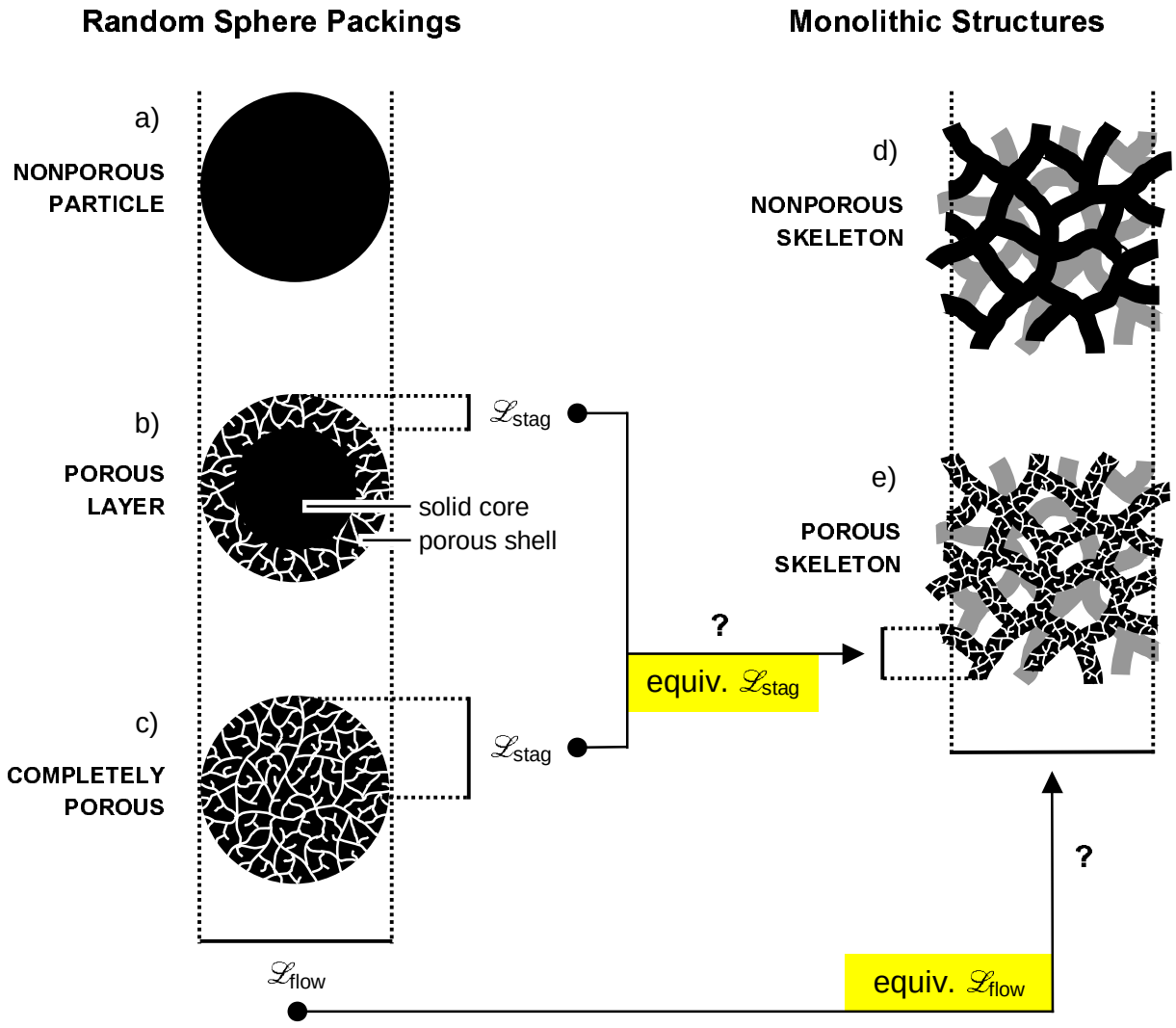

Figure 8. Characteristic lengths for the hydraulic permeability and hydrodynamic dispersion in a bed of spheres and monoliths [135]. While the particle diameter is useful to define a region impermeable for flow, the thickness of its porous layer (up to the particle radius) may be useful to address dispersion originating in stagnant zones of a random-close sphere packing.

6 EOF in sphere packings: Electrokinetic wall effect

Typically, CEC is carried out in a cylindrical capillary column of $d_c \leq 150$ µm packed with d_p = 3-10 µm porous adsorbent particles. Electrical fields up to 100 kV/m are applied for moving buffer solution and solute through the porous medium by electroosmosis (and electrophoresis, if analytes are charged) [19]. Thus, we usually have $d_c/d_p \leq 50$, with aspect ratios between 20 and 30 being most common. Particularly in this range the presence of the confining column wall has several implications for the EOF dynamics, as well as transport and hydrodynamic dispersion on a macroscopic scale.

First, the radial porosity distribution is systematically influenced over a substantial volume of the column. Concerning packing densities close to the wall it has been shown that radial distribution of the voidage in a random sphere packing is inhomogeneous [137-140], and that the interstitial porosity (ε_{inter}) begins with maximum value of unity at a column inner wall, then displays damped oscillations with period close to d_p over a distance of about 4-5 d_p into the bulk of the bed before reaching void fractions typical for bulk packing (ε_{inter} = 0.38-0.4). This geometrical wall effect can be explained by the decrease of packing order as the distance from the wall increases and may have strong impact on the macroscopic flow heterogeneity, axial dispersion, and particle-to-fluid heat and mass transfer, especially at an aspect ratio (d_c/d_p) below 15 [141-146] when the critical wall region occupies a substantial fraction of the column. Since any radial variations of transport properties have a much more serious effect on column performance than axial ones the packing aspect will be rather important for capillary HPLC, but it may have less impact on a macroscopic velocity inequality of the flow pattern in CEC. In close relation, it has been demonstrated that (in the thin EDL limit) average EOF velocity in a single pore is relatively independent of pore radius [78] which, on a macroscopic scale, is complemented by observing that average EOF in packed capillaries then is hardly influenced by the particle diameter [77].

Second, and rather than the radial porosity distributions, it is a radial distribution of electrokinetic potential (ζ) at solid-liquid interfaces which determines the EOF profile in a fixed bed. In addition to EOF generated locally at a particles surface (ζ_p) we also need to consider the capillary inner wall as a further source for EOF (ζ_w). In general, electrokinetic (and chromatographic) properties of these surfaces can be very different. This fact introduces an electrokinetic wall effect which depends on aspect ratio (d_c/d_p) and actual potential mismatch (ζ_w/ζ_p), as shown in Figure 9. The influence of the confining, charged capillary inner wall on the radial distribution of EOF velocities may be estimated by [147, 148]

$$\frac{v(r)}{v_p} = 1 + \left(\frac{\zeta_w}{\zeta_p} - 1 \right) \frac{I_0\left(\beta r / d_p\right)}{I_0\left(\beta r_{eff} / d_p\right)} \qquad \text{for } 0 \leq r \leq r_c - 7\lambda_D \cong r_{eff}\,, \tag{3}$$

where I_0 is the (zero-order modified) Bessel function of the first kind and r_{eff} an effective capillary radius accounting for the no-slip condition at the column inner wall. β characterizes the overall permeability of a bed [149]

$$\beta = 3\sqrt{\frac{\alpha(1-\varepsilon_{bed})}{2}} \quad . \tag{4}$$

The dimensionless parameter α depends on the drag forces provided by a particle and, thus, on packing structure, particle shape and permeability. On the basis of Eq. 3, Figure 9 demonstrates a strong effect of ζ_w/ζ_p on resulting trans-column EOF profiles. The wall effect in CEC is limited to a relatively narrow annulus at the wall that inreases in width with the magnitude of the excess zeta-potential $\zeta_{ex} = \zeta_w - \zeta_p$.

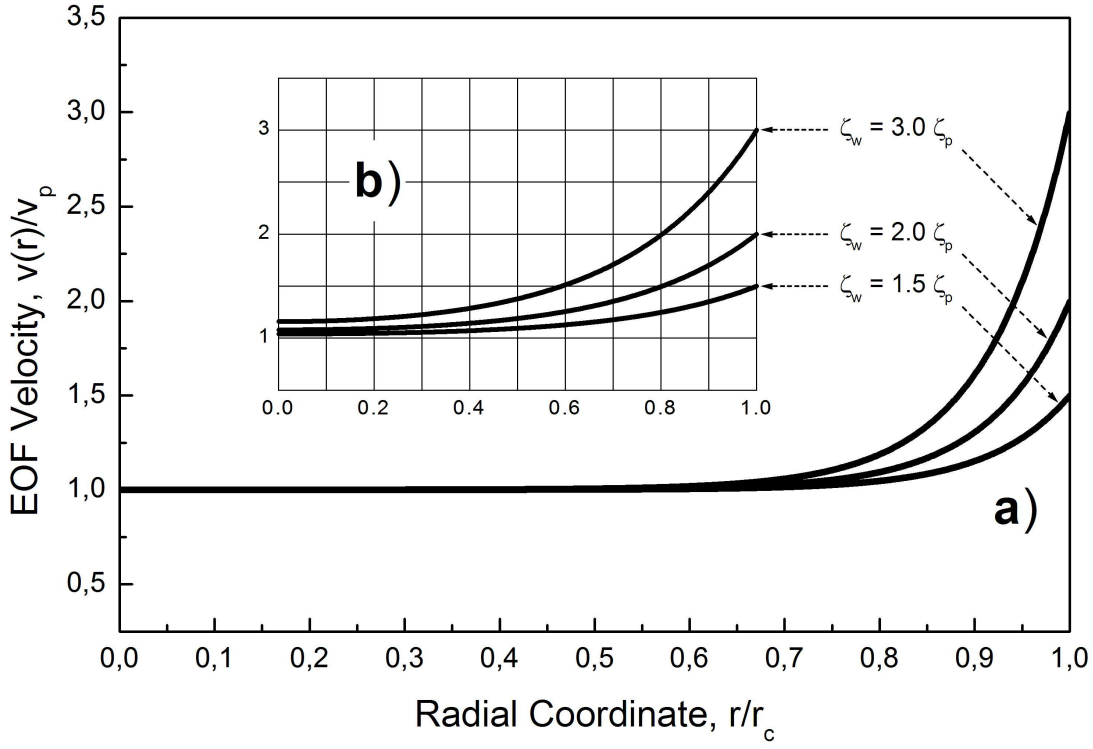

Figure 9. Prediction of radial EOF distribution based on Eq. 3 (normalized by v_p, the velocity generated locally at a particle surface) in random sphere packings for different values of ζ_w/ζ_p and aspect ratios, with r_c = 125 µm, λ_D = 3.9 nm, and β = 1.65 [150]. a) d_c/d_p = 15 and b) d_c/d_p = 5.

Although the particles surface and capillary inner wall both often carry a negative charge density the open fused-silica capillaries are known to give EOF velocities significantly higher than those of the packing materials used in CEC [50, 151, 152]. Electrokinetic potentials at the inner wall of

quartz capillaries up to –100 mV and even above are not unusual, although with the buffers and mobile phase ionic strengths typically encountered in CEC the value presents an upper limit and ζ_w realistically ranges between –50 and –100 mV [153-155]. By contrast, ζ_p of many commercial (silica-based and cation exchange) particles is smaller than ζ_w of the bare fused-silica capillaries [151] depending on the particles concrete surface chemistry and morphology. The electrokinetic wall effect recently has been spatially resolved and also analyzed by dynamic NMR microscopy with 40 µm in-plane resolution in a study of flow through a 250 µm i.d. fused-silica capillary that was packed with cation exchange particles [150]. That work has demonstrated that significantly higher velocities close to the inner wall than in the capillary center affect transient hydrodynamic dispersion. They are causing a long-time disequilibrium in the fluid molecules axial displacement probability distribution and the developing fronting behavior leads to broad averaged propagator distributions as clearly demonstrated in Figure 10. The spatial dimension of a wall annulus is the distance inward from the capillary inner surface over which the (local) fluid velocity is affected by ζ_w (Figure 9). This macroscopic flow heterogeneity (Figure 10) needs trans-column equilibration of the fluid molecules (i.e., their exchange via lateral dispersion over a complete capillary radius) to approach a uniform Gaussian.

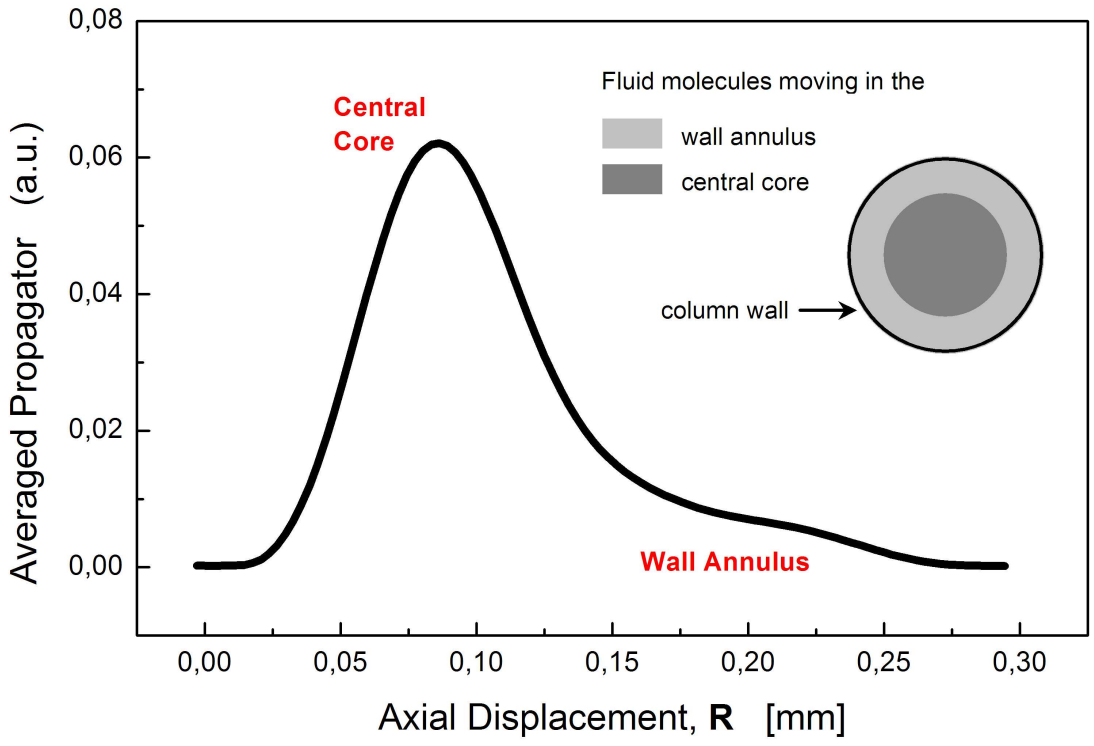

Figure 10. Electrokinetic wall effect. Propagator distribution measured by pulsed magnetic-field gradient nuclear magnetic resonance in a discrete time window. The massive fronting in this distribution is caused by fluid molecules moving in a wall annulus which can be resolved on the transient observation time scale of these measurements, here by encoding fluid motion (axial displacements) over 120 ms.

To summarize the electrokinetic wall effect is too important to be neglected in CEC practice with $d_c/d_p \leq 30$, unless $\zeta_w \approx \zeta_p$. Thus, in dependence of $\zeta_{ex} = \zeta_w - \zeta_p$ and the actual column-to-particle diameter ratio the resulting macroscopic flow heterogeneity will engender additional dispersion. Problems encountered with particulate packings in capillary HPLC and CEC such as sintering of frits, wall effects due to radial variation in porosity and ζ-potential or a preparation of stable beds can be overcome by the use of monoliths, directly fabricated as a continuous porous solid in the capillary [156-158]. Concerning electrokinetic wall effects, capillary inner surfaces can be coated by a fluid-impervious annulus of the same material, reducing the excess ζ-potential between the wall and monolith material.

7 Electroosmotic perfusion in sphere packings

With already basic understanding at hand of the EOF dynamics in a microfluidic channel and the bottleneck impact of stagnant zones (holdup dispersion) in classical HPLC, we now turn to one of the most attractive features of CEC in porous media concerning fluid transport and the achievable separation efficiencies, namely electroosmotic perfusive flow which is operating on a different dimension compared to hydraulic flow.

Perfusion chromatography in classical HPLC, i.e., a utilization of intraparticle forced-convection to reduce mobile phase mass transfer resistance originating in the intraparticle stagnant regions of packed beds has received significant attention over the last decade [159-172], although some beneficial consequences of this phenomenon have been recognized earlier, as in size-exclusion chromatography [173] and catalyst design [174, 175] or for nutrient transport in biological pellets [176]. By using porous particles with tailored hydraulic permeability such that the pressure drops typically encountered in packed columns act as decent driving force for intraparticle flow [177], a non-zero velocity component can assist or even dominate, depending on the magnitude relative to the time scale of analyte diffusion and adsorption-desorption processes the conventional, i.e., diffusion-limited intraparticle transport. It reduces the holdup dispersion due to stagnant regions, a contribution that begins to dominate the axial dispersion in packed beds of porous particles at Peclet numbers above ca. 25 (Figure 7) [127]. The result of these studies which have combined advanced numerical and experimental methods (a high-resolution lattice-Boltzmann flow field in computer-generated fixed beds and PFG-NMR, respectively) to differentiate between dispersion mechanisms that originate in stagnant and flowing regions of random sphere packings suggests that the holdup contribution to the dispersion is more important than it is often assumed [178]. In contrast, the term perfusion chromatography refers to any separation process characterized by a non-zero intraparticle velocity.

However, a mobile phase perfusion in beds of permeable, spherical-shaped particles is realized with hydraulic flow to any significant amount only when relatively high column pressure drop and particles with large pores are encountered. In turn, this limits the intraparticle surface-to-volume

ratio in view of the mechanical strength or adsorption capacity of a particle. But even with large pores, intraparticle fluid velocities remain small compared with velocities in the interparticle pore space [126, 177] and intraparticle flow is relevant only for transport of slowly diffusing molecules with a comparatively fast adsorption-desorption kinetics [169].

The electroosmotic perfusion through beds of porous particles proceeds with significantly higher intraparticle electroosmotic permeability [93, 179, 180]. This is in striking contrast to the intensity of efforts and prerequisites concerning an optimized particle technology, as well as the realized magnitude of any perfusive, but hydraulic flow and (still) remaining velocity inequalities between the inter- and intraparticle flow patterns. Indeed, a similar behaviour has been recognized earlier by selective applications in the physical and life sciences including the electrokinetic dewatering of waste sludge or efficient removal of contaminants from soil [46]. Concerning a permeability of packed capillary columns the EOF has shown a superior dispersion characteristics compared to pressure-driven flow which accompanies the reduction of velocity extremes in the mobile phase flow patterns on almost any time and length scale [90-94, 181]. In particular, axial plate heights and dispersion coefficients reduced by up to a decade with respect to those usually observed in pressure-driven flow (capillary HPLC) have been reported, especially for weakly and unretained solutes [90, 92, 93]. This is illustrated by Figure 11.

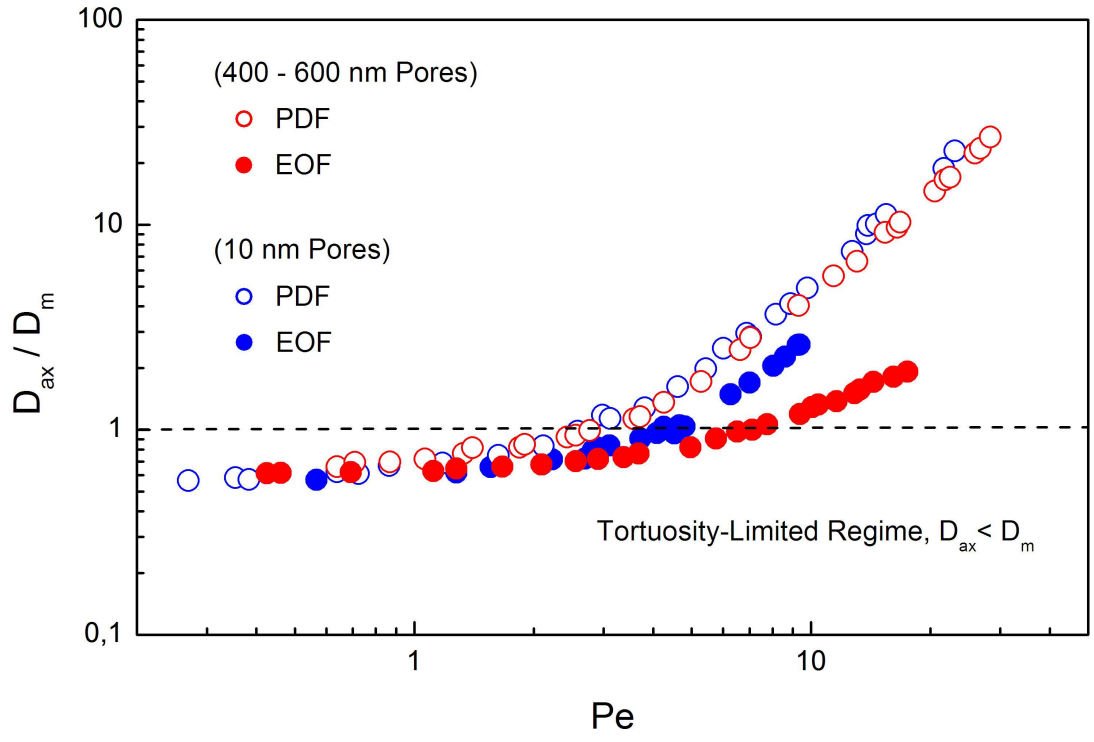

Figure 11. Hydrodynamic axial dispersivities (D_{ax}/D_m) vs. Pe = $v_{av}d_p/D_m$ measured directly in the packing by PFG-NMR [93, 126]. The mobile phase is water with 10^{-3} M borate buffer (pH 9.0).

Figure 11 clearly demonstrates that a change from pressure-driven flow (PDF) to electroosmotic flow (EOF) through the same capillary packed with porous particles can result in a tremendous improvement in hydrodynamic dispersion, represented by dispersion coefficients that are almost a decade smaller at similar Pe with EOF than for PDF (red circles). For the particles with smaller pores (blue circles) the improvement is significantly less. As we see later, but can understand at this point already intuitively, this observation is related to a stronger intraparticle EDL overlap for particles with smaller pores (at a constant mobile phase ionic strength) and expectedly leads to reduced intraparticle volumetric EOF. It becomes more evident when comparing with the results shown in Figure 3 for EOF in a single capillary of radius r_c depending on the EDL overlap (r_c/λ_D). Thus, based on the data in Figure 11, the possible intraparticle EOF may significantly contribute to a reduction of velocity extremes in the global flow field, improve hydrodynamic dispersion, but it depends on intraparticle EDL interaction (r_{pore}/λ_D).

As impressive as the results in Figure 11 (red circles) are, it is difficult to relate this improvement quantitatively to an electroosmotic perfusion mechanism because the dispersion data (and plate height data in CEC, in general) are inherently acquired over only a limited range of Pe. This fact is related to small particle sizes and limitations in applied electrical field strengths which restrict achievable values for $Pe = v_{av}d_p/D_m$. Consequently, the available flow rate range is not sufficient for adequate differentiation between dispersion processes originating in flowing and (remaining) stagnant regions of a packed bed [132, 178, 182, 183]. It is well known that with pressure-driven flow stochastic velocity fluctuations in the interparticle pore space cause mechanical dispersion which grows linearly with Pe, while regions of zero velocity inside the particles and close to their external surface give rise to nonmechanical contributions which grow as Pe^2 (holdup dispersion) and $Pe \cdot \ln(Pe)$ (boundary layer dispersion), respectively [182]. How these contributions coexist in CEC to determine the plate height dependence on Pe under a given set of conditions, including the distribution of pore sizes and EDL thickness, pore geometry and interconnectivity, the fractal nature and possible chemical heterogeneity of the surface, dissociation equilibria of the analytes and surface groups, buffer type, analyte charge, retention mechanism or a coupling of nonlinear adsorption with the local electrokinetics [58] is a yet unresolved, complex issue.

This situation underlines the need for experimental approaches which allow to measure (directly and on quantitative basis) individual electrokinetic transport phenomena on the scale of a single adsorbent particle in packed beds. A rather promising method concerning sensitivity and spatio-temporal resolution is confocal laser scanning microscopy (CLSM). While this method has been intensively used in biology over the last decades [184], it was only recently that its potential has been explored and further utilized in chemistry and physics [185-195] particularly with respect to the mass transfer characteristics in porous beads used for a variety of applications, including ion exchange chromatography, solid phase synthesis, or controlled drug delivery [196-200]. On the

other hand, the miniaturization demands for the electrokinetically-controlled transport in capillary columns and also microfluidic devices are excellently suited for an implementation with confocal microscopes. A key feature of these instruments is a pinhole (confocal aperture) in the detection optics which excludes light from any, but that location in the focal plane where the laser beam is focused (confocal spot) [201]. Two-dimensional images can then be generated by sweeping the specimen, e.g., a single porous particle of the fixed bed with the light beam at the focal plane of interest [202], as indicated in Figure 12 for the implemented device [203].

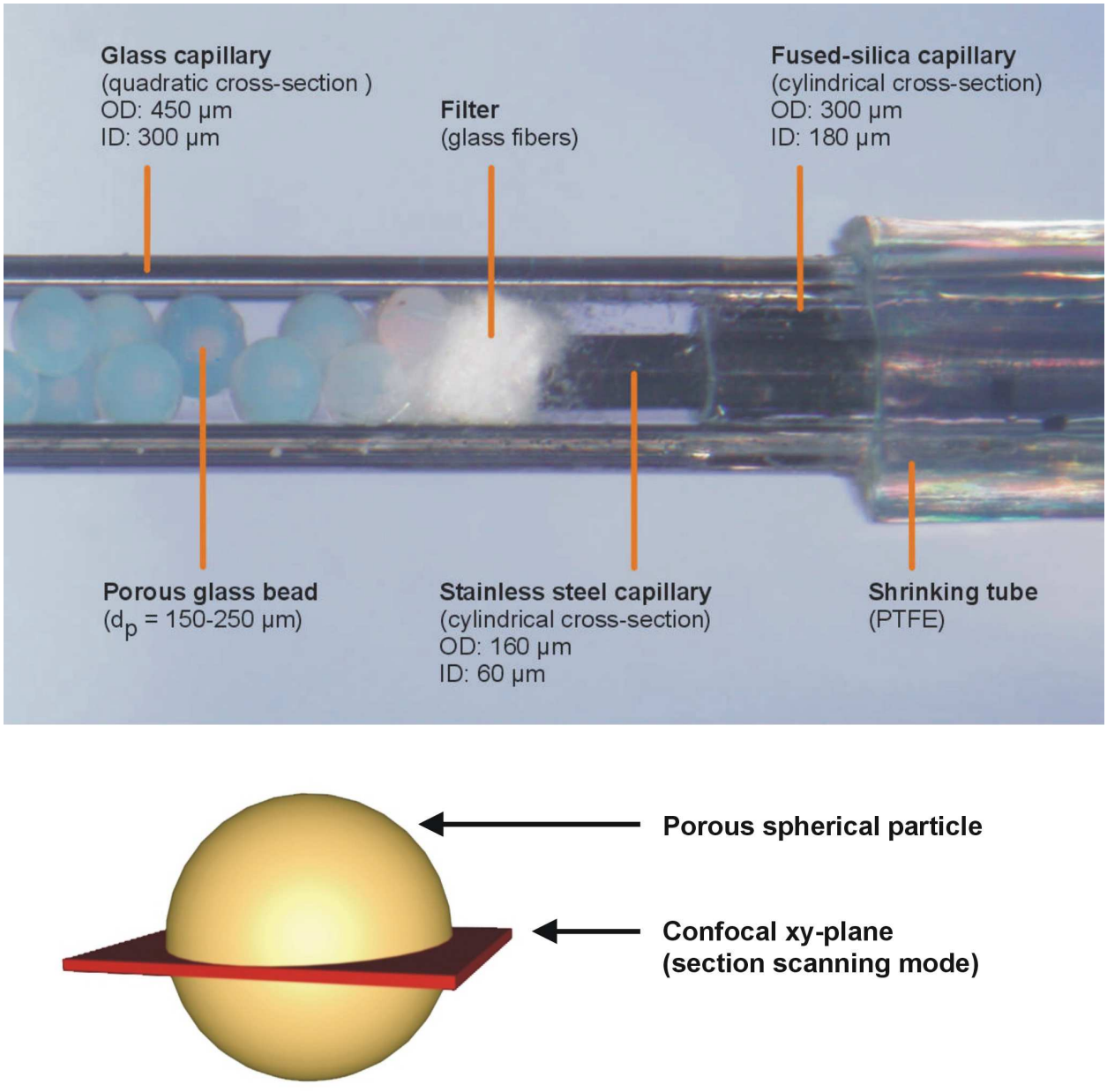

Figure 12. Inlet section of the packed capillary configuration used for quantitative study of electrokinetic transport phenomena in (and around) beads by confocal laser scanning microscopy [203]. Stainless-steel capillaries at both ends of the device are used as electrodes. Section scanning refers to image acquisition in a plane perpendicular to the optical (but parallel to the column) axis.

Because optical transparency of the porous medium is a prerequisite for analyzing quantitatively at any depth inside particles the distribution profiles of (un)charged fluorescent molecules during their uptake in or release from a single bead in view of the mass transfer mechanisms operating under the influence of an external electrical field [204-209] we used a widely applicable dynamic approach for matching the refractive index of a liquid to that of the solid skeleton of the particles (glass or silica-based particles, cf. Figure 12). To eliminate artifacts due to abberation caused by absorption and scattering of excitation and fluorescence light we selected dimethylsulphoxide, a versatile dipolar aprotic solvent with refractive index of 1.479 and tuned its mole fraction in water until the porous beads appeared optically transparent. A final refractive index mismatch over the whole experimental setup then could be adjusted to below 0.5%, and it was less than only 0.1% inside the beads [203]. With this setup and approach a series of experiments was conducted for a variety of conditions concerning electrokinetic intraparticle transport. For this purpose a slug of (un)charged fluorescent molecules was injected into the capillary and pressure-driven flow was applied to achieve fast interparticle convection of mobile phase and uniform distribution of tracer around a particle. Thus, the spherical glass beads were first loaded, saturated and then emptied by the unretained fluorescent (charged or uncharged) tracers, depending on a carefully adjusted combination of driving forces (additional electrical field), as illustrated in Figure 13.

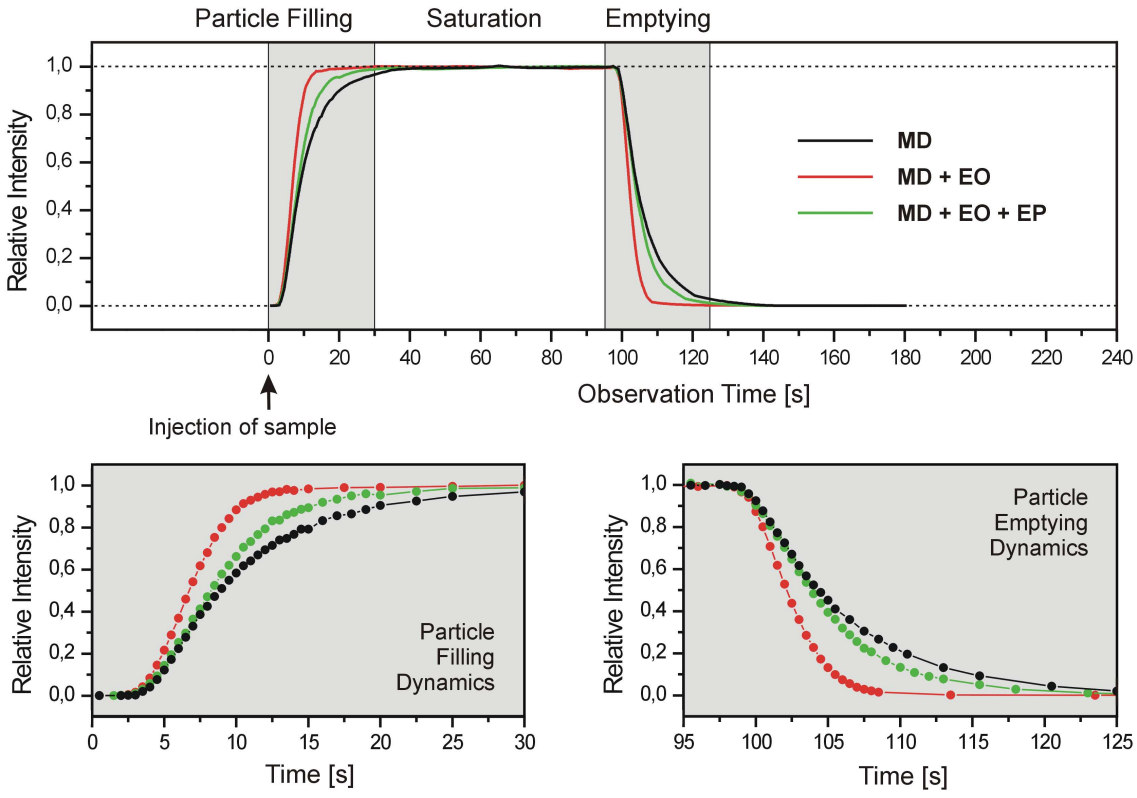

Figure 13. Intraparticle mass transfer kinetics (tracer uptake and release dynamics) during the elution of fluorescent tracer molecules without (MD only) and in the presence of an externally applied electrical field (neutral tracer: MD + EO, charged tracer: MD + EO + EP) [203].

As indicated by Figure 13, the electroneutral fluorescent tracer molecules are transported inside a particle by electroosmosis (EO) of the bulk mobile phase due to the external electrical field, in addition to molecular diffusion (MD), while for charged molecules we also expect electrophoretic migration (EP), in addition to EOF and a molecular diffusion along the concentration gradient. In the absence of an external electrical field intraparticle transport remains diffusion-limited. Thus, by a well-defined choice of the experimental conditions and adjusted properties of the saturating liquid (ionic strength in view of EDL thickness), fluorescent tracer (diffusivity, charge, adsorption behaviour) and involved surface (charge density, intraparticle pore size), the clean and stepwise analysis of a complex interplay between the diffusive, electrophoretic and electroosmotic driving forces is possible. The results (Figure 13) demonstrate that electrokinetic transport mechanisms (electroosmosis, electrophoresis) can significantly accelerate intraparticle uptake and release by target molecules. Compared to a purely-diffusive mass transfer these data indicate an existence of substantial intraparticle velocities for EOF and the electrophoretic migration. Because a glass beads surface has negative charge density, negatively charged (co-ionic) fluorescent molecules experience electrophoretic migration in a direction opposite to that of forced EOF. As evidenced by Figure 13 these different driving forces still result in a faster intraparticle mass transfer (MD + EO + EP) compared to the diffusion-limited transport (MD), but the kinetics is slower than for the EOF without electrophoresis (MD + EO).

Complementary to a mass transfer kinetics the intraparticle analyte profiles can be analyzed. As seen in Figure 14, the effect of non-zero electroosmotic and electrophoretic velocity in a particle leads to a clear deviation from spherical symmetry in transient analyte distribution profiles. Both the charged and uncharged tracer molecules respond to an electrical field (unidirectional driving force) by producing non-symmetric distribution profiles parallel to it, but in opposite directions. In particular, for presence of intraparticle EOF (electroneutral tracer, Figure 14b) the concentration minimum moves downstream compared to molecular diffusion alone (Figure 14a), resulting in a higher concentration in the upstream half of the sphere than the downstream. This is caused by the electroosmotic convection mechanism operating in the same direction as molecular diffusion in the upstream part of the particle, but opposite to diffusion downstream. Results become more instructive for a charged tracer when both the electroosmosis and electrophoresis are operating (Figure 14c). In this case, because intraparticle electrophoretic velocity ($\mathbf{v}_{ep}$) is sufficiently higher than the EOF velocity ($\mathbf{v}_{eo}$) and in the opposite direction, the sphere is effectively loaded from its downstream side with accompanying shift of the concentration minimum into the opposite half of a particle. Even under these conditions where the (fictitiously decoupled) electrokinetic transport mechanisms lead to countercurrent mass transport tracer uptake and release kinetics are faster than for the purely-diffusive case (Figure 13). Consequently, situations should be avoided where opposing intraparticle transports (EOF vs. diffusion and EOF vs. electrophoresis) would become of a similar magnitude.

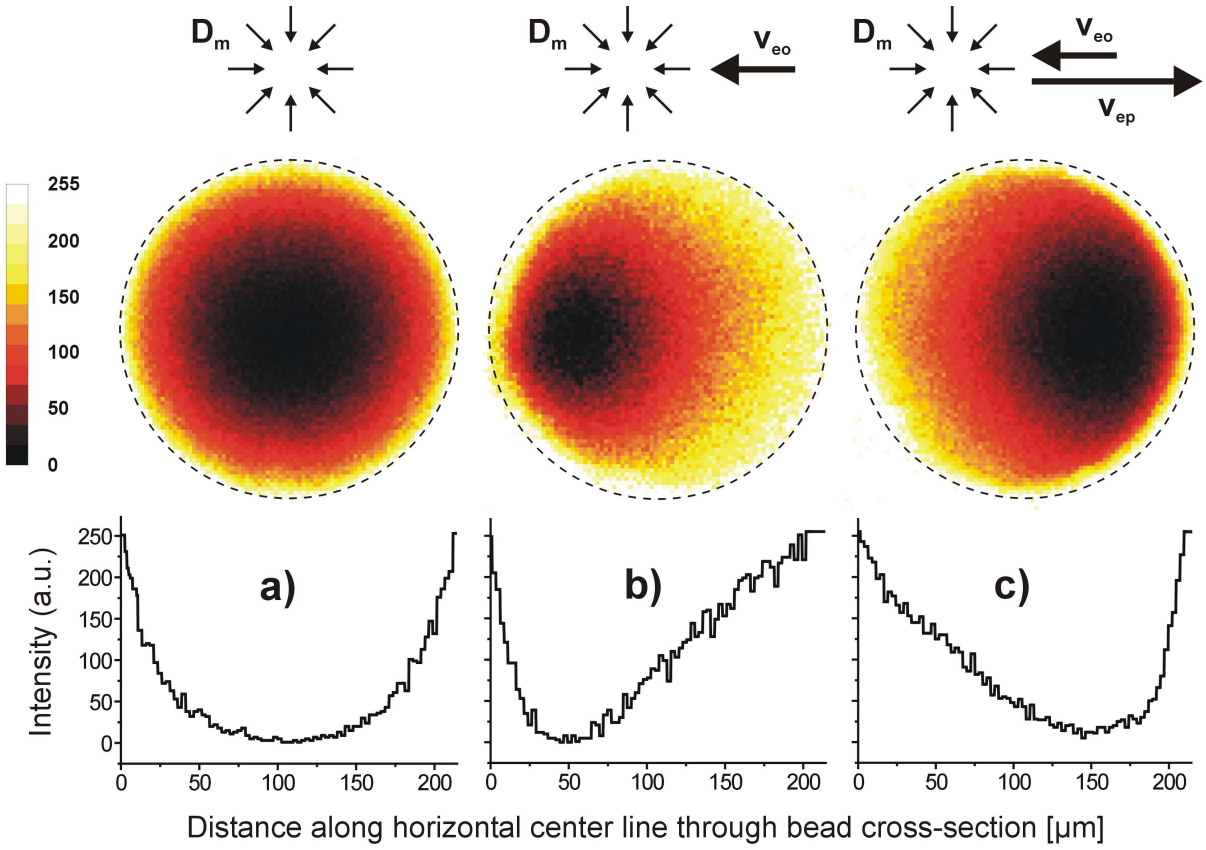

Figure 14. Single-bead CLSM analysis. Distribution of fluorescent tracers in a slice parallel to the axis of the capillary and through the center of a porous particle. a) Neutral tracer; PDF only, diffusive intraparticle transport. b) Neutral tracer; additional transport by EOF due to electrical field. c) Charged tracer (electrical field as before); transport by electrophoresis ($\mathbf{v}_{ep}$), electroosmosis ($\mathbf{v}_{eo}$) and diffusion (D_m).

This quantitative CLSM approach has been utilized to investigate both relevance and magnitude of an electroosmotic perfusion mechanism in electrochromatography for the devised transport of electroneutral, nonadsorbing tracer [210]. These studies have shown that even under conditions of a significant EDL overlap in the pores of a particle the resulting intraparticle EOF produces, in striking contrast to the symmetric, spherical distributions typical for the purely-diffusive transport (cf. Figure 14) strongly asymmetric concentration profiles inside spherical particles as the locally charged pore liquid begins to respond to the externally applied electrical field. However, profiles retain an axisymmetric nature, i.e., rotational symmetry with respect to the field direction. These data could be successfully interpreted and further analyzed with a compact mathematical model accounting for intraparticle molecular diffusion in a direction of decreasing concentration and the electroosmotic convection in the direction of the unidirectional d.c. electrical field for well-defined and realistic assumptions and proper boundary-conditions [210]. As a result, intraparticle Peclet numbers ($Pe_{intra} = v_{intra}d_p/D_m$) up to 150 have been realized in that work and found to significantly enhance mass transport on particle-scale toward the convection-dominated regime with respect to the diffusion-limited kinetics.

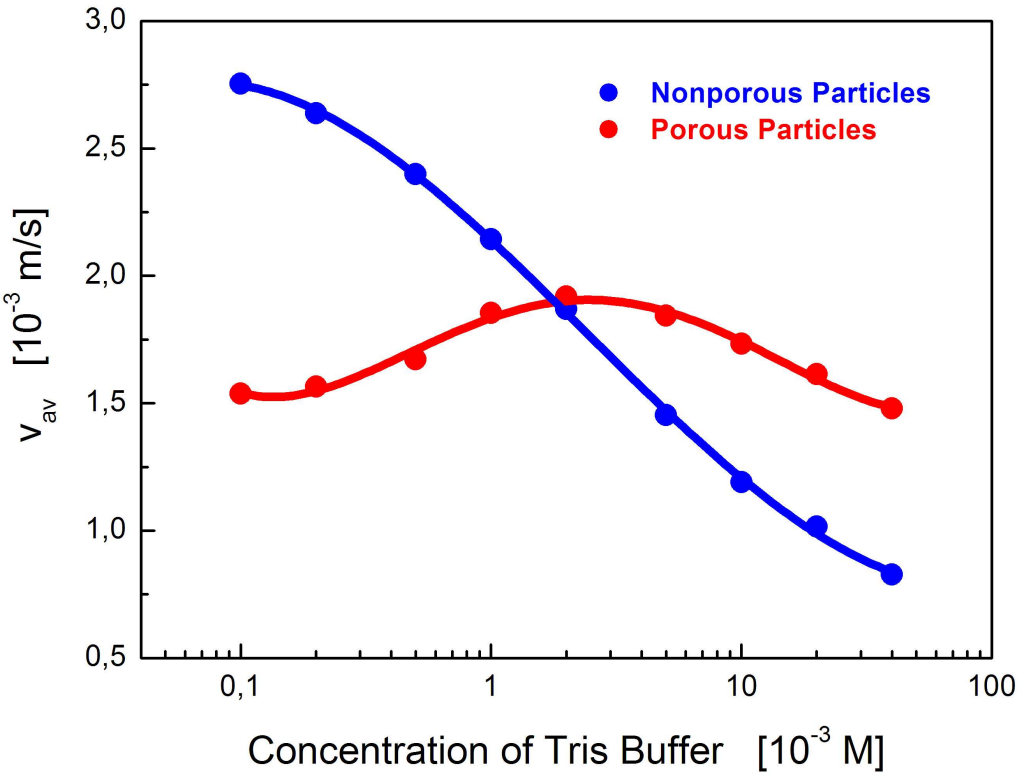

Figure 15. Effect of mobile phase Tris concentration on the average EOF through (100 µm i.d.) capillary columns packed with nonporous and porous silica-based, spherical particles [211]. The average diameter of the particles is about 2.5 µm and the mean pore size of porous beads is 105 nm. For all measurements the applied field strength was ca. 60 kV/m. Mobile phase: 80:20 acetonitrile/water (v/v). The ionic strength corresponds to half of the actual Tris concentration.

Complementary to the resolved and analyzed intraparticle tracer profiles, mass transfer kinetics, and calculated velocities based on the CLSM experiments and mathematical model the effect of the intraparticle EOF is also seen in a mobile phase ionic strength dependence of average EOF through columns packed with porous, as compared to those with nonporous particles [211]. The results shown in Figure 15 for the nonporous (i.e., impermeable, nonconducting) particles reveal normal electrokinetic behaviour in the sense that, as the ionic strength of the fluid increases, the EDL is compressed which results in a reduced shear plane potential at the solid-liquid interface and continuously decreasing values of average EOF velocity at an increasing Tris concentration [212]. By contrast, the porous particles are permeable for EOF and conducting depending on an intraparticle porosity and pore sizes. When originally solid dielectric spheres become permeable and conducting the ratio of specific conductivities within now porous particles and bulk liquid will increase from zero, bending the electrical field lines toward a particles interior which reduces the tangential field component at the particles external surface. Consequently, this contribution from the porosity reduces electroosmotic slip velocities at the external solid-liquid interface, and it can

explain the decreased values of v_{av} with respect to nonporous particles at a lower ionic strength (Figure 15, between 1 x 10^{-4} and about 2 x 10^{-3} M Tris) where a strong intraparticle EDL overlap prevails. However, this contribution to v_{av} of the porous particles is more than compensated with increasing buffer concentration by the perfusion effect due to intraparticle-forced EOF relative to the solid skeleton of the particle. In contrast to the first effect this phenomenon strongly depends on the buffer concentration, and it will begin to dominate v_{av} only when intraparticle EDL overlap is substantially reduced enabling a significant amount of volumetric EOF through particles [211]. As evidenced by Figure 15 this perfusion effect becomes responsible for the increasing average EOF velocities through the bed between 1 x 10^{-4} and 2 x 10^{-3} M Tris, and a maximum then is the consequence of competitive contributions from intraparticle EOF and normal EDL behaviour at a particles external surface. The latter effect which finally dominates and leads to the decrease of v_{av} above 2 x 10^{-3} M Tris, although the EDL overlap continues to be further reduced, has already been recognized as the origin of a continuous mobility decrease for the nonporous spheres. The presence of the perfusive EOF nevertheless can explain the finally higher values of v_{eo} for these porous compared to the nonporous particles (between 2 x 10^{-3} and 4 x 10^{-2} M Tris).

In general, the effect of EOF in porous particles, demonstrated by microscopic and macroscopic measurements, is advantageous for dispersion because it reduces in a global sense the velocity inequality of a flow pattern. Electroosmotic perfusion however becomes less effective compared to intraparticle diffusion, it should be recalled that $Pe_{intra} = v_{intra}d_p/D_m$, as the diameter of a porous particle is reduced. On the other hand, the diffusivities (D_m) of typically relevant analytes span a range from 10^{-9} to 10^{-12} m^2/s and, thus, they also determine inherently the relative importance of the electroosmotic perfusion. Concerning the remaining parameter in Pe_{intra} (v_{intra}), the presented CLSM results clearly demonstrate that the substantial EDL overlap presents no severe limitation for already significantly increased intraparticle mass transfer, and that the resulting pore velocity can be significant compared to a purely diffusive time scale even when r_{pore}/λ_D approaches unity and r_{pore} is only a few nanometers. Thus, CEC particle technology therefore should focus on the minimum mean pore size of the particles which allows still significant intraparticle EOF at decent mobile phase ionic strength, while keeping the surface-to-volume ratio high enough for complex separations. Based on perfusive EOF electrochromatography may be easily realized in effective nanoparticle dimensions leaving molecular diffusion as ultimate limitation to performance, but by employing micrometer-sized porous beads [213]. Thus, perfusive EOF translates to even higher separation efficiencies than actually achieved in CEC using narrow-pore supports or nonporous particles, an increased mass sensitivity in on-line coupling schemes like nano-ESI-MS, and (due to higher hydraulic permeability of beds of micron-sized particles) the possibility of implementing pressure-assisted CEC in view of higher speed of analysis, flow stability and reproducibility, but without significant increase in axial dispersion. Further, practical problems associated with direct nanoparticle packing like clogging or instable beds are avoided.

8 Concentration polarisation in electrical fields

Electrokinetic transport phenomena of charged species (simple ions, analyte molecules, or globular particles) in porous media with hierarchically-structured pore space (like in packed or monolithic chromatographic beds) are typically considered as occurring in a single macroporous compartment saturated with bulk (neutral) electrolyte solution, confined by a charged solid-liquid interface characterized by a thin, locally flat EDL. Any influence of (intraparticle or intraskeleton) mesoporous domains on possible ion-permselective transport of a charged analyte is commonly neglected. The general analysis of (non-equilibrium) space charge being responsible for relative motion of fluid with respect to the solid after application of an electrical field reduces to the small spatial dimension of a primary EDL along this interface (cf. Figure 2c). Thus, electrolyte systems are usually considered as quasi-equilibrium systems, and EOF velocity shows a linear dynamics concerning its dependence on applied field strength [46].

While the characterization and adjustment of an electroosmotic perfusive flow field and optimum particle dimensions in CEC have received much attention for improving the separation efficiency of mainly electroneutral analytes [214], the transport complexity for a charged analyte increases when in addition to the bulk electrolyte in the macroporous domain with locally balanced cationic and anionic molar fluxes another interconnected spatial domain with different transport numbers for one type of the ions is realized in the porous medium. For example, the fixed beds of porous spherical particles or monoliths are frequently characterized by rather discrete bimodal pore size distributions with macropores in the interparticle or the interskeleton pore space and mesopores inside a particle or monolith [136]. The favored permeation of counter-ions is one main transport characteristics of ion-exchange membranes, and ion-permselective mass transport constitutes a basis for electrochemical and electrokinetic processes like electrode reactions or electrodialysis [215, 216]. With respect to a permselective nature charged porous media containing mesopores with mean sizes of the order of and even below the EDL thickness act as ion-exchange material in which transport numbers for the counter-ion can approach unity (Figure 16). This behaviour is supported by low mobile phase ionic strength due to the increased EDL thickness which causes severe EDL overlap on a mesopore scale. Consequently, most of the particulate and monolithic stationary phases employed in CEC contain ion-permselective spatial domains which exlude the co-ions, but enrich the counter-ions (cf. Figure 16a) [217-219]. In addition to the EDL model, this situation can be alternatively analyzed with the Donnan potential. At electrochemical equilibrium in the electrolyte solution distributed between both compartments, the counter-ion concentration is higher and the co-ion concentration lower in the mesopore than in the macropore space. The Donnan potential balances the tendency of ions to level out existing concentration differences. It pulls the cations back into the negatively charged mesoporous domain and anions back into the positively charged macropore compartment. Thus, the ion-permselectivity in hierarchical porous media appears to be a phenomenon with general, rather than special significance.

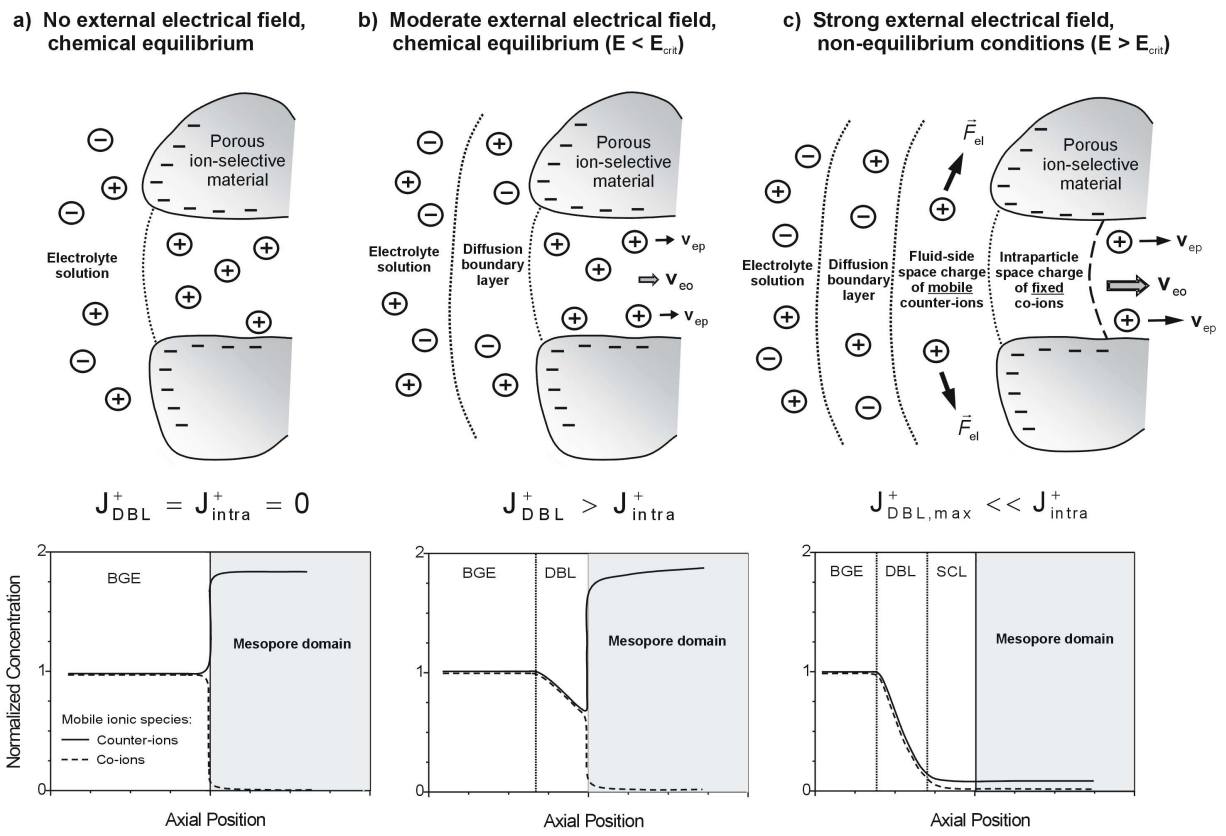

Figure 16. Schematic view of concentration distribution and the transport properties of charged species in an ion-permselective (mesoporous) region of a material and in the adjacent electrolyte. The normalized centerline concentration profiles of the co- and counter-ion species reflect various stages of concentration polarization. BGE: background electrolyte (electroneutral), DBL: diffusion boundary-layer (electroneutral), SCL: space charge layer which develops under non-equilibrium conditions and contains excess of mobile counter-ions. E_{crit} is a critical field strength above which intraparticle electrokinetic counter-ion flux density ($\mathbf{J}_{intra}$) due to velocities of electrophoretic migration ($\mathbf{v}_{ep}$) and electroosmosis ($\mathbf{v}_{eo}$) exceeds maximum flux density through the diffusion boundary-layer ($\mathbf{J}_{DBL}$). Consequently, E_{crit} marks the onset for local deviation from electroneutrality.

As compared to the Donnan-equilibrium (Figure 16a) an increased complexity is observed in the presence of superimposed (external) electrical fields for ion-distributions and the mass transport of charged tracer (including the background electrolyte and buffer components) in the attempt to satisfy mass continuity and local electroneutrality. Caused by the applied external electrical field electrolyte concentration is induced to decrease where counter-ions enter the ion-permselective domain from the bulk solution. Co-ions migrate in opposite direction away from the interface and because this withdrawal cannot be compensated by supply coming from the mesopores, the co-ion concentration decreases. The interplay of ion-permselectivity, electromigration, and diffusive flux leads to the formation of a diffusion boundary-layer which presents significant mass transfer resistance. At the opposite (i.e., downstream) side of the mesopore domain boundaries a region with increased ion concentrations develops. The electrolyte solution has become polarized, and

this phenomenon due to formation of concentration gradients in the electrolyte solution adjacent to ion-permselective (charge-selective) interfaces upon the passage of electrical current normal the interface is called concentration polarization (CP), illustrated in Figure 16b for the upstream CP zone with reduced ionic concentrations. In strong fields which can force the concentration of co-ions in the CP zone towards zero close to the interface while that of the counter-ions remains finite, a space charge can be induced in the fluid-side of the macropore compartment [220, 221] (Figure 16c). The induced space charge represents a nonequilibrium charge layer (or secondary double layer) which can interact with the tangential component of the electrical field to generate electroosmosis of the second kind along curved interfaces, including the skeletons of a monolith or spherical particle. The conditions and consequences of strong CP become quite important for the spatio-temporal dynamics of EOF in many materials with ion-permselective properties. It is a topic that has received significant attention in the past, both from a theoretical and experimental point of view [222-228]. The CP zone reaching towards the primary (quasi-equilibrium) EDL may be pictured as covering i) an induced space charge region where concentration of counter-ions significantly exceeds that of the co-ions, absent at lower voltage with an established equilibrium CP, and ii) the diffusion boundary-layer with a linear variation of the ion concentrations and local electroneutrality in the sense that $c^+ - c^- \ll c^+ + c^-$ (Figure 16c).

It should be mentioned that, in contrast to classical electroosmosis of the first kind (EO-1), which results from the interaction between the tangential electrical field and space charge of the usual, quasi-equilibrium (primary) EDL, electroosmosis of the second kind (EO-2) developing in strong electrical fields is caused by a force of the tangential field component on the induced, extended space charge of the non-equilibrium (secondary) double layer [227]. While the EOF velocity in a sphere packing responds linearly to the applied field strength concerning EO-1, it is expected to show a nonlinear dependence for EO-2 [147]. Electrokinetic phenomena of the second kind and especially EO-2 have hardly been investigated in the context of CEC although potential benefits of this phenomenon (EO-2) can be anticipated [147]. First, it provides a unique scheme towards increased EOF velocities compared to current CEC practice (dominated by the EO-1 dynamics). Second, electroosmotic whirlwinds (microvortex) associated with EO-2 around an isolated single spherical particle [222, 228] have implications for accelerated (primarily lateral) mixing in sphere packings, reducing the time scale for transverse equilibration of analyte. In the remaining figures effects of CP in sphere packings and monoliths with ion-permselective regions are illustrated. In particular, Figure 17 indicates the influence of diffusion boundary-layer mass transfer resistance on the intraparticle counter-ion transport and loading capacity. Figure 18 reveals an existence of irregular flow patterns in the macroporous compartment and their beneficial effect on separation efficiency (by enhanced lateral mixing) with charged analytes. Finally, Figure 19 demonstrates a systematic development of nonlinear EOF velocities in capillary monoliths depending on applied electrical field and mobile phase ionic strengths.

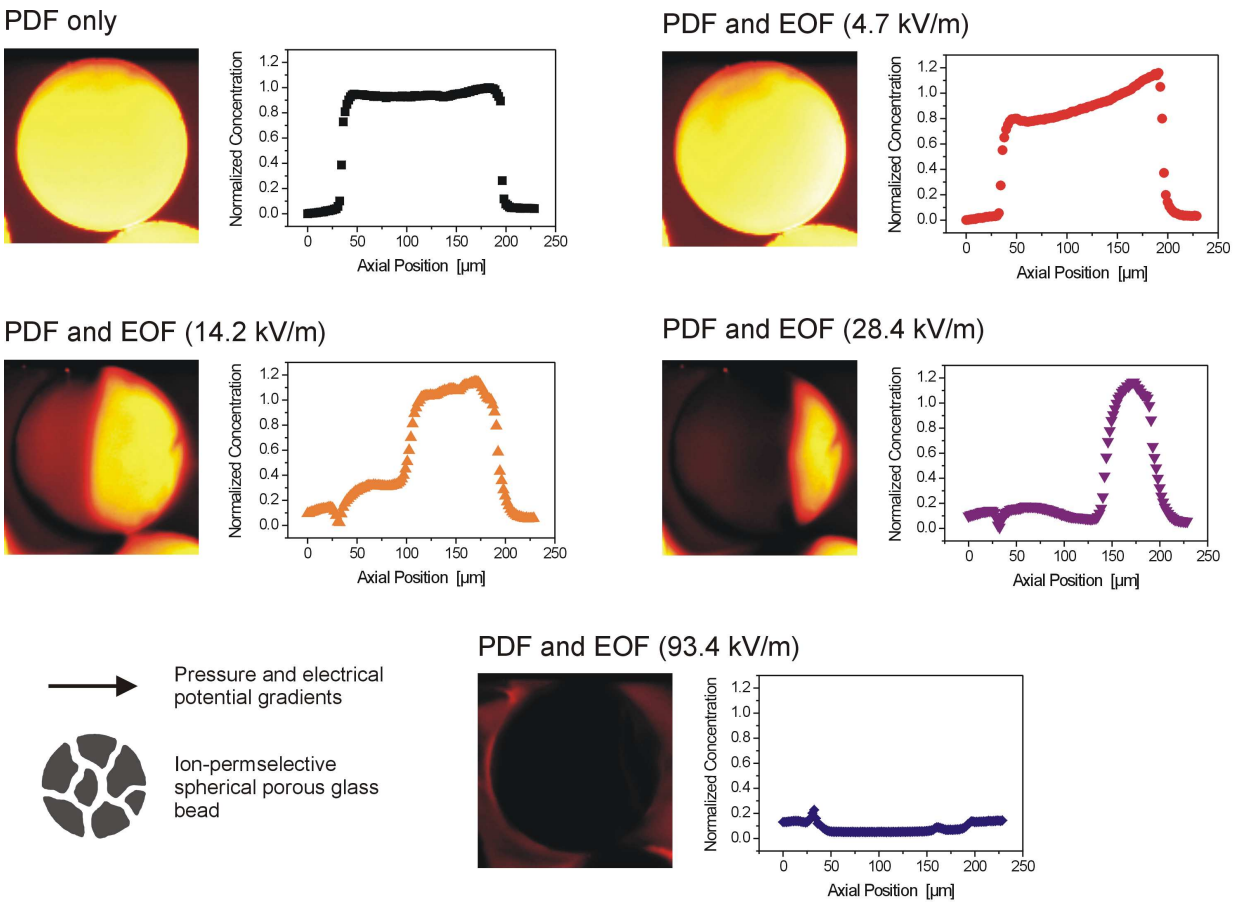

Figure 17. Representative CLSM images and corresponding normalized tracer concentration profiles for steady-state centerline distributions of strongly adsorbed counter-ion Rhodamine 6G. These profiles were acquired in a direction of applied (hydrodynamic and electrical) driving forces and normalized with respect to the maximum concentration observed for diffusive mass transfer [229].

A detailed investigation of the steady-state counter-ion concentration distributions of fluorescent tracer in ion-permselective particles by CLSM at different applied field strength revealed a rather unusual behaviour (Figure 17) [229]. This analysis proved an existence of extended intraparticle zones of depleted counter-ion concentrations arising from the anodic (counter-ionic) side or pole of a particle. These zones cover significant fractions of the particles cross-sectional area until, at a sufficiently strong field, they extend over the complete particle which then remains (effectively) emptied by the strongly adsorbing counter-ion tracer. Analysis of the external and internal molar flux densities for positively charged Rhodamine 6G allowed to calculate the critical field strength at which intraparticle transport begins to exceed transport through the diffusion-boundary layer [229]. Because inside the particle more counter-ions are removed at its frontal upstream surface than are actually supplied from bulk solution through the diffusion boundary-layer deviation from local electroneutrality can occur and space charge regions can develop outside a sphere (space charge of mobile counter-ions; Figure 16c) and inside it (space charge of fixed co-ions, which is actually charge due to surface groups; Figure 16c and depleted zones in Figure 17).

Basically because electrokinetically-induced intraparticle flux densities (EO and EP in Figure 16) exceed mass transfer toward the surface through the diffusion boundary-layer particles begin to remain empty. In other words, intraparticle ionic fluxes cannot be balanced any longer by supply from bulk solution and zones of depleted counter-ion concentrations develop inside particles. As evidenced by the CLSM data (in Figure 17) the area of these regions increases and, vice versa, the particle-averaged loading capacity decreases with the electrical field strength until the beads practically remain completely empty [229].

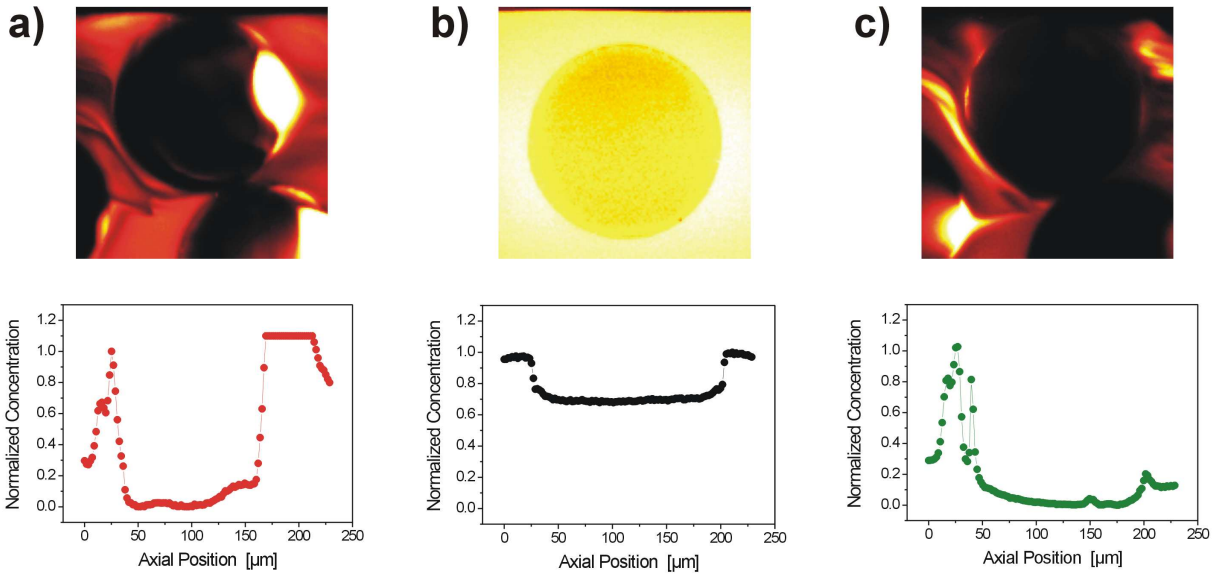

Figure 18. Representative CLSM images and corresponding centerline concentration profiles through a single (ion-permselective) glass bead and the adjacent solution for a) counter-ionic, b) electroneutral, and c) co-ionic tracer under conditions of strong concentration polarization [229].

The local deviation from electroneutrality in the bulk fluid-side induced by the normal component of the electrical field under conditions of nonequilibrium CP close to a curved, ion-permselective interface has unique consequences. First, and in contrast to a linear EOF dynamics known from EO-1, the resulting EO-2 naturally shows a nonlinear behaviour because it depends on both the normal and tangential components of the applied field via creation of a space charge (induction step) and force exerted on the mobile part of this secondary EDL (interaction step), respectively. Further, because normal and tangential field components vary locally along the curved surfaces in monoliths or sphere packings, also the intensity of nonequilibrium CP and EO-2 velocities are expected to change accordingly. Then, local back pressures must generate based on continuity, and complex coupling between the electrostatics and hydrodynamics may lead to a formation of micro-vortices. Although resulting patterns certainly depend on the pore space morphology, any potential operation of this phenomenon in porous media having technical or analytical relevance

is a challenging task. For example, to which extent can large recirculation zones that have been visualized for a spherical, isolated particle [222, 228] develop in random-close packings of these particles or in monolithic structures? If vortices develop locally, can they interact cooperatively to create even lateral mixing bands? – Accelerated column cross-sectional equilibration of analyte (here caused by an electrokinetic chaotic mixing) would be very beneficial as it may reduce axial dispersion further by orders of magnitude. This is demonstrated in Figure 18, again for the glass bead system and by CLSM studies. Bulk flow behaviour under strong non-equilibrium conditions is illustrated by snapshots of distributions of electroneutral and ionic tracer in the interstitial pore space. The local concentration of electroneutral tracer in bulk solution is constant, even a strong electrokinetic lateral mixing cannot affect its steady-state profiles. By contrast, because the ionic concentration due to CP varies significantly with geometrical position in the beds it is possible to detect strongly fluctuating areas with different ionic concentration indicating pronounced velocity streamlines around the bead and the existence of chaotic pattern in the flow field for sufficiently high electrical field strength (electrokinetic chaotic mixing, Figure 18a and 18c). This aggravated radial convective transport in the interparticle pore space (macropore compartment) has already indicated significant improvement in the extraparticle fluid-side variances of elution signals [229] because, as expected, the increasing lateral mixing with respect to diffusion-limited equilibration will cause axial spreading of a sample zone to decrease [230, 231].

Figures 16 to 18 have shown that in porous media with hierarchically-structured pore space like a bed of porous particles, and ion-permselective transport properties in at least one domain, the ion concentration distributions in bulk fluid cannot be treated as homogeneous any longer when an electrical field is applied. This induces regions of reduced and increased ionic concentrations in the solution close to a phase boundary to the ion-permselective domains, e.g., a mesoporous bead. The CP results in inhomogeneous (steady-state) ion distributions over the whole medium. While transport and the distributions of electroneutral tracer are little affected by CP, it becomes important for charged tracers. The region of depleted ion concentration close to the surface of a particle presents substantial electrokinetically-induced mass transfer resistance for counter-ions, and compared to intraparticle electrokinetic flux transport through the diffusion boundary-layer is expected to depend only little on applied field. Thus, there is a critical field strength above which intraparticle transport cannot be satisfied from bulk solution through the diffusion boundary-layer any longer, and regions of electrokinetically-induced local space charge, both inside and outside the ion-permselective particle can develop (Figure 16). The former results in extending zones of depleted counter-ion concentrations in a bead, so that the particle-averaged adsorption capacity is reduced until the particles remain completely emptied by strongly adsorbing counter-ions. The latter, i.e., mobile non-equilibrium space charge gives rise to strong tangential electroconvection around the particles (electroosmosis of the second kind). Drastic consequences of these effects,

in particular, arise for the elution efficiency in pulse injections. Since lateral dispersion increases and intraparticle mass transfer resistance decreases, also the overall separation efficiencies are expected to improve accordingly. In this context electrokinetic processes such as CEC involving fixed particulate or monolithic beds of ion-permselective media require more detailed analysis in view of CP and possible deviation from local electroneutrality due to nonequilibrium effects, both in the mesoporous (ion-permselective) domain and the macroporous compartment. It is an issue with a fundamental physico-chemical relevance.

After having analyzed and discussed potential benefits of CP in porous media for primarily mass transport and dispersion, Figure 19 rounds off this thematical issue by revealing the dynamics of nonlinear electroosmosis in (silica-based) capillary monoliths with bimodal pore size distribution. These monoliths are hierarchically-structured with (intraskeleton) mesopores and (interskeleton) macropores. While a linear dependence of average EOF velocities on the applied field strength could be observed with 5 x 10^{-3} M Tris (turning slightly nonlinear at higher concentrations due to thermal effects), this dependence becomes systematically nonlinear as the Tris concentration is reduced towards 10^{-4} M. Velocities increased by more than 50% with respect to those expected from a linear behaviour are realized at 10^5 V/m [232]. As shown in the inset EOF velocities even approaching 1 cm/s are observed when directly measured in a simple device by CLSM at higher electrical field strengths than available with the commercial instrumentation ($HP^{3D}CE$) employed for conventional use. A local deviation from electroneutrality in the bulk fluid-side induced by the normal component of the electrical field under conditions of nonequilibrium CP close to a curved ion-permselective interface has unique consequences also for the macroscopic hydrodynamics [147]. In sharp contrast to a linear EOF dynamics known from EO-1, the resulting EO-2 naturally shows nonlinear behaviour because it depends on both components (the normal and tangential) of the applied field via creation of space charge (induction step) and force exerted on the mobile part of this secondary EDL (interaction step), respectively. In view of the conditions favoring CP, the decreasing concentration of Tris buffer adjusts the mesopore space of the monolith skeleton (Figure 19) towards ideal ion-permselectivity. Its permeability for the co-ions decreases, and the critical field strength above which the nonequilibrium CP may start to contribute significantly to a global electrokinetics in the monolith also decreases, i.e. the lower the co-ion permeability of the mesopore domain the easier it becomes for an electrical field to decrease co-ion concentrations in the CP zone towards nonequilibrium conditions. We then observe a systematically developing nonlinear EOF dynamics in a certain range of decreasing ionic strength by increasing relevance of EO-2 in the macropore space of the monolith, in this case being most pronounced between 1 and 0.1 mM Tris (Figure 19) [232]. One of the goals is to characterize and taylor these effects in hierarchical porous media concerning ion-permselectivity, macropore space morphology, mobile phase composition, and applied field strength.

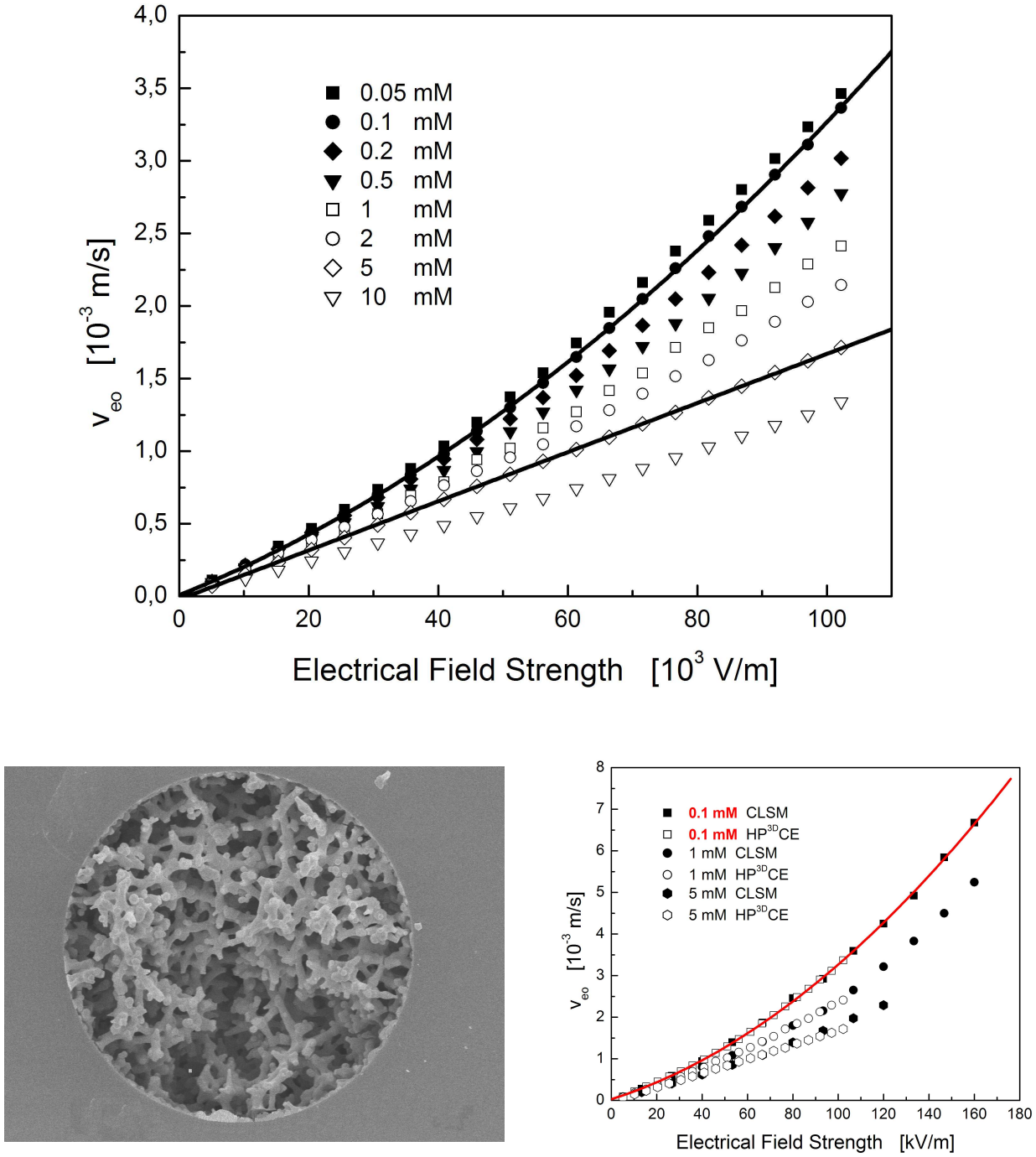

Figure 19. Average EOF velocity in the capillary monolith vs. applied electrical field strength for different mobile phase Tris concentrations as indicated [232]. Second-order polynomial and linear fits for 0.1 and 5 mM Tris, respectively, are a guide to the eye. While with the commercial equipment (here a $HP^{3D}CE$ from Agilent Technologies, Waldbronn) field strength over the monolithic column is limited to a maximum value of around 10^5 V/m, significantly higher values could be realized with a homebuilt device (shorter columns) used for CLSM measurements to demonstrate better the developing nonlinearity of EOF velocities (cf. red solid line) at decreasing ionic strength. The SEM image shows a silica-based monolith with bimodal pore size distribution due to interskeleton macopores and intraskeleton mesopores.

Compared to the electroosmotic perfusion mechanism [90-95], electrokinetic phenomena based on a nonequilibrium EDL develop in a different operational domain. While substantially perfusive EOF in particulate or monolithic beds requires a quasi-equilibrium EDL thickness (much) smaller than typical macro- and mesopore sizes, the nonequilibrium CP underlying EO-2 requires strong ion-permselectivity within a porous medium, meaning that the EDL dimension is large compared to pore sizes in the ion-permselective regions. Further, while electroosmotic perfusion effectively removes stagnant zones, which dramatically reduces velocity extremes in the mobile phase flow pattern in view of improved dispersion and increased average velocities, the conditions for EO-2 develop ion-permselectivity to leave these zones practically stagnant. In this case the mesopore space is used for indirect manipulation of EOF velocities in the macropore space where possible lateral mixing associated with the hydrodynamic pattern of EO-2 reduces axial dispersion. Thus, via the EDL interaction both phenomena (the perfusive electroosmosis and EO-2) may be tuned towards high-speed, high-efficiency electrokinetic transport mechanisms in porous media simply by adjusting the mobile phase ionic strength.

9 Literature cited

[1] Cs. Horváth, B. A. Preiss, S. R. Lipsky, *Anal. Chem.* **1967**, *39*, 1422.

[2] Cs. Horváth, S. R. Lipsky, *Anal. Chem.* **1969**, *41*, 1227.

[3] R. P. W. Scott, P. Kucera, *J. Chromatogr.* **1976**, *125*, 251.

[4] D. Ishii, K. Asai, K. Hibi, T. Jonokuchi, M. Nagaya, *J. Chromatogr.* **1977**, *144*, 157.

[5] D. Ishii (Ed.), *Introduction to Microscale High-Performance Liquid Chromatography*, VCH, Weinheim **1988**.

[6] J. P. C. Vissers, H. A. Claessens, C. A. Cramers, *J. Chromatogr. A* **1997**, *779*, 1.

[7] J. P. C. Vissers, *J. Chromatogr. A* **1999**, *856*, 117.

[8] J. Abian, A. J. Oosterkamp, E. Gelpi, *J. Mass Spectrom.* **1999**, *34*, 244.

[9] G. P. Rozing, M. Serwe, H.-G. Weissgerber, B. Glatz, *Am. Lab.* **2001**, *33*, 26.

[10] M. Szumski, B. Buszewski, *Crit. Rev. Anal. Chem.* **2002**, *32*, 1.

[11] E. Rapp, U. Tallarek, *J. Sep. Sci.* **2003**, *26*, 453.

[12] R. F. Probstein, R. E. Hicks, *Science* **1993**, *260*, 498.

[13] J. E. Sauer, E. J. Davis, *Environ. Sci. Technol.* **1994**, *28*, 737.

[14] A. T. Yeung, *Adv. Porous Media* **1994**, *2*, 309.

[15] M. M. Dittmann, K. Wienand, F. Bek, G. P. Rozing, *LC•GC* **1995**, *13*, 800.

[16] S. V. Ho, P. W. Sheridan, C. J. Athmer, M. A. Heitkamp, J. M. Brackin, D. Weber, P. H. Brodsky, *Environ. Sci. Technol.* **1995**, *29*, 2528.

[17] T. Tsuda (Ed.), *Electric Field Applications in Chromatography, Industrial and Chemical Processes*, VCH, Weinheim **1995**.

[18] Y. B. Acar, E. E. Ozsu, A. N. Alshawabkeh, M. F. Rabbi, R. J. Gale, *CHEMTECH* **1996**, *26*, 40.

[19] A. L. Crego, A. González, M. L. Marina, *Crit. Rev. Anal. Chem.* **1996**, *26*, 261.

[20] T. F. Coletta, C. J. Brunell, D. K. Ryan, H. I. Inyang, *J. Environ. Eng.* **1997**, *123*, 1227.

[21] C. Fujimoto, *Trends Anal. Chem.* **1999**, *18*, 291.

[22] L. A. Colón, G. Burgos, T. D. Maloney, J. M. Cintrón, R. L. Rodríguez, *Electrophoresis* **2000**, *21*, 3965.

[21] U. Pyell, *J. Chromatogr. A* **2000**, *892*, 257.

[24] C. Ericson, J. Holm, T. Ericson, S. Hjertén, *Anal. Chem.* **2000**, *72*, 81.

[25] C. Yu, F. Svec, J. M. J. Fréchet, *Electrophoresis* **2000**, *21*, 120.

[26] J. D. Hayes, A. Malik, *Anal. Chem.* **2000**, *72*, 4090.

[27] L. Bousse, C. Cohen, T. Nikiforov, A. Chow, A. R. Kopf-Sill, R. Dubrow, J. W. Parce, *Annu. Rev. Biophys. Biomol. Struct.* **2000**, *29*, 155.

[28] Q. L. Tang, M. L. Lee, *Trends Anal. Chem.* **2000**, *19*, 648.

[29] G. J. M. Bruin, *Electrophoresis* **2000**, *21*, 3931.

[30] Z. Deyl, F. Svec (Eds.), *Capillary Electrochromatography*, Journal of Chromatography Library, Vol. 62, Elsevier, Amsterdam **2001**.

[31] G. M. Whitesides, A. D. Stroock, *Phys. Today* **2001**, *54*, 42.

[32] N. Tanaka, H. Kobayashi, K. Nakanishi, H. Minakuchi, N. Ishizuka, *Anal. Chem.* **2001**, *73*, 420A.

[33] H. A. Stone, S. Kim, *AIChE J.* **2001**, *47*, 1250.

[34] N. A. Polson, M. A. Hayes, *Anal. Chem.* **2001**, *73*, 312A.

[35] H. Kobayashi, C. Smith, K. Hosoya, T. Ikegami, N. Tanaka, *Anal. Sci.* **2002**, *18*, 89.

[36] A. S. Rathore, *Electrophoresis* **2002**, *23*, 3827.

[37] A. R. Minerick, A. E. Ostafin, H.-C. Chang, *Electrophoresis* **2002**, *23*, 2165.

[38] K. Mistry, I. Krull, N. Grinberg, *J. Sep. Sci.* **2002**, *25*, 935.

[39] A. V. Delgado (Ed.), *Interfacial Electrokinetics and Electrophoresis*, Marcel Dekker, New York **2002**.

[40] D. J. Throckmorton, T. J. Shepodd, A. K. Singh, *Anal. Chem.* **2002**, *74*, 784.

[41] L. Ceriotti, N. F. de Rooij, E. Verpoorte, *Anal. Chem.* **2002**, *74*, 639.

[42] C. Legido-Quigley, N. D. Marlin, V. Melin, A. Manz, N. W. Smith, *Electrophoresis* **2003**, *24*, 917.

[43] I. Peric, E. Kenndler, *Electrophoresis* **2003**, *24*, 2924.

[44] A. B. Jemere, R. D. Oleschuk, D. J. Harrison, *Electrophoresis* **2003**, *24*, 3018.

[45] B. S. Broyles, S. C. Jacobson, J. M. Ramsey, *Anal. Chem.* **2003**, *75*, 2761.

[46] R. F. Probstein, *Physicochemical Hydrodynamics*, John Wiley & Sons, New York **1994**.

[47] S. Saksena, A. L. Zydney, *J. Membr. Sci.* **1995**, *105*, 203.

[48] G. R. Eykholt, *J. Hazard. Mater.* **1997**, *55*, 171.

[49] M. M. Dittmann, G. P. Rozing, *J. Microcolumn Sep.* **1997**, *9*, 399.

[50] G. Choudhary, Cs. Horváth, *J. Chromatogr. A* **1997**, *781*, 161.

[51] D. Erickson, D. Li, *Langmuir* **2002**, *18*, 1883.

[52] J. Jiskra, T. Jiang, H. A. Claessens, C. A. Cramers, *J. Microcolumn Sep.* **2000**, *12*, 530.

[53] B. Gaš, E. Kenndler, *Electrophoresis* **2000**, *21*, 3888.

[54] A. Banholczer, U. Pyell, *J. Chromatogr. A* **2000**, *869*, 363.

[55] T. Tanigawa, T. Nakagawa, K. Kimata, H. Nagayama, K. Hosoya, N. Tanaka, *J. Chromatogr. A* **2000**, *887*, 299.

[56] K. Bohinc, V. Kralj-Iglič, A. Iglič, *Electrochim. Acta* **2001**, *46*, 3033.

[57] T. L. Sounart, J. C. Baygents, *Colloids Surf. A* **2001**, *195*, 59.

[58] M. Pačes, J. Kosek, M. Marek, U. Tallarek, A. Seidel-Morgenstern, *Electrophoresis* **2003**, *24*, 380.

[59] B. D. Bath, H. S. White, E. R. Scott, *Anal. Chem.* **2000**, *72*, 433.

[60] G. Moy, B. Corry, S. Kuyucak, S.-H. Chung, *Biophys. J.* **2000**, *78*, 2349.

[61] B. Corry, S. Kuyucak, S.-H. Chung, *Biophys. J.* **2000**, *78*, 2364.

[61] T. C. Kuo, L. A. Sloan, J. V. Sveedler, P. W. Bohn, *Langmuir* **2001**, *17*, 6298.

[63] B. Zhao, J. S. Moore, D. J. Beebe, *Science* **2001**, *291*, 1023.

[64] G. E. Karniadakis, A. Beskok, *Micro Flows – Fundamentals and Simulation*, Springer-Verlag, New York **2002**.

[65] P. Vainshtein, C. Gutfinger, *J. Micromech. Microeng.* **2002**, *12*, 252.

[66] A. T. Conlisk, J. McFerran, Z. Zheng, D. Hansford, *Anal. Chem.* **2002**, *74*, 2139.

[67] O. D. Uitto, H. S. White, K. Aoki, *Anal. Chem.* **2002**, *74*, 4577.

[68] R. Qiao, N. R. Aluru, *Nano Lett.* **2003**, *3*, 1013.

[69] H. H. Bau, J. Z. Zhu, S. Z. Qian, Y. Xiang, *Sens. Actuators B* **2003**, *88*, 207.

[70] A. D. Stroock, G. M. Whitesides, *Acc. Chem. Res.* **2003**, *36*, 597.

[71] W. L. W. Hau, D. W. Trau, N. J. Sucher, M. Wong. Y. Zohar, Y., *J. Micromech. Microeng.* **2003**, *13*, 272.

[72] T. Tsuda, *Anal. Chem.* **1987**, *59*, 521.

[73] V. Pretorius, B. J. Hopkins, J. D. Schieke, *J. Chromatogr.* **1974**, *99*, 23.

[74] J. W. Jorgenson, K. D. Lukacs, *J. Chromatogr.* **1981**, *218*, 209.

[75] J. H. Knox, I. H. Grant, *Chromatographia* **1987**, *24*, 135.

[76] J. H. Knox, *Chromatographia* **1988**, *26*, 329.

[77] J. H. Knox, I. H. Grant, *Chromatographia* **1991**, *32*, 317.

[78] C. L. Rice, R. Whitehead, *J. Phys. Chem.* **1965**, *69*, 4017.

[79] R. J. Gross, J. F. Osterle, *J. Chem. Phys.* **1968**, *48*, 228.

[80] K.-L. K. Liu, K. L. Davis, M. D. Morris, *Anal. Chem.* **1994**, *66*, 3744.

[81] S. Arulanandam, D. Li, *Colloids Surf. A* **2000**, *161*, 89.

[82] P. H. Paul, M. G. Garguilo, D. J. Rakestraw, *Anal. Chem.* **1998**, *70*, 2459.

[83] U. Tallarek, E. Rapp, T. Scheenen, E. Bayer, H. Van As, *Anal. Chem.* **2000**, *72*, 2292.

[84] K. K. Unger, S. Lüdtke, M. Grün, *LC-GC Int.* **1999**, *12*, 870.

[85] K. K. Unger, D. Kumar, M. Grün, D. Büchel, S. Lüdtke, Th. Adam, K. Schumacher, S. Renker, *J. Chromatogr. A* **2000**, *892*, 47.

[86] T. Sakaki, S. Kitagawa, T. Tsuda, *Electrophoresis* **2000**, *21*, 3088.

[87] J. P. Kutter, S. C. Jacobson, N. Matsubara, J. M. Ramsey, *Anal. Chem.* **1998**, *70*, 3291.

[88] R. D. Oleschuk, L. L. Schultz-Lockyear, Y. B. Ning, D. J. Harrison, *Anal. Chem.* **2000**, *72*, 585.

[89] B. E. Slentz, N. A. Penner, E. Lugowska, F. E. Regnier, *Electrophoresis* **2001**, *22*, 3763.

[90] R. Stol, W. Th. Kok, H. Poppe, *J. Chromatogr. A* **1999**, *853*, 45.

[91] E. Wen, R. Asiaie, Cs. Horváth, *J. Chromatogr. A* **1999**, *855*, 349.

[92] P. T. Vallano, V. T. Remcho, *Anal. Chem.* **2000**, *72*, 4255.

[93] U. Tallarek, E. Rapp, H. Van As, E. Bayer, *Angew. Chem. Int. Ed.* **2001**, *40*, 1684.

[94] R. Stol, H. Poppe, W. Th. Kok, *Anal. Chem.* **2001**, *73*, 3332.
[95] U. Tallarek, E. Rapp, A. Seidel-Morgenstern, H. Van As, *J. Phys. Chem. B* **2002**, *106*, 12709.
[96] R. Xiang, Cs. Horváth, *Anal. Chem.* **2002**, *74*, 762.
[97] S. R. Dziennik, E. B. Belcher, G. A. Barker, M. J. DeBergalis, S. E. Fernandez, A. M. Lenhoff, *Proc. Natl. Acad. Sci. U.S.A.* **2003**, *100*, 420.
[98] I. Gusev, Cs. Horváth, *J. Chromatogr. A* **2002**, *948*, 203.
[99] L. Ren, D. Li, *J. Colloid Interface Sci.* **2001**, *243*, 255.
[100] C. Yang, D. Li, J. H. Masliyah, *Int. J. Heat Mass Transfer* **1998**, *41*, 4229.
[101] N. A. Patankar, H. H. Hu, *Anal. Chem.* **1998**, *70*, 1870.
[102] S. V. Ermakov, S. C. Jacobson, J. M. Ramsey, *Anal. Chem.* **1998**, *70*, 4494.
[103] S. K. Griffiths, R. H. Nilson, *Anal. Chem.* **1999**, *71*, 5522.
[104] F. Bianchi, R. Ferrigno, H. H. Girault, *Anal. Chem.* **2000**, *72*, 1987.
[105] E. B. Cummings, S. K. Griffiths, R. H. Nilson, P. H. Paul, *Anal. Chem.* **2000**, *72*, 2526.
[106] J. G. Santiago, *Anal. Chem.* **2001**, *73*, 2353.
[107] P. Dutta, A. Beskok, *Anal. Chem.* **2001**, *73*, 5097.
[108] R. J. Yang, L. M. Fu, Y. C. Lin, *J. Colloid Interface Sci.* **2001**, *239*, 98.
[109] H. J. Keh, H. C. Tseng, *J. Colloid Interface Sci.* **2001**, *242*, 450.
[110] P. Dutta, A. Beskok, T. C. Warburton, *J. Microelectromech. Syst.* **2002**, *11*, 36.
[111] L. M. Fu, R. J. Yang, G. B. Lee, *Electrophoresis* **2002**, *23*, 602.
[112] Y. J. Kang, C. Yang, X. Y. Huang, *J. Colloid Interface Sci.* **2002**, *253*, 285.
[113] Z. Zheng, D. J. Hansford, A. T. Conlisk, *Electrophoresis* **2003**, *24*, 3006.
[114] A. Chatterjee, *J. Micromech. Microeng.* **2003**, *13*, 758
[115] J. L. Anderson, W. K. Idol, *Chem. Eng. Commun.* **1985**, *38*, 93.
[116] B. Potoček, B. Gaš, E. Kenndler, M. Štědrý, *J. Chromatogr. A* **1995**, *709*, 51.
[117] P. Weidenhammer, H. J. Jacobasch, *J. Colloid Interface Sci.* **1996**, *180*, 232.
[118] R. A. Hayes, *Colloids Surf. A* **1999**, *146*, 89.
[119] A. E. Herr, J. I. Molho, J. G. Santiago, M. G. Mungal, T. W. Kenny, M. G. Garguilo, *Anal. Chem.* **2000**, *72*, 1053.
[120] S. Ghosal, *J. Fluid Mech.* **2002**, *459*, 103.
[121] D. Long, H. A. Stone, A. Ajdari, *J. Colloid Interface Sci.* **1999**, *212*, 338.
[122] F. E. Regnier, D. Wu, in *Capillary Electrophoresis Technology*, N. A. Guzman (Ed.), Marcel Dekker, New York **1993**, pp. 287-309.
[123] J. Bear, *Dynamics of Fluids in Porous Media*, Dover Publications, New York **1988**.
[124] F. A. L. Dullien, *Porous Media: Fluid Transport and Pore Structure*, Academic Press, San Diego **1992**.
[125] J. C. Giddings, *Dynamics of Chromatography. Part I: Principles and Theory*, Marcel Dekker, New York **1965**.
[126] U. Tallarek, F. J. Vergeldt, H. Van As, *J. Phys. Chem. B* **1999**, *103*, 7654.
[127] D. Kandhai, D. Hlushkou, A. G. Hoekstra, P. M. A. Sloot, H. Van As, U. Tallarek, *Phys. Rev. Lett.* **2002**, *88*, art. no. 234501.
[128] D. L. Koch, J. F. Brady, *Chem. Eng. Sci.* **1987**, *42*, 1377.

[129] J. Salles, J.-F. Thovert, R. Delannay, L. Prevors, J.-L. Auriault, P. M. Adler, *Phys. Fluids A* **1993**, *5*, 2348.

[130] J. P. Hulin, *Adv. Colloid Interface Sci.* **1994**, *49*, 47.

[131] D. Kandhai, U. Tallarek, D. Hlushkou, A. Hoektra, P. M. A. Sloot, H. Van As, *Phil. Trans. R. Soc. Lond.* **2002**, *360*, 521.

[132] D. L. Koch, J. F. Brady, *J. Fluid Mech.* **1985**, *154*, 399.

[133] E. Charlaix, J. P. Hulin, T. J. Plona, *Phys. Fluids* **1987**, *30*, 1690.

[134] J. P. Hulin, E. Charlaix, T. J. Plona, L. Oger, E. Guyon, *AIChE J.* **1988**, *34*, 610.

[135] U. Tallarek, F. C. Leinweber, A. Seidel-Morgenstern, *Chem. Eng. Technol.* **2002**, *25*, 1177.

[136] F. C. Leinweber, U. Tallarek, *J. Chromatogr. A* **2003**, *1006*, 207.

[137] O. Bey, G. Eigenberger, *Chem. Eng. Sci.* **1997**, *52*, 1365.

[138] M. Giese, K. Rottschäfer, D. Vortmeyer, *AIChE J.* **1998**, *44*, 484.

[139] A. J. Sederman, P. Alexander, L. F. Gladden, *Powder Technol.* **2001**, *117*, 255.

[140] J. C. Park, K. Raghavan, S. J. Gibbs, *J. Chromatogr. A* **2002**, *945*, 65.

[141] T. C. Hsiang, H. W. Haynes, Jr., *Chem. Eng. Sci.* **1977**, *32*, 678.

[142] H. Martin, *Chem. Eng. Sci.* **1978**, *33*, 913.

[143] R. G. Carbonell, *Chem. Eng. Sci.* **1980**, *35*, 1347.

[144] E. Tsotsas, E.-U. Schlünder, *Chem. Eng. Process.* **1988**, *24*, 15.

[145] B.-J. Ahn, A. Zoulalian, J. M. Smith, *AIChE J.* **1986**, *32*, 170.

[146] E. Tsotsas, *Über die Wärme- und Stoffübertragung in durchströmten Festbetten*, Fortschritt-Berichte VDI, Reihe 3, Nr. 223, VDI-Verlag, Düsseldorf **1990**.

[147] A. S. Rathore, Cs. Horváth, *J. Chromatogr. A* **1997**, *781*, 185.

[148] A. I. Liapis, B. A. Grimes, *J. Chromatogr. A* **2000**, *877*, 181.

[149] G. Neale, N. Epstein, W. Nader, *Chem. Eng. Sci.* **1973**, *28*, 1865.

[150] U. Tallarek, T. W. J. Scheenen, H. Van As, *J. Phys. Chem. B* **2001**, *105*, 8591.

[151] A. S. Rathore, E. Wen, Cs. Horváth, *Anal. Chem.* **1999**, *71*, 2633.

[152] Y. Liu, D. J. Pietrzyk, *Anal. Chem.* **2000**, *72*, 5930.

[153] J. Th. G. Overbeek, in *Colloid Science*, Kruyt, H. R. (Ed.), Elsevier, Amsterdam **1952**, chapter 5.

[154] R. J. Hunter, H. J. L. Wright, *J. Colloid Interface Sci.* **1971**, *37*, 564.

[155] J. Vindevogel, P. Sandra, *J. Chromatogr.* **1991**, *541*, 483.

[156] I. Gusev, X. Huang, Cs. Horváth, *J. Chromatogr. A* **1999**, *855*, 273.

[157] F. Svec, J. M. J. Fréchet, *Ind. Eng. Chem. Res.* **1999**, *38*, 34.

[158] N. Ishizuka, H. Minakuchi, K. Nakanishi, N. Soga, H. Nagayama, K. Hosoya, N. Tanaka, *Anal. Chem.* **2000**, *72*, 1275.

[159] N. B. Afeyan, N. F. Gordon, I. Mazsaroff, L. Varady, S. P. Fulton, Y. B. Yang, F. E. Regnier, *J. Chromatogr.* **1990**, *519*, 1.

[160] A. E. Rodrigues, Z. P. Lu, J. M. Loureiro, *Chem. Eng. Sci.* **1991**, *46*, 2765.

[161] A. I. Liapis, M. A. McCoy, *J. Chromatogr.* **1992**, *599*, 87.

[162] A. E. Rodrigues, J. C. Lopes, Z. P. Lu, J. M. Loureiro, M. M. Dias, *J. Chromatogr.* **1992**, *590*, 93.

[163] G. Carta, M. E. Gregory, D. J. Kirwan, H. A. Massaldi, *Sep. Technol.* **1992**, *2*, 62.

[164] D. D. Frey, E. Schweinheim, Cs. Horváth, *Biotechnol. Prog.* **1993**, *9*, 273.

[165] G. Carta, A. E. Rodrigues, *Chem. Eng. Sci.* **1993**, *48*, 3927.
[166] R. H. Davis, H. A. Stone, *Chem. Eng. Sci.* **1993**, *48*, 3993.
[167] D. H. Reeder, A. M. Clausen, M. J. Annen, P. W. Carr, M. C. Flickinger, A. V. McCormick, *J. Colloid Interface Sci.* **1996**, *184*, 328.
[168] P.-E. Gustavsson, P.-O. Larsson, *J. Chromatogr. A* **1996**, *734*, 231.
[169] M. McCoy, K. Kalghatgi, F. E. Regnier, N. Afeyan, *J. Chromatogr. A* **1996**, *743*, 221.
[170] D. C. Nash, H. A. Chase, *J. Chromatogr. A* **1998**, *807*, 185.
[171] J. J. Meyers, A. I. Liapis, *J. Chromatogr. A* **1998**, *827*, 197.
[172] Q. L. Li, E. W. Grandmaison, M. F. A. Goosen, D. Taylor, *AIChE J.* **2000**, *46*, 1927.
[173] M. E. Van Kreveld, N. Van den Hoed, *J. Chromatogr.* **1978**, *149*, 71.
[174] A. Nir, L. M. Pismen, *Chem. Eng. Sci.* **1977**, *32*, 35.
[175] A. E. Rodrigues, B. J. Ahn, A. Zoulalian, *AIChE J.* **1982**, *28*, 541.
[176] G. Stephanopoulos, K. Tsiveriotis, *Chem. Eng. Sci.* **1989**, *44*, 2031.
[177] J. F. Pfeiffer, J. C. Chen, J. T. Hsu, *AIChE J.* **1996**, *42*, 932.
[178] J. H. Knox, *J. Chromatogr. A* **1999**, *831*, 3.
[179] E. Venema, J. C. Kraak, H. Poppe, R. Tijssen, *J. Chromatogr. A* **1999**, *837*, 3.
[180] P. T. Vallano, V. T. Remcho, *J. Phys. Chem. B* **2001**, *105*, 3223.
[181] H. S. Dearie, N. W. Smith, F. Moffat, S. A. C. Wren, K. P. Evans, *J. Chromatogr. A* **2002**, *945*, 231.
[182] M. Sahimi, *Flow and Transport in Porous Media and Fractured Rock*, VCH, Weinheim **1995**.
[183] U. Tallarek, E. Bayer, G. Guiochon, *J. Am. Chem. Soc.* **1998**, *120*, 1494.
[184] J. B. Pawley (Ed.), *Handbook of Biological Confocal Microscopy*, Plenum, New York **1995**.
[185] M. Malmsten, K. Xing, A. Ljunglöf, *J. Colloid Interface Sci.* **1999**, *220*, 436.
[186] W. L. Whipple, C. Maltesh, *Langmuir* **2000**, *16*, 3124.
[187] J. R. Barone, S. Q. Wang, J. P. S. Farinha, M. A. Winnik, *Langmuir* **2000**, *16*, 7038.
[188] Y. Song, M. Srinivasarao, A. Tonelli, C. M. Balik, R. McGregor, *Macromolecules* **2000**, *33*, 4478.
[189] O. D. Velev, E. W. Kaler, A. M. Lenhoff, *J. Phys. Chem. B* **2000**, *104*, 9267.
[190] W. Hoheisel, W. Jacobsen, B. Lüttge, W. Weiner, *Macromol. Mater. Eng.* **2001**, *286*, 663.
[191] A. Spiess, V. Kasche, *Biotechnol. Prog.* **2001**, *17*, 294.
[192] F. Fergg, F. J. Keil, H. Quader, *Colloid Polym. Sci.* **2001**, *279*, 61.
[193] U. Reichert, T. Linden, G. Belfort, M.-R. Kula, J. Thömmes, *J. Membr. Sci.* **2002**, *199*, 161.
[194] E. H. C. Bromley, I. Hopkinson, *J. Colloid Interface Sci.* **2002**, *245*, 75.
[195] M. Lowry, Y. He, L. Geng, *Anal. Chem.* **2002**, *74*, 1811.
[196] H.-B. Kim, M. Hayashi, K. Nakatani, N. Kitamura, K. Sasaki, J. Hotta, H. Masuhara, *Anal. Chem.* **1996**, *68*, 409.
[197] A. Ljunglöf, J. Thömmes, *J. Chromatogr. A* **1998**, *813*, 387.
[198] P. Bouillot, N. Ubrich, F. Sommer, T. Minh Duc, J.-P. Loeffler, E. Dellacherie, *Int. J. Pharm.* **1999**, *181*, 159.
[199] T. Linden, A. Ljunglöf, M.-R. Kula, J. Thömmes, *Biotechnol. Bioeng.* **1999**, *65*, 622.
[200] J. Rademann, M. Barth, R. Brock, H.-J. Egelhaaf, G. Jung, *Chem. Eur. J.* **2001**, *7*, 3884.
[201] R. H. Webb, *Rep. Prog. Phys.* **1996**, *59*, 427.

[202] T. Wilson (Ed.), *Confocal Microscopy*, Academic Press, London **1990**.
[203] U. Tallarek, E. Rapp, H. Sann, U. Reichl, A. Seidel-Morgenstern, *Langmuir* **2003**, *19*, 4527.
[204] T. D. Visser, F. C. A. Groen, G. J. Brakenhoff, *J. Microsc.* **1991**, *163*, 189.
[205] C. J. R. Sheppard, P. Török, *J. Microsc.* **1997**, *185*, 366.
[206] M. J. Booth, M. A. A. Neil, T. Wilson, *J. Microsc.* **1998**, *192*, 90.
[207] A. Liljeborg, *Proc. SPIE* **1996**, *2655*, 11.
[208] M. J. Booth, T. Wilson, *J. Biomed. Opt.* **2001**, *6*, 266.
[209] A. Diaspro, F. Federici, M. Robello, *Appl. Opt.* **2002**, *41*, 685.
[210] U. Tallarek, M. Pačes, E. Rapp, *Electrophoresis* **2003**, *24*, 4241.
[211] G. Chen, U. Tallarek, *Langmuir* **2003**, *19*, 10901.
[212] J. Lyklema, *Fundamentals of Interface and Colloid Science. Vol. II: Solid-Liquid Interfaces*, Academic Press, London **1995**.
[213] G. Chen, M. Pačes, M. Marek, Y. Zhang, A. Seidel-Morgenstern, U. Tallarek, *Chem. Eng. Technol.* **2004**, *27*, 417.
[214] R. Stol, H. Poppe, W. Th. Kok, *Anal. Chem.* **2003**, *75*, 5246.
[215] I. Rubinstein, *Electro-Diffusion of Ions*, SIAM, Philadelphia **1990**.
[216] I. Rubinstein, *Physical Electrochemistry*, Marcel Dekker, New York **1995**.
[217] F. Helfferich, *Ion Exchange*, McGraw-Hill, New York **1962**.
[218] J. Ståhlberg, *J. Chromatogr. A* **1999**, *855*, 3.
[219] A. E. Yaroshchuk, *Sep. Purif. Technol.* **2001**, *22-23*, 143.
[220] I. Rubinstein, *J. Chem. Soc. Faraday Trans. II* **1981**, *77*, 1595.
[221] S. S. Dukhin, *Adv. Colloid Interface Sci.* **1991**, *35*, 173.
[222] N. A. Mishchuk, P. V. Takhistov, *Colloids Surf. A* **1995**, *95*, 119.
[223] N. A. Mishchuk, *Colloids Surf. A* **1998**, *140*, 75.
[224] I. Rubinstein, B. Zaltzman, in *Surface Chemistry and Electrochemistry of Membranes*, T. S. Sørensen (Ed.), Marcel Dekker, New York **1999**, pp. 591-621.
[225] I. Rubinstein, B. Zaltzmann, *Phys. Rev. E* **2000**, *62*, 2238.
[226] N. Mishchuk, F. Gonzalez-Caballero, P. Takhistov, *Colloids Surf. A* **2001**, *181*, 131.
[227] I. Rubinstein, B. Zaltzmann, *Math. Models Methods Appl. Sci.* **2001**, *11*, 263.
[228] Y. Ben, H.-C. Chang, *J. Fluid Mech.* **2002**, *461*, 229.
[229] F. C. Leinweber, U. Tallarek, *Langmuir* **2004**, *20*, 11637.
[230] S. G. Weber, P. W. Carr, in *High Performance Liquid Chromatography*, P. R. Brown, R. A. Hartwick (Eds.), Wiley, New York **1989**, chapter 1.
[231] U. Tallarek, K. Albert, E. Bayer, G. Guiochon, *AIChE J.* **1996**, *42*, 3041.
[232] I. Nischang, U. Tallarek, *Electrophoresis* **2004**, *25*, 2935.

Part 2:

Contributed Articles

Hydraulic flow in porous media:

Diffusive mass transfer and dispersion in sphere packings

U. Tallarek, F. J. Vergeldt, and H. Van As
Stagnant mobile phase mass transfer in chromatographic media: Intraparticle diffusion and exchange kinetics.
Journal of Physical Chemistry B **1999**, *103*, 7654-7664.

Pulsed field gradient nuclear magnetic resonance (PFG-NMR) is used to resolve directly in the packing of chromatographic columns intraparticle stagnant fluid and record the associated mass transfer kinetics for the fluid phase percolating through the porous medium. These data are well analysed by the diffusion equation for purely-diffusive intraparticle transport. Different particles are compared in view of the derived effective intraparticle diffusion coefficient and tortuosity factor. Further, the influence of the particle size distributions and interparticle (hydrodynamic) boundary-layer mass transfer resistance on the intraparticle transport dynamics is revealed and discussed. The results point out the importance of the particle morphology on stagnant mobile phase mass transfer and dispersion. The approach appears unique for separate studies of intraparticle diffusion and interparticle convection.

D. Kandhai, U. Tallarek, D. Hlushkou, A. G. Hoekstra, P. M. A. Sloot, and H. Van As
Numerical simulation and measurement of liquid holdup in biporous media containing discrete stagnant zones.
Philosophical Transactions of the Royal Society of London A **2002**, *360*, 521-534.

Complements the direct PFG-NMR measurements of transient axial averaged propagator (displacement probability) distributions in random sphere packings by a numerical simulation of the hydrodynamics in computer-generated fixed beds. The numerical approach is based on a hierarchical transport model using a discrete lattice-Boltzmann interparticle flow field. Simulated propagator distributions agree well with the experimental data and correctly reproduce the dynamics of the intraparticle diffusive and interparticle convective fluid. Further, finite-size effects in the simulations associated with a spatial discretization of the particles and boundaries of a bed are addressed and minimized.

D. Kandhai, D. Hlushkou, A. G. Hoekstra, P. M. A. Sloot, H. Van As, and U. Tallarek
Influence of stagnant zones on transient and asymptotic dispersion in macroscopically homogeneous porous media.
Physical Review Letters **2002**, *88*, 234501-1 – 234501-4.

Continues and rounds off the earlier work concerning complementary studies (PFG-NMR and numerical simulations) of the role of stagnant zones for hydrodynamic dispersion in liquid flow through a fixed bed of spherical, permeable particles. The numerical simulations in a bulk random-close sphere packing show good agreement with the experimental results on diffusion-limited mass transfer, transient and asymptotic axial dispersion. The data are compared to results for nonporous, impermeable particles and clearly demonstrate that intraparticle liquid holdup in (macroscopically homogeneous) porous media dominates over contributions arising from the flow field heterogeneity (mechanical dispersion) and the hydrodynamic boundary-layer mass transfer.

Hydraulic flow in porous media:
Permeability, dispersion and adsorption capacity in monolithic structures

---

U. Tallarek, F. C. Leinweber, and A. Seidel-Morgenstern
Fluid dynamics in monolithic adsorbents: Phenomenological approach to equivalent particle dimensions.
Chemical Engineering and Technology **2002**, *25*, 1177-1181.

Discusses the general problems of understanding fluid dynamics in monoliths with respect to the one in particulate beds. It presents a phenomenological analysis of the friction factor – Reynolds number relation and the axial dispersivity – Peclet number dependence for random sphere packings in order to derive characteristic lengths (equivalent particle dimensions) for monoliths concerning the hydraulic permeability and dispersion originating in stagnant zones. This phenomenological approach, simply based on liquid flow and stagnation in porous media, can successfully relate the hydrodynamic properties of a monolith to that of particulate beds from a very general point of view.

F. C. Leinweber, D. Lubda, K. Cabrera, and U. Tallarek
Characterization of silica-based monoliths with bimodal pore size distribution.
Analytical Chemistry **2002**, *74*, 2470-2477.

Investigates chromatographic band dispersion in analytical (silica-based) monoliths with bimodal pore size distribution. This work reveals diffusion-limited mass transfer in the mesoporous silica skeleton which was used to calculate an equivalent dispersion particle diameter (in relation to sphere packings) with the C-term parameter of the van Deemter plate height equation. The macroporous interskeleton network responsible for the hydraulic permeability of these monoliths was translated to the interparticle pore space of sphere packings, and an equivalent permeability particle diameter was obtained by scaling based on the Kozeny-Carman equation.

F. C. Leinweber and U. Tallarek
Chromatographic performance of monolithic and particulate stationary phases: Hydrodynamics and adsorption capacity.
Journal of Chromatography A **2003**, *1006*, 207-228.

Presents in more detail than before a simple, widely applicable, phenomenological approach for analysing single-phase incompressible flow through monolithic structures. It relies on a determination of equivalent particle (usually sphere) dimensions which characterize the corresponding behaviour in particulate, discontinuous beds. The equivalence is obtained by dimensionless scaling of the macroscopic behaviour (hydraulic permeability and hydrodynamic dispersion) in both types of materials, without need for direct geometrical translation of their constituent units. The differences in adsorption capacity for particulate and monolithic stationary phases show that silica-based monoliths with bimodal pore size distribution can provide comparable maximum loading capacities (with respect to beds of completely porous spheres) due to the high (total) porosity of this material. It is demonstrated that their pore structure provides the basis for unique combination of high bed permeability, short diffusion path lengths and high adsorption capacity which cannot be achieved with a fixed bed of adsorbent particles.

F. C. Leinweber, D. G. Schmid, D. Lubda, K.-H. Wiesmüller, G. Jung, and U. Tallarek
Silica-based monoliths for rapid peptide screening by capillary liquid chromatography hyphenated with ESI-FTICR-MS.
Rapid Communications in Mass Spectrometry **2003**, *17*, 1180-1188.

Demonstrates a superior performance (as was analysed in much detail in the earlier articles) of monoliths compared to sphere packings (i.e., a better combination of bed permeability, hydrodynamic dispersion and adsorption capacity) for the fast and efficient screening of complex libraries by electrospray-ionization Fourier transform ion cyclotron resonance mass spectrometry (ESI-FTICR-MS). Electrospraying was performed sheathless from an open-tubular transfer capillary into the ESI-interface. Libraries with more than 1000 different peptides could be screened in less than 20 min.

F. C. Leinweber, D. G. Schmid, D. Lubda, B. Sontheimer, G. Jung, and U. Tallarek
Sheathless electrospray ionization directly from a capillary monolith for fast liquid chromatography coupled to FT-ICR mass spectrometry.
Journal of Mass Spectrometry **2004**, *39*, 223-225.

Continues the earlier mass spectrometric work in that the electrospraying here is directly performed from the capillary monolith into the ESI-interface, i.e., the LC-MS configuration incorporates monolithic capillary columns over the complete distance from the injection module to the sheathless electrospray interface. The main advantage of this modification is a simple removal of adverse effects on chromatographic performance resulting from conventional spray capillaries, including post-column dispersion or significant back-pressure (if either large- or small-diameter open capillaries are used). Monoliths with continuous solid phase are ideally suited for that purpose compared to sphere packings with sintered frit because the latter may become instable and break easily, limiting the robustness of this realisation.

Electroosmotic flow in porous media:
Experimental realisation and general transport characteristics

---

E. Rapp and U. Tallarek
Liquid flow in capillary (electro)chromatography: Generation and control of micro- and nanoliter volumes.
Journal of Separation Science **2003**, *26*, 453-470.

Describes and discusses instrumental developments in capillary (electro)chromatography relevant for generating and controlling required volumetric flow rates in the micro- and nanoliter range through packed capillaries. Isocratic and gradient elution is considered. For capillary HPLC it inlvolves only commercial instrumentation, but also realizes the innovative concept of a high-pressure electrokinetic pump. Systems that have been used to generate electroosmotic flow in chromatographic beds are presented under the aspects of basically commercial capillary electrophoresis instruments adapted for electrochromatography, home-built configurations, and commercial capillary electrochromatography systems. An emphasis is given on feasibility, automation, as well as system-inherent delay times and dead-volumes.

G. Chen, M. Pačes, M. Marek, Y. Zhang, A. Seidel-Morgenstern, and U. Tallarek
Dynamics of capillary electrochromatography: Experimental characterization of flow and transport in particulate beds.
Chemical Engineering and Technology **2004**, *27*, 417-428.

Has partly the character of a review article by presenting general aspects of electroosmotic flow in porous media, but with original research results concerning electroosmotic perfusion. The chromatographic performance with respect to the flow behaviour and axial dispersion in packed beds of nonporous and macroporous particles was studied in capillary HPLC and electrochromatography. The existence of substantial electroosmotic intraparticle pore flow in columns packed with the macroporous particles was found to result in significant improvement of column efficiency compared to capillary HPLC. Based on these data an optimum chromatographic performance in view of speed and efficiency can be achieved by adjustment of the particle and (intraparticle) pore sizes, as well as electrolyte concentration.

Electroosmotic flow in porous media:
Velocity profiles in open channels and sphere packings

U. Tallarek, E. Rapp, T. Scheenen, E. Bayer, and H. Van As
Electroosmotic and pressure-driven flow in open and packed capillaries: Velocity distributions and fluid dispersion.
Analytical Chemistry **2000**, *72*, 2292-2301.

In this work the flow field dynamics in (open and packed) segments of a capillary column was studied with PFG-NMR using direct motion-encoding of fluid molecules. The method operates in a time window that allows a quantitative discrimination of electroosmotic against pressure-driven flow behavior. In contrast to the parabolic velocity profile and its impact on axial dispersion characterizing hydraulic flow through a cylindrical open capillary, a plug-like velocity distribution is revealed for electroosmotic flow. In the latter case, the variances of (radially averaged) axial displacement probability distributions can be quantitatively explained by molecular diffusion at the actual buffer temperature, while for Poiseuille flow classical Taylor-Aris dispersion and its preasymptotic regime could be resolved.

U. Tallarek, T. W. J. Scheenen, P. A. de Jager, and H. Van As
Using NMR displacement imaging to characterize electroosmotic flow in porous media.
Magnetic Resonance Imaging **2001**, *19*, 453-456.

PFG-NMR and NMR imaging were used to study temporal and spatial domains of electrokinetically-driven transport in porous media with a homebuilt NMR setup. Characteristics like the velocity distribution and dispersion were contrasted to viscous flow behavior. To characterize dispersion of electrokinetically driven mobile phase through the pore space of open and packed capillaries the access by PFG-NMR was utilized to a temporal domain covering the range from a few milliseconds up to seconds. By combining this technique with NMR imaging it was possible to study the microscopic fluid dynamics with a sufficient spatial resolution to address factors that influence dispersion on macroscopic scale.

U. Tallarek, T. W. J. Scheenen, and H. Van As
Macroscopic heterogeneities in electroosmotic and pressure-driven flow through fixed beds at low column-to-particle diameter ratio.
Journal of Physical Chemistry B **2001**, *105*, 8591-8599.

This work demonstrates by using dynamic NMR microscopy with 40 µm spatial resolution the existence of specific wall effects for electroosmotic and pressure-driven flow in fixed beds at low column-to-particle diameter ratio. While the geometrical wall effect with pressure-driven flow in the sphere packings is due to radial distribution of interstitial porosity, an electrokinetic wall effect is promoted by different values of the zeta-potential associated with the inner surface of a capillary and that of the particles. The wall effects cause a persistent disequilibrium in the axial dispersion dynamics, and correlation lengths in the flow field may cover the complete radius of the packed capillary. Characteristic times of these macroscopic flow heterogeneities exceed by far those for stagnant mobile phase mass transfer in the bed as was shown by complementary pulsed field gradient NMR measurements.

M. Pačes, J. Kosek, M. Marek, U. Tallarek, and A. Seidel-Morgenstern
Mathematical modelling of adsorption and transport processes in capillary electrochromatography: Open-tubular geometry.
Electrophoresis **2003**, *24*, 380-389.

Presents a compact mathematical modelling approach to open-tubular capillary electrochromatography. The model accounts for the coupling of (non)linear adsorption of charged analyte molecules (at a charged surface) with a local equilibrium electrokinetics, mobile phase transport by electroosmosis and hydraulic flow, as well as species transport by electrophoresis and diffusion. Thus, the local zeta-potential and electroosmotic mobility then become a function of the concentration of the charged analyte. The resulting inhomogeneity of electroosmotic flow through the capillary produces a compensating pore pressure as requirement for incompressible flow. These results are further discussed in view of the surface-to-volume ratio of a capillary, analyte concentration in combination with a Langmuir isotherm for the adsorption process, and buffer effects.

D. Hlushkou, D. Kandhai, and U. Tallarek
Coupled lattice-Boltzmann and finite-difference simulation of electroosmosis in microfluidic channels.
International Journal for Numerical Methods in Fluids **2004**, *46*, 507-532.

This article is concerned with an extension of the lattice-Boltzmann method for the numerical simulation of three-dimensional electroosmotic flow problems in porous media. The approach is evaluated for simple geometries as encountered in open-channel structures of microfluidic devices. The general case of nonuniform zeta-potential distributions requires a three-dimensional solution of the coupled Navier-Stokes equation for liquid flow, Poisson equation for electrical potential distribution, and Nernst-Planck equation for distribution of ionic species. The hydrodynamic problem has been treated with a high efficiency by code parallelization via the lattice-Boltzmann method. For their validation, velocity fields were simulated in several microcapillary systems and good agreement with results predicted either theoretically or obtained by alternative numerical methods could be established. The approach is particularly useful for more complex structures with arbitrary pore space morphologies (e.g., sphere packings or monoliths) and an arbitrary distribution of electrokinetic potential at the solid-liquid interface.

Electroosmotic flow in porous media:
Electroosmotic perfusion in beds of porous particles

U. Tallarek, E. Rapp, H. Van As, and E. Bayer
Electrokinetics in fixed beds: Experimental demonstration of electroosmotic perfusion.
Angewandte Chemie International Edition **2001**, *40*, 1684-1687.

This communication provides clear evidence for the existence (and impact) of an electroosmotic perfusion mechanism in porous media. Using pulsed field gradient nuclear magnetic resonance (PFG-NMR) as a noninvasive motion-encoding technique which operates directly on the nuclear spin of the fluid molecules (e.g., $^{1}H_2O$) the dynamics of pressure-driven and electroosmotic flow was studied in a bed of charged porous particles. Starting with an analysis of axial dispersion as a function of the Peclet number (for either mode of fluid flow) these data are complemented by the selectively measured dynamics of intraparticle mass transfer. Also the influence of thermal effects is addressed. The results are finally discussed in view of the hierarchical design of porous particles and important correlation of pore interconnectivity in a bidisperse pore network.

U. Tallarek, E. Rapp, A. Seidel-Morgenstern, and H. Van As
Electroosmotic flow phenomena in packed capillaries: From the interstitial velocities to intraparticle and boundary-layer mass transfer.
Journal of Physical Chemistry B **2002**, *106*, 12709-12721.

Detailed PFG-NMR studies of (intra- and interparticle) electrokinetic flow through a fused-silica capillary packed with spherical porous particles. Measurements reveal that (compared to only pressure driven flow through the porous medium) the intraparticle mass transfer rate constant significantly increases by the influence of a superimposed electrical potential gradient. This increase also depends clearly on the buffer concentration via electrical double layer overlap. The data show that fluid molecules in the porous particles remain diffusion-limited in the presence of a pressure gradient over the packed bed. By contrast, intraparticle Peclet numbers above unity (i.e., nonzero velocities) have been measured in electroosmotic flow and were found to increase with the applied voltage. Further, interparticle resistance to mass transfer appears to vanish on pore scale when the electrical double layer thickness is small compared to the relevant pore dimensions.

G. Chen and U. Tallarek
Effect of intraparticle porosity and double-layer overlap on electrokinetic mobility in multiparticle systems.
Langmuir **2003**, *19*, 10901-10908.

Experimental study of electrokinetic mobility (depending on mobile phase ionic strength) for different porous and nonporous silica-based spherical microparticles. Effects of intraparticle electrical double layer overlap and porosity on the electrophoretic mobility in dilute suspensions and electroosmotic mobility in fixed beds of the (non)porous particles were investigated. The electrokinetically consistent results demonstrate substantially different behaviour for the porous particles with respect to nonporous spheres.

It can be related to a porous particles dipole coefficient via the intraparticle void volume and, strongly depending on mobile phase ionic strength, to the actual magnitude of electroosmotic flow jetted through a particles interior. In contrast to the normal electrical double layer behaviour observed for solid spheres (continuous decrease of mobility with ionic strength) the competitive contributions give rise to pronounced maxima in the mobility curves for porous spheres. These studies resolve perfusive electroosmosis from the standpoint of average velocity as compared to its effect on dispersion.

U. Tallarek, E. Rapp, H. Sann, U. Reichl, and A. Seidel-Morgenstern
Quantitative study of electrokinetic transport in porous media by confocal laser scanning microscopy.
Langmuir **2003**, *19*, 4527-4531.

Based on the refractive index matching of liquid and solid phase in a bed of porous spherical glass beads confocal laser scanning microscopy allowed a quantitative study of intraparticle electrokinetic transport phenomena. By recording (transient) single-bead profiles for fluorescent, charged and uncharged tracer it was visualized that electrokinetic species transport produces, in contrast to the symmetric-spherical distributions observed with diffusion-limited operations, pronounced asymmetric concentration profiles in a particle. This behaviour is caused by the unidirectional character of electroosmosis and electrophoresis. It forms the basis for a significantly faster intraparticle mass transfer compared to the diffusion-limited kinetics. Further, quantitative image analysis permitted the direct determination of velocities underlying an intraparticle-forced electroosmotic convection and electrophoretic migration.

U. Tallarek, M. Pačes, and E. Rapp
Perfusive flow and intraparticle distribution of a neutral analyte in capillary electrochromatography.
Electrophoresis **2003**, *24*, 4241-4253.

Extends the earlier work with more detail. Systematic study of electroosmotic perfusion for transport of an electroneutral, nonadsorbing tracer. Quantitative analysis in real-time of spatio-temporal distribution of fluorescent tracer molecules during their uptake by and release from porous particles with confocal laser scanning microscopy. Results of measurements could be successfully interpreted and further analyzed by a compact mathematical model. Intraparticle Peclet numbers of up to 150 were realized and found to significantly enhance mass transport on a particle-scale towards the convection-dominated regime when compared to the conventional, diffusion-limited kinetics.

Electroosmotic flow in porous media:
Concentration polarisation and nonequilibrium effects

F. C. Leinweber and U. Tallarek
Nonequilibrium electrokinetic effects in beds of ion-permselective particles.
Langmuir **2004**, *20*, 11637-11648.

Electrokinetically-driven transport of neutral and charged analytes in porous glass beads was investigated by confocal laser scanning microscopy using a microfluidic setup. Investigations were carried out at low ionic strength leading to ion-permselective transport through a bead. Concentration polarisation was induced by external electrical fields resulting in a diffusion boundary-layer with reduced ion concentrations in the solution adjacent to a bead surface. It comprises extraparticle fluid-side mass transfer resistance. At increasing field strengths internal flux densities finally exceed extraparticle transport from bulk solution toward the surface and a nonequilibrium space charge develops, both inside the ion-permselective particles and in the adjacent electrolyte solution outside. As a consequence, the effective adsorption area of the intraparticle surface is reduced and beads ultimately remain unloaded for counter-ionic tracer. The induced diffuse space charge outside the particles gives rise to tangential electroosmotic convection stimulating electrokinetic chaotic mixing. Tracer pulse injections show that the overall signal variance can be improved by more than two orders of magnitude adjusting non-equilibrium electrokinetic conditions.

I. Nischang and U. Tallarek
Nonlinear electroosmosis in hierarchical monolithic structures.
Electrophoresis **2004**, *25*, 2935-2945.

Examines electrochromatographic separation efficiencies with electroneutral analytes and the dynamic behaviour of EOF in C18-silica capillary monoliths with bimodal pore size distribution over a wide range of mobile phase Tris concentration. The dependence of plate height and fluid dynamics on the applied electrical field and mobile phase ionic strengths is discussed in view of electroosmosis of the second kind, indicating a unique and yet unexplored potential of this electrokinetic transport mechanism in separation science. In particular, the onset of a nonlinear electroosmotic flow behaviour in the hierarchical monolithic structure and concomitant, significantly reduced dispersion were analyzed in view of concentration polarisation and possible nonequilibrium electrokinetic effects which may develop in porous media with ion-permselective regions due to the presence of strong electrical fields.

Stagnant Mobile Phase Mass Transfer in Chromatographic Media: Intraparticle Diffusion and Exchange Kinetics

Ulrich Tallarek,* Frank J. Vergeldt, and Henk Van As

Laboratory of Molecular Physics and Wageningen NMR Centre, Department of Biomolecular Sciences, Wageningen Agricultural University, Dreijenlaan 3, 6703 HA Wageningen, The Netherlands

Received: March 9, 1999

Pulsed field gradient nuclear magnetic resonance has been successfully applied to a direct and detailed experimental study of topological and dynamic aspects involved in the exchange of small, nonsorbed fluid molecules between the intraparticle pore network and the interparticle void space in chromatographic columns packed with spherical-shaped, porous particles. The approach provides quantitative data about the effective, intraparticle diffusion coefficients (and tortuosity factors) and about the associated, diffusion-limited mass transfer kinetics, including stagnant boundary layer contributions. In view of the recorded exchange kinetics, an analytical description for solute diffusion into/out of spherical particles is offered and addresses the influence of the particle size distribution and particle shape on the observed mass transfer rates and calculated diffusivities. The combined analyses of the steady-state intraparticle pore diffusion data and the associated exchange kinetics with Peclet numbers up to 500 reveals the existence of external stagnant fluid where all the interparticle fluid-side resistance to diffusion is localized. It is represented by a thin stagnant boundary layer around the particles and can be accounted for by the introduction of a hydrodynamically effective particle diameter which is found to depend on the Peclet number. The approach appears to be promising for a selective, detailed study of the boundary layer dynamics. Concerning the investigation of different chromatographic media and intraparticle morphologies, we demonstrate that the actual correlation (or randomness) of interconnection between intraparticle pores of different size has a profound effect on the observed tortuosity factors and the diffusion-limited stagnant mobile phase mass transfer kinetics. Compared to intraparticle pore networks with a random assignment of different pore sizes, hierarchically structured bidisperse porous particles offer a superior network topology, which can form the basis for an increased chromatographic performance.

Introduction

The packed and consolidated bed of a chromatographic column obtained with spherical-shaped, porous, rigid particles intrinsically bears a complex fluid dynamics. It is difficult to analyze exactly, due not least to the number of different mechanisms that actually contribute to the dispersion of a solute band as it passes through the column and to the complex geometries of the intraparticle pore network and the interparticle void space involved in this tortuous journey.[1−3] Under typical conditions, solute transport occurs mainly by interparticle convection and intraparticle diffusion, and chromatographic separations are generally achieved by a differential adsorption of the solutes on the large inner surface area of the packing materials. The adsorption process requires that solute first moves through a film of fluid at the outer surface of the adsorbent particles (most often assumed to be stagnant), where diffusion normal to the surface is at least the dominating transport mechanism,[4−7] and then diffuses through the pools of stagnant fluid entrained in the intraparticle pore network.[8−13] In most practical cases, the adsorption−desorption process is fast and the equilibrium kinetics are controlled by the mass transfer resistances. In this respect, the stagnant mobile phase mass transfer, i.e., the diffusion of solute molecules into and out of the fine pores of the particles, has been identified as the major source of band dispersion in liquid chromatography.[1,14−16] Especially with smaller partition coefficients of the solute and a larger particle radius, this diffusion-limited mass transfer within the particles may dramatically limit the overall kinetics.[9]

Advances in the design and preparation of adsorbents have included the use of small nonporous[17,18] and micropellicular particles,[19] continuous polymer phases[20] and monolithic structures[21] as an alternative to packed beds, as well as the development of hierarchically structured, macroporous[22] and gigaporous particles (with $d_{pore}/d_p > 10^{-2}$).[23,24] In the case of the latter, intraparticle fluid forced convection has been proposed to be operative under certain conditions, to assist and even dominate over the diffusive transport in the larger, particle-transecting ("flow-through") pores of the bidisperse pore network inside these particles.[25−28] Because of the higher mass transfer rates columns packed with these gigaporous media have shown significant performance advantages over columns obtained with conventional, purely diffusive adsorbent particles, especially in high-speed separations and purifications of slowly diffusing (bio)macromolecules.

Central to the understanding of a diffusion-controlled mass transfer kinetics in porous particles and to the prediction of the chromatographic performance of a material is the effective diffusivity (D_{eff}) of and in the stagnant fluid entrained in the intraparticle pore network. This parameter inherently contains a wealth of information and in the general case is related to the bulk diffusivity in free solution (D_m) by[29,30]

$$\frac{D_{eff}}{\epsilon_{intra}} = \frac{D_m}{\tau_{intra}} \frac{K_p}{K_H} \qquad (1)$$

* To whom correspondence should be addressed. Phone: + 31 (317) 48-2047. Fax: + 31 (317) 48-2725. E-mail: ulrich.tallarek@water.mf.wau.nl.

10.1021/jp990828b CCC: $18.00
Published on Web 08/21/1999

with ϵ_{intra}, the internal porosity of the particles and τ_{intra}, the tortuosity (more correctly,[31] the tortuosity factor) of the intraparticle pore network. The enhanced drag coefficient, K_H^{-1}, is a factor accounting for additional hydrodynamic hindrance within the pore when solute and pore size are of comparable magnitudes. K_P is the partition coefficient and characterizes the ratio of solute concentration inside the pores to the concentration outside the pores in bulk solution at equilibrium. This entropy-controlled, geometric exclusion effect is intimately related to the basic retention mechanism in gel permeation chromatography.[32,33] The restrictive factor $F_\lambda = K_P/K_H$ is a function dependent on λ, the ratio of the critical molecular diameter to the pore diameter, and ranges between 0 and 1.[30]

For diffusion-limited mass transfer kinetics and small values of λ ($F_\lambda \approx 1$) the effective diffusivity remains the ultimate transport parameter relating—commonly expressed by a single tortuosity factor (and the respective network porosity)—diffusive flux into and out of the particles pores to the intrinsic system morphology (geometry and topology) and range of inhomogeneities. It includes surface characteristics (e.g., chemical modification and roughness), the pore size and its distribution(s), pore shape, and pore interconnectivity. For a network made of cylindrical pore segments the effective diffusivity may be expressed by[34,35]

$$D_{eff} = \frac{1}{\tau_{intra}} \int_{\mathbf{r}} D(\mathbf{r}) \cdot \epsilon_{intra}(\mathbf{r})\, d\mathbf{r} \qquad (2)$$

where $\epsilon_{intra}(\mathbf{r})d\mathbf{r}$ stands for the porosity of pores having a radius in the interval $[\mathbf{r}, \mathbf{r} + d\mathbf{r}]$, and $\epsilon_{intra}(\mathbf{r})$ is the porosity density function which may account for the length and size distribution of the (cylindrical) pores.[35] Unfortunately, this equation does not contain much information about the actual correlation of the interconnection between pores of different size that contribute to $\epsilon_{intra}(\mathbf{r})$, an effect that certainly has a strong influence on the network permeability and value of τ_{intra}. The tortuosity factor is a very sensitive indicator for the presence of dead-end pores which adversely affect stagnant mobile phase mass transfer rates[36−38] and may cause excessive bandbroadening and peak tailing.[39,40] At a given porosity and pore size distribution the tortuosity is lower for pore networks with higher coordination numbers.[41,42]

Closely related to the effective diffusivity is the intraparticle diffusivity D_{intra}, but compared to D_{eff} it is based on the pore-level solute concentration and consequently does not account for the porosity factor and the equilibrium partition coefficient[43]

$$D_{intra} = \frac{D_m}{\tau_{intra}} \frac{1}{K_H} \qquad (3)$$

Thus, the problem now is to predict the values of the intraparticle tortuosity factor, τ_{intra} (for $K_H^{-1} \approx 1$). Finally, although with silica it is reasonable to assume that no mass transfer can take place through the walls between pores, this is not necessarily true for all the resins used as packing materials.[44] For this diffusion in and through the polymer matrix itself, the diffusion coefficient would be unusually small, causing low intraparticle sorption rates.[45,46] Although estimation procedures are available, it still remains very complicated to make accurate predictions of the diffusivities and tortuosities needed for liquid chromatography and bioreactor modeling, including diffusion and reaction in porous catalysts.[47] Despite its importance and historical background,[1,2] the direct and quantitative measurement of the classical stagnant (i.e., diffusion-limited) mobile phase mass transfer kinetics also has been extremely difficult.

Based on the averaged propagator formalism for nuclear spin (hence, molecular) displacements, pulsed field gradient nuclear magnetic resonance (PFG-NMR) is currently attracting increased interest—by choice acting as a contrast mechanism in an NMR imaging approach—in the experimental characterization of fluid flow and dispersion within a number of porous model systems.[48−56] This includes specific packed-bed applications in high performance liquid chromatography and heterogeneous catalysis, such as the study of axial and transverse plate height relations in analytical columns[57] or the performance of preparative-scale, radially compressed cartridges,[58] and effective diffusivity measurements in porous catalyst pellets.[59] In particular, it has been demonstrated most recently that this approach allows to observe directly, separately and quantitatively the purely diffusive, intraparticle and the diffusive-convective interparticle fluid molecules in chromatographic columns packed with porous adsorbent particles.[60]

In this article we report about an extended, detailed PFG-NMR investigation of the stagnant mobile phase mass transfer kinetics and intraparticle diffusivities of several single-fluid phases in selected chromatographic media. Special attention is given to the influence of structural parameters, such as the particle size and (intraparticle) pore size distributions, and to the actual correlation of interconnectivity between, e.g., large and small pores on the observed intraparticle fluid transport characteristics, such as the tortuosity factor and the rates of fluid exchange with the interparticle void space. It is demonstrated that this potential PFG-NMR approach provides important, in fact complementary data of both steady-state and transient nature concerning intraparticle diffusion and the associated, diffusion-limited mass transfer kinetics. The combined use of these series of data allows an unambiguous determination of intraparticle diffusivities and tortuosity factors and of the contribution to the observed mass transfer characteristics at a given Peclet number of stagnant regions in the interstitial space of packed beds, i.e., of those between and around the fine particles. The obtained results are compared to dimensional considerations concerning the stagnant boundary layer and its hydrodynamics available from literature data.

Experimental and Procedural Section

The 4.6 × 150 mm poly(arylether-ether-ketone) columns were professionally packed and consolidated using the slurry technique (Grom Analytik + HPLC GmbH, Herrenberg, Germany),[61,62] following the detailed instructions of the respective manufacturer. The PEEK material allows the columns to be packed and operated at pressures up to 350 bar and also shows an excellent magnetic susceptibility characteristics.[63] ^{1}H PFG-NMR measurements were made at 23 ± 0.5 °C on a 0.5 T NMR spectrometer. A more detailed description of the NMR hardware configuration and the liquid chromatography implementation can be found in a previous article.[54] Solvents were of LiChrosolv quality (Merck, Darmstadt, Germany) and degassed with helium before use.

Some characteristics of the packing materials used in this work are listed in Table 1. Particle characterization (mean diameter and standard deviation of particle size distribution) was performed by laser light scattering on a Coulter LS 130 particle size analyzer (Beckman Coulter, Inc., Fullerton, CA). Two of these supports are based on a polystyrene (PS) matrix cross-linked with divinylbenzene (DVB). One is a so-called perfusive support with a rather bimodal intraparticle pore network, which in this case is due to the hierarchical design of these particles (POROS 50 R2 from PerSeptive Biosystems,

TABLE 1: Some Characteristics of the Spherical-Shaped, Rigid Porous Particles

properties: material	YMC ODS-A S50	POROS 50 R2	SOURCE 30Q
mean diameter, d_p [μm]	50.2	49.6	30.7
standard deviation [μm]	10.6	9.5	0.7 ($<0.03d_p$)
matrix	C18-bonded silica, fully endcapped	cross-linked PS-DVB, hierarchically structured	cross-linked PS-DVB, quaternary ammonium
internal porosity[a]		~ 0.5	
average pore sizes [Å]	120 ± 15, unimodal distribution	6000−8000, 500−1500; bimodal distribution	200−10000, unimodal distribution

[a] According to the information provided by the respective manufacturer.

Wiesbaden, Germany).[23,64] The second consists of extremely monodisperse spheres, which is due to the salient features of the Ugelstad method[65] on which the particles are based, with a comparatively broad, unimodal intraparticle pore size distribution (SOURCE 30Q from Amersham Pharmacia Biotech, Freiburg, Germany). These monosized beads are substituted with quaternary ammonium groups which are attached to the matrix via long, hydrophilic spacer arms (strong anion exchanger). In addition to the two PS-DVB supports we used conventional reversed-phase particles based on a porous silica matrix (YMC•GEL ODS-A S50 from YMC Europe, Schermbeck, Germany).

For an ideal PFG-NMR experiment[66] and in the absence of any spatial localization gradients the normalized echo amplitude, $E(\mathbf{q},\Delta)$, bears a direct Fourier relation with the Lagrangian averaged propagator, $\bar{P}(\mathbf{R},\Delta)$, of the fluid molecules[67−69]

$$E(\mathbf{q},\Delta) = \frac{S(\mathbf{q},\Delta)}{S(0,\Delta)} = \int_{\mathbf{R}} \bar{P}(\mathbf{R},\Delta)\exp(i2\pi\mathbf{q}\cdot\mathbf{R})\, d\mathbf{R} \qquad (4)$$

The displacement probability distribution $\bar{P}(\mathbf{R},\Delta)$ gives the probability for any fluid molecule in the sample to travel a net displacement, $\mathbf{R}$, over time Δ in the direction of the applied pulsed magnetic field gradients of amplitude $|\mathbf{g}|$ and duration δ.[69] This gradient area defines the vector $\mathbf{q} = (2\pi)^{-1}\gamma\delta\mathbf{g}$ in $\mathbf{q}$-space, which is the space reciprocal to the dynamic displacement $\mathbf{R}$.[70−72] Thus, $\bar{P}(\mathbf{R},\Delta)$ can be reconstructed directly from the PFG-NMR signal by Fourier transform of $E(\mathbf{q},\Delta)$ with respect to $\mathbf{q}$. When on the observational time scale both the intraparticle diffusion and the convection-driven interparticle dispersion processes of the fluid molecules are Gaussian in nature,[54] the net amplitude attenuation of $E(\mathbf{q},\Delta)$ as a function of $\mathbf{q}$ is modulated, as long as the exchange between stagnant intraparticle and moving interparticle fluid is still incomplete over time Δ, by the respective two (also Gaussian) decay envelopes representing the intraparticle diffusivity D_{intra} and the apparent axial dispersion coefficient $D_{ap,a}$. Including in general the possibility of differences in the longitudinal (T_1) and transverse (T_2) relaxation time characteristics of the fluid molecules in the intra- and interparticle pore space environments,[73,74] we then obtain for $S(\mathbf{q},\Delta)$[68]

$$S(\mathbf{q},\Delta) = \sum_{n=1}^{2} A_n(\Delta)\exp\left[-4\pi^2\mathbf{q}^2 D_n\left(\Delta - \frac{\delta}{3}\right) - \frac{(\kappa_2 - \kappa_1)}{T_{1,n}} - \frac{2\kappa_1}{T_{2,n}}\right] \qquad (5)$$

Here, κ_1 and κ_2 denote the time of the (nonselective) second and third 90° r.f. pulse in the pulsed field gradient stimulated echo sequence used in this work.[75,76] On the basis of the dynamic displacements $\mathbf{R}$ over time Δ, the $A_n(\Delta)$ in this case represent the number of fluid molecules which have remained in stagnant regions of the packed bed or which have (at least once) participated in the interparticle flow, respectively. Experiments at different observation times Δ (κ_2 varied) were generally performed with a constant gradient pulse duration ($\delta = 2.5$ ms and $\delta \ll \Delta$) but incremented gradient amplitude, taking 64 $\mathbf{q}$-steps in the range of $\pm\mathbf{q}_{max}$ and up to 48 phase-alternated signal averages at each value of $\mathbf{q}$. By keeping κ_1 fixed, the contribution of transverse relaxation in eq 5 is also constant. Echoes were acquired on-resonance and were phased individually to extract the net amplitude modulation of $S(\mathbf{q},\Delta)$ at a given flow rate and observation time. For the calculation of D_{intra} and $A_{intra}(\Delta)$ individual measurements were repeated at least three times, with $r^2 > 0.9996$ for the best fit of the raw data to eq 5 and a reproducibility of the results within 5%.

All calculations were performed using IDL (Interactive Data Language, Research Systems Inc., Boulder, CO). To account for the contribution of intraparticle longitudinal relaxation over time $(\kappa_2 - \kappa_1) = (\Delta - \kappa_1)$ to the slope of the $A_{intra}(\Delta)$ vs Δ curve (cf. Equation 5), combined T_1/T_2 ^{1}H relaxation time measurements were made with a standard inversion−recovery technique (T_1), incorporating a proper echo-train (T_2). These measurements did not reveal the existence of discrete T_1 distributions for the intraparticle and the interparticle fluid molecules. Although the surface-to-volume ratios of the respective pore spaces are different, it suggests that surface relaxation is not strong enough to impart a significant difference in longitudinal relaxation behavior. It is probably caused by the low-field NMR measurements (^{1}H 20.35 MHz), combined with the extremely low amount of paramagnetic impurities present in these chromatographic media and the respective chemical modification of the particles (internal and external) surfaces. In the case of the porous silica particles (the only inorganic oxide-based particles used in this work), for example, the Fe^{3+} contamination of the parent silica is well below 10 ppm. From a chromatographic point of view, surface trace metal impurities would give strong Lewis acid adsorption sites which adversely affect performance.[77] Further, the originally polar, silanolic surface has been chemically derivatized by a bonded alkyl layer (high coverage of C_{18} chains), including a C_1-endcapping of residual silanols. It is a classical chromatographic support used for many reversed-phase separations, most applicable for polar to moderately nonpolar samples. Thus, returning to the NMR standpoint, surface (and bulk) trace metal activity is very small, and the respective sites become sterically almost inaccessible.

Results and Discussion

With respect to the actual fluid dynamics encountered in the experiments, Figure 1a shows a representative single-fluid phase averaged propagator distribution, $\bar{P}(\mathbf{R},\Delta)$, recorded in the axial (flow) direction, at a volumetric flow rate (F_v) of 8.0 mL/min and an observation time (Δ) of 25 ms. This quantitative displacement probability distribution illustrates both the potential steady-state character (regarding intraparticle diffusion) and transient nature (with respect to the stagnant mobile phase mass transfer kinetics) of these PFG-NMR measurements. For

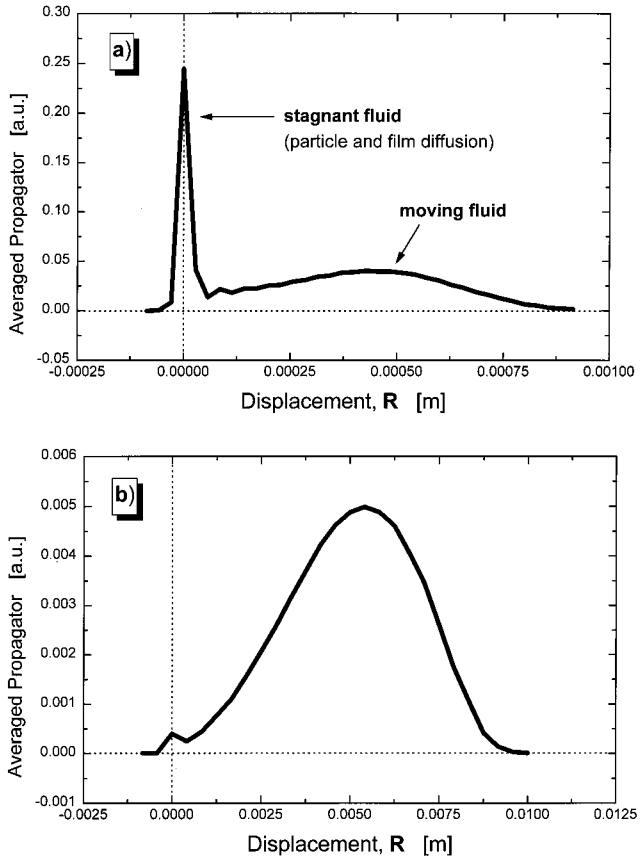

Figure 1. Axial displacement probability distributions of the fluid molecules (water) in a packed bed of porous particles (YMC ODS-A S50). 4.6 × 150 mm PEEK column; volumetric flow rate F_v of 8.0 mL/min. The stagnant, purely diffusive fluid is found centered at zero net displacement. Observation times, $\Delta = 25$ ms and $\Delta = 420$ ms.

example, under the experimental conditions (Figure 1a), we find 24.6% of the water molecules in the packed bed being left unexchanged in the deep stagnant pools inside the porous C18 silica particles. By a systematic variation of the observation time, this actually transient character of the measurement allows to record the stagnant mobile phase mass transfer kinetics toward a complete exchange between stagnant and moving fluid in the packed bed.[54] As is demonstrated in Figure 1b, at $\Delta = 420$ ms only less than 0.5% of the stagnant water remains unexchanged. On the basis of tortuosity factor, the average size and spherical shape of the particles it should be finished after some characteristic exchange time, Δ_e, assuming that the fluid molecules have to travel a net distance of $d_p/2$ (from the spheres center to its external surface) to leave the porous particles completely[1]

$$\Delta_e = \frac{\tau_{intra}}{2\,D_m}\left[\frac{d_p}{2}\right]^2 \qquad \text{with} \qquad (\sqrt{\langle \mathbf{R}^2_{intra}\rangle})_{\Delta=\Delta_e} = \frac{d_p}{2} \quad (6)$$

We will see how this dimensional consideration matches the experimental data. On the other hand, the root-mean-squared (rms) translational displacement of the yet unexchanged intraparticle fluid molecules (as long as $\Delta < \Delta_e$, cf. Figure 1a) probed in the direction of the applied magnetic field gradient is given by

$$\sqrt{\langle \mathbf{R}^2_{intra}\rangle} = (2\,D_{intra}\Delta)^{1/2} \quad (7)$$

For the particle dimensions of the chromatographic media, mobile phase diffusivities and observation times selected for this study, the corresponding diffusive displacements of the

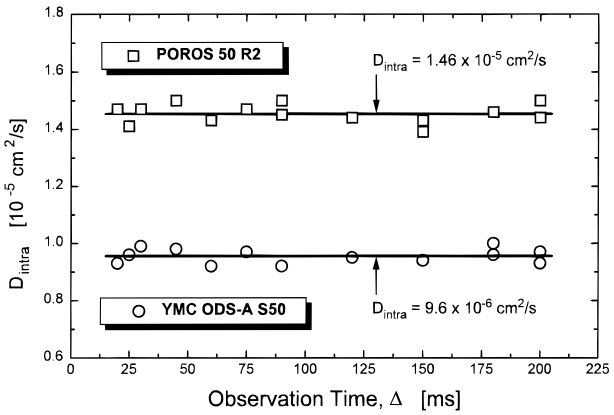

Figure 2. Intraparticle self-diffusion coefficient of water in two of the chromatographic media as a function of the observation (diffusion) time; $F_v = 8.0$ mL/min.

stagnant fluid molecules are much larger than the range of typical inhomogeneities in either intraparticle pore network. In this respect, the experiment then provides a steady-state pore diffusion measurement which allows to extract an effective intraparticle diffusion coefficient, D_{intra}. Furthermore, these data necessarily have to be consistent with the characteristic decay rates of the aforementioned, diffusion-limited exchange kinetics. These two series of data in fact provide us with complementary information, not only in view of the stagnant (diffusion-controlled) boundary layer existing at the particles external surface under laminar flow conditions.[5] Consequently, the obtained results are now discussed separately under the light of these aspects.

Intraparticle, Effective Self-Diffusion Coefficients. The single fluid phases used in this study consist of water, acetonitrile, methanol, 2-propanol, and methylene chloride. These nonsorbed molecules are rather small compared to the pore constrictions encountered inside the porous particles. Thus, hydrodynamic friction is negligible and the directly measured intraparticle rms translational displacements (and D_{intra}) at long enough times approach the values given by the topology, i.e., the interconnectiveness of the pore network, by means of eq 3 (with $K_H^{-1} \approx 1$). Because only single-fluid phases are used, the calculated values of D_{intra} represent the corresponding self-diffusion coefficients.[78]

Because of different mean pore sizes, pore size distributions, and pore interconnectivities in the particles (Table 1), the associated transport heterogeneities in the respective pore networks are expected to be characterized by different correlation times and length scales. Figure 2, however, demonstrates that, within the range of observation times Δ encountered in the measurements, D_{intra} in fact is found independent of this parameter and in the tortuosity-limited regime of the respective pore network, corresponding to a steady-state pore diffusion in either case (i.e., such that $D_{intra} \equiv D^{eff}_{intra} = D_m/\tau_{intra}$). Otherwise, D_{intra} would depend on Δ and still decrease toward the tortuosity asymptote. The attainment of a steady-state pore diffusion, together with its verification here by the data shown in Figure 2 is also important with respect to the average particle diameters (Table 1). For example, when larger pores start to contribute to the intraparticle porosity, the pore network becomes inhomogeneous on an increasing scale that may approach the size of the whole particle. On the other hand, as long as the asymptotic (tortuosity limited) diffusion regime is reached, the tortuosity factor of a network consisting of 100% small pores is the same as with 100% large pores.[42]

TABLE 2: Intraparticle Tortuosity Factors, $\tau_{intra} = D_m/D_{intra}$

fluid: material	YMC ODS-A S50	POROS 50 R2	SOURCE 30Q	D_m [10^{-5} cm^2/s]
water	2.24	1.47	2.08	2.15
acetonitrile	2.29	1.56	2.16	3.83
methanol	2.23	1.51	2.11	2.23
2-propanol	2.15	1.43	2.03	0.58
methylenechloride	2.21	1.53	2.09	3.07

The intraparticle tortuosities measured by PFG-NMR are summarized in Table 2, and the discussion necessarily focuses on the topology of the three pore networks. The most striking feature of these data is the tortuosity factor of the gigaporous particles (POROS 50 R2) which, for all the mobile phases considered in this work, is significantly lower than that of the other two supports. In contrast to conventional media, these POROS beads have two discrete classes of pores interconnected in a well-correlated manner.[23] The bidisperse particles are made by inter-adhering PS-DVB microspheres which are fused into the final, continuous particle structure by using several steps of clustering. This process creates a first set of 6000−8000 Å pores which transect the whole particle (throughpores) and a second, more abundant set of smaller pores with 500−1500 Å in diameter. Because of the hierarchical design of these particles, the spacing between throughpores is seldom greater than 1 μm, thereby reducing diffusion path lengths in the interconnecting smaller pores to below that distance.[23] Thus, the actual correlation of interconnectivity between the large and small pores creates a gigapore network ($d_{pore}/d_p > 10^{-2}$) that spans the whole particle and minimizes diffusion distances in the macroporous domain ($d_{pore} > 500$ Å). On the basis of the lower network tortuosities, the stagnant mobile phase mass transfer rates within such hierarchical bidisperse networks will be superior compared to bidisperse structures in which the pore sizes are assigned at random.[79,80] The transport behavior of such nonrandom bidisperse pore networks in fact is expected to be closer to that of the individual giga- and macropore (or macro- and mesopore) networks arrayed in parallel rather than to the behavior of the corresponding random network with bimodal pore size distribution.[81] Although the correlation of interconnectivity is now well-recognized as being of prime importance in the design of (bidisperse) porous particles,[79−83] surprisingly little experimental data (like D_{intra}) are available which directly characterize the topology of these hierarchically structured pore networks compared to less correlated ones.

In contrast to the 50-μm PS-DVB particles (POROS 50 R2), the pore network of the 30-μm beads (SOURCE 30Q) is characterized by a relatively broad, unimodal pore size distribution, with the interconnection of the larger and smaller pores being rather uncorrelated, i.e., comparatively random. Thus, the large and small pores do not form interconnected, distinct pore networks, and the tortuosity factor then increases due to the shielding of large pores by small ones (Table 2).[84] Finally, the yet slightly higher intraparticle tortuosity factors found for the mesoporous silica-based particles (YMC ODS-A S-50) could be caused by the presence of a larger number of dead-end pores. However, the exact topological differences of the latter two pore networks are hardly known with sufficient accuracy to allow such small distinctions to be made meaningfully. Nevertheless and as a more general trend in view of the arguments followed in this work, the tortuosity factors observed for the nonhierarchical intraparticle pore networks are significantly higher than those found for the hierarchical bidisperse particles; however, the values are still close to 2. This value has been predicted for an isotropic porous medium,[31] recalling the basic arguments of Carman[85] in context of the parallel-pore model. Other arguments suggest a tortuosity factor of 3 for a particle network consisting of randomly oriented, nonintersecting cylindrical pores where each straight capillary covers the length of the whole particle.[86]

TABLE 3: Cubic Lattices of Identical Spheres at Dense Packing

cubic lattice	coordination number	interstitial porosity	tortuosity factor
SC	6	0.476	1.38
BCC	8	0.320	1.47
FCC	12	0.259	1.62

With respect to the remarkably lower value of τ_{intra}, the hierarchical bidisperse particles can be viewed as consisting of loosely packed agglomerates being responsible for the several types of pores finally present in the matrix.[23] Thus, the actual network within a single support particle resembles itself, to some degree at least, the overall (intra- and interparticulate) pore space typically encountered in packed beds of porous particles. Using this similarity for a moment, Table 3 summarizes some properties of cubic, i.e., regular lattices of identical, impenetrable spheres at dense packing so that the hard spheres are just touching each other.[87,88] An increase in the distance between neighboring spheres (or corresponding decrease, while spheres start to overlap) causes also an increase (decrease) in the interstitial porosity and in the effective, translational diffusivity of small molecules entrained in the respective pore network.[89] Further, any kind of positional disorder introduced into the particle arrangement (at a constant porosity) leads to an increased lengthscale of heterogeneities and a higher tortuosity factor.

Given the fact that a conservative estimate for the intraparticle porosity of the hierarchically structured particles (POROS 50 R2) is 0.5,[23] comparison with Table 3 and the tortuosity factors given in Table 2 suggests that neither regular (cubic) lattice at dense packing is appropriate to describe well this pore network. On the basis of a pure value identification, the simple cubic arrangement comes closest. Not surprisingly, it is the one with the smallest coordination number. These observations are in agreement with recent findings that the pore structure of these particles rather behaves like an inhomogeneous assemblage of loosely packed microspheres.[90] This situation is quite different from the one typically encountered in random close-packed beds of chromatographic columns. Here, the interparticle porosity is usually found to vary between 0.36 and 0.4. More extreme values are possible, depending on packing and operational procedures, as well as on particle characteristics.[91]

Remarkably low intraparticle tortuosity factors have also been postulated for hierarchically structured, spherical, porous zirconia particles using PFG-NMR methods.[92,93] Even though the authors did not report the net effective, intraparticle diffusion coefficients, the trend in their diffusivity data at least indicates values of τ_{intra} between 1.5 and 2 (i.e., below the isotropic porous medium value). This behavior has been attributed to the very open packing of the colloids within the particles.[92] Higher tortuosity factors, yet close to 2, have been reported for protein diffusion within macroporous size-exclusion chromatographic media.[43,94] By restricting the diffusing species to individual

particles using excluding solvent in the interparticle void space, intraparticle labeled-protein (tracer) diffusion could be studied selectively by fluorine PFG-NMR.

All these data seem to indicate a general trend for the actual hierarchy in pore structure and the associated tortuosity factor. However, they also call for further studies demonstrating systematically its dependence on the processing conditions and thereby achieved correlation (or randomness) of interconnection between differently sized pores. These experimental data will help in the refinement of chromatographic separations[95] and in the development of a numerical approach (and model validation in general) for predicting the interrelationship of structure and transport in porous adsorbent particles.[96]

Another aspect closely related to the intraparticle diffusivity of the hierarchically structured particles (POROS 50 R2) merits attention. On the basis of dimensional considerations and morphological observations concerning the gigaporous (through-pore) network, it has been proposed that these hierarchically bidisperse particles can be operated under perfusion conditions, i.e., in such a mode that both intraparticle forced-convection and diffusion contribute to the fluid transport in the gigapores, while only diffusion is active in the smaller macropores.[23] According to Liapis and McCoy,[97] the term "perfusion chromatography" refers to any chromatographic system in which the intraparticle fluid velocity is nonzero. The effect of intraparticle convection is an enhancement of the overall rate of mass transfer in the particle, thereby improving the efficiency of diffusion-limited chromatographic operations. It has been pointed out conceptually that its contribution can be well-represented by a convection-augmented effective, intraparticle diffusivity.[23,98] The first experimental direct confirmation of net flow through gigaporous particles has been reported recently in a test apparatus that isolates single particles.[90] Figure 3a however shows that within the range of hydrodynamic conditions encountered in our current work, D_{intra} in all the chromatographic media remains constant in the purely diffusive, tortuosity-limited regime ($D_{intra} < D_m$ and $\tau_{intra} > 1$). As can be concluded from Figure 3b which records the accompanying pressure drop over the 4.6 × 150 mm columns and also from a comparison with the results reported by Pfeiffer et al.,[90] the actual pressure gradient across individual particles in the packed bed is probably too small to act as a driving force for any measurable intraparticle forced-convection assisting or even dominating fluid transport. Thus, compared to the other two supports, the low tortuosity factor recorded for the hierarchically bidisperse particle structure resembles diffusion control in a yet superior pore network, without the need to postulate, at this stage at least, the operation of a perfusive mechanism.

Next, we turn to the stagnant mobile phase mass transfer kinetics which is associated with the exchange of fluid molecules between the investigated purely diffusive intraparticle pore network (already with a preknowledge of the respective values of D_{intra}) and the diffusive-convective interparticle void space, how we can acquire and analytically describe it, and to the complementary information it provides.

Nonsteady-State Diffusion into/out of Spherical Particles. On the basis of the net (dynamic) displacements of the fluid molecules over time Δ, the propagator formalism provides a quantitative characterization of the stagnant and moving fluid in the packed bed using the PFG-NMR technique. Averaged propagator distributions recorded at increasing observation times thus directly monitor the progressive diffusion out of the spherical particles.[60] Those fluid molecules which leave the spheres and participate in the interparticle forced convection

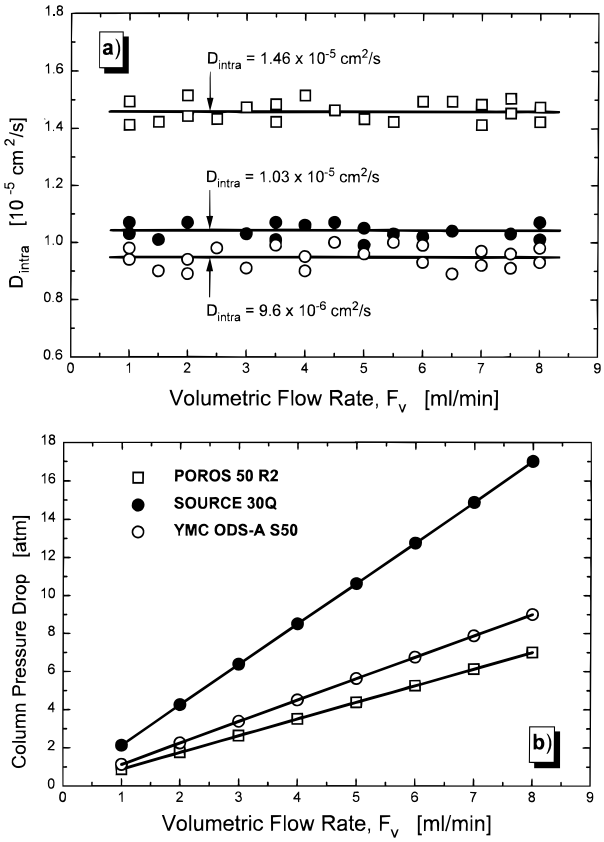

Figure 3. Intraparticle self-diffusion coefficients of water in (a) the chromatographic media and (b) column pressure drop as a function of the volumetric flow rate; Δ = 60 ms.

within (increased) time Δ will no longer contribute to the ensemble of purely diffusive fluid molecules which is found centered at zero net displacement. At long enough observation times the stagnant fluid fraction has disappeared and exchange is complete (cf. Figure 1). Consequently, this situation resembles the general case of an unsteady-state diffusion of a solute into/out of spherical, porous particles in which the spheres are emptied or, vice versa, filled by diffusion, and it can be treated analytically in the same manner. Thus, when we then consider the case in which the diffusion (no chemical reaction yet) from the bulk of the particle of radius r_p to its surface is radial, i.e., the initial and surface conditions are such that the concentration C of a solute only depends on r and time Δ, the diffusion equation for a constant diffusion coefficient takes the form[99]

$$\frac{\partial C}{\partial \Delta} = D_{intra}\left[\frac{\partial^2 C}{\partial r^2} + \frac{2}{r}\frac{\partial C}{\partial r}\right] \tag{8}$$

With the substitution $u = Cr$ and assuming an initial concentration $C_i(r)$ in the sphere and surface concentration $C_s(\Delta)$, the equations for u become[99]

$$\frac{\partial u}{\partial \Delta} = D_{intra}\frac{\partial^2 u}{\partial r^2} \qquad \text{for} \qquad 0 \le r < r_p \tag{9}$$

with

$u = 0$ when $r = 0$ and $\Delta > 0$

$u = C_s(\Delta)\cdot r_p$ when $r = r_p$ and $\Delta > 0$

$u = C_i(r)\cdot r$ when $0 \le r < r_p$ and $\Delta = 0$

These are the equations for diffusion in a slab of thickness r_p, with its ends at $r = 0$ and $r = r_p$ kept at zero and $C_s(\Delta)r_p$ respectively, and with the initial distribution $C_i(r)r$. Thus, the problem of radial diffusion in (uniform) spheres can be deduced from the solution of the corresponding linear problem. Equation 9 is of the same form as the analogous differential equation characterizing heat transfer for unsteady-state heat conduction in plane sheets (and spheres). For that case, Carslaw and Jaeger[100] have derived an analytical solution which is the product of a trigonometric and an exponential series. In terms of the differential equation (eq 9) and the boundary conditions that the sphere initially is at a uniform concentration ($C_i(r)$ = constant = C_0) and that the concentration at the surface of the sphere is maintained steady at zero ($C_s(\Delta)$ = constant = 0), which causes the sphere to be emptied by diffusion, the average amount of diffusing substance still remaining in the sphere at any time, $A_{intra}(\Delta)$, is given by[100]

$$\frac{A_{intra}(\Delta)}{A_{intra}(0)} = \frac{6}{\pi^2}\sum_{n=1}^{\infty}\frac{1}{n^2}\exp\left[-n^2\pi^2\frac{D_{intra}\Delta}{r_p^2}\right] \qquad (10)$$

The corresponding solution for small exchange times (and small values of the dimensionless parameter $\zeta = (D_{intra}\Delta/r_p^2)$ is

$$\frac{A_{intra}(\Delta)}{A_{intra}(0)} = 1-6\left[\frac{D_{intra}\Delta}{\pi r_p^2}\right]^{1/2} + \frac{3D_{intra}\Delta}{r_p^2} - 12\left[\frac{D_{intra}\Delta}{r_p^2}\right]^{1/2}\sum_{n=1}^{\infty}\text{ierfc}\frac{nr_p}{\sqrt{D_{intra}\Delta}} \cong 1-6\left[\frac{\zeta}{\pi}\right]^{1/2} + 3\zeta \qquad (11)$$

At large observation (exchange) times Δ, on the other hand, eq 10 approximates to a simple exponential decay function

$$\frac{A_{intra}(\Delta)}{A_{intra}(0)} = \frac{6}{\pi^2}\exp[-\pi^2\zeta] \qquad (12)$$

Figure 4a shows the dependence on the observation time of the amount of stagnant water entrained in the respective particle packings. At first glance, all the mass transfer data are well-described by eq 10 and values of the constant $B = D_{intra}\pi^2/r_p^2$ obtained from the best fit of the data to this equation are summarized in Table 4, together with the corresponding values obtained by use of eqs 11 and 12 at short and long times, respectively. Evidently, the experimental approach followed in this work using single-fluid phases, while monitoring a (fictitious) diffusional emptying of the porous particles (Figure 4a), avoids problems that could arise due to a nonconstant (i.e., concentration-dependent) diffusion coefficient during transient diffusion experiments.[101]

A closer look at the data however reveals slight, but characteristic deviations from the best fit to eq 10 which inherently assumes, apart from a constant diffusion coefficient, a uniform diameter of the spherical particles. In this respect, both the particle shape and a size distribution will have a pronounced effect on the experimental mass transfer curves.[102] Compared to the predictions of eq 10, smaller-than-average particles will cause a higher initial rate, while the larger-than-average particles will be responsible for lower decay rates at long times, especially when $A_{intra}(\Delta)/A_{intra}(0)$ becomes smaller than about 0.2. This is exactly what we observed for the supports with the larger particle size distribution (Figure 4b and Table 4). In view of the fact that the monodisperse polymer particles (SOURCE 30 Q) have a remarkably narrower particle size distribution than the other two supports (cf. Table 1),[65] the effect was investigated further. In passing we note that the influence of the particle shape is not addressed separately and that a perfect spherical shape of the particles is assumed, a fairly reasonable assumption for these modern supports as can be shown by electron microscopy of the media.

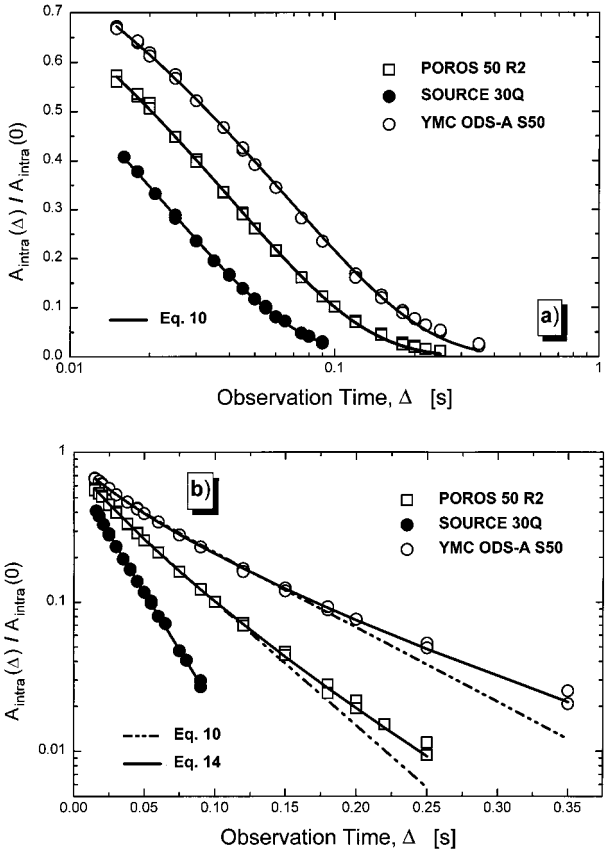

Figure 4. (a) Unsteady-state diffusion and total intraparticle fluid fraction unremoved as a function of the observation time. Mobile phase, pure water. F_v = 4.8 mL/min (30 μm particles) and 8.0 mL/min (50 μm particles). (b) The effect of the finite particle size distribution becomes evident, best fit of the data to eqs 10 and 14.

Introducing a particle size distribution function $f(r_p)$, where $f(r_p)dr_p$ is the fraction of particles having a radius in the range $(r_p + dr_p)$, the appropriate expression for describing diffusion out of the spherical particles is

$$\frac{A_{intra}(\Delta)}{A_{intra}(0)} = \frac{6}{\pi^2}\sum_{n=1}^{\infty}\frac{1}{n^2}\int_{r_p=0}^{\infty} f(r_p)\exp\left[-n^2\pi^2\frac{D_{intra}\Delta}{r_p^2}\right]dr_p \qquad (13)$$

The particle size distributions of the supports have been measured and particle sizes were found to be normally (Gaussian) distributed. When μ and σ, respectively, denote the mean and standard deviation of the particle radius, eq 13 then becomes[102]

$$\frac{A_{intra}(\Delta)}{A_{intra}(0)} = \frac{6}{\sigma\pi^2\sqrt{2\pi}}\sum_{n=1}^{\infty}\frac{1}{n^2}\int_{r_p=0}^{\infty}\times \exp\left[-\left(\frac{r_p-\mu}{\sigma\sqrt{2}}\right)^2 - n^2\pi^2\frac{D_{intra}\Delta}{r_p^2}\right]dr_p \qquad (14)$$

TABLE 4: Exchange Kinetics $B = D_{intra}\pi^2/r_p^2$ and D_{intra} for Water

parameter	material		
	YMC ODS-A S50	POROS 50 R2	SOURCE 30Q
B (eq 10)	11.51	19.11	35.48
B (eq 11)[a]	11.94	19.54	*e*
B (eq 12)[b]	8.62	16.47	35.53
D_{intra} [10^{-5} cm^2/s], eq 10[c]	0.73	1.21	0.81
D_{intra} [10^{-5} cm^2/s], eq 14[d]	0.80	1.30	0.83

[a] For $A_{intra}(\Delta)/A_{intra}(0) > 0.45$. [b] For $0 < A_{intra}(\Delta)/A_{intra}(0) < 0.15$. [c] Based on the mean particle radius alone. [d] Using the mean particle radius and its standard deviation (cf. Table 1). [e] The initial part of the mass transfer data is missing due to the smaller particle size and the lower limit of the observation times.

TABLE 5: D_{intra} from Exchange Kinetics and Steady-State Pore Diffusion

parameter	YMC ODS-A S50[a]		POROS 50 R2[a]		SOURCE 30Q[a]	
	H_2O[b]	CH_3CN[b]	H_2O[b]	CH_3CN[b]	H_2O[b]	CH_3CN[b]
D_{intra} [10^{-5} cm^2/s], eq 14	0.80	1.45	1.30	2.18	0.83	1.48
D_{intra} [10^{-5} cm^2/s], Table 2	0.96	1.67	1.46	2.46	1.03	1.77
δ_{film} [μm]	2.2	1.9	1.7	1.7	1.6	1.4
δ_{film}/d_p	0.044	0.038	0.034	0.034	0.052	0.046
Pe[c]	491	275	491	275	177	99

[a] Material. [b] Fluid. [c] Pe = particle Peclet number $= 4F_v d_p/(\epsilon_{inter}\pi d_c^2 D_m)$, with ϵ_{inter}, the interparticle porosity (assumed 0.38) and d_c, the column diameter (0.46 cm).

With the information about μ and σ, obtained by means of independent measurements, eq 14 was evaluated numerically and an indeed excellent agreement with the experimental data could be established (Figure 4b). The values of D_{intra} obtained by this procedure (eq 14) are also given in Table 4.

Thus, by taking proper account of the supports particle size distribution (and the shape), a very satisfactory quantitative description of the experimental mass transfer data may be obtained from the diffusion equation, and for the moderate particle size distributions encountered in this work, already eq 10 provides a good working definition of the intraparticle diffusivity. With the monodisperse particles hardly any error is introduced in the determination of D_{intra} by assuming a uniform particle size (eq 10). For the other two supports, the effect of the broader size distribution leads to an upward correction of D_{intra} of the order of 8%. These particle size distributions are still representative for today's high-performance packings where the distributions tend to be no wider than about 25% around the mean.[61] The results are in agreement with theoretical analyses on this topic,[103,104] which indicate that the particle size distribution has a significant influence on chromatographic performance only for much broader or asymmetric distributions.

The same series of measurements and calculations reported for water (Figure 4 and Table 4) were also made using acetonitrile as the mobile phase, with similar results. These values of D_{intra} for water and acetonitrile (eq 14), together with the corresponding data obtained from the steady-state pore diffusion measurements (Table 2) are summarized in Table 5. It is now instructive to compare the agreement between these two sets of D_{intra} values because they necessarily have to be consistent in terms of the inherently associated fluid dynamics, network topology and particle dimensions.

Comparison between Steady-State and Transient Measurements. There exists a fair qualitative agreement between these two approaches, but it becomes evident that the intraparticle diffusivities based on the exchange kinetics are systematically smaller (between 10 and 20%), even though these data have been corrected for the effects of the particle size distribution. In turn, the particles shape or size distribution does not influence the values of D_{intra} which are calculated from the steady-state pore diffusion measurement, because the rms translational displacement of the stagnant fluid over time Δ is here directly measured (cf. Figure 1 and eq 7). Thus, the latter values of D_{intra} represent the time-weighted average of the fluid molecules in stagnant regions of the packed bed. On the other hand, the values of D_{intra} extracted from the mass transfer curves are based on the predetermination of the stagnant fluid fractions over times Δ, which represent the volume-weighted average of fluid molecules in (any) stagnant regions of the packed bed, and D_{intra} is then obtained from the decay rate of these curves (using eq 10 or 14). Included in these data, $A_{intra}(\Delta)/A_{intra}(0)$ vs Δ (Figure 4), is the contribution of the stagnant boundary layer which exists under laminar flow conditions at the particles external surface.[5,13] When the fluid molecules diffuse out of the particles and reach the spheres boundaries they first move through this stagnant film, where the transport normal to the surface is dominated by diffusion,[4] before they enter the flow streamlines. The effect of the boundary layer, an idealized stagnant, spherically symmetric film, is to slightly enlarge each particle.[9]

Considering the effect of the stagnant boundary layer on the time-weighted average value of D_{intra}, any influence is due to the higher value of the diffusivity within this film ($D_{film} \approx D_m$) compared to the situation in the intraparticle pore space ($D_{intra} = D_m/\tau_{intra}$). Following a fluid molecule from the center of the spherical particle to its external surface, a characteristic time Δ_{intra} of 325 ms is calculated based on eq 6 for travelling this net distance of r_p (using water and the porous C18 silica particles as an example, $d_p = 50$ μm and $\tau_{intra} = 2.24$). Assuming a film thickness of 2.0 μm ($0.04d_p$), the time Δ_{film} it takes the fluid molecules to pass this stagnant boundary layer (moving normal to the particle surface) is less than 1 ms ($D_m = 2.15 \times 10^{-5}$ cm^2/s). When each stagnant fluid molecule has enough time to sample both the intraparticle pore space and the film region, the time-weighted average of the diffusion coefficients D_{stag} of the stagnant fluid can be expressed as

$$D_{stag} = \frac{\sum_n D_n \Delta_n}{\sum_n \Delta_n} = \frac{(D_{intra}\Delta_{intra}) + (D_{film}\Delta_{film})}{\Delta_{intra} + \Delta_{film}} \cong D_{intra} \qquad (15)$$

Using for D_n and Δ_n the values calculated in the above example, we find $D_{stag} = 1.0038D_{intra}$. Unfortunately, this

situation corresponds to observation times where the stagnant mobile phase mass transfer becomes already complete, because in terms of probability, fluid molecules originally located at the center of the particle must also be able to reach the stagnant boundary layer so that eq 15 can be applied (i.e., $\Delta \approx \Delta_{intra} = \Delta_e$, eq 6). But even at the shorter observation times, where the effective, intraparticle self-diffusion coefficients are typically measured (cf. Figure 2), a similar dimensional consideration shows that $D_{stag} \approx D_{intra}$ to within 1.5%. Thus, the influence of the slightly different diffusivity experienced by the fluid molecules in the stagnant film enveloping the spheres on the determined values of the steady-state intraparticle diffusivities (given in Table 2 in form of the respective tortuosity factors) can be neglected.

The situation is different for the reported transient measurements. The volumetric effect of the stagnant boundary layer manifests itself in an additional (diffusional) mass transfer resistance external to the spheres. Thus, the actually stagnant interstitial fluid in the packed bed at a given Peclet number dictates an effective interparticle porosity available for flow.[5] On the other hand, the mean particle radius enters in eqs 10 and 14 as a squared "constant". From an intraparticle viewpoint, this immediately suggests the introduction of a hydrodynamically effective particle radius (including the film thickness δ_{film}) to account for its contribution to the recorded mass transfer kinetics. It certainly represents an oversimplified picture of the (considerably streamlined) stagnant fluid at the free surface of the particles and in the cusp regions around their contact points, but nevertheless provides a tractable starting point within this study to cover the average effect.

For the calculation of the data reported in Tables 4 and 5, the mean particle radius was used as determined from the particle size distribution measurement. Now, the accurate values of the steady-state pore diffusivities act as a boarder line for D_{intra} and the systematically lower diffusivities obtained from the exchange kinetics are adjusted to these numbers by defining the hydrodynamically effective particle radius, $r_p^* = r_p + \delta_{film}$, i.e., the steady-state diffusivities (Table 2) are used as input parameters in eq 14 and the ("effective") mean particle radius, with $\mu = r_p^*$, is fitted. The values of δ_{film} obtained by this procedure are listed in Table 5. The measurements were made at a volumetric flow rate, F_v, of 8.0 mL/min in case of the 50 μm particles and at one of 4.8 mL/min with the smaller 30 μm particles due to a higher column pressure drop in this case. The corresponding (particle) Peclet numbers of each experiment are also given in Table 5. Depending on the actual hydrodynamic conditions, we find a film thickness for the different fluid phases and support particles ranging between 1.4 and 2.2 μm (i.e., up to $0.05d_p$). These data are now inspected in view of their dimension, but they are too limited to allow conclusions about the dependence of the stagnant boundary layer thickness on molecular diffusivity (H_2O and CH_3CN) and Peclet number. Compared to the 50 μm particles, the results obtained for the 30 μm spheres (Table 5, δ_{film}/d_p), however, indicate that the boundary layer is thicker at lower Peclet numbers.

The flow rate dependence (above Pe $\approx$ 50) of its thickness is an important criterion for the existence of a stagnant boundary at the interface. To confirm this observation, we conducted experiments at different flow rates and carefully recorded the complete mass transfer kinetics with purely diffusive particles. This ensures that the intraparticle diffusivity itself will be independent of Pe (cf. Figure 3a) and any significant differences in the observed exchange kinetics may then be traced back to a change in the hydrodynamically effective particle diameter. Figure 5 shows the results for acetonitrile in the column packed with the 50 μm C18 silica particles. The parameters obtained

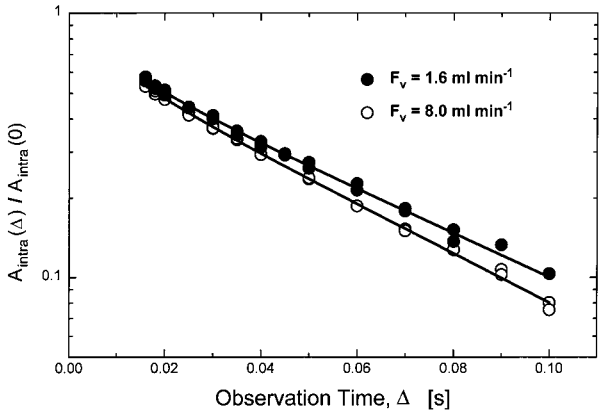

Figure 5. Influence of the flow rate on the diffusion-limited exchange kinetics. Mobile phase, pure acetonitrile. Column packed with porous C18 silica particles (YMC ODS-A S50). Best fit of the data to eq 14 (solid line).

with eqs 10 and 14 are summarized in Table 6. As may be seen, the flow rate probably has an effect and the value of D_{intra} apparently increases steadily when the mean particle radius is maintained strictly constant at its value obtained from the particle size distribution measurement.

The same kind of observation has already been made by Boyd et al.[9] in their classical work on the kinetics of ion exchange adsorption processes in a shallow-bed apparatus. For their diffusion-limited stagnant mobile phase mass transfer kinetics these authors found a clear dependence on the flow rate of the "constant" $B = D_{intra}\pi^2/r_p^2$ in eq 10. They concluded that the particles were made effectively slightly larger by a surrounding liquid film which should be an inverse function of the flow velocity.

Thus, by keeping now in our calculations the acetonitrile intraparticle diffusivity constant at its value known from the steady-state pore diffusion measurement ($D_{intra} = 1.67 \times 10^{-5}$ cm^2/s), the increase in Peclet number is accompanied by a steady decrease of the film thickness from 3.1 to 1.9 μm (r_p^* from 28.2 to 27.0 μm, Table 6). Due to the dimensions inherently involved (50 and 30 μm particles), the absolute effects are expectedly small. We now seek for dimensional estimates of the boundary layer and its dependence on the hydrodynamics available from literature data.

In an attempt to describe the interplay of convective and diffusional mixing of unsorbed solutes in the interstitial space of packed beds, Horváth and Lin[105] argued that eddy dispersion occurs only outside the stagnant film, i.e., in the liquid which is actually moving between the particles. To evaluate the thickness of this film they came up with the "free surface model" of Pfeffer and Happel[106,107] who developed it in their analytical study of heat and mass transfer to a bed of spherical particles at low Reynolds numbers. These authors found that at high Peclet (Pe) numbers the Sherwood (Sh) number depends on Pe by

$$\mathrm{Sh} \equiv \frac{k_{film} d_p}{D_m} = \Omega \mathrm{Pe}^{1/3} \qquad (16)$$

Here, k_{film} is the fluid film mass transfer coefficient and the value of Ω is a function of the interstitial porosity only, changing from 3.6 to 3.2 when ϵ_{inter} varies from 0.36 to 0.42. Fair agreement with this dependence has been obtained by Wilson and Geankoplis[108] on the basis of their electrochemical measurements (for $0.0016 < \mathrm{Re} < 55$).

TABLE 6: Flow Rate Dependence of Mass Transfer Kinetics[a]

F_v [ml/min]	Pe	D_{intra} [10^{-5} cm^2/s][b]	$r_p^* = r_p + \delta_{film}$ [μm][c]	δ_{film}/d_p	B[d]	δ_{film} [μm][e]
1.6	55	1.34	28.2	0.062	19.2	3.7
4.1	141	1.42	27.3	0.044	20.9	2.7
8.0	275	1.45	27.0	0.038	21.3	2.2

[a] Mobile phase: acetonitrile. Packing material: 50 μm C18 silica (YMC ODS-A S50). [b] Calculated with eq 14, assuming a constant mean particle radius, $r_p = 25.1$ μm (Table 1). [c] Obtained from eq 14, using a constant diffusivity, $D_{intra} = 1.67 \times 10^{-5}$ cm^2/s (Table 2). [d] $B = D_{intra}\pi^2/r_p^2$, eq 10. [e] Based on eq 17, with $\Omega = 3.6$.

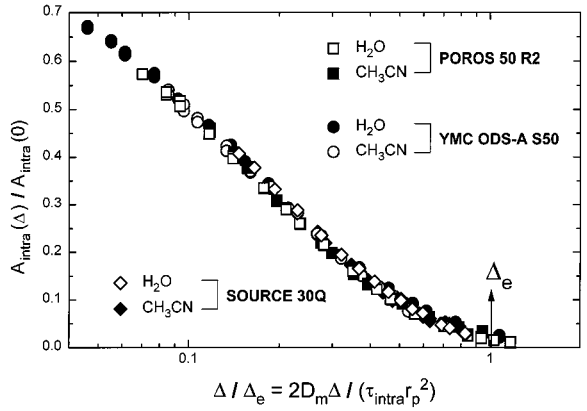

Figure 6. Total fraction of the stagnant fluid remaining unexchanged in the packed beds as a function of the observation time, normalized by the characteristic exchange time (Δ_e). Mobile phases, water and acetonitrile. $F_v = 4.8$ mL/min (30 μm particles) and 8.0 mL/min (50 μm particles).

The film thickness was then obtained by relating it to the mass transfer coefficient via the Nernst diffusion layer[105]

$$\delta_{film} = \frac{D_m}{k_{film}} = \frac{d_p}{\Omega Pe^{1/3}} \qquad (17)$$

The stagnant boundary layer thickness expected on the basis of eq 17 (strictly applicable for Pe > 50) is given in Table 6 for comparison. Although the absolute values of the film thickness obtained from our measurements are found to diverge from the calculated ones by up to 20%, they still fall into a reasonable order of magnitude and follow qualitatively the predictions of eq 17. It should be pointed out that at this stage and with the available data such a comparison should help to gain dimensional insight, rather than providing quantitative description or agreement.

Thus, by introducing a flow rate dependent, effective particle radius, which is similar to the definition of an effective (velocity dependent) interparticle porosity, the PFG-NMR approach appears promising to study the (relative) hydrodynamic behavior of the interstitial stagnant fluid volume in packed beds of porous particles. (N.B. For the sake of completeness, it has been pointed out correctly that the film mass transfer coefficient used by Horváth and Lin[105] was originally derived under conditions of a concentration boundary layer profile.[109] The correct film thickness thus would be the concentration boundary layer thickness which will be less than the Nernst diffusion layer thickness.)

Finally, we close by returning to the topological aspect of the intraparticle pore network. All mass transfer data recorded for the three packing materials are plotted in Figure 6 against the observation time which now has been normalized by the characteristic exchange time defined by eq 6. In the calculation for Δ_e the intraparticle tortuosity factors obtained from the steady-state pore diffusion measurement (Table 2) have been used. The exchange kinetics obtained for the small, nonsorbed fluid molecules in the different pore networks collapse onto a single decay curve characteristic of Fickian diffusion. It demonstrates that in this case simple geometrical aspects (particle shape, mean diameter, particle size distribution, and the tortuosity factor) are the only important parameters which characterize the stagnant mobile phase mass transfer resistance. In this respect, the results indicate again the importance of the actual correlation (or randomness) of pore interconnectivity in the particles.

Conclusions

The PFG-NMR approach followed in this work allows to record two series of data with complementary character regarding the diffusion and exchange kinetics in chromatographic media. The steady-state pore diffusion measurement gives an effective, intraparticle self-diffusion coefficient from which the respective tortuosity factor can be calculated. The results demonstrate the profound effect of the actual correlation of interconnectivity between different pore sizes and thereby achieved hierarchy in pore structure on the associated transport behavior. It has a strong impact on the chromatographic performance of the support. These data are independent of the actual packing quality of particles in the column, their shape or size distribution, and external contributions due to the stagnant boundary layer.

The observational time scale of the PFG-NMR method can also be used to record the complete stagnant mobile phase mass transfer kinetics in the packed bed of porous particles. These data are influenced by the respective particle shape and size distribution, and by the hydrodynamics of the stagnant boundary layer (consequently, also by the packing density), which presents diffusional mass transfer resistance external to the particles. The effects of the particle shape and size distribution can be accounted for by independent measurements and the diffusion equation provides an excellent quantitative description of the exchange kinetics including this information. Slight corrections (<10%) of the intraparticle diffusivity are found for moderate Gaussian particle size distributions. The remaining effect of the stagnant boundary layer can be accounted for by the introduction of a hydrodynamically effective particle diameter, which is found to depend on Peclet number.

The approach shows potential to study and differentiate between the mechanisms that may contribute to the mass transfer in porous particles. This points toward enhanced surface diffusion and intraparticle-forced convection, which both may be responsible for higher effective, intraparticle diffusivities than those within the tortuosity limited regime (i.e., $D_{intra} < D_m$ and $\tau_{intra} > 1$) encountered in this work. Further, the kinetics of adsorption/desorption could be derived more accurately if we correct properly for the intraparticle diffusivity contribution. Thus, it will be extremely useful to carry out similar determinations on a variety of other relevant chromatographic and ion exchange media.

Acknowledgment. One of the authors (U. T.) gratefully acknowledges the award of a Marie Curie Fellowship under

the Training and Mobility of Researchers (TMR) Program from the European Union (Contract ERBFMBI-CT98-3437).

References and Notes

(1) Giddings, J. C. *Dynamics of Chromatography*; Marcel Dekker: New York, 1965.
(2) Weber, S. G.; Carr, P. W. *The Theory of the Dynamics of Liquid Chromatography*. In *High Performance Liquid Chromatography*; Brown, P. R., Hartwick, R. A., Eds.; Wiley: New York, 1989; Chapter 1.
(3) Dullien, F. A. L. *Porous Media: Fluid Transport and Pore Structure*; Academic Press: New York, 1992.
(4) King, C. V. *J. Am. Chem. Soc.* **1935**, *57*, 828.
(5) Gottschlich, C. F. *AIChE J.* **1963**, *9*, 88.
(6) Deans, H. A.; Lapidus, L. *AIChE J.* **1960**, *6*, 656.
(7) Ergun, S. *Chem. Eng. Prog.* **1952**, *48*, 227.
(8) Martin, A. J. P.; Synge, R. L. M. *Biochem. J.* **1941**, *35*, 1358.
(9) Boyd, G. E.; Adamson, A. W.; Meyers, L. S., Jr. *J. Am. Chem. Soc.* **1947**, *69*, 2836.
(10) Boyd, G. E.; Meyers, L. S., Jr.; Adamson, A. W. *J. Am. Chem. Soc.* **1947**, *69*, 2849.
(11) Klinkenberg, A.; Sjenitzer, F. *Chem. Eng. Sci.* **1956**, *5*, 258.
(12) van Deemter, J. J.; Zuiderweg, F. J.; Klinkenberg, A. *Chem. Eng. Sci.* **1956**, *5*, 271.
(13) Rosen, J. B. *Ind. Eng. Chem.* **1954**, *46*, 1590.
(14) Done, J. N.; Knox, J. H. *J. Chromatogr. Sci.* **1972**, *10*, 606.
(15) Huber, J. F. K. *Ber. Bunsen-Ges. Phys. Chem.* **1973**, *77*, 179.
(16) Horváth, Cs.; Lin, H.-J. *J. Chromatogr.* **1978**, *149*, 43.
(17) Unger, K. K.; Jilge, G.; Kinkel, J. N.; Hearn, M. T. W. *J. Chromatogr.* **1986**, *359*, 61.
(18) Kirkland, J. J. *Anal. Chem.* **1992**, *64*, 1239.
(19) Kalghatgi, K.; Fellegvári, I.; Horváth, Cs. *J. Chromatogr.* **1992**, *604*, 47.
(20) Hjertén, S.; Liao, J.-I.; Zhang, R. *J. Chromatogr.* **1989**, *473*, 273.
(21) Petro, M.; Svec, F.; Gitsov, I.; Fréchet, J. M. J. *Anal. Chem.* **1996**, *68*, 315.
(22) Reeder, D. H.; Clausen, A. M.; Annen, M. J.; Flickinger, M. C.; Carr, P. W.; McCormick, A. V. *J. Colloid Interface Sci.* **1996**, *184*, 328.
(23) Afeyan, N. B.; Gordon, N. F.; Mazsaroff, I.; Varady, L.; Fulton, S. P.; Yang, Y. B.; Regnier, F. E. *J. Chromatogr.* **1990**, *519*, 1.
(24) Frey, D. D.; Schweinheim, E.; Horváth, Cs. *Biotechnol. Prog.* **1993**, *9*, 273.
(25) Nir, A.; Pismen, L. M. *Chem. Eng. Sci.* **1977**, *32*, 35.
(26) Rodrigues, A. E.; Lopes, J. C.; Lu, Z. P.; Loureiro, J. M.; Dias, M. M. *J. Chromatogr.* **1992**, *590*, 93.
(27) Heeter, G. A.; Liapis, A. I. *J. Chromatogr. A* **1997**, *761*, 35.
(28) Davis, R. H.; Stone, H. A. *Chem. Eng. Sci.* **1993**, *48*, 3993.
(29) Satterfield, C. N.; Colton, C. K.; Pitcher, W. H., Jr. *AIChE J.* **1973**, *19*, 628.
(30) Limbach, K. W.; Wei, J. *AIChE J.* **1990**, *36*, 242.
(31) Epstein, N. *Chem. Eng. Sci.* **1989**, *44*, 777.
(32) Yau, W. W.; Kirkland, J. J.; Bly, D. D. *Modern Size-Exclusion Liquid Chromatography*; John Wiley & Sons: New York, 1979; Chapter 2.
(33) Giddings, J. C.; Kucera, E.; Russel, C. P.; Myers, M. N. *J. Phys. Chem.* **1968**, *72*, 4397.
(34) Satterfield, C. N. *Mass Transfer in Heterogeneous Catalysis*; MIT Press: Cambridge, MA, 1970.
(35) Burganos, V. N.; Sotirchos, S. V. *AIChE J.* **1987**, *33*, 1678.
(36) Carberry, J. J.; Bretton, R. H. *AIChE J.* **1958**, *4*, 367.
(37) Aris, R. *Chem. Eng. Sci.* **1959**, *11*, 194.
(38) Koch, D. L.; Brady, J. F. *J. Fluid Mech.* **1985**, *154*, 399.
(39) Deans, H. A. *Soc. Pet. Eng. J.* **1963**, *3*, 49.
(40) Coats, K. H.; Smith, B. D. *Soc. Pet. Eng. J.* **1964**, *4*, 73.
(41) Sahimi, M.; Tsotsis, T. T. *J. Catal.* **1985**, *96*, 552.
(42) Hollewand, M. P.; Gladden, L. F. *Chem. Eng. Sci.* **1992**, *47*, 1761.
(43) Coffman, J. L.; Lightfoot, E. N.; Root, T. W. *J. Phys. Chem. B* **1997**, *101*, 2218.
(44) Li, J.; Cantwell, F. F. *J. Chromatogr. A* **1996**, *726*, 37.
(45) Li, J.; Litwinson, L.; Cantwell, F. F. *J. Chromatogr. A* **1996**, *726*, 25.
(46) Villermaux, J. *J. Chromatogr. Sci.* **1974**, *12*, 822.
(47) Haynes, H. W., Jr. *Catal. Rev.−Sci. Eng.* **1988**, *30*, 563.
(48) Ding, A.; Candela, D. *Phys. Rev. E* **1996**, *54*, 656.
(49) Tallarek, U.; Albert, K.; Bayer, E.; Guiochon, G. *AIChE J.* **1996**, *42*, 3041.
(50) Lebon, L.; Oger, L.; Leblond, J.; Hulin, J. P.; Martys, N. S.; Schwartz, L. M. *Phys. Fluids* **1996**, *8*, 293.
(51) Seymour, J. D.; Callaghan, P. T. *AIChE J.* **1997**, *43*, 2096.
(52) Tessier, J. J.; Packer, K. J.; Thovert, J.-F.; Adler, P. M. *AIChE J.* **1997**, *43*, 1653.
(53) Amin, M. H. G.; Gibbs, S. J.; Chorley, R. J.; Richards, K. S.; Carpenter, T. A.; Hall, L. D. *Proc. R. Soc. A* **1997**, *453*, 489.
(54) Tallarek, U.; van Dusschoten, D.; Van As, H.; Bayer, E.; Guiochon, G. *J. Phys. Chem. B* **1998**, *102*, 3486.
(55) Tessier, J. J.; Packer, K. J. *Phys. Fluids* **1998**, *10*, 75.
(56) Stapf, S.; Packer, K. J.; Graham, R. G.; Thovert, J.-F.; Adler, P. M. *Phys. Rev. E* **1998**, *58*, 6206.
(57) Tallarek, U.; Bayer, E.; Guiochon, G. *J. Am. Chem. Soc.* **1998**, *120*, 1494.
(58) Tallarek, U.; Bayer, E.; van Dusschoten, D.; Scheenen, T.; Van As, H.; Guiochon, G.; Neue, U. D. *AIChE J.* **1998**, *44*, 1962.
(59) Hollewand, M. P.; Gladden, L. F. *Chem. Eng. Sci.* **1995**, *50*, 309.
(60) Tallarek, U.; van Dusschoten, D.; Van As, H.; Guiochon, G.; Bayer, E. *Angew. Chem.* **1998**, *110*, 1983; *Angew. Chem., Int. Ed. Engl.* **1998**, *37*, 1882.
(61) Neue, U. D. *HPLC Columns: Theory, Technology, and Practice*; Wiley-VCH: New York, 1997.
(62) Poole, C. F.; Poole, S. K. *Chromatography Today*; Elsevier: Amsterdam, 1993.
(63) Schenck, J. F. *Med. Phys.* **1996**, *23*, 815.
(64) Regnier, F. E. *Nature* **1991**, *350*, 634.
(65) Ugelstad, J.; Soderberg, L.; Berge, A.; Bergstrom, J. *Nature* **1983**, *303*, 95.
(66) Stejskal, E. O.; Tanner, J. E. *J. Chem. Phys.* **1965**, *42*, 288.
(67) Stejskal, E. O. *J. Chem. Phys.* **1965**, *43*, 3597.
(68) Callaghan, P. T. *Principles of Nuclear Magnetic Resonance Microscopy*; Clarendon Press: Oxford, 1993; Chapter 6.3.
(69) Kärger, J.; Heink, W. *J. Magn. Reson.* **1983**, *51*, 1.
(70) Callaghan, P. T.; Coy, A.; MacGowan, D.; Packer, K. J.; Zelaya, F. O. *Nature* **1991**, *351*, 467.
(71) Callaghan, P. T.; MacGowan, D.; Packer, K. J.; Zelaya, F. O. *J. Magn. Reson.* **1990**, *90*, 177.
(72) Cotts, R. M. *Nature* **1991**, *351*, 443.
(73) Zimmerman, J. R.; Brittin, W. E. *J. Phys. Chem.* **1957**, *61*, 1328.
(74) Brownstein, K. R.; Tarr, C. E. *Phys. Rev. A* **1979**, *19*, 2446.
(75) Stilbs, P. *Prog. Nucl. Magn. Reson. Spectrosc.* **1987**, *19*, 1.
(76) Kärger, J.; Pfeifer, H.; Heink, W. *Adv. Magn. Reson.* **1988**, *12*, 1.
(77) Nawrocki, J. *Chromatographia* **1991**, *31*, 177.
(78) Albright, J. G.; Mills, R. *J. Phys. Chem.* **1965**, *69*, 3120.
(79) Reyes, S. C.; Iglesia, E. *J. Catal.* **1991**, *129*, 457.
(80) Hollewand, M. P.; Gladden, L. F. *Chem. Eng. Sci.* **1992**, *47*, 2757.
(81) Nicholson, D.; Petrou, J. K.; Petropoulos, J. H. *Chem. Eng. Sci.* **1988**, *43*, 1385.
(82) Petropoulos, J. H.; Liapis, A. I.; Kolliopoulos, N. P.; Petrou, J. K.; Kanellopoulos, N. K. *Bioseparation* **1990**, *1*, 69.
(83) Petropoulos, J. H.; Petrou, J. K.; Liapis, A. I. *Ind. Eng. Chem. Res.* **1991**, *30*, 1281.
(84) Sharratt, P. N.; Mann, R. *Chem. Eng. Sci.* **1987**, *42*, 1565.
(85) Carman, P. C. *Trans. Inst. Chem. Eng. (London)* **1937**, *15*, 150.
(86) Feng, C.; Stewart, W. E. *Ind. Eng. Chem. Fundam.* **1973**, *12*, 143.
(87) Venema, P.; Struis, R. P. W. J.; Leyte, J. C.; Bedeaux, D. *J. Colloid Interface Sci.* **1991**, *141*, 360.
(88) Blees, M. H.; Leyte, J. C. *J. Colloid Interface Sci.* **1994**, *166*, 118.
(89) Dunn, K.-J.; Bergman, D. J. *J. Chem. Phys.* **1995**, *102*, 3041.
(90) Pfeiffer, J. F.; Chen, J. C.; Hsu, J. T. *AIChE J.* **1996**, *42*, 932.
(91) Guiochon, G.; Golshan-Shirazi, S.; Katti, A. M. *Fundamentals of Preparative and Nonlinear Chromatography*; Academic Press: Boston, MA, 1994.
(92) Lorenzano-Porras, C. F.; Carr, P. W.; McCormick, A. V. *J. Colloid Interface Sci.* **1994**, *164*, 1.
(93) Lorenzano-Porras, C. F.; Annen, M. J.; Flickinger, M. C.; Carr, P. W.; McCormick, A. V. *J. Colloid Interface Sci.* **1995**, *170*, 299.
(94) Gibbs, S. J.; Lightfoot, E. N.; Root, T. W. *J. Phys. Chem.* **1992**, *96*, 7458.
(95) Lightfoot, E. N.; Athalye, A. M.; Coffman, J. L.; Roper, D. K.; Root, T. W. *J. Chromatogr. A* **1995**, *707*, 45.
(96) Rigby, S. P.; Gladden, L. F. *Chem. Eng. Sci.* **1996**, *51*, 2263.
(97) Liapis, A. I.; McCoy, M. A. *J. Chromatogr.* **1992**, *599*, 87.
(98) Rodrigues, A. E.; Ahn, B.; Zoulalian, A. *AIChE J.* **1982**, *28*, 541.
(99) Crank, J. *The Mathematics of Diffusion*; Clarendon Press: Oxford, 1956; Chapter 6.
(100) Carslaw, H. S.; Jaeger, J. C. *Conduction of Heat in Solids*; Clarendon Press: Oxford, 1959; Chapter 9.3.
(101) Westrin, B. A.; Zacchi, G. *Chem. Eng. Sci.* **1991**, *46*, 1911.
(102) Ruthven, D. M.; Loughlin, K. F. *Chem. Eng. Sci.* **1971**, *26*, 577.
(103) Rasmuson, A. *Chem. Eng. Sci.* **1985**, *40*, 621.
(104) Lin, Y. S.; Ma, Y. H. *AIChE J.* **1990**, *36*, 1569.
(105) Horváth, Cs.; Lin, H.-J. *J. Chromatogr.* **1976**, *126*, 401.
(106) Pfeffer, R.; Happel, J. *AIChE J.* **1964**, *10*, 605.
(107) Pfeffer, R. *Ind. Eng. Chem. Fundam.* **1964**, *3*, 380.
(108) Wilson, E. J.; Geankoplis, C. J. *Ind. Eng. Chem. Fundam.* **1966**, *5*, 9.
(109) Arnold, F. H.; Blanch, H. W.; Wilke, C. R. *J. Chromatogr.* **1985**, *330*, 159.

10.1098/rsta.2001.0952

THE ROYAL SOCIETY

Numerical simulation and measurement of liquid hold-up in biporous media containing discrete stagnant zones

By D. Kandhai[1,2], U. Tallarek[3]†, D. Hlushkou[3]‡, A. Hoekstra[1], P. M. A. Sloot[1] and H. Van As[3]

[1]*Section of Computational Science, University of Amsterdam, Kruislaan 403, 1098 SJ Amsterdam, The Netherlands*

[2]*Kramers Laboratorium voor Fysische Technologie, Delft University of Technology, Prins Bernhardlaan 6, 2628 BW Delft, The Netherlands*

[3]*Laboratory of Molecular Physics and Wageningen NMR Centre, Wageningen University, Dreijenlaan 3, 6703 HA Wageningen, The Netherlands*

Published online 12 February 2002

We have studied hydrodynamic dispersion in single-phase incompressible liquid flow through a fixed bed made of spherical, permeable (porous) particles. The observed behaviour was contrasted with the corresponding fluid dynamics in a random packing of impermeable (non-porous) spheres with an interparticle void fraction of 0.37. Experimental data were obtained in the laminar flow regime by pulsed field gradient nuclear magnetic resonance and were complemented by numerical simulations employing a hierarchical transport model with a discrete (lattice Boltzmann) interparticle flow field. Finite-size effects in the simulation associated with the spatial discretization of support particles or dimension and boundaries of the bed were minimized and the simulation results are in reasonable agreement with experiment.

Keywords: fixed beds; stagnant zones; diffusion-limited mass transfer; lattice Boltzmann flow field; pulsed magnetic-field gradient NMR

1. Introduction

An understanding of transport phenomena in porous media is important for many technological and environmental processes such as enhanced oil recovery, paper manufacturing, subterranean transport of hazardous wastes, filtration, or fixed-bed operations in catalysis and separation science (see, for example, Bear 1988; Dullien 1992; Sahimi 1995). In the past, several approaches have been developed to study transport phenomena in porous media and numerical simulations, in particular, were

† Present address: Lehrstuhl für Chemische Verfahrenstechnik, Otto-von-Guericke Universität Magdeburg, Universitätsplatz 2, 39106 Magdeburg, Germany (ulrich.tallarek@vst.uni-magdeburg.de).

‡ Present address: Max Planck Institute for Dynamics of Complex Technical Systems, Sandtorstr. 1, 39106 Magdeburg, Germany.

often employed to connect theoretical analysis with experimental measurements. The extremely complex geometry inherent to porous media, however, has always been one of the major difficulties in these studies. Several simplifications in pore structure or transport mechanisms have been introduced to allow more efficient computer simulations. In the last decade, lattice-gas and lattice Boltzmann simulations (see, for example, Rothman & Zaleski 1997; Chen & Doolen 1998; Chopard & Droz 1998) have proven to be versatile tools in simulating a wide variety of applications related to transport in porous media. Examples of such applications are diffusion and flow, including multi-component or multi-phase flows in several models of porous media such as spherical bead packings (Maier *et al.* 2000), fibrous media (Koponen *et al.* 1998; Clague *et al.* 2000) and even digitized samples of real porous media (Ferréol & Rothman 1995).

In this contribution we are interested in the hydrodynamic dispersion in porous media, i.e. transport of tracer particles in a solvent by flow and molecular diffusion within a complex pore network. This problem, also known as pore-scale dispersion, has been the subject of many studies (see, for example, Gunn & Price 1969; Han *et al.* 1985; Koch & Brady 1985, 1987; Gunn 1987; Salles *et al.* 1993; Lebon *et al.* 1996; Lowe & Frenkel 1996; Stapf *et al.* 1998; Tallarek *et al.* 1998*b*, 1999; Manz *et al.* 1999; Maier *et al.* 1998, 2000). In these studies a wide variety of techniques have been applied to probe the motion of tracer particles in a porous medium. Significant progress has been obtained by using theoretical methods, experimental measurements based on pulsed field gradient nuclear magnetic resonance (PFG NMR) and numerical simulations based on traditional finite-difference schemes and lattice Boltzmann algorithms in combination with Monte Carlo methods.

To the best of our knowledge all the numerical modelling efforts conducted so far has focused on porous media composed of impermeable spherical beads. Therefore, transport is solely restricted to the void space between the bead particles or the so-called interparticle transport. Here we consider porous materials with additional purely diffusive stagnant regions inside the beads, thus allowing for intraparticle mass transport. Our model porous medium is composed of permeable spherical beads with a rather complex tortuous network. These extra stagnant zones have a substantial influence on dispersion, since fluid molecules entrained in the deep diffusive pools of the particles give rise to a hold-up contribution and affect both the time-scale of (transient) dispersion and the value of the asymptotic dispersion coefficient (Koch & Brady 1987; Salles *et al.* 1993; Hulin 1994).

From a computational point of view, the main difference between our system and those studied previously is that characteristic time- and length-scales associated with an exchange of fluid molecules moving in velocity extremes of the flow field may differ by several orders of magnitude. Therefore, a direct numerical simulation that resolves transport processes including geometrical details of the tortuous pore network inside the permeable beads is not feasible, even with current state-of-the-art high-performance computer systems. Instead we followed a hierarchical and semi-empirical modelling approach. The flow field in a computer-generated model of the interparticle pore space was computed by means of a lattice Boltzmann algorithm. A particle tracking method was then used to record tracer dispersion in the entire interconnected (interparticle and intraparticle) pore network. The actual morphology of the intraparticle pore space is lumped into the model by an effective intraparticle diffusion coefficient D_{intra}, itself obtained from the PFG NMR measurements.

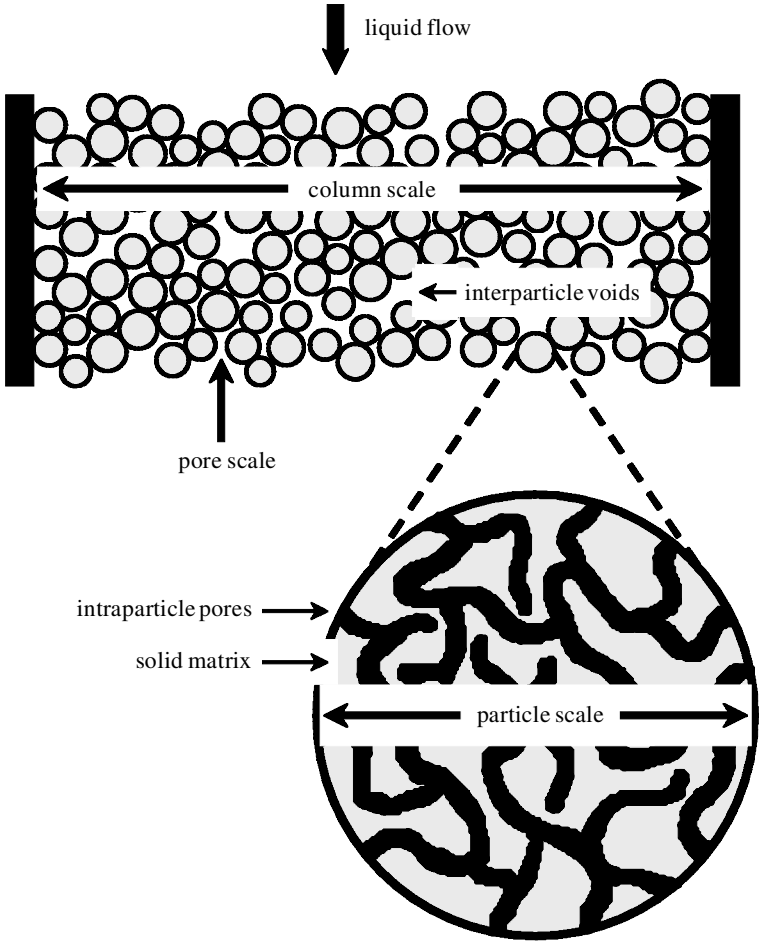

Figure 1. Illustration of different spatio-temporal scales concerning possible velocity extremes in the mobile phase (and associated mass transfer phenomena based on molecular diffusion or lateral dispersion) in a packed bed.

Mass transfer through the interparticle–intraparticle interface is accounted for by a stochastic approach.

2. Simulation methods

It has already been indicated in the Introduction that fluid transport through the packed bed involves a hierarchy of time- and length-scales. In the measurements, for example, we used spherical, totally porous particles with average diameter 50 μm packed into a 4.6 mm internal diameter (d_c) cylindrical column. Pores inside the particles have a mean diameter (d_{pore}) of only 12 nm. The size of interparticle voids is *ca.* 25–40% of the particle size (Dullien 1992) and exceeds the intraparticle pore size by a factor of more than 10^3. Mainly due to this variety of spatial and corresponding temporal scales with respect to the flow heterogeneity and mass transfer (see figure 1), we did not attempt a model which simultaneously resolves details at all scales, but exploited a hierarchical approach.

(a) Interparticle transport

Fluid transport in the voids between bead particles is due to a combination of pressure-driven convection and molecular diffusion. Similar to the detailed work reported by Maier *et al.* (2000) we used a lattice Boltzmann (LB) algorithm for the computation of the fluid flow field and a particle-tracking method to calculate tracer motion in the LB velocities. In LB methods local streaming and collision rules define a mesoscopic world from which the correct hydrodynamic behaviour in certain flow regimes emerges at a macroscopic level (Chopard & Droz 1998; Chen & Doolen 1998). In this paper we use the D3Q19 lattice Bhatnagar–Gross–Krook (BGK) model, where the collision operator is based on a single-time relaxation to the local equilibrium distribution (Qian *et al.* 1992; Chopard & Droz 1998). To define the displacement probability distributions or averaged propagators $P_{\mathrm{av}}(\boldsymbol{R}, \Delta)$, a large number of tracer molecules has been distributed in the computational domain. Since interparticle transport is driven by flow and diffusion, the position of each tracer particle during an elementary time-step δt is determined by convective and diffusive contributions and its time evolution can be described by (Maier *et al.* 2000)

$$\boldsymbol{r}(t + \delta t) = \boldsymbol{r}(t) + \boldsymbol{u}(\boldsymbol{r}(t))\delta t + \delta \boldsymbol{r}^{\mathrm{D}}. \tag{2.1}$$

$\boldsymbol{u}(r)$ is the local velocity at $\boldsymbol{r}$ approximated with the computed flow field by a linear interpolation of velocities at neighbouring lattice nodes. $\delta \boldsymbol{r}^{\mathrm{D}}$ is the displacement due to molecular diffusion and can be modelled by a random-walk process:

$$\delta \boldsymbol{r}^{\mathrm{D}} = \xi \sqrt{6 D_{\mathrm{m}} \delta t}, \tag{2.2}$$

where D_{m} is the free molecular diffusion coefficient ($D_{\mathrm{m}} = 2.15 \times 10^{-9}\ \mathrm{m^2\ s^{-1}}$ for water at 25 °C) and ξ is the unit vector with a random orientation in space. $P_{\mathrm{av}}(\boldsymbol{R}, \Delta)$ is then determined by calculating the number of particles with a net displacement $\boldsymbol{R}$ after time Δ. The total number of tracer particles is chosen such that statistical fluctuations in $P_{\mathrm{av}}(\boldsymbol{R}, \Delta)$ are small, and the time-step in these simulations is constrained by the maximum net displacement and the lattice spacing (Maier *et al.* 2000).

(b) Intraparticle transport

Transport inside the bead is purely diffusive because the mean velocity through a network of interconnected pores increases with the square of the pore diameter (Bear 1988). Thus, intraparticle pores (assuming that they are well interconnected like interparticle pores in a bed of uniform hard spheres—and even this is not guaranteed) restrain fluid motion to a velocity approximately a factor of 10^6 less than the interparticle average. Intraparticle diffusion is incorporated in the simulation semi-empirically, i.e. we use $D_{\mathrm{intra}} = 7.3 \times 10^{-6}\ \mathrm{cm^2\ s^{-1}}$ obtained experimentally for this packing material by PFG NMR (Tallarek *et al.* 1999). The motion of tracer particles is modelled by equation (2.1), neglecting the convective term.

(c) Mass transfer between intraparticle and interparticle pore space

Close to the particle's external surface, in the thin hydrodynamic boundary layer, transport normal to the solid–liquid interface is dominated by diffusion. In the case of porous beads, molecules can enter or leave the deep pools of stagnant fluid only

through pores that lead from the particles interior to the external surface. Initially, tracer molecules are distributed uniformly in the interconnected pore space. In dealing with the geometrical restrictions for the tracer flux through the sphere's external surface we follow a probabilistic approach. Close to this interface fluid transport is diffusive in both the inner (D_{intra}) and outer (*ca.* D_{m}) pore space. Corresponding differences in diffusive displacements within the interparticle and intraparticle pore space become apparent in different probabilities for entering or leaving a sphere. By using mass-balance arguments the following relation can be derived for the entrance and exit probabilities p_{enter} and p_{exit}:

$$p_{\mathrm{enter}} = \frac{D_{\mathrm{intra}} c_{\mathrm{intra}}}{D_{\mathrm{m}} c_{\mathrm{inter}}} p_{\mathrm{exit}} = \frac{D_{\mathrm{intra}}}{D_{\mathrm{m}}} \frac{n_{\mathrm{intra}} \varepsilon_{\mathrm{inter}}}{n_{\mathrm{inter}}(1-\varepsilon_{\mathrm{inter}})} p_{\mathrm{exit}}. \tag{2.3}$$

Here $\varepsilon_{\mathrm{inter}}$ is the porosity of the interparticle pore space and n_{inter} and n_{intra} are the number of particles in the interparticle and intraparticle pore space, respectively. $c_{\mathrm{intra}} = n_{\mathrm{intra}}/(1-\varepsilon_{\mathrm{inter}})V$ and $c_{\mathrm{inter}} = n_{\mathrm{inter}}/\varepsilon_{\mathrm{inter}}V$ are the intraparticle and interparticle tracer concentrations, and V is the total volume of the porous medium.

In the simulations, we assume that the probability for leaving a particle is 1. This choice is optional because the important aspect is the ratio of entrance and exit probabilities.

3. Experimental set-up and measurements

(*a*) *Packed column*

A 4.6 mm internal diameter $\times 150\ \mathrm{mm}^2$ long cylindrical poly(arylether-ether-ketone) column was packed and consolidated using the slurry technique (see, for example, Neue 1997). We used conventional silica-based particles as packing material. These spherical particles have a relatively narrow and Gaussian size distribution, which has been measured on a Coulter LS 130 particle size analyser (Beckman Coulter, Fullerton, CA). Particles are porous (by 50%) and intraparticle pores have an average size of 120 ± 15 Å. The mean particle diameter (d_{p}) is 50.2 μm, with a standard deviation of 10.6 μm. In general, the interparticle porosity $\varepsilon_{\mathrm{inter}}$ in columns packed by using slurry technology (as in our case) ranges between 0.38 and 0.4 (Stanley *et al.* 1997), but can be smaller (*ca.* 0.35) when compression techniques like hydraulic axial or radial compression are applied (Neue 1997; Stanley *et al.* 1996).

(*b*) *Displacement probability distributions by PFG NMR*

In an ideal PFG NMR experiment (Stejskal & Tanner 1965) without spatial localization gradients, the complex signal, $E(\boldsymbol{q}, \Delta)$, bears a direct Fourier relation with the Lagrangian averaged propagator, $P_{\mathrm{av}}(\boldsymbol{R}, \Delta)$, of the fluid molecules (Stejskal 1965; Kärger & Heink 1983; Callaghan 1993):

$$E(\boldsymbol{q}, \Delta) = \frac{S(\boldsymbol{q}, \Delta)}{S(0, \Delta)} = \int P_{\mathrm{av}}(\boldsymbol{R}, \Delta) \exp(\mathrm{i}2\pi \boldsymbol{q} \cdot \boldsymbol{R})\, \mathrm{d}\boldsymbol{R}. \tag{3.1}$$

$P_{\mathrm{av}}(\boldsymbol{R}, \Delta)$ gives the average probability for any particle to travel a dynamic (net) displacement $\boldsymbol{R}$ over time Δ in the direction of the pulsed magnetic field gradients of amplitude $\boldsymbol{g}$ and duration δ (Kärger & Heink 1983). This gradient area

defines a wavevector $\boldsymbol{q} = (2\pi)^{-1}\gamma\delta\boldsymbol{g}$ in q-space, which is space reciprocal to the dynamic displacement $\boldsymbol{R}$ (Callaghan *et al.* 1991; Cotts 1991). Thus $P_{\mathrm{av}}(\boldsymbol{R}, \Delta)$ can be reconstructed from the PFG NMR signal by Fourier transformation of $E(\boldsymbol{q}, \Delta)$ with respect to $\boldsymbol{q}$. Due to the inherent time-scale (including values for Δ from a few milliseconds up to a few seconds), it is possible to recover convective and stagnant fluid in $P_{\mathrm{av}}(\boldsymbol{R}, \Delta)$ and study the associated mass transfer kinetics if, in general, $\Delta \ll l_{\mathrm{stag}}^2/2D_{\mathrm{stag}}$, where l_{stag} is a characteristic dimension of the stagnant zone and D_{stag} is the diffusion coefficient. In this way PFG NMR has been used to measure the intraparticle effective diffusion coefficient D_{intra} that we subsequently employ in the simulation to account for the actual morphology of the intraparticle pore space (Tallarek *et al.* 1998*a*, 1999). Experiments were performed with a constant gradient pulse duration ($\delta = 2.5$ ms), but gradient amplitude was incremented using the stimulated echo sequence (Kärger *et al.* 1988), taking 64 $\boldsymbol{q}$-steps in the range of $\pm\boldsymbol{q}_{\max}$ and 56 phase-alternated signal averages at each value of $\boldsymbol{q}$. Details of the NMR hardware configuration can be found in an earlier publication (Tallarek *et al.* 1998*a*).

4. Results and discussion

(*a*) *Porous medium*

Prior to a presentation of the actual results concerning the inherent dispersion process we briefly discuss some important aspects of our model porous medium. The packed bed used in the NMR experiments is characterized by a column-to-particle diameter (aspect) ratio, $\psi = d_{\mathrm{c}}/d_{\mathrm{p}}$, of the order of 100. For the simulations, however, we needed to restrict ourselves to a much smaller system ($\psi = 10$ and a length of $40d_{\mathrm{p}}$) because of computational limitations. In this respect it is well known that for beds of identical spheres the interstitial porosity ($\varepsilon_{\mathrm{inter}}$) starts with a maximum value of unity at the column wall and displays damped oscillations with a period close to d_{p} over a distance of up to $5d_{\mathrm{p}}$ into the bulk until the void fraction reaches values which are typical for random packings ($\varepsilon_{\mathrm{inter}} = 0.38$–$0.40$) (Bey & Eigenberger 1997; Giese *et al.* 1998). It is caused by a decrease of packing order as the distance from the wall increases.

The consequences of this geometrical wall effect for macroscopic flow heterogeneity on a column scale (see figure 1), axial dispersion, and particle-to-fluid heat and mass transfer are particularly severe at aspect ratios below 15 where the critical 'wall annulus' occupies a substantial fraction of the bed's cross-section (Hsiang & Haynes 1977; Martin 1978; Carbonell 1980; Ahn *et al.* 1986). For systems with a larger ψ, however, these effects become smaller and it was found that, for example, the dispersion in beds of spheres is then independent of ψ (Gunn & Price 1969). To represent closer the column cross-sectional average of fluid transport in the PFG NMR measurements ($\psi \approx 100$) we considered periodic packings in the simulations ($\psi = 10$).

There exist a number of algorithms which may be used to generate a random packing of spheres even though the expression of actual randomness in such a system still poses challenges (Torquato *et al.* 2000). In particular, Monte Carlo schemes (Tobochnik & Chapin 1988) and drop-and-roll methods (Visscher & Bolsterli 1972; Lebon *et al.* 1996) have been used. To obtain an adequate representation of our porous medium, a random packing of identical hard spheres has been simulated using the Jodrey–Tory algorithm (Jodrey & Tory 1985). This method was chosen because of its efficiency and the dense bed that we actually required ($\varepsilon_{\mathrm{inter}} = 0.37$). Since

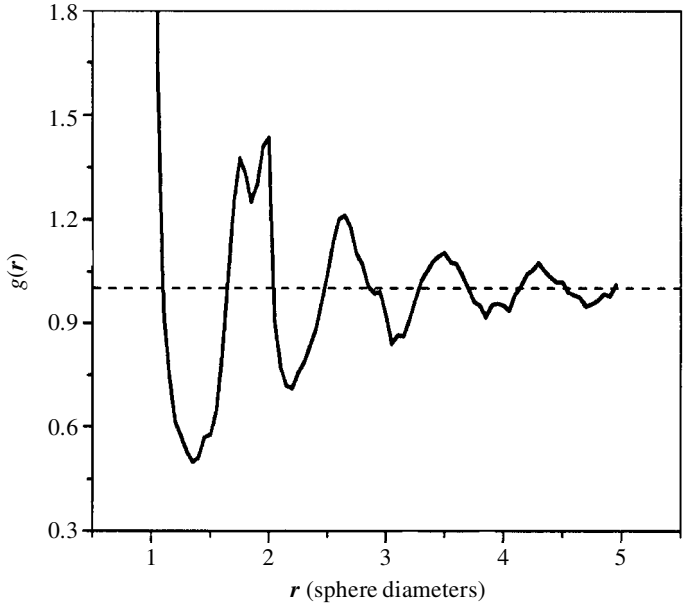

Figure 2. Pair-correlation function for a sphere packing of dimension $10D \times 10D \times 10D$.

we have reproduced this algorithm with only slight differences we will not discuss it. One of the most widely known tools for investigating 'randomness' of a bed structure is an analysis of the pair-correlation function $g(\boldsymbol{r})$. $g(\boldsymbol{r})d_{\mathrm{p}}^3\boldsymbol{r}$ is proportional to the probability of finding a sphere with its centre in a volume $d_{\mathrm{p}}^3\boldsymbol{r}$ at distance $\boldsymbol{r}$ from a given point. It is normalized to unity when $\boldsymbol{r}$ goes to infinity. We checked whether $g(\boldsymbol{r})$ of the bed exhibits features well known for random structures (Gusak 1987). In particular, a double-peak characteristic for close packing appears in the range 1.7–2.0, and oscillations decay to unity at larger $\boldsymbol{r}$ (figure 2).

(*b*) *Finite-size effects*

LB methods have proven to be versatile tools in the simulation of fluid flow through porous media (Chen & Doolen 1998; Koponen *et al.* 1998; Clague *et al.* 2000), mainly due to their flexibility in dealing with arbitrary and complex geometries. Further, the inherent spatial and temporal locality of the simulation algorithm makes it ideal for parallel processing, facilitating large-scale simulations (Kandhai *et al.* 1998). Commonly, the no-slip condition at the solid–liquid interface is implemented by a simple bounce-back formalism. However, it has been pointed out that problems related to this bounce-back boundary condition may lead to a significant error in the flow field (see, for example, Kandhai *et al.* 1999). In practice, a sufficiently large computational grid is often required to reduce these effects. To gain more insight into this artefact we performed preliminary simulations for flow in a periodic box of dimension $10D \times 10D \times 10D$ (with D equal to the diameter of the beads in lattice units) and $\varepsilon_{\mathrm{inter}} = 0.37$. The BGK relaxation parameter is unity and viscous flow is driven by a constant body force. From the flow field we computed the hydraulic permeability, K, using sphere diameters of 10, 15, 20, 25 and 30 lattice points. K is often used to characterize flow through porous media and expresses the flow resistance by the solid

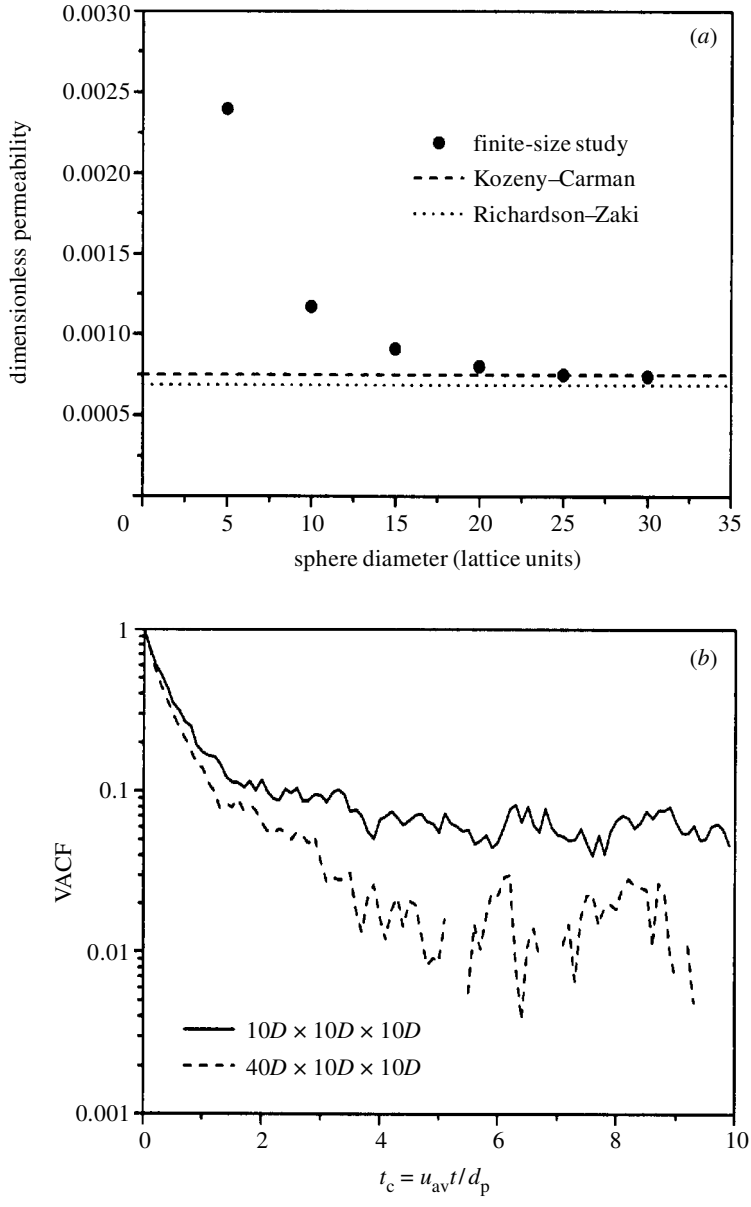

Figure 3. Finite-size effects. (*a*) Dimensionless bed permeability ($k = K/r_p^2$) versus the spatial discretization of a particle. (*b*) Velocity autocorrelation function $C_L(t)/C_L(0)$ versus dimensionless convective time in random sphere packings of different length, $\varepsilon_{inter} = 0.37$.

phase (Bear 1988). Figure 3*a* shows computed values of dimensionless permeability $k = K/r_p^2$ for a different sphere discretization. It is obvious that as the resolution is increased k approaches a constant value and the difference between results obtained with a diameter of 20 lattice points is less than 11% compared with 25 lattice points. A further increase does not significantly improve the results.

Besides numerical errors associated with the boundary conditions, recorrelation

effects due to the periodic boundaries may also influence dispersion. These effects were studied in detail by Maier *et al.* (2000) and can be analysed to some extent via the velocity autocorrelation function (VACF) for a simulation box and Peclet number while changing dimensions. The VACF measures the decay of the velocity autocovariance from its initial value. The longitudinal velocity autocovariance $C_{\mathrm{L}}(t)$ is defined as

$$C_{\mathrm{L}}(t) = \sum_{i=1}^{N} (u_i(t) - u_{\mathrm{av}})(u_i(0) - u_{\mathrm{av}}), \tag{4.1}$$

with $u_i(t)$ the velocity of tracer particle i at time t, u_{av} is the mean velocity of tracers, and the VACF is given by $C_{\mathrm{L}}(t)/C_{\mathrm{L}}(0)$. Figure 3*b* compares the behaviour of systems with dimension $10D \times 10D \times 10D$ and $40D \times 10D \times 10D$. It is clear that stronger recorrelation effects are present in the smaller system. They tend to slow down the decay of the VACF, thereby increasing the longitudinal dispersion coefficient by an artificial contribution (Maier *et al.* 2000). Based on these observations we used the system with $40D \times 10D \times 10D$, $D = 20$ lattice points, and, thus, a grid size of $800 \times 200 \times 200$ in our final simulations.

(*c*) *Propagator distributions*

Figure 4 begins with a comparison of simulated propagator distributions for the random packings of non-porous (impermeable) and porous (permeable) uniform spheres. The characteristic differences in propagator position and shape for the otherwise identical sphere packings originate in the existence of a pronounced intraparticle stagnant zone in the case of porous particles. The volumetric flow rate (F_{v}) is the same in both cases, but it results in different averaged linear velocities through the bed ($u_{\mathrm{av}} = F_{\mathrm{v}}/\varepsilon_{\mathrm{T}}A$ with A the column's free cross-sectional area) according to the total porosity ε_{T} of the respective pore space: $\varepsilon_{\mathrm{T}} = \varepsilon_{\mathrm{inter}} = 0.37$ for non-porous spheres and $\varepsilon_{\mathrm{T}} = \varepsilon_{\mathrm{inter}} + (1 - \varepsilon_{\mathrm{inter}})\varepsilon_{\mathrm{intra}} = 0.68$ for porous spheres ($\varepsilon_{\mathrm{intra}} = 0.5V_{\mathrm{sphere}}$). Consequently, at observation times $\Delta < r_{\mathrm{p}}^2/2D_{\mathrm{intra}}$ (r_{p} is the particle radius) we observe a stagnant, i.e. diffusion-limited, fluid fraction in $P_{\mathrm{av}}(\boldsymbol{R}, \Delta)$ very close to zero net displacement (figure 4).

It contains molecules that have remained only inside the particles over time Δ (diffusive ensemble), while those molecules leaving or entering the sphere gain a net displacement due to interparticle flow. By contrast, $P_{\mathrm{av}}(\boldsymbol{R}, \Delta)$ for the random packing of non-porous spheres does not reveal any diffusion-limited fluid, i.e. molecules which temporarily experience the no-slip condition at the solid–liquid interface exchange rapidly with downstream velocities in the interparticle channels of only a few micrometres in dimension. Thus, boundary-layer mass transfer is already in a steady state (achieved by diffusion normal to the interface) at the shortest observation time realized in our study ($\Delta = 15$ ms). Intraparticle motion of tracer molecules is computed via equations (2.1) and (2.2) with zero velocity field and by using the experimental $D_{\mathrm{intra}} = 7.3 \times 10^{-6}\ \mathrm{cm^2\ s^{-1}}$ for water inside these particles (Tallarek *et al.* 1999) instead of D_{m} to represent tortuosity-limited effective diffusion. When comparing simulated bimodal propagator distributions obtained for porous particles with the results of our PFG NMR measurements we observe a reasonable agreement regarding the reproduction and scaling with time of interparticle convective–diffusive and intraparticle stagnant fluid (cf. figure 5).

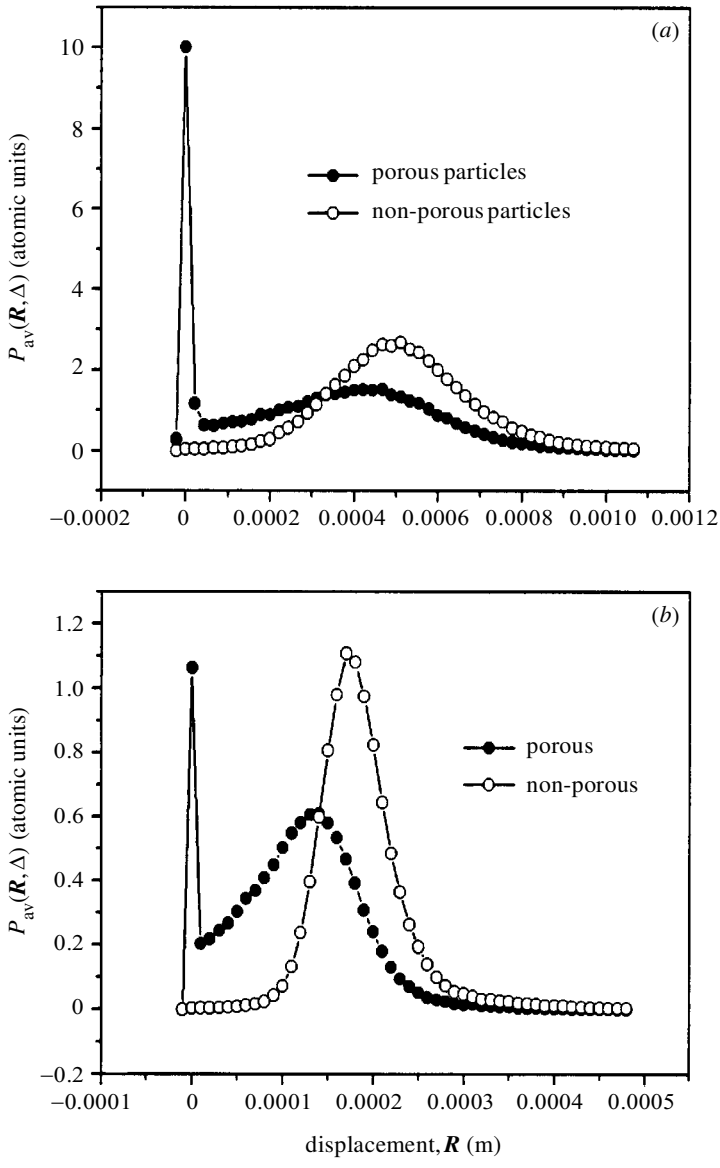

Figure 4. Simulated displacement probability distributions for pressure-driven flow of water through a random packing of spheres. The system size is $40D \times 10D \times 10D$ with $D = 20$ lattice points. (*a*) $\Delta = 25$ ms, (*b*) $\Delta = 90$ ms.

5. Conclusion and outlook

Compared with non-porous (impermeable) spheres, a fixed bed of porous (permeable) particles contains an additional contribution to the dispersion which arises from liquid hold-up (diffusion-limited mass transfer) in the particles. Both PFG NMR measurements and numerical simulations characterizing diffusion and convection on a time-scale short enough to capture the disequilibrium of intraparticle fluid transport indicate, in an encouraging agreement, that liquid hold-up strongly affects

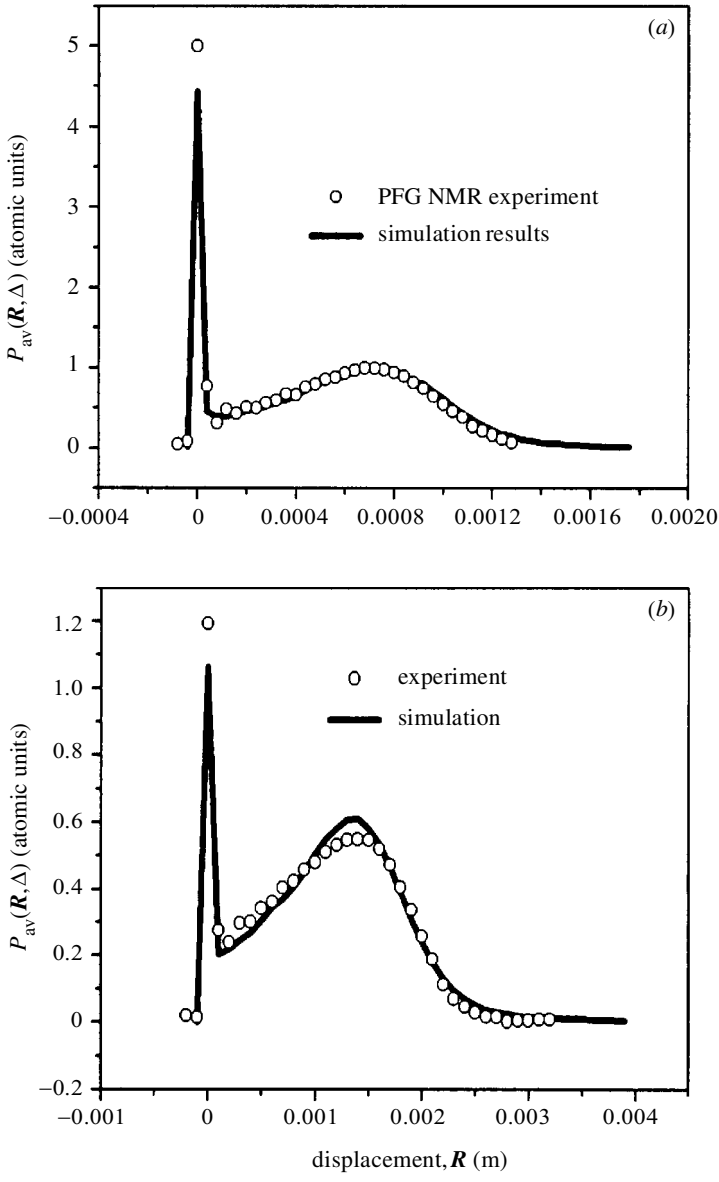

Figure 5. Comparison of the simulated and measured displacement probability distributions for liquid flow through a bed of porous particles ($d_p = 50$ μm, $\varepsilon_T = 0.68$). $Pe = u_{av} d_p / D_m = 274$, $Re = u_{av} d_p / \nu = 0.66$, kinematic viscosity $\nu = 8.9 \times 10^{-3}$ cm^2 s^{-1} at 25 °C. (*a*) $\Delta = 45$ ms, (*b*) $\Delta = 90$ ms.

longitudinal dispersion. Thus, the hierarchical simulation approach presented and validated in our work enables us to study in more detail the associated (diffusion-limited) mass-transfer kinetics and influence of stagnant zones on both transient and asymptotic longitudinal and transverse dispersion. This, in turn, will allow us to discriminate directly between dispersion mechanisms that originate in flowing and stagnant regions of the medium and helps to determine whether an inequality of the

macroscopic flow pattern or mobile phase stagnation contributes most persistently to transient dispersion at given Peclet and Reynolds numbers. This topic is of fundamental importance in many areas ranging from reservoir engineering to separation science.

We gratefully acknowledge the award of a Marie Curie Fellowship (U.T.) under the Training and Mobility of Researchers Programme from the European Union (contract ERBFMBI-CT98-3437). This work was further supported by the European Community activity Large-Scale Facility Wageningen NMR Centre (contract ERBCHGE-CT95-0066).

References

Ahn, B.-J., Zoulalian, A. & Smith, J. M. 1986 Axial dispersion in packed beds with large wall effect. *AIChE J.* **32**, 170–174.

Bear, J. 1988 *Dynamics of fluids in porous media*. New York: Dover.

Bey, O. & Eigenberger, G. 1997 Fluid flow through catalyst filled tubes. *Chem. Engng Sci.* **52**, 1365–1376.

Callaghan, P. T. 1993 *Principles of nuclear magnetic resonance microscopy*. Oxford University Press.

Callaghan, P. T., Coy, A., MacGowan, D., Packer, K. J. & Zelaya, F. O. 1991 Diffraction-like effects in NMR diffusion studies of fluids in porous solids. *Nature* **351**, 467–469.

Carbonell, R. G. 1980 Flow non-uniformities in packed beds: effect on dispersion. *Chem. Engng Sci.* **35**, 1347–1356.

Chen, S. & Doolen, G. D. 1998 Lattice Boltzmann method for fluid flows. *A. Rev. Fluid Mech.* **30**, 329–364.

Chopard, B. & Droz, M. 1998 *Cellular automata modelling of physical systems*. Cambridge University Press.

Clague, D. S., Kandhai, B. D., Zhang, R. & Sloot, P. M. A. 2000 Hydraulic permeability of (un)bounded fibrous media using the lattice-Boltzmann method. *Phys. Rev.* E **61**, 616–626.

Cotts, R. M. 1991 Diffusion and diffraction. *Nature* **351**, 443–444.

Dullien, F. A. L. 1992 *Porous media: fluid transport and pore structure*. Academic.

Ferréol, B. & Rothman, D. H. 1995 Lattice-Boltzmann simulations of flow through Fontainebleau sandstone. *Transport Porous Media* **20**, 3–20.

Giese, M., Rottschäfer, K. & Vortmeyer, D. 1998 Measured and modeled superficial flow profiles in packed beds with liquid flow. *AIChE J.* **44**, 484–490.

Gunn, D. J. 1987 Axial and radial dispersion in fixed beds. *Chem. Engng Sci.* **42**, 363–373.

Gunn, D. J. & Price, C. 1969 Dispersion in packed beds. *Trans. IChE* **47**, T341–T350.

Gusak, N. E. 1987 *The physics of structurally disordered matter*. Bristol: Adam Hilger.

Han, N.-W., Bhakta, J. & Carbonell, R. G. 1985 Longitudinal and lateral dispersion in packed beds: effect of column length and particle size distribution. *AIChE J.* **31**, 277–288.

Hsiang, T. C. & Haynes Jr, H. W. 1977 Axial dispersion in small diameter beds of large, spherical particles. *Chem. Engng Sci.* **32**, 678–681.

Hulin, J. P. 1994 Porous media: a model system for the physics of disorder. *Adv. Colloid Interface Sci.* **49**, 47–84.

Jodrey, W. S. & Tory, E. M. 1985 Computer simulation of close random packing of equal spheres. *Phys. Rev.* A **32**, 2347–2351.

Kandhai, D., Koponen, A., Hoekstra, A., Kataja, M., Timonen, J. & Sloot, P. M. A. 1998 Lattice-Boltzmann hydrodynamics on parallel systems. *Comput. Phys. Commun.* **111**, 14–26.

Kandhai, D., Koponen, A., Hoekstra, A., Kataja, M., Timonen, J. & Sloot, P. M. A. 1999 Implementation aspects of 3D lattice-BGK: boundaries, accuracy and a new fast relaxation method. *J. Computat. Phys.* **150**, 482–501.

Kärger, J. & Heink, W. 1983 The propagator representation of molecular transport in microporous crystallites. *J. Magn. Reson.* **51**, 1–7.

Kärger, J., Pfeifer, H. & Heink, W. 1988 Principles and application of self-diffusion measurements by nuclear magnetic resonance. *Adv. Magn. Reson.* **12**, 1–89.

Koch, D. L. & Brady, J. F. 1985 Dispersion in fixed beds. *J. Fluid Mech.* **154**, 399–427.

Koch, D. L. & Brady, J. F. 1987 Nonlocal dispersion in porous media: nonmechanical effects. *Chem. Engng Sci.* **42**, 1377–1392.

Koponen, A., Kandhai, D., Hellén, E., Alava, M., Hoekstra, A., Kataja, M., Niskanen, K., Sloot, P. M. A. & Timonen, J. 1998 Permeability of three-dimensional random fiber webs. *Phys. Rev. Lett.* **80**, 716–719.

Lebon, L., Oger, L., Leblond, J., Hulin, J. P., Martys, N. S. & Schwartz, L. M. 1996 Pulsed gradient NMR measurements and numerical simulation of flow velocity distribution in sphere packings. *Phys. Fluids* **8**, 293–301.

Lowe, C. P. & Frenkel, D. 1996 Do hydrodynamic dispersion coefficients exist? *Phys. Rev. Lett.* **77**, 4552–4555.

Maier, R. S., Kroll, D. M., Kutsovsky, Y. E., Davis, H. T. & Bernard, R. S. 1998 Simulation of flow through bead packs using the lattice-Boltzmann method. *Phys. Fluids* **10**, 60–74.

Maier, R. S., Kroll, D. M., Bernard, R. S., Howington, S. E., Peters, J. F. & Davis, H. T. 2000 Pore-scale simulation of dispersion. *Phys. Fluids* **12**, 2065–2079.

Manz, B., Gladden, L. F. & Warren, P. B. 1999 Flow and dispersion in porous media: lattice-Boltzmann and NMR studies. *AIChE J.* **45**, 1845–1854.

Martin, H. 1978 Low Peclet number particle-to-fluid heat and mass transfer in packed beds. *Chem. Engng Sci.* **33**, 913–919.

Neue, U. D. 1997 HPLC columns: theory, technology, and practice. New York: Wiley-VCH.

Qian, Y. H., d'Humières, D. & Lallemand, P. 1992 Lattice BGK models for Navier–Stokes equation. *Europhys. Lett.* **17**, 479–484.

Rothman, D. H. & Zaleski, S. 1997 *Lattice gas cellular automata.* Cambridge University Press.

Sahimi, M. 1995 *Flow and transport in porous media and fractured rock.* Weinheim: VCH.

Salles, J., Thovert, J.-F., Delannay, R., Prevors, L., Auriault, J.-L. & Adler, P. M. 1993 Taylor dispersion in porous media. Determination of the dispersion tensor. *Phys. Fluids* A **5**, 2348–2376.

Stanley, B. J., Sarker, M. & Guiochon, G. 1996 Consolidation of the packing material in chromatographic columns under dynamic axial compression. 4. Mechanical properties of some packing materials. *J. Chromatogr.* A **741**, 175–184.

Stanley, B. J., Foster, C. R. & Guiochon, G. 1997 On the reproducibility of column performance in liquid chromatography and the role of the packing density. *J. Chromatogr.* A **761**, 41–51.

Stapf, S., Packer, K. J., Graham, R. G., Thovert, J.-F. & Adler, P. M. 1998 Spatial correlations and dispersion for fluid transport through packed glass beads studied by pulsed field-gradient NMR. *Phys. Rev.* E **58**, 6206–6221.

Stejskal, E. O. 1965 Use of spin echoes in a pulsed magnetic-field gradient to study anisotropic, restricted diffusion and flow. *J. Chem. Phys.* **43**, 3597–3603.

Stejskal, E. O. & Tanner, J. E. 1965 Spin diffusion measurements: spin echoes in the presence of a time-dependent field gradient. *J. Chem. Phys.* **42**, 288–292.

Tallarek, U., van Dusschoten, D., Van As, H., Bayer, E. & Guiochon, G. 1998*a* Study of transport phenomena in chromatographic columns by pulsed field gradient NMR. *J. Phys. Chem.* B **102**, 3486–3497.

Tallarek, U., Bayer, E., van Dusschoten, D., Scheenen, T., Van As, H., Guiochon, G. & Neue, U. D. 1998*b* Dynamic NMR microscopy of chromatographic columns. *AIChE J.* **44**, 1962–1975.

Tallarek, U., Vergeldt, F. V. & Van As, H. 1999 Stagnant mobile phase mass transfer in chromatographic media: intraparticle diffusion and exchange kinetics. *J. Phys. Chem.* B **103**, 7654–7664.

Tobochnik, J. & Chapin, E. M. 1988 Monte Carlo simulation of hard spheres near random closest packing using spherical boundary conditions. *J. Chem. Phys.* **88**, 5824–5830.

Torquato, S., Truskett, T. M. & Debenedetti, P. G. 2000 Is random close packing of spheres well defined? *Phys. Rev. Lett.* **84**, 2064–2067.

Visscher, W. M. & Bolsterli, M. 1972 Random packing of equal and unequal spheres in two and three dimensions. *Nature* **239**, 504–507.

Influence of Stagnant Zones on Transient and Asymptotic Dispersion in Macroscopically Homogeneous Porous Media

D. Kandhai,[1,2] D. Hlushkou,[3,4] A. G. Hoekstra,[1] P. M. A. Sloot,[1] H. Van As,[5] and U. Tallarek[5,6,*]

[1]*Section Computational Science, Faculty of Science, University of Amsterdam, Kruislaan 403 1098 SJ Amsterdam, The Netherlands*

[2]*Kramers Laboratorium voor Fysische Technologie, Faculty of Applied Sciences, Delft University of Technology, Prins Bernhardlaan 6, 2628 BW Delft, The Netherlands*

[3]*Max Planck Institute for the Dynamics of Complex Technical Systems, Sandtorstrasse 1, 39106 Magdeburg, Germany*

[4]*Department of System Analysis, Belarusian State University, 4, Francisk Scoryna Avenue, Minsk, 220050, Belarus*

[5]*Laboratory of Molecular Physics and Wageningen NMR Centre, Wageningen University, Dreijenlaan 3, 6703 HA Wageningen, The Netherlands*

[6]*Lehrstuhl für Chemische Verfahrenstechnik, Otto-von-Guericke Universität Magdeburg, Universitätsplatz 2, 39106 Magdeburg, Germany*

(Received 27 November 2001; published 24 May 2002)

The role of stagnant zones in hydrodynamic dispersion is studied for creeping flow through a fixed bed of spherical permeable particles, covering several orders of characteristic time and length scales associated with fluid transport. Numerical simulations employ a hierarchical model to cope with the different temporal and spatial scales, showing good agreement with our experimental results on diffusion-limited mass transfer, transient, and asymptotic longitudinal dispersion. These data demonstrate that intraparticle liquid holdup in macroscopically homogeneous porous media clearly dominates over contributions caused by the intrinsic flow field heterogeneity and boundary-layer mass transfer.

DOI: 10.1103/PhysRevLett.88.234501 PACS numbers: 47.15.Gf, 05.60.–k, 47.55.Mh

A detailed understanding of transport in porous media over the intrinsic temporal and spatial scales is important in many technological and environmental processes [1]. For example, natural and industrial materials such as soil, rock, filter cakes, or catalyst pellets often contain low-permeability zones with respect to hydraulic flow of liquid through the medium or even stagnant regions which then remain purely diffusive. The relevance of stagnant zones stems from their influence on dispersion: Fluid molecules entrained in the deep diffusive pools cause a substantial holdup contribution and thereby affect the time scale of transient dispersion, as well as the value of the asymptotic dispersion coefficient (if the asymptotic long-time limit can be reached at all) [2–4]. Consequently, the associated kinetics of mass transfer between fluid percolating through the medium and stagnant fluid becomes rate limiting in a number of dynamic processes, including the separation and reaction efficiency of chromatographic columns and reactors, or economic oil recovery from a reservoir.

In this respect, transport phenomena observed in model systems such as random packings of spheres may help to characterize materials with a higher disorder [5–7]. For random packings of *nonporous* (impermeable) particles, for example, the long-time longitudinal dispersion coefficient is dominated by the boundary-layer contribution (due to the no-slip condition at the solid-liquid interface) or by medium and large-scale velocity fluctuations in the flow field depending on the actual disorder of the medium and the Peclet number, $Pe = \frac{u_{av} d_p}{D_m}$ (with u_{av}, the average velocity; d_p, particle diameter; and D_m, the molecular diffusivity) [6,8]. This behavior contrasts with random packings of *porous* (permeable) particles. In that case, liquid holdup associated with stagnant zones inside the particles may dominate dispersion when convective times $t_c = \frac{u_{av} t}{d_p}$ significantly exceed the dimensionless time for diffusion, $t_d = \frac{D_m t}{d_p^2}$ [9]. In many situations, however, both a macroscopic flow heterogeneity and solute trapping in stagnant zones contribute to transient and asymptotic dispersion [3,7,9].

Despite numerous theoretical, experimental, and numerical studies (e.g., [1,7,8,10–12]), the transient and asymptotic behavior of dispersion in porous media is not completely understood [13]. In particular, the influence of stagnant zones with respect to the actual mesoscopic and macroscopic flow field heterogeneity of the medium has found little attention in theory and experiment, and furthermore, the additional length and time scale associated with transport in stagnant regions complicates numerical simulations. Therefore it leaves the controversy about the dominating contribution to dispersion and the origin of long-time tails in residence-time distributions unresolved [3,7,14], let alone the question whether hydrodynamic dispersion coefficients exist at all [13]. In this Letter, we are able to resolve this issue experimentally and numerically for a macroscopically homogeneous medium by considering transient and asymptotic dispersion in a random packing of porous spheres, i.e., in a medium with bimodal porosity and associated length scales that differ by orders of magnitude. The results are contrasted to the behavior observed in packed beds of nonporous spheres.

In the experiments we used pulsed field gradient nuclear magnetic resonance (PFG-NMR) [15] to measure over

discrete temporal and spatial domain longitudinal nuclear spin (hence, molecular) displacement probability distributions of the fluid molecules in single-phase incompressible flow through beds of porous particles with average diameter (d_p) of 50 and 34 μm packed into a 4.6 mm internal diameter (d_c) cylindrical column. Pores inside the particles have a mean diameter (d_{pore}) of only 12 nm. In this hierarchical pore network the size of interparticle voids is about 25%–40% of the particle size and exceeds the intraparticle pore size by a factor of more than 10^3. One of the consequences is that transport of solutes also occurs on separate scales and is governed by different mechanisms [7,9], i.e., while the forced convection dominates transport between particles, diffusion is the only effective mechanism—based on pore space permeability [1]—that operates inside the particles.

Mainly due to this large variety of spatial and temporal domains we did not attempt a model which simultaneously resolves the fluid dynamics on column, particle, and pore scale, but exploited a hierarchical approach in the numerical simulations: A lattice-Boltzmann (LB) algorithm [16,17] was implemented for computing the flow field in computer-generated models of the interparticle pore space, and a particle tracking method was then used to record tracer dispersion in the total interconnected pore network (between and inside particles) [12]. The influence of pore space morphology in a single particle on the effective intraparticle diffusivity (D_{intra}) is not modeled explicitly, but is lumped into the model by using D_{intra} obtained from the PFG-NMR measurements. In dealing with the geometrical restrictions for tracer flux through the spheres external surface, we followed a probabilistic approach. Close to this interface fluid transport is diffusive in the inner (D_{intra}) and outer ($D_{\text{inter}} = D_m$) pore space. Corresponding differences in diffusive displacements become apparent in different probabilities for entering (p_e) or leaving (p_l) particles and can be shown by using mass balance arguments to follow the relation

$$\frac{p_e}{p_l} = \frac{D_{\text{intra}} \times \epsilon_{\text{intra}}}{D_m}, \tag{1}$$

with ϵ_{intra} the porosity of the intraparticle pore space. In the final flow simulations a periodic packing with dimension $800 \times 200 \times 200$ (with bead particles of diameter 20 lattice points) was used, and the particle tracking calculations were performed by using 500 000 particles and a time step of $0.1h$ (with h the lattice spacing). A more detailed description of the numerical methods and generated porous media including finite-size effects can be found elsewhere [18]. It should be noted that this numerical approach involves only a single free parameter, D_{intra}.

Figure 1 compares simulated displacement probability distributions (propagators) $P_{av}(R, \Delta)$ in random packings of nonporous and porous spheres where R is the net displacement of the tracer over time Δ. Characteristic differences in propagator position and shape for the otherwise identical sphere packings originate in the existence of an intraparticle stagnant zone in the case of porous particles. While the volumetric flow rate is identical

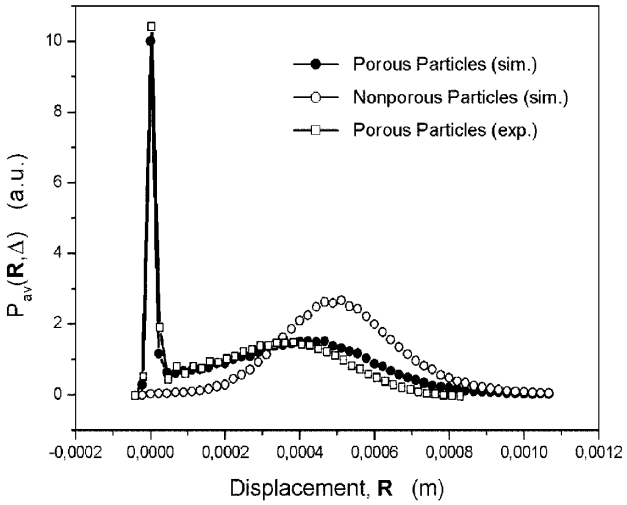

FIG. 1. Simulated and measured displacement probability distributions for liquid flow through a fixed bed of spheres after $\Delta = 25$ ms (porosity of the inter- and intraparticle pore space, $\epsilon_{\text{inter}} = 0.37$ and $\epsilon_{\text{intra}} = 0.45$, $D_{\text{intra}} = 7.3 \times 10^{-6}$ cm^2 s^{-1}, $d_p = 50$ μm, $Pe = \frac{u_{av} d_p}{D_m} = 274$ and $Re = \frac{u_{av} d_p}{\nu} = 0.66$ with kinematic viscosity: $\nu = 8.9 \times 10^{-3}$ cm^2 s^{-1}). Liquid phase: degassed water.

in both cases, it results in different averaged velocities through the bed according to the total porosity of the respective pore space. Consequently, at observation times $\Delta < \frac{r_p^2}{2D_{\text{intra}}}$ (r_p is the particle radius) we expect a stagnant, i.e., diffusion-limited fluid fraction in $P_{av}(R, \Delta)$ very close to zero net displacement containing molecules that have remained inside the particles over time Δ (diffusive ensemble). Fluid molecules leaving (or entering) the sphere gain (have gained) a net displacement due to interparticle convection. By contrast, $P_{av}(R, \Delta)$ for the random packing of nonporous spheres does not reveal diffusion-limited fluid molecules. Those which temporarily experience the no-slip condition at the solid-liquid interface exchange rapidly with downstream velocities in channels of only a few micrometers in dimension. As also seen in Fig. 1 the simulated bimodal propagator distributions obtained for porous particles are in good agreement with the results of PFG-NMR measurements. By recording the amount of stagnant fluid molecules at increasing Δ that remain unexchanged with interparticle velocities, $A_{\text{intra}}(\Delta)$, we can monitor a (fictitious) emptying of the spherical particles characterized by the classical mass transfer rate constant $B_{\text{intra}} = \pi^2 \frac{D_{\text{intra}}}{r_p^2}$ [19]

$$\frac{A_{\text{intra}}(\Delta)}{A_{\text{intra}}(0)} = \frac{6}{\pi^2} \sum_{n=1}^{\inf} \frac{1}{n^2} \exp(-n^2 B_{\text{intra}} \Delta). \tag{2}$$

Figure 2 demonstrates that the experimental and simulated intraparticle mass transfer kinetics match satisfactorily (within 3%) using $D_{\text{intra}} = 7.3 \times 10^{-6}$ cm^2 s^{-1} and $r_p = 2.5 \times 10^{-5}$ m in both cases. As mentioned, this value for D_{intra} is obtained from the experimental data ($B_{\text{intra}} = 11.52$ s^{-1}) [19] and then used in the simulations to reconstruct diffusion-limited mass transfer. The

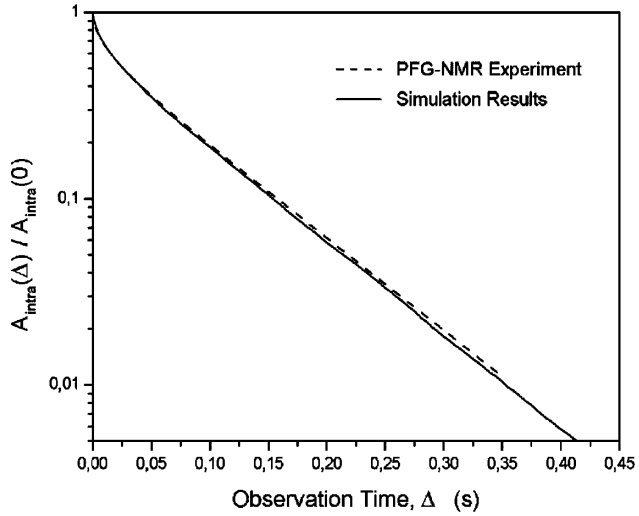

FIG. 2. Intraparticle stagnant mobile phase mass transfer kinetics ($d_p = 50$ μm, $Pe = 274$).

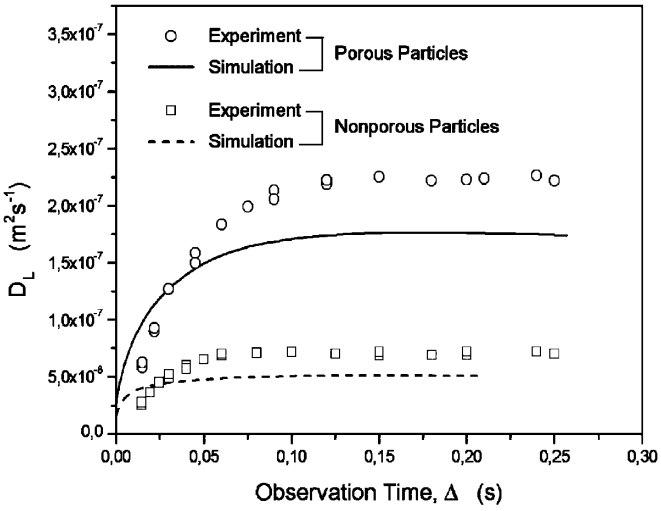

FIG. 3. Time-dependent longitudinal dispersion for flow through random packings of porous and nonporous spheres. In both cases $d_p = 34$ μm, $\epsilon_{\text{inter}} = 0.37$, $Pe = 54$ and $Re = 0.13$.

results in Fig. 2 demonstrate that the semiempirical simulation procedure followed in this Letter works well, as does Eq. (2) in describing both data sets.

Thus, mass transfer in these spatially discrete stagnant zones (uniform spheres) has been adequately accounted for and allows us to focus now on its influence on longitudinal dispersion which we analyze by [12]

$$D_L(t) = \int_0^t C_L(t')\, dt', \tag{3}$$

where $C_L(t) = \sum_{i=1}^{N} [u_i(t) - u_{av}][u_i(0) - u_{av}]$ is the velocity autocovariance [N is the number of tracer particles and $u_i(t)$ is the longitudinal velocity of particle i at time t]. Figure 3 compares transient behavior at constant Pe ($d_p = 34$ μm, $d_c = 4.6$ mm). In both experiment and simulation $D_L(t)$ for the nonporous particles reaches its asymptotic value (D_L^*) in a much shorter time (after approximately 50 ms) than with the porous particles (ca. 160 ms). While we observe a good agreement between simulation and experiment concerning this time scale, D_L^* itself is underestimated by the simulation in either case (by up to 25%). This effect seems to be systematic as it appears for packings of porous and nonporous particles and is probably caused by inaccuracies in the LB flow field (notice that the relative error in the hydraulic permeability, a measure of the flow resistance by the solid phase, is around 11%) [18]. Other possible explanations are related to the influence of the column wall confining the sphere packing [20], bead particles not being perfectly monodisperse (as evident from Fig. 2, cf. [19]), and the fact that the nonporous particles actually have small (micro)pores at the surface which contribute to a finite but small particle holdup. With the independently measured D_{intra} and known r_p, intraparticle diffusion can be identified as the most persistent contribution to transient dispersion in the random packing of porous spheres, i.e., the holdup dispersion mechanism reaches its long-time behavior after $t_h = \frac{r_p^2}{2D_{\text{intra}}}$ [19]. For nonporous particles, on the other hand, we find a qualitative agreement between the corresponding time scale (about 50 ms, Fig. 3) and characteristic time for boundary-layer dispersion ($t_b = 40$ ms) based on the nonlocal dispersion theory of Koch and Brady [2]. This transient behavior may be also due to mechanical dispersion [12,18]. Further work is needed to resolve these contributions in macroscopically homogeneous beds of nonporous particles.

Figure 4 compares the velocity dependence of asymptotic dispersion coefficients for random packings of porous and nonporous spheres in the range $0.1 < Pe < 100$. While the simulated data again underestimate experimental values of D_L^* (cf. Fig. 3) the effect of intraparticle liquid holdup on a significantly increased dispersion is evident. Already Aris [21] showed that this contribution scales with Pe^2, a result that was rediscovered later by Koch and Brady [8]. When analyzing the dependence of D_L^* on Pe we have to account for longitudinal diffusion, mechanical dispersion (Θ_m), boundary layer mass transfer (Θ_b) and, of course, the intraparticle holdup (Θ_h) [7,8]

$$\frac{D_L^*}{D_m} = \tau + \Theta_m Pe + \Theta_b Pe \ln(Pe) + \Theta_h Pe^2. \tag{4}$$

For $Pe \to 0$ $\frac{D_L^*}{D_m}$ approaches the packed beds tortuosity factor (τ) which represents the long-time diffusion coefficient in the interconnected pore space. This value has been measured independently by PFG-NMR (without flow) and is subsequently used in the analysis. We then fitted the experimental data, D_L^* vs Pe (Fig. 4), to Eq. (4) and the values of the parameters $(\tau, \Theta_m, \Theta_b, \Theta_h)$ thus obtained are $(0.51, 0.153 \pm 9 \times 10^{-3}, 0.080 \pm 5 \times 10^{-3}, 1.65 \times 10^{-3} \pm 2 \times 10^{-4})$ and $(0.74, 0.144 \pm 0.016, 0.101 \pm 0.011, 0.020 \pm 6 \times 10^{-4})$ for the packings of nonporous and porous spheres, respectively. The most striking feature of this analysis is the substantial difference in Θ_h characterizing holdup dispersion. Further, mechanical

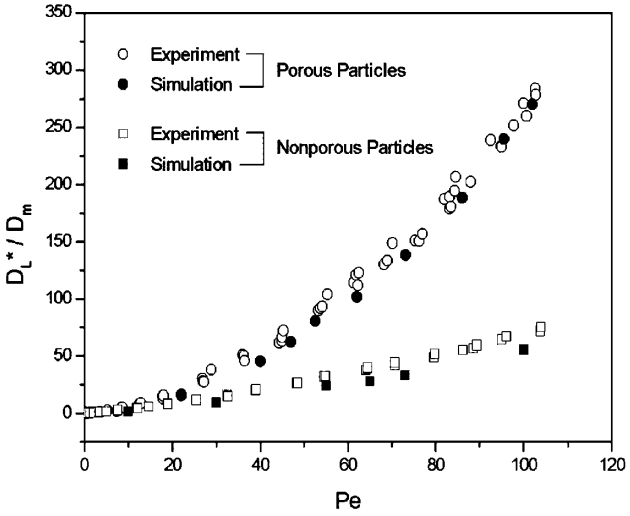

FIG. 4. Dependence of asymptotic longitudinal dispersion on Peclet number in fixed beds of porous and nonporous particles ($d_p = 34$ μm, $d_c = 4.6$ mm). Liquid phase: water. The experimental data in Figs. 3 and 4 were obtained with an accuracy of better than 5%.

dispersion is very similar in both columns which were packed and consolidated by the same procedure. Values for Θ_m (0.153 and 0.144) are actually of the same order as $\Theta_m = 0.25$ reported by Maier *et al.* [12] for their simulation of dispersion in random packings of nonporous spheres, in the range $1 < Pe < 5000$ and with $\epsilon_{\text{inter}} = 0.44$. As has already been pointed out by these authors, values for Θ_b found in our work (0.08 and 0.101), together with their own value (0.03) suggest that boundary layer dispersion is much lower than predicted by the theory of Koch and Brady [8]. A possible explanation for this discrepancy may be found in the significantly different porosities considered in that theory, on one hand, and the simulations and experiment on the other. Even the relatively small difference in particle volume fractions of the systems used by Maier *et al.* [12] ($\epsilon_{\text{inter}} = 0.44$) and in this work ($\epsilon_{\text{inter}} = 0.37$) may contribute significantly to the observed differences in Θ_m and Θ_b.

To conclude, the present work combines experimental and numerical elements to differentiate between dispersion mechanisms that originate in stagnant and flowing regions of a macroscopically homogeneous porous medium. The numerical simulations employ a semiempirical hierarchical model with a single free parameter to cope with the large variety of temporal and spatial scales. The results are in good agreement with our experimental data and clearly demonstrate the dominating contribution of liquid holdup to transient (Fig. 3) and asymptotic (Fig. 4) longitudinal dispersion in a random packing of porous spheres with column-to-particle diameter ratio above 100. Persistent effects due to flow field nonuniformities were not identified which suggests that characteristic times for mechanical dispersion are short compared to the diffusive time of this nonmechanical contribution. These findings suggest that holdup dispersion in porous media may be more important than assumed in many cases [3,7,14]. One of the remaining challenges is to characterize the relative importance of mechanical and nonmechanical dispersion mechanisms when the heterogeneity length scale is increased, e.g., in a confined random sphere packing with smaller column-to-particle diameter ratio. Then, the macroscopic flow profile may start to dominate dispersion and prevent an observation of Gaussian residence-time distributions [20,22].

*Corresponding author.
Email address: ulrich.tallarek@vst.uni-magdeburg.de

[1] J. Bear, *Dynamics of Fluids in Porous Media* (Dover, New York, 1988).
[2] D. L. Koch and J. F. Brady, Chem. Eng. Sci. **42**, 1377 (1987).
[3] J. Salles, J.-F. Thovert, R. Delannay, L. Prevors, J.-L. Auriault, and P. M. Adler, Phys. Fluids A **5**, 2348 (1993).
[4] J. P. Hulin, Adv. Colloid Interface Sci. **49**, 47 (1994).
[5] J.-C. Bacri, N. Rakotamala, and D. Salin, Phys. Rev. Lett. **58**, 2035 (1987).
[6] E. Charlaix, J. P. Hulin, and T. J. Plona, Phys. Fluids **30**, 1690 (1987).
[7] M. Sahimi, *Flow and Transport in Porous Media and Fractured Rock* (VCH, Weinheim, 1995).
[8] D. L. Koch and J. F. Brady, J. Fluid Mech. **154**, 399 (1985).
[9] J. C. Giddings, *Dynamics of Chromatography: Principles and Theory* (Marcel Dekker, New York, 1965), Part I.
[10] L. Lebon, L. Oger, J. Leblond, J. P. Hulin, N. S. Martys, and L. M. Schwartz, Phys. Fluids **8**, 293 (1996).
[11] S. Stapf, K. J. Packer, R. G. Graham, J.-F. Thovert, and P. M. Adler, Phys. Rev. E **58**, 6206 (1998).
[12] R. S. Maier, D. M. Kroll, R. S. Bernard, S. E. Howington, J. F. Peters, and H. T. Davis, Phys. Fluids **12**, 2065 (2000).
[13] C. P. Lowe and D. Frenkel, Phys. Rev. Lett. **77**, 4552 (1996).
[14] J. H. Knox, J. Chromatog. A **831**, 3 (1999).
[15] P. T. Callaghan, *Principles of Nuclear Magnetic Resonance Microscopy* (Oxford University Press, Oxford, 1993).
[16] R. Benzi, S. Succi, and M. Vergassola, Phys. Rep. **222**, 145 (1992).
[17] S. Chen and G. D. Doolen, Annu. Rev. Fluid Mech. **30**, 329 (1998).
[18] D. Kandhai, U. Tallarek, D. Hlushkou, A. G. Hoekstra, P. M. A. Sloot, and H. Van As, Philos. Trans. R. Soc. London A **360**, 521 (2002).
[19] U. Tallarek, F. J. Vergeldt, and H. Van As, J. Phys. Chem. B **103**, 7654 (1999).
[20] R. S. Maier, D. M. Kroll, R. S. Bernard, S. E. Howington, J. F. Peters, and H. T. Davis, Philos. Trans. R. Soc. London A **360**, 497 (2002).
[21] R. Aris, Chem. Eng. Sci. **11**, 194 (1959).
[22] U. Tallarek, T. W. J. Scheenen, and H. Van As, J. Phys. Chem. B **105**, 8591 (2001).

Fluid Dynamics in Monolithic Adsorbents: Phenomenological Approach to Equivalent Particle Dimensions

By *Ulrich Tallarek*, *Felix C. Leinweber*, and *Andreas Seidel-Morgenstern**

Due to the complex, often sponge-like structure of monolithic adsorbents it is difficult to define appropriate constituent units that characterize the hydrodynamics of the material, or to determine relevant shape and size distribution factors comparable to those for spherical particles in (particulate) fixed beds. Based on a phenomenological analysis of the friction factor (Reynolds number relation and the longitudinal dispersivity – Peclet number dependence for random sphere packings) we derive characteristic lengths (i.e., equivalent particle dimensions) for a monolith with regard to its hydraulic permeability and dispersion originating in stagnant zones. Equivalence to the hydrodynamic behavior in "reference" sphere packings is established by dimensionless scaling of the respective data for the monolithic structure. This phenomenological approach, which is simply based on liquid flow and stagnation in a porous medium, can successfully relate hydrodynamic properties of the monolith to that of particulate beds.

1 Introduction

The recent development of rigid monolithic support structures has contributed to many technological and environmental processes, including selective high surface area materials (e.g., microcellular foams, nanostructured films, hierarchically-ordered composites, molded polymers) for emission control of industrial and automobile gases, high throughput catalysis and (bio)medical screening, chromatographic separations, or as an important component in supercapacitors and sensors [1–10]. By controlling chemical composition, pore and surface structure, as well as physical properties down to the nanometer scale it is possible to produce materials with tailored optical, mechanical, electrical or hydrodynamic properties and increased selectivity for adsorption/reaction and catalytic processes. The introduction of hierarchical order in the interconnected pore network and independent manipulation of the contributing sets of pores [11] allows the design of highly permeable media and optimization of solute transport to and from the active surface sites. Compared to conventional particulate fixed-bed adsorbers monolithic materials combine high selectivity and capacity, mobile phase velocity and mass transfer efficiency in a unique manner [4,6,12].

2 Problem Formulation

While the solid phase in random sphere packings is discontinuous, monoliths have a continuous rigid skeleton. Although differences between monolithic and particulate stationary phases are obvious with regard to morphology, the major principles underlying the advanced processing of a high surface area into appropriate structures, (i.e. suitable permeability, heterogeneity and associated mass transfer resistances) remain identical, for example the physical mechanisms responsible for dispersion. These involve molecular diffusion in the interconnected pore network, a mechanical contribution due to velocity fluctuations in the flow field induced by the randomly distributed solid phase, nonmechanical dispersion associated with the no-slip condition at the solid-liquid interface (in general), and the particular access to intraparticle or intraskeleton stagnant zones in which diffusion remains the dominating transport mechanism [13]. While equivalence between different geometries concerning the convection, diffusion and reaction is well recognized for particulate systems [14], a direct comparison with monolithic structures is less obvious due, not least, to the complex shape of the skeleton domain. Although monoliths are considered as a new generation of adsorbents, appropriate characteristic lengths that competitively relate their hydrodynamic properties (i.e. flow and stagnation of the mobile phase) to those of particulate fixed beds are not readily available (Fig. 1).

3 Materials and Methods

Particulate beds were prepared with either nonporous or completely porous spherical C18-silica particles, the latter having mesopores of 30 nm average diameter. These packings were compared to a C18-silica monolith with bimodal pore size distribution (Fig. 2) purchased from Merck KGaA (Darmstadt, Germany). Relevant column, particle and packing characteristics are summarized in Tab. 1. The mobile phase in all experiments was a water/acetonitrile (50:50 v/v) mixture containing 0.1 % trifluoroacetic acid. Thus, following tracer pulse injection, the elution of analytes (acetone, angiotensin II and insulin) occured under nonretained conditions. The longitudinal dispersion coefficients were determined by analysis of residence time distributions with an exponentially modified Gaussian function [15].

[*] Dr. rer. nat. U. Tallarek (author to whom correspondence should be addressed), Dipl.-Chem. F. C. Leinweber, Prof. Dr.-Ing. A. Seidel-Morgenstern, Lehrstuhl für Chemische Verfahrenstechnik, Institut für Verfahrenstechnik der Otto-von-Guericke-Universität Magdeburg, Universitätsplatz 2, D-39106 Magdeburg, Germany (E-mail: ulrich.tallarek@vst.uni-magdeburg.de).

  0930-7516/02/1212-1177 $ 17.50+.50/0

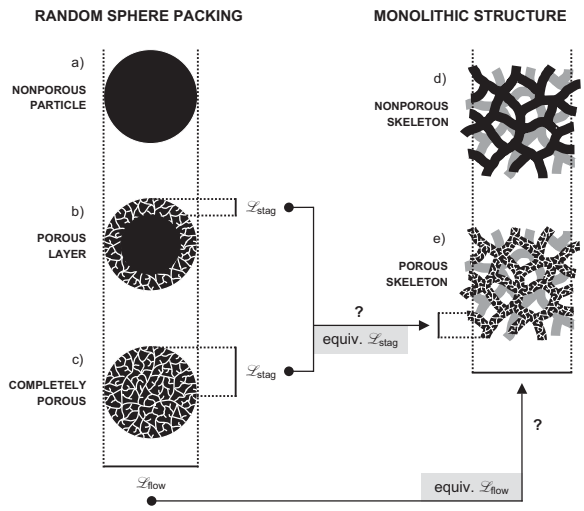

Figure 1. Characteristic lengths for hydraulic permeability and hydrodynamic dispersion in a bed of spheres and monoliths. While the particle diameter is useful to define a region impermeable for flow, the thickness of its porous layer may be used to address dispersion originating in stagnant zones of a sphere packing. Apparently, $\mathscr{L}_{flow}$ and $\mathscr{L}_{stag}$ are different.

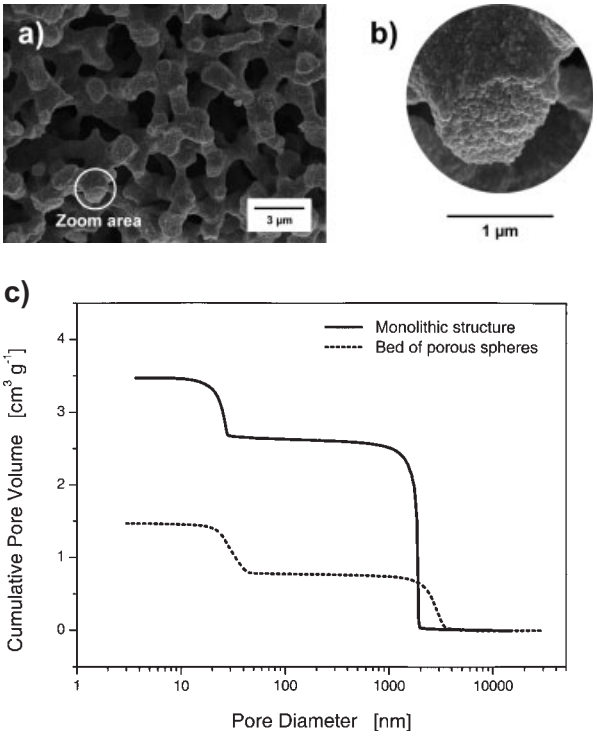

Figure 2. Morphology of the silica-based monolith. a) SEM picture showing the macroporous interskeleton pore space with d_{macro} = 1.9 µm, and b) the mesoporous skeleton, d_{meso} = 25 nm. c) Discrete bimodal pore size distribution.

4 Results and Discussion

In this communication we use a simple, general, phenomenological approach for analyzing single-phase incompressible flow through porous media with a continuous solid phase. It relies on equivalent particle (sphere) dimensions which characterize the corresponding behaviour in a particulate bed. Equivalence is obtained by the dimensionless scaling of macroscopic flow behaviour (pore space permeability and longitudinal dispersion) for both types of media, without the need for a direct geometrical translation of their constituent units. In this approach, the Reynolds number $Re = u_{sf}\mathscr{L}_{flow}/\nu$ (defined with respect to the superficial velocity, u_{sf}) is used to analyse the resistance of the porous medium to liquid flow, and the Peclet number $Pe = u_{av}\mathscr{L}_{stag}/D_m$ (defined with respect to the average velocity of an analyte through the bed, u_{av}) is used in the analysis of longitudinal dispersion. D_m is the diffusivity of the analyte in the mobile phase and ν its (kinematic) viscosity. Most important in the present context, $\mathscr{L}_{flow}$ and $\mathscr{L}_{stag}$ are appropriate lengths of the medium characterizing flow permeability and dispersion originating in stagnant zones, respectively (cf. Fig. 1)[1)].

4.1 Hydraulic Permeability

Based on a general phenomenological analysis, the resistance of (incompressible) random close packings of spherical particles to liquid flow can be expressed by the following relationship between dimensionless variables (with, as usual, the mean sphere diameter d_p for $\mathscr{L}_{flow}$) [16]

$$\frac{\Delta P}{\rho u_{sf}^2}\frac{d_p}{L} = \mathscr{F} = f\left(Re = \frac{u_{sf}d_p}{\nu}, \varepsilon_{inter}, q_i, \psi_i\right) \quad (1)$$

where $\Delta P/L$ is pressure drop over length $\mathscr{L}$ of the bed (in the macroscopic flow direction), ρ is the density of the liquid, and q_i and ψ_i are parameters for particle shape and size distribution. Eq. (1) may be much simplified when the deviation from a uniform spherical shape and differences in particle size distribution, surface roughness, interparticle porosity (ε_{inter}) and bed structure for different sphere packings may be considered insignificant. Eq. (1) then reduces to a simple unique relation between friction factor $\mathscr{F}$ and Re [16,17].

1) List of symbols at the end of the paper.

Table 1. Characteristic dimensions and parameters of the porous media. d_{col} is the column diameter and $\mathscr{L}$ denotes the bed length. ε_{total}, ε_{inter} and ε_{intra} are the total, interparticle (interskeleton) and intraparticle (intraskeleton) porosities of the porous medium, respectively [12]. A_{spec} is the specific and A_{rel} the volume-weighted surface area.

Fixed bed	L [mm]	d_{col} [mm]	d_p [µm]	ε_{total}	ε_{inter}	ε_{intra}	A_{spec} [$m^2\ g^{-1}$]	A_{rel} [$m^2\ cm^{-3}$]	$\mathscr{L}_{flow}$ [µm]	$\mathscr{L}_{stag}$ [µm]
Spheres (nonporous)	53	4.6	3.0	0.36	0.36	–	0.6	0.7	3.0	–
Spheres (porous)	55	2.0	6.4	0.75	0.37	0.60	76	65	6.4	3.2
Monolithic structure	100	4.6	–	0.92	0.72	0.70	147	39	9.5	1.0

Fig. 3 demonstrates, as then expected, a superposition of these data for different sphere packings having similar ε_{inter}, q_i and ψ_i. The linear dependence of $\mathscr{F}$ on Re represents the validity of Darcy's law. An equivalent permeability length ($\mathscr{L}_{flow}$) for the monolithic structure, i.e., a particle diameter d_p for a fictitious bed (with similar ε_{inter}, q_i, ψ_i, and structure as the other two sphere packings) is obtained by dimensionless scaling of the pressure drop – flow rate dependence for monoliths to the $\mathscr{F}$ – Re relation characterizing particulate beds (Fig. 3). It is achieved by adjusting d_p which gives $\mathscr{L}_{flow}$ = 9.5 μm in the present case. The fact that the data for porous and nonporous sphere packings coincide by means of their mean d_p shows that the intraparticle pore network of these porous particles does not contribute measurably to macroscopic flow. The actual macro-to-mesopore diameter ratio in the sphere packing (and monolith) is of the order of 100, thus, hydraulic permeability of the intraparticle (and intraskeleton) mesopore space is some 10^4 times lower than that of the interparticle (and interskeleton) macroporous network, and the assumption that the former constitutes a stagnant zone seems to be justified.

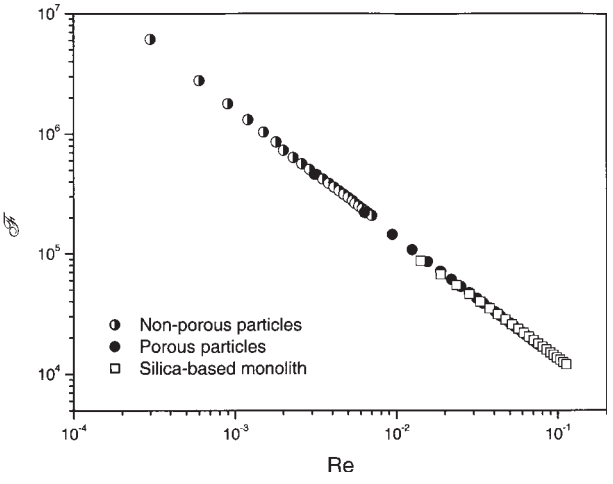

Figure 3. Friction factor vs. Reynolds number for the liquid in beds of (non)porous spheres, with d_p as $\mathscr{L}_{flow}$ in Re (Fig. 1). Dimensionless scaling for the monolith gives $\mathscr{L}_{flow}$ = 9.5 μm. Re = 0.1 corresponds to a pressure drop ΔP over the monolith (L = 100 mm) of about 15 MPa.

4.2 Hydrodynamic Dispersion

The spatial dimension of stagnant zones is often used as characteristic length for hydrodynamic dispersion in macroscopically homogeneous, microscopically disordered media like random packings of porous spheres because liquid holdup, i.e., diffusion-limited mass transfer in these regions, dominates dispersion for Pe >> 1 [13]. Similar to Eq. (1) we may write for the longitudinal dispersion coefficient D_L

$$\frac{D_L}{D_m} = \mathscr{D} = f\left(Pe = \frac{u_{av}\mathscr{L}_{stag}}{D_m}, \varepsilon_{inter}, q_i, \psi_i, \frac{D_{stag}}{D_m}\right) \qquad (2)$$

which, in contrast to Eq. (1), includes features of both the convection-dominated interparticle and diffusion-limited intraparticle pore space. Eq. (2) can also be simplified for packed beds with comparable ε_{inter}, q_i, ψ_i and structure, resulting in a relationship between the dispersivity $\mathscr{D}$ and Pe almost as simple as that between $\mathscr{F}$ and Re. The remaining difficulty in Eq. (2) is associated with an evaluation of the analyte diffusivity in stagnant zones (D_{stag}), as in general it depends on the morphology of the intraparticle pore space. However, when D_{stag} is similar the dispersion data for different particulate beds and monoliths are expected to collapse on a unique curve by means of the characteristic dimension $\mathscr{L}_{stag}$. This is demonstrated by the data in Tab. 2 and Fig. 4 which show D_{stag} is very similar for the porous particles and monolith used in this work. For completely porous spheres $\mathscr{L}_{stag} = r_p$ is easily measured (cf. Fig. 1), and has been used to calculate Pe in Fig. 4.

As with the permeability data (Fig. 3), the next step consists of dimensionless scaling, this time of the monoliths dispersion data to those obtained with the fixed bed of porous spheres, giving $\mathscr{L}_{stag}$ = 1.0 μm (Fig. 4). The equivalence in this case states that dispersion in the monolith associated with liquid holdup in the intraskeleton pore space resembles the contribution from stagnant zones (characterized by the same D_{stag}) in a bed of spherical particles with porous layer of thickness $\mathscr{L}_{stag}$. It is important to note that, if liquid holdup exists in a monolith and dominates dispersion, nonporous spheres are not appropriate for evaluating an equivalence based on this particular (nonmechanical) contribution.

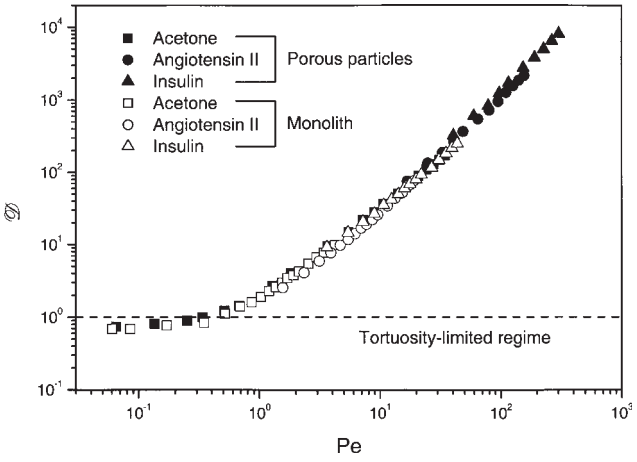

Figure 4. Longitudinal dispersivity vs. Peclet number for nonretained analytes in a bed of porous spheres, with r_p as $\mathscr{L}_{stag}$ in Pe (Fig. 1). Dimensionless scaling for the monolith gives $\mathscr{L}_{stag}$ = 1.0 μm.

5 Conclusions

It is possible to phenomenologically translate the macroscopic hydraulic permeability and longitudinal dispersion characteristics (dominated by the holdup contribution) of a monolith with bimodal pore size distribution and hierarchi-

Table 2. Physical properties of the analytes. R_G is the radius of gyration and D_{stag} denotes the effective diffusion coefficient of analyte molecules in the (intraparticle or intraskeleton) stagnant zone. $D_{stag} = \varepsilon_{intra} K_p D_m/\tau_{intra}$ where $\tau_{intra} = \varepsilon_{intra} + 1.5\,(1 - \varepsilon_{intra})$ is the tortuosity factor [18] and K_p characterizes hindered pore diffusion depending on the molecule size [19].

Analyte	M_w [g mol^{-1}]	R_G [nm]	D_m [10^{-10} m^2 s^{-1}]	D_{stag} [10^{-10} m^2 s^{-1}]	
				Porous particle	Monolith skeleton
Acetone	58.1	n.a.	12.8	6.6	8.1
Angiotensin II	1046	< 0.2	3.1	1.5	1.9
Insulin	5807	0.54	1.4	0.7	0.8

cally-structured pore network into distinct particle dimensions of what is most conventionally understood by a "random-close" sphere packing. The actual ratio of equivalent lengths, $\mathscr{R}_{hp} = \mathscr{L}_{flow}/\mathscr{L}_{stag}$, may be used as a parameter characterizing the hydrodynamic performance (hp) of a monolith. While this material provides relatively large flow-through pores ($\mathscr{L}_{flow}$ = 9.5 μm), it only needs a comparatively short diffusion length ($\mathscr{L}_{stag}$ = 1.0 μm) to combine the high permeability with a large surface area. With regard to $\mathscr{R}_{hp}$, the monolithic column resembles a fixed bed of (solid core-porous shell) spheres with $d_p = \mathscr{L}_{flow}$ and a porous layer of thickness $\mathscr{L}_{stag}$ (cf. Fig. 1). Thus, the volume-weighted surface area for a monolith can much larger than for a bed of core-shell spheres with the same $\mathscr{R}_{hp}$, and may be the origin of the superior performance displayed by the monolith in many applications. Vice versa, completely porous particles provide a higher surface area than the core-shell particles, which is still of the same order as that of the monolith, but in this case $\mathscr{R}_{hp}$ = 2 (while $\mathscr{R}_{hp} \approx 10$ for the monolith). Thus, due to the high porosity ($\varepsilon_{total} > 0.9$) and its unique, rigid structure that can withstand high pressure, this type of monolith offers substantial adsorption capacity (see A_{spec} and A_{rel} in Table 1) for fast and efficient liquid phase separations.

Acknowledgements

We gratefully acknowledge support of this work by the Deutsche Forschungsgemeinschaft (DFG) under grant SE 586/7–1.

Received: June 12, 2002 [CET 1628]

Symbols used

A_{col}	[m^2]	column cross-sectional area
A_{rel}	[m^2 m^{-3}]	relative surface area of particulate bed (monolith)
A_{spec}	[m^2 kg^{-1}]	specific surface area
d_{col}	[m]	column diameter
D_L	[m^2 s^{-1}]	longitudinal dispersion oefficient
D_m	[m^2 s^{-1}]	analytes free molecular diffusion coefficient in mobile phase
$\mathscr{D}$	[–]	reduced dispersivity, $\mathscr{D} = D_L/D_m$
D_{stag}	[m^2 s^{-1}]	effective diffusion coefficient in stagnant zone, $D_{stag} = \varepsilon_{intra} K_p D_m/\tau_{intra}$
u_{sf}	[m s^{-1}]	superficial mobile phase velocity, $u_{sf} = F_v/A_{col}$
u_{av}	[m s^{-1}]	average analyte velocity through the bed, $u_{av} = u_{sf}/\varepsilon_{total}$
F_v	[ml min^{-1}]	volumetric flow rate
Re	[–]	Reynolds number
Pe	[–]	Peclet number
d_p	[m]	mean diameter of spherical particles
K_p	[–]	hindrance factor concerning pore-level diffusion
$\mathscr{F}$	[–]	friction factor
$\mathscr{L}_{stag}$	[m]	characteristic length for liquid holdup in porous medium
$\mathscr{L}_{flow}$	[m]	characteristic length for hydraulic permeability
q_i	[–]	parameter(s) of particle size distribution
$\mathscr{R}_{hp}$	[–]	hydrodynamic performance factor, $\mathscr{R}_{hp} = \mathscr{L}_{flow}/\mathscr{L}_{stag}$
V_{col}	[m^3]	column volume
V_{inter}	[m^3]	interparticle (interskeleton) pore volume
V_{intra}	[m^3]	intraparticle (intraskeleton) pore volume
V_{solid}	[m^3]	volume of particle (skeleton) solid

Greek symbols

ε_{inter}	[–]	interparticle (interskeleton) porosity, $\varepsilon_{inter} = V_{inter}/V_{col}$
ε_{intra}	[–]	intraparticle (intraskeleton) porosity, $\varepsilon_{intra} = V_{intra}/(V_{intra} + V_{solid})$
ε_{total}	[–]	total porosity
ψ_i	[–]	particle shape parameter
ν	[m^2 s^{-1}]	kinematic viscosity of mobile phase
τ_{intra}	[–]	intraparticle (intraskeleton) tortuosity factor, $\tau_{intra} = \varepsilon_{intra} + 1.5\,(1 - \varepsilon_{intra})$
ρ	[kg m^{-3}]	density of mobile phase

References

[1] R. M. Heck, R. J. Farrauto, *Catalytic Air Pollution Control: Commercial Technology*, John Wiley & Sons, New York **1995**.

[2] R. A. Dunbar, J. D. Jordan, F. V. Bright, *Anal. Chem.* **1996**, *68,* 604.
[3] F. Kapteijn, J. J. Heiszwolf, T. A. Nijhuis, J. A. Moulijn, *CatTech*. **1999**, *3,* 24.
[4] F. Svec, J. M. J. Fréchet, *Ind. Eng. Chem. Res.* **1999**, *38,* 34.
[5] D. Josic, A. Buchacher, *J. Biochem. Biophys. Methods* **2001**, *49*, 153.
[6] N. Tanaka, H. Kobayashi, K. Nakanishi, H. Minakuchi, N. Ishizuka, *Anal. Chem.* **2001**, *73,* 420A.
[7] A. Kirschning, C. Altwicker, G. Dräger, J. Harders, N. Hoffmann, U. Hoffmann, H. Schönfeld, W. Solodenko, U. Kunz, *Angew. Chem. Int. Ed.* **2001**, *40,* 3995.
[8] J. L. Williams, *Catal. Today* **2001**, *69,* 3.
[9] P. Sepulveda, J. R. Jones, L. L. Hench, *J. Biomed. Mater. Res.* **2002**, *59,* 340.
[10] H. Pröbstle, C. Schmitt, J. Fricke, *J. Power Sources* **2002**, *105,* 189.
[11] K. Nakanishi, R. Takahashi, T. Nagakane, K. Kitayama, N. Koheiya, H. Shikata, N. Soga, *J. Sol-Gel Sci. Technol.* **2000**, *17,* 191.
[12] F. C. Leinweber, D. Lubda, K. Cabrera, U. Tallarek, *Anal. Chem.* **2002**, *74,* 2470.
[13] D. Kandhai, D. Hlushkou, A. G. Hoekstra, P. M. A. Sloot, H. Van As, U. Tallarek, *Phys. Rev. Lett.* **2002**, *88,* article no. 234501.
[14] Z. P. Lu, M. M. Dias, J. C. P. Lopes, G. Carta, A. E. Rodrigues, *Ind. Eng. Chem. Res.* **1993**, *32,* 1839.
[15] V. B. Di Marco, G. G. Bombi, *J. Chromatogr. A* **2001**, *931,* 1.
[16] H. Rumpf, A. R. Gupte, *Chem. Ing. Tech.* **1971**, *43,* 367.
[17] I. F. Macdonald, M. S. El-Sayed, K. Mow, F. A. L. Dullien, *Ind. Eng. Chem. Fundam.* **1979**, *18,* 199.
[18] M. Suzuki, J. M. Smith, *Chem. Eng. J.* **1972**, *3*, 256.
[19] H. Brenner, L. J. Gaydos, *J. Colloid Interface Sci.* **1977**, *58,* 312.

Anal. Chem. **2002,** *74,* 2470−2477

Characterization of Silica-Based Monoliths with Bimodal Pore Size Distribution

Felix C. Leinweber,[†] Dieter Lubda,[‡] Karin Cabrera,[‡] and Ulrich Tallarek*,[†]

Lehrstuhl für Chemische Verfahrenstechnik, Otto-von-Guericke Universität Magdeburg, Universitätsplatz 2, 39106 Magdeburg, Germany, and R&D Biochemistry and Separation, Merck KGaA, Frankfurter Strasse 250, 64293 Darmstadt, Germany

Band dispersion was studied and the retention thermodynamics addressed for insulin and angiotensin II on C18 silica monoliths with a bimodal pore size distribution, covering linear mobile-phase velocities up to 1 cm/s and different temperatures. These data suggest that the influence of average column pressure on retention (between 0 and 10 MPa) is not negligible. Plate height curves were interpreted with the van Deemter equation by assuming an independent contribution from mechanical and nonmechanical dispersion mechanisms. This analysis revealed diffusion-limited mass transfer in the mesoporous silica skeleton which, in turn, allowed us to calculate an equivalent dispersion particle diameter ($d_{\mathrm{disp}} = 3\ \mu\mathrm{m}$) using the *C*-term parameter of the van Deemter equation. The resulting superposition of reduced plate height curves for monolithic and particulate beds confirmed that this view presents an adequate analogy. The macroporous interskeleton network responsible for the hydraulic permeability of a monolith was translated to the interparticle pore space of particulate beds, and an equivalent permeability particle diameter ($d_{\mathrm{perm}} = 15\ \mu\mathrm{m}$) was obtained by scaling based on the Kozeny−Carman equation.

Monolithic structures, as compared to particulate chromatographic beds, have a continuous solid phase.[1−12] In this respect, at least, they resemble consolidated natural porous media which, on the other hand, are often characterized by a low average porosity and large-scale permeability heterogeneity.[13] Skeleton and domain sizes of monoliths, by contrast, can be small and repeated uniformly, resulting in microscopically disordered, but macroscopically homogeneous materials.[14−16] Again compared to particulate beds where the packing procedure and actual column-to-particle diameter ratio strongly influence a velocity correlation of the flow field on mesoscopic and macroscopic scale,[17−21] it is largely the manufacturing process of monolithic beds that determines the existence and amplitude of velocity extremes in the mobile phase on any time and length scale and, in turn, the mechanical contribution to transient and asymptotic dispersion. A particular flow regime is described by Peclet and Reynolds numbers defined with respect to a characteristic dimension of the medium, e.g., the average diameter of spherical particles in a particulate bed. By analogy, the domain size may be used as equivalent dimension in the case of monoliths.[14] However, the individual skeleton units are not randomly close packed as particles in a fixed bed but, rather, (in combination with the relatively large interskeleton flow channels) build a monolith domain of much higher porosity. Further, because the skeleton itself (like particles) may cover the range from totally porous to nonporous or, more correctly, contains (un)accessible pores depending on experimental conditions, we also need, in general, two lengths for permeability and diffusion-limited mass transfer when comparing different monoliths or relating these materials to particulate beds.

In this work, we are concerned with silica-based monoliths that possess a rather discrete bimodal pore size distribution and a high correlation of interconnectivity between these two sets of pores.[8,10] The larger macropores form a flow-channel network outside the monolith skeleton that rapidly transports solute molecules by

* To whom correspondence should be addressed. Phone: +49 (0)391-67-18644. Fax: +49 (0)391-67-12028. E-mail: ulrich.tallarek@vst.uni-magdeburg.de.
[†] Otto-von-Guericke Universität Magdeburg.
[‡] Merck KGaA.

(1) Hjertén, S.; Liao, J.-L. *J. Chromatogr.* **1988**, *457*, 165−174.
(2) Hjertén, S.; Liao, J.-L.; Zhang, R. *J. Chromatogr.* **1989**, *473*, 273−275.
(3) Tanaka, N.; Ebata, T.; Hashizume, K.; Hosoya, K.; Araki, M. *J. Chromatogr.* **1989**, *475*, 195−208.
(4) Nakanishi, K.; Soga, N. *J. Am. Ceram. Soc.* **1991**, *74*, 2518−2530.
(5) Nakanishi, K.; Soga, N. *J. Non-Cryst. Solids* **1992**, *139*, 1−13.
(6) Svec, F.; Fréchet, J. M. J. *Anal. Chem.* **1992**, *64*, 820−822.
(7) Wang, Q. C.; Svec, F.; Fréchet, J. M. J. *J. Chromatogr.* **1994**, *669*, 230−235.
(8) Minakuchi, H.; Nakanishi, K.; Soga, N.; Ishizuka, N.; Tanaka, N. *Anal. Chem.* **1996**, *68*, 3498−3501.
(9) Ericson, C.; Liao, J.-L.; Nakazato, K.; Hjertén, S. *J. Chromatogr., A* **1997**, *767*, 33−41.
(10) Nakanishi, K.; Minakuchi, H.; Soga, N.; Tanaka, N. *J. Sol-Gel Sci. Technol.* **1997**, *8*, 547−552.
(11) Sýkora, D.; Svec, F.; Fréchet, J. M. J. *J. Chromatogr., A* **1999**, *852*, 297−304.
(12) Svec, F.; Fréchet, J. M. J. *Ind. Eng. Chem. Res.* **1999**, *38*, 34−48.
(13) Sahimi, M. *Flow and Transport in Porous Media and Fractured Rock*; VCH: Weinheim, 1995.
(14) Minakuchi, H.; Nakanishi, K.; Soga, N.; Ishizuka, N.; Tanaka, N. *J. Chromatogr., A* **1997**, *762*, 135−146.
(15) Peters, E. C.; Svec, F.; Fréchet, J. M. J. *Chem. Mater.* **1997**, *9*, 1898−1902.
(16) Minakuchi, H.; Nakanishi, K.; Soga, N.; Ishizuka, N.; Tanaka, N. *J. Chromatogr., A* **1998**, *797*, 121−131.
(17) Knox, J. H.; Laird, G. R.; Raven, P. A. *J. Chromatogr.* **1976**, *122*, 129−145.
(18) Tsotsas, E.; Schlünder, E. U. *Chem. Eng. Process.* **1988**, *24*, 15−31.
(19) Guiochon, G.; Farkas, T.; Guan-Sajonz, H.; Koh, J.-H.; Sarker, M.; Stanley, B. J.; Yun, T. *J. Chromatogr., A* **1997**, *762*, 83−88.
(20) Giese, M.; Schäfer, K.; Vortmeyer, D. *AIChE J.* **1998**, *44*, 484−490.
(21) Shalliker, R. A.; Broyles, B. S.; Guiochon, G. *J. Chromatogr., A* **2000**, *888*, 1−12.

10.1021/ac011163o CCC: $22.00
Published on Web 04/26/2002

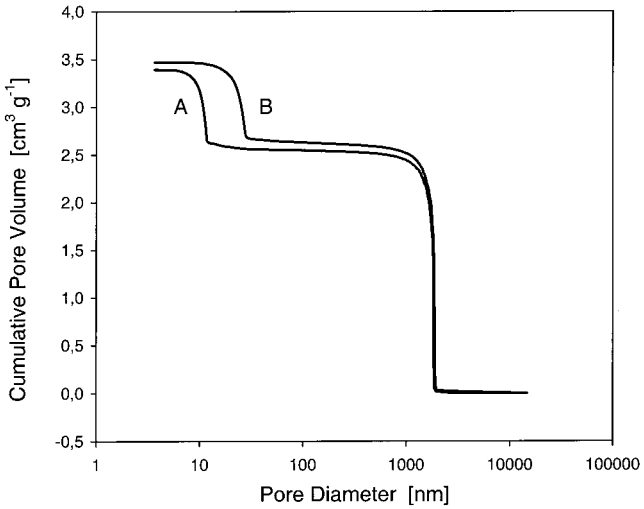

Figure 1. Cumulative specific pore volume for silica-based monoliths with 1.9-μm macrocopres and 12.5- (A) or 20-nm (B) mesopores.

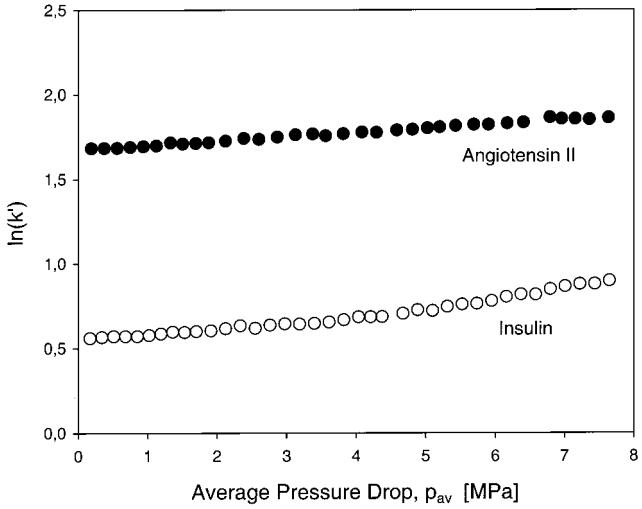

Figure 2. Dependence of the separation factor on average column pressure at 24 °C using the silica-based monolith with 12.5-nm average mesopore diameter.

convection down the column and to the smaller mesopores inside the silica matrix. The porous skeleton provides a relatively large surface area compared to the interskeleton pore space but, at the same time, needs only very short diffusion lengths and does not contain micropores to any significant amount. It has been shown that the macropore size can be varied independently from the skeleton size.[14] Thus, a careful control of the macropore permeability (transport dominated by convection) relative to mesopore residence times (diffusion-limited mass transfer) can be used to optimize the performance of this monolithic support in terms of throughput, dispersion, and capacity. For particulate structures, by contrast, a similar (independent) adjustment of permeability and dispersion length scales includes the transition from totally porous via pellicular to nonporous particles (or vice versa), with a concomitant drastic decrease in surface area (or increase of intraparticle residence times). In this study, we first address retention thermodynamics as column pressure drop spans more than 2 orders of magnitude, then characterize band dispersion, and finally determine equivalent sphere dimensions to interpret the observed behavior in view of particulate structures.

EXPERIMENTAL SECTION

Chemicals and Apparatus. Thiourea, trifluoroacetic acid (TFA), and acetonitrile (gradient grade) were obtained from Merck (Darmstadt, Germany). Deionized, purified water was prepared with a MilliQ water purification system. Angiotensin II ($M_w = 1180$) and insulin ($M_w = 5807$) were purchased from Sigma. All experiments were run on a Merck/Hitachi LaChrom HPLC system including quaternary low-pressure gradient pump, autosampler, column oven, and UV detector. The configuration was controlled by Merck/Hitachi HSM software.

Measurements were made with Chromolith Performance RP18e columns (100 × 4.6 mm) having interskeleton macropores of 1.9 μm and 12.5 or 20 nm intraskeleton mesopores, as can be seen in Figure 1. Pore size distributions were measured by nitrogen adsorption and mercury porosimetry at Merck. LiChrospher RP18 columns (100 × 4.6 mm) packed with spherical particles having 10-nm mesopores were also obtained from Merck, including their particle size distributions. Plate numbers were determined by a computer algorithm based on an exponentially modified Gaussian (EMG). Relative errors made by using an EMG are within 1.5% for peaks with asymmetry factors between 1 and 2.76, while statistical moment analysis leads to similar accuracy.[22] Peak shapes of angiotensin II and insulin had asymmetry factors smaller than 1.5 and, thus, remained in the range for adequate use of an EMG.

Separation Conditions. The premixed eluent for insulin separation was prepared from 1500 mL of deionized (DI) water, 643 mL of acetonitrile, and 2.143 mL of TFA, which translates to 70:30 (W/CH_3CN) eluent mixed by the gradient delivery system. For angiotensin II, the eluent consisted of 2000 mL of DI water, 440 mL of acetonitrile, and 2.440 mL of TFA corresponding to a 82:18 (W/CH_3CN) eluent. The pump was operated at volumetric flow rates between 0.1 and 9.0 mL/min (5% accuracy). Angiotensin II and insulin were dissolved at 20 and 100 μg/mL, respectively, in the eluent to avoid concentration effects due to different elution strengths. The injection volume was 10 μL with thiourea (4 μg/mL) as the t_0 marker, and detection was carried out at 215 nm (16-μL detection cell volume). Plate height curves were measured at increasing flow rate. After reaching the maximum bed velocities (~1 cm/s), this sequence was repeated to minimize systematic errors. Data emerge as mean values of two independent runs; all temperatures are given as oven temperature.

RESULTS AND DISCUSSION

Retention Thermodynamics. One of the main advantages of bimodal silica-based monoliths is their increased hydraulic permeability compared to random close packings of porous spheres with similar dispersion characteristics. It allows comparatively high mobile-phase velocities. When under isocratic conditions, the volumetric flow rate is increased from 1 to 2 mL/min in particulate packings to 5 to 10 mL/min through monolithic structures, the actual influence of pressure drop on retention, peak capacity, and selectivity may not be negligible any longer. This becomes particularly important for larger molecules. As shown in Figure 2, the separation factor of both angiotensin II and insulin

(22) Foley, J. P.; Dorsey, J. G. *Anal. Chem.* **1983**, *55*, 730−737.

Table 1. Parameters Considered in the Band Dispersion Analysis

eddy dispersion[36]	A	$A = 2\gamma d_p$
longitudinal diffusion[36]	B/u_{av}	$B = 2k_D D_m$
mass transfer[43]	Cu_{av}	$C = \dfrac{\epsilon_p^2(1-\epsilon_b)m^2 d_p^2}{30[\epsilon_b + \epsilon_p(1-\epsilon_b)m]^2 \tilde{D}_{eff}}$
effective diffusivity[43]	$\tilde{D}_{eff}$	$\tilde{D}_{eff} = \dfrac{D_{eff}}{f(\lambda)} = \dfrac{\epsilon_p K_p D_m}{\tau}\left[\dfrac{3}{\lambda}\left(\dfrac{1}{\tanh \lambda} - \dfrac{1}{\lambda}\right)\right]^{-1}$
retention parameter[45]	m	$m = 1 + (1-\epsilon_p)k'/\epsilon_p\Phi$

clearly depends on the average column pressure. Possible thermodynamic explanations have been discussed for many years.[23−31] In contrast to Martire and Boehm,[25] who presented a unified theory of chromatography using statistical thermodynamics, other authors obtained equivalent results from macroscopic solution thermodynamics. The isothermal change in Gibbs free energy with pressure equals the change of the analyte's standard partial molar volume ($\Delta V°_{assoc}$) for its association process with a stationary phase. By relating Gibbs free energy to the chemical equilibrium constant expressed by the phase ratio Φ and separation factor k' we obtain eq 1. It describes the dependence of k'on

$$\left(\frac{\partial \ln k'}{\partial p}\right)_T = -\frac{\Delta V°_{assoc}}{RT} \qquad (1)$$

pressure if the influence of the latter on Φ and an isothermal change in molar concentration due to mobile-phase compressibility are negligible.[27,30] Since retention of polyelectrolytes such as peptides and polypeptides depends on their ionization, shifts in ionization equilibrium strongly affect the separation factor, especially at pH values close to the p*I*. In our studies, the pH was adjusted to 2.1. Under these conditions, angiotensin II and insulin are fully protonated and changes of the pK_a and pH with pressure have a negligible effect. An analysis of the data in Figure 2 by use of eq 1 revealed changes of the standard partial molar volume of −63 and −109 mL/mol for angiotensin II and insulin, respectively. These differences are consistent with earlier observations for peptides and polypeptides.[28,31] We obtained similar results for monoliths with 20-nm average mesopore diameter suggesting that the C18 end-capped surface modification is comparable on each column. Our data indicate that for peptides and proteins the molecular size becomes important in retention thermodynamics. For example, the Stokes' radius of insulin is ∼1.1 nm.[32] Thus, changes in pressure drop may not be negligible any longer as normally assumed for small, uncharged solutes.[33]

Band Dispersion. Although from a general point of view the solid phase in monoliths is continuous (while it is discontinuous in a bed of spheres), the inherent physical mechanisms leading to axial spreading of a solute band in particulate packings also prevail in monolithic structures: (a) molecular diffusion, (b) a mechanical contribution due to the stochastic velocity field (outside the spherical particles or solid monolith skeleton) induced by the randomly distributed pore boundaries, and (c) nonmechanical effects associated with liquid holdup inside the particles or (in the present case mesoporous) monolith skeleton and no-slip condition at the solid−liquid interface.[13,34] This very last effect still exists in a monolith with nonporous skeleton as in a bed of nonporous spheres. Further, it is known that the dispersion in consolidated and unconsolidated media is similar concerning individual contributions, but characteristic time and length scales may differ significantly.[35] By considering these processes as independent, their rate constants add inversely, and in view of a typical chromatographic analysis performed in our present study, we return to the familiar van Deemter equation[36] for characterizing axial dispersion also in monolithic structures (parameters are listed in Table 1).

Plate height curves at different temperatures were measured for angiotensin II and insulin using silica monoliths with 12.5- or 20-nm mesopores (Figures 3 and 4). The contribution of axial diffusion (*B*-term) resulting from the relatively low solute diffusivities remains small. Due to the very few data points (usually) acquired in that region of the curves where the *B*-term dominates, fitting procedures did not result in reliable parameters. Thus, prior to our data analysis, in view of the van Deemter equation, diffusion coefficients of the analytes were calculated by the Young−Carroad−Bell method.[37,38] Although originally developed for large globular proteins, this approach only requires the molecular mass and also recognizes the influence of temperature and viscosity. Diffusion coefficients in Table 2 were then used to calculate the *B*-term parameter (cf. Table 1), and results of our subsequent plate height analysis are summarized in Table 3. We compared the regression coefficients obtained on the basis of the van Deemter model (*A*-term independent of velocity) to an analogous procedure by using the Knox equation with $u_{av}^{1/3}$ dependence of the eddy dispersion term.[39] In all cases, the regression analysis favored the van Deemter equation, which may be due to the fact that we

(23) Bidlingmeyer, B. A.; Hooker, R. P.; Lochmüller, C. H.; Rogers, L. B. *Sep. Sci.* **1969**, *4*, 439−446.
(24) Bidlingmeyer, B. A.; Rogers, L. B. *Sep. Sci.* **1972**, *7*, 131−158.
(25) Martire, D. E.; Boehm, R. E. *J. Phys. Chem.* **1987**, *91*, 2433−2446.
(26) McGuffin, V. L.; Evans, C. E. *J. Microcolumn Sep.* **1991**, *3*, 513−520.
(27) Guiochon, G.; Sepaniak, M. J. *J. Chromatogr.* **1992**, *606*, 248−250.
(28) McGuffin, V. L.; Chen, S.-H. *J. Chromatogr., A* **1997**, *762*, 35−46.
(29) Ringo, M. C.; Evans, C. E. *Anal. Chem.* **1997**, *69*, 643−649.
(30) Ringo, M. C.; Evans, C. E. *Anal. Chem.* **1997**, *69*, 4964−4971.
(31) Chen, S.-H.; Ho, C.-T.; Hsaio, K.-Y.; Chen, J.-M. *J. Chromatogr., A* **2000**, *891*, 207−215.
(32) Olesen, H.; Rehfeld, J.; Hom, B. L.; Hippe, E. *Biochim. Biophys. Acta* **1969**, *194*, 67−70.
(33) Guiochon, G.; Golshan-Shirazi, S.; Katti, A. M. *Fundamentals of Preparative and Nonlinear Chromatography*; Academic Press: Boston, 1994.
(34) Koch, D. L.; Brady, J. F. *J. Fluid Mech.* **1985**, *154*, 399−427.
(35) Sahimi, M. *Rev. Mod. Phys.* **1993**, *65*, 1393−1534.
(36) van Deemter, J. J.; Zuiderweg, F. J.; Klinkenberg, A. *Chem. Eng. Sci.* **1956**, *5*, 271−289.
(37) Young, M. E.; Carroad, P. A.; Bell, R. L. *Biotechnol. Bioeng.* **1980**, *22*, 947−955.
(38) Tyn, M. T.; Gusek, T. W. *Biotechnol. Bioeng.* **1990**, *35*, 327−338.
(39) Knox, J. H. *J. Chromatogr. Sci.* **1977**, *15*, 352−364.

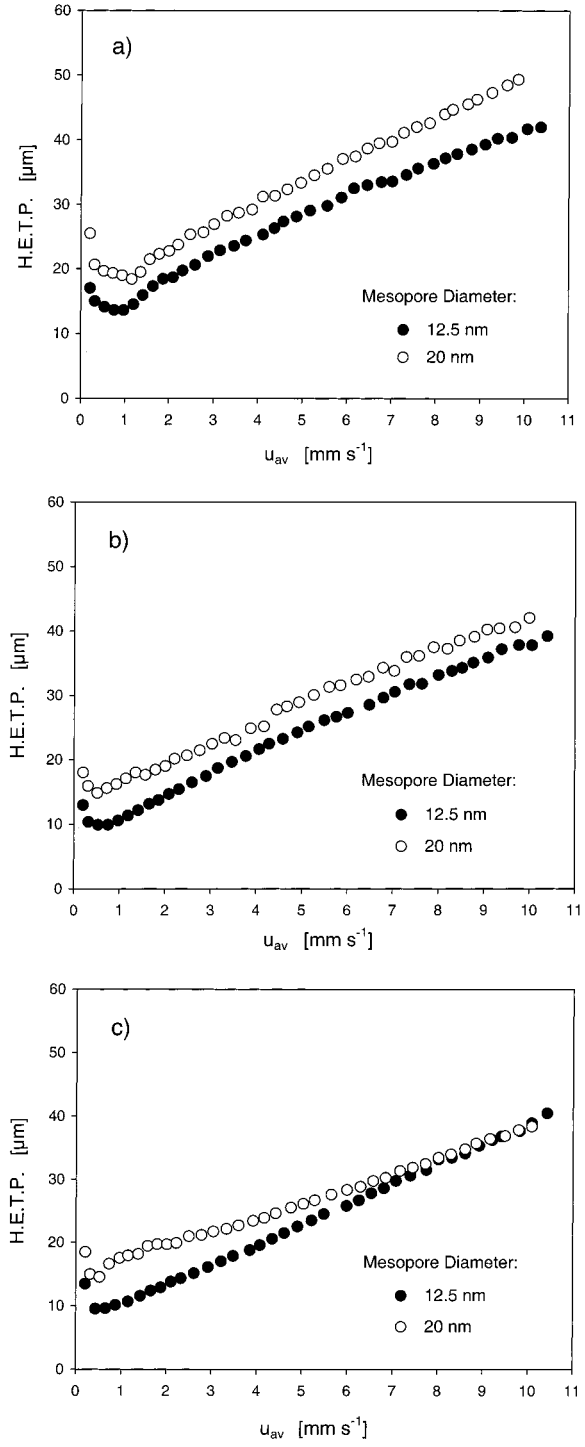

Figure 3. Plate height curves for angiotensin II with C18e silica monoliths: (a) 16, (b) 24, and (c) 32 °C oven temperature; average macropore diameter, 1.9 μm.

worked in a relatively narrow range (of only two decades) and at low values (below 10^2) of Peclet numbers; for the calculation of Peclet numbers, we refer to our forthcoming discussion. This observation, however, is not surprising when diffusion-limited mass transfer of stagnant fluid entrained in the monolith skeleton dominates the band spreading at higher flow rates (it should be remembered that we also work under retained conditions). Then, plate height curves are expected to taper off only slightly, if at all, due to that particular dispersion contribution arising from the

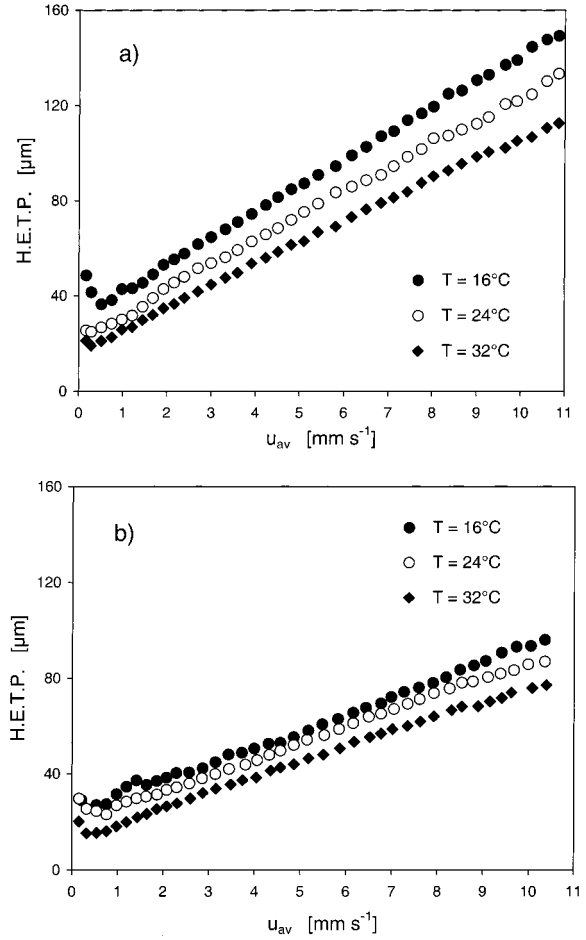

Figure 4. Temperature dependence of the plate height curves for insulin on C18e silica monoliths with different mesopore diameters: (a) 12.5 and (b) 20 nm, macropore diameter, 1.9 μm.

Table 2. Calculated Mobile-Phase Viscosity and Solute Diffusivities

	angiotensin II		insulin	
temp (°C)	η_{mp} (10^{-3} Pa s)	D_m (10^{-6} cm^2 s^{-1})	η_{mp} (10^{-3} Pa s)	D_m (10^{-6} cm^2 s^{-1})
16	1.10	2.1	0.94	1.4
24	0.85	2.8	0.79	1.8
32	0.75	3.2	0.68	2.1

stochastic flow field outside the monolith skeleton coupled with lateral dispersion.[40]

Another question arising in relation to high linear flow rates and column pressure drops is whether a perfusion mechanism is operative in the bimodal silica monoliths. It refers to the particular situation in which the intraskeleton velocity in the hierarchic network of interconnected (interskeleton) macropores and (intraskeleton) mesopores becomes nonzero. Then, mass transfer in the porous skeleton is enhanced by convection and the effective pore diffusivity increases. This phenomenon has been studied in much detail for particulate beds.[41−46] In the laminar flow regime

(40) Giddings, J. C. *Dynamics of Chromatography.* Part I: *Principles and Theory*; Marcel Dekker: New York, 1965.
(41) Afeyan, N. B.; Gordon, N. F.; Mazsaroff, I.; Varady, L.; Fulton, S. P.; Yang, Y. B.; Regnier, F. E. *J. Chromatogr.* **1990**, *519*, 1−29.
(42) Liapis, A. I.; McCoy, M. A. *J. Chromatogr.* **1992**, *599*, 87−104.

Table 3. van Deemter Parameters for Angiotensin II and Insulin (cf. Table 1)

	angiotensin II						insulin					
	A (10^{-6} m)		B_{calc} (10^{-9} m^2 s^{-1})		C (10^{-3} s)		A (10^{-6} m)		B_{calc} (10^{-9} m^2 s^{-1})		C (10^{-3} s)	
temp (°C)	12.5 nm	20 nm	12.5 nm	20 nm	12.5 nm	20 nm	12.5 nm	20 nm	12.5 nm	20 nm	12.5 nm	20 nm
16	12.35	16.75	0.25	0.25	3.05	3.34	32.87	23.94	0.17	0.17	10.85	6.98
24	8.30	13.59	0.33	0.33	3.12	2.98	22.03	20.66	0.21	0.21	10.28	6.61
32	7.23	14.33	0.39	0.39	3.17	2.40	17.30	13.29	0.25	0.25	9.00	6.39

and with equivalent particulate material, perfusive flow may be approximated by a linear relationship between the intraparticle and bed superficial velocities, i.e., $u_{intra} = a_0 u_{sf}$.[43] However, an analysis of our plate height curves using the *C*-term parameter that incorporates the influence of intraparticle (or intraskeleton) convection through a convection-augmented diffusivity (cf. Table 1) gives values for a_0 statistically indistinguishable from zero. Thus, inside the monoliths mesopores, which provide most of the effective surface area, the mobile phase is stagnant and associated mass transfer remains diffusion-limited. Possible reasons are (i) the pore network connectivity of the silica skeleton is unfavorable,[47] (ii) the solute diffusivity is too large compared to a small intraskeleton velocity component,[47,48] and (iii) mesopores are too small compared to macropores (factor 10^2) so that the typical pressure drop is not sufficient to create a significant intraparticle (or intraskeleton) flow.[49] Our results suggest that these bimodal silica monoliths inherently show diffusion-limited mass transfer similar to conventional particulate beds of spheres having 12.5-nm (or 20-nm) intraparticle pores.

The fact that the term perfusion has been associated recently with monolithic columns in which the intraskeleton pores were largely unaccessible for solute molecules is misleading.[50,51] In these cases, the tracer only samples dedicated flow pores of an (effectively) monomodal interskeleton pore network where convection naturally exists. This situation simply translates to liquid chromatography with a packed bed of nonporous particles for which the plate height data are well known to taper off at increasing flow rate because a classical holdup contribution is not present. It does not resemble the case in which a subnetwork of pores, e.g., in a hierarchically structured medium having bimodal (or higher order) pore size distribution like a bed of porous particles, is permeated by any significant amount of convection (in addition to diffusion and, of course, in addition to convection in the primary set of pores).

The data in Table 3 (and corresponding Figures 3 and 4) indicate a strong influence of temperature on band spreading by eddy dispersion; i.e., the *A*-term parameter is reduced by almost half as temperature increases from 16 to 32 °C. Elevated temperature increases molecular diffusion and, thus, enhances lateral mass transfer (more correctly, lateral dispersion), which equilibrates between molecules residing temporarily in velocity extremes of the mobile phase.[40] Similarly, concerning stagnant zones in the monolith, intraskeleton mass-transfer resistance (as indicated by the *C*-term parameter in Table 3) is decreased by increasing diffusion. Further, when addressing different behavior of the solutes, hindered pore diffusion needs attention: angiotensin II is about one-fifth of the molecular mass of insulin and gives much smaller *C*-term parameters, a fact that is certainly influenced by its higher pore diffusivity.[52] The only general conclusion concerning these still complex data with contributions from (stagnant and flowing) mobile and stationary phase is that an elevated temperature favors separation efficiency over the range studied.

Equivalent Sphere Dimensions. The foregoing analysis indicates that it could be beneficial (and not only tempting from an intuitive or historical point of view) to introduce equivalent particle dimensions for hydraulic permeability and the dispersion characteristics of monoliths. This may be particularly important and helpful when compiling these data for a dimensionless analysis or scaling purposes using particulate and monolithic beds.[39] Nonporous, pellicular, and totally porous, but spherical particles are most widely used in liquid chromatography today. Thus, we focus on equivalent sphere dimensions when considering a particular hydrodynamic property of monoliths, but could also extend our view to, for example, slab-shaped particles.[43]

Silica-based monoliths with bimodal pore size distribution can offer high bed permeability, low dispersion, and relatively high surface area at the same time, so they cannot be described by just one characteristic length. Rather, equivalent particle (sphere) dimensions must be attributed to the following factors influencing the overall performance: band dispersion, bed permeability, and column surface-to-volume ratio. As a characteristic dimension for band dispersion, we consider the spatial domain of diffusion-limited mass transfer in the monolith and calculate the diameter of an equivalent, totally porous spherical particle by using the *C*-term value obtained in our previous van Deemter analysis of plate height data (Table 3). Before rearranging the expression for the *C*-term (Table 1) in view of an equivalent dispersion particle diameter (d_{disp}), parameters in this equation have to be addressed by measuring pore volume of the monolithic structure. Together with the total porosity (ϵ_{total}) obtained by dividing the elution volume of an inert tracer by the total column volume, the pore volume ratio $\Theta = V_{macro}/V_{meso}$ forms the basis for calculating

(43) Rodrigues, A. E.; Lopes, J. C.; Lu, Z. P.; Loureiro, J. M.; Dias, M. M. *J. Chromatogr.* **1992**, *590*, 93−100.
(44) Carta, G.; Gregory, M. E.; Kirwan, D. J.; Massaldi, H. A. *Sep. Technol.* **1992**, *2*, 62−72.
(45) Frey, D. D.; Schweinheim, E.; Horváth, Cs. *Biotechnol. Prog.* **1993**, *9*, 273−284.
(46) Davis, R. H.; Stone, H. A. *Chem. Eng. Sci.* **1993**, *48*, 3993−4005.
(47) Meyers, J. J.; Liapis, A. I. *J. Chromatogr., A* **1999**, *852*, 3−23.
(48) McCoy, M.; Kalghatgi, K.; Regnier, F. E.; Afeyan, N. *J. Chromatogr., A* **1996**, *743*, 221−229.
(49) Pfeiffer, J. F.; Chen, J. C.; Hsu, J. T. *AIChE J.* **1996**, *42*, 932−939.
(50) Hahn, R.; Jungbauer, A. *Anal. Chem.* **2000**, *72*, 4853−4858.
(51) Ghose, S.; Cramer, S. M. *J. Chromatogr., A* **2001**, *928*, 13−23.
(52) Brenner, H.; Gaydos, L. J. *J. Colloid Interface Sci.* **1977**, *58*, 312−356.

Table 4. Physical Properties of the Monolithic Structures (cf. List of Symbols)

d_{macro} (μm)	d_{meso} (nm)	ϵ_{total}	ϵ_b	ϵ_p	Φ	τ
1.9	12.5	0.862	0.597	0.658	0.160	1.171
1.9	20	0.915	0.676	0.738	0.093	1.131

skeleton porosity ϵ_p (which translates to the intraparticle porosity of a spherical particle)

$$\epsilon_p = \frac{V_{meso}}{V_{skeleton}} = \frac{\epsilon_{total}}{1 + \Theta(1 - \epsilon_{total})} \quad (2)$$

and bed porosity ϵ_b characterizing the pore space outside the monolith skeleton (which translates to the interparticle porosity in a packed bed of spheres)

$$\epsilon_b = \frac{V_{macro}}{V_{column}} = \frac{\epsilon_{total}}{1 + 1/\Theta} \quad (3)$$

Physical properties of the monoliths are summarized in Table 4. Both bed and skeleton porosities (thus, the total porosity) of these bimodal monolithic structures are significantly increased compared to random close packings of spherical, porous particles.[53] For example, LiChrospher RP18 (5-μm particle diameter and 10-nm pore diameter) has a total porosity of 0.69, i.e., a pore porosity (ϵ_p) of 0.50 combined with a bed porosity (ϵ_b) of typically 0.38. In addition to these parameters, the effective pore diffusion coefficient (D_{eff}) of the solute, the experimental *C*-term parameter in Table 3, and corresponding retention parameter *m* (Table 1) are needed for calculating d_{disp}. This quantity can be regarded as an equivalent length scale that solute molecules travel in stagnant zones of the porous medium. Thus, the monolith is viewed as an ensemble (but not a close packing; see ϵ_b in Table 4!) of spheres with diameter d_{disp} and, of course, the identical intraparticle pore network morphology (including ϵ_p, Table 4).

$$d_{disp} = \left[30 D_{eff} C \frac{[\epsilon_b + \epsilon_p(1 - \epsilon_b)m]^2}{\epsilon_p^2(1 - \epsilon_b)m^2}\right]^{1/2} \quad (4)$$

In view of fixed beds based on random close packings of spheres with ϵ_b of 0.37−0.4, a porous medium consisting of spherical particles located (fixed) in space such that the resulting interparticle porosity of this geometry gives a permeability approaching that of the monoliths, although satisfying the dispersion criterion by the size (d_{disp}) and porosity (ϵ_p) of the particles, can only result in a fictitious equivalent as it requires $\epsilon_b \gg 0.37-0.4$. It is more realistic to introduce a second (and larger) equivalent particle diameter based on hydraulic permeability (d_{perm}) and combine it with d_{disp} to a pellicular particle that satisfies both dispersion and permeability of a monolith. For this purpose, we rearrange the

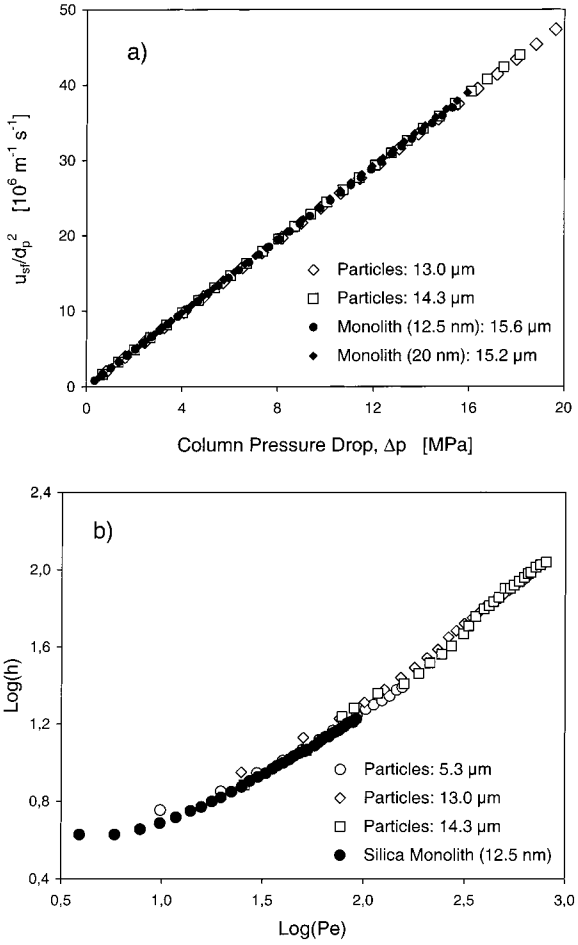

Figure 5. (a) Scaling of hydraulic permeability data originating from particulate and monolithic beds according to the Kozeny−Carman equation, based on d_p for particles and leading to d_{perm} for monoliths. (b) Reduced plate height curves for particulate and monolithic structures (based on $d_{disp} = 2.5$ μm and d_p), with angiotensin II as the solute.

Kozeny−Carman equation[54]

$$\frac{u_{sf}}{d_{perm}^2} = -\frac{\epsilon_b^3}{180\eta_{mp}(1 - \epsilon_b)^2}\frac{\Delta p}{L} \quad (5)$$

Figure 5a demonstrates how d_{perm} for monoliths is determined by using particulate packings as a reference. The bed's superficial velocity, normalized by the respective (well-characterized) average particle diameter, is plotted against column pressure drop for both monolithic and particulate material. This scaling procedure gives an equivalent permeability particle diameter of slightly more than 15 μm for the silica-based monoliths.

Table 5 summarizes equivalent permeability and dispersion particle dimensions calculated with eqs 4 and 5. Based on this result, Figure 5b presents reduced plate height curves for angiotensin II obtained with monoliths and beds of porous particles under similar conditions. An equivalent particle Peclet number (*Pe*) is defined via the dimensionless times for diffusion ($t_D = D_m t/d_{disp}^2$) and convection ($t_C = u_{av} t/d_{disp}$), $Pe = t_C/t_D =$

(53) Neue, U. D. *HPLC Columns: Theory, Technology, and Practice;* Wiley-VCH: New York, 1997.

(54) Bear, J. *Dynamics of Fluids in Porous Media*; Dover Publications: New York, 1988.

Table 5. Equivalent Sphere Dimensions for Silica-Based Monoliths with Bimodal Pore Size Distribution

pore diameter		equivalent sphere diameter			
macropore (μm)	mesopore (nm)	d_{perm} (μm)	$d_{disp,Ang.\ II}$ (μm)	$d_{disp,Insulin}$ (μm)	relative surface area (%)
1.9	12.5	15.6	2.5	3.9	79
1.9	20	15.2	2.5	3.4	73

$u_{av}d_{disp}/D_m$ and characterizes the relative importance of these contributions at a given flow rate. It should be noted that our values for d_{disp} between 2.5 and 3.9 μm (Table 5) are very close to the monoliths' domain size, which has been used as an effective particle dimension in earlier work by Minakuchi et al.[14,16] This domain includes the macropore size and thickness of the silica skeleton at the narrower (saddle) portions. Thus, our approach for estimating d_{disp} based on a characteristic dimension of diffusion-limited mass transfer and, in turn, the morphological approach lead to conservative estimates. Then, under most ideal conditions and as clearly seen in Figure 5b, the monolithic and particulate axial dispersion data collapse on a single universal reduced plate height curve. Deviations from that behavior are expected, e.g., when a particulate column (or monolith) is irreproducibly packed (more irregularly manufactured) and flow field heterogeneities of that particular structure become more important relative to stagnant mobile-phase mass transfer.

Because the silica monoliths show a relatively high bed porosity ϵ_b of about two-thirds (Table 4), which forms the basis for their substantial permeability ($d_{perm} \approx 15$ μm), the question naturally arises whether this material can still provide a significant intraskeleton surface. In fact, these monoliths also have a highly porous backbone as indicated by the mesopore porosity (ϵ_p) in Table 4. Compiled data from Merck KGaA (Darmstadt, Germany) on the specific surface area and density of totally porous, spherical particles confirm that the effective surface of a column does not depend on the particle diameter, but rather on intraparticle pore size (at constant ϵ_p), illustrated in Figure 6. The silica-based monoliths with bimodal pore size distribution show an only slightly smaller surface area with respect to beds of totally porous particles (cf. Table 5).

CONCLUSIONS

There exists no diffusive particle type that offers all of the three main advantages of silica-based monoliths with bimodal pore size distribution: high separation efficiency, low pressure drop, and a large effective, specific surface area for high adsorption/reaction capacity. Intraskeleton mass transfer is diffusion-limited as in porous particles with identical pore network morphology, but it is characterized by only short diffusion path lengths. While for beds of totally porous spheres, efficiency and permeability are usually analyzed by using the same mean particle diameter, the monoliths with bimodal pore size distribution can be described by pellicular particles with an overall diameter d_{perm} (15 μm), having a diffusive porous layer of $d_{disp}/2$ (1.5 μm). We express characteristic lengths for dispersion in stagnant zones of the monolith and its hydraulic permeability by two independent equivalent particle diameters and, thus, account for an also independent variation of the macropore and skeleton size. Consequently, the associated fluid dynamics in the monolith is comparable (equivalent) to that in random close packings of the resulting pellicular particles. The benefit of this monolithic structure is, however, that due to its porous skeleton it can offer a much higher surface area than these pellicular particles.

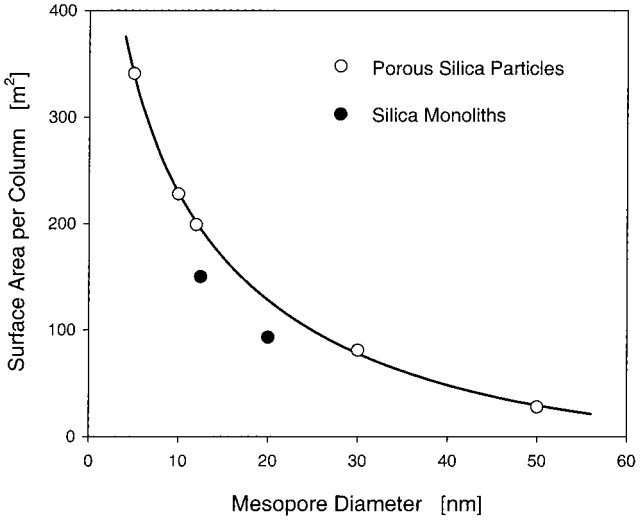

Figure 6. Absolute surface area of a 4.6 mm i.d. × 100 mm column depending on the (intraparticle or intraskeleton) mesopore diameter of particulate beds and monoliths.

Monoliths with a nonporous skeleton or an unaccessible intraskeleton pore network resemble beds of nonporous spheres ($d_p = d_{perm}$). In this case, the characteristic diffusion length is expectedly small as it is associated with the no-slip condition at the skeletons external surface, giving rise to a velocity boundary layer that needs transchannel equilibration only. By introducing different characteristic (permeability and dispersion) lengths, monoliths can combine short diffusion paths (high separation efficiency), large specific surface (loading capacity), and high bed permeability (mobile-phase velocity) for a superior performance compared to fixed beds of particulate, diffusive adsorbents. They may also be an alternative to perfusive particulate media that develop their potential, i.e., a dynamically reduced intraparticle diffusion length at increasing superficial flow rates only for slowly diffusing molecules and relatively large intraparticle pores, which either reduces the surface-to-volume ratio of a particle or the amount of intraparticle flow.

GLOSSARY

A, B, C	parameters in van Deemter equation,[36] Table 1
D_{eff}	effective pore diffusivity (m^2/s)
D_m	molecular free diffusion coefficient[37] (m^2/s)
$\tilde{D}_{eff}$	convection-augmented diffusivity (m^2/s), Table 1
d_p	particle diameter (μm)
$d_{disp/perm}$	equivalent particle diameter for monoliths (μm), eqs 4 and 5
HETP	height equivalent to one theoretical plate (μm)
k'	separation factor
k_D	obstruction parameter (taken as 0.6)
K_p	hindrance parameter for pore-level diffusion[52]
m	retention parameter, Table 1

p_{av}	average column pressure (MPa)
Δp	column pressure drop (MPa)
R	universal gas constant (J mol^{-1} K^{-1})
u_{av}	average linear velocity through the bed (mm/s)
u_{sf}	mobile-phase superficial velocity (mm/s)
ΔV°_{assoc}	difference in standard partial molar volume (cm^3/mol)
V_{macro}	macropore volume (cm^3)
V_{meso}	volume of mesopores (cm^3)
$V_{skeleton}$	volume of silica skeleton (including mesopores) (cm^3)
Φ	phase ratio: $(1 - \epsilon_p)\ (1 - \epsilon_b)/(\epsilon_b + \epsilon_p\ (1 - \epsilon_b))$
Θ	pore volume ratio: V_{macro}/V_{meso}
ϵ_p	pore porosity (inside spheres or intraskeleton), eq 2
ϵ_b	bed porosity (between spheres/interskeleton), eq 3
ϵ_{total}	total column porosity
γ	eddy-diffusivity parameter
η_{mp}	dynamic viscosity of mobile phase (Pa s)
λ	intraparticle (or intraskeleton) Peclet number
τ	intraskeleton tortuosity factor: $\epsilon_p + 1.5\ (1 - \epsilon_p)$

ACKNOWLEDGMENT

We thank Edith Dicks, Gisela Jung, Martina Witzenbacher, and Alexander Kraus from Merck KGaA (Darmstadt, Germany) for their technical support.

Received for review November 8, 2001. Accepted February 23, 2002.

AC011163O

Available online at www.sciencedirect.com
SCIENCE DIRECT®
Journal of Chromatography A, 1006 (2003) 207–228
JOURNAL OF CHROMATOGRAPHY A
www.elsevier.com/locate/chroma

Chromatographic performance of monolithic and particulate stationary phases
Hydrodynamics and adsorption capacity

Felix C. Leinweber, Ulrich Tallarek*
Institut für Verfahrenstechnik, Otto-von-Guericke-Universität Magdeburg, Universitätsplatz 2, D-39106 Magdeburg, Germany

Abstract

Monolithic chromatographic support structures offer, as compared to the conventional particulate materials, a unique combination of high bed permeability, optimized solute transport to and from the active surface sites and a high loading capacity by the introduction of hierarchical order in the interconnected pore network and the possibility to independently manipulate the contributing sets of pores. While basic principles governing flow resistance, axial dispersion and adsorption capacity are remaining identical, and a similarity to particulate systems can be well recognized on that basis, a direct comparison of sphere geometry with monolithic structures is less obvious due, not least, to the complex shape of the skeleton domain. We present here a simple, widely applicable, phenomenological approach for treating single-phase incompressible flow through structures having a continuous, rigid solid phase. It relies on the determination of equivalent particle (sphere) dimensions which characterize the corresponding behaviour in a particulate, i.e. discontinuous bed. Equivalence is then obtained by dimensionless scaling of macroscopic fluid dynamical behaviour, hydraulic permeability and hydrodynamic dispersion in both types of materials, without needing a direct geometrical translation of their constituent units. Differences in adsorption capacity between particulate and monolithic stationary phases show that the silica-based monoliths with a bimodal pore size distribution provide, due to the high total porosity of the material of more than 90%, comparable maximum loading capacities with respect to random-close packings of completely porous spheres.

Keywords: Monolithic columns; Stationary phases, LC; Hydrodynamic; Adsorption; Packed columns; Permeability; Dispersion

1. Introduction

Monolithic high surface area materials have found a number of applications in industrial and environmental technologies, e.g. as ceramic supports for high-temperature heterogeneous solid-phase–gas phase catalysis (especially as automotive exhaust gas catalysts and in industrial gas purification), as condensators, and in liquid chromatography [1–7]. Due to the reduced dynamic viscosity of gases at elevated temperatures, solid-phase catalysts for gas reactions usually are highly ordered microporous media with a monomodal pore size distribution. Stationary phases for liquid chromatography, however, preferably have a hierarchically-structured pore space with macropores dedicated for convective mass transport through the column and mesopores inside the (itself

*Corresponding author. Tel.: +49-391-611-0465; fax: +49-391-671-2028.
E-mail address: ulrich.tallarek@vst.uni-magdeburg.de (U. Tallarek).

0021-9673/03/$ – see front matter
doi:10.1016/S0021-9673(03)00391-1

porous) support material. This offers a large surface area accessible via diffusion-limited mass transfer. Such bimodal pore size distributions can be realized by packing micrometre-sized mesoporous particles into the desired column geometry. A reduced axial dispersion, one of the goals in high-performance liquid chromatography, is accomplished when the large and irregularly shaped particles first used in (low-pressure) liquid chromatography are replaced by spheres of only a few micrometres in diameter with a narrow size distribution (Fig. 1), because dispersion associated with the liquid hold-up (intraparticle stagnant mobile phase mass transfer resistance) can be then significantly reduced due to a decreased characteristic diffusion path length in the stagnant zone [8]. Additionally, mechanical dispersion may be reduced by an increased packing homogeneity due to a uniform particle shape [9]. Although hydrodynamic dispersion analysis suggests the use of spheres as small as possible, any further reduction of particle size to the submicrometre range is of only limited value because the resulting beds create an unacceptably high back pressure [10] and, further, slurry packing of these columns is impeded by problems in getting the submicron spheres settled reasonably into a ''fixed'' bed [11].

Another aspect concerning the hydrodynamics in a random-close packing of completely porous spheres is that the mean interparticle macropore diameter (affecting the hydraulic permeability) and particle or domain size (influencing axial dispersion) cannot be manipulated independently as both parameters are ultimately coupled with the mean particle diameter. Pellicular [12] and nonporous particles [13,14] may be an alternative but lack a large effective surface area. In order to overcome these limitations for a fixed bed of spheres with its particulate (and, therefore, discontinuous) solid-phase, monolithic structures can be a solution because, in their continuous solid-phase, the macropore diameter and domain size can be adjusted independently over the complete length of the bed. Monolithic media for liquid chromatography can be distributed into two main categories based on their manufacturing material: organic polymer [15–20] and silica-based monoliths [21–26]. The macroscopic differences in bed morphology are revealed by SEM pictures of some of the commercially available monolithic stationary phases

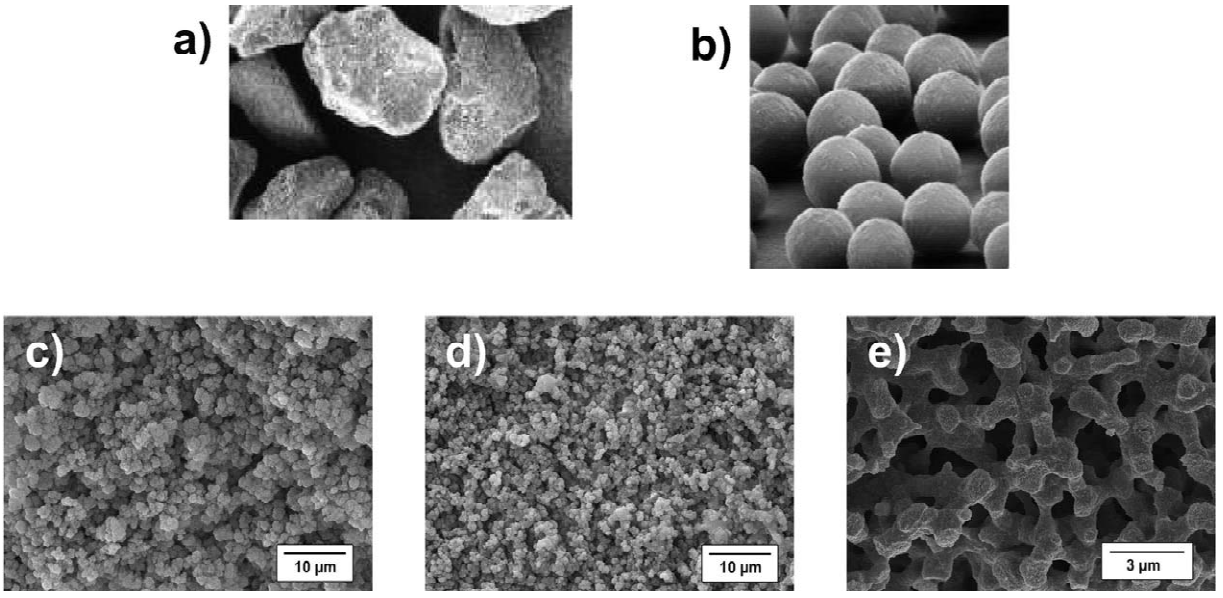

Fig. 1. Scanning electron microscopy pictures of different types of porous chromatographic materials. (a) Irregularly-shaped silica particles, (b) spherical silica particles, (c) organic polymer monolith A (UNO S), (d) organic polymer monolith B (CIM Disk), and (e) silica-based monolith (Chromolith).

(Fig. 1). Since the bed structure of organic polymer monoliths more or less resembles that of a loose packing of spherical or nearly so particles (microglobules) with a broad size distribution, the silica monoliths show a more fractal morphology with large interskeleton pore space. Differences in macroscopic stationary phase structures are intensified by the pore size distribution measurements (Fig. 2, although these measurements do not contain information about the actual pore interconnectivity) and these can be, by referring to the original literature, directly related to the respective preparation process: the organic polymer monoliths are synthesized by a thermally initiated one-step radical polymerization process in the presence of a mixture of porogens that induces phase separation and creates the interskeleton macropores [5]. The reaction temperature and composition of the porogenic mixture determine the macropore, as well as the microglobule diameter, but both also influence the development of micropores in the microglobules, hence in the stationary phase, so that reaction conditions are normally adjusted to lead to a nearly nonporous skeleton and, for sufficiently large molecules, to an effectively monomodal pore size distribution [27]. Silica-based monoliths, in contrast, are prepared through a two-step process involving a sol–gel mechanism overlapped by a spinodal phase transition process as the first step (this determines domain size and macropore diameter), followed by a solvent exchange as the second one, leaching out the silica skeleton to create the intraskeleton mesopore space [28–32]. Consequently, the resulting pore space shows a bimodal pore size distribution [21]. Up to date, only the use of silica as the basis material for monoliths in chromatography allows to create a hierarchically-structured pore space with independent adjustment of all skeleton parameters. Based on preparation aspects, most of the applications for polymer monoliths are in the purification (downstreaming) process of biomacromolecules like proteins and plasmid-DNA [33–35], while the silica-based monoliths as stationary phase material in partitioning chromatography are mainly used for low- and medium molecular mass substances [36–38].

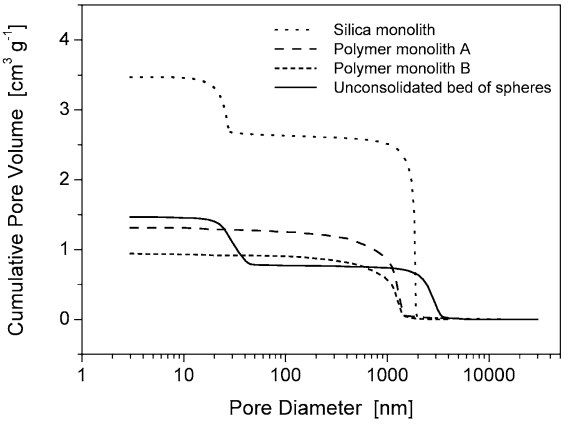

Fig. 2. Cumulative pore volume data for the monolithic and particulate fixed beds indicating monomodal pore size distributions in the case of the polymer monoliths and bimodal pore size distributions for both the silica-based monolith and the bed of porous silica beads.

Polymeric continuous stationary phases for liquid chromatography offer, in comparison with the particulate fixed beds, the possibility to be easily prepared in any dimension desired, in normal tube [15] and in disk format [19], and in radial flow geometry [39] or on microfluidic devices [40,41], whereas for silica-based materials the column geometry has to be fitted to the stationary phase due to the syneresis of the silica-gel [21,32]. One main restriction for both polymeric and silica-based monolithic structures is, since the stationary phase cannot be packed under a high pressure into the confining column geometry, the proper attachment of the stationary phases to the column wall. This results in a maximum operating pressure (recommendation) ranging from 1 to 5 MPa for the organic polymers and up to 20 MPa for the silica monoliths. Another problem concerning highly permeable monolithic structures or those in an extraordinary geometry like a disk or radial flow type is the proper (radial) sample introduction. In comparison to packed beds of small particles in narrow-diameter columns, there exists no sufficiently high back pressure to create a more homogeneous radial flow distribution [42]. Further, polymeric monolithic stationary phases are, like the conventional polymer beads, restricted to an eluent composition prohibiting the use of strong organic solvents due to swelling of the skeleton [5].

In any confining geometry the description of the respective flow regime via Reynolds and Peclet numbers relies on the definition of some characteris-

tic and, over the length of the bed, constant dimension $\mathscr{L}$ of the respective medium [10,43]. In open-tubular geometry this dimension is the inner column diameter, while for a fixed bed of (completely) porous spheres the mean particle diameter is a good measure for the determination of Reynolds and Peclet numbers (Fig. 3). In the monolithic structures there also exists a continuously repeating geometrical unit, for the silica monoliths it is the average domain size [22,26], or for polymer monoliths the mean microglobule diameter [27]. However, monolithic resins are not closely packed and they rather provide a large interskeleton porosity impeding the direct use of some characteristic geometrical skeleton units to determine a particular flow regime. The hydraulic permeability is certainly a function of interstitial porosity, macropore diameter, and domain size (as well as of their distribution functions). Axial dispersion depends on the size and porosity of the domain, on the macropore diameter and the pore (inter)connectivity. The consideration of permeability functions similar to those established for random-close packings of spheres [44–46] may actually fail because pore space morphology of each monolith offers unique geometrical properties and the differences between monoliths cannot, in contrast to that for fixed beds of nearly spherical particles, be easily reduced to only a few macroscopically relevant bed parameters. To obtain insight into the hydrodynamic behaviour of the various monolithic stationary phases it is, thus, favourable not to try to set up a model for a particular monolithic system, but to rather scale their hydrodynamic behaviour to that of the (well established) systems of particulate fixed beds via introduction of ''equivalent sphere dimensions'' for permeability and dispersion in monoliths, in general [47,48]. By defining $\mathscr{L}_{flow}$ and $\mathscr{L}_{disp}$ (Fig. 3 [48]) for hydrodynamics in different monoliths their behaviour

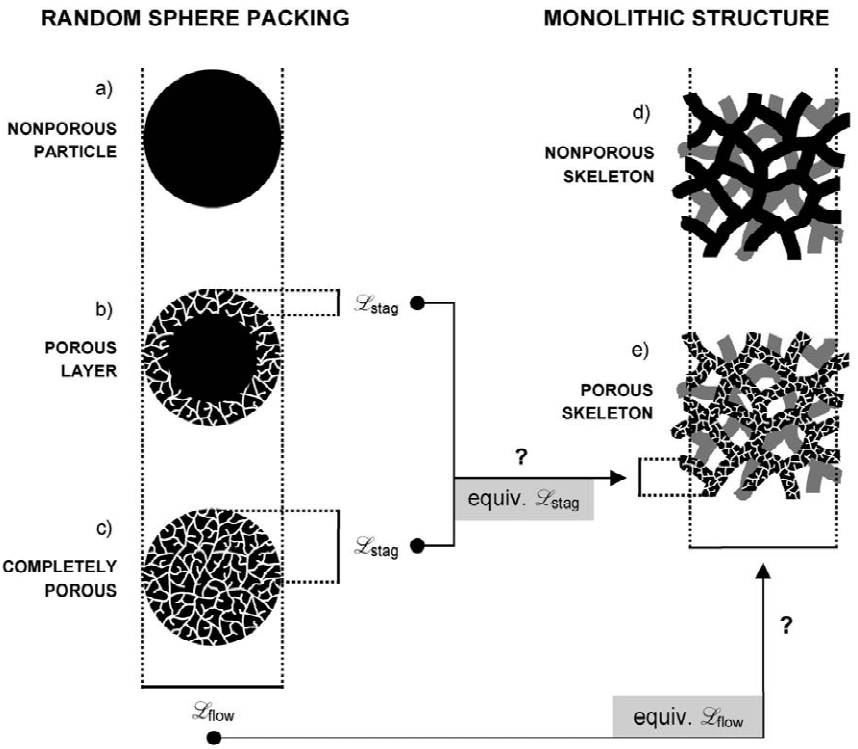

Fig. 3. Characteristic length-scales for hydraulic permeability and hydrodynamic dispersion in a bed of spheres and in monoliths. While the particle diameter is useful to define a region impermeable for flow, the actual thickness of the porous layer may be used to address the dispersion originating in stagnant zones of a sphere packing. Apparently $\mathscr{L}_{stag}$ and $\mathscr{L}_{flow}$ are different. Adapted with permission from Tallarek et al. [48].

is translated into the diameter and porosity of a spherical particle in a fixed bed of such spheres which shows an identical macroscopic flow resistance and/or the identical longitudinal dispersion characteristics.

The purpose of our current investigation is to analyze the hydrodynamics of monolithic stationary phase materials in comparison to some particulate reference materials. The general (and widely applicable) phenomenological approach of dimension analysis allows the scaling of permeability and dispersivity data from particulate media and from both polymer and silica-based monoliths. The hydrodynamic analysis is complemented by adsorption capacity studies for the silica-based materials covering RP4e, RP8e and RP18e surface modification. The monolithic and particulate chromatographic media are quantitatively compared via three main chromatographically relevant parameters: pressure drop, efficiency and adsorption capacity.

2. Experimental

2.1. Chemicals

Acetone, caffeine, trifluoroacetic acid (TFA), and acetonitrile (gradient grade) were purchased from Merck (Darmstadt, Germany). Purified water was prepared on a Milli-Q water purification system. Angiotensin II, insulin and bovine serum albumin (BSA) were purchased from Sigma.

2.2. Columns

Silica-based monoliths (Chromolith Performance RP18e) with mean intraskeleton mesopores of 25 nm, as well as a column of LiChrospher WP300 RP18e spheres having 30 nm mesopores were obtained from Merck. A Zorbax SB300-C_{18} column was obtained from Agilent Technologies (Waldbronn, Germany), a Micra NPS column packed with nonporous particles was purchased from Bischoff Analysentechnik (Leonberg, Germany). The particle size distribution functions of all particulate porous media were measured after the completion of experiments on a CILAS 968 laser light diffraction and diffusion system (CILAS, Marcoussis, France). An integration of each population distribution led to the mean surface-averaged particle diameter ($\bar{d}_{p,2}$). Polymer-based monoliths CIM Disk SO_3 and UNO S Polishing Kit were purchased from BiaSeparation (Lubljana, Slovenia) and from Bio-Rad (Munich, Germany). The pore size distributions and specific surface area data of all porous materials were determined by mercury intrusion and nitrogen adsorption at Merck. Scanning electron microscopy pictures were taken at the Mikrostrukturzentrum of the Otto-von-Guericke-Universität Magdeburg. A comprehensive overview of the properties of different fixed beds used in the permeability and dispersion analysis is given in Table 1.

Chromolith Performance monolithic columns (100×4.6 mm) with an RP4e, RP8e and RP18e surface modification containing 12.5 nm mesopores and macropores of 1.9 μm were obtained from Merck. PurospherSTAR RP18e in a particulate reference column (55×4.0 mm) for the adsorption capacity studies (3 μm particle diameter and 12 nm mesopore diameter) was also obtained from Merck.

2.3. Apparatus

All measurements on hydraulic permeability, van Deemter curves and adsorption capacity were conducted on a Merck–Hitachi HPLC system. Each column material was first thoroughly wetted with pure acetonitrile (except organic polymer monoliths) and, thereafter, the total pressure drop was recorded with purified, degassed water until the maximum possible flow-rate was reached. Correction by the system back pressure gave the column pressure drop. All dispersion experiments were conducted on an Agilent 1100 capillary HPLC system including a binary low-pressure gradient pump, an autosampler, and UV detector. The microlitre flow control sensor was bypassed and the eluent was directly delivered in isocratic mode in the range from 100 to 2500 μl/min by the pump. The volumetric flow-rate through each column was determined by measuring elution volume over time behind the detection cell. The actual flow-rate deviated within 2% of the system value. All connecting tubes were replaced by 200 μm I.D. capillary tubing from Agilent with a maximum length of 10 cm between injection valve and column, both to avoid a high system pressure-

Table 1
Characteristic dimensions and parameters of porous media used in this study

Fixed bed[a]	L_{bed} (mm)	d_{col} (mm)	V_{extra}/V_{bed} [b]	$\bar{d}_{p,2}$ (μm)	d_{macro} (μm)	ρ_{bed} (g/ml)	ε_{total}	ε_{inter}	ε_{intra}	τ_{intra}	Φ	A_{spec} (m^2/g)	A_{rel} (m^2/ml)
Nonporous spheres	53	4.6	0.02	3.2	–	1.20	0.36	0.36	–	–	1.78	1	1
Porous spheres A	50	2.1	0.10	4.3	–	0.87	0.65	0.37	0.44	1.28	0.54	51	44
Porous spheres B	55	2.0	0.10	7.2	–	0.85	0.75	0.37	0.60	1.20	0.33	76	65
Silica monolith	100	4.6	0.01	–	1.9	0.26	0.92	0.72	0.70	1.15	0.09	147	39
Polymer monolith A	10	4.6	0.10	–	1.1	0.76	0.70	0.70	–	–	0.43	4.4	3.3
Polymer monolith B	3	12	0.42	–	1.1	1.06	0.47	0.47	–	–	1.13	3.6	3.8

[a] Nonporous spheres, Micra NPS; porous sphere packing A, Agilent Zorbax SB300-C_{18}; porous sphere packing B, Merck LiChrospher WP300 RP18e; silica monolith, Merck Chromolith; polymer monolith A, BioRad UNO S Polishing Kit; polymer monolith B, BiaSeparations CIM Disk SO_3.

[b] $V_{extra} = 17$ μl, except with polymer monolith B for which $V_{extra} = 142$ μl (resulting from the disk housing).

drop at maximum flow-rates and to minimize extra-column volume. The column was directly connected to a 5 μl semi-micro detection cell. Data acquisition rate was increased up to 50 Hz at highest volumetric flow-rates to prevent artificial band broadening due to an insufficient detector response time.

2.4. Elution conditions

Dispersion analysis under non-retained elution conditions was achieved for all tracers by the use of premixed eluents consisting of a water–acetontrile (50:50) mixture, adjusted to acidic conditions for reversed-phase materials by addition of 0.1% (v/v) trifluoroacetic acid and to basic conditions for the strong cation-exchange polymer monoliths with 10 m*M* sodium phosphate buffer (pH 11). Prior to use, the eluents were filtered with 0.45 μm membrane filters and degassed with helium. The injection volume ranged between 1 and 5 μl (depending on the bed volume) with sample concentrations of 0.5% (v/v) for acetone, 20 μg/ml for angiotensin II and 50 μg/ml for insulin and BSA. Each sample was dissolved in the mobile phase to avoid concentration effects due to different elution strengths. Detection was carried out at 215 nm (ref.: 250 nm) with 10 nm bandwidth, except for acetone (254 nm, ref.: 330 nm). Elution was made at controlled room temperature (21 °C).

Van Deemter curves for caffeine were recorded at increasing flow-rate in two independent runs. The retention factor was adjusted to $k' = 5$ for all stationary phase materials yielding in eluent compositions of water–acetonitrile of 92:8, 94:6, 94.5:5.5 and 95:5 for the RP18e particles, the RP18e, RP8e and RP4e silica monolith, respectively. All eluents were premixed, thoroughly degassed with helium and filtered with membrane filters prior to their use. The injection volume ranged between 2 and 10 μl depending on column volume. The detection wavelength was 254 nm and all experiments were carried out at controlled room temperature (21 °C).

2.5. Analysis of dispersion data

Signal response obtained under nonretained conditions is usually characterized by asymmetric peak shapes whereas the asymmetry mainly depends on the tracer residence times in the column. It is, thus, necessary to deconvolute the detector signal into two functions: (i) a Gaussian function describing the signal variance caused by extra- and intracolumn band broadening, and (ii) a first order exponential decay function resulting in a time constant for first order dilution effects. The latter one accounts only for peak tailing due to incomplete axial equilibrium and increases as tracer residence times decrease. In order to distinguish between these complementary effects a convenient approach consists of using an exponentially modified Gaussian function (EMG) [49–51]:

$$f(t) = y_0 + \frac{h_0\sigma_t}{\tau}\sqrt{\frac{\pi}{2}}\exp\left[\frac{1}{2}\left(\frac{\sigma_t}{t}\right)^2 - \frac{t-t_0}{\tau}\right] \times \left\{1 - \mathrm{erf}\left[\frac{1}{\sqrt{2}}\left(\frac{\sigma_t}{t} - \frac{t-t_0}{\tau}\right)\right]\right\} \quad (1)$$

where t_0, σ_t^2 and h_0 represent mean residence time, variance and area of the Gaussian function and τ is the time constant of the first order decay function. As the extracolumn system geometry and, hence, extracolumn band broadening remained identical for each column during the whole experiment, and by taking into account only the Gaussian part of the deconvoluted elution profile, it allows to suppress the influence of an incomplete axial equilibration and offers the possibility of comparing axial dispersion in different column geometries. Chromatographic data were therefore exported from ChemStation software and imported into Origin 6.0 (Microcal, Northhampton, USA) in order to fit each signal response by an EMG. A transformation of the Einstein diffusion equation yields the apparent axial dispersion coefficient D_{ax} describing the sum of the intra- and extracolumn dispersion effects as derived from the detector output:

$$D_{ax} = \frac{\sigma_L^2}{2\Delta t} = \frac{u_{av}^2\sigma_t^2}{2t_{el,i}} \quad (2)$$

A time-scale-based signal response variance, however, has to be transferred into a length-scale-based variance by multiplication with the square of the average mobile phase velocity.

2.6. Analysis of adsorption data

Adsorption isotherms of caffeine on particulate

and monolithic RP18e material were determined via frontal analysis at room temperature. Eluent composition was the same as with the van Deemter analysis and the retention factor was kept at $k' = 5$ for all materials. Step gradients were run by the gradient pump at constant superficial velocity of 1 mm s^{-1} with pure mobile phase in the first and caffeine solution (20 mg/ml in the eluent) in the second channel. The accuracy of the step gradient was confirmed a priori with an acetone solution (0.5%, v/v), confirming a deviation below 1% for all steps. To avoid exceeding the detector's dynamic range the detection wavelength was 300 nm. The inflection point of each step was determined by fitting a Boltzmann function through the corresponding breakthrough curve. The calculation of adsorption isotherms was carried out as described in the literature [52].

3. Results and discussion

3.1. Hydraulic permeability

Unconsolidated porous media (either particulate or monolithic) usually exhibit a macroscopically coherent pore network system as evidenced by the average macropore diameters seen in the pore size distributions (Fig. 2), together with an inspection of scanning electron microscopy (SEM) pictures (Fig. 1) which reveal irregular, but geometrically congruent media. Even though these systems are macroscopically homogeneous (i.e. time and length scales on which transport processes occur are much smaller than the scales of variations in the velocity field experienced by the analyte) all porous media are characterized by a more or less broad distribution of diameter, characteristic lengths and shape (thus, morphology) of their respective interparticle (or interskeleton) macropore system, resulting in microscopically disordered structures. The general physical law governing flow resistance to a Newtonian fluid through such a fixed bed (particulate or monolithic) is Darcy's law (Eq. (3)), which presents a linear relationship between cross-sectional averaged superficial velocity and pressure gradient over the length of the bed [43]:

$$u_{sf} = -\frac{K}{\eta}\nabla p \tag{3}$$

This linear relationship is valid for the case of laminar flow and that both the Newtonian fluid and porous medium remain incompressible.

The hydraulic permeability data for (porous and nonporous) particulate and monolithic resins are shown in Fig. 4a. These data indeed confirm a linear increase of pressure drop (per metre) over the whole velocity range which reproduces nothing else than Darcy's law. For each material the flow regime remains in the laminar regime and both the bed and

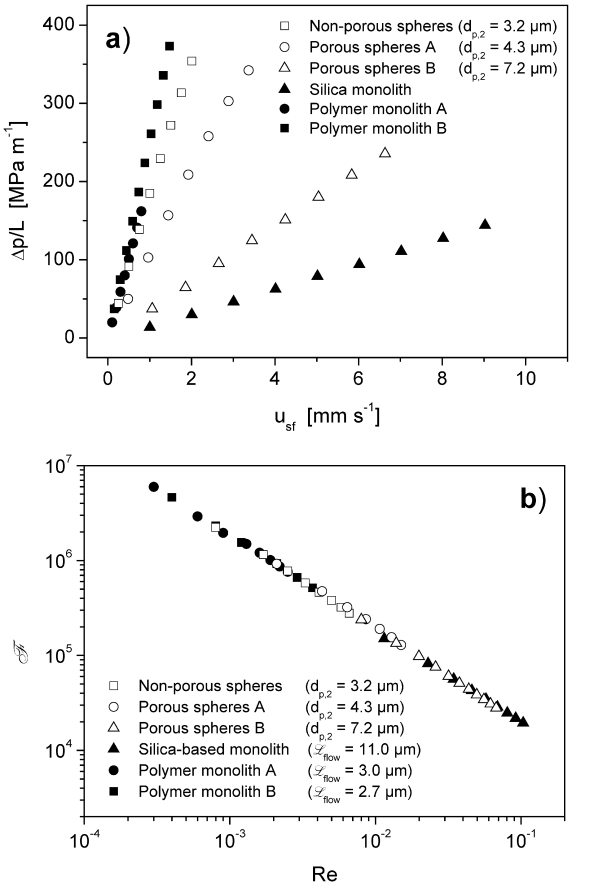

Fig. 4. Hydraulic permeability (using water as a liquid) of particulate and monolithic beds. (a) Flow resistance against superficial velocity, (b) dimensionless Darcy–Weißbach friction factor–Reynolds number relation (with $\bar{d}_{p,2}$ as $\mathscr{L}_{flow}$ for the particulate media, leading to $\mathscr{L}_{flow}$ for the monoliths via scaling of their data).

fluid can be regarded as being incompressible. Besides the fact that particulate media show different slopes according to their different particle dimensions this figure, in general, reveals quite strong differences in hydraulic permeability, especially between organic polymer and silica-based monoliths. The silica monolith offers the highest permeability of the systems investigated, while both polymer monoliths show a permeability less than that of a random-close packing of the smallest particles, i.e. the nonporous beads with an average diameter of 3.2 μm. Although these curves already indicate some trends, for a quantitative treatment of hydraulic permeability accounting for different interstitial porosities and particle diameters (as indicated by $\mathscr{L}_{\text{flow}}$ in Fig. 3) a transformation of the absolute data into a dimensionless form has to be performed and first properly applied to the particulate beds. Then, a direct comparison of the monolith's hydraulic permeability to those of particulate beds can be carried out by defining an appropriate characteristic length ($\mathscr{L}_{\text{flow}}$) for which both types of curves (monoliths, particulate beds) coincide.

Due to the fact that the specific permeability K can be determined exactly from Darcy's law but, vice versa, an exact prediction of the actual bed permeability from its characterizing macroscopic properties like porosity or average pore diameter fails, simplified geometrical models of the pore network (especially for particulate fixed beds) were developed to allow an estimation of the bed's permeability by knowing macroscopic properties like the interstitial porosity, mean particle shape or diameter [44–46].

For example, the Kozeny–Carman equation [53] is based on the assumption that an irregular distribution of pore dimensions in a fixed bed of particles can be replaced by a bundle of twisted, nonintersecting channels with a similar diameter in which flow resistance is governed by the Hagen–Poiseuille law for laminar flow in open tubes. If the permeability data shall be normalized through this approach also the limitations of this model have to be considered: the equation is based on empirical data that were acquired for random-close packings of nearly spherical particles, having narrow particle size distribution and an interstitial porosity of about 0.4 [53]. An extension of the porosity function obtained for this model to porous media with an interstitial porosity much higher than that of a random-close sphere packing is physically not consistent and will therefore lack accuracy. Despite such restrictions the Kozeny–Carman equation gives reasonable results when permeability data based on similar column and particle dimensions are considered [47]. To avoid limitations and allow for a comparison of chromatographic media with very different porosities we here adopt the approach of the dimension analysis. This phenomenological approach was used by Rumpf and Gupte [54,55] in their study of liquid flow through porous media covering a wide range of porosities (for $10^{-2} \leq Re \leq 10^{2}$, using sphere packings prepared by a special procedure, with interparticle porosities between 0.35 and 0.68). In dimension analysis all the experimentally available system parameters are first defined and then calculated against each other, leading to a dimensionless number which specifically characterizes the system under investigation.

In the case of laminar flow of a Newtonian fluid through a fixed bed (fluid and bed are considered incompressible and, therefore, Darcy's law is valid) the general approach of dimension analysis for hydraulic permeability can be represented as [55]:

$$\frac{\Delta p}{\rho u_{\text{sf}}^2} = f\left(Re = \frac{u_{\text{sf}}\bar{x}}{\nu}, \frac{L}{\bar{x}}, \varepsilon_{\text{inter}}, q_i, \psi_i, \text{packing structure}\right) \quad (4)$$

System parameters affecting flow resistance are: (i) total pressure drop Δp over the fixed bed, (ii) cross-sectionally averaged superficial velocity u_{sf}, and (iii) volumetric density of the liquid ρ. Their ratio (see left-hand side of Eq. (4)) is a function of several also dimensionless variables characterizing liquid flow, packing material and structure: (i) Reynolds number, (ii) interstitial porosity $\varepsilon_{\text{inter}}$, (iii) particle shape and size distribution factors (ψ_i and q_i) and (iv) the ratio of bed length L divided by a mean characteristic length $\bar{x}$ of the porous medium orthogonal to the flow direction which governs the flow resistance, defined as $\mathscr{L}_{\text{flow}}$ for both the particulate and monolithic media. In a random-close packing for which L strongly exceeds $\mathscr{L}_{\text{flow}}$ all factors affecting the axial flow resistance can be considered as constant over the bed length, leading to a linear

relationship between $\Delta p/(\eta u_{sf}^2)$ and $L_{bed}/\mathscr{L}_{flow}$, summarized in the Darcy–Weißbach friction factor $\mathscr{F}$:

$$\mathscr{F} = \frac{\Delta p}{\rho u_{sf}^2}\frac{\mathscr{L}_{flow}}{L_{bed}} = f\left(Re = \frac{u_{sf}\mathscr{L}_{flow}}{\nu}, \varepsilon_{inter}, q_i, \psi_i\right) \quad (5)$$

The (dimensionless) Darcy–Weißbach friction factor itself is a function of several dimensionless parameters but if spherical particles with a narrow particle size distribution are used, deviations in the interstitial porosity, particle shape and size distributions have a negligible influence, reducing $\mathscr{F}$ to a function of only one dimensionless variable, the Reynolds number. Taking $\mathscr{L}_{flow}$ as the mean surface-averaged particle diameter, the friction factor–Reynolds number relation for the different sphere packings leads to a coincidation of these data onto a linear master curve (open symbols in Fig. 4b), justifying the assumption that the phenomenological approach of dimension analysis is well suited for comparing different sphere packings, porous and nonporous, and that also the resulting packing properties in view of ε_{inter}, q_i, and ψ_i are sufficiently similar. (Because the viscous drag on a spherical particle in laminar flow is proportional to the surface area orthogonal to the flow direction [10], it is physically meaningful to use the mean surface-averaged particle diameter $d_{p,2}$ for characterizing $\mathscr{L}_{flow}$. Also other authors dealing with the flow resistance in porous media have used $d_{p,2}$ [46,55].)

The close correlation of hydraulic permeability data for porous and nonporous beads suggests an extension of this phenomenological approach to the monolithic resins in order to relate their specific permeability data to those of particulate beds simply by scaling them with an appropriate $\mathscr{L}_{flow}$ to the particles' master curve (closed symbols for the monoliths, Fig. 4b). The data for both silica-based and polymer monoliths fit well into the master curve, suggesting the usefulness of this approach. The equivalent sphere dimensions for permeability ($\mathscr{L}_{flow}$) are 3.0 μm and 2.7 μm for the polymer monoliths A and B, respectively, whereas the permeability of the silica monolith equals that for a fixed bed of 11.0 μm spheres ($d_{p,2}$). Differences in flow resistances between the monolithic resins are more difficult to explain by only their mean individual bed properties. For example, based on macropore diameters (and by considering the Hagen–Poiseuille law) the expected permeability ratio concerning the silica and polymer monoliths should be about 4, but it actually ranges between 12 and 16. Certainly the porosities also need to be considered here, but because the monoliths span a quite substantial range of porosities, the resulting difficulty lies in the estimation of an accurate porosity function which is able to cover the total range. Already an extrapolation based on the Kozeny–Carman equation for sphere packings with higher interstitial porosity than the typical 0.4 becomes inaccurate. For example, as shown by Rumpf and Gupte the porosity function $(1-\varepsilon_{inter})^2/\varepsilon_{inter}^3$ after Blake, Kozeny and Carman should be better replaced by $\varepsilon^{-5.5}$ or by the still more meaningful function $4(1-\varepsilon_{inter})\varepsilon_{inter}^{-4.55}$ [55].

Hence, there seems to exist no clear relationship between bed structure properties like porosity or macropore diameter and permeability according to Darcy's law (cf. $\mathscr{L}_{flow}$ and Table 1). It points towards the usefulness of a pragmatic approach, to relate hydrodynamic properties of monoliths to those of the well-defined and understood system comprised by a fixed bed of spheres via the phenomenological approach of dimension analysis, taking into account only directly measurable macroscopic system properties.

Absolute permeability data for various organic polymer-based monoliths adapted from the literature were subsequently scaled to obtain $\mathscr{L}_{flow}$ with the help of particulate reference materials and with water as the liquid. The resulting equivalent sphere dimensions are listed in Table 2. Data for the commercially available polymer monoliths A and B adapted from different authors reveal that the permeabilities of these monoliths result in an $\mathscr{L}_{flow}$ of similar magnitude as in this study. Polymer-based monolithic resins offer an individual permeability characteristic depending on preparation conditions. Therefore, no general relationship between the nature of these monolithic stationary phases (organic polymer or inorganic silica skeleton) and permeability can be drawn.

A phenomenological approach relying on the Darcy–Weißbach friction factor–Reynolds number

Table 2
Relative permeability of selected monolithic materials

Author	Svec et al.	Wang et al.	Liao et al.	Mayr et al.	Premstaller et al.	Luo et al.	Hahn et al.	Ghose et al.
Year	1992 [15]	1994 [16]	1996 [56]	2001 [57]	2000 [58]	2001 [59]	2001 [60]	2001 [61]
Type of monolith	HPLC-format polymer monolith, laboratory-made	HPLC-format polymer monolith, laboratory-made	Capillary polymer monolith, laboratory-made	HPLC-format polymer monolith, laboratory-made	Capillary polymer monolith, laboratory-made	HPLC-format polymer monolith, laboratory-made	HPLC-format polymer monolith, CIM Disk	HPLC-format polymer monolith, UNO S
Purpose of use	Ion-exchange liquid chromatography of proteins	RP liquid chromatography of peptides and alkylbenzenes	Electro-chromatography of polycyclic aromatic hydrocarbons	Liquid chromatography of proteins and oligonucleotides	Ion pair RP chromatography of oligonucleotides	Immobilized metal affinity chromatography of proteins	Analysis of hydrodynamics	Analysis of hydrodynamics
$\mathscr{L}_{\mathrm{flow}}$ (μm)	5.5	9.5	16.0	16.0	2.5	11.5	2.5	3.5

relation, which is not based on any confining model and which takes into account only directly measureable system parameters, is shown to be a sufficient, yet extremely practical tool for the dimensionless scaling of permeability data for porous media with a quite different porosity and structure. By introducing the radial length scale $\mathscr{L}_{\mathrm{flow}}$ (an equivalent sphere diameter for hydraulic permeability), it is possible to attribute to each monolithic bed a single value which describes its macroscopic permeability in terms of the average particle diameter of spheres in the equivalent sphere packing and, thus, allows a convenient and straightforward comparison of monolithic and particulate chromatographic beds, at least under this point of view.

3.2. Hydrodynamic dispersion

For a quantitative comparison of the axial dispersion coefficients of the solute a method has to be devised which also allows to evaluate the apparently diverging data for the various media in a dimensionless form. Prerequisite is a constant and sufficiently small extracolumn contribution to the band broadening. Then, a possible approach consists of applying the Van Deemter model for band dispersion in chromatographic media [62] which uses the theoretical plate height (H), an already reduced parameter, for indicating the effectiveness of a column via the first derivative of the axial variances of the detector response signals with respect to the column length (i.e. $H = \mathrm{d}\sigma_{\mathrm{L}}^2/\mathrm{d}L$). The introduction of three parameters for mechanical (eddy) dispersion, axial molecular diffusion and nonmechanical dispersion (stagnant mobile phase mass transfer) results in the well-known Van Deemter equation in which all processes are considered to occur independently and, therefore, their offered resistances add in series. Then, the dispersion data for silica-based monoliths with a bimodal pore size distribution can be scaled on the basis of a lumped mass transfer kinetics (C-term parameter) to those observed for fixed beds of porous spheres (also with a bimodal pore size distribution cf. Fig. 2) by introduction of an equivalent sphere dimension concerning axial dispersion [47]. For this purpose, the mass transfer in the stagnant part of the mobile phase, here the intraskeleton or intraparticle pore space, has to remain diffusion-limited (as a function of Pe) in order to use the Van Deemter equation. Reduced plate height plots originating from the dispersion data for particulate and monolithic beds then may coincide by appropriate dimensionless scaling.

To verify this simple approach with uncharged analyte molecules on reversed-phase materials, Van Deemter curves for monolithic columns with different surface modification (RP4e, RP8e and RP18e), as well as for a 3.0 μm particulate RP18e ‘‘reference’’ material are shown in Fig. 5. They were obtained with caffeine under strong retention conditions ($k' = 5$). Regression data for both the A-term and C-term parameters are (for all the reversed-phase monolithic media) very similar to those for the random-close packing of these 3.0 μm spheres (cf. Table 3). Thus, the monoliths equivalent particle diameter for axial dispersion representing that in a bed of completely porous spheres of 3 μm (this dimension is obtained here without the need for concrete calculation of the C-term parameter, but just—accidentally—by optical inspection) is consistent with our previous findings [47]. One advantage of the Van Deemter analysis is a convenient direct derivation based on readily obtainable plate height curves of equivalent sphere dimensions for axial dispersion under conditions of retained elution. These conditions guarantee relatively long tracer residence times in the column, resulting in accurate experimental data concerning the C-term

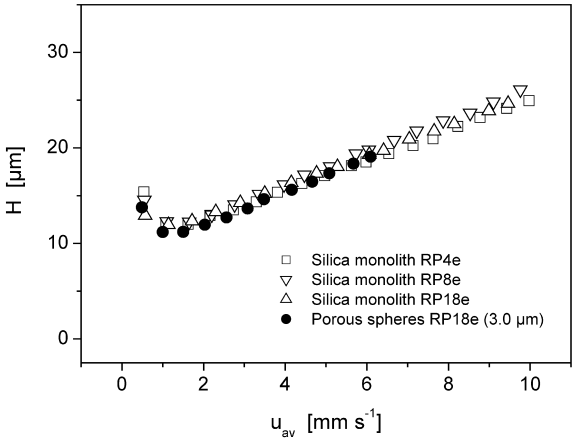

Fig. 5. Van Deemter curves for caffeine on silica-based monolithic and particulate stationary phases obtained under conditions of strong retention ($k' = 5$).

Table 3
Van Deemter parameters for caffeine elution

Stationary phase	A (μm)	B_{calc} (10^{-9} m^2/s)[a]	C (10^{-3} s)
Silica monolith RP4e	10.1±0.5	0.7	1.4±0.1
Silica monolith RP8e	10.0±0.4	0.7	1.6±0.1
Silica monolith RP18e	9.7±0.2	0.7	1.6±0.1
Fixed bed of spheres RP18e	9.3±0.6	0.7	1.5±0.2

[a] $B_{calc} = 2k_b D_m$ with k_b being the obstruction factor (0.7), and $D_m = 0.5\times10^{-9}$ m^2/s [62].

(significant slope in the plate height curves) which then clearly dominates the overall dispersion. But, at the same time, the use of retained conditions is also one of the major drawbacks of this approach. Comparisons of dispersion behaviour will then be complicated by the surface-specific adsorption kinetics, in addition to the differences in diffusion path lengths in the particulate and monolithic materials. Thus, the main focus of this work (the hydrodynamic dispersion) will be, at least partly, obscured by thermodynamic effects. To circumvent these difficulties elution under nonretained conditions is favored because dominating mass transfer resistances in the mobile phase then arise from diffusive processes that itself originates in stagnant zones characterized by a different spatial dimension (and pore space morphology), depending on the material under consideration. But, as a consequence, the C-term parameter is then reduced to a magnitude which represents the actual experimental error in its determination and this, in turn, prohibits a meaningful data evaluation.

Therefore, the plate height H is first replaced by the dispersivity $\mathscr{D}$, the dimensionless ratio of the effective axial dispersion coefficient to the analytes molecular diffusivity. By applying dimension analysis to axial dispersion in fixed beds of porous spheres we can formulate Eq. (6), describing $\mathscr{D}$ as a function of several (also dimensionless) factors [48]:

$$\mathscr{D} = \frac{D_{ax}}{D_m} = f\left(Pe = \frac{u_{av}\mathscr{L}_{disp}}{D_m}, \varepsilon_{inter}, q_i, \psi_i, \varepsilon_{intra}, \frac{D_{stag}}{D_m}\right) \quad (6)$$

The same parameters as for the permeability data are used to characterize interstitial porosity, particle shape and size distribution, and they can be neglected for a random close packing of spheres with relatively narrow particle size distribution and reasonable sphericity. $\mathscr{D}$ depends on the Peclet number, on intraparticle porosity and reduced pore diffusivity (D_{stag}/D_m), where D_{stag} is the effective diffusion coefficient of analyte molecules in the stagnant zone. However, in order to scale the dispersion data for porous and nonporous spheres via dimension analysis in a similar way as for the permeability data, we have to introduce a common (appropriate) length scale $\mathscr{L}_{disp}$ for the consistent determination of the dispersive flow regime (cf. Eq. (6)).

For studying the axial dispersivity $\mathscr{D}$ of a neutral, nonreacting solute in incompressible liquid flow through a random sphere packing as a function of Pe we have to take into account the bed's tortuosity (τ_{bed}), a mechanical dispersion contribution (coefficient Θ_m) and two nonmechanical mechanisms, namely boundary-layer mass transfer (Θ_b) and the liquid hold-up in the intraparticle stagnant zone (Θ_h) [63]:

$$\mathscr{D} = \frac{D_{ax}}{D_m} = \tau_{bed} + \Theta_m Pe + \Theta_b Pe \ln(Pe) + \Theta_h Pe^2 \quad (7)$$

Apparently, the liquid hold-up contribution is not present with nonporous particles (unless some of the particles crush and lead to an appreciable amount of dead-end blockage, or the ''nonporous'' particles have micropores to a finite extent). The relevant flow regime for mechanical dispersion and boundary layer mass transfer can be characterized by $\mathscr{L}_{flow}$ because both contributions are physically related to the (velocity and shear stress at/close to the) particles external surface. By contrast, the liquid hold-up in beds of porous spheres is inherently coupled to $\mathscr{L}_{stag}$ (cf. Fig. 3), the effective intraparticle diffusion pathlength that we determine, in this study, for

completely porous spherical particles from their mean surface-averaged particle diameter ($\bar{d}_{p,2}$).

In beds of nonporous spheres, i.e. in the absence of liquid hold-up, $\mathscr{L}_{disp}$ is determined uniquely by $\mathscr{L}_{flow}$, but for the porous particles both $\mathscr{L}_{flow}$ and $\mathscr{L}_{stag}$ are important. Apparently, they are not identical (Fig. 3). The intraparticle liquid hold-up contribution begins to dominate axial dispersion when completely porous spheres are used and Peclet numbers *Pe* sufficiently exceeding unity are encountered ($Pe > 20$; it is, thus, most relevant in liquid chromatography practice). This has been re-evaluated and demonstrated recently by the complementary pulsed field gradient NMR measurements, combined with a numerical simulation (using high-resolution flow fields) of axial dispersion coefficients in packings of porous and nonporous spherical particles (Fig. 6a) [64], an aspect to which we will return to below.

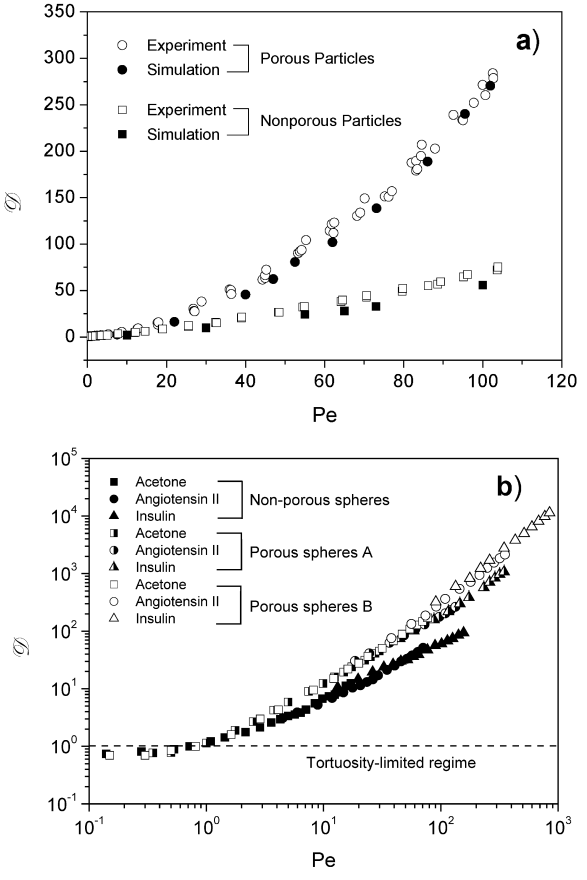

Fig. 6. Dimensionless dispersivity versus the Peclet number for random packings of totally porous and nonporous spheres. (a) Data obtained with PFG-NMR measurements and numerical simulations, reprinted with permission from Kandhai et al. [64]. Regression analysis results in the following values for τ_{bed}, Θ_m, Θ_b, and Θ_h: 0.74, 0.144, 0.101 and 0.020 in the case of the porous particles, and 0.51, 0.153, 0.080 and 0.0016 for the nonporous spheres. (b) Data obtained by tracer elution experiments under unretained conditions. For all curves (porous or nonporous particles) *Pe* has been calculated, as is usually done, on the basis of the mean particle diameter.

Axial dispersion in random-close packings of totally porous and completely nonporous spheres represents two limiting cases for which the flow regime can be conveniently characterized by a single length scale ($\mathscr{L}_{disp}$) which is $\mathscr{L}_{stag}$ in the former and $\mathscr{L}_{flow}$ in the latter situation. The actual flow regime for pellicular particles (cf. Fig. 3), however, needs two different length scales and the dimensionless dispersivity is not expressed easily in a reduced form. Because liquid hold-up in these particles is strongly reduced (this is one of the main purposes of the pellicular particles), it may not be the dominating contribution to band dispersion any longer, yet not be negligible, and $\mathscr{L}_{disp}$ cannot be replaced simply by $\mathscr{L}_{stag}$ without introducing an ambiguity.

Before we continue with a demonstration of the importance of liquid hold-up in stagnant zones for a determination of an equivalent dispersion length for monoliths compared with that in particulate beds, it should be pointed out that Eq. (7) apparently contains a coupling (via the boundary-layer contribution) between mechanical dispersion and mass transfer resistances arising in the mobile phase. This is in contrast to the Van Deemter model (*A*-term independent of velocity) and it is still incomplete compared to the Giddings coupling theory [8]. Giddings has addressed the important role played by lateral diffusion (or, more correctly, by lateral dispersion, although it is only a very weak function of *Pe*) in the relaxation of radial concentration gradients. For this purpose, he has identified several velocity inequalities of the flow pattern in a packed bed, covering length scales from the radius of an individual interparticle pore (transchannel contribution), via short and long range interchannel effects (including a few particle diameters), up to the whole diameter of the column (transcolumn contribution) [65]. For the sake of completeness, Eq. (7) expresses

coupling only between the pore-scale velocity inequality arising due to the no-slip condition at the solid–liquid interface and diffusion normal to that surface. This pore-level Taylor dispersion translates to the Giddings transchannel effect. Velocity inequalities on a higher length-scale (like short and long range interchannel, or even transcolumn effects) are not considered [63]. Thus, ''coupling'' between mechanical and nonmechanical effects in Eq. (7) represents a situation between the Van Deemter model and the comprehensive Giddings equation [8]. Nevertheless, the importance of intraparticle liquid hold-up, irrespective of the foregoing discussion, stems from the fact that this contribution (proportional to $\Theta_h Pe^2$, cf. Eq. (7))—as there is no flow inside the particles and, thus, no coupling with mobile phase velocities—starts to dominate overall dispersion at higher values of *Pe*. But how high must *Pe* get to clearly distinguish between mechanical and nonmechanical effects? The answer is provided by Fig. 6a.

By having used well-defined computer-generated, as well as physical sphere packings of porous and nonporous particles, lattice-Boltzmann flow field simulations and pulsed field gradient NMR measurements have revealed (Fig. 6a), in excellent agreement, that for both types of particles (porous and nonporous) the parameters for mechanical dispersion and boundary-layer mass transfer are indeed very similar (most probably because surface chemistries, particle shape and size, as well as their distribution parameters were comparable), but that the coefficient for liquid hold-up shows an increase by more than a decade with the porous particles [64]. It should also be mentioned that both columns (porous vs. nonporous particles) were packed and consolidated by the same procedure. As clearly demonstrated in Fig. 6a the liquid hold-up contribution starts to dominate dispersion in the bed of porous spheres at Peclet numbers exceeding about 20. Thus, liquid hold-up as a particular dispersion mechanism is also suited to study and compare the band broadening in monolithic and particulate beds, as long as this contribution is sufficiently present in a material and dispersion data are acquired over a sufficiently wide range of *Pe*.

Compared to these results based on the direct measurement and simulation of axial dispersive processes in packed beds, the classical chromatographic tracer dispersion data derived from an external detector response are strongly affected by the respective extracolumn volumes and, therefore, are usually more scattered (Fig. 6b). Dispersion data for porous particles A and B (cf. Table 1) in Fig. 6b have a different dependence of $\mathcal{D}$ on *Pe*, caused mainly by differences in the intraparticle porosity and different reduced pore diffusivities D_{stag}/D_m (Table 4), as both quantities contribute to the coefficient Θ_h characterizing the liquid hold-up. Consequently, these parameters (ε_{intra} and D_{stag}/D_m) also directly influence the slope of dispersivity curves in a regime where the hold-up contribution dominates the overall dispersion [48].

The direct comparison of axial dispersion in monolithic and particulate media having a bimodal pore size distribution (one set of pores for convection-dominated transport, the other set of pores for achieving a large surface area, but with diffusion-limited mass transfer) can be accomplished, in analogy to the permeability data, by defining an $\mathcal{L}_{stag}$ for the monolithic structures so that their dispersion data collapse onto the dispersivity curve for the particulate media. This dimensionless scaling strategy will work perfectly when both axial dispersion curves (i.e. for the monolithic and particulate beds) are characterized by a similar slope, meaning

Table 4
Physical properties of the tracer molecules used in dispersion analysis

Tracer	Molecular mass (g/mol)	R_G (nm)	D_m (10^{-10} m^2/s)	D_{stag}/D_m			Ref.
				Porous spheres A	Porous spheres B	Silica monolith	
Acetone	58.1	n.a.	12.8	0.35	0.50	0.64	[66]
Angiotensin II	1046	<0.2	3.1	0.20	0.37	0.36	[67]
Insulin	5807	0.54	1.4	0.14	0.29	0.25	[68,69]
BSA	67 000	3.06	0.6	0.05	Size exclusion	Size exclusion	[70]

that the reduced effective pore diffusivities (cf. Table 4 and the list of symbols) become similar. Otherwise, the dispersivity plots will not coincide exactly, a behaviour that is well known from the reduced plate height curves for different particulate media in liquid chromatography.

The elution under nonretained conditions allows to derive the effective total porosity experienced by each analyte from its residence time distribution (Table 5). Acetone, angiotensin II and insulin are able to enter the intraparticle or intraskeleton pore space of all silica-based chromatographic materials. Further, liquid hold-up dominates dispersion at $Pe \gg 1$ in these hierarchically-structured porous materials (with intraparticle or intraskeleton mesopores and interparticle or interskeleton macropores). For the porous spheres B and the silica-based monolith the dispersion data for all analytes demonstrate a unique behaviour when defining an $\mathcal{L}_{stag}$ for the monolith of 1.0 μm (Fig. 7a). This actually means that dispersion in this monolithic structure corresponds to (is equivalent to) that in a random close packing of porous spheres with an average particle diameter of 2.0 μm having similar stagnant zone pore space morphology as the porous spheres B (which were used as a ''reference'' in this analysis). In contrast to the above-mentioned analytes, effective porosity data for BSA elution (Table 5) indicate that this molecule is size-excluded from the mesoporous intraparticle pore space of the porous spheres B and also from the mesoporous skeleton of the silica monolith (see also Table 1). Because BSA does not experience a substantial liquid hold-up (if any at all—boundary layer mass transfer resistance is still present and it is certainly diffusion-limited close to the surface, normal to it, but its characteristic length-scale is small and it does not constitute a liquid hold-up mechanism) and undergoes convec-

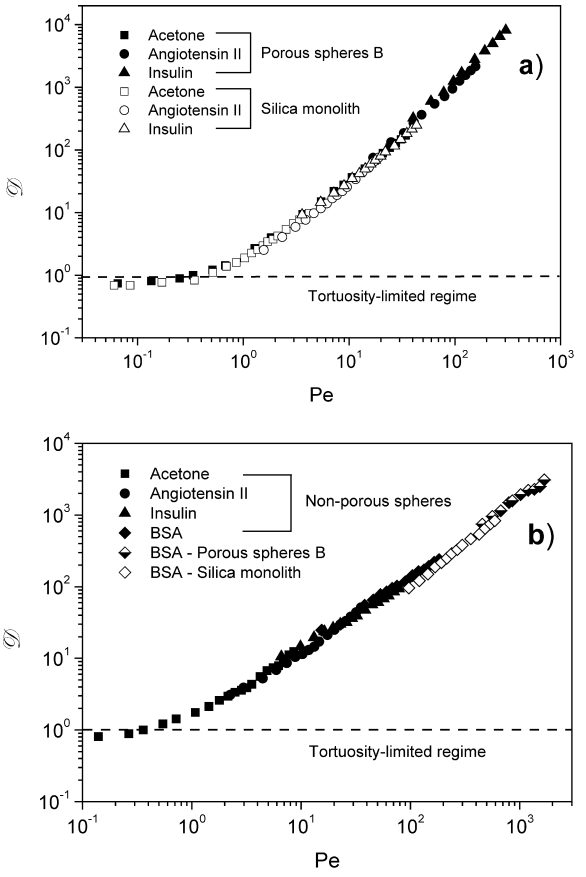

Fig. 7. Dimensionless scaling of tracer dispersion data for the silica-based monolith. (a) Axial dispersivity in the monolithic structure and in the random packing of porous particles B, with the analyte experiencing liquid hold-up in the stagnant part of the mobile phase (intraparticle or intraskeleton pore space). The data are plotted and scaled versus *Pe* calculated based on the thickness of the porous layer of completely porous particles which is $\bar{d}_{p,2}/2$ (cf. Fig. 3). This procedure leads to an $\mathcal{L}_{stag}$ for the monolith of 1.0 μm. Reprinted with permission from Tallarek et al. [48]. (b) $\mathcal{D}$ vs. *Pe* for the nonporous spheres, together with the BSA elution data for porous spheres B and the monolith (size exclusion). In all cases, *Pe* is now calculated based on $\mathcal{L}_{flow}$.

Table 5
Effective tracer porosities in the different porous media

Tracer	Sphere packings			Monoliths		
	Nonporous	Porous spheres A	Porous spheres B	Silica-based	Organic polymer A	Organic polymer B
Acetone	0.36	0.65	0.75	0.92	0.70	0.47
Angiotensin II	0.36	0.55	0.68	0.84	0.60	0.35
Insulin	0.36	0.51	0.63	0.80	0.58	0.34
BSA	0.36	0.37	0.36	0.70	0.55	0.32

tion-dominated dispersion in the interparticle or interskeleton pore space, these dispersion data resemble more those for beds of nonporous spheres. Then, the best measure for $\mathscr{L}_{\mathrm{disp}}$ in this limiting case appears to be $\mathscr{L}_{\mathrm{flow}}$ like $d_{\mathrm{p},2}$ for the nonporous particles, as pointed out earlier. By representing the BSA dispersion data with an $\mathscr{L}_{\mathrm{flow}}$ of 11.0 μm for the silica monolith (obtained from the permeability analysis) and 7.2 μm for the porous spheres B and by comparing these data to those for the packing of nonporous spheres, we arrive at a unique scaling and finally obtain an equivalence for the axial dispersion behaviour in the interstitial (interparticle or interskeleton) pore space of these media (Fig. 7b).

The axial dispersion data for both polymer monoliths could not be scaled in a meaningful way to the behaviour observed in the reference beds of porous or nonporous particles. While the pore size measurement by mercury intrusion and a surface area determination by nitrogen adsorption could not prove any significant amount of micro- and/or mesopores, the effective porosity data in Table 5 indicate that these two monoliths are not completely nonporous concerning liquid hold-up meaning that their pore size distribution (Fig. 2) remains not necessarily monomodal for all of the analytes. Moreover, the data for polymer monolith B cannot be further differentiated because of the relatively high extra-column volume engendered by the disk housing system (cf. Table 1).

3.3. Adsorption capacity

In preparative chromatography the sample amount loaded on a column is increased to a stage in which the surface concentrations of adsorbed analyte molecules cannot be treated independent from the already adsorbed molecules any longer and the adsorption isotherm begins to show a nonlinear behavior [52,71,72]. In view of high-throughput processes, stationary phase materials have to be designed for nonlinear chromatography which offer large specific surface areas [73]. This aspect clearly favours completely porous support structures over nonporous ones (Table 1). Differences in the maximum loading capacity for different stationary phases can be derived from the determination of the adsorption isotherms under identical retention conditions, preferably for molecules obeying a Langmuir isotherm type [73] because the monolayer saturation capacity, in contrast to the nitrogen adsorption data, inherently contains the influence of the respective pore space morphology, e.g. it accounts for differences in accessible pore space for larger analytes.

All adsorption isotherms in this study were determined by frontal analysis [74–78] under strong retention conditions ($k' = 5$) for RP18e porous spheres and the silica monoliths with RP4e, RP8e and RP18e surface modification. Caffeine was chosen as analyte because it adsorbs reversibly on reversed-phase materials and shows Langmuir behaviour (as has been determined a priori). Further, its high solubility in water (of more than 20 g l^{-1}) allows to realize sufficiently high surface concentrations so that the monolayer saturation capacity can be approached. Adsorption studies were not carried out for polymer monoliths because both are fabricated from different monomers and, therefore, they show different SCX surface characteristics. Moreover, a suitable (polymer-based) particulate reference material was not available. In addition, an extensive capacity study for proteins on polymer monolith B has already been published [33].

For complementary information about the specific adsorption behaviour of caffeine, its adsorption isotherms were plotted with respect to the following parameters (Fig. 8): volumetric solid-phase concentration (mass of caffeine per stationary phase volume), surface concentration (mass of caffeine per BET surface area of the solid-phase), and the relative column volume-weighted concentration (mass of caffeine per column volume). Differences in phase ratio between the two columns (particulate and monolithic bed) indicate that the volume-weighted adsorption isotherm, although useful for modelling chromatograms with a single stationary phase [71], is not suited for describing variations in adsorption capacity for different materials because adsorption occurs on the surface of the solid, but not within its volume. Therefore, the adsorption is better represented by the surface-weighted isotherm, indicating that the monolith's loading capacity (per squared metre of the BET surface area) is increased compared to sphere packings with a similar surface modification. But also this illustration allows only limited conclusions about adsorption behaviour on

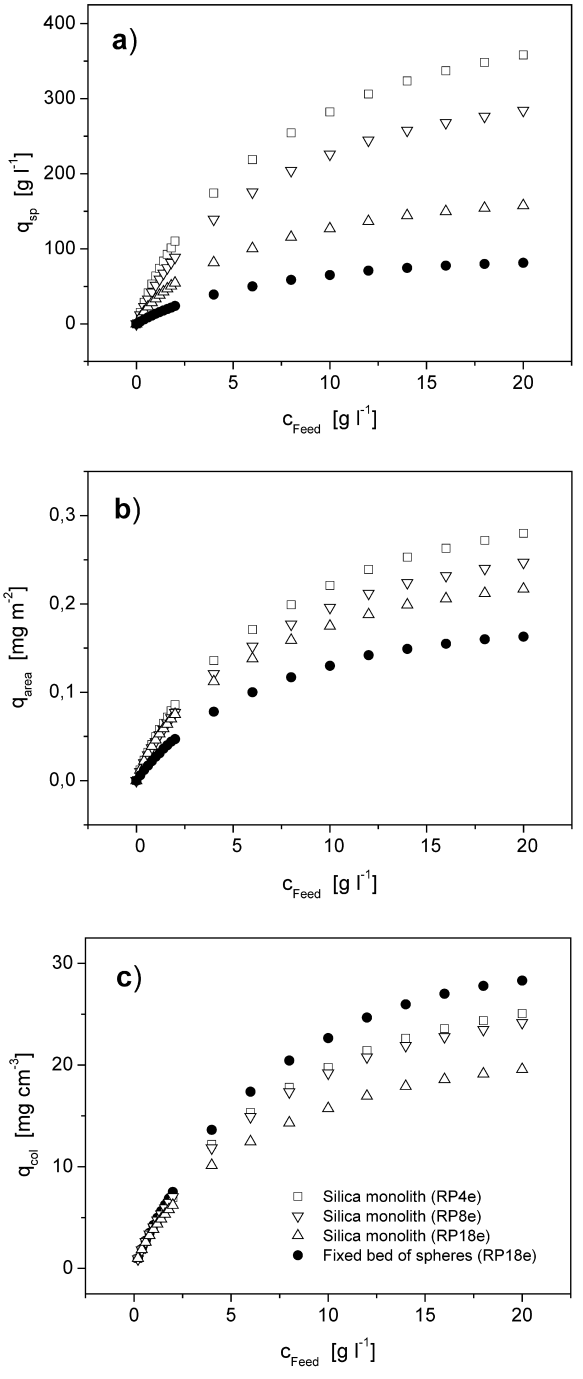

Fig. 8. Adsorption of caffeine on monolithic and particulate stationary phase materials under conditions of strong retention. Reference parameter: (a) the solid-phase concentration (q_{sp}), (b) solid-phase surface concentration (q_{area}), and (c) the column volume-weighted concentration (q_{col}).

different porous media, because the area determination was carried out by using nitrogen, a molecule assumed to enter the whole meso- and micropore space. However, the BET analysis does not describe the effective surface area for caffeine. Possible explanation for differences in surface loading capacities may be found in a reduced accessibility of parts of the pore network, (i) in reversed-phase modifications with longer chain lengths (RP18e) compared to materials with a shorter carbon chain (RP4e and RP8e) and (ii) in the silica spheres compared to monoliths due to the higher solid-phase content of the particles (cf. phase ratio in Table 1).

Quantitative information about adsorption capacity in different chromatographic beds is obtained by illustrating the adsorption isotherm with respect to the column volume-weighted concentration (Fig. 8c), because this representation includes the materials-specific adsorption and solid-phase content in the actual column. Adsorption data were fitted to the Langmuir isotherm and resulted in a maximum column volume-weighted loadability for the porous spheres of 40.4 mg/ml and one of 25.7, 33.1 and 34.9 mg/ml for the silica monoliths with RP18e, RP8e and RP4e surface modification, respectively. In all cases, regression coefficients were better than 0.999. Reduction of chain length from RP18e to RP8e and RP4e leads to a significant increase in the maximum adsorption capacity for the monolithic columns. A possible explanation may be found by a better accessibility of the mesopore space (combined with a larger effective surface area) when shorter chain lengths are used. In general, however, the silica-based monoliths offer a lower adsorption capacity than particulate beds, e.g. the monolayer saturation capacity for caffeine on the RP18e silica monolith is about 64% of that for the corresponding RP18e modified fixed bed of porous spheres. This difference is mainly caused by the actual amount of solid-phase in each column. In the particulate chromatographic beds the total mass of solid is about three times higher than for the highly porous silica monolith. But the significantly higher intraskeleton porosity, possibly also providing better accessible intraskeleton pore space, compensates partly the solid-phase ratio of these materials of only 0.34: the resulting surface ratio is 0.58 and the actual ratio of maximum loading capacities amounts to 0.64. Thus,

compared to conventional particulate stationary phase materials the silica-based monoliths with bimodal pore size distribution provide a still comparable and only slightly decreased dynamic adsorption capacity.

4. Conclusions

The phenomenological approach of dimension analysis, suitable for scaling the hydrodynamics in different fixed beds of (porous and nonporous) spheres via their mean particle diameter, also allows to relate hydraulic permeability and axial dispersion data for monolithic chromatographic supports to the behaviour of well characterized random-close packings of spheres. It is achieved by the introduction of equivalent sphere dimensions for the monolithic structures. Although the continuous solid-phase of monoliths leads to a different bed morphology, this approach provides an excellent competitive analysis concerning the hydraulic permeability of all monoliths (organic polymer, silica-based) and the axial dispersion behaviour of, at least, the porous silica monoliths. The hydrodynamics in these monoliths can now be characterized in terms of particle dimensions via single values of $\mathscr{L}_{\mathrm{flow}}$ and $\mathscr{L}_{\mathrm{disp}}$.

In general, the hydrodynamic properties of a porous medium can be described by the ratio of the aforementioned dimensions for axial dispersion and hydraulic flow resistance:

$$\mathscr{R}_{\mathrm{HP}} = \frac{\mathscr{L}_{\mathrm{disp}}}{\mathscr{L}_{\mathrm{flow}}} \tag{8}$$

It characterizes the hydrodynamic performance of stationary phases [48]. For completely porous spheres this ratio is 0.5 (Fig. 3), meaning that the mean sphere diameter, respectively the mean radius, can determine the flow regime for permeability and dispersion.

The hydrodynamic properties of the silica-based monoliths with a bimodal pore size distribution correspond to those of a bed of totally porous spheres with a radius of $\mathscr{L}_{\mathrm{stag}} = 1.0$ μm concerning dispersion originating in the monoliths mesopore space (under nonretained elution condition and with liquid hold-up in the mesopore space as the dominating contribution to the axial dispersion), as well as to a packing with equivalent sphere diameter for hydraulic permeability and dispersion in the macroporous interskeleton pore space of $\mathscr{L}_{\mathrm{flow}} = 11.0$ μm. The hydrodynamic performance ratio for analytes experiencing liquid hold-up thus is reduced to $\mathscr{R}_{\mathrm{HP}} = 0.09$. To realize this ratio in sphere geometry, pellicular particles have to be applied with a total diameter of 11 μm (as $\mathscr{L}_{\mathrm{flow}}$), and with a thickness of the porous layer (in the first approximation) of $\mathscr{L}_{\mathrm{stag}}$. However, a geometrical analysis of this diffusive layer suggests that its thickness can be treated as small in comparison with the total radius of the resulting solid core–porous shell sphere. This allows to apply the one-dimensional diffusion equation (Fick's second law) for infinite plane sheets [79,80] (i.e. for slab geometry) in the case of the pellicular particle. The corresponding thickness of the porous layer leading to a similar dispersion as the (completely porous) sphere with a radius $\mathscr{L}_{\mathrm{stag}}$ is derived by solving the diffusion equation in slab and sphere geometries for transient diffusion and assuming equivalent mean residence times of the analyte molecules in both media [81,82]. Rodrigues et al. [83,84] have solved this problem and have obtained a value of $1/\sqrt{5}$ for the ratio of the slabs half thickness to the sphere radius, assuming purely diffusive mass transport. Pellicular particles having an overall $d_{\mathrm{p}} = 11$ μm to account for permeability, with similar hydrodynamic performance ratio as the silica-based monoliths (i.e. $\mathscr{R} = 0.09$), then have a porous layer that is only 0.45 μm thick. For such a pellicular particle, the resulting nonporous core contains more than 77% of the spheres volume so that the effective surface area and the adsorption capacity per column are strongly reduced compared to both the completely porous spheres and silica monoliths (Table 6). In this respect, these pellicular particles provide no alternative to the silica-based monoliths with a bimodal pore size distribution.

The bimodal pore size distribution of silica-based monoliths with large macropores and a thin, highly porous (but pressure-stable) skeleton, is the basis for the unique combination of high bed permeability, short diffusion path lengths and high adsorption capacity which cannot be achieved in a fixed bed of any diffusive particle type. Since, up to date, only silica-based monoliths show a distinct bimodal pore

Table 6
Hydrodynamic and adsorption properties of selected porous media

Fixed bed	$\mathscr{L}_{flow}$ (μm)	$\mathscr{L}_{stag}$ (μm)	$\mathscr{R}_{HP}$ liquid hold-up	A_{sp} (m^2/g)	A_{rel} (m^2/ml)	q_{max} (mg/ml)
Silica monolith	11.0	1.0	0.09	91	39	25.7
Pellicular particle	11.0	0.45	0.09	13	14	9.1
Porous spheres B	7.2	3.6	0.5	161	65	40.4

size distribution as a result of their two-step manufacturing process, these columns are clearly favored for use in chromatographic applications especially in those for which the combination of a high bed permeability, short diffusion pathlengths and high surface area is stringently needed like in high-throughput routine analysis, process-scale chromatography using, e.g., simulated moving bed technology, and for determination of compounds in complex mixtures by liquid chromatography on-line coupled to mass spectrometry.

On the other hand, organic polymer monoliths which are characterized by monomodal pore size distributions due to their one-step polymerization process, have been designed for purification processes of biomacromolecules by gradient elution. Since the monomodal pore size distribution provides, for sufficiently large molecules, almost exclusively flow-through pores leaving diffusion-limited mass transfer on transchannel length-scale, the transport of these molecules in polymer monoliths can be considered as being convection-dominated in the pore space available for the analyte. This certainly results in a reduced axial dispersion compared to the high surface area monoliths like the bimodal silica structures. Thus, the hydrodynamic behavior in organic polymer monoliths more resembles that in beds of nonporous spheres. However, the slight, but yet finite porosity of the skeleton, as seen from porosity data and the broad pore size distribution (cf. Fig. 2) suggests that organic polymer monoliths are not completely nonporous and that their skeleton provides, even for molecules of BSA size, accessible pores with a stagnant mobile phase.

5. Nomenclature

A_{spec} specific surface area of the porous medium (m^2/g)
A_{rel} column volume-weighted surface area of porous medium (m^2/ml)
c_{Feed} feed concentration [52] (g/l)
d_{macro} macro or flow-through pore diameter (μm)
d_p average particle diameter (μm)
$\mathscr{D}$ dimensionless dispersivity, Eq. (6)
D_{ax} effective axial dispersion coefficient (m^2/s)
D_m molecular diffusion coefficient (m^2/s)
D_{stag} effective diffusion coefficient in stagnant mobile phase, $D_{stag} = \varepsilon_{intra} K_p D_m / \tau_{intra}$ (m^2/s)
$\bar{d}_{p,2}$ surface area-averaged particle diameter, $\bar{d}_{p,2} = \Sigma\, d_{n,i}^3 n_i / \Sigma d_{n,i}^2 n_i$ (μm)
$\mathscr{F}$ Darcy–Weißbach friction factor
H theoretical plate height (m)
K bed permeability (m^2)
K_p hindrance parameter for pore level diffusion [86]
$\mathscr{L}_{stag}$ characteristic length for liquid hold-up in porous medium
$\mathscr{L}_{disp}$ characteristic length for axial dispersion
$\mathscr{L}_{flow}$ characteristic length for hydraulic permeability
L_{bed} length of packed bed (m)
ΔP pressure drop along column (Pa)
Pe Peclet number
q_i parameter(s) of particle size distribution
q_{area} stationary phase surface concentration (mg/m^2)
q_{max} maximum (monolayer) adsorption capacity (mg/ml)
q_{col} column volume-weighted concentration (mg/ml)
q_{sp} solid-phase concentration (g/l)
Re Reynolds number
$\mathscr{R}_{HP}$ hydrodynamic performance ratio, Eq. (8)
R_G radius of gyration (nm)

$t_{el,i}$ tracer residence time on column (s)
u_{sol} average linear velocity of solute band, $u_{sol} = u_{sf}/\varepsilon_{eff,i}$ (m/s)
u_{av} average mobile phase velocity, $u_{av} = u_{sf}/\varepsilon_{total}$ (m/s)
u_{sf} mobile phase superficial velocity (volumetric flow-rate divided by the column cross sectional area) (m/s)
V_{bed} fixed bed volume (m^3)
V_{extra} extra-column volume (m^3)
$V_{el,i}$ elution volume of solute (m^3)
$\dot{V}$ volumetric flow-rate of the mobile phase (m^3/s)
$\bar{x}$ characteristic radial length scale (m)
σ_L^2 length-scale based variance of a solute band (m^2)
σ_t^2 time-scale based variance of solute band (detector signal) (s^2)
ρ volumetric density of the mobile phase (kg/m^3)
ρ_{bed} volumetric density of fixed bed (kg/m^3)
ε_{total} total porosity of fixed bed (mobile phase volume divided by the column volume)
ε_{inter} interstitial porosity (interstitial void volume—interparticle or interskeleton—divided by column volume) [47]
ε_{intra} porosity of support structure (intraparticle or intraskeleton mobile phase volume divided by the particle or skeleton volume) [47]
$\varepsilon_{eff,i}$ effective bed porosity for analyte i (column residence time divided by the column volume)
τ_{intra} intraparticle or intraskeleton tortuosity factor, $\tau_{intra} = \varepsilon_{intra} + 1.5(1 - \varepsilon_{intra})$ [85]
τ_{bed} bed tortuosity [8,64]
Φ phase ratio (solid-phase volume divided by the liquid phase volume), $\Phi = (1 - \varepsilon_{total})/\varepsilon_{total}$
η dynamic viscosity of the mobile phase (Pa s)
ν kinematic mobile phase viscosity (m^2/s)
ψ_i particle shape distribution parameter(s)
$\Theta_{m,b,h}$ coefficients for mechanical, boundary-layer and hold-up dispersion [63]

Acknowledgements

We are grateful to Dieter Lubda from Merck (Darmstadt, Germany) for the kind donation of the silica-based monoliths and the gift of the particulate media, as well as for his support in providing physical data of the stationary phase materials. We also thank Dr. Gerard Rozing from Agilent Technologies (Waldbronn, Germany) for the donation of HPLC columns. This work was supported by the Deutsche Forschungsgemeinschaft (DFG) under grant SE 586/7-1.

References

[1] R.M. Heck, R.J. Farrauto, Catalytic Air Pollution Control: Commercial Technology, Wiley, New York, 1995.
[2] R.A. Dunbar, J.D. Jordan, F.V. Bright, Anal. Chem. 68 (1996) 604.
[3] F. Kapteijn, J.J. Heiszwolf, T.A. Nijhuis, J.A. Moulijn, CatTech 3 (1999) 24.
[4] A. Kirschning, C. Altwicker, G. Dräger, J. Harders, N. Hoffmann, U. Hoffmann, H. Schönfeld, W. Solodenko, U. Kunz, Angew. Chem. Int. Ed. Engl. 40 (2001) 3995.
[5] F. Svec, J.M.J. Fréchet, Ind. Eng. Chem. Res. 38 (1999) 34.
[6] N. Tanaka, H. Kobayashi, K. Nakanishi, H. Minakuchi, N. Ishizuka, Anal. Chem. 73 (2001) 420A.
[7] D. Josic, A. Buchacher, J. Biochem. Biophys. Methods 49 (2001) 153.
[8] J.C. Giddings, Dynamics of Chromatography. Part I: Principles and Theory, Marcel Dekker, New York, 1965.
[9] P.A. Bristow, J.H. Knox, Chromatographia 10 (1977) 279.
[10] R.F. Probstein, Physiochemical Hydrodynamics, Wiley, New York, 1994.
[11] K.K. Unger, Handbuch der HPLC, GIT Verlag, Darmstadt, 1994.
[12] Cs. Horváth, B.A. Preiss, S.R. Lipsky, Anal. Chem. 39 (1967) 1422.
[13] R.N. Kellerey, F.W. Billmeyer, Anal. Chem. 41 (1969) 874.
[14] K.K. Unger, G. Jilge, J.N. Kinkel, M.T.W. Hearn, J. Chromatogr. 359 (1986) 61.
[15] F. Svec, J.M.J. Fréchet, Anal. Chem. 64 (1992) 820.
[16] Q.C. Wang, F. Svec, J.M.J. Fréchet, J. Chromatogr. A 669 (1994) 230.
[17] F. Svec, J.M.J. Fréchet, Science 273 (1996) 205.
[18] E.C. Peters, F. Svec, J.M.J. Fréchet, Chem. Mater. 9 (1997) 1898.
[19] M.B. Tennikov, N.V. Gazdina, T.B. Tennikova, F. Svec, J. Chromatogr. A 798 (1998) 55.
[20] S. Xie, R.W. Allington, F. Svec, J.M.J. Fréchet, J. Chromatogr. A 865 (1999) 169.
[21] H. Minakuchi, K. Nakanishi, N. Soga, N. Tanaka, Anal. Chem. 68 (1996) 3498.
[22] H. Minakuchi, K. Nakanishi, N. Soga, N. Ishizuka, N. Tanaka, J. Chromatogr. A 762 (1997) 135.
[23] K. Nakanishi, H. Minakuchi, N. Soga, N. Tanaka, J. Sol–Gel Sci. Technol. 8 (1997) 547.

[24] N. Ishizuka, H. Minakuchi, K. Nakanishi, N. Soga, N. Tanaka, J. Chromatogr. A 797 (1998) 133.
[25] K. Cabrera, G. Wieland, D. Lubda, K. Nakanishi, N. Soga, H. Minakushi, K.K. Unger, Trends Anal. Chem. 17 (1998) 50.
[26] H. Minakuchi, K. Nakanishi, N. Soga, N. Ishizuka, N. Tanaka, J. Chromatogr. A 797 (1998) 121.
[27] F. Sinner, M.R. Buchmeiser, Macromolecules 33 (2000) 5777.
[28] K. Nakanishi, N. Soga, J. Am. Ceram. Soc. 74 (1991) 2518.
[29] K. Nakanishi, Y. Sagawa, N. Soga, J. Non-Cryst. Solids 134 (1991) 39.
[30] K. Nakanishi, N. Soga, J. Non-Cryst. Solids 139 (1992) 14.
[31] K. Nakanishi, N. Soga, J. Non-Cryst. Solids 139 (1992) 1.
[32] K. Nakanishi, J. Porous Mater. 4 (1997) 67.
[33] I. Mihelic, T. Koloini, A. Podgornik, A. Strancar, J. High Resolut. Chromatogr. 23 (2000) 39.
[34] M. Vodopivec, A. Podgornik, M. Berovic, A. Strancar, J. Chromatogr. Sci. 38 (2000) 489.
[35] D. Josic, A. Strancar, Ind. Eng. Chem. Res. 38 (1999) 333.
[36] N. Tanaka, H. Nagayama, H. Kobayashi, T. Ikegami, K. Hosoya, N. Ishizuka, H. Minakuchi, K. Nakanishi, K. Cabrera, D. Lubda, J. High Resolut. Chromatogr. 23 (2000) 111.
[37] K. Cabrera, D. Lubda, H.-M. Eggenweiler, H. Minakuchi, K. Nakanishi, J. High Resolut. Chromatogr. 23 (2000) 93.
[38] D. Lubda, K. Cabrera, W. Kraas, C. Schäfer, D. Cunningham, LC–GC Int. 14 (2001) 730.
[39] A. Podgornik, M. Barut, A. Strancar, D. Josic, T. Koloini, Anal. Chem. 72 (2000) 5693.
[40] C. Yu, M.H. Davey, F. Svec, J.M.J. Fréchet, Anal. Chem. 73 (2001) 5088.
[41] D.S. Petersen, T. Rohr, F. Svec, J.M.J. Fréchet, Anal. Chem. 74 (2002) 4081.
[42] Q.S. Yuan, A. Rosenfeld, T.W. Root, D.J. Klingenberg, E.N. Lightfoot, J. Chromatogr. A 831 (1999) 149.
[43] J. Bear, Dynamics of Fluids in Porous Media, Dover Publications, New York, 1988.
[44] S. Ergun, Chem. Eng. Sci. 48 (1952) 89.
[45] K.E.B. Andersson, Chem. Eng. Sci. 15 (1961) 276.
[46] I.F. Macdonald, M.S. El-Sayed, K. Mow, F.A.L. Dullien, Ind. Eng. Chem. Fundam. 18 (1979) 199.
[47] F.C. Leinweber, D. Lubda, K. Cabrera, U. Tallarek, Anal. Chem. 74 (2002) 2470.
[48] U. Tallarek, F.C. Leinweber, A. Seidel-Morgenstern, Chem. Eng. Technol. 25 (2002) 1177.
[49] J.P. Foley, J.G. Dorsey, Anal. Chem. 55 (1983) 730.
[50] M.S. Jeansone, J.P. Foley, J. Chromatogr. Sci. 29 (1991) 258.
[51] V.B.D. Marco, G.G. Bombi, J. Chromatogr. A 931 (2001) 1.
[52] R.M. Nicoud, A. Seidel-Morgenstern, Isolation Purif. 2 (1996) 165.
[53] P.C. Carman, Trans. Inst. Chem. Eng. 15 (1937) 150.
[54] A.R. Gupte, Ph.D. dissertation, Fakultät für Chemieingenieurwesen, Technische Hochschule Karlsruhe, Karlsruhe, 1970.
[55] H. Rumpf, A.R. Gupte, Chem.-Ing.-Tech. 43 (1971) 367.
[56] J.I. Liao, N. Chen, C. Ericson, S. Hjertén, Anal. Chem. 68 (1996) 3468.
[57] B. Mayr, R. Tessadri, E. Post, M.R. Buchmeiser, Anal. Chem. 73 (2001) 4071.
[58] A. Premstaller, H. Oberacher, C.G. Huber, Anal. Chem. 73 (2001) 4386.
[59] Q. Luo, H. Zou, X. Xiao, Z. Guo, L. Kong, X. Mao, J. Chromatogr. A 926 (2001) 255.
[60] R. Hahn, A. Jungbauer, Anal. Chem. 72 (2000) 4853.
[61] S. Ghose, S.M. Cramer, J. Chromatogr. A 928 (2001) 13.
[62] J.J. van Deemter, F.J. Zuiderweg, A. Klinkenberg, Chem. Eng. Sci. 5 (1956) 271.
[63] D.L. Koch, J.F. Brady, J. Fluid Mech. 154 (1985) 399.
[64] D. Kandhai, D. Hlushkou, A.G. Hoekstra, P.M.A. Sloot, H. Van As, U. Tallarek, Phys. Rev. Lett. 88 (2002) art. no. 234501.
[65] S.G. Weber, P.W. Carr, in: P.R. Brown, R.A. Hartwick (Eds.), High Performance Liquid Chromatography, Wiley, New York, 1989, Chapter 1.
[66] D.R. Lide, CRC Handbook of Chemistry and Physics, CRC Press, Boca Raton, 1997.
[67] A.E. Kamholz, E.A. Schilling, P. Yager, Biophys. J. 80 (2001) 1967.
[68] H. Olesen, J. Rehfeld, B.L. Hom, E. Hippe, Biochim. Biophys. Acta 194 (1969) 67.
[69] M.E. Young, P.A. Carroad, R.L. Bell, Biotechnol. Bioeng. 22 (1980) 947.
[70] M.T. Tyn, T.W. Gusek, Biotechnol. Bioeng. 35 (1990) 327.
[71] G. Guiochon, S. Golshan-Shirazi, A.M. Katti, Fundamentals of Preparative and Nonlinear Chromatography, Academic Press, Boston, 1994.
[72] T. Fornstedt, G. Guiochon, Anal. Chem. 73 (2001) 608A.
[73] D.M. Ruthven, Principles of Adsorption and Adsorption Processes, Wiley, New York, 1984.
[74] E. Glückauf, Nature 156 (1945) 748.
[75] G. Schay, G. Székely, Acta Chim. Acad. Sci. Hung. 5 (1954) 167.
[76] D.H. James, C.S.G. Phillips, J. Chem. Soc (1954) 1066.
[77] J.M. Jacobson, J.H. Frenz, Cs. Horváth, J. Chromatogr. 316 (1984) 53.
[78] J.M. Jacobson, J.H. Frenz, Cs. Horváth, Ind. Eng. Chem. Res. 26 (1987) 43.
[79] H.S. Carslaw, J.C. Jaeger, Conduction of Heat in Solids, Oxford University Press, Oxford, 1959.
[80] J. Crank, The Mathematics of Diffusion, Oxford University Press, Oxford, 1975.
[81] G. Greco, G. Iorio, G. Tola, S.P. Waldram, Trans. Inst. Chem. Eng. 53 (1975) 55.
[82] E.D. Heyse, D.J. Mika, T.P. deVenoge, D.L. Couliette, A. McGowin, Environ. Toxicol. Chem. 18 (1999) 1964.
[83] Z.P. Lu, M.M. Dias, J.C.B. Lopes, A.E. Rodrigues, Ind. Eng. Chem. Res. 32 (1993) 1839.
[84] A.E. Rodrigues, J.C.B. Lopes, M.M. Dias, G. Carta, Sep. Technol. 2 (1992) 208.
[85] M. Suzuki, J.M. Smith, Chem. Eng. J. 3 (1972) 256.
[86] H. Brenner, L.J. Gaydos, J. Colloid Interface Sci. 58 (1977) 312.

RAPID COMMUNICATIONS IN MASS SPECTROMETRY
Rapid Commun. Mass Spectrom. 2003; **17**: 1180–1188
Published online in Wiley InterScience (www.interscience.wiley.com). DOI: 10.1002/rcm.1039

RCM

Silica-based monoliths for rapid peptide screening by capillary liquid chromatography hyphenated with electrospray ionization Fourier transform ion cyclotron resonance mass spectrometry

Felix C. Leinweber[1†], Dietmar G. Schmid[2†], Dieter Lubda[3], Karl-Heinz Wiesmüller[4], Günther Jung[2] and Ulrich Tallarek[1]*

[1]Otto-von-Guericke-Universität Magdeburg, Institut für Verfahrenstechnik, Universitätsplatz 2, D-39106 Magdeburg, Germany
[2]Eberhard-Karls-Universität Tübingen, Institut für Organische Chemie, Auf der Morgenstelle 18, D-72076 Tübingen, Germany
[3]Merck KGaA, Frankfurter Straße 250, D-64271 Darmstadt, Germany
[4]EMC microcollections GmbH, Sindelfinger Straße 3, D-72070 Tübingen, Germany

Received 17 January 2003; Revised 26 March 2003; Accepted 26 March 2003

Capillary liquid chromatography based on particulate and monolithic stationary phases was used to screen complex peptide libraries by fast gradient elution coupled on-line to electrospray ionization Fourier transform ion cyclotron resonance mass spectrometry (ESI-FTICRMS). A slightly modified commercial electrospray interface consisting of a fused-silica transfer capillary and low dead volume stainless steel union at which the electrospray voltage was grounded enabled the effluent of all the capillary columns to be directly sprayed into the mass spectrometer. Stable electrospray conditions were generated over a wide range of mobile phase compositions, alleviating the need for a tapered end of the spray capillary, pneumatic assistance or preheated nebulizer gas. Since the identification of complex samples containing numerous isobaric substances is facilitated by chromatographic separation prior to mass spectrometry, stationary phase materials have been employed which offer a fast, efficient elution and, due to the complexity of samples, a high loading capacity. Silica-based monolithic capillary columns combine these three characteristics in a unique manner due to a tailored adjustment of both macro- and mesopore sizes in the highly porous silica structure. As we demonstrate by a comparative study of the silica-based monolithic and packed capillaries for LC/MS analysis of complex peptide libraries, silica monoliths show superior performance over packed beds of small-diameter particles with respect to analysis time and separation efficiency. Libraries with more than 1000 different peptides could be screened in less than 20 min.

High-resolution mass spectrometry in combination with electrospray ionization presents one of the most powerful systems in use for the analysis of complex biological samples encountered, for example, in proteomics and drug discovery.[1–4] Fourier transform ion cyclotron resonance mass spectrometry (FTICRMS) with superconducting magnets up to 25 Tesla provides a mass resolving power exceeding $m/\Delta m_{50\%} = 10^6$ for the analysis of single peptides, allowing an identification of individual analytes directly by their molecular mass without needing time-consuming in-cell dissociation.[5,6] Especially with complex mixtures the extremely high signal capacity in FTICRMS provides a basis for the simultaneous analysis of numerous compounds, as was demonstrated for a broad range of different samples.[7–10] The possibility of a direct identification via the molecular mass significantly reduces analysis time for samples in which the molecular mass of all components is known or can be calculated in advance, e.g., for tryptic digests of proteomes expressed by sequenced genomes and, of course, synthetic libraries. However, two major drawbacks arise for a direct, accurate mass spectrometric identification: in complex mixtures a signal suppression becomes possible due to the different efficiencies of ionization within the ESI process,[11] an effect that is also observed in ESI-FTICRMS.[12] The second problem is that isobaric components, e.g., those containing structural isomeric amino acids leucine and iso-leucine, are hardly distinguishable and usually have to be identified by further high-energy fragmentation, although there have been attempts to overcome this limitation.[13]

Capillary separation techniques based on liquid chromatography which are applied prior to mass spectrometric

*Correspondence to: U. Tallarek, Otto-von-Guericke-Universität Magdeburg, Institut für Verfahrenstechnik, Universitätsplatz 2, D-39106 Magdeburg, Germany.
E-mail: ulrich.tallarek@vst.uni-magdeburg.de
†These authors contributed equally to this work.

detection, and coupled on-line through an ESI interface, provide a suitable means for meeting the requirements for a fast identification of samples containing isobaric compounds because, after efficient chromatographic separation, analytes enter the mass spectrometer in concentrated elution bands with only a few or, in the case of baseline separation, without any further components that would decrease the sensitivity and resolution of the MS detection. Its low sample consumption (injection volumes are of the order of some tens of nanoliters) and volumetric flow rates of about 1 μL/min make the capillary separation techniques well suited to the optimum operation conditions of ESI interfaces.[14] To date, chromatographic capillary columns conventionally consist of a random-close packing of small-diameter spherical particles packed under high pressure into fused-silica capillaries. The use of small spheres (1.5–3 μm) significantly enhances the separation efficiency[15] under the limitation, however, of a drastically increased column back-pressure.[16] The capillaries packed with these particles (either porous or non-porous) are capable of providing high separation efficiency in reasonably short elution times only if they are operated as very short beds or with expensive ultra-high pressure LC equipment enabling system pressure drops between 700 and 1100 bar.[17–19]

To circumvent limitations of packed and therefore discontinuous stationary phases (in these beds the interstitial pore diameter and particle size are inherently coupled), monolithic stationary phases, based on either silica[20–23] or on organic polymers,[24–27] can provide useful alternatives because the morphology of their continuous solid phase can be tailored by an independent manipulation of both the macropore diameter and skeleton domain size via appropriate reaction conditions. Since the manufacturing process of the silica-based monoliths involves solvent exchange as the second step, the internal porosity of their skeleton may be varied in addition to and independently from the other skeleton parameters,[28] a feature that can hardly be realized for polymer monoliths due to their one-step polymerization manufacturing process.[29] The silica-based monoliths consequently show a distinct bimodal pore size distribution with relatively large macropore diameters (providing a favorable hydraulic permeability to the porous medium), small skeleton domain sizes (resulting in short diffusion path lengths) and large mesopore space which guarantees high adsorption capacity (Fig. 1).

The hydrodynamic behavior of silica-based monoliths (and monoliths in general) can be expressed in terms of 'equivalent particle (sphere) dimensions' for the permeability (d_{perm}) and band broadening (d_{disp}).[30,31] Due to the unique manipulation of their skeleton morphology, silica-based monoliths are characterized by quite different values for d_{perm} (10 μm) and d_{disp} (2 μm). This means that these silica monoliths offer the separation efficiency of a packed bed of 2 μm porous spheres, but with only the back-pressure that a bed of 10 μm spheres will generate, while keeping the adsorption capacity similar to that of a bed of porous spheres (Table 1).[30,31]

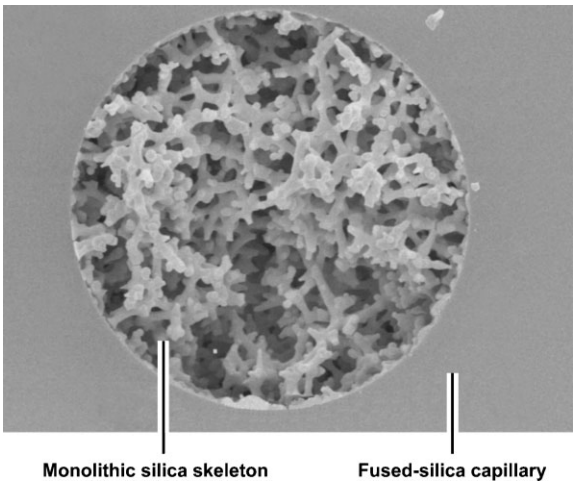

Figure 1. Scanning electron microscopy picture of the (silica-based) monolithic capillary column showing a bimodal pore size distribution with large flow-through pores (1.9 μm), small skeleton domains and a high internal skeleton porosity (12.5 nm mesopores).

Silica-based capillary columns have already been successfully used for highly efficient separations of neutral and charged analytes under isocratic elution conditions (as in μLC and CEC).[23,32] In this communication we demonstrate the use of silica-based capillary monoliths with internal diameter of 100 μm for a fast and efficient gradient-LC elution, directly coupled with FTICRMS detection in view of synthetic library screening. Due to the combination of a high permeability, separation efficiency and their large surface area, there was no need to use ultra-high pressure equipment with these monoliths. Rather, a standard high-pressure chromatographic system with maximum pressure drop of about 350 bar was well sufficient to realize short elution times.

To demonstrate the differences between particulate and monolithic stationary phases, three different capillary columns of identical dimension and similar reversed-phase surface modification were employed; these were either packed with two different porous particulate materials or contained the silica-based monolith. These materials were

Table 1. Characteristic physical properties of the different capillary columns

Fixed bed	Stationary phase	$\overline{d}_p$ [μm]	ρ_{bed} [g cm^{-3}]	ε_{total}	ε_{inter}	ε_{intra}	A_{spec} [m^2/g]
Small porous spheres (nominal 5 μm)	discontinuous, silica-based	6.1	0.85	0.65	0.37	0.44	about 300
Large porous spheres (nominal 10 μm)	discontinuous, silica-based	10.7	0.87				
Silica monolith	continuous, silica-based	—	0.29	0.92	0.72	0.70	

$\overline{d}_p$: mean particle diameter; ρ_{bed}: chromatographic bed density; ε_{total}: total bed porosity; ε_{inter}: interstitial porosity; ε_{intra}: intraparticle or intraskeleton porosity; A_{spec}: specific surface area (for further details see ref. 30).

compared in the context of achieving a fast and efficient analysis of complex synthetic peptide libraries.

EXPERIMENTAL

Chemicals

Acetonitrile (ACN), purified water (both HPLC grade) and formic acid were purchased from VWR International (Darmstadt, Germany). The synthetic peptide library VS*X*LY (*X* = all 20 proteinogenic amino acids) was donated by the Institute of Organic Chemistry, University of Tübingen (Germany), and library CW*XXX*G (*X* = 10 different amino acids E, N, R, F, P, S, W, Y, L, and H) came from EMC Microcollections GmbH (Tübingen, Germany).[7,8]

Capillary columns

Three different capillary columns of 100 μm i.d. (365 μm o.d.), 50 cm length and with a similar reversed-phase RP18 surface modification, were used in this study. Two of these capillaries were packed with 5 μm or 10 μm porous silica spheres (PurospherSTAR, Merck KGaA, with mesopore diameter of 12 nm), and the third one contained a monolithic chromatographic bed (Chromolith^{TM}, Merck KGaA; 1.9 μm as mean macropore diameter and mesopore diameter of 12.5 nm). Packed capillaries were prepared by the following procedure: briefly, fused-silica capillaries were cut to the desired length and first both ends were ground (grid 4000 sand paper) to ensure rectangular cuts. A glass fibre filter was then pre-cut and placed into a 1/16″ stainless steel coupling union (Upchurch, Oak Harbor, USA; 25 nL dead volume). On this side of the union the fused-silica capillary was inserted to ensure proper direct contact with the glass fibre filter. Tubing sleeves and PEEK finger-tight ferrules (Upchurch) sealed the capillary properly in the union. The glass fibre filter now functions as a low dead-volume in-line retaining frit for the stationary phase material (Fig. 2). The packing of capillary columns was achieved by preparing a slurry of 10% (w/v) of the respective stationary phase material in methanol, ultrasonicating for about 5 min and packing with a methanol/water mixture (1:4) for about 3 h at 550 bar. Afterwards, the flushing liquid was changed to pure water and a small inlet frit was burned with a laser splicing machine at a distance of 50 cm from the middle of the stainless steel union. The capillary then was directly cut at this frit and the pressure released very slowly. All packed capillaries were inspected under the microscope for homogeneity prior to their use.

Nano-LC system and gradient elution

Solvent delivery was achieved by an Eldex MicroPro dual syringe pumping system (SunChrom, Friedrichsdorf, Germany) at a constant volumetric flow rate of 20 μL/min which was then split in a graduated micro-splitting device from Upchurch. The splitting device was adjusted individually for each column to reach the maximum possible volumetric flow rate (as indicated by system pressure drops of about 320 bar). Injection (20 nL) was performed with a micro-injection valve and the separation capillary was directly connected to this valve in order to avoid pre-column band broadening.

Gradient elution for the two synthetic peptide libraries was conducted with 0.1% (v/v) formic acid in both water and acetonitrile serving as eluents A and B, respectively. For all separations of peptide library VS*X*LY a linear gradient of 10% to 30% B in 10 min was applied; for the large peptide library CW*XXX*G, the gradient increased linearly from 15% to 50% B in 20 min, and for the tryptic BSA digest from 10% to 55% B in 15 min. In all analyses the final percentage of organic modifier was held at its maximum value until the end of data acquisition.

Nano-ESI interface

The built-in, conventional stainless steel transfer capillary (192 mm long, 100 μm i.d., 1500 nL dead volume) of the ESI

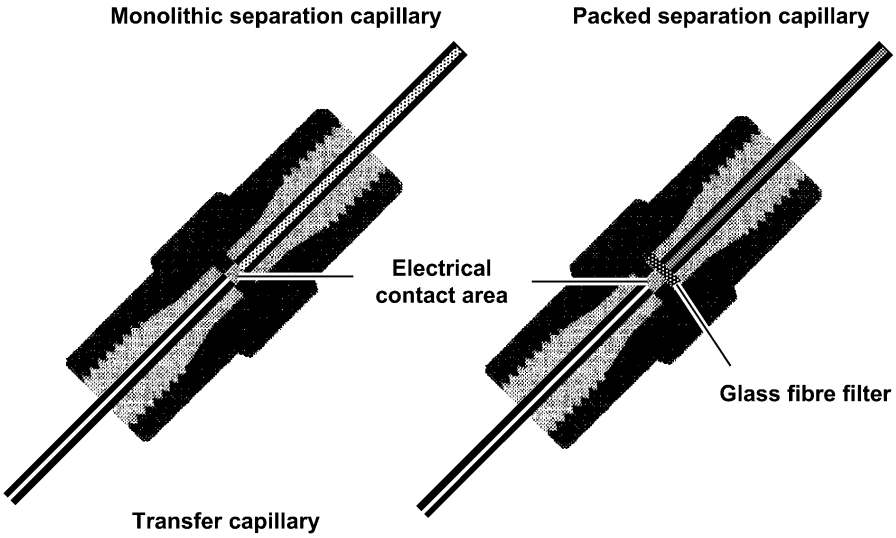

Figure 2. Schematic representation of a liquid junction between the capillary column and spray capillary of the electrospray interface (using a stainless steel union). While for packed capillaries an in-line glass fibre filter has to be used to retain the chromatographic beds, monolithic columns can be directly connected to the union. Note that the glass fibre filter is enlarged; after fingertight-fitting, it is only a few micrometers thick.

interface (Analytica of Branford, Branford, USA) was replaced by a fused-silica capillary having a similar length, but with 25 μm i.d. and 160 μm o.d., which possesses only 92 nL dead volume. The spraying end was ground to provide a flat surface, and the polyimide coating was carefully removed at this end of the capillary. The electrospray voltage (−4300 V) was grounded via the acidic mobile phase at the stainless steel coupling union. If necessary the electrical contact area between ground and solvent may be increased by the use of stainless steel filter disks for retaining the column packing.[33] However, a stable electrospray was obtained with all eluent compositions, and neither pneumatic assistance nor sheath liquid or heated nebulizer gas had to be used. Spraying was done at 60° off-axis.

FTICRMS conditions

ESI-FTICRMS was performed with a passively shielded 4.7 Tesla APEXII-ESI/MALDI-FTICR mass spectrometer (Bruker Daltonik, Bremen, Germany). The software XMASS version 5.0.10 (Bruker Daltonik), running on a Silicon Graphics O2 workstation, was used for data acquisition and processing. Mass calculation was performed with the standard elemental mass compilation of Audi and Wapstra.[34] A cylindrical 'infinity' cell is integrated in the superconducting magnet,[35] and is primarily used to avoid ion ejection in the z-direction during the excitation by simulating an rf field of an infinitely long cell. Instead of pulsed cooling gas, the 'sidekick' cell component of the 'infinity' cell was used to trap ions. Vacuum with a base pressure of 2.5×10^{-10} mbar at the cell side was provided by turbomolecular pumps (Edwards, Sussex, UK). In general, 512 k data points were acquired. For the monitoring of HPLC peaks, 256 sequential experiments were used and four spectra per experiment accumulated. A voltage of 1.0 V was applied to the trapping plates within the analyzer cell. An external four-point calibration was made by using compounds with an m/z of 364, 922, 1522 and 2122. The mass ranges were m/z 200–2000 for the peptide library VS*X*LY, and m/z 300–3000 for the peptide library CW*XXX*G and the tryptic BSA digest, resulting in data acquisition times of 22 and 28 min, respectively.

RESULTS AND DISCUSSION

Nano-electrospray interface

A nano-electrospray interface which is mainly based on commercial equipment has been designed for coupling capillary liquid chromatography with FTICR mass spectrometry. It allows a convenient exchange of capillary columns and contains a robust spray needle that guarantees constant (long-term) electrospray conditions and only negligible post-column dead volume. In order to meet these requirements, the built-in stainless steel transfer capillary was replaced by a 25 μm i.d. fused-silica capillary, and the built-in coupling union was replaced by one with a lower dead volume. Otherwise, the commercial interface remained unchanged for the analytical LC/MS coupling. Although the transfer capillary was not equipped with a tapered end, stable electrospray conditions could be achieved for eluent compositions between 0 and 50% acetonitrile (with 0.1% formic acid added to both the aqueous and the organic phases) while spraying directly out of the transfer capillary at 60° off-axis to prevent contamination of the ESI interface. With this setup, post-column dead volume is reduced to approximately 120 nL for the union and transfer capillary, which amounts to less than 2% of the volume of mobile phase in the different separation capillaries. Since this setup successfully meets the prerequisites for strongly reduced post-column band broadening, all the capillary columns were directly connected to the interface as indicated in Fig. 2. Due to its continuous stationary phase, a monolith could be simply connected to the union by appropriate fittings, but for the capillaries containing particulate beds a precut glass fibre filter had to be placed between capillary and union to retain the discontinuous stationary phase (cf. Fig. 2, note that the thickness of the glass fibre filter is exaggerated). In order to virtually remove all post-column dead volume the monolith may be cut in two pieces of appropriate length that can be placed on both sides of the union. Spraying is then performed directly out of the monolith.

Comparative gradient LC elution

Gradient elution usually starts with mobile phase compositions of weak elution strength, so most of the analytes are first (relatively) strongly adsorbed on the stationary phase material and thereafter, at increasing elution strength, continuously desorbed in different chromatographic bands according to their intensity of interaction. This technique inherently incorporates a chromatographic focusing (zone sharpening) step resulting in narrow bands also for the late-eluting compounds, especially if a steep gradient is run.[15,36] To demonstrate the suitability of the three different stationary phase materials for a fast, efficient gradient elution of complex samples, a preliminary comparative study was conducted using the smaller peptide library VS*X*LY. A linear gradient with 10–30% organic modifier in 10 min was applied to all capillaries, and the micro-splitting device was adjusted to set maximum flow rate through each separation column as indicated by a maximum system pressure drop of 320 bar (close to the pressure limit for standard PEEK fittings of ca. 350 bar). Since all pre-injection system capillaries had at least 100 μm i.d., the total back-pressure recorded at the pump mainly originated from the separation and the transfer capillary. By using the results of a previous study on the hydraulic flow resistance of particulate and monolithic resins, the observed pressure drop could be translated to a volumetric flow rate of about 250 nL/min for the (nominal) 5 μm material and to about 1000 nL/min for the 10 μm particles and the silica monolith (all capillaries with a 100 μm i.d. and 50 cm length).[30,31] An LC/MS analysis of peptide library VS*X*LY with these three stationary phases indicates significant differences between monolithic and particulate media with respect to elution time and peak width under otherwise similar elution conditions and column dimensions (the gradient LC/MS contour plots are shown in Fig. 3).

From these contour plots two main conclusions concerning the separation characteristics of the particulate media can be drawn. First, the zone sharpening effect in gradient elution reduces strong differences in separation efficiency normally observed in isocratic elution mode for the 5 and 10 μm spheres.[30,31] Both materials now lead to almost identical peak broadening. Second, the hydraulic permeability has the most

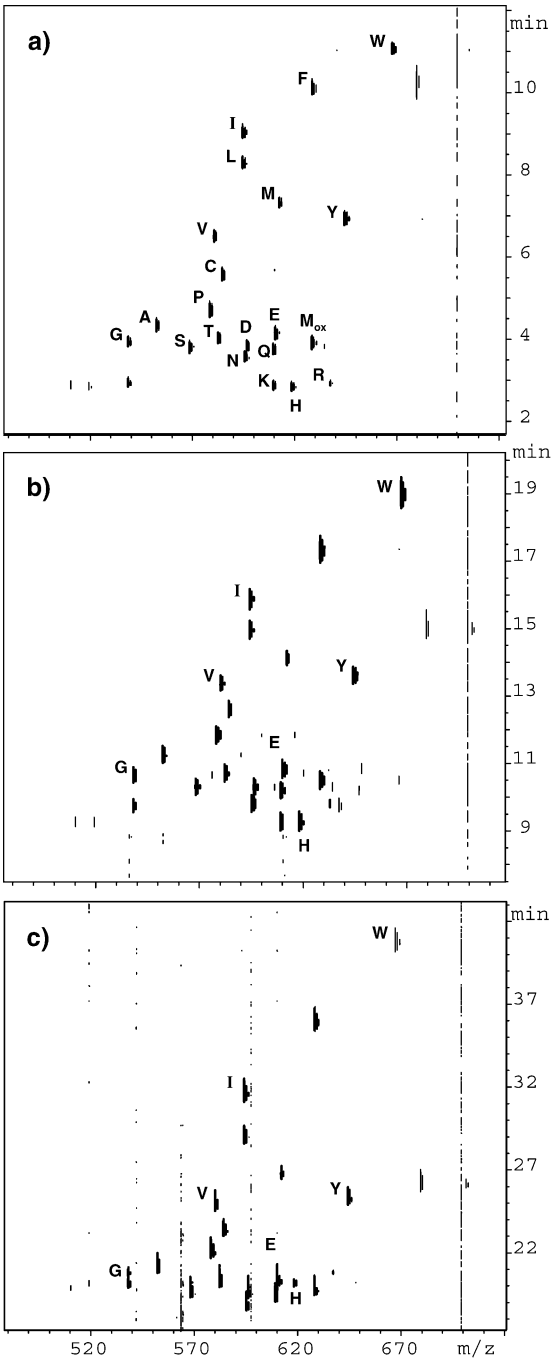

Figure 3. Contour plots of a gradient LC/MS analysis (at the highest attainable linear velocity) of synthetic peptide library VS*X*LY with both particulate and monolithic chromatography stationary phases. Capillary columns: (a) the silica-based monolith (Chromolith™ from Merck KGaA, Darmstadt, Germany) with a bimodal pore size distribution, (b) and (c) capillaries packed with the 10 and 5 μm porous spheres, respectively.

pronounced influence on separation time. Despite a constant pre-split volumetric flow rate of 20 μL/min resulting in a constant gradient delay time of less than 1 min for each capillary column, the reduced volumetric flow rate (and, concomitantly, the reduced linear mobile phase velocity) through the 5 μm sphere packing causes a strongly increased elution time, and therefore the total analysis time for this small peptide library takes more than 40 min. A further reduction of particle diameter would even more drastically decrease the speed of separation since column pressure drop is inversely related to the squared particle diameter.[16] Thus, packed beds of particles smaller than 5 μm are less suitable for a fast screening of complex mixtures with standard high-pressure equipment and were, for this reason, not a subject of this study on rapid peptide screening.

The main critical issue for high-throughput separations of complex mixtures (which usually require large column adsorption capacity to avoid overloading effects) is, therefore, the highest linear mobile phase velocity through the chromatographic bed that is attainable on a routine basis. One possibility for overcoming the limitation of decently high linear flow velocities through a packing would be the use of an ultra-high pressure system, but this is quite expensive and needs special operating precautions. An alternative is the use of much shorter columns; however, this approach has the limitation of a reduced loading capacity, especially when the particles are only superficially porous or even completely non-porous. A still more convenient alternative is the implementation of monolithic adsorption columns having a distinct bimodal pore size distribution which, to date, are available only as silica-based materials. As mentioned above[30,31] these columns combine the advantages of a large hydraulic permeability ($d_{perm} = 10\,\mu m$) and high separation efficiency ($d_{disp} = 2\,\mu m$), while keeping the adsorption capacity comparable to that of particulate beds consisting of completely porous spherical particles (Table 1). When using the capillary monolith for gradient elution of the peptide library VS*X*LY a highly efficient separation in short elution times can be realized (Fig. 3). Peak width and overall elution time are significantly reduced compared with those achieved using both particulate ''reference'' materials.

Data for the elution order according to relative hydrophobicity of the various peptides, as well as for the accuracy of the mass determination by an on-line MS analysis, are listed in Table 2. With an external four-point mass calibration in the range *m/z* 200–2000 a mean relative mass error of 4.9 ppm was obtained, a value that can be further decreased by injection of less concentrated samples to avoid undesired space charge effects due to ion/ion interaction. Mass spectra for the co-eluting basic peptides in the elution window from 3.8 to 4.2 min (with the silica monolith) demonstrate the unambiguous identification by high-resolution FTICRMS (Fig. 4).

LC/MS analysis of complex samples

In order to demonstrate the need in high-throughput LC/MS analysis of complex samples for both a high permeability and high separation efficiency, as well as a large surface area, the silica monolith and a column packed with 10 μm porous spheres were used to screen the synthetic peptide library CW*XXX*G, with *X* varied among ten different amino acids. This library contains 1000 different peptides in total, and the LC/MS contour plots for both capillaries are shown in Fig. 5. An efficient chromatographic elution with the silica monolith permits the identification also of doubly and triply charged peptides. This characteristic is hardly distinguishable with the packed capillary due to the broadened (and therefore diluted) peaks. The elution data for this large peptide library indicate that this new type of monolithic

Table 2. Mass accuracy of the MS detection of peptide library VS*X*LY after gradient elution on the silica monolith

Peptide VS*X*LY	Order of elution	exp. *m/z* $[M+H]^+$	theo. *m/z* $[M+H]^+$	$\Delta m/z$	δ [ppm]
X = G	9	538.28870	538.28714	0.00156	2.9
A	12	552.30563	552.30279	0.00284	5.1
S	7	568.30068	568.29770	0.00298	5.2
P	13	578.31800	578.31844	−0.00044	−0.8
V	15	580.33667	580.33409	0.00258	4.4
T	10	582.31614	582.31335	0.00279	4.8
C	14	584.27632	584.27486	0.00146	2.5
L	18	594.35234	594.34974	0.00260	4.4
I	19	594.35234	594.34974	0.00260	4.4
N	4	594.35174	594.34974	0.00200	3.4
D	5	595.30839	595.30860	−0.00021	−0.4
Q	6	596.29814	596.29262	0.00552	9.3
K	2	609.32589	609.32425	0.00164	2.7
E	11	609.36235	609.36064	0.00171	2.8
M	17	610.31085	610.30827	0.00258	4.2
H	1	612.31035	612.30616	0.00419	6.8
M_{ox}	8	618.32993	618.32459	0.00534	8.6
F	20	628.30763	628.30108	0.00655	10.4
R	3	628.33809	628.33409	0.00400	6.4
Y	16	637.37198	637.36679	0.00519	8.1
W	21	644.33137	644.32901	0.00236	3.7
				Mean	4.9
				Std. dev.	2.9

capillary column is capable of resolving complex libraries in very short analysis times due to its bimodal pore size distribution characterized by $d_{perm} = 10\,\mu m$ and $d_{disp} = 2\,\mu m$: it provides rapid access to a large surface area at a high volumetric flow rate. The zoomed insert in Fig. 5(a) reveals two well-separated peaks which represent the isobaric compounds CW*SSE*G, CW*ESS*G or CW*SES*G ($m/z = 668.23$, peak width 0.15 min), whereas with the particulate material the two peptides could not be chromatographically separated (cf. Fig. 5(b), peak width 0.5 min). The detailed sequence of each peptide can, of course, be further elucidated by MS/MS studies. For the particulate capillary column packed with 10 μm porous particles intraparticle diffusion path lengths are strongly increased and, as demonstrated in Fig. 5, lead to a significant band broadening and retarded gradient elution profiles. This becomes evident by an elution window of about 22 min (to be compared with only 11 min for the monolith), even though the same gradient was applied to both columns and, secondly, this particulate column offers a hydraulic permeability comparable to that of the monolith.

In addition to the analysis of synthetic peptides with their clearly predefined amino acid sequences and controlled purity, the monolithic capillary column was now used to demonstrate its feasibility for fast peptide mapping using real biological samples. We used a tryptic protein digest which represents a common, wide-spread separation problem in modern biotechnology. The contour plot of a gradient elution of a tryptic BSA digest (20 μM) as the model sample is shown in Fig. 6. Selective peptide masses obtained by single LC/MS runs were analyzed using the on-line Internet research software PROWL and, as expected, the fragment peptides could be unambiguously attributed to the protein BSA. Although the monolithic capillary column shows good

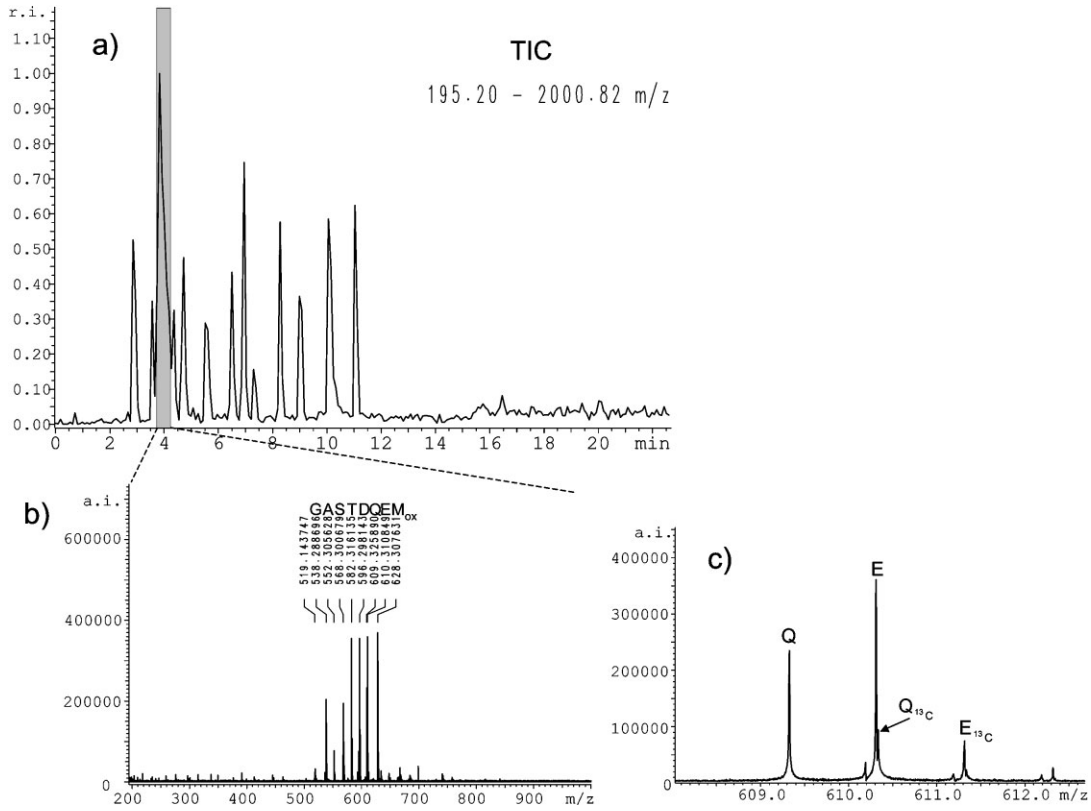

Figure 4. (a) TIC of peptide library VS*X*LY obtained using gradient elution with the silica monolith and (b) mass spectrum of the elution window from 3.8 to 4.2 min, including (c) the zoomed region for *m/z* 608–612.

RCM

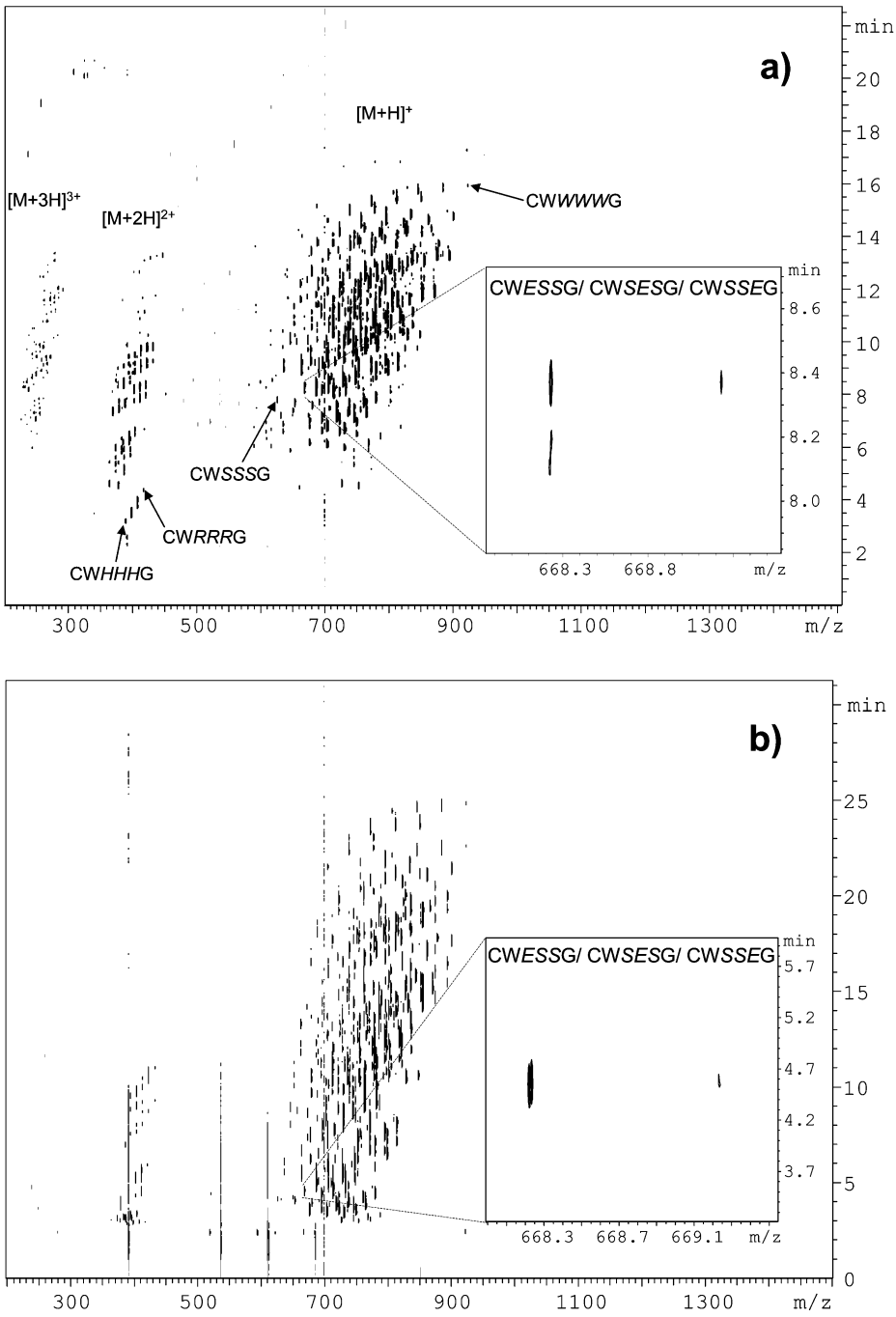

Figure 5. Contour plots (retention time vs. *m/z*) for the gradient elution of synthetic peptide library CW*XXX*G. (a) Monolithic capillary column and (b) a column packed with 10 μm porous spheres. The zoomed areas show the isobaric peptides CW*XXX*G (with *X* varied among S, S and E), but baseline separation is obtained only for the monolith.

separation efficiency, many fragment peptides are still co-eluting due to the variation in composition and chain length for each individual peptide and a possible post-translational modification. They have to be identified by the high mass resolving power of the FTICR mass spectrometer, as demonstrated in Fig. 7 for a pair of co-eluting peptides: the isotopic distribution of a five-fold charged peptide ($m/z = 997.486$, M = 4982.4) interferes with the signal pattern of a singly charged peptide ($m/z = 997.622$). The closest isotopic signals of these peptides differ by only 0.07 and 0.04 Th, but, with a mean mass resolving power of $m/\Delta m_{50\%} \approx 55\,000$, they could be resolved on-line in a single run.

CONCLUSIONS

For the high-throughput screening of low-volume and, at the same time, complex samples, capillary LC coupled to ESI-FTICRMS provides a general approach to fulfil the requirements for fast elution, high separation efficiency and high loading capacity. However, not all chromatography columns are equally suited. When using standard high-pressure

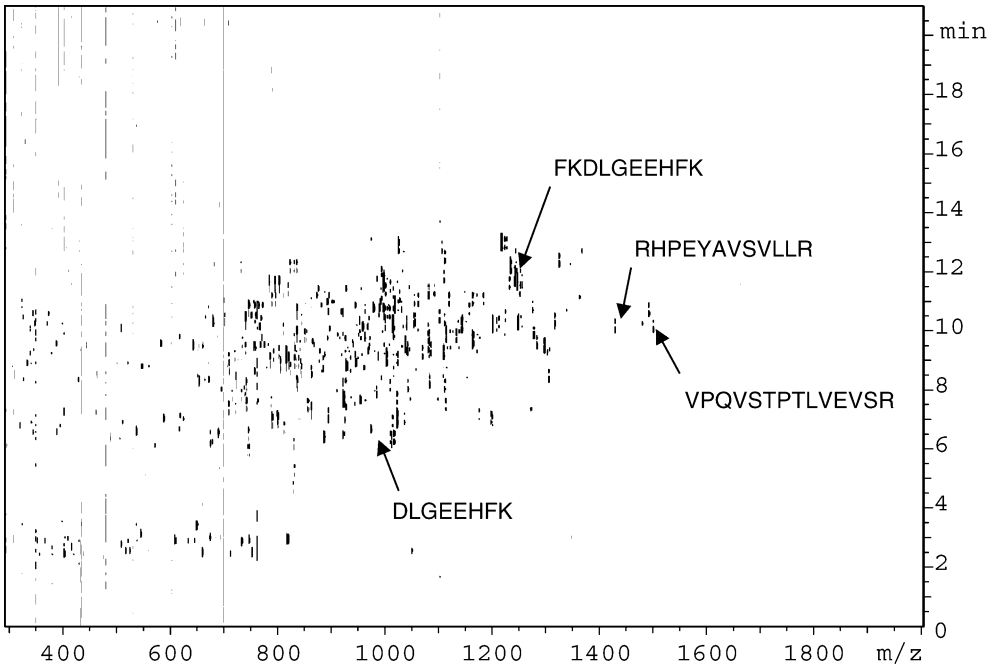

Figure 6. Contour plot (retention time vs. *m/z*) for gradient elution of a tryptic digest of BSA on the silica-based monolithic capillary column.

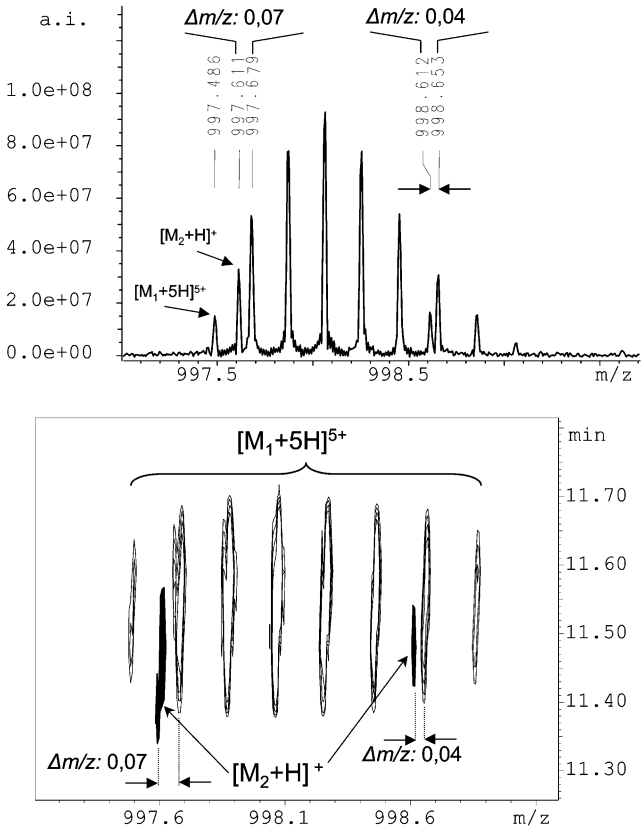

Figure 7. Mass spectrometric on-line detection of co-eluting peptides of a tryptic BSA digest using the silica capillary monolith. FTICRMS mass resolving power is higher than $m/\Delta m_{50\%} \approx 55\,000$.

laboratory equipment, long packed beds of small-diameter spheres can offer severe disadvantages with respect to the achievable elution time due to their strongly increased hydraulic flow resistance. While the pressure drop characteristics may be improved by a reduced column length, the overall adsorption capacity of the bed may be insufficient for complex mixtures. In addition, the short columns necessitate use of comparatively long (open channel) transfer capillaries that causes additional band broadening and, consequently, restricts a convenient implementation of on-line capillary LC/MS coupling. Further, the separation efficiency remains nearly identical for particulate columns of different particle sizes when operated in gradient elution mode because the band broadening (usually increased by the size of larger spheres in an isocratic elution) can be largely compensated by zone sharpening.

The silica-based monoliths can offer a further increased chromatographic performance due to their continuous solid phase, exhibiting a distinguished bimodal pore size distribution for which relevant skeleton parameters are adjusted independently. It allows the unique combination of low pressure drop (comparable to that of a 10 μm sphere packing, $d_{perm} = 10\,\mu m$), high separation efficiency (like that of a 2 μm sphere packing, $d_{disp} = 2\,\mu m$), much higher than that for the reference columns, and a loading capacity similar to that of random-close packings of porous spheres (despite the strongly reduced solid-phase content). Further, the increased volumetric flow rate of about 1 μL/min through the capillary monolith generates stable electrospray conditions over a wide range of mobile phase composition. Thus, the high separation efficiency of the monolithic capillary columns coupled to the outstanding mass resolving power of FTICRMS provides a very sensitive tool for the direct analysis of complex mixtures, especially in combinatorial chemistry or proteomics.

Acknowledgements

This work is funded by research grants from the Landesgraduiertenförderungsgesetz to D.G.S. and the DFG Sonderforschungsbereich 510 to G.J. The authors would

also like to thank A. Beck and R. Lehmann for providing the BSA digest. F.C.L. and U.T. acknowledge financial support from the Deutsche Forschungsgemeinschaft (DFG) under grant SE 586/7-2.

REFERENCES

1. Zhang X, Herring CJ, Romano PR, Szczepanowska J, Brzeska H, Hinnebusch AG, Qin J. *Anal. Chem*. 1998; **70**: 2050.
2. Gygi SP, Rochon Y, Franza BR, Aebersold R. *Mol. Cell Biol*. 1999; **19**: 1720.
3. Link AJ, Eng J, Schieltz DM, Carmack E, Mize GJ, Morris DR, Garwik BM, Yates JR. *Nat. Biotechnol*. 1999; **17**: 676.
4. Süßmuth RD, Jung G. *J. Chromatogr. B* 1999; **725**: 49.
5. Marshall AG, Hendrickson CL, Jackson GS. *Mass Spectrom. Rev*. 1998; **17**: 1.
6. Shi SD, Drader JJ, Hendrickson CL, Marshall AG. *J. Am. Soc. Mass Spectrom*. 1999; **10**: 265.
7. Jung G. *Combinatorial Peptide and Nonpeptide Libraries: A Handbook*, Wiley-VCH: Weinheim, 1996.
8. Jung G. *Combinatorial Chemistry: Synthesis, Analysis, Screening*, Wiley-VCH: Weinheim, 1999.
9. Schmid DG, Grosche GP, Bandel H, Jung G. *Biotechnol. Bioeng*. 2001; **71**: 149.
10. Hughey CA, Rogers RP, Marshall AG. *Anal. Chem*. 2002; **74**: 4145.
11. Enke C. *Anal. Chem*. 1997; **69**: 4885.
12. Sterner JL, Johnston MV, Nicol GR, Ridge DP. *J. Mass Spectrom*. 2000; **35**: 385.
13. Bossio RE, Marshall AG. *Anal. Chem*. 2002; **74**: 1674.
14. Abian J, Oosterkamp AJ, Gelpi E. *J. Mass Spectrom*. 1999; **34**: 244.
15. Brown PR, Hartwick RA. In *High Performance Liquid Chromatography*, Weber SG, Carr PW (eds). John Wiley: New York, 1989; 1–115.
16. Bear J. *Dynamics of Fluids in Porous Media*, Dover Publications: New York, 1988.
17. MacNair JE, Opitech GJ, Jorgenson JW, Moseley MA. *Rapid Commun. Mass Spectrom*. 1997; **11**: 1279.
18. Shen Y, Zhao R, Belov ME, Conrads TP, Anderson GA, Tang K, Pasa-Tolic L, Veenstra TD, Lipton MS, Udseth HR, Smith RD. *Anal. Chem*. 2001; **73**: 1766.
19. Tolley L, Jorgenson JW, Moseley MA. *Anal. Chem*. 2001; **73**: 2985.
20. Minakuchi H, Nakanishi K, Soga N, Ishizuka N, Tanaka N. *J. Chromatogr. A* 1997; **762**: 135.
21. Minakuchi H, Nakanishi K, Soga N, Ishizuka N, Tanaka N. *J. Chromatogr. A* 1997; **797**: 121.
22. Minakuchi H, Nakanishi K, Soga N, Tanaka N. *Anal. Chem*. 1996; **68**: 3498.
23. Tanaka N, Nagayama H, Kobayashi H, Ikegami T, Hosoya K, Ishizuka N, Minakuchi H, Nakanishi K, Cabrera K, Lubda D. *J. High Resolut. Chromatogr*. 2000; **23**: 111.
24. Svec F, Fréchet JMJ. *Anal. Chem*. 1992; **64**: 820.
25. Wang QC, Svec F, Fréchet JMJ. *J. Chromatogr. A* 1994; **669**: 230.
26. Svec F, Fréchet JMJ. *Ind. Eng. Chem. Res*. 1999; **38**: 34.
27. Gusev I, Huang X, Horváth C. *J. Chromatogr. A* 1999; **855**: 273.
28. Nakanishi K. *J. Porous Mater*. 1997; **4**: 67.
29. Sinner F, Buchmeiser MR. *Macromolecules* 2000; **33**: 5777.
30. Leinweber FC, Lubda D, Cabrera K, Tallarek U. *Anal. Chem*. 2002; **74**: 2470.
31. Tallarek U, Leinweber FC, Seidel-Morgenstern A. *Chem. Eng. Technol*. 2002; **25**: 1177.
32. Ishizuka N, Minakuchi H, Nakanishi K, Soga N, Nagayama H, Hosoya K, Tanaka N. *Anal. Chem*. 2000; **72**: 1275.
33. Schmid DG, Behnke B, Kempter C, Metzger JW, Kuhn R. *Microchim. Acta* 2001; **137**: 111.
34. Audi G, Wapstra AH. *Nucl. Phys. A* 1995; **595**: 409.
35. Caravatti PM, Allemann M. *Org. Mass Spectrom*. 1991; **26**: 514.
36. Snyder LR, Kirkland JJ. *Introduction to Modern Liquid Chromatography*, John Wiley: New York, 1979.

JOURNAL OF MASS SPECTROMETRY
J. Mass Spectrom. 2004; **39**: 223–225
Published online in Wiley InterScience (www.interscience.wiley.com). DOI: 10.1002/jms.544

JMS

JMS Letters

Received 11 September 2003; Accepted 13 September 2003

Dear Sir,

Sheathless electrospray ionization directly from a capillary monolith for fast liquid chromatography coupled to Fourier transform ion cyclotron resonance mass spectrometry

High-resolution Fourier transform ion cyclotron resonance (FTICR) mass spectrometry (MS) has emerged as one of the most efficient analytical tools for the identification of numerous different compounds in complex biological and synthetic samples only by means of the precisely determined molecular mass.[1] Especially in active areas such as proteomics or high-throughput library screening, relevant samples may contain several isobaric compounds. Their exact identification requires either a further and time-consuming in-cell fragmentation and/or a preceding chromatographic gradient elution.[2–6] Liquid chromatography (LC) with nanobore capillaries (up to 100 μm i.d.) and volumetric flow-rates in the lower microliters per minute range meet best the optimum conditions for electrospray ionization[7] and, in addition, the inherent chromatographic focusing step in gradient elution allows low-abundance molecules to be identified even from complex mixtures. However, to guarantee highly efficient chromatographic separations, a large surface area (column adsorption capacity) in sufficiently long capillaries is also required. Capillaries packed with small-diameter porous spheres generate high back-pressure and the resulting increased analysis time limits their use in fast LC. Monolithic columns provide an alternative because the devised preparation of their constituting solid skeleton allows a tailored adjustment of all relevant stationary phase characteristics.[8,9] To date only monoliths based on porous silica are capable of offering the unique combination of high hydraulic bed permeability, high separation efficiency and large surface area,[6,10] a combination which cannot be realized with any type of particulate stationary phase material.

For an efficient ionization process, the commonly used interfaces operating with sheath flow remain unsuitable for capillary

*Correspondence to: U. Tallarek, Otto-von-Guericke-Universität Magdeburg, Institut für Verfahrenstechnik, Universitätsplatz 2, D-39106 Magdeburg, Germany.
E-mail: ulrich.tallarek@vst.uni-magdeburg.de
†Both authors contributed equally to this work.
‡Present address: Novartis Pharma AG, Lichtstrasse 35, CH-4056 Basel, Switzerland.

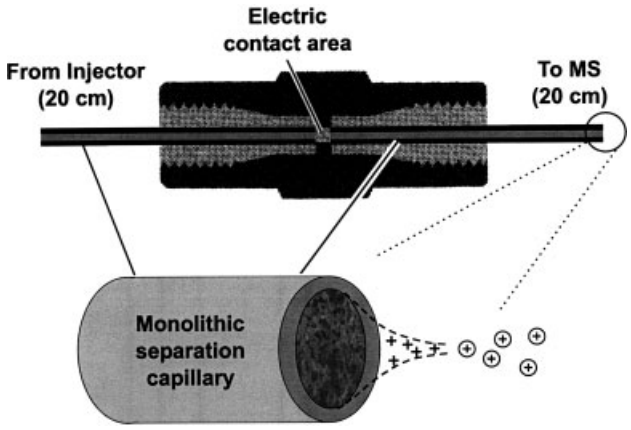

Figure 1. Schematic representation of the sheathless liquid junction interface with electrospray performed directly out of the silica-based monolithic separation column (capROD RP18e, 100 μm i.d.) (Merck, Darmstadt, Germany). The system's dead volume reduces to that of the liquid junction (25 nl).

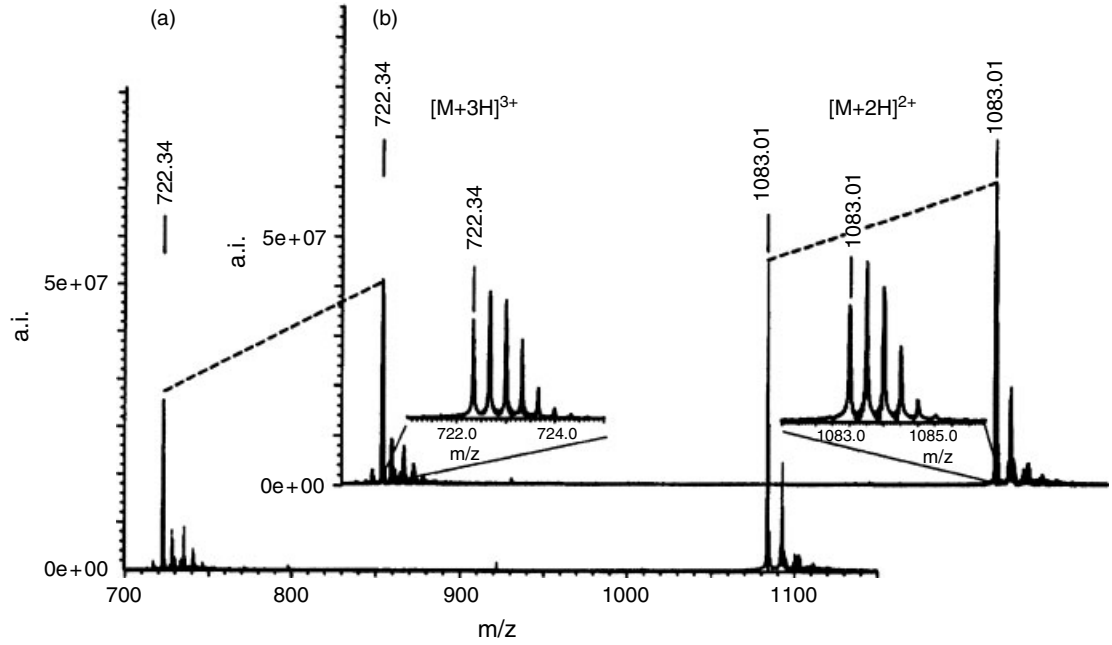

Figure 2. Comparison of the ionization performance of the peptide-based antibiotic gallidermin[15] using (a) a commercial electrospray ionization set-up incorporating an open-tube stainless-steel transfer capillary and (b) the silica-based monolithic capillary column (both 100 μm i.d.). Capillary LC/FTICR-MS settings: 200 individual scans to obtain reliable statistics; electrospray voltage, −4000 V; mobile phase: water–acetonitrile (50 : 50) + 0.1% (v/v) TFA; flow-rate, 1 μl min^{-1}; other conditions similar to those in Ref. 6.

JMS

separation techniques owing to severe sample dilution and a significant decrease in detection sensitivity.[11] Thus, sheathless interfaces based on liquid junctions are preferably used in LC/MS coupling owing to the versatile implementation of either open narrow-bore spray capillaries or packed separation columns with a tapered end.[11–13] In addition, metal-coated spray tips as an alternative for sheathless electrospray show only very limited long-term stability of a few hours at the maximum.[14]

Here we present an LC/MS configuration which incorporates monolithic capillary columns over the complete distance from the injection module to the sheathless electrospray interface. The commercially built-in stainless-steel spray capillary is replaced with a silica-based monolith sealed in a fused-silica capillary of the same dimensions (Fig. 1). Since the electrospray was performed directly out of the plain-cut end of this monolithic separation capillary, the main advantage of the device is a simple removal of the adverse effects on chromatographic performance resulting from the spray capillary. These include post-column band broadening or significant back-pressure if either large- or small-diameter open capillaries are used. A comparison of the ionization efficiency with respect to the commercially built-in stainless-steel spray capillary where the electrospray voltage can be conducted directly to the spraying tip was made by eluting the antibiotic peptide gallidermin[15] (M_w = 2164 g mol^{-1}) under unretained conditions (Fig. 2). The signal intensities and ionization patterns show similar qualitative and quantitative results concerning the electrospray process. With both configurations no additional preheated nebulizer gas or pneumatic assistance was needed to establish stable electrospray conditions at the respective capillary end.

The almost dead volume-free configuration in combination with the monolithic stationary phase allows fast and efficient gradient elution at volumetric flow-rates up to 4 µl min^{-1} (350 bar with standard micro-LC pumping systems) because these silica-based monoliths offer a relatively high permeability of a bed of 11 µm diameter hard spheres and a separation efficiency corresponding to that of 2 µm porous spheres.[10] The chromatographic performance is demonstrated by the capillary LC/FTICR-MS analysis of a synthetic pyrrole collection containing 284 different target molecules. The complete collection could be screened within 6 min (Fig. 3). Especially the separation at elevated flow-rates is accompanied by two advantages: first, in combination with short gradient delay times, a strong reduction of the total analysis time can be achieved compared with that reported in earlier work on the elution of complex samples with different monolithic or particulate stationary phase materials;[5,6] second, the increased flow-rates alleviate the need for tapered ends to generate stable electrospray conditions and successfully circumvent the risk of clogging at the spraying outlet. Not only fast and efficient chromatographic elution but also an accurate mass determination is possible. The FTICR mass spectrum in Fig. 4 taken directly from the gradient elution LC/MS analysis indicates a mass resolving power of more than

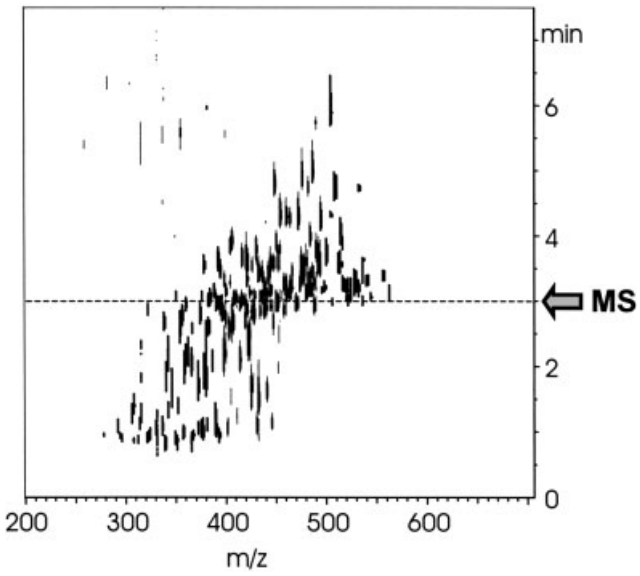

Figure 3. Fast gradient elution of a synthetic pyrrole library containing 284 different heterocyclic molecules each at a concentration of about 30 nmol l^{-1}. Elution conditions: (A) deionized water 1; (B) acetonitrile, both with addition of 0.1% TFA; gradient 0 min 30% B, 1 min 50% B, 6 min 80% B; flow-rate, adjusted to a maximum back-pressure of 350 bar corresponding to a flow-rate of about 4 µl min^{-1}. FTICR-MS settings similar to those in Ref. 6.

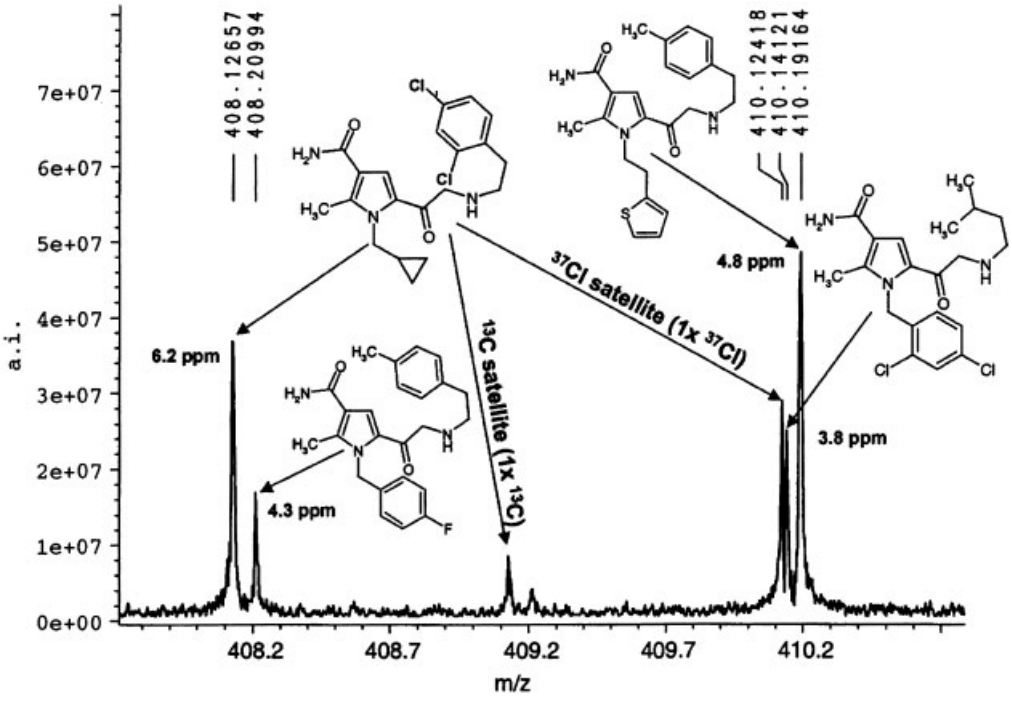

Figure 4. On-line mass spectrometric resolution of three structurally different, co-eluting pyrrole derivatives with a mass resolving power of more than $m/\Delta m_{50\%} \approx 24\,000$ (at an elution time of 3 min in Fig. 3).

$m/\Delta m_{50\%} \approx 24\,000$ and an average mass accuracy of below 5 ppm with external calibration for structurally different but co-eluting pyrrole derivatives. It is sufficient to allow the fast, efficient and direct on-line identification of relevant library components including the determination of their elemental composition.

In conclusion, the presented modified sheathless electrospray configuration with silica-based monolithic capillary columns allows fast LC because this stationary phase material may be used continuously to cover the complete distance from the injector to the mass analyzer including the electrospray ion source. Mechanically unstable parts such as sintered frits, tapered ends or coated spraying tips are successfully replaced and the presented chromatographic, ionization and mass spectrometric properties and also the robust nature of the monolith demonstrate that the direct electrospray out of the monolithic separation capillary is compatible with the demands of high-throughput LC/MS screening.

Yours,

FELIX C. LEINWEBER,[1†] DIETMAR G. SCHMID,[2†‡] DIETER LUBDA,[3] BERND SONTHEIMER,[4] GÜNTHER JUNG[2] and ULRICH TALLAREK[1*]

[1] Otto-von-Guericke-Universität Magdeburg, Institut für Verfahrenstechnik, Universitätsplatz 2, D-39106 Magdeburg, Germany

[2] Eberhard-Karls-Universität Tübingen, Institut für Organische Chemie, Auf der Morgenstelle 18, D-72076 Tübingen, Germany

[3] Merck KGaA, Frankfurter Strasse 250, D-64271 Darmstadt, Germany

[4] EMC Microcollections GmbH, Sindelfinger Strasse 3, D-72070 Tübingen, Germany

References

1. Marshall AG, Hendrickson CL, Jackson GS. Fourier transform ion cyclotron resonance mass spectrometry: a primer. *Mass Spectrom. Rev.* 1998; **17**: 1.
2. Süssmuth RD, Jung G. Impact of mass spectrometry on combinatorical chemistry. *J. Chromatogr. B* 1999; **725**: 49.
3. Wolters DA, Washburn MP, Yates JR. An automated multidimensional protein identification technology for shotgun proteomics. *Anal. Chem.* 2001; **73**: 5683.
4. Schmid DG, Grosche GP, Bandel H, Jung G. FTICR-mass spectrometry for high-resolution analysis in combinatorical chemistry. *Biotechnol. Bioeng.* 2001; **71**: 149.
5. Smith RD, Anderson GA, Lipton MS, Pasa-Tolic L, Shen Y, Conrads TP, Veenstra TD, Udseth HR. An accurate mass tag strategy for quantitative and high-throughput proteome measurements. *Proteomics* 2002; **2**: 513.
6. Leinweber FC, Schmid DG, Lubda D, Wiesmüller KH, Jung G, Tallarek U. Silica-based monoliths for rapid peptide screening by capillary liquid chromatography hyphenated with electrospray ionization Fourier transform ion cyclotron resonance mass spectrometry. *Rapid Commun. Mass Spectrom.* 2003; **17**: 1180.
7. Abian J, Oosterkamp AJ, Gelpi E. Comparison of conventional, narrow-bore and capillary liquid chromatography mass spectrometry for electrospray ionization mass spectrometry: practical considerations. *J. Mass Spectrom.* 1999; **34**: 244.
8. Svec F, Fréchet JMJ. Molded rigid monolithic porous polymers: an inexpensive, efficient and versatile alternative to beads for the design of materials for numerous applications. *Ind. Eng. Chem. Res.* 1999; **38**: 34.
9. Tanaka N, Nagayama H, Kobayashi H, Ikegani T, Hosoya K, Ishizuka N, Minakuchi H, Nakanishi K, Cabrera K, Lubda D. Monolithic silica columns for HPLC, Micro-HPLC, and CEC. *J. High Resolut. Chromatogr.* 2000; **23**: 111.
10. Leinweber FC, Tallarek U. Chromatographic performance of monolithic and particulate stationary phases: hydrodynamics and adsorption capacity. *J. Chromatogr. A* 2003; **1006**: 207.
11. Gelpi E. Interfaces for coupled liquid-phase separation/mass spectrometry techniques. An update on recent developments. *J. Mass Spectrom.* 2002; **37**: 241.
12. Davis MT, Stahl DC, Hefta SA, Lee TD. A microscale electrospray interface for online, capillary liquid-chromatography tandem mass-spectrometry of complex peptide mixtures. *Anal. Chem.* 1995; **67**: 4549.
13. Link AJ, Eng J, Schieltz DM, Carmack E, Mize GJ, Morris DR, Garvik BM, Yates JR. Direct analysis of protein complexes using mass spectrometry. *Nat. Biotechnol.* 1999; **17**: 676.
14. Valaskovic GA, McLafferty FW. Long-lived metallized tips for nanoliter electrospray mass spectrometry. *J. Am. Soc. Mass Spectrom.* 1996; **7**: 1270.
15. Kellner R, Jung G, Hoerner T, Zaehner H, Schnell N, Entian K-D, Goetz F. Gallidermin, a new lanthionine-containing polypeptide antibiotic. *Eur. J. Biochem.* 1998; **177**: 53.

Erdmann Rapp, Ulrich Tallarek

Lehrstuhl für Chemische Verfahrenstechnik, Institut für Verfahrenstechnik, Otto-von-Guericke Universität Magdeburg, Universitätsplatz 2, 39106 Magdeburg, Germany

In memory of our teacher and mentor Professor Dr. Ernst Bayer

Liquid flow in capillary (electro)chromatography: Generation and control of micro- and nanoliter volumes

We describe and discuss instrumental developments in capillary (electro)chromatography which are of particular relevance for generating (and controlling) required volumetric flow rates in the micro- and nanoliter range through packed capillaries. Both isocratic and gradient elution are considered. For capillary HPLC this practically involves only commercial instrumentation, with systems based on syringe or piston pumps, but it also realizes the innovative concept of a high-pressure electrokinetic pump. The numerous systems that have been used to generate electroosmotic flow through chromatographic beds are classified under the following headings: i) basically commercial capillary electrophoresis instruments (adapted for electrochromatography); ii) home-built configurations; and iii) commercial capillary electrochromatography systems. Concerning the reviewed instrumentation, emphasis is placed on feasibility, automation, as well as system-inherent delay times and dead volumes.

Key Words: Miniaturization; Packed capillaries; HPLC; CEC; Instrumentation; Pump systems; Dead volume

Received: March 19, 2002; revised: June 17, 2002; accepted: September 6, 2002

1 Introduction

Miniaturization with regard to the column inner diameter (ID) of high-performance liquid-phase separation systems utilizing fixed beds of (nowadays) typically porous, spherically shaped, slurry-packed adsorbent particles was initiated more than 25 years ago [1–5]. This continuing trend is mainly driven by the need to handle small volumes of complex sample, e.g., for the elucidation of physiological processes and identification of successful drug candidates, especially in the context of high-throughput screening technologies. On moving from analytical and narrow-bore LC with 2.1–4.6 mm ID columns, an average particle size in the range 3–10 μm, and bed lengths rarely exceeding 200 mm towards nano-scale LC and sub-microliter flow rates (see **Table 1** for definitions [6–9]), the ensuing benefits include:

i) an increased mass sensitivity (in combination with concentration-sensitive detection) due to reduced chromatographic dilution,

ii) the possibility of using smaller particle diameters which – at constant average flow velocity through the bed – translates into an increased efficiency as it (mainly) reduces the stagnant mobile phase mass transfer resistance,

iii) the achievement of a high column efficiency per unit time and pressure drop which translates into a low separation impedance [10],

iv) a lower stationary phase, solvent, and sample volume consumption which facilitates the use of exotic liquids, expensive solids, and/or long columns (if pressure drop is not a limiting factor),

v) compatibility with flow rate requirements of a nano-ESI interface for on-line coupling to mass spectrometry, and

vi) the possibility of applying high electric fields for an additional (or exclusive) transport of solute molecules by electroosmosis and/or electrophoresis.

This last aspect has stimulated a tremendous interest in capillary electrochromatography (CEC) which combines retention mechanisms and stationary phase selectivities known from HPLC with the miniaturization potential of capillary electrophoresis (CE) [11–17]. Tsuda [18] described electrochromatography as an electrophoretic procedure where sorptive interactions with the stationary phase of the support particles are a major contribution, i.e., the separation is achieved by differential partitioning and migration. Compared to pressure-driven flow, the superior performance of electroosmosis in bulk transport of liquid through a single, straight, and open (unpacked) cylindrical capillary accrues from the fact that, in the limit of thin electrical double layers, the liquid moves as in plug flow, i.e., the velocity field apparently slips at the inner wall of the capillary [19, 20] and that, further, the ratio of electroosmotic to hydraulic volumetric flow rates (at a fixed

Correspondence: U. Tallarek, Lehrstuhl für Chemische Verfahrenstechnik, Otto-von-Guericke Universität Magdeburg, Universitätsplatz 2, D-39106 Magdeburg, Germany. Phone: +49 (0)391 6110 465. Fax: +49 (0)391 67 12028. E-mail: ulrich.tallarek@vst.uni-magdeburg.de.

 1615-9306/2003/0605–0453$17.50+.50/0

Table 1. Suggested nomenclature for various regimes in LC practice.

Regime	Column type	Column diameter, cross-section	Flow rates	Typical loading
Analytical LC	normal-bore column	5.0–3.9 mm, 20–12 mm^2	5–1.5 mL/min	2–10 mg
Narrow-bore LC	narrow-bore column	3.9–2.1 mm, 12–3.5 mm^2	1.5–0.2 mL/min	0.5–2 mg
Micro LC	micro-bore column	2.1–0.5 mm, 3.5–0.2 mm^2	300–10 μL/min	50–500 μg
Capillary LC	packed capillaries	0.5–0.15 mm, 0.2–0.02 mm^2	15–1 μL/min	1–50 μg
Nano(scale) LC	packed capillaries	< 0.15 mm, < 0.02 mm^2	< 1 μL/min	< 1 μg

potential and pressure gradient) is inversely proportional to the square of the capillary radius [21]. The flat flow profile typical for CE under conditions of pure electroosmotic flow (EOF) [22, 23] and negligible or moderate thermal effects [24] has also clear implications for the dynamics of the EOF in CEC, which involves porous media like random sphere packings or monolithic structures. Compared to pressure-driven flow, solute dispersion and the medium geometry can be improved

i) due to a relatively flat microscopic (pore-level) velocity profile of the EOF in the interparticle pore space of the packing (under most practical conditions the electrical double layer is thin compared to interparticle pore dimensions),

ii) because, again for thin electrical double layers, volumetric pore-level EOF is fairly independent of the pore diameter which reduces interparticle flow heterogeneity on a mesoscopic scale,

iii) due to intraparticle EOF [25–28]. Although under many conditions the electrical double layer cannot be regarded as thin in the intraparticle pore space with its smaller pore dimensions the resulting volumetric EOF can be still substantial,

iv) because intraparticle transport of charged species (applying to most solutes) can be increased by migration and surface electrodiffusion [29], and

v) because the contrasting pore-scale dependence of electroosmotic and hydraulic permeabilities allows operation of comparatively long packed columns in CEC and the use of nanoparticles as packing material [30, 31]. Vice versa, CEC can achieve fast, efficient separations already with very short chromatographic beds [32].

These contributions leave longitudinal molecular diffusion as the only limitation to performance in CEC, as in CE, but in a porous medium with much higher surface-to-volume ratio. On the other hand, returning to the benefits of miniaturization in HPLC, the electrokinetic transport of liquid and solute through packed capillaries or monolithic structures increases separation efficiency and mass sensitivity further towards a new dimension. Despite the clear advantages, CEC still awaits a comprehensive validation including the interface electrokinetics [33] and, in this respect, especially the influence of the sample on the matrix, and it is far from being an alternative to HPLC and/or CE on any routine basis. Among other problems, including the preparation of chromatographic beds with long-term stability (that indeed deserve the attribute "fixed bed"), the minimization of system dead volume and fast mixing of small amounts of liquid for gradient elution, an important issue in CEC and cHPLC practice is related to the generation and control of micro- and nanoliter flow rates.

Following this line of thought, our present paper is concerned with a hardware overview and the comparison of instrumental configurations that can be used to address the volumetric flow rate requirements bridging capillary and nano-scale LC (cf. Table 1). While for pressure-driven flow, which we will discuss first, it effectively involves only commercial devices (Section 2 and **Table 2**), the great variety of setups that have been presented and successfully used for realizing electrokinetic flow through chromatographic beds can be divided into

i) (in most cases) commercial, but also home-built CE instruments adapted for CEC, implemented directly or only slightly modified, without an option for pressure-assisted CEC (pCEC) or cHPLC (see Section 3 and **Table 3**), and

ii) instruments designed for CEC, cHPLC, and pCEC which, in the past, were realized almost exclusively via home-built configurations (commercial systems have become available only recently, cf. **Table 4**) discussed in Section 4.

2 Commercial μHPLC and cHPLC instruments

The continuing interest in (μ/c)HPLC is reflected in the large number of articles that have been published about with these techniques, including reviews that cover general aspects [34–42], column technology [43–47], detection [48–56], and instrumentation [57, 58]. A significant decrease of bed volume puts stringent demands on instrumentation for μHPLC and especially cHPLC as all the volumetric extra-column dispersion (and delay) sources

Table 2. Selection of commercial (μ/c)HPLC instruments.

Specifications	Agilent 1100 series	Waters CapLC™	LC Packings UltiMate™	Eldex MicroPro™
Hydraulics	two serial dual pistons, servo-controlled variable stroke drive and active inlet valves	two controlled, parallel, positive-displacement syringe-style pistons [h]	reciprocating double-piston pump, electronic suppression of residual pulsation	up to four high-pressure syringe pumps with 2 mL or 10 mL volume
Flow rates	0.01 to 2500 μL/min in 0.01 μL/min increments	0.25 to 40 μL/min, increments of 0.01 μL/min	0.05 to 1000 μL	0.01 to 10000 μL/min in increments of 0.01 μL/min
Recommended flow rates[a]	1–100 μL/min by EFC, 0.1–2.5 mL/min without split [b]	1–40 μL/min without split	0.05–1000 μL with different calibrator cartridges[j]	1–200 μL/min without split [k]
Gradient mixing	(binary) presplit high-pressure mixing[c] followed by EFC	(binary or ternary) splitless high-pressure mixing	low pressure (quarternary) mixing	(up to quarternary) splitless high-pressure mixing
Delay volumes	presplit mixer: 420 μL, 1–20 μL/min kit: 5 μL [d] 20–100 μL/min kit: 14 μL [d] >100 μL/min: 180–480 μL	< 20 μL without sample loop	without autosampler, depending on calibrator cartridge: μHPLC ≈ 120 μL, cHPLC ≈ 12 μL, nano-HPLC ≈ 0.6 μL	dynamic mixer: 15 and 85 μL, static: 5 μL down to 29 nL (e.g., micro-tee P · 775 from Upchurch) [l]
Pressure range	up to 400 bar	up to 5000 psi (≈ 345 bar)	up to 400 bar	up to 10000 psi (≈ 700 bar)
pH range	1.0 to 8.5 recommended	no information available	2.0 to 10.0 recommended	no information available
Degasser	4-channel vacuum degasser [e]	no information available	four bottles helium sparkled	not integrated
Fully integrated autosampler	thermostatted, 0.01–40 μL injection volume; 10–100 μL delay volume[f]	0.02–100 μL injection volume, no information about delay volume available	can be connected to the LC Packings Famos™ autosampler	can be connected to the Spark [m] autosamplers
Column oven	✓	✓	✓	not integrated
Available integrated detected	UV-Vis, MWD, and PDA, MS systems from Agilent and other manufacturers	PDA and MS systems, especially from Micromass [i]	fast scanning UV-Vis, several MS systems	a variety of detectors from different manufacturers detectors
UV flow cells	500 nL; flow cell with 10 mm path length and larger ones [g]	250 nL, 5 mm path length flow cell for pressures up to 1000 psi (≈ 70 bar)	3 nL, 45 nL, and 180 nL flow cells, each with 10 mm path length, for pressures up to 400 bar	depends on detector manufacturer

[a] Especially for solvent gradients. [b] With by-passed EFC. [c] Using adjusted primary flow rates (200–800 μL/min). [d] From the EFC to the column inlet (without sample loop). [e] Each channel has an internal volume of 1 mL. [f] Depending on sample-loop volume; automatic reduction of system delay volume down to 5 μL (cf. [d] and delay volumes) is possible via by-passing the autosampler after injection. [g] Semi-micro flow cell, standard flow cell, high-pressure flow cell. [h] With active check valve control for continuous solvent delivery. [i] Micromass UK Limited, Manchester, United Kingdom (http://www.micromass.co.uk). [j] Non-controlled flow splitters. [k] In any case allows a minimum run time of 50 min before syringe refill is required. [l] Additional volumes only by injection device and transfer lines. [m] Spark Holland Instrumenten, Emmen, The Netherlands (http://www.spark-holland.nl).

have to be scaled down accordingly. It is particularly important for injection and detection, as well as for sample and solvent preparation. In gradient elution attention has to be given to minimization of extra-column volumes and associated delay times arising from mobile phase transfer and mixing. Commercial instruments have become available in (μ/c)HPLC (Table 2) following different approaches for providing constant flow rates in the lower and sub-microliter range through the packed beds (i.e., against substantial back-pressure) which are based on

Table 3. Commercial CE instruments adapted for CEC applications.

Specifications	Agilent Technologies CE	Beckman Coulter P/ACE MDQ	Prince Technologies PrinCE-C 660
Operation modes	constant (or ramped) voltage, current or power	constant (or ramped) voltage, current or power	constant (or ramped) voltage or current
Injection modes	elektrokinetic (0 to ±30 kV), pressure	elektrokinetic (0 to ±10 kV), pressure	elektrokinetic (0 to ±30 kV), pressure
Pressure range	0–50 mbar bidirectional for injection. 1 bar and 2–12 bar for rinsing, or 2–12 bar for vial pressurization with (external) N_2 or He	−5 to +25 psi (≈ 1.8 bar) for injection, –5 to +100 psi (≈ 7 bar) for rinsing or vial pressurization	−180 to 250 mbar for injection, up to 2.5 bar by DCI [g] or 10 bar with external N_2 or He pressurization for rinsing or vial pressurization
Voltage range	±30 kV	±30 kV	±30 kV
Current range	±300 μA	±300 μA	±200 μA
Thermostatting of capillary at 25°C	forced air convection (15–60°C)	recirculating liquid cooling (15–60°C)	forced air convection (20–60°C)
Sample/buffer tray	48-position carousel for samples, buffer vials and buffer replenishment	sample tray: 2 × 96 well plates or 2 × 48 vial plates, buffer tray: 2 × 36 vial plates or (2 × 2) 25 mL vial plates	carousel with 30–48 positions for sample and buffer vials
Fraction collection	possible	no information available	no information available
Sample thermostatting	10–40°C	5–60°C	4–40°C
Capillary lengths	L_{eff} (bed) down to 24.5 cm [a] and L_{total} down to 33.0 cm	L_{eff}: 21–100 cm [d] and L_{total}: 31.2–110 cm	no information available
Capillary and window geometries	restricted due to the hollow electrodes and the alignment interface for UV detection [b]	restricted due to the liquid cooling system and aperture device [e]	relatively free due to the flexible design of the forced air cooling and external detection
Available integrated detectors	UV/VIS-PDA, fluorescence and LIF [c] as well as several Agilent MS systems	UV/VIS with several wavelengths, UV/VIS-PDA, LIF and Finnigan[f] LCQ_{DUO}-MS system	variety of detectors from different manufacturers (more or less integratable)

[a] $L_{eff} \approx 8.5$ cm for short-end injection. [b] Different interfaces and the hollow electrodes allow installation of 365 μm OD capillaries with different ID; bubble cells can also be installed and a special Z-shaped sensitivity detection cell is available. [c] Fluorescence detector, e.g., from Flux Instruments (Basel, Switzerland; http://www.flux.ch) and LIF detector from Picometrics (Ramonville, France; http://www.picometrics.com). [d] $L_{eff} \approx 10$ cm for short-end injection. [e] Aperture and the coolant fittings allow installation of 365 μm OD capillaries with different ID and also bubble cells. The 4 mm ID tubing for liquid cooling restricts the use of (high-pressure) unions for coupling of capillaries. [f] Thermo Finnigan, San Jose, CA (http://www.thermofinnigan.com). [g] DCI: (patented) Dynamic Compression Injection.

i) conventional reciprocating piston pump systems reconfigured for this flow rate range by requiring (in most cases) a flow splitter,

ii) the use of a syringe pump system which directly produces nanoliter flow rates without needing flow splitting, and

iii) electrokinetic pumping by an intersegmental pressure that develops as a consequence of nonuniform electroosmosis in a segmented setup.

2.1 Agilent [59] 1100 series (μ/c)HPLC

This system belongs to the first category which relies on a flow splitter. It has been developed on a modular basis and can run HPLC columns of 0.18–2 mm ID with similar functionality, performance characteristics, robustness, and ruggedness as the established 1100 series (designed for analytical and semi-prep scale). The operational optimum of this capillary system covers columns with ID between 0.3 and 1.0 mm and a flow rate range of

Table 4. Commercial (μ/c)HPLC/CEC/pCEC instruments.

Specifications	Unimicro Tri-Sep™ 2000GV	Micro-Tech Ultra-Plus II™	ProLab Evolution 200
Hydraulic system	two PU-1580 μHPLC pumps	binary gradient pump with reciprocating single pistons	double-piston pumps for binary high pressure gradients [h]
Settable flow rates	1 μL/min to 10 mL/min [a], lower flow rates only by splitting [b]	5–300 μL/min without split, splited down to 10 nL/min [e]	isocratic: 0.02–200 μL/min (no split) gradient: 1–200 μL/min (no split) [i]
Gradient generation	binary back-pressure regulated pre-split mixing [c]	binary two-stage dynamic high-pressure pre-split mixing [f]	high-pressure passive mixing inside a mixing tee
Delay volumes	no information available	mixer: 1, 20, 80 or 400 μL	no information available
Pressure range	up to 1000 psi (≈ 70 bar)[d]	up to 10000 psi (≈ 700 bar)	up to 400 bar
Degasser	no information available	two bottles helium sparkled	4-channel vacuum degasser
Available integrated detectors	UV/Vis, variable or fixed wavelength	electrochemical or UV/VIS (variable wavelength)	variety of detectors from different manufacturers, more or less integratable
UV flow cells	capillary flow cell for on-line detection	250 nL cell or an on-capillary column flow cell	depending on detector manufacturer
Operation modes	(μ/c)HPLC, (p)CEC, CE in isocratic and gradient mode	(μ/c)HPLC, (p)CEC, CE in isocratic and gradient mode	(μ/c)HPLC and (p)CEC in isocratic and gradient mode
Injection modes	pressure, no more information	pressure, no more information	pressure and electrokintetics
Injection device	10 and 20 nL injection valves	autosampler (>100 nL) or injection valve (low nanoliter range)	autosampler in combination with a 7-port valve
Voltage range	±30 kV	0–60 kV [g]	±30 kV
Current range	no information available	no information available	±200 μA
Column thermostatting	not implemented	column oven for cHPLC, cooling for (p)CEC; no further information available	dry, Peltier-thermostatted forced air
Sample thermostatting	not implemented	not implemented	possible
Column lengths	no information available	no information available	up to 50 cm
Capillary and window geometries	relatively free due to the flexible design	relatively free due to the flexible design	quite free due to flexible injector position, forced air cooling, external detection

[a] Isocratically; limits for gradient elution not available. [b] Non-controlled flow splitter. [c] Compare Figure 10.b. [d] Limited by the back-pressure regulator. [e] Isocratic split rate is non-controlled; limits for gradient elution not available. [f] This dual-chamber dynamic mixing system allows to adjust the mixer volume to the flow rate. [g] No polarity switching possible. [h] Includes four high-pressure linear drives, electric pump-head selector valves (patent pending) with pressure-compensation channel and software tool for pulsation suppression and syringe pump mode. [i] Additional splitting is possible, but limits for split gradient elution were not available.

1–100 μL/min. In this range the flow rate is electronically controlled and regulated (**Figure 1.a**). As shown in **Figure 1.b** flow control is achieved by an electromagnetic purge valve (EMPV) that splits solvent delivered by the pump in a controlled manner. This valve has one outlet (waste) with an adjustable flow restrictor and a second

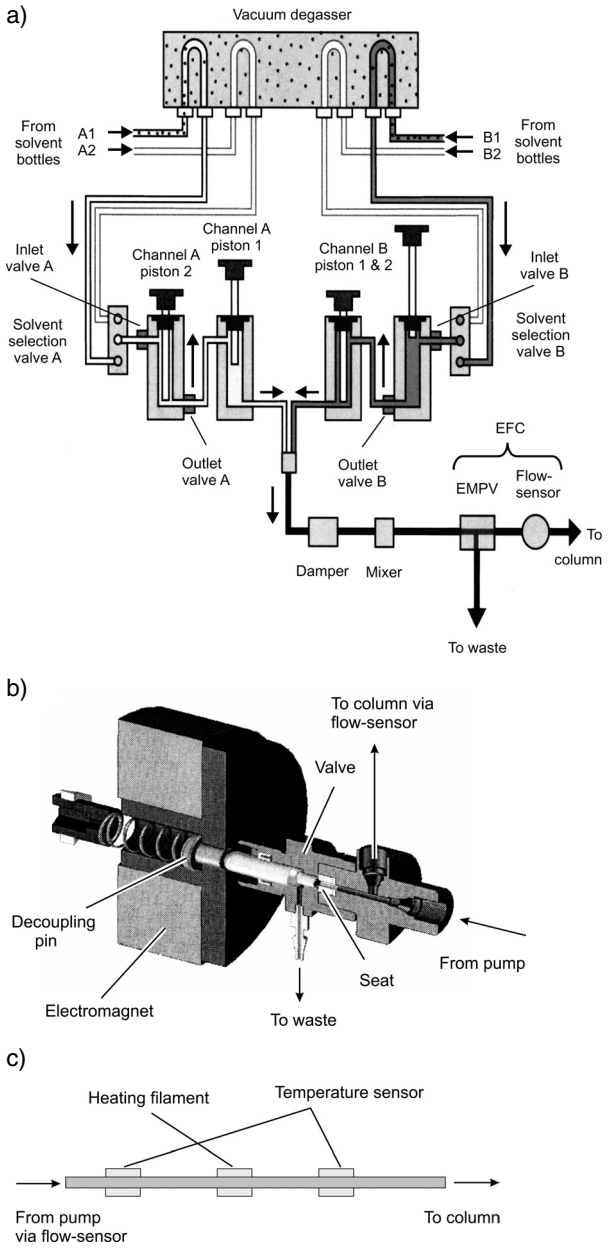

Figure 1. a) Illustration of the Agilent 1100 series (μ/c)HPLC system incorporating electronic flow control (EFC). Cycle of pumping procedure: Outlet valve A is closed, channel A (piston 1) pushes the fluid towards the column, while piston 2 refills with fluid from the degasser via the opened inlet valve A. After the refill of channel A (piston 2) the inlet valve A closes because piston 2 now compresses the fluid inside the cylinder until system pressure is reached. This opens outlet valve A, fluid is pushed towards the column via the (now refilling) piston 1, afterwards the cycle starts again. The same procedure applies to channel B. b) Electromagnetic purge valve (EMPV) regulating the split rate to the waste after feedback with the thermal flow sensor. c) Thermal flow sensor based on mass-flow measurement which has to be calibrated for each solvent pairing using software-implemented calibration data for most common solvents and mixtures. (All figures adapted with permission from Agilent Technologies.)

outlet comprising the micro-flow path containing a flow sensor that measures the flow rate (**Figure 1.c**). A feedback control loop regulates the flow resistance in the waste outlet to maintain a constant flow rate from 1–100 μL/min (down to 10 nL/min is, in principle, possible in isocratic mode, but is not recommended by the manufacturer). Both devices together constitute the electronic flow control (EFC). In this (regulated) range the flow rate is independent of column back-pressure up to 400 bar (cf. Table 2), which is the biggest advantage compared to the passive split-flow arrangements realized, for example, in the LC Packings system (see below). If the flow rate decreases because of an increase in column back-pressure it will be counteracted by increasing flow resistance in the split waste path. Thus, the capillary pump will be insensitive to pressure variations induced by changes in mobile phase composition (as in gradient elution) or by a gradually plugging column, demonstrated in **Figure 2**. A disadvantage of this system is that flow rates below 1 μL/min (which, in principle, can be regulated in a controlled manner) are not recommended by the manufacturer as they exceed the calibrated range and reasonable volume ratios, i.e., of the split-flow to system and detection-cell volume. But precisely those flow rates from 1000 down to 20 nL/min are relevant for capillary columns with an ID smaller than 150 μm and for the on-line coupling of nano-ESI-MS to HPLC. Another problem at lower flow rates is the relatively large UV-detection cell with a volume of 500 nL and a 10 mm path length, contributing measurably to extra-column dispersion below 5 μL/min.

2.2 LC Packings [60] UltiMate™ (μ/c/nano)HPLC

This system is also a reciprocating pump with proprietary micro-flow processing based on flow splitting, but without electronic split control and regulation. Flow rates for different column geometries and packings are realized by an automatic pump flow adjustment and predefined split ratio selected with different calibrator cartridges. The system is able to maintain flow rates from 200 μL/min (optionally 1 mL/min) down to 50 nL/min, even for solvent gradients generated with a quaternary low-pressure gradient former. If the flow path does not become plugged, this system works reproducibly also for gradient elution, but the split ratio changes over a single run due to mobile phase viscosity changes. Thus, the flow rate also changes in gradient elution, but can be reproducible from run to run. Unlike the Agilent system the LC Packings system can generate solvent gradients at flow rates below 1 μL/min and handle capillary and nano-HPLC columns in isocratic and gradient mode. Further, LC Packings offers a variety of UV-detection cells for their UltiMate™ (nano/μ/c)HPLC System reaching from 180 nL down to 3 nL cell volume.

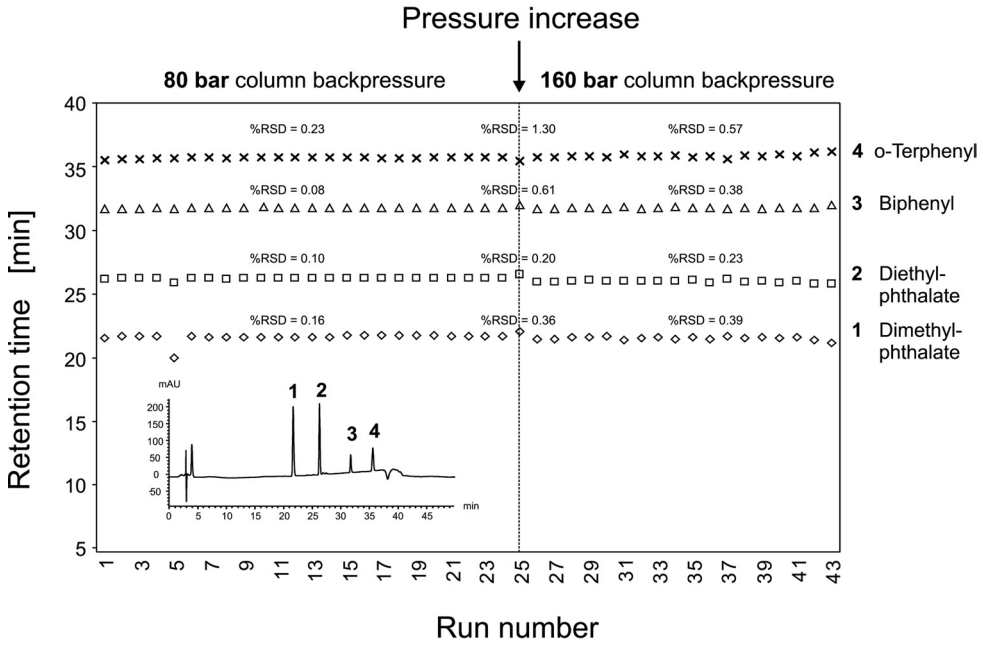

Figure 2. Flow rate precision during repetitive injection at different column back-pressures. Column: Hypersil ODS (Thermo Hypersil Ltd., Runcorn Cheshire, U.K.), 5 μm particles, 150 × 0.3 mm, flow rate: 4 μL/min, solvent: water/acetonitrile, gradient: 5–85% acetonitrile, injection volume: 0.1 μL, temperature: 25°C, detection wavelength: 250 nm. The column back-pressure increased from 80 to 160 bar after run 24. (Adapted with permission from Agilent Technologies.)

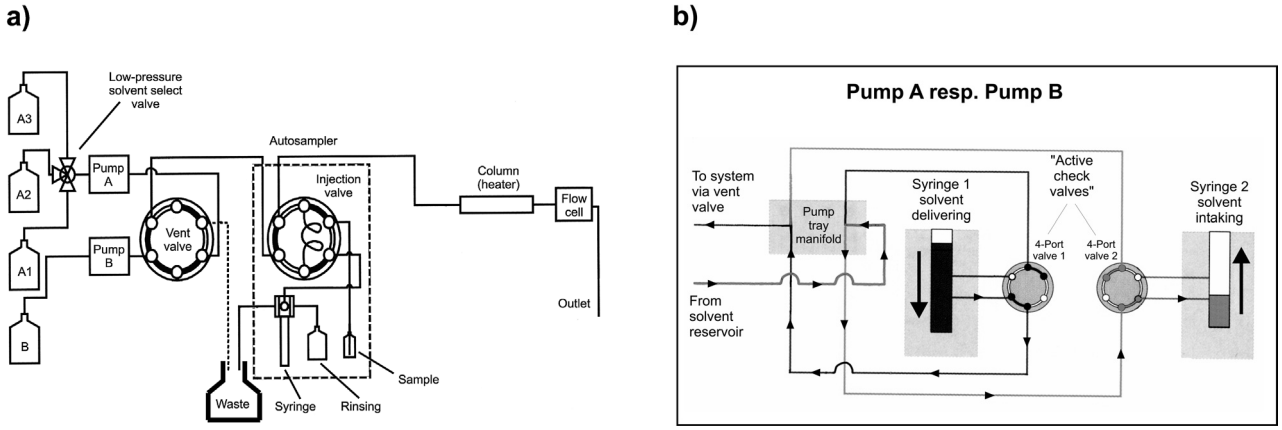

Figure 3. a) CapLC™ system configured for the generation of binary gradients. Each solvent has an individual, binary, continuous-flow, positive-displacement pump (pump A, respectively pump B) delivering pulse-free gradient flow in the 1–40 μL/min range and isocratic flow down to 250 nL/min. b) Binary, continuous-flow, positive-displacement pump (CFPD): Each pump tray (pump A and B, optionally C) has two syringe pumps, each with a pressure transducer and an active check valve, i.e., a 4-port valve. While syringe 1 is delivering, syringe 2 is refilling. When syringe 1 is almost empty, syringe 2 compresses its liquid to system pressure with an intermediate "dead-end position" of its 4-port valve. Then, the 4-port valve 1 opens toward the low pressure side (refilling), the 4-port valve 2 switches to the high-pressure side and eluent flow continues at system pressure. Syringe 1 refills and the cycle repeats. (Adapted with permission from Waters Corporation.)

2.3 Waters [61] CapLC™ (μ/c)HPLC

This system is based on a patented syringe-style, positive displacement, continuous delivery design (**Figure 3**). It can be used to run isocratic (down to 250 nL/min) and gradient separations from 1–40 μL/min. Each syringe is motor-driven and software-controlled so that crossover-related flow phenomena are eliminated. Gradients are mixed under high pressure and the overall system volume is below 20 μL (according to the manufacturer). Syringe

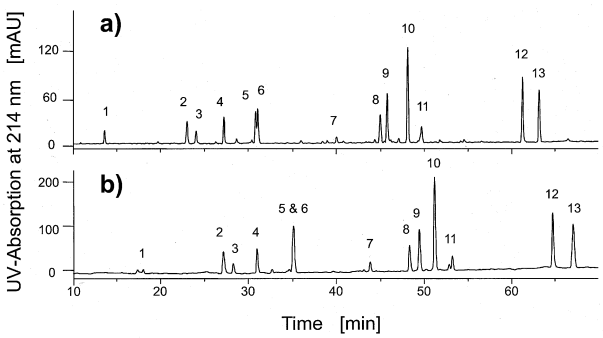

Figure 4. Separation of a cytochrome C tryptic digest, comparison of cHPLC results with those of analytical HPLC. a) Analytical system: Waters Alliance™ (Symmetry™C_{18} column: 3.9 mm ID, 5 μm particles with 100 Å pores, flow rate: 800 μL/min, 810 pmol sample). b) Capillary system: Waters CapLC™ (Symmetry™C_{18} column: 320 μm ID, 5 μm particles with 100 Å pores, flow rate: 5 μL/min, 20 pmol sample). Joint conditions: Mobile phase 0–40% B in 80 min (A = 0.1% TFA in H_2O, B = 0.085% TFA in acetonitrile), UV detection at 214 nm. (Adapted with permission from Waters Corporation.)

pumps are self-priming and self-purging. A high-pressure switching valve permits running of binary (as seen in Figure 3) and optionally ternary gradients, as well as on-column pre-concentration and post-column solvent delivery. Similarly to the Agilent system, the Waters system includes only a relatively large 250 nL UV-detection cell volume with a 5 mm path length. **Figure 4** demonstrates that the actual performance achieved with the CapLC™ system can be comparable to that of an analytical HPLC system. Both chromatograms show the same separation (with the same sample, column chemistry, and programmed gradient), only scaling down the flow rate to the same linear velocity and the sample load to column volume. With fourty times less sample, the CapLC™ system generates a two times greater peak height response, yielding an 80-fold enhancement in mass sensitivity. (Because the optical path length for the analytical system is 10 mm, while it is only 5 mm for the capillary flow cell, this enhancement factor is correspondingly smaller than the expected 149 for the case of identical path lengths.) In general, however, and as also indicated by the chromatograms in Figure 4, the significance of gradient mixing and transfer volumes (relevant for the delay and steepness of the gradient) and detector dead volume (engendering additional dispersion) should not be underestimated.

2.4 Eldex [62] MicroPro (μ/c)HPLC pumping system

This is a modular syringe-based system that allows practicable flow rates from 200 μL/min (10 mL/min possible) down to 10 nL/min in isocratic and, down to 1 μL/min, in gradient elution mode without split. Mixing is provided by a (85 μL or 15 μL) dynamic mixer or, for the lower microliter flow rates, by (≦ 5 μL) static mixers. A single MicroPro™ pump can interact with up to three other MicroPro™ pumps, offering the possibility of generating quaternary gradients or of using the syringes in reciprocating mode (i.e., one syringe delivers while another one is refilling). The fully integrated system provides stable flow without pressure pulsation, thereby increasing the UV-detector sensitivity by decreased baseline noise. Syringe plungers are displaced by software-controlled micro-stepper motors (0.1 nL/step) and are fitted to a pressure transducer for high flow rate and gradient reproducibility. The MicroPro™ can be programmed for positive and negative flow rates, constant pressure, as well as constant flow mode and for the generation of pressure gradients. These pressure gradients are mainly used for rapid automatic, software-controlled pressure ramps necessary for fast, reproducible column pre-pressurization between two separations or after syringe refill. The complete pumping system (including syringes, transfer lines, and solvent mixer) is thermostatted to suppress temperature fluctuations which can significantly affect the flow stability, especially at low flow rates. Due to free access to this modular setup, it is (relatively) easy to configure the system for specific needs without loosing software control. For example, mixer and transfer lines can be replaced by smaller devices for the minimization of gradient volume and delay at lower microliter flow rates.

2.5 Electrokinetic pump technology

For miniaturization in LC, basic instrumental requirements have remained essentially unchanged over the years, especially concerning the high pressure pumping devices which are either reciprocating piston or syringe pumps. However, these pump systems besides mixers, valves and detectors, appear to be of enormous size compared to nano-scale (or even on-chip) separations. A size match seems to be difficult (if not impossible) due to the fact that individual components of the pumping device have to be fabricated separately and then assembled manually. An approach that seems to overcome this limitation relies on the design of a high-pressure electrokinetic pump (EKP) [63–65]. This can utilize conventional fused-silica capillaries arranged in a segmented configuration, where each capillary segment contains porous material, but for a different purpose. The EKP segment itself is packed with a high surface area material showing a stable and substantial surface charge density under operating conditions. Two electrodes are immersed in the electrolyte at the ends of this segment and an applied electric field generates EOF through the medium. As a consequence pressure is developed at the outlet until (pressure-driven) back-flow through this segment matches the EOF. The

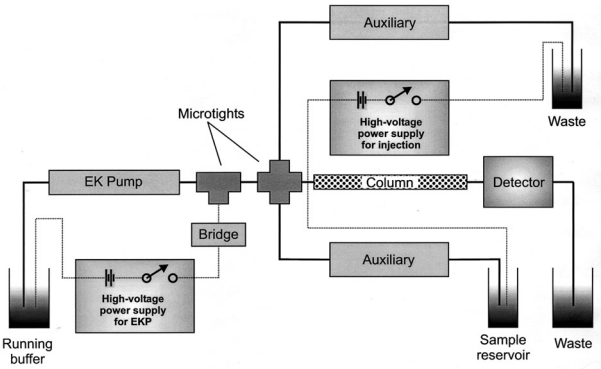

Figure 5. Schematics of an isocratic EKP (μ/c/nano)HPLC system. The heart of the high-pressure electrokinetic SmartFlow™ system from Eksigent is the EKP segment producing high-pressures by EOF. It is connected to the electrodes of a high-voltage power supply via running buffer vial and a bridge. This bridge (borosilicate glass with 4 nm pore size – small enough to suppress EOF and pressure-induced flow) acting as a ionic conductor enables to separate the electrodes from the primary flow stream. The EKP segment and auxiliary elements are packed with 1.5 μm non-porous silica spheres having a non-retentive surface optimized for EOF, giving interparticle pores sufficiently small to suppress hydrostatic flow, but still large enough to generate a substantial EOF. The separation segment is packed with 3 μm porous C_{18} silica particles for achieving a higher hydraulic permeability and chromatographic suitability. Sample injection is supported electrokinetically by applying a potential difference across the auxiliary sections.

ratio of maximum pressure to applied voltage depends on inherent properties of the porous medium (like surface-to-volume ratio, surface roughness, charge density) and the working electrolyte solution (viscosity, permittivity, salt concentration, pH). A second, connected, packed capillary segment then contains porous material for the separation. Liquid is driven through this segment by the pressure gradient that develops at its ends. Consequently, the separation segment needs an adjusted hydraulic permeability and surface (area) optimized for chromatography, while for the EKP segment its electroosmotic permeability is important. The EKP contains no moving parts and controls pressure-driven flow (in the mL to nL/min flow rate range) through the separation segment by EOF generated in the EKP segment, thus, by an easily controllable gradient in electric potential. Based on this approach the Eksigent company [66] was founded in May 2000, commercialising the (in the meantime patented) EKP as the Eksigent Smart Flow™ HPLC system (schematically shown in **Figure 5**). This technology allows generation of pressures in excess of 10000 psi (≈ 700 bar) without flow pulsation [63, 64]. Because the pumping unit is a porous medium, devices can be realized in a variety of geometries. Eksigent's development in EKP materials and design enabled 10 psi/volt to be exceeded in high-pressure devices and flow rates of 5 mL/min in low-pressure (ca. 150 psi) devices. **Figure 6** demonstrates how the Eksigent Smart Flow™ HPLC system (in a dual configuration) can repeatedly run steep water/acetonitrile solvent gradients allowing, for example, the reproducible gradient separation of angiotensin peptides [66].

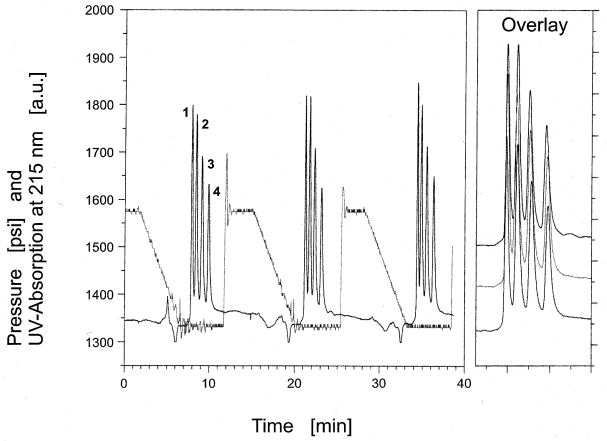

Figure 6. Solvent gradients generated by water/acetonitrile pressure-gradients (at constant overall system pressure) with a dual setup of the electrokinetic SmartFlow™ pump can be run repeatedly with reset times less than one minute. Example: Gradient separation of angiotensin peptides (**1:** [Ile^7] Angiotensin III, **2:** [Val^4] Angiotensin III, **3:** Angiotensin III, **4:** Angiotensin I) and monitored pressure plot for water representing the water/acetonitrile gradient. Run-to-run reproducibility is demonstrated by the overlay. (Adapted with permission from Eksigent Technologies.)

The (μ/c)HPLC systems offered by Micro-Tech [67] and ProLab [68] are considered later in Section 4.2 because, in addition to configurations presented so far, they allow application of electric fields on a modular basis.

3 Commercial CE instruments adapted for CEC

Commercial instruments originally developed for CE are not ideally suited for CEC. Especially the first generations of these systems had several disadvantages. Unlike in CE, bubble formation is a practical problem in CEC. Along with noisy baselines and spikes, bubbles can even cause a breakdown of electrical current and, consequently, of the EOF [69–72]. This was a problem when adapting the first generations of commercial CE instruments for CEC because they usually had no feature for pressurizing capillary ends to avoid bubble formation. Thus, CE systems had to be modified along these lines, as was reported, e.g., by Smith and Evans [71, 73] or Boughtflower et al. [70], and later described in more detail by Smith and Carter-Finch [74]. They used modified CE intruments from ABI [75] and Prince [76] enabling the application of up to 35 bar to inlet and outlet buffer vials. The latest generation of commercial CE instruments now

allows application of pressure (He, N_2, or air) to the inlet and/or outlet vial, but only up to 7–12 bars (depending on the manufacturer, cf. Table 3). While this may be sufficient to prevent bubble formation, it is definitely not enough for a hydrodynamic conditioning of packed capillaries or, if the accompanying pressure drop is not too high (as may be expected for relatively permeable monoliths), for conditioning in a reasonable time. Further, nearly all CE instruments of the first generation only allowed in-built on-capillary UV detection. Coupling to other detection devices such as PDA, RI, EC, LIF, or even the hyphenation with MS and NMR was originally not intended. However, due to the growing interest additional in-built detectors and upgrade kits became available for later versions. Another problem with CE instruments is the lack of flexibility in performing continuous solvent gradients. The only possibility for an unmodified commercial CE instrument (for interesting modifications undertaken with the HP^{3D}CE system see Section 4.2) is to perform step-gradients where the mobile phase composition is varied by first stopping the applied voltage in order to change the inlet vial to another one with a different elution strength, followed by a continued application of voltage [77–79]. A problem besetting most commercial CE instruments lies in restrictions concerning column geometry and configuration, especially with Beckmann Coulter [80] systems which, in this case, is mainly due to the small dimensions of the liquid capillary-cooling system. The outer diameter of the capillary, its length, and the position and geometry of the detection window can only be chosen within certain limits. However, modern CE instruments are fully integrated systems which permit automation. They show a sufficient run-to-run reproducibility concerning injection volumes or retention times, and they allow parallel acquisition of data (multiple detector signals, voltage, current, temperature) and effective control of column temperature by either air or liquid cooling, depending on the manufacturer (cf. Table 3). Thus, today, for the most part, CEC (can be and) is carried out by using commercial instrumentation originally designed for CE. In this review we consider only the latest generation of these devices as they offer the mentioned advantages.

4 Instruments specifically designed for CEC

In order to better utilize the inherent potential of CEC it is necessary to employ instrumentation with gradient elution capability for improving peak capacity, to speed up the separation via zone compression, but particularly for solving problems too complex for standard isocratic elution. Besides temperature [25] and voltage [81] gradients (which can already be run with commercial CE systems) the most powerful elution gradient is the continuous mobile phase gradient well known from HPLC. Here, we focus on pressurizable gradient systems performing separations in chromatographic beds because of the above-mentioned reasons and a several dimensions higher loadability of these media compared to open-tubular or isocratic systems (an important factor for the microscale).

4.1 Home-built instruments for (p)CEC

The need for gradient elution, together with an opportunity to perform cHPLC, CEC, pCEC (and even CE), inspired several CEC-pioneering groups to construct and use instruments despite their lack of user-friendliness and automation. Nevertheless, some of these configurations were highly flexible for solvent delivery, injection by pressure or electrokinetics, column dimensions, design, and geometry. They also show compatibility with a wide variety of detectors and are well suited for hyphenation with NMR and especially MS. Because home-built instrumentation for CEC has been repeatedly reviewed recently [82–84], in this work we are concerned only with the most practicable and innovative configurations.

4.1.1 Subjective selection of home-built instruments for (p)CEC

To provide a useful classification of the numerous configurations we divide them into pre-split and post-split injection systems.

4.1.1.1 Pressurizable gradient cHPLC/(p)CEC systems with pre-split injection

The pre-split injection design schematically shown in **Figure 7.a** is quite suitable for building up systems with an (optional) automation of sample injection and it shows a high stability regarding EOF. Due to the spatial separation of individual components in this arrangement including gradient pump, injection device and splitter, and due to the tolerance of larger injection volumes by the post-injection split, it is straightforward to install an autosampler for running sequences. Concerning band broadening, a delay volume between split and column inlet, and dead volume between column outlet and detector has to be minimized. The pre-split injection setup also causes problems: First, the column flow rate and consequently the injected sample volume and sample amount can only be examined by determining the actual split ratio. Measuring flow rate changes in the lower micro- or even nanoliter range caused by changing solvent viscosities (gradients) or by a partial column clogging is time-consuming and laborious. Secondly, if the split ratio changes so does the flow velocity. Thus, the run-to-run reproducibility can deteriorate, especially in the presence of an ongoing column clogging. But this is a problem for all types of non-controlled and unregulated flows. Still, however, the biggest disadvan-

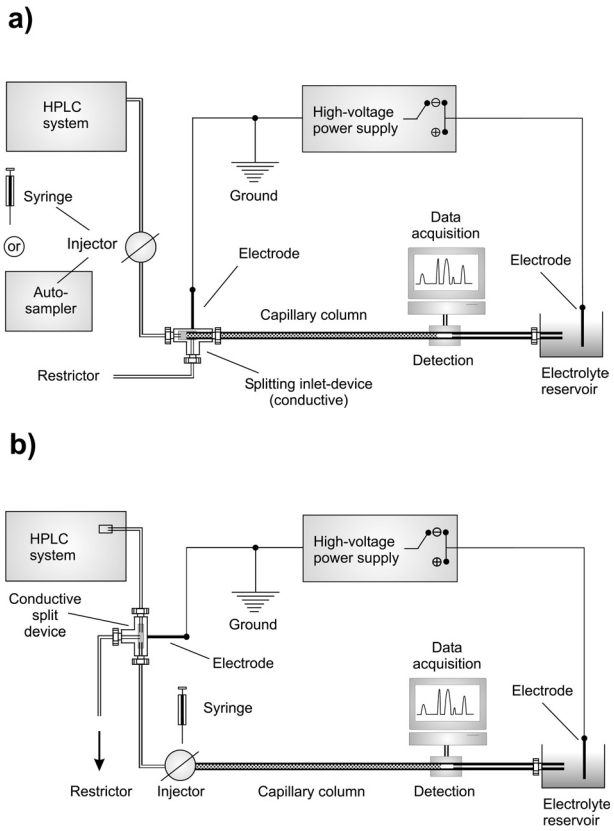

Figure 7. a) Pressurizable gradient (μ/c)HPLC/(p)CEC system with pre-split injection mode. b) Pressurizable gradient (μ/c)HPLC/(p)CEC system with post-split injection mode.

tage of this setup is the tremendous waste of sample by the split, a severe problem for sample-limited applications.

The pre-split injection design was first presented 1994 by Behnke and Bayer [85], then by Eimer et al. [86], and was further developed by Huber et al. [87], Kitagawa et al. [88], and Zhang et al. [89]. Later, optimized setups, e.g., with autosampler, minimized dead volume, in-line filters to prevent clogging, and outlet restrictor capillary to prevent bubble-formation were presented by Taylor et al. [90, 91] (similar to the Unimicro [92] starter kit configuration shown in Figure 10.b), Behnke and Metzger [93], Strickmann et al. [94], and Alexander et al. [95]. Nearly all publications demonstrated the importance of an optimized design of the capillary column inlet device which is schematically shown in Figure 7.a. The interface should be resistant to high pressure and high voltage, show a low dead volume, and include one of the two electrodes, a flow-restricting split, a connection for the transfer line from the pump (respectively injector), and a connection for the column inlet. Geometry should be optimized such that solvent and sample pass the capillary inlet coaxially and mainly leave the interface through the split. Due to this arrangement the peak tailing and broadening caused by the injection can be minimized. Further, bubbles formed at the electrode due to high voltage are immediately removed from the system by the coaxial pump flow and cannot reach the column inlet. What may happen if this interface is not optimized with respect to the aspects listed above has been shown by Lister et al. [96]. Low-pressure solvent gradients were generated with a μHPLC system which was connected to the CEC column via a flow-injection analysis (FIA) interface. After having compared the performance of their instrumental setup with that of a standard one the authors found an increase in asymmetry (tailing) of about 70% and an increased peak width by a factor of 2.5. The authors report a dwell volume of ca. 250 μL, an injection loop volume of 10 μL, and suspected turbulent flow causing sample dilution inside the FIA interface.

4.1.1.2 Pressurizable gradient cHPLC/(p)CEC systems with post-split injection

Because this setup (**Figure 7.b**), as compared to pre-split injection, contains the injection device and split in reversed order, dead volume between split, injector, and column inlet has to be minimized. It is not simple to install an autosampler for running sequences because of the inherent size (e. g. injection needle, sample loop, transfer lines) and resulting delays. The problems associated with the split (changes in split ratio), the determination of column flow rate, and amount of injected sample are the same as mentioned for pre-split injection. Flow velocity can change for the same reasons, but compared to the pre-split injection design, waste of sample is minimized. This is an advantage for sample-limited applications, but presents a problem for automation because autosamplers with an overall dead volume in the lower microliter or (even better) nanoliter range are not available. A first step in this direction can be made with mirco- or nano-injection valves supplied by VICI [97], Rheodyne [98], or Upchurch [99]. The post-split injection design was first presented in 1991 by Verheij et al. [100], followed by Tsuda [101], Behnke et al. [102], and was recently re-examined by Anderson and Bloomberg [103] and Sander et al. [104]. However, gradient elution has been demonstrated in only two of these articles [100, 104].

4.1.2 Hardware aspects of home-built instruments

4.1.2.1 Splitless isocratic cHPLC/(p)CEC system

Guo et al. [105] describe a splitless cHPLC/(p)CEC system schematically shown in **Figure 8.a**. An ISCO [106] Model 3850 capillary electropherograph was used for CEC operation and a Valco 20 nL injector for sample injection. In some of their experiments, smaller injections were achieved by switching the injection valve back to "load" after a certain time interval (typically 5 s, corre-

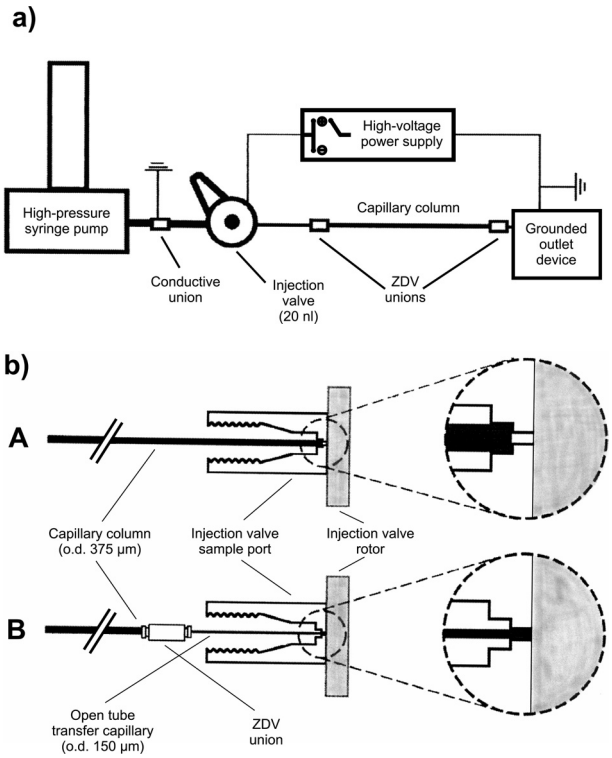

Figure 8. a) Splitless isocratic cHPLC/(p)CEC system. Due to the grounded outlet device the connection between pump and high-voltage inlet has to be grounded somewhere (e.g., with a conductive union) to protect the syringe pump from being damaged by high voltage. The grounded outlet device can be a buffer vial, a nucleation light-scattering detection system, a (nano-)ESI interface to the MS, or a grounded union for the transfer capillary to an NMR spectrometer. b) Different connections to the sample port. (Figures adapted with permission from [105]. Copyright (1999) Elsevier Science.)

sponding to a 5 nL injection at 1200 psi). A high-pressure syringe pump (Model 100 DM from ISCO) was used to provide supplementary flow to the CEC column. The high voltage for CEC operation was applied to the injector after the injection. A stainless steel union placed in the transfer line from pump to injector was grounded to protect the pump from possible damage caused by high voltage (as current can also flow back through the solution from the high voltage end of the CEC power supply to the pump). Two 10 cm open-tube segments (25 µm ID, 150 µm OD fused-silica) were connected to the inlet and outlet of the CEC column with two identical Upchurch microtight zero dead volume (ZDV) unions. The syringe pump was operated in isocratic constant-pressure mode. An initial attempt to employ the injection valve via direct connection of the separation column resulted in broad, but basically symmetrical peaks. This led the authors to suspect dead volume acting as a mixing chamber just in front of the column inlet. In fact, they observed a void volume in the sample port of the injection valve. The smallest ID of the sample port was 180–200 µm so that the column (375 µm OD) could not reach through the port to approach the rotor (Scheme A in **Figure 8.b**). The dead volume between column inlet and the rotor surface has been reduced by the mentioned 10 cm long, 150 µm OD fused-silica segment which comes so close as to almost touch the rotor (Scheme B in Figure 8.b). The authors compared chromatograms obtained with and without this minimization of dead volume and found that peak areas in both cases were at comparable level. However, a (two times) better sensitivity and (four times) increased separation efficiency were obtained with the smaller OD of the capillary.

4.1.2.2 Elektrokinetically generated eluent gradient CEC system

Yan et al. [107, 108] developed a setup for gradient CEC (**Figure 9**) without any need for HPLC devices to form the gradient. An electrokinetically generated gradient is achieved by coupling the inlet of the capillary column (via a T-piece) to two independent, voltage-controlled solvent delivery capillary channels, each ending in a vial with different mobile phase and a high-voltage electrode. The outlet of the capillary column ends in a reservoir containing the grounded electrode. By utilizing two high-voltage power supplies, one connected to each inlet vial, and applying voltage at various (computer-controlled) rates, the mobile phase gradient can be mixed by the ratio of EOF rates between the two delivery channels. Shortcomings of this approach are the need to disconnect the column from the mixing tee prior to each sample injection and the difficult control of the exact mobile phase composition as it enters the column. Further, it has to be recognized that EOF changes with the composition of the mobile

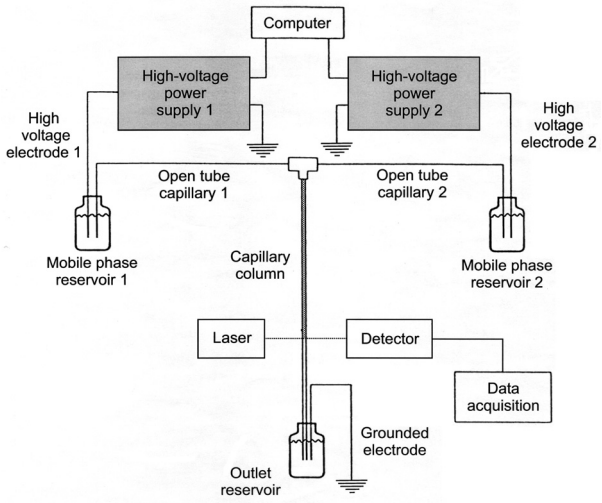

Figure 9. Outline of a CEC system using electrokinetically generated solvent gradients. (Adapted with permission from [107]. Copyright (1996) American Chemical Society.)

phase as the zeta potential sensitively depends on its ionic strength, viscosity, pH, and dielectric constant.

4.1.2.3 Ultrahigh-voltage capillary electrophoresis system

Here, we address the significant problems and hardware requirements arising when operating at voltages far above 30 kV. Although demonstrated for open tube appplications these considerations are also relevant for packed bed operation (in view of, e.g., frit stability and bubble formation, or pressure-assisted CEC which exerts additional stress on the capillary wall). Hutterer and Jorgenson [109] reported an ultrahigh-voltage CE system based on a commercial 30 kV power supply, extensively modified in order to provide electric potentials up to 120 kV. To prevent capillary breakdown and corona or spark discharges they developed an electric shield system. Their electrophoretic studies with peptides showed that the number of theoretical plates increased linearly with the applied voltage (up to 6.1 million plates at 120 kV). The resolution increased with the square root of the applied voltage, as predicted by theory. However, a routine use of potentials far beyond 30 kV becomes difficult owing to the possible electrical breakdown of the fused-silica wall, as well as to an increased risk of electric discharge and shock. By applying a potential difference across the capillary, electric fields are induced both axially (along the capillary axis) and radially (through the capillary walls). An appropriate choice of capillary length, inner diameter, and electrolyte conductivity can reduce problems associated with the heat dissipation in the capillary. The radial electric field strength increases from the grounded end of the capillary to the high-potential end and is responsible for stress on the fused-silica wall and its eventual dielectric breakdown.

4.2 Commercial instruments for (μ/c)HPLC, CEC, and pCEC

4.2.1 The Unimicro [92] TriSep™ 2000GV

This instrument from Unimicro combines (μ/c)HPLC, (p)CEC, and CE. It enables operation with high voltages and pressure at the same time. The instrument even allows gradient pCEC to be run with orthogonal (chromatographic and electrophoretic) selectivity. Ru et al. [110] used it to manipulate the selectivities (by solvent and voltage gradients) in a separation of 18 amino acids (**Figure 10.a**). Besides different types of TriSep™ instruments (for further technical information see Table 4), Unimicro offers a CEC Starter™ which includes micro-filters, mixer, micro-splitter, back-pressure regulator, micro-injector, high-voltage power supply, and restrictor (schematically shown in **Figure 10.b**), and a complete upgrade kit including the starter kit, UV/Vis-detector, and data system to

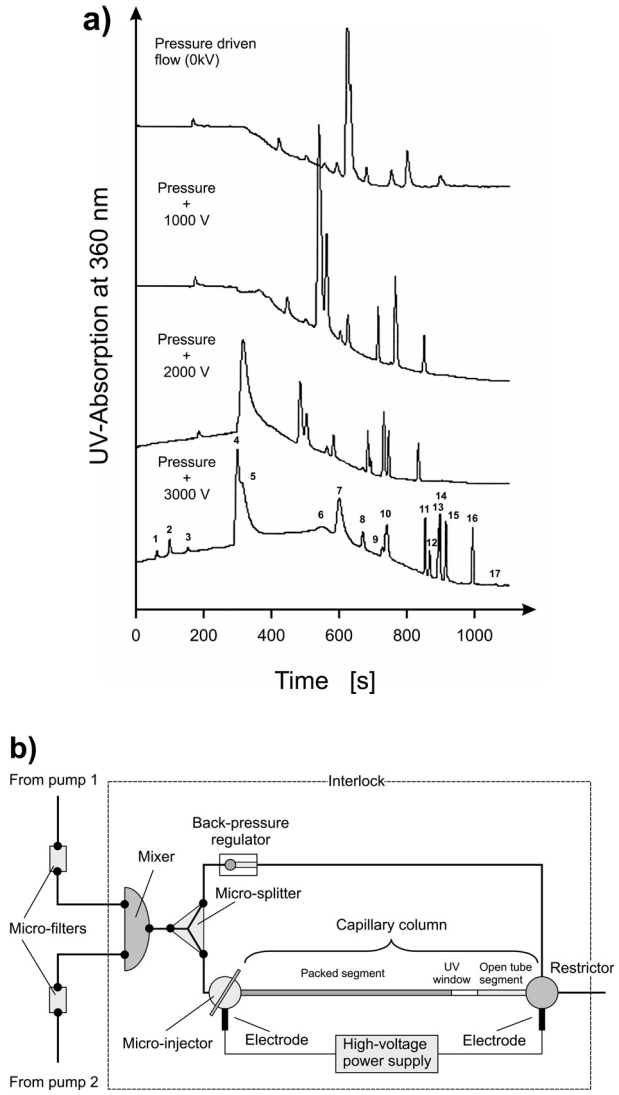

Figure 10. a) Effect of voltage on the chromatograms of a (18 amino acids) standard separated by gradient nano-HPLC and pCEC. The sensitivity, resolution, and number of detected amino acid peaks increases with the applied voltage. Further, the order of the peaks changes. Column: PS-C_{18} (3 μm), 130 mm × 75 μm ID, injection volume: 20 nL. **1:** aspartate, **2:** glutamate, **3:** tyrosine, **4:** derivate, **5:** serine, **6:** tryptophan, **7:** glycine, **8:** threonine, **9:** proline, **10:** alanine, **11:** valine, **12:** methionine, **13:** isoleucine, **14:** leucine, **15:** phenylalanine, **16:** lysine, **17:** arginine. (Adapted with permission from [110]. Copyright (2000) Elsevier Science.).
b) Schematics of the CEC Starter™ which is also implemented in the TriSep™ instruments. It includes i) micro-filters to prevent a plugging of the splitter, column and back-pressure regulator, ii) static mixer, iii) micro-splitter that divides the flow coming from the mixer into two lines, one going to the injector and the other directly going towards the restrictor, by-passing the capillary column, iv) back-pressure regulator (ca. 3–70 bar), v) micro-injector enabling the injection of 10 or 20 nL samples, vi) high-voltage power supply providing up to 30 kV, and vii) restrictor that constrains the out-flow, minimizing bubble formation at the interface between packed segment and UV-detection window.

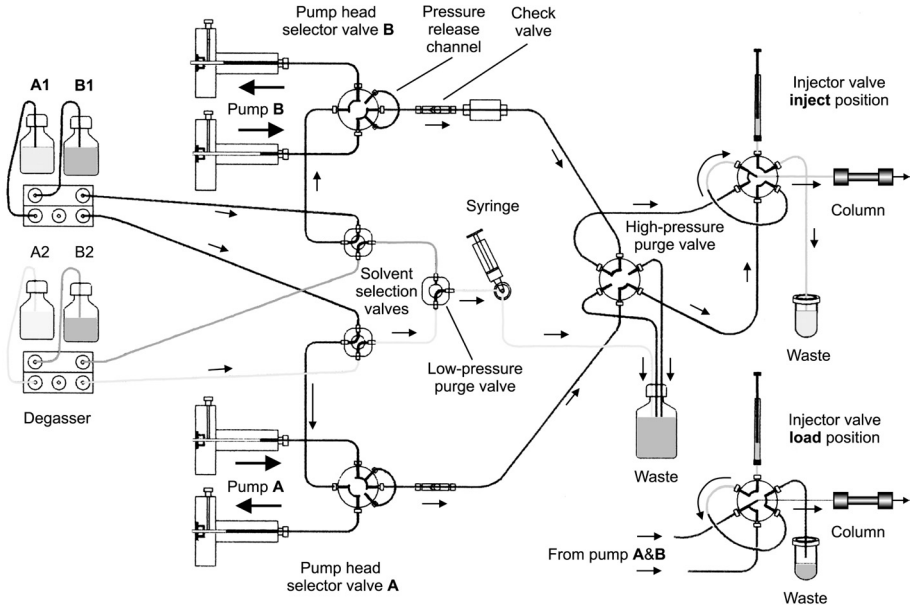

Figure 11. Flow scheme of the ProLab Evolution 200 (μ/c) HPLC/(p)CEC binary dual-piston high-pressure gradient pump system. The option for (p)CEC is not included in this scheme. Switch-over between the two pistons of a channel is realized by an electrically driven pump head selector valve. Channels A and B are separated by (almost dead volume-free) check valves. By switching the pump head selector valve it connects the two pistons of the channel for a short moment via the so-called pressure release channel, thus pressure-matching both pump heads. In addition, the actually delivering piston uses some compression steps to reach the original pressure. Altogether, it minimizes pressure fluctuations or pulsation and enables to circumvent pulsation dampers which, further, would increase the system dead volume. (Adapted with permission from ProLab Instruments.)

convert a conventional HPLC to a CEC system which can also be used for cHPLC (but only up to 70 bar, cf. Table 4) and CE.

4.2.2 The Micro-Tech [67] Ultra-Plus II™

Micro-Tech developed the Ultra-Plus II™ System for solvent delivery and gradient mixing down to sub-microliter flow rates. Sample injector, detector flow cell, and interconnecting tubing volume have been optimized accordingly. This instrument enables isocratic flow rates down to 0.1 μL/min, while 3 μL/min micro-gradients can be generated without split. The latter are provided by a micro-dynamic mixer which allows the user to configure the mixer volume down to 320 μm ID capillary column operation. The Ultra-Plus II™ gradient system combines cHPLC and (p)CEC. Like the Unimicro system this apparatus combines the selectivity tunings of cHPLC and CE/CEC via an additional high-voltage power supply (but only with a single polarity). The system can utilize capillary columns down to 25 μm ID by adopting the split-technique and a time-controlled Valco cHPLC injector for nanoliter sample injection. It allows either electric field assisted-cHPLC or pCEC. The combination of gradient elution and electrophoretic migration fosters increased sensitivity, complex sample resolution and analysis speed. Further details are given in Table 4.

4.2.3 The ProLab [68] Evolution 200

The Evolution 200 (μ/c)HPLC/CEC system from ProLab integrates a (μ/c)HPLC high-pressure gradient pump, a solvent degasser, a (readily accessible) thermostatted column chamber with injection valve for manual or automatic injection, and a high-voltage power supply (with switchable polarity). The Evolution 200 can be used for (μ/c)HPLC, CEC, and pCEC. It contains a binary dual-piston high-pressure gradient pump system (**Figure 11**) delivering from 20 nL/min to 200 μL/min which enables the use of columns down to 200 μm ID for gradient elution without split-flow (columns with a smaller ID can still be run isocratically without split, but gradient mode then requires flow-splitting). The electrically driven injection valve is located on a sliding carriage within the thermostatted column chamber and can be adjusted to the capillary length. This simplifies the connection of capillaries and a change of sample loops. The incorporated LabSource 7-port valve, especially developed for the Evolution 200 (μ/c)HPLC/CEC system, is connected to the high-voltage electrode and has an (electrically insulated) elec-

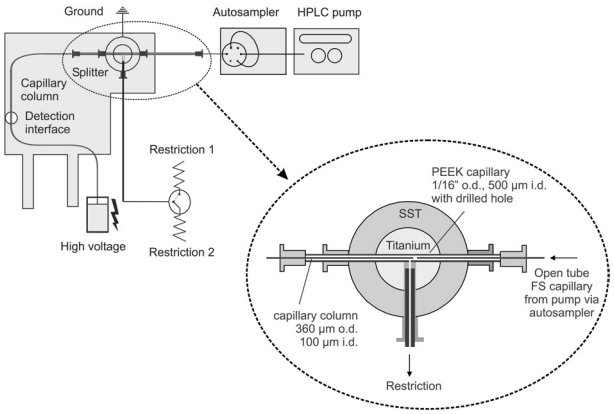

Figure 12. Schematics of the cassette (originally used for CE-MS coupling) interfacing the HP[3D]CE with an 1100 series HPLC system via flow splitter, depicted in more detail in the zoomed section. (Adapted with permission from Agilent Technologies.)

tric drive. Thus, the capillary column inlet, directly connected to the valve, can be set to high potential. This provides the option of electrokinetic injection and, even more important, the direct hyphenation with MS or NMR (setting the capillary column outlet to ground). The valve simultaneously fulfils the function of a static mixer and a splitter. Technical details of the Evolution 200 can be found in Table 4. This apparatus has been used by Mayer et al. [111] for enantiomer separation by cHPLC on a cellulose-based stationary phase (while they employed a Prince CE and a Beckman P/ACE instrument for CEC).

4.2.4 Agilent 1100 HPLC coupled to Agilent CE

Agilent studied the performance of an automated cHPLC/(p)CEC apparatus via two different approaches. The first one was realized by coupling a 1100 series ternary gradient pump (in combination with a HP 1100 autosampler) via flow split and CE/MS-capillary-cassette to the HP[3D]CE instrument, first published in 1997 by Dittmann et al. [112], performing cHPLC, CEC, and pCEC in isocratic and gradient elution mode. The setup depicted in **Figure 12** shows that this cassette was modified to allow grounding of the T-piece which acts as the flow splitter and column inlet. Since high voltage in the HP[3D]CE can only be applied at the position normally used as the capillary inlet vial; the path of the separation capillary and voltage polarity have to be changed to enable its use as an outlet. The capillary column and capillary transfer line from the pump were both mounted in 1/16″ OD (500 µm ID) PEEK tubing with a drilled hole to enable split-flow and grounding of the column inlet (cf. Figure 12). A similar setup was used by Apffel et al. [113] to investigate the separation of peptide digests. They also performed all the chromatographic modes that have already been mentioned, but with an extension to electrically assisted cHPLC (pressure-driven chromatography with enhanced selectivity for charged molecules by an electric field). This can be realized by suppressing EOF at low pH or by using a stationary phase unsuitable for producing any EOF.

The second approach followed by Agilent was the development of a prototype high-pressure standing seal vial and hollow (concentric double-tube) electrode. This setup enabled an upgrade of the existing HP[3D]CE instrument serving as the platform for capillary chromatographic separations coupled (via this prototype) to a HP 1100 pump. In contrast to the first approach, injection is performed with the intrinsic autosampler of the HP[3D]CE and the capillary path could stay as usual. The seal-vial (cross-sectional view in **Figure 13**) allows different chro-

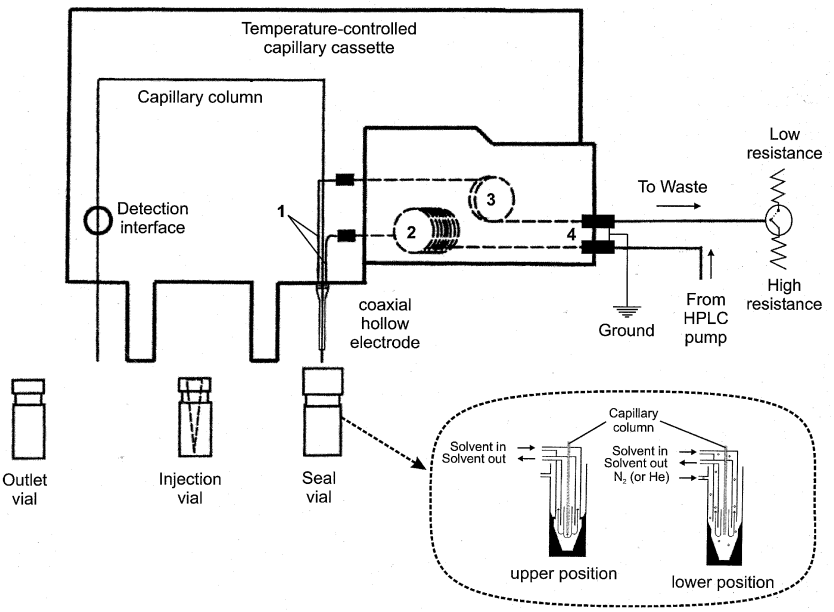

Figure 13. Illustration of the integrated platform of the Agilent prototype gradient cHPLC/(p)CEC system. (**1**) stainless-steel tubes, (**2**) 1 m × 100 µm open-tube fused-silica capillary, (**3**) 0.5 m × 100 µm open-tube fused-silica capillary, and (**4**) grounded stainless-steel unions. (Adapted with permission from [114]. Copyright (1999) Elsevier Science.) The inset illustrates details of the seal-vial. (Adapted with permission from Agilent Technologies.)

matographic modes by a dedicated positioning of the inlet lift. In its lower position, isocratic and gradient CEC is possible. The pump delivers liquid via the inner channel of the concentric double-tube electrode, which passes the N_2 (or He) pressurized vial and mostly leaves it through the outer channel by using the low-resistance flow path of the outlet restrictor. Pressures in this and the outlet vial are matched to suppress bubble formation and hydraulic flow. Liquid required for CEC is pulled into and moved through the column electrokinetically. The upper position of the seal-vial enables isocratic and gradient (μ/c)HPLC and pCEC. In this position, the vial functions as a high-pressure flow splitter in combination with the high-resistance flow path of the outlet restrictor. In all cases sample is injected electrokinetically using a standard sample-vial and injection procedure of the CE system. The whole configuration shown in Figure 13, presented by Choudhary et al. [114] and Rozing et al. [84], remained a prototype.

5 Conclusions and outlook

Despite recent instrumental developments in (μ/c)HPLC and (p)CEC, a further miniaturization of individual component volumes which are involved in the bulk transport of liquid (adequately accounting for the actual bed dimension) seems to be necessary as they cause delay times and result in dispersion. While injectors, static mixers, and detection cells are already available from sub-microliters down to a few nanoliters, pumping devices, autosamplers, and dynamic mixers are still too large. A controlled and regulated split is certainly an attractive feature, but it should be reasonably adaptable down to low nanoliter flow rates. Preferably, single split-regulated solvent channels should be introduced for these flow rates, allowing solvent recycling by splitting prior to mobile phase mixing. However, this technique and the splitless high-pressure solvent delivery of sub-microliter flow rates requires nanoliter dynamic mixers to provide a perfect mixing also for more critical solvent mixtures without adding significant delay volumes. Despite an ongoing miniaturization, pump systems still appear enormously overdimensioned in relation to generated flow rates. In this context (and especially for splitless systems) the relative expansion of the pressurized setup, fluid compressibilities, and volumetric mixing effects also have to be considered carefully. Commercial CE instruments (Section 3) are often used today for CEC applications, but alongside the above-mentioned home-built configurations (Section 4.1) which were (and still are) necessary to explore and validate CEC, especially gradient pCEC, commercial gradient (μ/c)HPLC/(p)CEC instruments are now on the market (Section 4.2). However, they are still based on more or less modified conventional components. The future hopefully will see the enhanced development of new LC device concepts, as illustrated by the hardware innovations described in Section 4.1.2 or the EKP (cf. Section 2).

Acknowledgement

We gratefully acknowledge support of this work by the Deutsche Forschungsgemeinschaft (DFG) under grant SE 586/7-1.

References

[1] Cs. Horváth, B.A. Preiss, S.R. Lipsky, *Anal. Chem.* **1967**, *39*, 1422.

[2] Cs. Horváth, S.R. Lipsky, *Anal. Chem.* **1969**, *41*, 1227.

[3] R.P.W. Scott, P. Kucera, *J. Chromatogr.* **1976**, *125*, 251.

[4] D. Ishii, K. Asai, K. Hibi, T. Jonokuchi, M. Nagaya, *J. Chromatogr.* **1977**, *144*, 157.

[5] D. Ishii (Ed), *Introduction to Microscale High-Performance Liquid Chromatography*, VCH, Weinheim 1988.

[6] J.P.C. Vissers, H.A. Claessens, C.A. Cramers, *J. Chromatogr. A* **1997**, *779*, 1.

[7] J.P.C. Vissers, *J. Chromatogr. A* **1999**, *856*, 117.

[8] J. Abian, A.J. Oosterkamp, E. Gelpi, *J. Mass Spectrom.* **1999**, *34*, 244.

[9] G.P. Rozing, M. Serwe, H.-G. Weissgerber, B. Glatz, *Am. Lab.* **2001**, *33*, 26.

[10] P.A. Bristow, J.H. Knox, *Chromatographia* **1977**, *10*, 279.

[11] J.H. Knox, I.H. Grant, *Chromatographia* **1991**, *32*, 317.

[12] M.M. Dittmann, K. Wienand, F. Bek, G.P. Rozing, *LC · GC* **1995**, *13*, 800.

[13] A.L. Crego, A. González, M.L. Marina, *Crit. Rev. Anal. Chem.* **1996**, *26*, 261.

[14] L.A. Colón, K.J. Reynolds, R. Alicea-Maldonado, A.M. Fermier, *Electrophoresis* **1997**, *18*, 2162.

[15] C. Fujimoto, *Trends Anal. Chem.* **1999**, *18*, 291.

[16] L.A. Colón, G. Burgos, T.D. Maloney, J.M. Citrón, R.L. Rodriguez, *Electrophoresis* **2000**, *21*, 3965.

[17] Z. Deyl, F. Svec (Eds), *Capillary Electrochromatography*, Journal of Chromatography Library, vol. 62, Elsevier, Amsterdam 2001.

[18] T. Tsuda, *Anal. Chem.* **1987**, *59*, 521.

[19] C.L. Rice, R. Whitehead, *J. Phys. Chem.* **1965**, *69*, 4017.

[20] R.J. Gross, J.F. Osterle, *J. Chem. Phys.* **1968**, *49*, 228.

[21] R.F. Probstein, *Physicochemical Hydrodynamics: An Introduction*, John Wiley & Sons, New York 1994.

[22] P.H. Paul, M.G. Garguilo, D.J. Rakestraw, *Anal. Chem.* **1998**, *70*, 2459.

[23] U. Tallarek, E. Rapp, T. Scheenen, E. Bayer, H. Van As, *Anal. Chem.* **2000**, *72*, 2292.

[24] K.-L.K. Liu, K.L. Davis, M.D. Morris, *Anal. Chem.* **1994**, *66*, 3744.

[25] E. Wen, R. Asiaie, Cs. Horváth, *J. Chromatogr. A* **1999**, *855*, 349.

[26] P.T. Vallano, V.T. Remcho, *Anal. Chem.* **2000**, *72*, 4255.

[27] R. Stol, H. Poppe, W.Th. Kok, *Anal. Chem.* **2001**, *73*, 3332.

[28] U. Tallarek, E. Rapp, H. Van As, E. Bayer, *Angew. Chem. Int. Ed.* **2001**, *40*, 1684.

[29] R. Xiang, Cs. Horváth, *Anal. Chem.* **2002**, *74*, 762.

[30] K.K. Unger, S. Lüdtke, M. Grün, *LC · GC Int.* **1999**, *12*, 870.

[31] K.K. Unger, D. Kumar, M. Grün, G. Büchel, S. Lüdtke, Th. Adam, K. Schumacher, S. Renker, *J. Chromatogr. A* **2000**, *892*, 47.

[32] T. Sakaki, S. Kitagawa, T. Tsuda, *Electrophoresis* **2000**, *21*, 3088.

[33] I. Gusev, Cs. Horváth, *J. Chromatogr. A* **2002**, *948*, 203.

[34] M. Novotny, *Anal. Chem.* **1981**, *53*, 1294A.

[35] F.J. Yang, *J. High Resol. Chromatogr.* **1983**, *6*, 348.

[36] M. Verzele, C. Dewaele, in: *The Science of Chromatography*, F. Bruner (Ed), Journal of Chromatography Library, vol. 32, Elsevier, Amsterdam 1985, p. 435.

[37] M. Novotny, *J. High Resol. Chromatogr.* **1987**, *10*, 248.

[38] K. Jinno, *Chromatographia* **1988**, *25*, 1004.

[39] M. Verzele, C. Dewaele, M. de Weerdt, *LC · GC* **1988**, *6*, 966.

[40] M. Novotny, *Anal. Chem.* **1988**, *60*, 502A.

[41] K. Jinno, C. Fujimoto, *LC · GC* **1989**, *7*, 328.

[42] D. Ishii, T. Takeuchi, *Trends Anal. Chem.* **1990**, *9*, 152.

[43] M. Novotny, *J. Chromatogr. Sci.* **1980**, *18*, 473.

[44] D. Ishii, T. Takeuchi, *Adv. Chromatogr.* **1983**, *21*, 131.

[45] M. Verzele, C. Dewaele, *J. High Resol. Chromatogr.* **1987**, *10*, 280.

[46] M. Verzele, C. Dewaele, *J. Chromatogr. Sci.* **1989**, *45*, 37.

[47] T. Takeuchi, *Fresen. J. Anal. Chem.* **1990**, *337*, 631.

[48] E.S. Yeung, in: *Microcolumn Separations*, M.V. Novotny, D. Ishii (Eds), Journal of Chromatography Library, vol. 30, Elsevier, Amsterdam 1985, p. 117.

[49] K. Jinno, C. Fujimoto, Y. Hirata, D. Ishii, in: *Microcolumn Separations*, M.V. Novotny, D. Ishii (Eds), Journal of Chromatography Library, vol. 30, Elsevier, Amsterdam 1985, p. 177.

[50] M. Goto, in: *Microcolumn Separations*, M.V. Novotny, D. Ishii (Eds), Journal of Chromatography Library, vol. 30, Elsevier, Amsterdam 1985, p. 309.

[51] N. Sagliano, R.A. Hartwick, *J. Chromatogr. Sci.* **1986**, *24*, 506.

[52] B.G. Belenkii, *J. Chromatogr.* **1988**, *434*, 337.

[53] J.C. Gluckman, M.V. Novotny, *J. Chomatogr. Sci.* **1989**, *45*, 145.

[54] E.S. Yeung, W.G. Kuhr, *Anal. Chem.* **1991**, *63*, 275A.

[55] C.E. Kientz, U.A.Th. Brinkmann, *Trends Anal. Chem.* **1993**, *12*, 363.

[56] A.G. Ewing, J.M. Mesaros, P.G. Galvin, *Anal. Chem.* **1994**, *66*, 527A.

[57] J.C. Gluckman, M.V. Novotny, in: *Microcolumn Separations*, M.V. Novotny, D. Ishii (Eds), Journal of Chromatography Library, vol. 30, Elsevier, Amsterdam 1985, p. 57.

[58] V.V. Berry, H.E. Schwartz, *J. Chromatogr. Sci.* **1989**, *45*, 67.

[59] Agilent Technologies, Waldbronn, Germany; http://www.chem.agilent.com

[60] LC Packings, Amsterdam, The Netherlands; http://www.lcpackings.nl

[61] Waters Corporation, Milford, MA; http://www.waters.com

[62] Eldex Laboratories Inc., Napa, CA; http://www.eldex.com

[63] P.H. Paul, D.W. Arnold, D.J. Rakestraw, in: *Micro Total Analysis Systems '98*, D.J. Harrison, A. van den Berg (Eds), Kluwer, Dordrecht 1998, p. 49.

[64] P.H. Paul, D.W. Arnold, D.W. Neyer, K.D. Smith, D.J. Rakestraw, in: *Micro Total Analysis Systems 2000*, A. van den Berg, W. Olthuis, P. Bergveld (Eds), Kluwer, Dordrecht 2000, p. 583.

[65] S. Zeng, C.-H. Chen, J.C. Mikkelsen, J.G. Santiago, *Sens. Actuators B* **2001**, *79*, 107.

[66] Eksigent Technologies, Livermore, CA; http://www.eksigent.com

[67] Micro-Tech Scientific, Sunnyvale, CA; http://www.microlc.com

[68] ProLab Instruments GmbH, Reinach, Switzerland; http://www.prolab.ch

[69] H. Poppe, *J. Chromatogr. A* **1997**, *781*, 3.

[70] R.J. Boughtflower, T. Underwood, C.J. Paterson, *Chromatographia* **1995**, *40*, 329.

[71] N.W. Smith, M.B. Evans, *Chromatographia* **1994**, *38*, 649.

[72] M.M. Dittmann, G.P. Rozing, *J. Chromatogr. A* **1996**, *744*, 63.

[73] N.W. Smith, M.B. Evans, *Chromatographia* **1995**, *41*, 197.

[74] N.W. Smith, A.S. Carter-Finch, *J. Chromatogr. A* **2000**, *892*, 219.

[75] Now: Applied Biosystems, Foster City, CA; http://www.appliedbiosystems.com (CE instrument no longer available.)

[76] Prince Technologies, Emmen, The Netherlands; http://www.princetechnologies.nl

[77] M.R. Euerby, D. Gilligan, C.M. Johnson, K.D. Bartle, *Analyst* **1997**, *122*, 1087.

[78] J. Ding, J. Sceliga, A. Dipple, P. Vouros, *J. Chromatogr. A* **1997**, *781*, 327.

[79] L.H. Zhang, H.F. Zou, W. Shi, J.Y. Ni, Y.K. Zhang, *J. Cap. Elec.* **1998**, *5*, 97.

[80] Beckman Coulter Inc., Fullerton, CA; http://www.beckmancoulter.com

[81] B. Xin, M.L. Lee, *J. Microcol. Sep.* **1999**, *11*, 271.

[82] F. Steiner, B. Scherer, *J. Chromatogr. A* **2000**, *887*, 55.

[83] U. Pyell, *J. Chromatogr. A* **2000**, *892*, 257.

[84] G.P. Rozing, A. Dermaux, P. Sandra, in: Z. Deyl, F. Svec (Eds), *Capillary Electrochromatography*, Journal of Chromatography Library, vol. 62, Elsevier, Amsterdam 2001, p. 39.

[85] B. Behnke, E. Bayer, *J. Chromatogr. A* **1994**, *680*, 93.

[86] Th. Eimer, K.K. Unger, T. Tsuda, *Fresen. J. Anal. Chem.* **1995**, *352*, 649.

[87] C.G. Huber, G. Choudhary, Cs. Horváth, *Anal. Chem.* **1997**, *69*, 4429.

[88] S. Kitagawa, A. Tsuji, H. Watanabe, M. Nakashima, T. Tsuda, *J. Microcol. Sep.* **1997**, *9*, 347.

[89] Y. Zhang, W. Shi, L. Zhang, H. Zou, *J. Chromatogr. A* **1998**, *802*, 59.

[90] M.R. Taylor, P. Teale, *J. Chromatogr. A* **1997**, *768*, 89.

[91] M.R. Taylor, P. Teale, S.A. Westwood, *Anal. Chem.* **1997**, *69*, 2554.

[92] Unimicro Technologies Inc., Pleasanton, CA; http://www.unimicrotech.com

[93] B. Behnke, J.W. Metzger, *Electrophoresis* **1999**, *20*, 80.

[94] D.B. Strickmann, B. Chankvetadze, G. Blaschke, C. Desiderio, S. Fanali, *J. Chromatogr. A* **2000**, *887*, 393.

[95] J.N. Alexander, J.B. Poli, K.E. Markides, *Anal. Chem.* **1999**, *71*, 2398.

[96] A.S. Lister, C.A. Rimmer, J.G. Dorsey, *J. Chromatogr. A* **1998**, *828*, 105.

[97] VICI (Valco International Co. Inc.), Houston, TX; http://www.vici.com

[98] Rheodyne L.P., Rohnert Park, CA; http://www.rheodyne.com

[99] Upchurch Scientific, Oak Harbor, WA; http://www.upchurch.com

[100] E.R. Verheij, U.R. Tjaden, W.M.A. Niessen, J. van der Greef, *J. Chromatogr.* **1991**, *554*, 339.

[101] T. Tsuda, *LC · GC Int.* **1992**, *5*, 26.

[102] B. Behnke, E. Grom, E. Bayer, *J. Chromatogr. A* **1995**, *716*, 207.

[103] M.B.O. Anderson, L.G. Blomberg, *J. Sep. Sci.* **2001**, *24*, 304.

[104] L.C. Sander, M. Pursch, B. Märker, S.A. Wise, *Anal. Chem.* **1999**, *71*, 3477.

[105] W. Guo, J.A. Koropchak, C. Yan, *J. Chromatogr. A* **1999**, *849*, 587.

[106] ISCO Inc., Lincoln, NE; http://www.isco.com

[107] C. Yan, R. Dadoo, R.N. Zare, D.J. Rakestraw, D.S. Anex, *Anal. Chem.* **1996**, *68*, 2726.

[108] R. Dadoo, C. Yan, R.N. Zare, D.S. Anex, D.J. Rakestraw, G.A. Hux, *LC · GC* **1997**, *15*, 630.

[109] K.M. Hutterer, J.W. Jorgenson, *Anal. Chem.* **1999**, *71*, 1293.

[110] Q.-H. Ru, J. Yao, G.-A. Luo, Y.-X. Zhang, C. Yan, *J. Chromatogr. A* **2000**, *894*, 337.

[111] S. Mayer, X. Briand, E. Francotte, *J. Chromatogr. A* **2000**, *875*, 331.

[112] M.M. Dittmann, G.P. Rozing, G. Ross, Th. Adam, K.K. Unger, *J. Cap. Elec.* **1997**, *4*, 201.

[113] A. Apffel, H. Yin, W.S. Hancock, D. McManigill, J. Frenz, S.-L. Wu, *J. Chromatogr. A* **1999**, *832*, 149.

[114] G. Choudhary, W. Hancock, K. Witt, G. Rozing, A. Torres-Duarte, I. Wainer, *J. Chromatogr. A* **1999**, *857*, 183.

[JSS 1228]

Dynamics of Capillary Electrochromatography: Experimental Study of Flow and Transport in Particulate Beds

By *Guofang Chen*, *Martin Pačes*, *Miloš Marek*, *Yukui Zhang*, *Andreas Seidel-Morgenstern*, and *Ulrich Tallarek**

The chromatographic performance with respect to the flow behavior and dispersion in fixed beds of nonporous and macroporous particles (having mean intraparticle pore diameters of 41, 105, and 232 nm) has been studied in capillary HPLC and electrochromatography. The existence of substantial electroosmotic intraparticle pore flow (perfusive electroosmosis) in columns packed with the macroporous particles was found to reduce stagnant mobile mass transfer resistance and decrease the global flow inhomogeneity over the column cross-section, leading to a significant improvement in column efficiency compared to capillary HPLC. The effect of electroosmotic perfusion on axial dispersion was shown to be sensitive to the mobile phase ionic strength and mean intraparticle pore diameter, thus, on an electrical double layer interaction within the particles. Complementary and consistent results were observed for the average electroosmotic flow through packed capillaries. It was found to depend on particle porosity and distinct contributions to the electrical double layer behavior within and between particles. Based on these data an optimum chromatographic performance in view of speed and efficiency can be achieved by straightforward adjustment of the electrolyte concentration and characteristic intraparticle pore size.

1 Introduction

1.1 Miniaturization in High Performance Liquid Chromatography

Miniaturization in high performance liquid chromatography (HPLC) concerning the column inner diameter (i.d.) and associated volumetric flow rates was initiated more than 25 years ago [1–5], and is an ongoing development mainly because of the need to handle small amounts of complex samples. While the typical dimensions in analytical and narrow-bore HPLC include a 2.1–4.6 mm column i.d., bed lengths of less than 200 mm and random sphere packings of 5–15 μm average diameter particles, the further miniaturization towards nano-LC (see Tab. 1) can offer distinct advantages [6–11] including:

i. reduced consumption of stationary phase, solvent, and chemicals, facilitating the use of expensive stationary phase, exotic mobile phases, and minute samples in the environmental and biomedical sciences,
ii. increased mass sensitivity due to reduced chromatographic dilution,
iii. use of smaller, but still porous particles (d_p = 3–5 μm)[1)] leading to higher column efficiencies by a significantly reduced contribution of the intraparticle stagnant zone to hydrodynamic dispersion,
iv. compatibility with flow rate requirements of a nano-ESI interface in view of an on-line coupling to mass spectrometry, and
v. application of high electrical fields for the additional (or exclusive) transport of bulk liquid and solute molecules through a porous medium by electroosmosis and/or electrophoresis.

Table 1. Suggested nomenclature for different HPLC regimes [11].

ategory	olumn diameter (cross-sectional area)	Vol. flow rates	Typical loading
Analytical HPLC	5.0–3.9 mm (20–12 mm^2)	5–1.5 mL/min	2–10 mg
Narrow-bore HPLC	3.9–2.1 mm (12–3.5 mm^2)	1.5–0.2 mL/min	0.5–2 mg
Micro HPLC	2.1–0.5 mm (3.5–0.2 mm^2)	300–10 μL/min	50–500 μg
apillary HPLC	0.5–0.15 mm (0.2–0.02 mm^2)	15–1 μL/min	1–50 μg
Nano(scale) LC	< 0.15 mm (< 0.02 mm^2)	< 1 μL/min	< 1 μg

Related to the last aspect, in general, mass transport in porous media induced by an externally applied electrical field nowadays plays a central role in a number of analytical, technological, and environmental processes, including the dewatering of waste sludge and soil remediation, capillary electrophoresis or electrochromatographic separations in capillaries and microfluidic devices [12–28]. However, there still exists a lack of mechanistic understanding concerning the interrelation between external control variables like the electrical field strength or current and parameters controlling macroscopic electrokinetic transport like the dispersion

[*] Dr. rer. nat. U. Tallarek (author to whom correspondence should be addressed, e-mail: ulrich.tallarek@vst.uni-magdeburg.de), Dipl.-Ing. G. Chen, Prof. Dr.-Ing. A. Seidel-Morgenstern, Institut für Verfahrenstechnik der Otto-von-Guericke Universität, Universitätsplatz 2, D-39106 Magdeburg, Germany; Dipl.-Ing. M. Pačes, Prof. Dr.-Ing. M. Marek, Department of Chemical Engineering and Center for Nonlinear Dynamics of Chemical and Biological Systems, Prague Institute of Chemical Technology, Technická 5, CZ-16628 Prague, Czech Republic; Prof. Dr. rer. nat. Y. Zhang, National Chromatography Research & Analysis Center, Dalian Institute of Chemical Physics, Chinese Academy of Sciences, 161 Zhongshan Road, Dalian 116011, Peoples Republic of China.

1) List of symbols at the end of the paper.

 DOI: 10.1002/ceat.200401939

coefficient or effective mobility. It is intimately related to the physico-chemical nature of the surface and its dynamic behavior, pore space morphology, and properties of the liquid. The characterization of these parameters is of fundamental relevance as it critically guides the performance and compelling advantages, as well as design strategies of a particular electrokinetic process with respect to any alternative diffusive-convective transport schemes.

The present work is concerned with the dynamics of electroosmotic flow (EOF) and solute transport in capillary electrochromatography (CEC). While the column efficiencies in HPLC may be increased by a reduction of the particle size this option is limited via the maximum operating pressure with conventional instrumentation. A significantly improved performance in view of the dispersion and permeability can be achieved in CEC by utilizing EOF for the transport of bulk mobile phase. In this introduction a brief survey is given of some of the most important features of the EOF in porous media (like random sphere packings) because it may be a relatively unfamiliar topic to many readers. A hardware overview with a comparison of instrumental configurations used for the generation and control of the required micro- and nanoliter volumes of liquid in capillary (electro)chromatography and nano-LC has been presented recently [11].

1.2 Capillary Electrochromatography

CEC is a relatively new separation technique carried out most commonly in a capillary column packed with conventional HPLC adsorbent material by utilizing an electroosmotically driven mobile phase at high electrical field strength (50–100 kV/m) in an apparatus similar to that used in capillary zone electrophoresis (CZE). Consequently, CEC combines the variety of retention mechanisms and stationary phase selectivities popular in HPLC with the miniaturization potential of CZE. Tsuda [29] described electrochromatography as an electrophoretic analysis where sorptive interactions with the stationary (retentive) phase of the support material are a major contribution, i.e., the separation is achieved by a differential partitioning and migration. Although the origin of CEC traces back to 1974 when Pretorius *et al.* [30] reported the successful electrokinetic transport of eluent through a (comparatively large) chromatographic column, it was Jorgenson and Lukacs [31] who demonstrated the feasibility of CEC for the separation of neutral compounds by applying a potential gradient across a packed column of capillary dimension, before Knox and Grant [32–34] examined more fundamental aspects and the advantages of CEC.

1.2.1 Advantages of CEC over Capillary HPLC

CEC is commonly performed in a 50–150 μm i.d. (fused-silica) capillary column setup, which is usually composed of a packed bed and open tubular segment, as well as a detection window immediately behind the outlet frit of the fixed bed. Compared to pressure-driven flow a superior performance of EOF through a single, straight and open capillary originates from the fact that in the limit of a thin electrical double layer (EDL) the velocity apparently slips at the inner wall of the capillary and, thus, the fluid moves as in plug-flow (assuming isothermal conditions) [35–38]. Further, for fixed pressure and potential gradients, the ratio of volumetric EOF to hydraulic flow rates is inversely proportional to the square of the capillary radius [39]. The flat "pore-level" velocity profile of EOF observed for a single-pore geometry (as in CZE) [40,41] and permeability criterion also have important implications for the fluid dynamics (an improved dispersion behavior, in particular) in CEC where actually many pores are connected, as in a random particulate fixed bed, including:

i. the use of micron- and submicron-sized particles as the packing material [42,43] for reduction of band spreading toward the diffusion-limited regime,
ii. the operation of relatively long packed columns (if needed) or, vice versa, the use of very short chromatographic beds [44],
iii. further reduction of the column diameter toward chip format [45–49],
iv. the generation of a substantial EOF within the porous particles (electroosmotic perfusion), which reduces intraparticle mass transfer resistance and associated hold-up dispersion [50–55],
v. a higher separation efficiency based on the superior hydrodynamic dispersion characteristics (see Fig. 1) in the interstitial pore space of a sphere packing over a wide range of experimental conditions [34], and

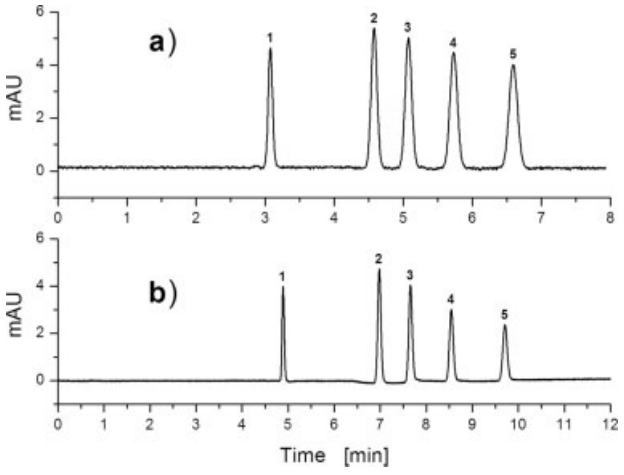

Figure 1. Separation efficiency at similar mobile phase average velocity. a) Capillary HPLC, packed bed of 150 mm length in a 100 μm i.d. capillary, in-column detection (215 nm); analytes: (1) thiourea, (2) methylbenzoate, (3) ethylbenzoate, (4) propylbenzoate, and (5) butylbenzoate. b) CEC, 325 mm long capillary setup (effective packed bed length of 240 mm) × 100 μm i.d., applied voltage: 20 kV. Stationary phase: Porous C18-silica particles (d_p = 2.45 μm and d_{pore} = 14 nm). The mobile phase is a 5 mM aqueous Tris (pH 8.3)/acetonitrile 20:80 (v/v) buffer solution. The separation efficiency in CEC is about 2×10^4 N/m.

vi. the enhancement of intraparticle transport of charged species by their migration and surface (electro)diffusion [56,57].

Thus, CEC offers the potential for implementation into miniaturized systems allowing high sample throughput and resolution, speed, and sensitivity. Compared to liquid chromatography CEC offers a better permeability and efficiency, as well as selectivity (in the case of charged analytes), and concerning CZE it operates in systems with far higher surface-to-volume ratio in view of sample capacity and dynamic changes in surface properties. As in capillary HPLC the actual flow rates are inherently compatible with direct mass spectrometric detection.

As demonstrated by Fig. 1, the separation efficiency in CEC is about twice as high as that in HPLC when using particles with a pore size ($d_{pore} \approx 10$ nm) of the order of the EDL thickness of typically 1–10 nm. It will be seen below how this improvement can still be substantially increased by optimizing intraparticle EOF with macroporous particles ($d_{pore} > 30$ nm).

1.2.2 EOF in a Fixed Bed of Spherical Particles

1.2.2.1 Simple Considerations

Consider a random close packing of spherical-shaped, solid, and dielectric (i.e., impermeable and nonconducting) particles with a uniform distribution of the electrokinetic or shear-plane potential (ζ_p) at their external surface and an EDL thickness (typically represented by the Debye screening length λ_D) much smaller than the particle radius (r_p). In this thin EDL limit ($r_p/\lambda_D \gg 1$) the macroscopic, average EOF velocity $\langle \mathbf{u}_p \rangle$ through a column of volume V_c is obtained by integration over the interparticle bed volume V_{inter} [58]

$$\langle \mathbf{u}_p \rangle = \frac{1}{V_c} \int_{V_{inter}} \mathbf{u}_p \, dV_c = -\frac{\varepsilon_0 \varepsilon_r \zeta_p}{\eta_f V_c} \int_{V_{inter}} \mathbf{E} \, dV_c \quad (1)$$

where ε_0, ε_r, and η_f are the permittivity of a vacuum, and the relative permittivity and viscosity of the electrolyte solution, respectively. $\mathbf{u}_p$ is the local slip velocity along the particles surface just outside the thin EDL, which results from the lines of force (in the EDL) due to the interaction of the electrical field of local strength $\mathbf{E} = -\nabla\Phi$ with a locally charged fluid [59,60]

$$\mathbf{u}_p = -\frac{\varepsilon_0 \varepsilon_r \zeta_p \mathbf{E}}{\eta_f} \quad (2)$$

Because the incompressible flows of electricity and fluid are parallel and proportional to each other at the solid/liquid interface, Eq. (2) is also supposed to hold throughout the whole liquid phase [60]. Although the no-slip condition is usually assumed for the fluid adjoining a surface [61], i.e., the velocity rises from zero at the shear plane to a limiting value beyond the EDL, it seems to slip past the surface from a macroscopic point of view. λ_D is given by

$$\lambda_D = \left(\frac{\varepsilon_0 \varepsilon_r RT}{F^2 \sum_i z_i^2 c_{i,\infty}} \right)^{1/2} \quad (3)$$

where R is the gas constant, T the absolute temperature, and F Faraday's constant, z_i is the valence of the ionic species i and $c_{i,\infty}$ its molar concentration in the electro-neutral solution (that is, beyond the EDL). For the macroscopic electrical current density

$$\langle \mathbf{i}_{el} \rangle = K^* \langle \mathbf{E} \rangle = \frac{K^\infty}{V_c} \int_{V_{inter}} \mathbf{E} \, dV_c = \frac{K^\infty}{V_c} \int_{V_{inter}} \frac{\mathbf{i}_{el}}{K^\infty} \, dV_c \quad (4)$$

K^∞ is the conductivity of the equilibrium electrolyte beyond the EDL and K* stands for the conductivity of the packed column. By combining Eqs. (1) and (4) the following is obtained

$$\langle \mathbf{u}_p \rangle = -\frac{\varepsilon_0 \varepsilon_r \zeta_p \langle \mathbf{i}_{el} \rangle}{\eta_f K^\infty} = -\frac{\varepsilon_0 \varepsilon_r \zeta_p \langle \mathbf{E} \rangle}{\eta_f} \left(\frac{K^*}{K^\infty} \right) \quad (5)$$

Thus, the EOF velocity averaged over the column cross-section can be expressed by means of the conductivity ratio K^*/K^∞, which becomes accessible experimentally via conductivities of a packed column and an identical, but open tube saturated with the same electrolyte solution. It is further assumed that the EDL only makes a negligible contribution to the total conductivity of the sphere packing [62,63]. The above considerations are valid for beds of nonporous (and porous) particles with arbitrary shape and size distribution.

1.2.2.2 Electrokinetic Wall Effect

Typically, CEC is carried out in a cylindrical capillary column of $d_c \leq 150$ μm packed with $d_p = 3$–10 μm porous adsorbent particles. Electrical fields of up to 100 kV/m are applied to move a buffer solution and solute molecules through the porous medium by electroosmosis (and electrophoresis, if the analytes were charged) [18,64]. Thus, $d_c/d_p \leq 50$, with aspect ratios between 20 and 30 being most common. In this range the presence of a column wall has several consequences for macroscopic flow and transport.

First, the radial porosity distribution is systematically influenced over a substantial volume of the column.

Concerning the packing density close to the wall, it has been shown that the radial distribution of voidage in a random sphere packing is inhomogeneous [65–68], and that the interstitial porosity (ε_{inter}) starts with a maximum value of unity at the column inner wall, then displays damped oscillations with a period close to d_p over a distance of about 4–5 d_p into the bulk of the bed, before reaching void fractions typical for bulk packing ($\varepsilon_{inter} = 0.38$–$0.4$). This geometrical wall effect can be explained by the decrease of packing order as the distance from the wall increases and may have a strong impact on the macroscopic flow heterogeneity, axial

dispersion, and particle-to-fluid heat and mass transfer, especially at aspect ratios, d_c/d_p, below 15 [69–74] when this critical wall region occupies a substantial fraction of the column. Since radial variations of transport properties have a far more serious effect on column performance than axial ones, this packing aspect will be quite important for capillary HPLC, but may have less impact on a macroscopic velocity inequality of the flow pattern in CEC. In close relation, it has been demonstrated that in the thin EDL limit the average EOF velocity in a single pore is relatively independent of pore radius [35], which, on a macroscopic scale, is complemented by observing that the average EOF in packed capillaries is hardly influenced by the particle diameter [34].

Rather than a radial porosity distribution, it is the radial distribution of electrokinetic potential (ζ) at the solid-liquid interface which determines the EOF profile in a fixed bed. In addition to EOF generated locally at the particles surface (ζ_p) the capillary inner wall must also be considered as a source of EOF (ζ_w). In general, the electrokinetic (and chromatographic) properties of these surfaces can be very different. This fact introduces an electrokinetic wall effect, which depends on the aspect ratio (d_c/d_p) and actual potential mismatch (ζ_w/ζ_p) as depicted in Fig. 2.

The influence of a charged capillary inner wall on the radial distribution of EOF velocities may be estimated by [58,75]

$$\frac{u(r)}{u_p} = 1 + \left(\frac{\zeta_w}{\zeta_p} - 1\right)\frac{I_0(\beta r/d_p)}{I_0(\beta r_{eff}/d_p)} \text{ for } 0 \le r \le r_c - 7\lambda_D \cong r_{eff} \quad (6)$$

where I_0 is the zero-order modified Bessel function of the first kind, r_{eff} an effective capillary radius accounting for the no-slip condition at the inner wall of the column, and β characterizes the overall permeability of a bed [76]

$$\beta = 3\sqrt{\frac{\alpha(1-\varepsilon_{bed})}{2}} \quad (7)$$

The dimensionless parameter, α, depends on the drag force provided by a particle and, thus, on packing structure, particle shape, and permeability. Based on Eq. (6), Fig. 2 demonstrates the strong effect of ζ_w/ζ_p on the resulting trans-column EOF profiles. The wall effect in CEC is limited to a relatively narrow annulus at the wall that increases in width with the magnitude of the excess Zeta potential $\zeta_{ex} = \zeta_w - \zeta_p$.

Although the particles surface and capillary inner wall both typically carry a negative charge density, the open fused-silica capillaries are known to give EOF velocities significantly higher than those of many packing materials in CEC [77–79]. The electrokinetic wall effect has recently been spatially resolved by dynamic NMR microscopy with 40 μm in-plane resolution in a study of flow through a 250 μm i.d. fused-silica capillary packed with 50 μm cation exchange particles [80]. This work has clearly demonstrated that a significantly higher velocity close to the wall than in the center of the column affects transient hydrodynamic dispersion, leading to a long-time disequilibrium in the fluid molecules axial displacement probability distribution. Thus, the electrokinetic wall effect is too significant to neglect in current CEC practice with $d_c/d_p \le 30$ (unless $\zeta_w \approx \zeta_p$).

1.2.2.3 Electroosmotic Perfusive Flow

The general tendency towards the use of submicron-size particles in chromatography is based on the popular models of, e.g., van Deemter *et al.* [81], Giddings [82], or Kennedy and Knox [83] for dispersion in packed columns. These predict a lower height equivalent to a theoretical plate (HETP) at the same linear velocity and, thus, higher separation efficiency as the particle size is reduced. An alternative to nanoparticles (which are difficult to pack in the form of stable and sufficiently long beds) in capillary HPLC and CEC is the utilization of pore flow within much larger, but macro- or even gigaporous particles. Perfusion chromatography refers to separation processes with non-zero intraparticle velocity and has received much attention in the past [84–92]. However, signifcant mobile phase perfusion in beds of permeable particles is only realized with hydraulic flow when high column pressure drops and particles with large (giga)pores are encountered, which limits the intra-

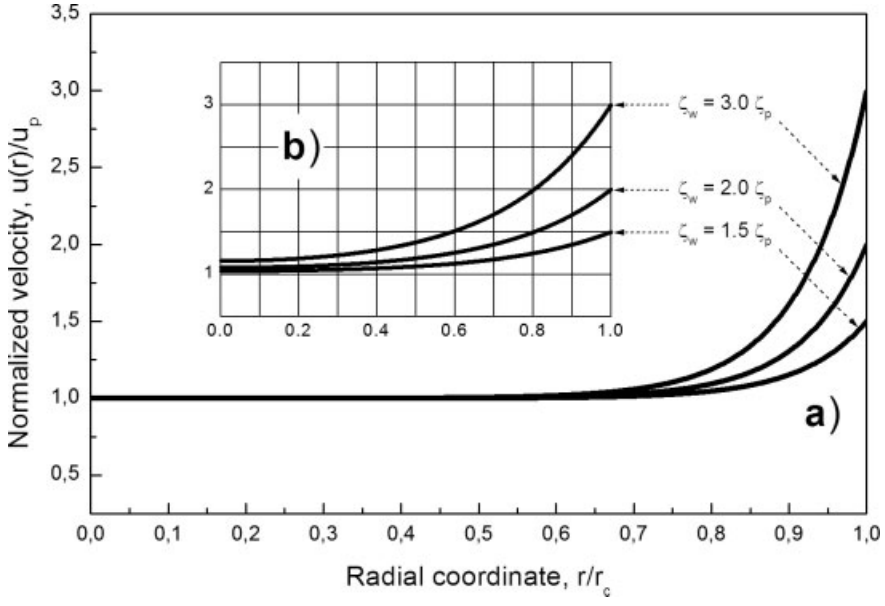

Figure 2. Prediction of radial EOF distributions normalized by u_p (the velocity generated locally at the external particle surface) in a sphere packing for different values of ζ_w/ζ_p and aspect ratios as based on Eq. (6) with r_c = 125 μm, λ_D = 3.9 nm, and β = 1.65 [80]. a) d_c/d_p = 15 and b) d_c/d_p = 5.

particle surface-to-volume ratio in view of a particles mechanical strength or adsorption capacity. But even then, the intraparticle velocities remain small compared to velocities in the interparticle pore space and they are relevant only for the transport of slowly diffusing (bio)molecules [93–95].

The hierarchical design of wide-pore material has been an important aspect from a particle engineering point of view [96,97]. As illustrated in Fig. 3 hierarchically-structured spheres are made by inter-adhering primary particles in several clustering steps.

The resulting particle can have two sets of pores, the large gigapores with $d_{pore}/d_p > 10^{-2}$ [90] and macropores. More importantly, hierarchical design produces a good correlation of interconnectivity between these discrete sets of pores and minimizes any dead-end branching. The gigapores transect the particle as a whole (see Fig. 3) and are the only basis for the, still small, intraparticle convection in hydraulic flow. By contrast, even the macropores are large enough for allowing substantial intraparticle EOF by an adjustment of the mobile phase ionic strength to the pore dimensions such that $r_{pore}/\lambda_D \gg 1$ or that, at least, $r_{pore}/\lambda_D > 1$ is guaranteed [50–55].

Thus, due to the strikingly different possibilities for tuning experimentally electroosmotic and hydraulic permeabilities of the packed bed, an important performance advantage of CEC over capillary HPLC lies in the new dimension of the perfusion mechanism. It has been shown that electroosmotic perfusion through fixed beds of porous particles proceeds with a significantly higher intraparticle permeability [55,98,99] and that, compared with hydraulic flow, the EOF offers far superior dispersion characteristics [50–53]. Gigapores are definitely not needed for electroosmotic perfusion, and the pore space morphology should rather be optimized in view of the surface-to-volume ratio while maintaining substantial intraparticle EOF at a modest ionic strength. As these considerations point toward a macropore domain the influence of intraparticle EDL overlap on flow and dispersion in random sphere packings was studied systematically using macroporous C18-silica particles with almost identical mean particle diameter and a monomodal pore size distribution, but with different mean intraparticle pore sizes. Thus, EDL overlap could be complementary adjusted by changing either the mobile phase ionic strength or the particle pore size.

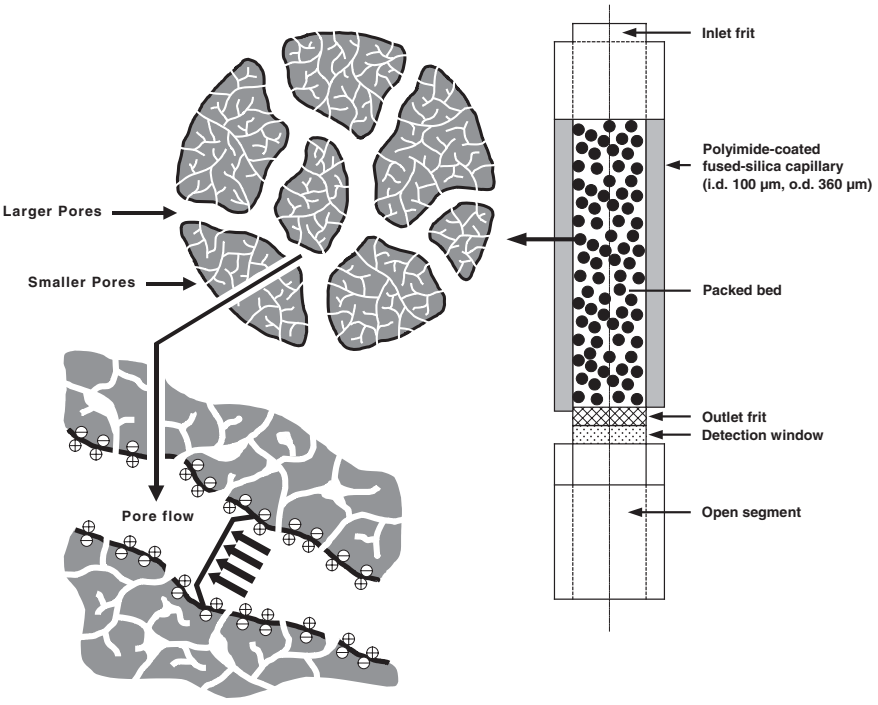

Figure 3. Column configuration representative for CEC and capillary HPLC with typical parameters ($L_{bed}/d_c > 1000$, $d_c/d_p = 10–50$, $d_p/d_{pore} > 100$, and $d_{pore}/\lambda_D = 5–50$), and the pore space morphology of a hierarchically-structured single particle with bimodal pore size distribution [53].

2 Experimental

2.1 Characterization of the Silica-Based Particles

Physical data for the (non)porous, spherical-shaped C18-silica particles are summarized in Tab. 2.

Table 2. Physical data for the (non)porous silica-based particles.

Particles	d_p [µm][a)]	V_{pore} [mL/g]	d_{pore} [nm][b)]	ε_{intra}[c)]	r_{pore}/λ_D[d)]	A_s [m^2/g][e)]
Porous spheres	2.45	0.88	41	0.66	0.6–12.8	64.7
	2.46	0.65	105	0.59	1.6–32.8	21.1
	2.42	0.34	232	0.43	3.6–72.5	7.5
Nonporous	2.45	–				a. 1

a) Refers to the external surface-averaged value.
b) Mean intraparticle pore diameter based on mercury porosimetry.
c) $\varepsilon_{intra} = (1 + (1/\rho_{SiO}V_{pore}))^{-1}$, with ρ_{SiO} taken as 2.24 g/mL .
d) For buffer concentrations used in this work (1×10^{-4}–4×10^{-2} M Tris).
e) Specific surface area based on nitrogen adsorption.

While all particles have almost the same average diameter, the mean intraparticle pore size is different. Thus, at a given column diameter (d_c) the aspect ratio d_c/d_p was constant for all packings, which allowed for a systematic evalution of the influence of an intraparticle EDL overlap on EOF behavior (electroosmotic perfusion) and associated dispersion in fixed beds without a conflicting contribution

from the electrokinetic wall effect (which depends on d_c/d_p). Further, at the aspect ratio realized in the experiments ($d_c/d_p = 40$) this wall effect is expected to play a less significant role. Particles were received from Merck KGaA (Darmstadt, Germany), together with the mercury intrusion and nitrogen adsorption data needed for the determination of pore volume and surface area, respectively. Tab. 2 indicates that a particles surface-to-volume ratio decreases significantly while its mean pore diameter is increased. Size distributions were analyzed with a 1180 laser particle size analyzer from CILAS (Marcoussis, France) using dilute suspensions in isopropanol. All macroporous particles have a monomodal intraparticle pore size distribution.

2.2 Column Packing Procedure

The setup devised for the packing procedure is shown in Fig. 4.

Fused-silica capillaries of 100 μm i.d. and 360 μm o.d. (Polymicro Technologies, Phonenix, AZ) were packed by a slurry packing method [100] using a WellChrom K-1900 pneumatic pump (KNAUER GmbH, Berlin, Germany). 500 μm i.d. glass-lined metal tubing was used as the slurry reservoir. MicroTight zero-dead-volume unions (including the fittings and gauge-plug) with MicroTight tubing sleeve, inlined with a glass-fibre filter providing a temporary outlet frit during packing, were obtained from Upchurch Scientific (Oak Harbor, WA, USA). An SSI two-way valve and SSI (dual-stem) three-way valve (ERC, Riemerling, Germany) were used between the pneumatic pump and the slurry reservoir for pressure release and slurry injection, respectively. Slurries were prepared by suspending 10 mg of the dry particles in 100 μL of ethanol under ultrasonication for 15 min. The slurry reservoir was filled with a syringe. Subsequently, using water as a pushing fluid, particles were forced into the fused-silica capillary at a set pressure. During the packing process the capillary (and optionally also the slurry reservoir) was placed in an ultrasonic bath to compact and stabilize the beds, which reached a length of at least 300 mm within 5–10 min. Finally, the pump was switched off, the pressure allowed to release, and the bed inspected for uniformity under a microscope.

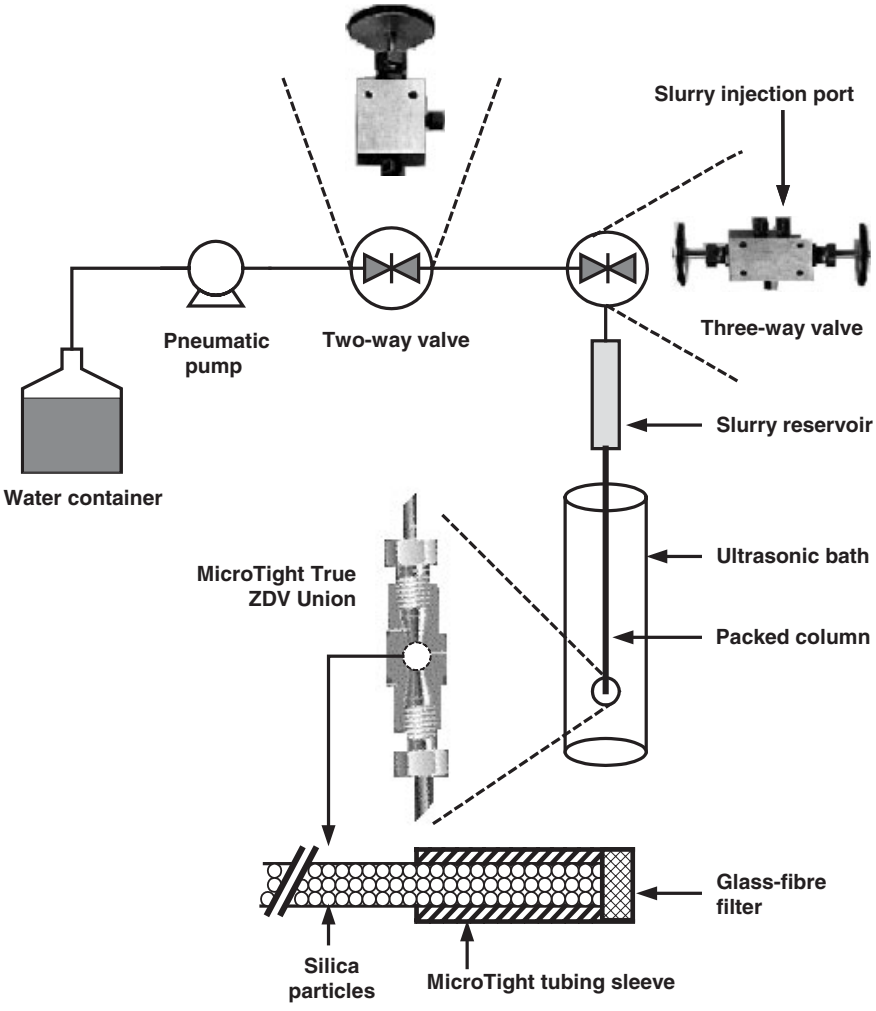

Figure 4. Schematics of the experimental setup implemented for packing the cylindrical (fused-silica) capillary columns with particulate stationary phase material.

Then, the packed capillary was again flushed with water for 45 min. At a pressure slightly higher than used for the packing, permanent inlet and outlet frits for the bed were made by sintering the silica particles for 350 ms with an arc fusion splicer FSM-05S (Fujikura, Tokyo, Japan) in its prefusion mode. Pressure was released to 200 bar, the MicroTight union disconnected from the column, and the remainder of the particles were flushed out with water. The detection window was prepared by scraping off some of the polyimide-coating 2 mm immediately downstream of the outlet frit. Protocols for column packing and frit sintering were optimized with respect to the pore-sizes of a material in order to produce packed beds of uncrushed wide-pore particles. For example, a packing pressure of 350, 300, and 250 bar was selected for particles with 40, 120, and 220 nm mean pore size, respectively, while for the nonporous silica particles 400 bar were used. Packed columns were preconditioned electrokinetically by applying a voltage of 5 kV for 5 min, a voltage ramp up to 20 kV within 20 min, and a constant voltage of 20 kV for another 20 min. When changing between mobile phases, the capillaries were also conditioned

electrokinetically by applying a voltage ramp up to 20 kV within 20 min, and a constant voltage of 20 kV for another 20 min.

2.3 Hardware Configuration

CEC experiments at a controlled temperature of 298 K with electrical potential gradients between both ends of a capillary setup of up to 30 kV were performed in a HP^{3D}CE instrument (Hewlett-Packard, Waldbronn, Germany) equipped with a diode array detector that was operated at 215 nm. An external helium pressure of 10 bar was applied on inlet and outlet mobile phase vials for minimizing bubble formation. Samples were injected electrokinetically (3 kV for 3 s). EOF velocities were calculated using the actual potential drop over the bed and residence time distributions of an unretained, uncharged flow field marker (thiourea), which is transported through the column by molecular diffusion and the EOF. HPLC experiments were carried out using a capillary liquid chromatography setup containing the MicroPro^{TM} syringe pumping system (Eldex Laboratories Inc., Napa, CA) and a SpectraFlow 501 UV/VIS-detector (SunChrom, Friedrichsdorf, Germany) operated at 215 nm. This pump allows practicable flow rates from 200 μL/min down to 10 nL/min in isocratic and down to 1 μL/min in gradient elution mode without split. Mixing is provided by a (85 μL or 15 μL) dynamic mixer or, for the lower microliter flow rates, by (≤ 5 μL) static mixers [11].

2.4 Mobile Phase Composition

Tris(hydroxymethyl)aminomethane (Tris) buffer solutions in 80:20 acetonitrile/water (v/v) were used as the liquid electrolyte. Mobile phases were generally filtered over a 0.45 μm nylon membrane filter and degassed by ultrasonication. An aqueous stock solution of 0.2 M Tris (base form) was prepared using water purified on a Milli-Q-Gradient (Millipore GmbH, Eschborn, Germany). The pH was adjusted to 8.3 by titration with concentrated hydrochloric acid. Appropriate volumes of this stock solution, MilliQ water, and HPLC grade acetonitrile were mixed to yield Tris buffer solutions of the desired ionic strength in 80:20 acetonitrile/water (v/v) covering the range from 1×10^{-4}–4×10^{-2} M effective Tris concentration, e.g., 2×10^{-3} M Tris in the final electrolyte corresponds to 0.01 M Tris in the aqueous part. The concentration of protonated Tris (acid form) needed for estimating the EDL thickness by means of λ_D (Eq. (3)) was calculated from the Henderson-Hasselbalch equation in which pH ≈ pK_a. The relative permittivity (ε_r) and viscosity (η_f) at 298 K of the final mobile phases were taken as 44.53 and 5.03×10^{-4} kgm^{-1}s^{-1}, respectively [101]. When needed, the mobile phase diffusivity (D_m) of an analyte was calculated according to the Wilke-Chang equation [102].

2.5 Sample Properties

Thiourea, tris(hydroxymethyl)aminomethane (Tris) and hydrochloric acid of analytical grade, as well as HPLC grade acetonitrile were purchased from Fluka (Sigma-Aldrich Chemie GmbH, Taufkirchen, Germany). The alkylbenzoates all came from Merck KGaA (Darmstadt, Germany). Under the conditions encountered in this work the analyte concentration remained within the linear range of the adsorption isotherm and, generally, the sample was prepared in running mobile phase. Only a few experimental studies of preparative electrochromatographic separations have been published to date [103–106]. Uncharged analytes were selected because the transport behavior of a charged molecule would be complicated further by its electrophoretic migration and possible effects originating from a coupling of the charge adsorption with the local electrokinetics [107]. This issue becomes even more complex when analyte and surface groups (relevant for EOF) are involved in pH-dependent equilibria [108].

3 Results and Discussion

3.1 Influence of Intraparticle Pore Size on Separation Efficiency

The equilibrium-dispersive model of chromatography [102] assumes that mobile and stationary phases are constantly in equilibrium, and that contributions to dispersion including kinetic effects like mass transfer resistances and finite adsorption/desorption kinetics can be combined together in an apparent axial dispersion coefficient (D_{ax}). Then, from the variance of a Gaussian peak in linear chromatography D_{ax} is calculated by:

$$D_{ax} = \frac{H\, u_{av}}{2} = \frac{L_{bed}\, u_{av}}{2N} \tag{8}$$

The effect of mean intraparticle pore size on the separation efficiency in CEC was studied by monitoring the axial dispersivity's, D_{ax}/D_m, dependence on the particle Peclet number Pe for C18-silica particles with a different mean pore diameter (see Tab. 2). Fig. 5 shows that D_{ax}/D_m at constant Pe decreases with the pore diameter (41, 105, and 232 nm).

At the same time, the increase in D_{ax}/D_m with Pe (indicative of stagnant mobile phase mass transfer resistance and flow heterogeneity) is smaller for the material with wider pores, and the regime in which axial molecular diffusion controls the dispersion ($D_{ax}/D_m < 1$) can extend to higher Pe. The EDL thickness remained constant in this series of experiments (with λ_D around 10 nm, Eq. (3)).

The observed behavior (see Fig. 5) can be attributed to electroosmotic perfusion. According to classical HPLC theory, diffusion-limited mass transfer inside the stationary phase particles and mechanical dispersion in the surrounding (dif-

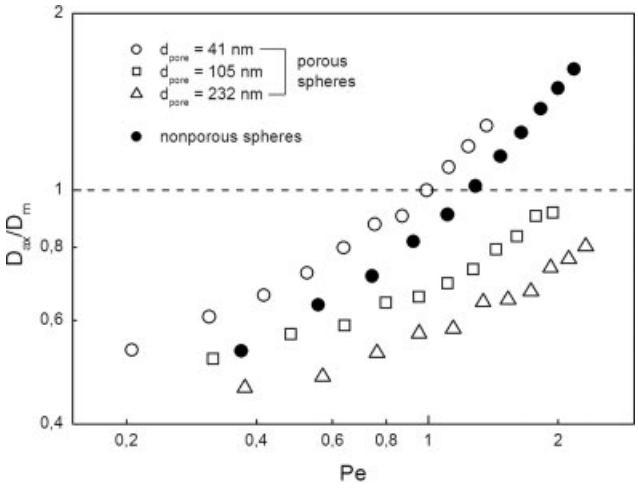

Figure 5. Effect of the mean intraparticle pore size on D_{ax}/D_m vs. particle Peclet number $Pe = u_{av}d_p/D_m$ (EOF) for methylbenzoate. Packed beds: 240 mm long consisting of the different particles. The mobile phase is acetonitrile-Tris (pH 8.3) 80:20 (v/v) with an effective Tris concentration of 10^{-3} M.

fusive-convective) mobile phase become the main sources of band spreading at increasing velocities [82,109]. It has been shown that with hydraulic flow the holdup due to intraparticle stagnant fluid starts to dominate hydrodynamic dispersion in random packings of porous particles at a Pe above about 25 [110]. Electroosmotic intraparticle convection reduces this mass transfer resistance, and wider pores (at constant λ_D) further suppress EDL overlap, which, in turn, produces stronger EOF inside the particle. When ultimately the velocity inside a particle equals that outside, there will be no contribution from this mass transfer resistance to the overall separation efficiency, and axial dispersion due to the nonuniformity of the flow velocity distribution over the whole column cross-section will be substantially reduced [111]. It should also be noted that D_{ax}/D_m (for particles with larger pore diameters, 105 and 232 nm) is smaller than for the nonporous (or solid) particles. From the standpoint of efficiency, the nonporous particles are ideal in that they eliminate the intraparticle stagnant mobile phase [83,112,113], whereas for the nonporous particles, the mechanical or eddy dispersion dominates band spreading over a wide range of Pe. From the comparison between these wide-pore and nonporous particles (see Fig. 5) it can be concluded that a more homogeneous column cross-sectional flow velocity distribution (including the particle-scale) is reached in perfusive electrochromatography. This contrasts with HPLC where nonporous particles result in higher efficiencies than porous ones. It may be explained via an analogy that substantial intraparticle EOF reduces the hydrodynamically effective particle diameter of the wide-pore packings well below that of the nonporous spheres, although (from a physical point of view) both solid and permeable spheres have almost the same mean diameter, as shown by Tab. 2.

3.2 Effect of Mobile Phase Ionic Strength on Separation Efficiency

As an alternative to the adjustment of mean pore size the mobile phase ionic strength (now at constant pore size) can be varied to systematically tune an intraparticle EDL overlap represented by r_{pore}/λ_D. The range of values realized for this characteristic ratio in the present work for the different particles and mobile phase concentrations of Tris buffer is summarized in Tab. 2. Fig. 6 demonstrates that the dispersion obtained with pressure-driven flow is much higher (by up to a factor of 5) than for EOF with any ionic strength through a capillary packed with the same wide-pore particles (d_{pore} = 105 nm).

Due to the dominating effect of intraparticle EDL overlap-suppression at increased Tris concentration intraparticle EOF is enhanced. It results in a higher pore-to-interstitial flow ratio. Thus, increasing intraparticle EOF improves flow homogeneity over the column cross-section and decreases mass transfer resistance in the mobile and stationary phases [54,111].

Although qualitatively sound, it becomes difficult to relate this improvement quantitatively to the electroosmotic perfusion mechanism because dispersion coefficients in CEC are, inherently, only acquired over a limited range of Pe. This results from the relatively small particle diameter (d_p = 2.45 μm) and limitations in maximum electrical field strength (and current) due to Joule heating [18]. In turn, the results appear insufficient to allow an adequate separation based on the scaling of D_{ax}/D_m with Pe between dispersion processes that originate in the flowing and stagnant zones of a bed [109,114–116]. For example, it is well-known that for pressure-driven flow stochastic velocity fluctuations between

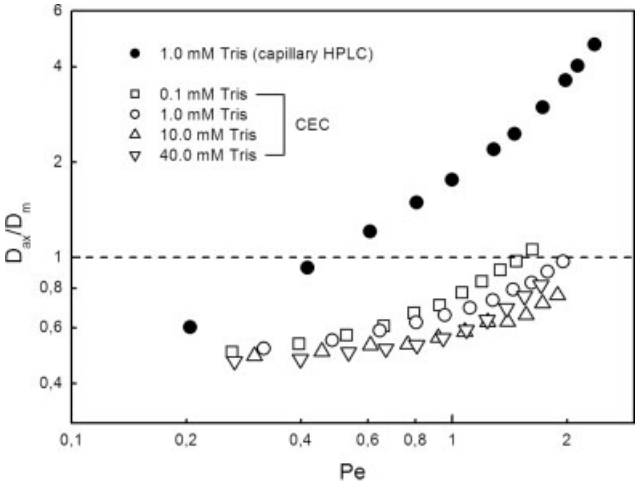

Figure 6. Effect of the Tris buffer concentration on D_{ax}/D_m of methylbenzoate vs. $Pe = u_{av}d_p/D_m$. CEC: 325 mm long column setup (240 mm bed length), bed of porous C18-silica-particles with d_p = 2.45 μm and d_{pore} = 105 nm. Mobile phase: acetonitrile-Tris (pH 8.3) 80:20 (v/v). For capillary HPLC: 150 mm long × 100 μm i.d. column (140 mm bed). The ionic strength of the electrolyte solution corresponds to half of the actual Tris concentration.

the particles cause mechanical dispersion, which grows linearly with Pe, while regions of zero velocity inside a particle and close to its external surface cause non-mechanical contributions growing as Pe^2 (holdup dispersion) and Pe·ln(Pe) (boundary-layer dispersion), respectively [115].

It needs further study to resolve the coexistence and relative importance of these contributions in CEC over a wide range of conditions, which determine the dependence of D_{ax}/D_m on Pe, like the distribution of pore sizes and EDL overlap, pore geometry and interconnectivity, the fractal nature and chemical heterogeneity of a surface, dissociation equilibria of both the analyte and surface groups, type of buffer, specific adsorption, charge of analyte, retention mechanism, or the coupling of a nonlinear adsorption with the local electrokinetics. In this respect, selective techniques like spectroscopic imaging methods, which allow for a focus on particular mechanical or nonmechanical contributions to dispersion, are promising approaches in resolving combined kinetics and thermodynamics [55,80,117–120]. For example, by using quantitative confocal laser scanning microscopy in combination with a microfluidic device it has been visualized that electrokinetic species transport through a fixed bed of spheres produces, in striking contrast to the symmetric-spherical distributions observed for diffusion-limited operations, pronounced asymmetric intraparticle concentration profiles caused by the unidirectional nature of electroosmosis and electrophoresis [119,120]. Quantitative image analysis permitted a direct determination of the velocities of intraparticle EOF and electrophoretic migration.

Results based on such experimental approaches corroborate data of the kind shown in Fig. 6 in that they provide EOF velocities and electrophoretic mobilities underlying macroscopic behavior and any improvement in separation efficiency. As also shown by Fig. 6, the reduction of particle size, which accompanies to some extent general miniaturization, together with limitations in maximum velocity (possibly due to hardware considerations, temperature effects, or particle surface properties) places the hydrodynamics in a regime characterized by low Reynolds and Peclet numbers where most kinetic processes are diffusion-controlled. For example, in contrast to hydraulic flow the dispersion data acquired with EOF hardly leave the tortuosity-limited regime where molecular diffusion in the tortuous pore space dominates the overall dispersion (see Fig. 6, $D_{ax}/D_m < 1$). The fact that an increased dispersion for the highest effective Tris concentration of 40 mM was found within the series of ionic strengths is explained by the actual power dissipation in the packed bed leading to development of Joule heat [121]. In the absence of Joule heating (and other nonlinear effects) the conductivity of an electrolyte solution is a constant and the current varies linearly with the applied field. As demonstrated in Fig. 7, the temperature increase associated with insufficient heat dissipation manifests itself in nonlinear Ohm plots, and deviation from linearity is most pronounced for the highest ionic strength.

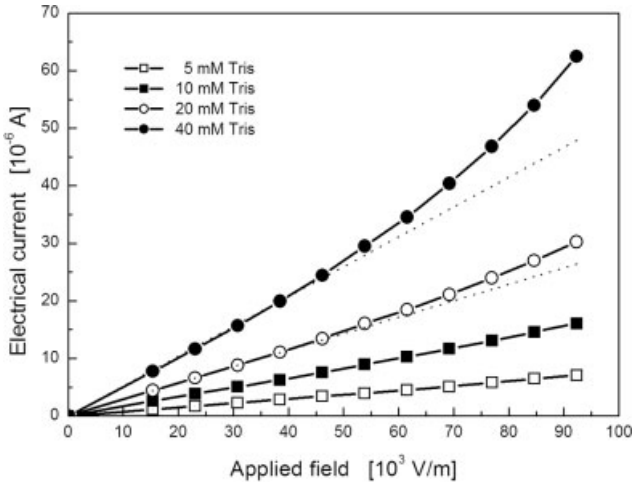

Figure 7. Ohm plots for a 100 μm i.d. packed capillary (d_p = 2.45 μm, d_{pore} = 105 nm). Mobile phase: acetonitrile-Tris (pH 8.3) 80:20 (v/v) with different effective concentrations.

This effect causes an uncorrected increase of the analytes diffusion coefficient in the bed, which, because the dispersion data are acquired in the diffusion-limited regime, is seen in higher dispersivities. The radial temperature profile is usually not strong enough to engender additional significant dispersion due to macroscopic flow heterogeneity [37,122].

3.3 Effect of Ionic Strength on Average EOF Velocity

In close relation to the dispersion data (see Fig. 6) the associated flow behavior is seen in Fig. 8, i.e., the dependence of the average EOF velocity through the bed on the effective Tris concentration in the mobile phase.

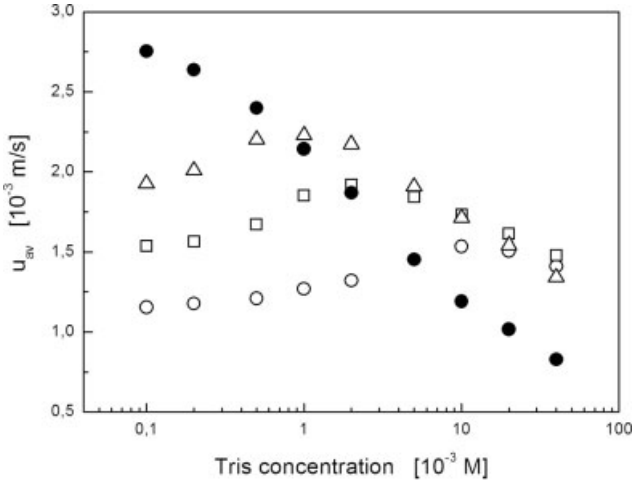

Figure 8. Effect of mobile phase Tris concentration on the average EOF through packed beds of the C18-silica particles (applied voltage: 20 kV). Nonporous particles (●), porous particles: d_{pore} = 41 nm (○), d_{pore} = 105 nm (□), and d_{pore} = 232 nm (△).

The actual ionic strength is given by:

$$I = \frac{1}{2}\sum_i z_i^2 c_{i,\infty} \quad (9)$$

In relation to this work this corresponds to half of the Tris concentration. Another important relation is that between the ionic strength and the ζ-potential, which, for a locally flat surface and (sufficiently) low values of ζ, may be approximated as [123]:

$$\zeta = \frac{\sigma_s \lambda_D}{\varepsilon_0 \varepsilon_r} = \sigma_s \left(\frac{RT}{2F^2 \varepsilon_0 \varepsilon_r I} \right)^{1/2} \quad (10)$$

where σ_s represents surface charge density insofar as it corresponds with opposite sign to the total (fluid-side) excess charge density up to the surface where the shear plane is located. As seen in Fig. 8, the average EOF for nonporous (impermeable and nonconducting) particles reveals a normal electrokinetic behavior [63], i.e., as the ionic strength increases the EDL is compressed, which results in a reduced shear plane (ζ) potential at the solid-liquid interface (Eq. (10)) and causes the continuously decreasing EOF velocities. The EDL thickness remained small with respect to a particle radius (r_s) over the whole range of buffer concentrations ($38 < r_s/\lambda_D < 766$). Thus, EDL overlap in the interparticle pore space (although already moderate at lower ionic strength) was not significant enough to dominate the electrokinetic behavior and lead to an intermediate increase of the EOF velocity with ionic strength. The behavior of the solid particles can thus be understood in view of Eq. (10).

This situation is different for the porous (permeable and conducting) particles. Before (cf. Fig. 8) the velocity finally decreases with increasing ionic strength, it displays pronounced maxima. This behavior is due to the significant suppression of intraparticle EDL overlap (leading to an increase of intraparticle EOF), which causes the average EOF through a bed to increase intermediately. The dependence of average EOF velocity with porous particles on ionic strength (see Fig. 8) is in principle a consequence of the following contributions [122–127]:

i. usual EDL behavior at the external particle surface leading to a decrease in velocity with increasing ionic strength,
ii. the generation of intraparticle EOF, which increases with ionic strength, and
iii. particle porosity (independent of ionic strength).

The last contribution results from the fact that conducting electrolyte in the particle introduces a normal component to the electrical field at its outer surface. This reduces the fields tangential component, but because the latter determines velocity at the particles external surface it is expected to decrease compared to a solid particle the more the porosity increases [125]. While the first contribution dominates overall velocities at higher ionic strengths (above 1×10^{-2} M Tris, see Fig. 8), the perfusive EOF is responsible for an increased velocity at lower ionic strengths. Similar behavior has been observed for porous particles when subjected to an electrophoresis experiment [127]. Based on previously measured porosimetry data for porous particles, simple cylindrical capillary models of a packed bed, together with the approximate expressions of Rice and Whitehead [35] for single-pore EOF, have already successfully explained relative magnitudes of intraparticle and interparticle EOF depending on EDL overlap inside the particles [52,128].

4 Conclusions

The data demonstrate that a tremendous performance advantage of CEC over capillary HPLC lies in the different dimension and experimental realization of a substantially perfusive flow field. Development in CEC particle technology, therefore, should focus on the minimum mean pore size of the throughpore network, which still allows a significant intraparticle EOF at decent mobile phase ionic strength, while keeping the surface-to-volume ratio of a medium high enough for separations of complex mixtures (gigapores, as with pressure-driven flow, are not required in an electroosmotic perfusion). With CEC in perfusive mode the fluid in most of the pore space is no longer stagnant and the system has the characteristics of a bed composed of much smaller, essentially nonporous particles being ideal from the standpoint of efficiency. CEC can then easily be realized in effective nanoparticle dimensions, but by employing porous supports of micrometer-size. This, in turn, leaves molecular diffusion as an ultimate limitation to performance (as shown in this work). Thus, the perfusive EOF field in fixed beds of porous particles translates to an even higher separation efficiency than currently achieved in CEC using narrow-pore supports or nonporous particles, an increased mass sensitivity in on-line coupling schemes like nano-ESI-MS, and, due to the higher hydraulic permeability of beds of micron-sized particles, the possibility of implementing pressurized CEC in view of a higher analysis speed, flow stability and reproducibility, but without much increase in dispersion. Further, the practical problems associated with direct nanoparticle packing like clogging or the generation of instable beds are then avoided.

Acknowledgements

We are grateful to Dieter Lubda from Merck KGaA (Darmstadt, Germany) for the preparation of the C18-silica particle research samples. We further acknowledge financial support from the Landesgraduiertenförderung Sachsen-Anhalt (Germany) to Guofang Chen. Martin Pačes was supported by the Czech grant agency under grant 104/02/0339, and we are also grateful to the Deutsche Forschungsgemeinschaft for financial support of this work (grant SE 586/7–2).

Received: September 26, 2003 [CET 1939]

Symbols used

$c_{i,\infty}$	[mol L^{-1}]	equilibrium concentration of type i ions beyond the EDL
d_c	[m]	column inner diameter
d_{pore}	[m]	mean intraparticle pore diameter
d_p	[m]	mean particle diameter
D_{ax}	[m^2 s^{-1}]	axial dispersion coefficient
D_m	[m^2 s^{-1}]	free molecular diffusion coefficient of analyte in mobile phase
E	[V m^{-1}]	electrical field strength
F	[C mol^{-1}]	Faraday constant
H	[m]	height equivalent to a theoretical plate
I	[mol L^{-1}]	mobile phase ionic strength
L_{bed}	[m]	length of the packed bed
N	[–]	plate number
Pe	[–]	particle Peclet number
R	[J $mol^{-1}K^{-1}$]	gas constant
u_{av}	[m s^{-1}]	average mobile phase velocity through the packed column
u_p	[m s^{-1}]	local EOF (slip) velocity close to a particles surface
V_c	[m^3]	total column volume
V_{inter}	[m^3]	volume of the interparticle pore space
ε_0	[$C^2J^{-1}m^{-1}$]	permittivity of vacuum
ε_{intra}	[–]	intraparticle porosity
ε_r	[–]	relative permittivity of the electrolyte solution
ε_{bed}	[–]	total porosity of packed column
η_f	[Pa s]	dynamic viscosity of the mobile phase
λ_D	[m]	Debye screening length
ζ_p	[V]	Zeta potential at a particle surface
ζ_w	[V]	Zeta potential at the capillary inner wall

References

[1] C. Horváth, B. A. Preiss, S. R. Lipsky, *Anal. Chem.* **1967**, *39*, 1422.
[2] C. Horváth, S. R. Lipsky, *Anal. Chem.* **1969**, *41*, 1227.
[3] R. P. W. Scott, P. Kucera, *J. Chromatogr.* **1976**, *125*, 251.
[4] D. Ishii, K. Asai, K. Hibi, T. Jonokuchi, M. Nagaya, *J. Chromatogr.* **1977**, *144*, 157.
[5] D. Ishii, *Introduction to Microscale High-Performance Liquid Chromatography*, VCH, Weinheim **1988**.
[6] J. P. C. Vissers, H. A. Claessens, C. A. Cramers, *J. Chromatogr., A* **1997**, *779*, 1.
[7] J. P. C. Vissers, *J. Chromatogr., A* **1999**, *856*, 117.
[8] J. Abian, A. J. Oosterkamp, E. Gelpi, *J. Mass Spectrom.* **1999**, *34*, 244.
[9] G. P. Rozing, M. Serwe, H.-G. Weissgerber, B. Glatz, *Am. Lab.* **2001**, *33*, 26.
[10] M. Szumski, B. Buszewski, *Crit. Rev. Anal. Chem.* **2002**, *32*, 1.
[11] E. Rapp, U. Tallarek, *J. Sep. Sci.* **2003**, *26*, 453.
[12] R. F. Probstein, R. E. Hicks, *Science* **1993**, *260*, 498.
[13] J. E. Sauer, E. J. Davis, *Environ. Sci. Technol.* **1994**, *28*, 737.
[14] M. M. Dittmann, K. Wienand, F. Bek, G. P. Rozing, *LC-GC North. Am.* **1995**, *13*, 800.
[15] S. V. Ho, P. W. Sheridan, C. J. Athmer, M. A. Heitkamp, J. M. Brackin, D. Weber, P. H. Brodsky, *Environ. Sci. Technol.* **1995**, *29*, 2528.
[16] T. Tsuda, *Electric Field Applications in Chromatography, Industrial and Chemical Processes*, VCH, Weinheim **1995**.
[17] Y. B. Acar, E. E. Ozsu, A. N. Alshawabkeh, M. F. Rabbi, R. J. Gale, *Chem. Tech.* **1996**, *26*, 40.
[18] A. L. Crego, A. González, M. L. Marina, *Crit. Rev. Anal. Chem.* **1996**, *26*, 261.
[19] T. F. Coletta, C. J. Brunell, D. K. Ryan, H. I. Inyang, *J. Environ. Eng.* **1997**, *123*, 1227.
[20] C. Fujimoto, *Trends Anal. Chem.* **1999**, *18*, 291.
[21] L. A. Colón, G. Burgos, T. D. Maloney, J. M. Cintrón, R. L. Rodríguez, *Electrophoresis* **2000**, *21*, 3965.
[22] U. Pyell, *J. Chromatogr., A* **2000**, *892*, 257.
[23] Q. L. Tang, M. L. Lee, *Trends Anal. Chem.* **2000**, *19*, 648.
[24] N. A. Polson, M. A. Hayes, *Anal. Chem.* **2001**, *73*, 312A.
[25] Z. Deyl, F. Svec, *J. Chromatogr. Libr.* **2001**, *62*.
[26] A. S. Rathore, *Electrophoresis* **2002**, *23*, 3827.
[27] K. Mistry, I. Krull, N. Grinberg, *J. Sep. Sci.* **2002**, *25*, 935.
[28] *Interfacial Electrokinetics and Electrophoresis* (Ed: A. V. Delgado), Marcel Dekker, New York **2002**.
[29] T. Tsuda, *Anal. Chem.* **1987**, *59*, 521.
[30] V. Pretorius, B. J. Hopkins, J. D. Schieke, *J. Chromatogr.* **1974**, *99*, 23.
[31] J. W. Jorgenson, K. D. Lukacs, *J. Chromatogr.* **1981**, *218*, 209.
[32] J. H. Knox, I. H. Grant, *Chromatographia* **1987**, *24*, 135.
[33] J. H. Knox, *Chromatographia* **1988**, *26*, 329.
[34] J. H. Knox, I. H. Grant, *Chromatographia* **1991**, *32*, 317.
[35] C. L. Rice, R. Whitehead, *J. Phys. Chem.* **1965**, *69*, 4017.
[36] R. J. Gross, J. F. Osterle, *J. Chem. Phys.* **1968**, *48*, 228.
[37] K.-L. K. Liu, K. L. Davis, M. D. Morris, *Anal. Chem.* **1994**, *66*, 3744.
[38] S. Arulanandam, D. Q. Li, *Colloids Surf., A* **2000**, *161*, 89.
[39] R. F. Probstein, *Physicochemical Hydrodynamics*, John Wiley & Sons, New York **1994**.
[40] P. H. Paul, M. G. Garguilo, D. J. Rakestraw, *Anal. Chem.* **1998**, *70*, 2459.
[41] U. Tallarek, E. Rapp, T. Scheenen, E. Bayer, H. Van As, *Anal. Chem.* **2000**, *72*, 2292.
[42] K. K. Unger, S. Lüdtke, M. Grün, *LC-GC* **1999**, *12*, 870.
[43] K. K. Unger, D. Kumar, M. Grün, D. Büchel, et al., *J. Chromatogr., A* **2000**, *892*, 47.
[44] T. Sakaki, S. Kitagawa, T. Tsuda, *Electrophoresis* **2000**, *21*, 3088.
[45] J. P. Kutter, S. C. Jacobson, N. Matsubara, J. M. Ramsey, *Anal. Chem.* **1998**, *70*, 3291.
[46] C. Ericson, J. Holm, T. Ericson, S. Hjerten, *Anal. Chem.* **2000**, *72*, 81.
[47] R. D. Oleschuk, L. L. Schultz-Lockyear, Y. B. Ning, D. J. Harrison, *Anal. Chem.* **2000**, *72*, 585.
[48] B. E. Slentz, N. A. Penner, E. Lugowska, F. E. Regnier, *Electrophoresis* **2001**, *22*, 3763.
[49] D. J. Throckmorton, T. J. Shepodd, A. K. Singh, *Anal. Chem.* **2002**, *74*, 784.
[50] R. Stol, W. T. Kok, H. Poppe, *J. Chromatogr., A* **1999**, *853*, 45.
[51] E. Wen, R. Asiaie, Cs. Horváth, *J. Chromatogr., A* **1999**, *855*, 349.
[52] P. T. Vallano, V. T. Remcho, *Anal. Chem.* **2000**, *72*, 4255.
[53] U. Tallarek, E. Rapp, H. Van As, E. Bayer, *Angew. Chem. Int. Ed.* **2001**, *40*, 1684.
[54] R. Stol, H. Poppe, W. T. Kok, *Anal. Chem.* **2001**, *73*, 3332.
[55] U. Tallarek, E. Rapp, A. Seidel-Morgenstern, H. Van As, *J. Phys. Chem., B* **2002**, *106*, 12709.
[56] R. Xiang, Cs. Horváth, *Anal. Chem.* **2002**, *74*, 762.
[57] S. R. Dziennik, E. B. Belcher, G. A. Barker, M. J. DeBergalis, S. E. Fernandez, A. M. Lenhoff, *Proc. Natl. Acad. Sci. U.S.A.* **2003**, *100*, 420.
[58] A. S. Rathore, C. Horváth, *J. Chromatogr., A* **1997**, *781*, 185.
[59] M. von Smoluchowski, in *Handbuch der Elektrizität und des Magnetismus* (Ed: I. Grätz), Barth, Leipzig **1921**, 366.
[60] J. T. G. Overbeek, in *Colloid Science* (Ed. H. R. Kruyt), Elsevier, New York **1952**, 194.
[61] R. W. O'Brien, *J. Colloid Interface Sci.* **1986**, *110*, 477.
[62] J. T. G. Overbeek, P. W. O. Wijga, *Rec. Trav. Chim.* **1946**, *65*, 556.
[63] J. Lyklema, *Fundamentals of Interface and Colloid Science*, Vol. II: Solid-Liquid Interfaces; Academic Press, London **1995**.
[64] L. A. Colón, K. J. Reynolds, R. Alicea-Maldonado, A. M. Fermier, *Electrophoresis* **1997**, *18*, 2162.
[65] O. Bey, G. Eigenberger, *Chem. Eng. Sci.* **1997**, *52*, 1365.
[66] M. Giese, K. Rottschäfer, D. Vortmeyer, *AIChE J.* **1998**, *44*, 484.
[67] A. J. Sederman, P. Alexander, L. F. Gladden, *Powder Technol.* **2001**, *117*, 255.
[68] J. C. Park, K. Raghavan, S. J. Gibbs, *J. Chromatogr., A* **2002**, *945*, 65.
[69] T. C. Hsiang, H. W. Haynes, Jr., *Chem. Eng. Sci.* **1977**, *32*, 678.
[70] H. Martin, *Chem. Eng. Sci.* **1978**, *33*, 913.
[71] R. G. Carbonell, *Chem. Eng. Sci.* **1980**, *35*, 1347.
[72] E. Tsotsas, E.-U. Schlünder, *Chem. Eng. Process.* **1988**, *24*, 15.
[73] B.-J. Ahn, A. Zoulalian, J. M. Smith, *AIChE J.* **1986**, *32*, 170.
[74] E. Tsotsas, Über die Wärme- und Stoffübertragung in durchströmten Festbetten, *Fortschr.-Ber. VDI, Reihe 19* **1990**, *3 (223)*.

[75] A. I. Liapis, B. A. Grimes, *J. Chromatogr., A* **2000**, *877*, 181.
[76] G. Neale, N. Epstein, W. Nader, *Chem. Eng. Sci.* **1973**, *28*, 1865.
[77] G. Choudhary, C. Horváth, *J. Chromatogr., A* **1997**, *781*, 161.
[78] A. S. Rathore, E. Wen, C. Horváth, *Anal. Chem.* **1999**, *71*, 2633.
[79] Y. Liu, D. J. Pietrzyk, *Anal. Chem.* **2000**, *72*, 5930.
[80] U. Tallarek, T. W. J. Scheenen, H. Van As, *J. Phys. Chem., B* **2001**, *105*, 8591.
[81] J. J. Van Deemter, F. J. Zuiderweg, A. Klinkenberg, *Chem. Eng. Sci.* **1956**, *5*, 271.
[82] J. C. Giddings, *Dynamics of Chromatography*, Part I: Principles and Theory, Marcel Dekker, New York **1965**.
[83] B. J. Kennedy, J. H. Knox, *J. Chromatogr. Sci.* **1985**, *10*, 549.
[84] M. E. van Kreveld, N. Van den Hoed, *J. Chromatogr.* **1978**, *149*, 71.
[85] N. B. Afeyan, N. F. Gordon, I. Mazsaroff, L. Varady, S. P. Fulton, Y. B. Yang, F. E. Regnier, *J. Chromatogr.* **1990**, *519*, 1.
[86] A. E. Rodrigues, Z. P. Lu, J. M. Loureiro, *Chem. Eng. Sci.* **1991**, *46*, 2765.
[87] A. I. Liapis, M. A. McCoy, *J. Chromatogr.* **1992**, *599*, 87.
[88] A. E. Rodrigues, J. C. Lopes, Z. P. Lu, J. M. Loureiro, M. M. Dias, *J. Chromatogr.* **1992**, *590*, 93.
[89] G. Carta, M. E. Gregory, D. J. Kirwan, H. A. Massaldi, *Sep. Technol.* **1992**, *2*, 62.
[90] D. D. Frey, E. Schweinheim, C. Horváth, *Biotechnol. Prog.* **1993**, *9*, 273.
[91] P.-E. Gustavsson, P.-O. Larsson, *J. Chromatogr., A* **1996**, *734*, 231.
[92] M. McCoy, K. Kalghatgi, F. E. Regnier, N. Afeyan, *J. Chromatogr., A* **1996**, *743*, 221.
[93] D. C. Nash, H. A. Chase, *J. Chromatogr., A* **1998**, *807*, 185.
[94] J. F. Pfeiffer, J. C. Chen, J. T. Hsu, *AIChE J.* **1996**, *42*, 932.
[95] U. Tallarek, F. J. Vergeldt, H. Van As, *J. Phys. Chem., B* **1999**, *103*, 7654.
[96] D. H. Reeder, A. M. Clausen, M. J. Annen, P. W. Carr, M. C. Flickinger, A. V. McCormick, *J. Colloid Interface Sci.* **1996**, *184*, 328.
[97] D. Whitney, M. McCoy, N. Gordon, N. Afeyan, *J. Chromatogr., A* **1998**, *807*, 165.
[98] E. Venema, J. C. Kraak, H. Poppe, R. Tijssen, *J. Chromatogr., A* **1999**, *837*, 3.
[99] P. T. Vallano, V. T. Remcho, *J. Phys. Chem., B* **2001**, *105*, 3223.
[100] U. D. Neue, *HPLC Columns: Theory, Technology, and Practice*, Wiley-VCH, New York **1997**.
[101] A. Banholczer, U. Pyell, *J. Chromatogr., A* **2000**, *869*, 363.
[102] G. Guiochon, S. G. Shirazi, A. M. Katti, *Fundamentals of Preparative and Nonlinear Chromatography*, Academic Press, Boston **1994**.
[103] K. D. Cole, H. Cabezas Jr., *J. Chromatogr., A* **1997**, *760*, 259.
[104] C. Keim, M. Ladisch, *Biotechnol. Bioeng.* **2000**, *70*, 72.
[105] C. M. Tellez, K. D. Cole, *Electrophoresis* **2000**, *21*, 1001.
[106] G. Yin, Z. Liu, R. Zhou, J. Zhan, J. Wang, N. J. Yuan, *J. Chromatogr., A* **2001**, *918*, 393.
[107] M. Pačes, J. Kosek, M. Marek, U. Tallarek, A. Seidel-Morgenstern, *Electrophoresis* **2003**, *24*, 380.
[108] M. Pačes, U. Tallarek, A. Seidel-Morgenstern, J. Kosek, M. Marek, in *Proc. of the 1st Int. Symp. on Process Intensification and Miniaturization* (Eds: G. Akay, M. Dogru), University of Newcastle **2003**.
[109] J. H. Knox, *J. Chromatogr., A* **1999**, *831*, 3.
[110] D. Kandhai, D. Hlushkou, A. G. Hoekstra, P. M. A. Sloot, H. Van As, U. Tallarek, *Phys. Rev. Lett.* **2002**, *88*, art. no. 234501.
[111] H. Poppe, R. Stol, W. T. Kok, *J. Chromatogr., A* **2002**, *965*, 75.
[112] Y. L. Yang, M. L. Lee, *J. Microcol. Sep.* **1999**, *11*, 131.
[113] S. R. Witowski, R. T. Kennedy, *J. Microcol. Sep.* **1999**, *11*, 723.
[114] D. L. Koch, J. F. Brady, *J. Fluid Mech.* **1985**, *154*, 399.
[115] M. Sahimi, *Flow and Transport in Porous Media and Fractured Rock*, VCH, Weinheim **1995**.
[116] U. Tallarek, E. Bayer, G. Guiochon, *J. Am. Chem. Soc.* **1998**, *120*, 1494.
[117] U. Tallarek, T. W. J. Scheenen, P. A. de Jager, H. Van As, *Magn. Reson. Imag.* **2001**, *19*, 453.
[118] B. R. Locke, M. Acton, S. J. Gibbs, *Langmuir* **2001**, *17*, 6771.
[119] U. Tallarek, E. Rapp, H. Sann, U. Reichl, A. Seidel-Morgenstern, *Langmuir* **2003**, *19*, 4527.
[120] U. Tallarek, M. Pačes, E. Rapp, *Electrophoresis* **2003**, *24*, 4241.
[121] A. S. Rathore, K. J. Reynolds, L. A. Colón, *Electrophoresis* **2002**, *23*, 2918.
[122] J. H. Knox, K. A. McCormack, *Chromatographia* **1994**, *38*, 207.
[123] A. W. Adamson, A. P. Gast, *Physical Chemistry of Surfaces*, John Wiley & Sons, New York **1997**.
[124] S. Levine, G. H. Neale, *J. Colloid Interface Sci.* **1974**, *47*, 520.
[125] N. P. Miller, J. C. Berg, R. W. O'Brien, *J. Colloid Interface Sci.* **1992**, *153*, 237.
[126] N. P. Miller, J. C. Berg, *J. Colloid Interface Sci.* **1993**, *159*, 253.
[127] G. Chen, U. Tallarek, *Langmuir* **2003**, *19*, 10 901.
[128] R. Stol, H. Poppe, W. T. Kok, *J. Chromatogr., A* **2000**, *887*, 199.

Anal. Chem. **2000,** *72,* 2292−2301

Electroosmotic and Pressure-Driven Flow in Open and Packed Capillaries: Velocity Distributions and Fluid Dispersion

Ulrich Tallarek,*,† Erdmann Rapp,‡ Tom Scheenen,† Ernst Bayer,‡ and Henk Van As†

Laboratory of Molecular Physics and Wageningen NMR Centre, Department of Biomolecular Sciences, Wageningen University, Dreijenlaan 3, 6703 HA Wageningen, The Netherlands, and Research Center of Nucleic Acid and Peptide Chemistry, Institute of Organic Chemistry, University of Tübingen, Auf der Morgenstelle 18, 72076 Tübingen, Germany

The flow field dynamics in open and packed segments of capillary columns has been studied by a direct motion encoding of the fluid molecules using pulsed magnetic field gradient nuclear magnetic resonance. This noninvasive method operates within a time window that allows a quantitative discrimination of electroosmotic against pressure-driven flow behavior. The inherent axial fluid flow field dispersion and characteristic length scales of either transport mode are addressed, and the results demonstrate a significant performance advantage of an electrokinetically driven mobile phase in both open-tubular and packed-bed geometries. In contrast to the parabolic velocity profile and its impact on axial dispersion characterizing laminar flow through an open cylindrical capillary, a pluglike velocity distribution of the electroosmotic flow field is revealed in capillary electrophoresis. Here, the variance of the radially averaged, axial displacement probability distributions is quantitatively explained by longitudinal molecular diffusion at the actual buffer temperature, while for Poiseuille flow, the preasymptotic regime to Taylor−Aris dispersion can be shown. Compared to creeping laminar flow through a packed bed, the increased efficiency observed in capillary electrochromatography is related to the superior characteristics of the electroosmotic flow profile over any length scale in the interstitial pore space and to the origin, spatial dimension, and hydrodynamics of the stagnant fluid on the support particles' external surface. Using the Knox equation to analyze the axial plate height data, an eddy dispersion term smaller by a factor of almost 2.5 than in capillary high-performance liquid chromatography is revealed for the electroosmotic flow field in the same column.

The actual flow pattern of a fluid undergoing slow, laminar flow in a packed bed of particles depends on the morphology (i.e., the topology and geometry) of the pore space that is available for the flow, and the existence of a point-to-point difference in flow velocity is a fundamental property of the fluid flow field under the most general conditions.[1] However, not only the inherent structural heterogeneity of the porous medium but also the actual physical origin(s) of the flow may very sensitively influence the correlation time and length which characterize velocity fluctuations in the mobile phase.

In contrast to the more conventional pressure-driven mode, capillary electrochromatography (CEC) utilizes the hydrodynamics of an electroosmotic flow (EOF) to transport solute molecules through the interconnected pore space of capillary columns packed with small adsorbent particles.[2−7] The ideal EOF in a narrow cylindrical channel should be characterized by a flat, i.e., pluglike velocity profile at distances from the surface that are of the order of the electric double-layer thickness. This intrinsic property makes the channel cross-sectional profile and magnitude of the EOF independent of the actual channel diameter, provided that the latter is significantly larger than the electric double-layer thickness.[8] The situation is in sharp contrast to the parabolic (Poiseuille) velocity profile encountered in pressure-driven flow, which directly results from the distribution of shear stress in a viscous fluid under laminar flow conditions. Further, the cross-sectional average velocity in the (cylindrical) channel here depends on the square of its diameter.

These characteristics have important implications for the eddy dispersion contribution to the overall band spreading expected in CEC and capillary high-performance liquid chromatography (CHPLC).[9] In general, eddy dispersion is caused by any velocity inequality of the flow pattern over the whole column cross section. Due to the anatomy of the available stream paths in the packed bed and local or systematic changes in packing density, fluctuations in permeability and mobile-phase velocity also exist at

* To whom correspondence should be addressed: (phone) + 31 (317) 48-2047; (fax) + 31 (317) 48-2725; (e-mail) ulrich.tallarek@water.mf.wau.nl.

† Wageningen University.

‡ University of Tübingen.

(1) Sahimi, M. *Applications of Percolation Theory*; Taylor & Francis: London, 1994.
(2) Knox, J. H.; Grant, I. H. *Chromatographia* **1987**, *24*, 135−143.
(3) Dittmann, M. M.; Wienand, K.; Bek, F.; Rozing, G. P. *LC-GC* **1995**, *13*, 800−814.
(4) Crego, A. L.; González, A.; Marina, M. L. *Crit. Rev. Anal. Chem.* **1996**, *26*, 261−304.
(5) Colón, L. A.; Reynolds, K. J.; Alicea-Maldonado, R.; Fermier, A. M. *Electrophoresis* **1997**, *18*, 2162−2174.
(6) Rathore, A. S.; Horváth, Cs. *J. Chromatogr., A* **1997**, *781*, 185−195.
(7) Colón, L. A.; Guo, Y.; Fermier, A. *Anal. Chem.* **1997**, *69*, 461A−467A.
(8) Rice, C. L.; Whitehead, R. *J. Phys. Chem.* **1965**, *69*, 4017−4024.
(9) Knox, J. H. *Chromatographia* **1988**, *26*, 329−337.

10.1021/ac991303i CCC: $19.00
Published on Web 04/12/2000

different length scales in the packing with laminar flow.[10] In addition to the convective mechanism of exchange, the time scale of lateral diffusion between the slow and fast stream paths largely governs the actual extent of band spreading.[10,11] Velocity extremes within and (on any time and length scale) between different channels in the packing may be absolutely minimized with electroosmotic flow, resulting in a much smaller eddy dispersion contribution. An improvement in efficiency by a factor of almost 2 over CHPLC has been demonstrated experimentally for CEC when carried out with the same column.[12] It was concluded that only axial diffusion constitutes the ultimate limitation to performance in CEC when achieved with nanoparticles.

Due to the high efficiencies that may be obtained with electrokinetically driven fluid flows in open tubes[13] (CE) and packed capillaries[5] (CEC), any factor influencing fluid dispersion under these hydrodynamic conditions should be well characterized and under control. The actual profile of the EOF and its stability have a large effect in improving the resolution and efficiency and certainly belong to the most important aspects controlling reproducibility.[14] Temperature effects may constitute a further source of difficulties.

The goal of our work is the development of an experimental approach toward the intrinsic fluid dynamics of capillary electroseparation techniques. In this first article, we report about a qualitative and quantitative characterization of pressure- and electrokinetically driven flows through open and packed capillaries. The discrimination is based on the respective fluid flow field and axial dispersion behavior which are both directly measured over discrete temporal and spatial domains by pulsed field gradient nuclear magnetic resonance (PFG-NMR).[15−17] A setup has been devised that allows measurements in capillary columns to be performed with a 0.5-T (^{1}H 20.35 MHz) electromagnet. Due to its open access, the presented NMR configuration offers a most flexible and convenient implementation of the CE, CHPLC, and CEC equipment, and the approach holds great promise for a fundamental study of many hydrodynamic aspects within these open tube and packed bed segments.

EXPERIMENTAL SECTION

NMR Hardware Configuration. The schematics of the setup is shown in Figure 1. ^{1}H 20.35-MHz PFG-NMR measurements were made on a 0.5-T NMR spectrometer with open access, consisting of a SMIS console (Surrey Medical Imaging Systems, Guildford, U.K.), an iron core magnet (Bruker, Karlsruhe, Germany), and a 45-mm-i.d. actively shielded gradient system (Doty Scientific, Columbia, OH) capable of producing pulsed magnetic field gradients of up to 0.5 T/m in the direction of the column axis (*y*-direction). The solenoidal radio frequency (rf) coil[18] was directly wound on a 35-mm-long, 1.57-mm-o.d. (381-μm- i.d.) PEEK tubing sleeve, which accommodates the 360-μm-o.d. (open or packed) capillary columns and which can be properly fixed within the setup (Figure 1a). For this purpose, a 300-μm-o.d. varnished copper wire was used in combination with a 200-μm-diameter Nylon strand—the latter keeping constant the distance between individual turns of the copper wire—to obtain a regular, ~11-mm-long solenoid (22 closely wound turns of the copper−nylon pair). The gradient system including the rf coil assembly can be rotated by 90° (i.e., from the *y*- into the *x*-direction, Figure 1a). This horizontal configuration was used for all CE experiments to prevent any pressure-driven flow component in the capillary due to gravity.

PFG-NMR Background. With this technique, the quantitative measurement of nuclear spin (hence, molecular) displacements over an adjustable time Δ relies on motion encoding by a pair of identical magnetic field gradients of amplitude (and direction) $\mathbf{g}$.[19] These are applied (pulsed) for a short time δ at the beginning and the end of this period Δ, respectively. The PFG-NMR time domain may cover a range for Δ from a few milliseconds up to a few seconds. Thus, several parameters of the involved fluid dynamics, e.g., dispersion in the axial and transverse direction[20−22] or the stagnant mobile-phase mass transfer,[23] can be studied in packed beds over any discrete evolution time within this range. For a PFG-NMR experiment in the narrow gradient pulse approximation ($\delta \ll \Delta$),[24] the echo signal amplitude and phase $E_\Delta(\mathbf{g})$ depend on the nuclear spin self-correlation function, $P_s(\mathbf{r}/\mathbf{r}_0,\Delta)$, which is the conditional probability that a spin initially at $\mathbf{r}_0$ has migrated to $\mathbf{r}$ over time Δ

$$E_\Delta(\mathbf{g}) = \int \rho(\mathbf{r}_0) \int P_s(\mathbf{r}/\mathbf{r}_0,\Delta) \exp[i\gamma\delta\mathbf{g}\cdot(\mathbf{r} - \mathbf{r}_0)]\, d\mathbf{r}\, d\mathbf{r}_0 \quad (1)$$

Here, $\rho(\mathbf{r}_0)$ denotes the normalized density of the initial spin positions, γ is the magnetogyric ratio of the nucleus considered (e.g., ^{1}H), and as usual, $i^2 = -1$. Introducing the concept of the dynamic displacement $\mathbf{R}$ (with $\mathbf{R} = \mathbf{r} - \mathbf{r}_0$) and defining an averaged propagator $P_{av}(\mathbf{R},\Delta)$ as the ensemble-averaged probability that *any* molecule will move a net distance $\mathbf{R}$ over time Δ,[25] we obtain

$$E_\Delta(\mathbf{q}) = \int P_{av}(\mathbf{R},\Delta) \exp(i2\pi\mathbf{q}\cdot\mathbf{R})\, d\mathbf{R} \quad (2)$$

The signal is acquired in the $\mathbf{q}$-space (with $2\pi\mathbf{q} = \gamma\delta\mathbf{g}$) which is the space reciprocal to the dynamic (i.e., net) displacement $\mathbf{R}$.[26] The key feature of eq 2 is that it bears a direct Fourier relation between the normalized echo signal, $E_\Delta(\mathbf{q})$, and the averaged

(10) Giddings, J. C. *Dynamics of Chromatography, Part I: Principles and Theory*; Marcel Dekker: New York, 1965.
(11) Tallarek, U.; Bayer, E.; Guiochon, G. *J. Am. Chem. Soc.* **1998**, *120*, 1494−1505.
(12) Knox, J. H.; Grant, I. H. *Chromatographia* **1991**, *32*, 317−328.
(13) Gaš, B.; Štědrý, M.; Kenndler, E. *Electrophoresis* **1997**, *18*, 2123−2133.
(14) Rathore, A. S.; Horváth, Cs. *Anal. Chem.* **1998**, *70*, 3069−3077.
(15) Stilbs, P. *Prog. Nucl. Magn. Reson. Spectrosc.* **1987**, *19*, 1−45.
(16) Kärger, J.; Pfeifer, H.; Heink, W. *Adv. Magn. Reson.* **1988**, *12*, 1−89.
(17) Callaghan, P. T. *Principles of Nuclear Magnetic Resonance Microscopy*; Clarendon Press: Oxford, U.K., 1993.
(18) Hoult, D. I.; Richards, R. E. *J. Magn. Reson.* **1976**, *24*, 71−85.
(19) Callaghan, P. T. *Aust. J. Phys.* **1984**, *37*, 359−387.
(20) Tallarek, U.; Albert, K.; Bayer, E.; Guiochon, G. *AIChE J.* **1996**, *42*, 3041−3054.
(21) Seymour, J. D.; Callaghan, P. T. *AIChE J.* **1997**, *43*, 2096−2111.
(22) Stapf, S.; Packer, K. J.; Graham, R. G.; Thovert, J.-F.; Adler, P. M. *Phys. Rev. E* **1998**, *58*, 6206−6221.
(23) Tallarek, U.; van Dusschoten, D.; Van As, H.; Guiochon, G.; Bayer, E. *Angew. Chem., Int. Ed. Engl.* **1998**, *37*, 1882−1885; *Angew. Chem.* **1998**, *110*, 1983−1986.
(24) Stejskal, E. O.; Tanner, J. E. *J. Chem. Phys.* **1965**, *42*, 288−292.
(25) Kärger, J.; Heink, W. *J. Magn. Reson.* **1983**, *51*, 1−7.
(26) Callaghan, P. T.; Eccles, C. D.; Xia, Y. *J. Phys. E: Sci. Instrum.* **1988**, *21*, 820−822.

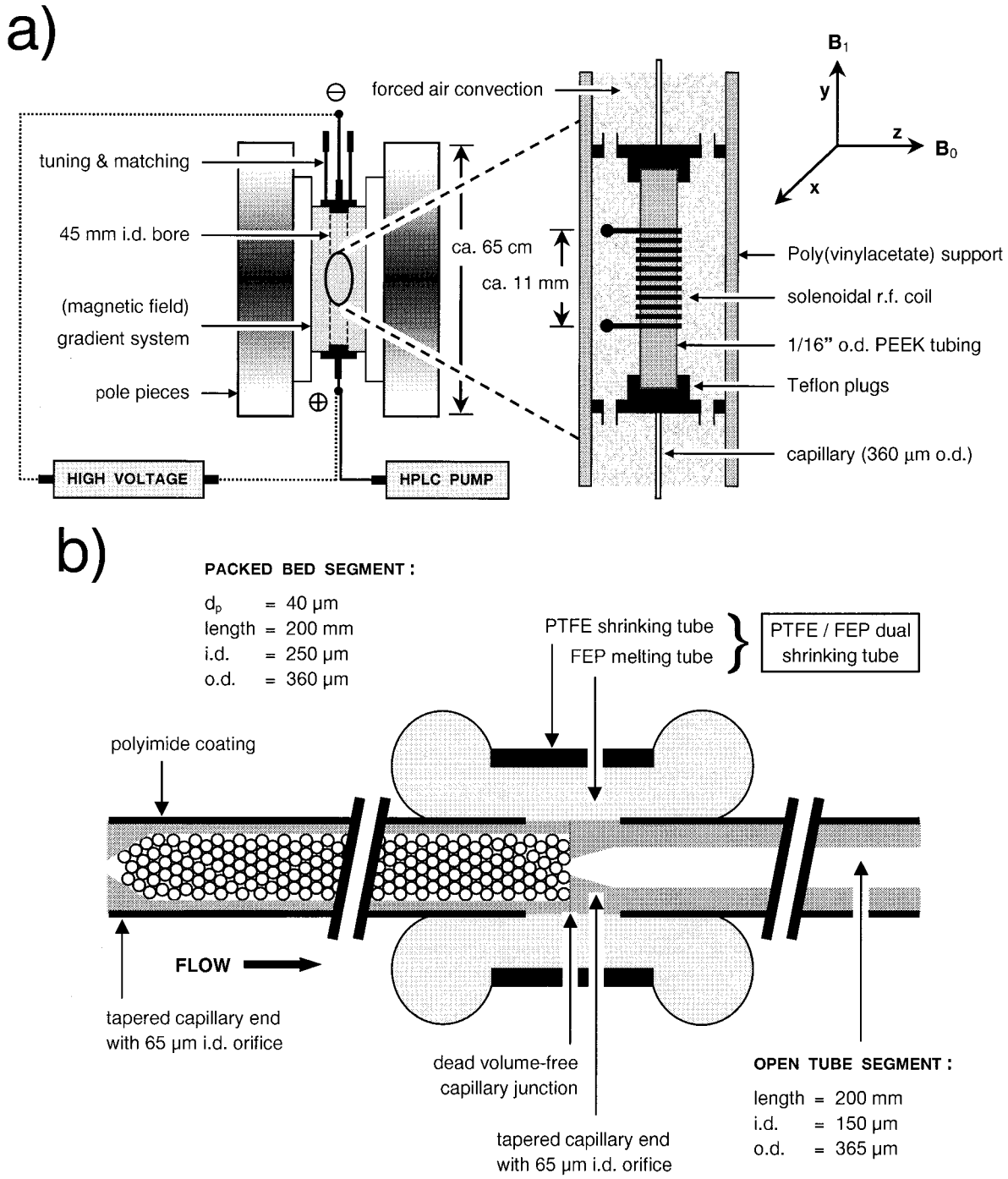

Figure 1. (a) Experimental setup used for the fluid dynamics studies in open and packed capillaries by pulsed field gradient nuclear magnetic resonance on a 0.5-T (^{1}H 20.35 MHz) electromagnet. For CE and CEC measurements, the gradient system with the incorporated home-built rf probe head is rotated into the *x*-direction and allowed to operate the capillaries in a horizontal orientation. The electrodes can be placed within a few centimeters from either edge of the gradient system and the capillary configuration thus may be as short as 0.4 m. (b) Fritless design of the packed column.

propagator, $P_{av}(\mathbf{R},\Delta)$, of the fluid molecules. Thus, the complete spectrum of molecular displacements over time Δ can be obtained by adequate sampling of $\mathbf{q}$-space and subsequent Fourier transformation of $E_\Delta(\mathbf{q})$ with respect to $\mathbf{q}$. For the measurement of $P_{av}(\mathbf{R},\Delta)$ using the stimulated echo version of the PFG-NMR technique, we typically chose for 32 $\mathbf{q}$-steps equidistant between $+\mathbf{q}_{max}$ and $-\mathbf{q}_{max}$, with up to 24 phase-alternated averages at each value of $\mathbf{q}$ for a sufficient signal-to-noise ratio (SNR). To minimize errors due to data discretization, the $E_\Delta(\mathbf{q})$ data were zero-filled to 64 points prior to Fourier transformation.[27] Truncation effects were here avoided by acquiring $E_\Delta(\mathbf{q})$ properly into the noise level at $\pm\mathbf{q}_{max}$. For the case that the distribution of molecular displacements over time Δ is a Gaussian, the PFG-NMR measurement

(27) Marshall, A. G.; Verdun, F. R. *Fourier Transforms in NMR, Optical, and Mass Spectrometry*; Elsevier: Amsterdam, 1990.
(28) Callaghan, P. T.; Stepisnik, J. *Adv. Opt. Magn. Reson.* **1996**, *19*, 325−388.

yields an echo signal modulated in amplitude and phase by[28]

$$E_\Delta(\mathbf{q}) = \exp(i2\pi\mathbf{q}\cdot\mathbf{u}_{av}\Delta - 4\pi^2q^2D\Delta) = \exp(i2\pi\mathbf{q}\cdot\mathbf{u}_{av}\Delta)|E_\Delta(\mathbf{q})| \quad (3)$$

The first term in the exponent of eq 3 can then be used to obtain the column cross-sectional averaged velocity, $\mathbf{u}_{av}$ (when $\mathbf{q} \parallel \mathbf{u}_{av}$), while the second term accounts for the contribution due to the incoherent motion of the fluid. Thus, depending on the actual hydrodynamics, D may represent pure molecular diffusion in an open capillary (D_m) or effective diffusion in the pore space of a packed bed (D_{eff}), as well as convection-driven apparent dispersion (D_{ap}).

PFG-NMR Measurements in the Presence of an Electric Current. With respect to the analytical techniques involving a strong axial electric field and steady electric current (I_y) in the capillary (of radius r_c), i.e., in the y-direction (Figure 1a), it should be noted that (on the basis of the classical physics Biot−Savart law) this current produces a uniform radial magnetic field gradient ($\mathbf{g}_x$) in the x-direction, i.e., perpendicular to that of the current given by[29]

$$|g_x| = \partial B_z/\partial x \approx 0.2I_y/{r_c}^2 \quad (4)$$

This linear field gradient within the capillary does not interfere with the motion-encoding pulsed magnetic field gradients $\mathbf{g}$ when the latter are applied in the fluid flow direction (i.e., in the y-direction such that $\mathbf{g} \perp \mathbf{g}_x$), because their vector product vanishes. Further, $\mathbf{g}_x$ can be compensated for with the proper external shim coil.[30] Electric currents typically involved in the CE and CEC measurements were below 80 and 30 μA, respectively ($r_c = 125$ μm), and the field gradient associated with this current density ($I_y/{r_c}^2$) is very small compared to the magnetic field gradient amplitudes $|\mathbf{g}| = g$ that are normally applied during the PFG-NMR measurements. Thus, the electric current manifests itself as a small background gradient perpendicular to the fluid flow direction, without influence on the determination of the (axial) averaged propagator, $P_{av}(\mathbf{R},\Delta)$.

Implementation of CE, CHPLC, and CEC Equipment. The polyimide-coated, fused-silica capillaries were purchased from Polymicro Technologies (Phoenix, AZ). For the study of electroosmotic flow, they were connected to a modular CE and (pressurizable) CEC system (Grom, Herrenberg, Germany; 0−30 kV, 0−0.2 mA). A conventional HPLC pump with splitter (Sykam, Gilching, Germany) was used for measurements involving pressure-driven flow. Borate buffers were prepared from a 0.01 M stock solution of sodium tetraborate (Merck, Darmstadt, Germany) and adjusted to pH 9.0 at 26 °C with 2 M HCl. Freshly cut capillaries (between 0.55 and 0.7 m long) were first flushed with 0.1 M NaOH and then with buffer solution and were run for at least 30 min at 15 kV/m.[31] Before use, the buffer solutions were filtered through a 0.2-μm syringe filter and then degassed with helium, followed by ultrasonication under vacuum. To ensure steady and reproducible conditions within the NMR setup, e.g., to avoid sample heating due to factors other than the Ohmic loss in the capillary itself, forced air convection thermostats the system to 26 ± 0.5 °C (Figure 1a).

In general, the electrokinetically or pressure-driven aqueous phase is continuously flowing through the column while the displacement probability distribution of water molecules (^1H_2O) is measured over an adjustable observation time (Δ) by ^{1}H PFG-NMR. The approach directly focuses on the fluid flow field (including diffusion over time Δ) under either condition. When the inner radius of the open capillary (or typical flow channel in a packed bed) is considerably larger than the electric double-layer thickness, the linear EOF velocity ($\mathbf{u}_{eo}$) is given by the Helmholtz−Smoluchowski equation[32]

$$\mathbf{u}_{eo} = \mu_{eo}\mathbf{E} = -\epsilon_0\epsilon_r(\zeta/\eta)\mathbf{E} \quad (5)$$

Here, μ_{eo} denotes the electroosmotic mobility and η the viscosity of the buffer solution, ζ the zeta potential (assumed to be constant over the whole surface), and E the electric field strength. ϵ_0 is the permittivity of vacuum and ϵ_r the relative permittivity of the electrolyte solution. Typical measurement times of a single axial displacement probability distribution, $P_{av}(\mathbf{R},\Delta)$, are of the order of 15 min.

For dispersion studies in packed beds, specially prepared capillaries[33] were slurry-packed with spherical-shaped, rehydroxylated silica particles (Hewlett-Packard, Newport, DE). The slurry was prepared in methanol, and the material was consolidated for ~35 min at 250 bar (under ultrasonication). During this packing process, the totally porous, high-purity particles ($d_p = 40$ μm with 9-nm average pore size) were retained in the 250-μm-i.d. (360-μm-o.d.) fused-silica columns by a taper (65-μm orifice) through a keystone effect.[34] Afterward, this tapered end served as the inlet retainer of the packed capillary, while the tapered end of an open tube segment (150 μm i.d.) was fitted to the packed-bed outlet (Figure 1b).[33] Great care was taken that particles did not settle before injecting the slurry via an injection valve and slurry reservoir into the destination capillary. The final bed length of this fritless design was 20 cm.

RESULTS AND DISCUSSION

Fluid Flow Field in Cylindrical Open Tubes. Figure 2 shows representative axial averaged propagator distributions of the buffer solution obtained for pure electroosmotic and pressure-driven flow through a 250-μm-i.d. fused-silica capillary. A rather short observation time ($\Delta = 14.2$ ms) was chosen for these measurements, and column cross-sectional averaged axial convective displacements clearly dominated over those due to radial molecular diffusion, i.e., $(2D_m\Delta)^{1/2} \ll u\Delta$ and r_c.

Two features become immediately evident: (a) $P_{av}(\mathbf{R},\Delta)$ for electroosmotic flow shows a perfect Gaussian shape and all fluid molecules apparently move at a single velocity (u_{eo}) with diffusional broadening only. (b) In the case of pressure-driven flow, the radially averaged axial displacement profile mostly reveals the

(29) Holz, M.; Müller, C. *J. Magn. Reson.* **1980**, *40*, 595−599.
(30) Holz, M.; Lucas, O.; Müller, C. *J. Magn. Reson.* **1984**, *58*, 294−305.
(31) van de Goor, A. A. A. M.; Wanders, B. J.; Everaerts, F. M. *J. Chromatogr.* **1989**, *470*, 95−104.
(32) Lyklema, J. *Fundamentals of Interface and Colloid Science*, *Vol. II: Solid−Liquid Interfaces*; Academic Press: London, 1995.
(33) Rapp, E.; Bayer, E. *J. Chromatogr., A*, in press.
(34) Lord, G. A.; Gordon, D. B.; Myers, P.; King, B. W. *J. Chromatogr., A* **1997**, *768*, 9−16.

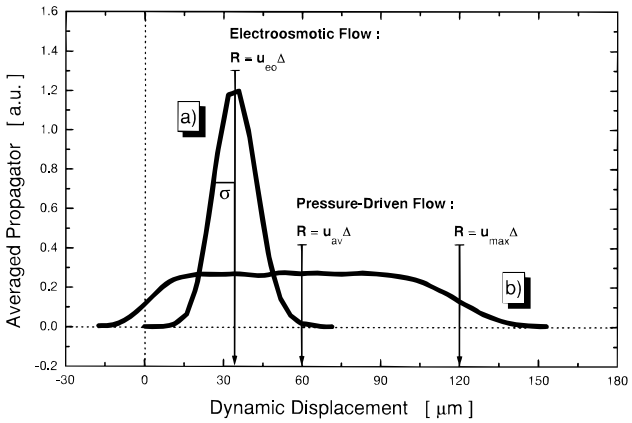

Figure 2. Axial displacement probability distributions, $P_{av}(\mathbf{R},\Delta)$, of the fluid molecules in a 0.65 m × 250 μm i.d. (360 μm o.d.) fused-silica capillary. (a) Electroosmotic flow (E = 23.1 kV/m, I = 49 μA). (b) Pressure-driven flow. Mobile phase, borate buffer (2×10^{-3} M, pH 9.0); observation time, Δ = 14.2 ms; ambient temperature, 26 ± 0.5 °C.

boxcar shape readily anticipated for the velocity distribution under these laminar flow conditions.[35] $P_{av}(\mathbf{R},\Delta)$ is far from a Gaussian and the no-slip boundary condition (i.e., $u = 0$ at the capillary surface), together with the contribution of molecular diffusion over time Δ of fluid molecules near the surface, is responsible for the negative net displacements that are still observed (in sharp contrast to the electroosmotic displacement profile). The local velocity is therefore a function of the radial position in the capillary, as expressed by the Hagen−Poiseuille equation

$$u(r) = 2u_{av}[1 - (r/r_c)^2] \tag{6}$$

where u_{av} is the column cross-sectional average linear velocity, with $u_{max} = 2u_{av}$ (cf. Figure 2). The total variance of this propagator distribution (including contributions from molecular diffusion and the Poiseuille flow spread) is given by[35]

$$\sigma^2 = 2D_m\Delta + (u_{av}\Delta)^2/3 \tag{7}$$

At ambient temperature (26 ± 0.5 °C) and in the absence of any flow, we find the diffusion coefficient of water at $D_m = 2.35 \times 10^{-5}$ cm^2/s.[36,37] Thus, a total variance of ~1266 μm^2 is calculated for the pressure-driven displacement distribution shown in Figure 2. By contrast, a variance of $\sigma^2 = 2D_m\Delta = 66$ μm^2 may be predicted for the electroosmotic displacement distribution when molecular diffusion is considered as the only source of axial dispersion.[38] However, from an analysis of the raw data using eq 3, we calculate a variance of 78 μm^2; i.e., pure molecular diffusion at ambient temperature cannot account quantitatively for the observed width of this Gaussian distribution (Figure 2). As we will demonstrate, the most probable explanation for this fact is that the buffer temperature has increased due to Joule heating in the capillary and that the variance then obtained can be well accounted for by the diffusion coefficient at the actual temperature of the solution, $D_m(T)$. The Gaussian propagator characterizing EOF thus becomes

$$P_{av}(\mathbf{R},\Delta) = \frac{1}{\sqrt{2\pi\sigma^2}} \exp\left[\frac{-(\mathbf{R} - \mathbf{u}_{eo}\Delta)^2}{2\sigma^2}\right] \tag{8}$$

with

$$\sigma^2 = 2D_m(T)\Delta \tag{9}$$

The (single) electroosmotic linear flow velocity is obtained from the center position of the distribution at $\mathbf{R}_c = \mathbf{u}_{eo}\Delta$. For example, an analysis of the measurement shown in Figure 2a gives u_{eo} = 2.29 mm/s. Note that column cross-sectional average velocities differ by a factor of 1.85 (Figure 2). Thus, for a velocity u_{av} identical to that in electroosmotic flow, the variance of the "diffusion-weighted" boxcar distribution is expected around 420 μm^2 (eq 7), which is still a factor of 5.4 larger than for the electrokinetically driven fluid flow (and a factor of 6.4 larger than a purely diffusive contribution at ambient temperature).

In calculating the actual buffer temperature under a given set of conditions, we follow the treatment of Knox and McCormack.[39] As a starting point, Figure 3 presents the EOF velocity and electric current against the electric field strength (for natural and forced air convection). With this forced convective cooling that we generally apply throughout the measurements, the equipment actually performs (solid circles) between the limiting cases of a perfect forced cooling (linear behavior) and still air (open circles) regarding a temperature rise of the buffer solution.

On the basis of eq 5 and Ohms law, a linear relationship is predicted for both the EOF velocity and the electric current. However, above ~10 kV/m, the degree of curvature increases at higher electric field strengths. It is important to note that the deviation from linearity observed for u_{eo} vs E exactly parallels that for I vs E; i.e., a plot of u_{eo} vs I, in turn, is linear over the whole range of data.[39−41] Figure 4 shows the variance and apparent dispersion coefficient that characterize the Gaussian displacement distributions obtained with forced air cooling at the respective field strength (open circles). At moderate values (below 10 kV/m), the variance can be quantitatively explained by pure molecular diffusion of water at ambient temperature (measured at 0 kV/m), which certainly is the ultimate limitation to performance in CE. When the EOF velocity starts to deviate from the linear behavior above ~10 kV/m (cf. Figure 3), the averaged propagator still retains its Gaussian shape, but with an increasing width (Figure 4). These combined results suggest that self-heating of the buffer solution is responsible for the curvature observed in Figures 3 and 4, most likely via the temperature dependence of the viscosity (u_{eo} and I vs E, Figure 3) and the diffusion coefficient (σ^2 and D_{ap} vs E, Figure 4) of the liquid.

To confirm that the apparent dispersion coefficient (D_{ap}) in fact represents the molecular diffusion coefficient at the actual buffer temperature, $D_m(T)$, and as such can fully account for the

(35) Golay, M. J. E.; Atwood, J. G. *J. Chromatogr.* **1979**, *186*, 353−370.
(36) Mills, R. *J. Phys. Chem.* **1973**, *77*, 685−688.
(37) Weingärtner, H. *Z. Phys. Chem. (N. F.)* **1982**, *132*, 129−149.
(38) Jorgenson, J. W.; Lukacs, K. D. *J. Chromatogr.* **1981**, *218*, 209−216.
(39) Knox, J. H.; McCormack, K. A. *Chromatographia* **1994**, *38*, 207−214.
(40) Terabe, S.; Otsuka, K.; Ando, A. *Anal. Chem.* **1985**, *57*, 834−841.
(41) Tsuda, T.; Nomura, K.; Nakagawa, G. *J. Chromatogr.* **1983**, *264*, 385−392.

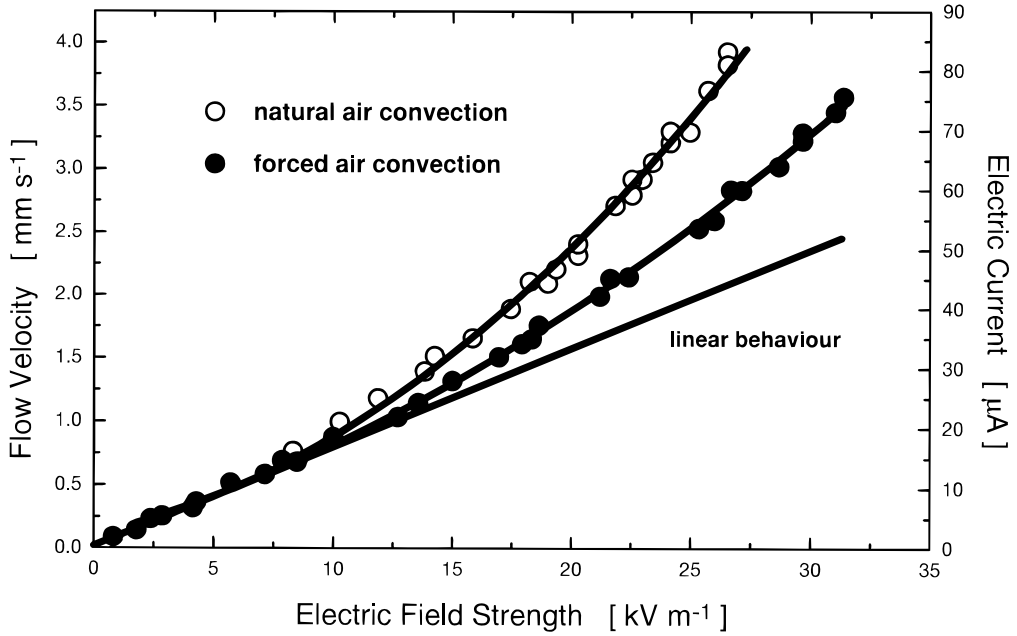

Figure 3. Electroosmotic flow velocity (u_{eo}) and electric current (I) vs the electric field strength. The velocities are calculated from the center position of the Gaussian displacement probability distributions, $P_{av}(\mathbf{R},\Delta)$, found at $\mathbf{R}_c = \mathbf{u}_{eo}\Delta$. Experiments: 250-$\mu$m-i.d. (360-$\mu$m-o.d.) fused-silica capillary, 2×10^{-3} M sodium tetraborate buffer (pH 9.0); observation time, $\Delta = 60$ ms ($\delta = 3.5$ ms).

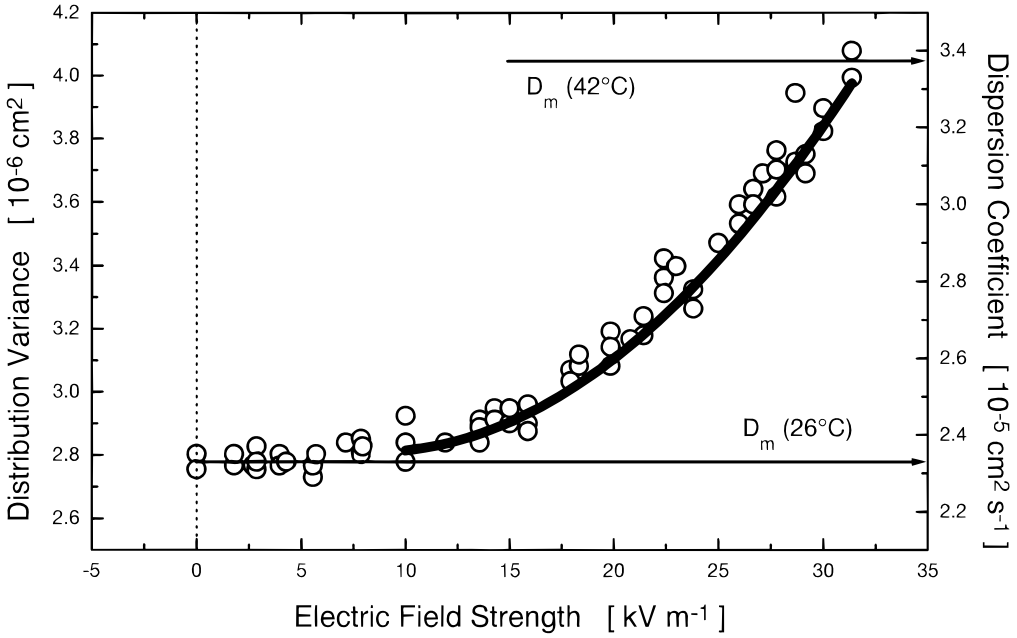

Figure 4. Displacement distribution variance (σ^2) and apparent dispersion coefficient ($D_{ap} = \sigma^2/2\Delta$) against the electric field strength (forced convective air cooling, experimental conditions as in Figure 3). Both σ^2 and D_{ap} are calculated from the PFG-NMR raw data acquired in the **q**-space using eq 3 (open circles). Solid line: Expected molecular diffusion coefficient of water at temperatures that were calculated from the corresponding viscosity data, $\eta(T)$, itself based on eq 5 and the u_{eo} vs E data shown in Figure 3 (solid circles).

observed distribution variance, this temperature has to be calculated. It is based on the nonlinearity of the u_{eo} vs E data itself (Figure 3). Considering the temperature dependence of the viscosity and neglecting a variation of $\epsilon_r\zeta$ with temperature, which may be justified by the linearity of u_{eo} with I,[39,40] the actual slope defined by eq 5, i.e., $u_{eo}/E = -\epsilon_0\epsilon_r\zeta/\eta(T)$ can then account for any deviation from linear behavior by a decrease of the buffer viscosity at the respective level of heat dissipation in the capillary.

In the initial linear domain of that curve (Figure 3), the slope is determined by the viscosity at ambient temperature. For water, this value is readily available[42] ($\eta = 0.8705$ cP) and provides $\epsilon_0\epsilon_r\zeta/\eta(26\ °C)$. With this information, $\eta(T)$ and thus the actual temperature can be calculated for any $u_{eo}-E$ pair in the nonlinear region. These temperatures are then used to estimate the trend in molecular diffusivity, $D_m(T)$. Both the viscosity[42] and the diffusion coefficient[36,37] of water are very accurately known as a function of the temperature that facilitates the conversion of u_{eo} at E to T and $D_m(T)$ via $\eta(T)$. Following this procedure, Figure 4

(42) *Handbook of Chemistry and Physics*, 66th ed.; CRC Press: Boca Raton, FL, 1986−1987.

shows the expected increase of the molecular diffusion coefficient of water (solid line) in comparison with the experimental data. Calculated temperatures cover a range from 26 to 42 °C; i.e., we find a temperature increase of ~16 °C above ambient at the highest power level in the capillary (which is $EI = 2.42$ W/m at $E = 31.4$ kV/m and $I = 77$ μA; Figure 3). The striking feature is that the measured distribution variance and the apparent dispersion coefficient can be well accounted for by the temperature dependence of the molecular diffusivity, and there is no need to propose any contribution of a laminar flow component or effect of a radial temperature gradient in the capillary lumen (at least within the moderate temperature range encountered here). In fact, the experimental data presented in Figures 3 and 4 suggest a plug-flow profile for electroosmosis with axial dispersion only due to molecular diffusion (as implied by eqs 8 and 9). The results agree with Raman spectroscopic measurements of temperature gradients in operating CE capillaries.[43] Those studies have shown that, if the average operating temperature is not 25 °C or more above ambient, radial gradients are small enough that the associated Taylor dispersion can be neglected.

A similar conclusion about the temperature effects in CE was reached by Knox and McCormack,[39] who showed that the increased value of the diffusion coefficient (at the actual buffer temperature) can largely explain the reduced number of theoretical plates obtained for a given separation. They pointed out that the differences still observed at higher linear velocities are partly due to an extra column dispersion caused by injection and detection effects.[44,45] Clearly, these factors are absent in the present PFG-NMR study in which the fluid flow field with any (intrinsic) source of dispersion is measured directly, i.e., without introducing a tracer. In this respect, our approach is similar to that of Paul et al.,[46] who recently used fluorescence imaging of a photoactivatable rhodamine dye to demonstrate a pure electrokinetic flow behavior in a 75-μm-i.d. fused-silica capillary (within the resolution of the technique). Images collected at a series of time delays after the uncaging event indicate a pluglike velocity profile, and peak widths were found to have increased only by axial diffusion of the tracer. The caged fluorescent dye is uniformly seeded throughout the active fluid phase (perfectly mixed) and can be activated at any position in the system. Thus, the injection of a dye, a process that may affect the initial conditions and dispersion characteristics,[47] is circumvented.

Starting with the situation in Figure 2 ($\Delta = 14.2$ ms), it is now instructive to follow the time evolution of either displacement distribution and see the interplay between axial convection and radial diffusion. The (Gaussian) electroosmotic displacement profiles shown in Figure 5a reveal a constant diffusion coefficient, i.e., $D_{ap} \equiv D_m(28\ °C) = 2.47 \times 10^{-5}$ cm^2/s at 15.1 kV/m (cf. Figure 4), and the increase in distribution variance scales exactly with the increase in observation time (eq 9). As demonstrated in Figure 5b, the assumption of a perfect Gaussian shape is reasonable and hardly any symmetric deviation (indicative of a laminar flow component) can be resolved by statistical analysis.[35] These observations again indicate a very narrow (if any) velocity distribution over the whole column cross section (on the inherent time scale of the measurements), with diffusional broadening at the actual buffer temperature only.

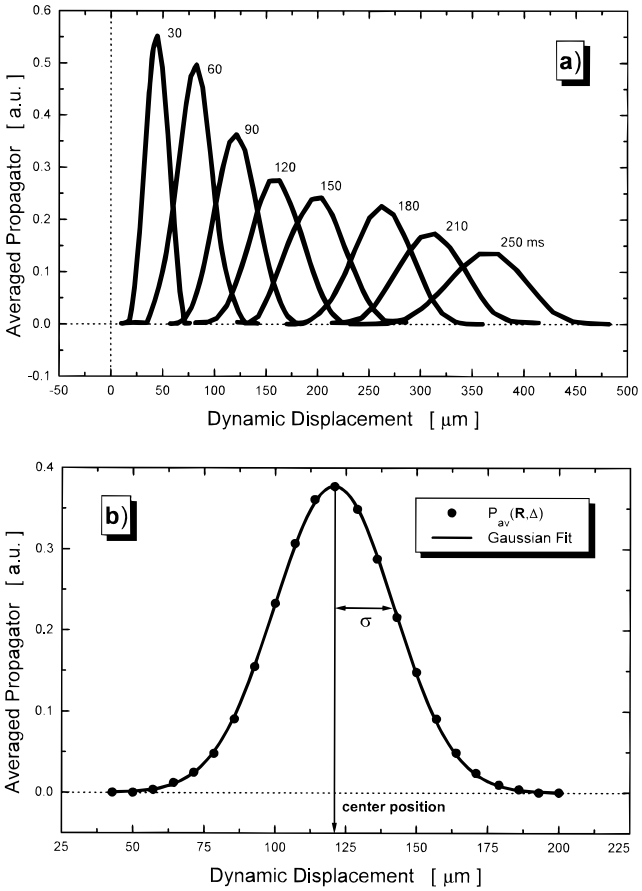

Figure 5. (a) Electroosmotic displacement profiles as a function of the observation time (Δ as indicated). $E = 15.1$ kV/m, $I = 29$ μA ($u_{eo} = 1.34$ mm/s). Mobile phase: 2×10^{-3} M sodium tetraborate buffer (pH 9.0); 0.7 m × 250 μm i.d. (360 μm o.d.) fused-silica capillary. (b) $P_{av}(\mathbf{R},\Delta)$ at $\Delta = 90$ ms and best Gaussian fit (center position, $\mathbf{R}_c = \mathbf{u}_{eo}\Delta = 121$ μm).

In contrast to the already constant electroosmotic displacement pattern, the influence of radial diffusion in the regime $(2D_m\Delta)^{1/2} \ll r_c$ under now laminar flow conditions manifests itself in an exchange between the involved velocity extremes (cf. Figure 2). The Lagrangian correlation length of this flow velocity field is much higher than for an ideal EOF profile, and exchange by radial diffusion proceeds over the whole capillary radius (125 μm), i.e., on the time scale of a few seconds. Because the velocity gradient changes with radial position, rather unique axial displacement profiles are observed at increasing observation times (Figure 6).[35,48] In the region of steep velocity gradients near the capillary surface, for example, an inward diffusion leads to a bump at the rear which then grows to consume the former boxcar shape. Due to the fact that the velocity varies only quadratically with distance from the capillary axis (eq 6), the leading edge of the boxcar substantially retains its shape in this early stage. Finally, however, the central front also will lose its sharpness and the displacement

(43) Liu, K.-L. K.; Davis, K. L.; Morris, M. D. *Anal. Chem.* **1994**, *66*, 3744−3750.
(44) Sternberg, J. C. *Adv. Chromatogr.* **1966**, *2*, 205−270.
(45) Huang, X.; Coleman, W. F.; Zare, R. N. *J. Chromatogr.* **1989**, *480*, 95−110.
(46) Paul, P. H.; Garguilo, M. G.; Rakestraw, D. J. *Anal. Chem.* **1998**, *70*, 2459−2467.
(47) Tsuda, T.; Ikedo, M.; Jones, G.; Dadoo, R.; Zare, R. N. *J. Chromatogr.* **1993**, *632*, 201−207.
(48) Shankar, A.; Lenhoff, A. M. *AIChE J.* **1989**, *35*, 2048−2052.

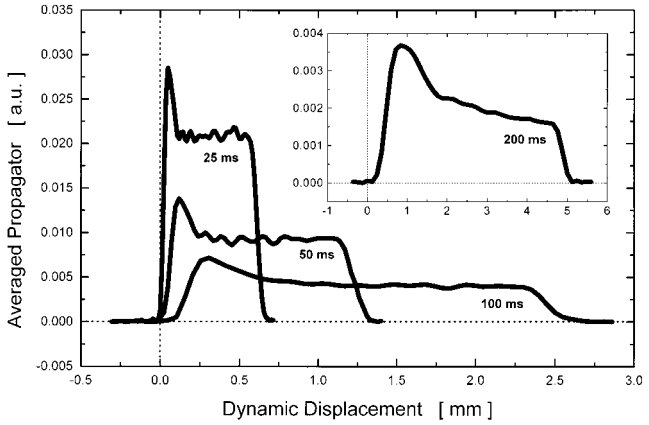

Figure 6. Axial displacement probability distributions, $P_{av}(\mathbf{R},\Delta)$, of the fluid molecules in laminar flow as a function of the observation time (Δ as indicated). Note the higher averaged flow velocity compared to Figure 2.

distribution becomes a skewn Gaussian.[35] These observations concerning the underlying fluid flow field demonstrate that the (Gaussian) Taylor−Aris limit[49,50] for the axial dispersion of an injected tracer pulse is valid only for sufficiently long capillaries or residence times, most conveniently expressed in terms of a dimensionless minimum transit time.[51] For a pure electrokinetic behavior, by contrast, the characteristic length scale of velocity fluctuations in the mobile phase is of the order of the electric double-layer thickness, which is a few nanometers under the most typical conditions. Exchange of fluid molecules over this spatial domain falls into the nanosecond regime and the total effect on dispersion must be extremely small (Figure 5). However, the contribution from resistance to mass transfer in the mobile phase may increase significantly when retention becomes more important, but is expected to be still smaller than in pressure-driven flow, at any given value of the retention factor.[52,53]

The velocity distributions reported and characteristic length scales indicated for pressure-driven and electroosmotic flow through open cylindrical capillaries bear a close resemblence to the so-called transchannel effect[10] in the interparticulate pore space of packed beds. It manifests itself as part of the eddy dispersion contribution to the overall band spreading, which we consider next.

Fluid Dispersion in Packed Capillaries. In laminar flow through a fixed bed, not only the transchannel effect between particles, i.e., the distribution of velocities in individual interstitial flow channels with a considerably more complex geometry than cylindrical capillaries, but a fluctuation in packing density and permeability on any time and length scale over the cross-sectional area of the column contributes to velocity extremes in the mobile phase. Although there exists a fairly continuous distribution of these scales in the interstitial pore space of the column, Giddings[10] further divided them into a short-range and long-range interchannel effect, as well as a transcolumn contribution. For electrokinetically driven fluid flow, however, as implied by eq 5, the EOF velocity is expected to be independent of the actual pore diameter and shape and this spatial hierarchy of heterogeneity length scales has lost (at least substantially) its conceptual impact on fluid dispersion.

With the PFG-NMR methodology presented in this work, axial displacement probability distributions of the fluid molecules are measured directly over discrete domains of time (Δ) and space (total length of the rf coil; cf. Figure 1a). Consequently, the bulk apparent axial dispersion coefficients ($D_{ap,a}$) do not include contributions from any effects other than due to the intrinsic dispersive nature of the flow field in this particular region of the column packing. They are related to the reduced plate heights via the conventional relationship[54]

$$h_a = (2/\nu)(D_{ap,a}/D_m) \tag{10}$$

The corresponding column cross-sectional average flow velocity (u_{av}) used to calculate the reduced flow velocity (ν) is derived from the center position of the Gaussian propagator distribution (at $\mathbf{R}_c = \mathbf{u}_{av}\Delta$) in displacement space

$$u_{av} = F_v/\epsilon_T A = R_c/\Delta \tag{11}$$

Because the fluid molecules have explored both the intraparticle and interparticle pore space environments, i.e., the associated exchange is complete over time Δ, the *total* porosity of the packing (ϵ_T) appears in the denominator of eq 11. F_v is the volumetric flow rate and A the cross-sectional area of the column.

Kennedy and Knox[55] showed that a simple additive contribution, $a\nu^n$, to the plate height equation can account for the combined effect of the four different scales of velocity extremes in the mobile phase distinguished by Giddings.[10] The exponent n is between 0.25 and 0.35, but often taken as 0.33 in the chromatographic literature.[56] The resulting plate height equation is known as the Knox equation

$$h_a = b/\nu + a\nu^{1/3} + c\nu \tag{12}$$

This totally empirical correlation is in agreement with most experimental results, and for the moment we assume that it applies to both our CHPLC and CEC dispersion data. The silica particles have rather small pores (∼9 nm in diameter), and together with the low buffer concentration used (10^{-3} M), intraparticle convection is not expected to be operative in CEC at any measurable level. A rough calculation of the electric double-layer thickness (∼10 nm) indicates a complete double-layer overlap.[4] Thus, an electroosmotic perfusion[57,58] is considered as being inactive under these conditions and any differences in plate height can then be traced back to velocity extremes that may exist in the interparticle mobile phase under pressure-driven and electroosmotic flow conditions. The results from a systematic study of the axial reduced plate height versus the reduced flow velocity in CEC and

(49) Taylor, G. I. *Proc. R. Soc. (London) A* **1953**, *219*, 186−203.
(50) Aris, R. *Proc. R. Soc. (London) A* **1956**, *235*, 67−77.
(51) Shankar, A.; Lenhoff, A. M. *J. Chromatogr.* **1991**, *556*, 235−248.
(52) Martin, M.; Guiochon, G.; Walbroehl, Y.; Jorgenson, J. W. *Anal. Chem.* **1985**, *57*, 559−561.
(53) McEldoon, J. P.; Datta, R. *Anal. Chem.* **1992**, *64*, 227−230.
(54) Giddings, J. C. *J. Chem. Phys.* **1959**, *31*, 1462−1467.
(55) Kennedy, G. J.; Knox, J. H. *J. Chromatogr. Sci.* **1972**, *10*, 549−556.
(56) Knox, J. H. *J. Chromatogr. Sci.* **1977**, *15*, 352−364.
(57) Li, D.; Remcho, V. T. *J. Microcolumn Sep.* **1997**, *9*, 389−397.
(58) Venema, E.; Kraak, J. C.; Poppe, H.; Tijssen, R. *J. Chromatogr., A* **1999**, *837*, 3−15.

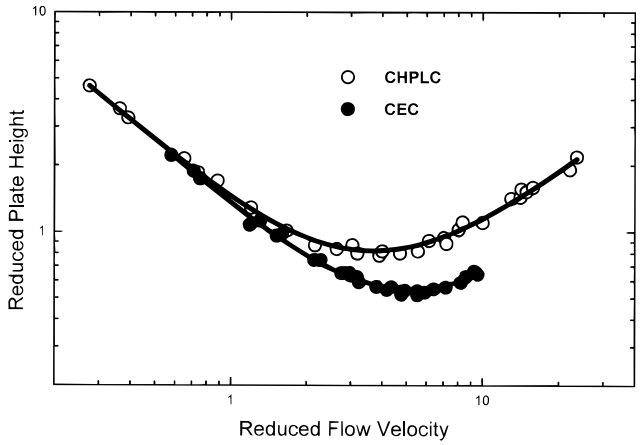

Figure 7. Reduced axial plate height ($h_a = H_a/d_p$) versus the reduced flow velocity ($\nu = d_p u_{av}/D_m$) for the CHPLC and CEC modes; solid line, eq 12. CHPLC ($r^2 = 0.997$): $a = 0.14$, $b = 1.25$, $c = 0.07$, $h_{min} = 0.83$, $\nu_{min} = 3.6$. CEC ($r^2 = 0.996$): $a = 0.06$, $b = 1.26$, $c = 0.04$, $h_{min} = 0.55$, $\nu_{min} = 5.3$. Capillary column: 250-μm-i.d. (360-μm-o.d.) fused silica. Packing: 40 μm rehydroxylated, spherical-shaped silica particles. Aspect ratio, $d_c/d_p = 6.25$. Buffer solution, 10^{-3} M sodium tetraborate (pH 9.13); observation time, $\Delta = 120$ ms ($\delta = 3.5$ ms).

CHPLC with the same column are shown in Figure 7, together with the best fit of these data to the Knox equation. The observation time ($\Delta = 120$ ms) has been chosen high enough to include the total contribution of stagnant (diffusion-limited) intraparticle and interparticle (boundary layer) mobile-phase mass transfer in the variance of both propagator distributions. These are then adequately represented as being single Gaussians.[59] Although the minimum plate height (h_{min}) in CHPLC, at a reduced flow velocity (ν_{min}) of 3.6, is already as small as 0.83, thereby demonstrating how efficient the fluid flow field is actually performing under these conditions, the value achieved by CEC (at $\nu_{min} = 5.3$) is still 1.6 times smaller. Starting with the eddy dispersion term ($a\nu^{1/3}$), which accounts for a combination of transverse diffusion and tortuous flow,[60] the interparticle charateristics of the EOF (in view of eq 5 and its validity), i.e., the temporal and spatial domain of velocity extremes in the mobile phase, can explain the much smaller a-term for electrokinetically driven fluid flow. Not surprisingly, the b-term, which represents an obstructed axial molecular diffusion, is identical for both separation modes. This parameter is related to the tortuosity factor of the interconnected pore space in the column (τ) by

$$\frac{b}{2} = \gamma = \frac{1}{\tau} = \frac{D_{eff}}{D_m} \quad \text{with} \quad D_{eff} = \frac{\sum_n D_n \Delta_n}{\sum_n \Delta_n} \qquad (13)$$

In the present case (no retention), the effective diffusion coefficient, D_{eff}, is the time-weighted average of diffusion coefficients in the intra- and interparticle pore space environments.[61] It should be noted that the tortuosity factor is the squared of the tortuosity and the inverse of the obstruction factor, γ, which is often used in the chromatographic literature.[10] The value of $\gamma = 0.63$ (obtained under both conditions) is very typical for randomly packed beds.[60] It is in an excellent agreement with the effective diffusivity measured separately in the absence of any flow, $D_{eff} = 1.43 \times 10^{-5}$ cm^2/s, which gives $\gamma = 0.61$ ($D_m = 2.35 \times 10^{-5}$ cm^2/s). The c-term remaining in the Knox equation mainly includes mass-transfer resistance from stagnant fluid entrained in the deep tortuous pools of the intraparticle pore network. However, in creeping laminar flow through a packed bed (with negligible turbulence), the stagnant fluid on the particles' external surface and in the cusp regions between particles provides an additional mass-transfer resistance and it makes particles effectively slightly larger. In this surrounding liquid film, molecular diffusion normal to the surface is at least the dominating transport mechanism.[62] This contribution manifests itself in the stagnant mobile-phase mass-transfer kinetics and may actually explain its flow rate dependence.[59,63] What, however, happens to the concept of the stagnant boundary layer and associated interparticle fluid-side resistance to mass transfer in electroosmotic flow? Here, the spatial dimension of this diffusion-limited mass transfer external to the particles is largely reduced and practically all the fluid external to the hard-sphere boundaries of the particles is flowing, except close to contact points between particles where the electric double layers may overlap completely. In laminar flow, a substantial fraction of the interparticle fluid can be regarded as being stagnant and is an inverse function of the flow rate. This basic difference in the hydrodynamically effective particle diameter or, vice versa, in the effective external porosity that is available for fluid flow, may explain differences in the c-term also under conditions that do not favor electroosmotic perfusion.

The results concerning the parameters in the Knox equation are in qualitative agreement with data recently published by Wen et al.[64] Comparing the efficiency in CHPLC and CEC for an unretained neutral marker (acrylamide) in a 50-μm-i.d. column packed with 6-μm Zorbax ODS particles having 8-nm pores (aspect ratio, 8.3), they reported a decrease in the a-term by a factor of 2.5 for the CEC mode and a c-term 1.3 times smaller than in CHPLC. For the same material, but with 30-nm pores, the corresponding decrease in a- and c-terms was by a factor of 3.0 and 1.6, respectively. In their study, Wen et al.[64] used particles with average pore diameter up to 100 nm (10^{-2} M phosphate buffer) and concluded that electroosmotic perfusion then contributes significantly to the increased performance in CEC, documented by a further decrease in the c-term as compared to CHPLC. We are currently performing PFG-NMR studies on intraparticle-forced electroosmotic flow in columns packed with large-pore materials, where the experimental approach presented here will be extremely helpful in revealing a perfusive electroosmotic fluid flow field at work.

CONCLUSIONS

The open-tubular work indicates that superimposed onto a flat (i.e., pluglike) velocity profile over the column cross section,

(59) Tallarek, U.; Vergeldt, F. J.; Van As, H. *J. Phys. Chem. B* **1999**, *103*, 7654−7664.
(60) Knox, J. H. *J. Chromatogr., A* **1999**, *831*, 3−15.
(61) Knox, J. H.; Scott, H. P. *J. Chromatogr.* **1983**, *282*, 297−313.
(62) King, C. V. *J. Am. Chem. Soc.* **1935**, *57*, 828−831.
(63) Boyd, G. E.; Adamson, A. W.; Myers, L. S., Jr. *J. Am. Chem. Soc.* **1947**, *69*, 2836−2848.
(64) Wen, E.; Asiaie, R.; Horváth, Cs. *J. Chromatogr., A* **1999**, *855*, 349−366.

axial molecular diffusion presents the ultimate limitation to performance in CE (for an unretained solute), and the plate height becomes

$$h_a = 2D_m(T)/d_c u_{eo} \quad (14)$$

Temperature effects were quantitatively characterized and can explain, via the temperature dependence of the molecular diffusion coefficient, the increasing variance of the Gaussian axial displacement probability distributions recorded at higher electroosmotic flow velocities (and associated levels of heat dissipation in the capillary).

The low values of reduced plate height observed with both the CHPLC and CEC modality ($h_a < 1$) demonstrate the excellent performance of the underlying fluid flow field in the packed bed region, even with an aspect ratio of only 6.25. Compared to the pressure-driven mobile phase ($h_{min} = 0.83$), however, the electroosmotic flow shows a still superior efficiency ($h_{min} = 0.55$). It is attributed to the improved flow uniformity on any time and length scale over the whole column cross section and to the difference in the hydrodynamically effective particle diameter concerning the total fraction of stagnant fluid in the column and associated, diffusion-limited mass transfer. These effects, which affect the *a*- and *c*-terms in the Knox equation but leave unchanged the *b*-term, also explain the shift of the minimum of the CEC plate height curve to higher reduced flow velocities.

ACKNOWLEDGMENT

U.T. gratefully acknowledges the award of a Marie Curie Fellowship under the Training and Mobility of Researchers (TMR) Program from the European Union (Contract ERBFMBI-CT98-3437). This research was further supported by the European Community activity Large-Scale Facility Wageningen NMR Centre (Contract ERBCHGE-CT95-0066) and by the Technology Foundation STW (Project WBI.3493), Applied Science Division of the Dutch Science Foundation NWO.

Received for review November 15, 1999. Accepted February 22, 2000.

AC991303I

ELSEVIER

Magnetic Resonance Imaging 19 (2001) 453–456

MAGNETIC RESONANCE IMAGING

Using NMR displacement imaging to characterize electroosmotic flow in porous media

Ulrich Tallarek*, Tom W.J. Scheenen, P. Adrie de Jager, Henk Van As

Laboratory of Molecular Physics and Wageningen NMR Centre, Department of Biomolecular Sciences, Wageningen University, Wageningen, The Netherlands

Abstract

Pulsed field gradient nuclear magnetic resonance (PFG-NMR) and NMR imaging were used to study temporal and spatial domains of an electrokinetically-driven mobile phase through open and packed segments of capillaries. Characteristics like velocity distribution and an asymptotic dispersion are contrasted to viscous flow behavior. We show that electroosmotic flow in microchannel geometries can offer a significant performance advantage over the pressure-driven flows at comparable Peclét numbers, indicating that velocity extremes in the pore space of open tubes and packed beds are drastically reduced. An inherent problem of capillary electrochromatography that we finally address is the existence of wall effects when in the general case the surface zeta-potentials of the capillary inner wall and the adsorbent particles are different. Using dynamic NMR microscopy we were able resolve this systematic velocity inequality of the flow pattern which strongly influences axial dispersion and may be responsible for long time-tails of velocity distribution in the mobile phase.

Keywords: Electroosmotic flow; Capillaries; Dispersion; Dynamic NMR imaging; Fixed beds

1. Introduction

The use of electroosmosis to drive mobile phase and solute through packed capillaries has received tremendous attention in capillary electrochromatography (CEC) over the last decade [1–3], because an electroosmotic flow (EOF) may offer significant advantages over pressure-driven flows. They include an essentially flat (i.e., plug-like) flow profile in individual channels of the pore space similar to the situation in capillary electrophoresis (CE) [4], as well as the fact that the average velocity (u_{av}) in channels is found relatively independent of the pore radius over a wide range of conditions [5]. This translates to high separation efficiencies, increased mass sensitivity and the potential of using extremely small particle diameters ($d_p < 1$ μm), while retaining still those separation mechanisms and selectivities that have already been established in HPLC. Thus, CEC is actually a hybrid between CE and HPLC.

To characterize the transient (and asymptotic) dispersion of an electrokinetically driven mobile phase through the pore space of open and packed capillaries we have used the access by PFG-NMR to a temporal domain covering the range from a few milliseconds up to several seconds [6]. By combining this technique with NMR imaging it is possible to study the microscopic fluid dynamics with sufficient spatial resolution to address those factors that influence dispersion on a macroscopic scale.

2. Materials and methods

The ^{1}H PFG-NMR and NMR imaging studies were performed on a 0.7 T electromagnet (Bruker, Karlsruhe, Germany), interfaced with a SMIS console (Surrey Medical Imaging Systems, Guildford, U.K.) and an actively shielded gradient system from Doty Scientific (Columbia, SC). The 250 μm i.d. (365 μm o.d.) fused-silica capillaries were fixed within a homebuilt radiofrequency setup based on a solenoidal r.f. coil which is manufactured on a PEEK microtight tubing sleeve (cf. Fig. 1). Degassed sodium tetraborate solutions (pH 9.13) were chosen as the mobile phase in all experiments. Capillaries were packed with either rehydroxylated spherical silica particles or strong cation-exchange particles by the slurry-technique [7]. In general, when both motion-encoding (**q**-space) and spatial localiza-

* Corresponding author. Tel.: +31-317-48-2047; fax: +31-317-48-2725.

E-mail address: ulrich.tallarek@water.mf.wau.nl (U. Tallarek).

0730-725X/01/$ – see front matter
PII: S0730-725X(01)00266-1

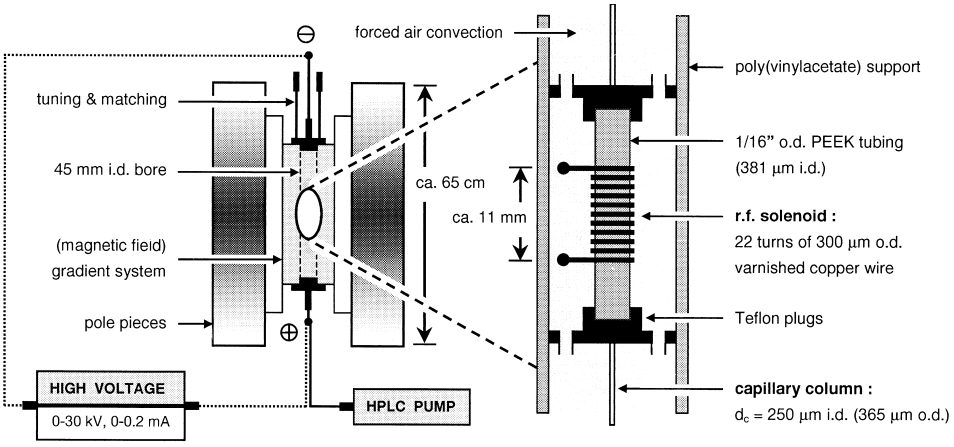

Fig. 1. Experimental setup for ^{1}H 30 MHz measurements in a capillary. The electrodes of the CE instrument were placed close to the edges of the 30 cm long gradient system and forced air convection thermostates the probe to 26 ± 0.5°C. For the experiments involving EOF a horizontal configuration could be used to prevent pressure-driven flow in the capillary due to gravity.

tion (**k**-space) gradients are applied, the modulation of the complex echo signal (in the narrow gradient pulse limit) is given by [6]

$$S(\mathbf{q},\mathbf{k}) = \int \rho(\mathbf{r}) \int P_{av}(\mathbf{R},\Delta) \cdot \exp(i2\pi\mathbf{q}\cdot\mathbf{R})d\mathbf{R}\, \exp(i2\pi\mathbf{k}\cdot\mathbf{r})d\mathbf{r} \qquad (1)$$

Fourier transformation of S(**k,q**) with respect to both **k** and **q** returns $\rho(\mathbf{r})P_{av}(\mathbf{R},\Delta)$, and a normalization of this function by the image density $\rho(\mathbf{r})$ acquired with $\mathbf{q} = 0$ then allows to reconstruct the averaged propagator of the fluid molecules, $P_{av}(\mathbf{R},\Delta)$, for each pixel of the image. In spatially non-resolved studies we used the stimulated echo version of the PFG-NMR approach [8], while for imaging of dynamic displacements we implemented a turbo spin-echo sequence that has recently been developed [9].

3. Results and conclusions

Fig. 2 expresses the flow field dynamics in EOF and pressure-driven (Poiseuille) flows through an open cylindrical capillary. At short observation times, $(2D_m\Delta)^{1/2} \ll u_{av}\Delta$ and the axial displacement probability distribution mostly reflects the column cross-sectional flow profile (cf. dashed lines). While $P_{av}(\mathbf{R},\Delta)$ in EOF already shows a Gaussian shape (Fig. 2a) and an asymptotic dispersion (Fig. 2c) with broadening only due to molecular diffusion at the actual buffer temperature ($\sigma^2 = 2D_m\Delta$) [10,11], $P_{av}(\mathbf{R},\Delta)$ in Poiseuille flow at this early stage of dispersion reveals the well known box-car shape for the distribution of instantaneous velocities [10–13]. It causes a significantly higher dispersion, $\sigma^2 = (u_{av}\Delta)^2/3 + 2D_m\Delta$ [14], as compared to pure electrokinetic flow. In contrast to EOF, the development toward a Gaussian shape must proceed by lateral diffusion on a time- and lengthscale covering the total column radius (i.e., $\Delta = r_c^2/2D_m \approx 3.3$ s) [13,14]. Although for both types of fluid flow the "no-slip" condition requires a zero velocity at the solid-liquid interface, the profile in EOF becomes plug-like beyond the electrical double layer (which is only a few tens of nanometers compared to $r_c = 125$ μm) [4], while the parabolic profile in Poiseuille flow results from the distribution of shear stress over r_c.

These single-channel flow characteristics with plug-like profile in EOF and the parabolic profile in Poiseuille flow have important implications for the dispersion expected in the pore space of a packed capillary (Fig. 3). The use of an electrokinetically driven mobile phase through a bed of charged particles (with rehydroxylated silica surface, pH 9.13) gives rise to a significantly smaller dispersion as compared to pressure-driven flow. For electrical double

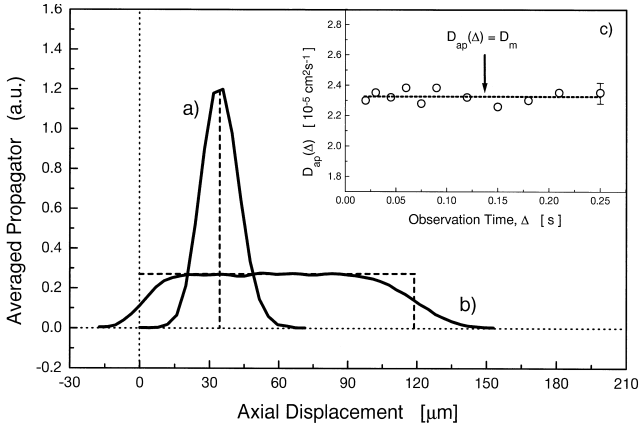

Fig. 2. Displacement probability distribution of fluid molecules in (a) EOF with a column cross-sectional averaged velocity u_{av} of 2.29 mm/s (E = 23.1 kV/m, I = 49 μA) and (b) pressure-driven flow (note that the u_{av} differ by a factor of 1.85). Sodium tetraborate buffer (2×10^{-3} M), Δ = 14.2 ms and molecular diffusivity (D_m) of 2.35×10^{-5} cm^2/s. (c) Apparent dispersion coefficient in EOF vs. the observation time (u_{av} = 1 mm/s). Technique: stimulated echo PFG-NMR.

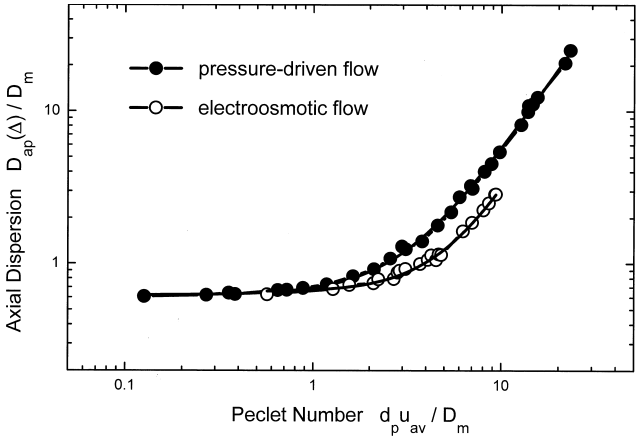

Fig. 3. Apparent dispersion coefficient (determined in the low-**q** limit[6] of Eq. 1) in EOF and pressure-driven flow normalized by the molecular diffusivity (D_m) vs. particle Péclet number. The capillary is packed with rehydroxylated silica particles (d_p = 40 μm). Sodium tetraborate buffer (10^{-3} M), Δ = 120 ms. Technique: stimulated echo PFG-NMR.

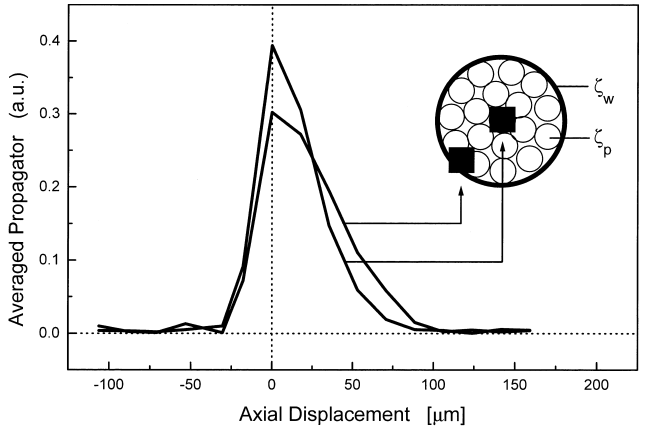

Fig. 4. Pixel displacement probability distributions of the fluid molecules in EOF close to the capillary wall and in the center of the fixed bed. The capillary is packed with strong cation exchange particles (d_p = 50 μm), both ζ_w and ζ_p are negative. Sodium tetraborate buffer (10^{-3} M), Δ = 35 ms. Data were acquired for pixels of dimension 65 × 65 μm in a slice of thickness 6 mm. Technique: turbo spin-echo NMR displacement imaging.

layers which are thin with respect to characteristic pore diameters, this performance advantage can be attributed to the relatively flat profile of the EOF in the individual channels and to the similar magnitude of the cross-sectional average of the EOF velocity in pores of different size [5]. Thus, mechanical dispersion effects caused by an intrinsic velocity heterogeneity of the flow pattern over any time- and lengthscale are strongly reduced.

However, one particular problem may arise in CEC when the ζ-potentials at the inner wall of the column (ζ_w) and the surface of the particles (ζ_p) are different. It creates a systematic EOF heterogeneity which is aggravated at low column-to-particle diameter (d_c/d_p) ratio and engenders additional dispersion [15]. To detect this wall effect we applied pulsed field gradient tubo spin-echo imaging to a capillary packed with cation exchange particles at low aspect ratio (d_c/d_p = 5). While both the capillary and particles surfaces have a negative charge density, ζ_w in this case is still more negative than ζ_p [16]. Because we are looking for a systematic effect, high spatial resolution in the third (i.e., the axial) direction is not needed. The results in Fig. 4 show that it is possible to resolve this wall effect with higher EOF close to the capillary wall (as expected), and they demonstrate that in current CEC practice (with $d_c/d_p < 50$) aspects concerning the column-to-particle diameter ratio and any mismatch of ζ-potentials must receive proper attention [15,16].

Acknowledgments

One of the authors (U.T.) gratefully acknowledges the award of a Marie Curie Fellowship under the Training and Mobility of Researchers (TMR) Program from the European Union (Contract ERBFMBI-CT98–3437). This research was further supported by the European Community activity Large-Scale Facility Wageningen NMR Center (Contract ERBCHGE-CT95–0066) and the Dutch Technology Foundation STW, Applied Science Division of NWO (Project WBI-3439). We like to thank Erdmann Rapp (University of Tübingen, Germany) for the preparation of the packed capillaries.

References

[1] Dittmann MM, Wienand K, Bek F, Rozing, GP. Theory and practice of capillary electrochromatography. LC·GC 1995;13:800–14.
[2] Crego AL, González A, Marina, ML. Electrochromatography. Crit Rev Anal Chem 1996;26:261–304.
[3] Colón LA, Reynolds KJ, Alicea-Maldonado R, Fermier AM. Advances in capillary electrochromatography. Electrophoresis 1997;18: 2162–74.
[4] Rice CL, Whitehead R. Electrokinetic flow in a narrow cylindrical capillary. J Phys Chem 1965;69:4017–24.
[5] Knox JH, Grant, IH. Electrochromatography in packed tubes using 1.5 to 50 μm silica gels and ODS bonded silica gels. Chromatographia 1991;32:317–28.
[6] Callaghan PT, Stepišnik, J. Generalized analysis of motion using magnetic field gradients. Adv Magn Opt Reson 1996;19:325–88.
[7] Neue, UD. HPLC Columns: Theory, Technology, and Practice. Wiley-VCH: New York, 1997.
[8] Kärger J, Pfeifer H, Heink, W. Principles and application of self-diffusion measurements by nuclear magnetic resonance. Adv Magn Reson 1988;12:1–89.
[9] Scheenen TWJ, van Dusschoten D, de Jager PA, Van As H. Microscopic displacement imaging with pulsed field gradient turbo spin-echo NMR. J Magn Reson A 2000;142:207–15.
[10] Tallarek U, Rapp E, Scheenen T, Bayer E, Van As H. Electroosmotic and pressure-driven flow in open and packed capillaries: velocity distributions and fluid dispersion. Anal Chem 2000;72:2292–301.
[11] Paul PH, Garguilo MG, Rakestraw, DJ. Imaging of pressure- and electrokinetically driven flows through open capillaries. Anal Chem 1998;70:2459–67.
[12] Wu D, Chen A, Johnson CS, Jr. Flow imaging by means of 1D pulsed field gradient NMR with application to electroosmotic flow. J Magn Reson A 1995;115:123–6.

[13] Codd SL, Manz B, Seymour JD, Callaghan, PT. Taylor dispersion and molecular displacements in Poiseuille flow. Phys Rev E 1999; 60:R3491–R3494.
[14] Golay MJE, Atwood JG. Early phases of the dispersion of a sample injected in Poiseuille flow. J Chromatogr 1979;186:353–70.
[15] Liapis AI, Grimes BA. Modeling the velocity field of the electroosmotic flow in charged capillaries and in capillary columns packed with charged particles: interstitial and intraparticle velocities in capillary electrochromatography systems. J Chromatogr A 2000;877: 181–215.
[16] Horváth, Cs, Choudhary G. Dynamics of capillary electrochromatography. Experimental study on the electroosmotic flow and conductance in open and packed capillaries. J Chromatogr A 1997;781: 161–83.

Macroscopic Heterogeneities in Electroosmotic and Pressure-Driven Flow through Fixed Beds at Low Column-to-Particle Diameter Ratio

Ulrich Tallarek,* Tom W. J. Scheenen, and Henk Van As

Laboratory of Molecular Physics and Wageningen NMR Centre, Department of Biomolecular Sciences, Wageningen University, Dreijenlaan 3, 6703 HA Wageningen, The Netherlands

Received: April 3, 2001; In Final Form: June 25, 2001

By using dynamic NMR microscopy with 40 μm spatial resolution we have demonstrated the existence of specific wall effects in electroosmotic and pressure-driven flows through a fixed bed at low column-to-particle diameter ratio. While the geometrical wall effect encountered in pressure-driven flow through the packed capillary is due to the radial distribution of interstitial porosity, with increasing void space closer to the wall, the electrokinetic wall effect is caused by different values of the zeta-potential associated with the inner surface of the capillary and those of the particles. It is shown that these wall effects are very systematic along the column axis for both types of fluid flow. They can cause a persistent (i.e., long-time) disequilibrium in the axial dispersion behavior, and associated correlation lengths of the flow field may cover the total radius of the packed capillary needing trans-column equilibration. The characteristic times of these macroscopic flow heterogeneities in electroosmotic and pressure-driven flows exceed by far those of the stagnant mobile phase mass transfer in the bed as we show by complementary pulsed field gradient NMR measurements.

Introduction

Due to the nonuniform radial distribution of voidage, permeability, and interstitial velocity in a critical region close to the wall,[1−13] the column diameter (d_c) to particle diameter (d_p) ratio may influence transport properties in fixed-bed catalytic reactors and chromatographic columns. It has already been shown in early studies and for uniform spheres with a smooth surface that the interstitial porosity (ϵ_{inter}) starts with a maximum value of unity at the column wall and then displays damped oscillations with a period close to d_p over a distance of 4−5 d_p into the bulk of the bed until the void fraction reaches values typical for random close packings of particles ($\epsilon_{inter} = 0.38 - 0.4$, Figure 1).[14−16] This behavior is explained by a decrease of packing order as the distance from the wall increases. To calculate the isothermal steady-flow profiles from a radial porosity distribution function $\epsilon_{inter}(r)$, which sensitively depends on particle shape, size distribution, and surface roughness, Vortmeyer and co-workers[13] employed a classical model based on the Brinkman equation.[17] They extended it to higher flow rates by adding an inertia term (incorporating the Ergun pressure-loss relation[18])

$$\frac{\partial p}{\partial z} = -150\,\eta_f \frac{(1-\epsilon_{inter}(r))^2}{\epsilon_{inter}(r)^3}\frac{v}{{d_p}^2} - 1.75\rho_f \frac{(1-\epsilon_{inter}(r))}{\epsilon_{inter}(r)^3}\frac{v^2}{d_p} + \frac{\eta_{eff}}{r}\frac{\partial}{\partial r}\left(r\frac{\partial v}{\partial r}\right) \quad (1)$$

An effective viscosity η_{eff} is used to compensate the failure of the pressure-loss relation close to the wall,[13] while η_f and ρ_f are the fluid dynamic viscosity and density. The consequences of this geometrical wall effect for the flow heterogeneity, axial dispersion, and particle-to-fluid heat and mass transfer may be particularly severe at aspect ratios $\psi = d_c/d_p$ below 15 where the wall region occupies a substantial fraction of the total column.[19−22] For larger aspect ratios it was found that (within limits of experimental precision) the dispersion in beds of spheres is independent of ψ.[23]

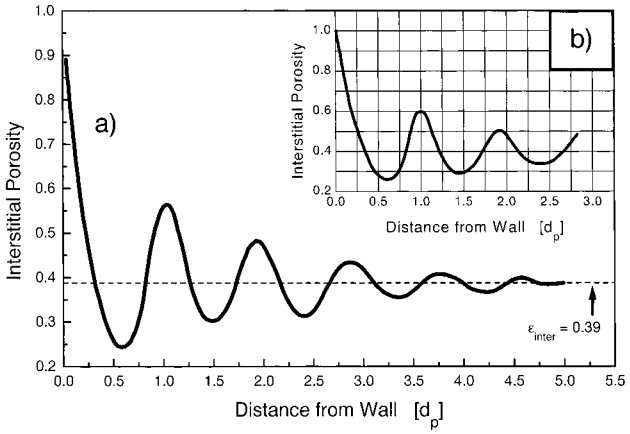

Figure 1. The radial porosity distribution function $\epsilon_{inter}(r)$ for fixed beds of monodisperse particles with perfect spherical shape and smooth surface. Experimental data for different column-to-particle diameter ratios: (a) $d_c/d_p = 14.1$, (b) $d_c/d_p = 5.6$ (after Benenati and Brosilow[15]).

A second wall effect has been shown to exist in analytical and preparative-scale columns ($\psi \gg 100$), which is probably caused by friction between the bed and the column wall.[24−26] This effect strongly depends on the packing procedure and operational characteristics. It is related to the relatively high compressibility of pulverulent materials and complex distribution of axial and radial stress during the compression of the bed.[27,28] For small slurry-packed columns it was found that the packing density is higher near the column exit and wall than in the upper and central regions.[29] The fractional volume affected by this

* To whom correspondence should be addressed. Present address: Lehrstuhl für Chemische Verfahrenstechnik, Otto-von-Guericke Universität Magdeburg, Universitätsplatz 2, 39106 Magdeburg, Germany. Phone: +49 (0)391 67-18644. Fax: +49 (0)391 67-12028. E-mail: ulrich.tallarek@vst.uni-magdeburg.de.

10.1021/jp0112471 CCC: $20.00
Published on Web 08/15/2001

interaction (compared to the first, purely geometrical effect) is much larger and may extend to about 50 d_p into the bulk of the bed.[30,31] It may be even thicker for preparative columns.[32] Both wall effects and the interplay as a function of ψ are critical in chromatography since radial variations of transport properties have a far more serious effect on column performance than do axial ones.

In sharp contrast to the radial porosity distribution function and its influence on the velocity heterogeneity in pressure-driven flows (wall effects in particular), it is the radial distribution of the zeta-potential (ζ) at the solid−liquid interface, i.e., a variation of the electrokinetic potential at the hypothetical plane of shear,[33,34] that determines the flow profile of an electrokinetically driven mobile phase through fixed beds. Electroosmotic flow (EOF) originates in the electrical double layer which exists when the liquid is in contact with charged surfaces such as those of ion exchange media.

Capillary electrochromatography (CEC) is typically carried out in capillary columns (i.d. < 150 μm) packed with 3−5 μm porous adsorbent particles (thus, ψ < 50). Electric fields of up to 100 kV/m are applied to move a buffer solution and solute through the medium by electroosmosis (and electrophoresis if the solute is charged).[35−39] Basically CEC is a hybrid between capillary electrophoresis (CE) and capillary high performance liquid chromatography (CHPLC), as the partitioning between two phases (e.g., a differential adsorption on the particles surfaces) still constitutes one major factor, as in CHPLC.[40,41] Concerning the interstitial flow characteristics, mainly two aspects may contribute to an improved efficiency of the EOF in chromatographic separations (as compared to pressure-driven flows).[42] They largely reflect implications of the parallel-pore model for a porous medium, although the exact microscopic details of the EOF are more complex than it suggests.[43,44] It is expected that the velocity distribution in a single pore of the network carries features of a plug-like profile which is predicted[45−49] and has also been observed[50,51] for pure electrokinetic flow in open capillaries, if the electrical double layer thickness (κ^{-1}) is small compared to the pore radius (r_{pore}). Second, with thin double layers ($\kappa r_{pore} \gg 1$), the average velocity in a pore is relatively independent of the pore radius and the actual porosity distribution has largely lost its impact on a flow heterogeneity.[46] This aspect is supported by observing that the average EOF in packed capillaries is hardly influenced by the particle diameter.[52]

For the EOF through fixed beds at a low aspect ratio (ψ < 50), however, it has been shown theoretically by Rathore and Horváth[53] and Liapis and Grimes[54] that the excess zeta-potential $\zeta_{ex} = (\zeta_w - \zeta_p)$, i.e., the difference between ζ associated with the capillary surface (ζ_w) and the particles surface (ζ_p), can have a deleterious effect on the column cross-sectional flow profile and average velocity. In general, the electrokinetic (and chromatographic) properties of these surfaces are quite different. Using the mathematical model constructed and solved by Liapis and Grimes,[54] the influence of the capillary wall (via ζ_w) on the radial distribution of the EOF can be expressed by (cf. Figure 2)

$$\frac{v_{eo}(r)}{v_p} = 1 + \left(\frac{\zeta_w}{\zeta_p} - 1\right)\frac{I_0(\beta r/d_p)}{I_0(\beta r_{eff}/d_p)} \qquad (2)$$

with $0 \le r \le r_c - 7/\kappa \equiv r_{eff}$ and where I_0 is the zero-order modified Bessel function of the first kind and r_{eff} is an effective capillary radius that accounts for the no-slip condition at the inner wall of the column, i.e., $v_{eo}(r_c) = 0$.[54] The constant β characterizes the overall permeability of the bed and can be evaluated from the following relationship[55]

$$\beta = \left(\frac{9}{2}(1 - \epsilon_{inter})\Phi\right)^{1/2} \qquad (3)$$

The dimensionless parameter Φ depends on the drag force that is provided by a spherical porous (permeable) particle in the packing.[54,55] As demonstrated in Figure 2, both the excess zeta-potential and the aspect ratio contribute to the actual EOF profile. These effects are too significant to neglect in current CEC practice with ψ < 50 unless $\zeta_w \approx \zeta_p$. Although one of the ultimate goals,[52,56] the use of submicron particles in CEC columns (ψ > 100) is still far from a routine application.

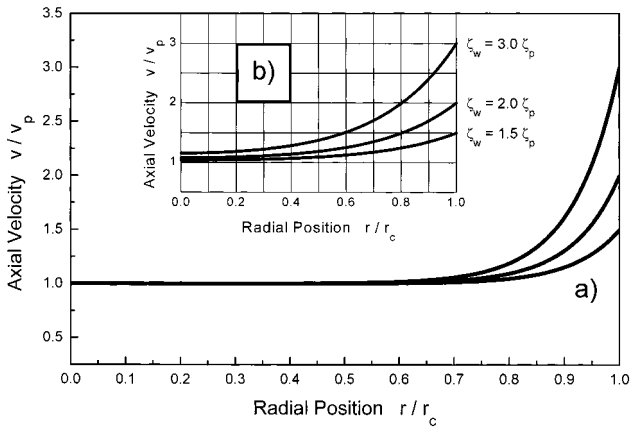

Figure 2. Radial distribution of the EOF velocity in packed beds (normalized by v_p, the velocity that is generated locally at the particle's external surface) for different values of ζ_w/ζ_p and aspect ratios, based on eq 2. (a) $d_c/d_p = 15$; (b) $d_c/d_p = 5$.

The present work was motivated by a very discrete influence of the column wall on the fluid dynamics of electroosmotic and pressure-driven flow fields in fixed beds. Because these wall effects are aggravated at a low aspect ratio, they are relevant to (electro)separation science when ψ < 50. We used pulsed field gradient (PFG) NMR and dynamic NMR microimaging to assign the origin and severe consequences of a systematic velocity heterogeneity to specific wall effects that are expected in either type of fluid flow. Our first direct documentation of wall effects for the EOF through a bed of charged porous particles in a charged capillary actually addresses the importance of that issue for a further optimization in CEC column engineering and surface chemistry.

Theoretical Background

Dispersion in Fixed Beds. In the asymptotic (long-time) limit, dispersion of a passive tracer in single-phase incompressible fluid flow through random porous media can be described by the local, averaged convection-diffusion equation in form of a macroscopic Fick law with an effective, i.e., constant dispersion tensor (**D**)[57]

$$\frac{\partial\langle c\rangle}{\partial t} + \mathbf{V}\cdot\nabla\langle c\rangle = \mathbf{D}\cdot\nabla^2\langle c\rangle \qquad (4)$$

It assumes implicitly that the dispersion process is Gaussian where $\langle c\rangle$ denotes the average concentration of tracer molecules and **V**, the mean interstitial velocity, is an average over the local (instantaneous) velocities, **v**. Then, **D** can be expressed by the autocorrelation function of the fluctuations in the velocity field[58]

$$\mathbf{D} = \lim_{t\to\infty} \int_0^t \langle [\mathbf{v}(0) - \mathbf{V}]\cdot[\mathbf{v}(t') - \mathbf{V}]\rangle \, dt' \quad (5)$$

Actually, eq 5 reflects the Lagrangian description of fluid motion since **D** is determined by an integral over the whole path of a molecule (in the limit of long times) and not by an average of local values as in the Eulerian approach, which involves an instantaneous picture of all the points in the flow field.[59] Eulerian ($\mathbf{D}_E$) and Lagrangian ($\mathbf{D}_L$) definitions give the same effective dispersion tensor **D** with the exception of possible antisymmetric components of $\mathbf{D}_E$ arising in media whose structures lack a reflectional symmetry (since $\mathbf{D}_L = \text{sym}\, \mathbf{D}_E$).[60] When the porous medium is isotropic on a macroscopic scale, **D** can be decomposed into axial and transverse components, i.e., those parallel (D_a) and perpendicular (D_t) to **V**, and the convection-diffusion equation becomes

$$\frac{\partial\langle c\rangle}{\partial t} + \mathbf{V}\cdot\nabla\langle c\rangle = D_a\frac{\partial^2\langle c\rangle}{\partial z^2} + D_t\nabla_t^2\langle c\rangle \quad (6)$$

In the preasymptotic dispersion regime (at intermediate times) and for heterogeneous porous media, in general, when the average displacements of tracer molecules are comparable to the spatial fluctuations in the velocity field and **D** is time-dependent, the nonlocal dispersion formalism due to Koch and Brady could be adapted.[61,62] Although this transport theory was originally developed for dilute systems of noninteracting spheres, experimental evidence for the applicability of that approach to random close packings has been recently presented by Ding and Candela.[63] **D** can be considered as a nonlocal generalization of the traditional (or Fickian) diffusivity, depending on the tracer particle shifts in space and time[61,62]

$$\mathbf{D} = \langle [\mathbf{v}(\mathbf{r}',t') - \mathbf{V}]\, P(\mathbf{r}',t'/\mathbf{r},t)\, [\mathbf{v}(\mathbf{r},t) - \mathbf{V}]\rangle \quad (7)$$

In this respect, $P(\mathbf{r}',t'/\mathbf{r},t)$ is the transition probability (or propagator) of finding a molecule at $\mathbf{r}'$ at time t' given that it was at **r** at time *t*. The nonlocal dispersion theory of Koch and Brady may be used to obtain the average concentration response to any source, regardless of its length scale or time scale, and allows to recognize non-Fickian behavior simply as dispersion processes that have not reached their asymptotic, i.e., (pseudo)-diffusive limits.

Analysis of Motion via Magnetic Field Gradients. The general analysis of fluid transport in fixed beds based on magnetic field gradients has found considerable potential (see Seymour and Callaghan[64] for a detailed description) and it includes the axial and transverse dispersion characteristics,[64−68] structure-flow and dispersion correlations,[69,70] scaling behavior,[71,72] and the stagnant mobile phase mass transfer kinetics.[73,74] In the context of dispersion, PFG-NMR can be used to obtain directly the nuclear spin (hence, a molecular) displacement probability distribution of the fluid (tracer) molecules in both electroosmotic and pressure-driven flows through packed capillaries, on an experimental time scale between 15 ms and ca. 1.5 s. The motion-encoding field gradients of amplitude (and direction) **g** and duration δ define a vector in **q**-space, i.e., $2\pi\mathbf{q} = \gamma\delta\mathbf{g}$[75−77] and γ is the gyromagnetic ratio of the nucleus. Introducing an averaged propagator, $P_{av}(\mathbf{R},\Delta)$,[78,79] as the probability that any molecule (e.g., ^1H_2O) travels a net distance $\mathbf{R} = \mathbf{r}'(t') - \mathbf{r}(t)$ over the experimental observation time $\Delta = (t' - t)$, we get a direct Fourier relation between $P_{av}(\mathbf{R},\Delta)$ and the normalized signal, $E(\mathbf{q},\Delta)$, acquired in the **q**-space, characterizing a PFG-NMR measurement in the narrow gradient pulse limit ($\delta \ll \Delta$)[80,81]

$$E(\mathbf{q},\Delta) = \frac{S(\mathbf{q},\Delta)}{S(0,\Delta)} = \int P_{av}(\mathbf{R},\Delta)\exp(i2\pi\mathbf{q}\cdot\mathbf{R})\, d\mathbf{R} \quad (8)$$

Thus, **q**-space is reciprocal to the (dynamic) displacement space **R** and $\mathbf{P}_{av}(\mathbf{R},\Delta)$ is recovered by Fourier transformation of $E(\mathbf{q},\Delta)$ with respect to **q**. The averaged propagator, $P_{av}(\mathbf{R},\Delta)$, of the fluid molecules is related to their conditional probability, $P(\mathbf{r}',t'/\mathbf{r},t)$, by the probability (i.e., nuclear spin) density, $\rho(\mathbf{r})$, for the original positions

$$P_{av}(\mathbf{R},\Delta) = \int \rho(\mathbf{r})\, P(\mathbf{r}',t'/\mathbf{r},t)\, d\mathbf{r} \quad (9)$$

In columns packed with porous particles we may distinguish (via the net displacements over time Δ) between convective-diffusive interparticle and purely diffusive fluid molecules that have remained in the deep stagnant pools inside the particles.[74] When on the experimental time scale both intraparticle diffusion and interparticle dispersion are Gaussian processes, the amplitude modulation of $S(\mathbf{q},\Delta)$ is given by

$$S(\mathbf{q},\Delta) = \sum_{n=1}^{2} A_n(\Delta)\exp\left[-4\pi^2\mathbf{q}^2 D_n\left(\Delta - \frac{\delta}{3}\right)\right] \quad (10)$$

$A_n(\Delta)$ represents the number of moving and stagnant fluid molecules. By recording $A_{intra}(\Delta)$ it is possible to monitor the fictitous emptying of the porous particles and characterize stagnant mobile phase mass transfer and its contribution to hold-up dispersion in the packed bed. The use of eq 10 assumes that adequate correction has been made for the nuclear spin−lattice (T_1) and spin−spin (T_2) relaxation times.[74]

In the context of our present PFG-NMR measurements, typical average axial displacements of the fluid molecules in both electroosmotic and pressure-driven flows through the packed capillary are not much larger than the spatial scale of the actual flow heterogeneity. Thus, the long-time limit of the apparent (transient) axial dispersion coefficient $D_{ap,a}$ taken with respect to the correlation time of the velocity fluctuations is not reached on the intrinsic experimental time scale. In this case, the low-**q** limit of $E(\mathbf{q},\Delta)$, corresponding to long-range displacements of fluid molecules in view of eq 8, may be analyzed to estimate $D_{ap,a}$. It has been shown by Callaghan and Stepišnik[82] that the initial slope of the amplitude modulation of $E(\mathbf{q},\Delta)$ can be expressed as

$$\lim_{\mathbf{q}\to 0}\frac{\partial}{\partial\mathbf{q}^2}\log|E(\mathbf{q},\Delta)| = -4\pi^2 D_a(\Delta)\Delta \quad (11)$$

Although eq 11 is exact only in the case that the distribution of corresponding displacements is Gaussian, this asymptotic analysis with $4\pi^2\mathbf{q}^2 D_a(\Delta)\Delta \ll 1$ provides a good working definition for the apparent (time-dependent) dispersion coefficient, i.e., $D_a(\Delta) \approx D_{ap,a}$.[64] In the long-time limit, this quantity corresponds to the effective (time-independent) dispersion coefficient that is defined by eq 6, i.e., $D_a(\Delta) \equiv D_a$. Then, when the exchange between mobile phase velocity extremes including intraparticle mass transfer is complete, $P_{av}(\mathbf{R},\Delta)$ becomes a Gaussian and eq 10 has reduced to a single exponent containing D_a.

When in addition to the motion-encoding field gradients **g** also spatial localization gradients of amplitude (and direction) **G** and duration λ are applied, the acquired signal is modulated in **q**-space and **k**-space ($2\pi\mathbf{k} = \gamma\lambda\mathbf{G}$)[82−84]

$$S(\mathbf{q},\mathbf{k}) = \int \rho(\mathbf{r}) \int P_{av}(\mathbf{R},\Delta) \exp(i2\pi\mathbf{q}\cdot\mathbf{R})\, d\mathbf{R}$$
$$\exp(i2\pi\mathbf{k}\cdot\mathbf{r})\, d\mathbf{r} = \int \rho(\mathbf{r})\, E(\mathbf{q},\mathbf{r},\Delta) \exp(i2\pi\mathbf{k}\cdot\mathbf{r})\, d\mathbf{r} \quad (12)$$

Thus, **k**-space is reciprocal to the (static) image space **r** and $P_{av}(\mathbf{R},\Delta)$ is implicitly a function of the pixel coordinate **r**. Double inverse Fourier transformation of $S(\mathbf{k},\mathbf{q})$ with respect to both **k** and **q** returns $\rho(\mathbf{r})P_{av}(\mathbf{R},\Delta)$. Normalizing this function by the image density $\rho(\mathbf{r})$ acquired with $\mathbf{q} = 0$, $P_{av}(\mathbf{R},\Delta)$ can be reconstructed for each pixel of the image. This dynamic NMR imaging (eq 12) naturally contains elements of both a Lagrangian (via motion-encoding) and Eulerian (via the spatial localization) information encoding.[64]

Experimental Section

Capillary (Electro)Chromatography. The 250 μm i.d. (365 μm o.d.) cylindrical fused-silica capillary (Polymicro Technologies, Phoenix, AZ) was slurry-packed[85] with spherical-shaped, strong cation-exchange particles ($d_p = 50$ μm, thus $\psi = 5$) at pressures up to 100 bar. These particles (POROS HS from PerSeptive Biosystems, Framingham, MA) have a high density of sulphopropyl groups (i.e., permanent charges over a wide range of pH) at their surface which provide the basis for an electrical double layer at the solid−liquid interface and the generation of an EOF through the fixed bed, in addition to the EOF being generated at the inner surface of the capillary due to the silanol groups of the fused-silica wall.[34] The final bed length was 20 cm. A degassed 10^{-3} M sodium tetraborate buffer solution (pH 9.13) was used as the mobile phase in all our experiments, usually run in the creeping laminar flow regime with Reynolds numbers of the order of 0.05.[59] For the measurements requiring a steady EOF in the packed capillary, the electrodes of a modular CE instrument operating from 0 to 30 kV and up to 0.2 mA (Fa. Grom, Herrenberg-Kayh, Germany) were connected to the column by a home-built PEEK block with flow splitter and a buffer vessel through open fused-silica capillary segments.[51] An integrated HPLC pump could be used for pressure-driven flows. Electrical field strengths and currents typically involved were around 35 kV/m and 20 μA, respectively.

Nuclear Magnetic Resonance. The ^{1}H NMR measurements were made at 30.7 MHz on an electromagnet (Bruker, Karlsruhe, Germany) interfaced with a SMIS console (Surrey Medical Imaging Systems, Guildford, U.K.) and an actively shielded gradient system (Doty Scientific, Columbia, SC) providing magnetic field gradients of up to 0.6 T/m. The packed capillary was fixed within a home-built radio frequency (r.f.) insert[51] based on a 1.5 mm i.d. and 11 mm long solenoidal r.f. coil which allows a convenient sample access in the magnet. For spatially nonresolved measurements of $P_{av}(\mathbf{R},\Delta)$ we used the stimulated echo sequence of the PFG-NMR methodology,[84] with Δ up to 1.5 s. $S(\mathbf{q},\Delta)$ is generally acquired with a constant gradient pulse duration ($\delta = 2.5$ ms, $\delta \ll \Delta$), but incremented gradient amplitude **g** by taking 40 **q**-steps in the range of $\pm\mathbf{q}_{max}$ and up to 64 signal averages at each value of **q**. Echo signals were acquired on-resonance and phased individually to extract the net amplitude modulation of $S(\mathbf{q},\Delta)$. The dispersion coefficient is characterized in the low-**q** limit, with $4\pi^2\mathbf{q}^2D_a(\Delta)\Delta \ll 1$ (cf. eqs 10 and 11). All calculations were made by using IDL (Interactive Data Language, Research Systems Inc., Boulder, CO).

For the microimaging of molecular displacements in the packed capillary, we implemented a pulse sequence that combines motion-encoding pulsed field gradients with a multiple spin−echo imaging module.[86] It is the unique feature of this approach that not only an amplitude attenuation but also phase-information is maintained over the whole echo-train at each value of **q**. Figure 3 illustrates the information of the multiecho PFG-NMR experiment after Fourier transformation of $S(\mathbf{k},\mathbf{q})$ with respect to **k**. Horizontally shown in Figure 3a is the modulation of the real part of $\rho(\mathbf{r})S(\mathbf{q})$ as a function of **q**, whereas the signal decay in the echo-train is displayed vertically. After Fourier transformation of $\rho(\mathbf{r})S(\mathbf{q})$ with respect to **q** (zero-filling of the data is possible here), we obtain $\rho(\mathbf{r})P_{av}(\mathbf{R},\Delta)$ in Figure 3b. The signal decay in the echo-train is usually characterized by T_2, but with a used nominal in-plane resolution of 40 × 40 μm the imaging gradients become large enough that this decay is also affected by the dispersive motion of the fluid molecules.[87] In principle, such a multiecho PFG-NMR imaging experiment can relate an initial signal amplitude and a characteristic decay time to any pixel and value of **R**. We used an additional multiecho imaging experiment (i.e., $\mathbf{q} = 0$) with increased signal-to-noise ratio (40 averages and 20 echoes) to examine the characteristic decay time for each pixel in the column. No systematic differences in decay times could be retrieved and we used the mean value (32 ms) to filter signals in the echo-train for each pixel in order to add filtered signals when needed and increase the signal-to-noise ratio of the final pixel propagators.

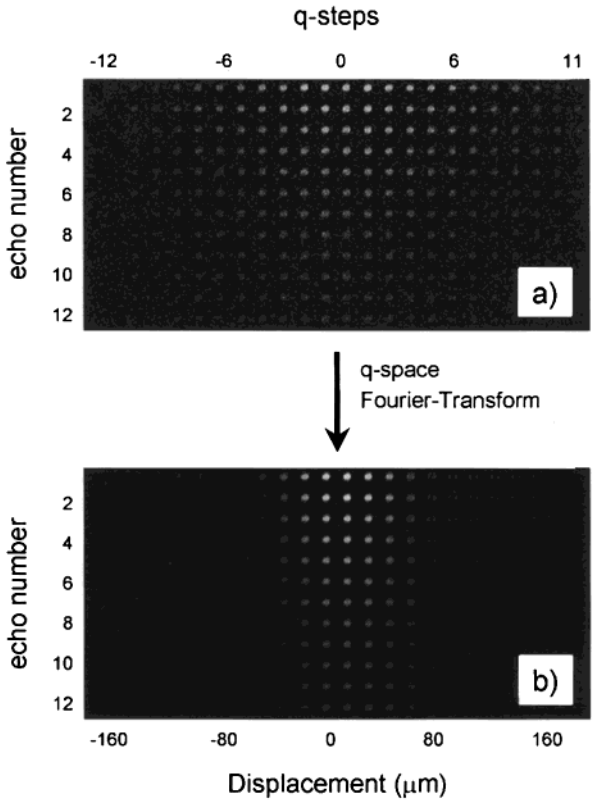

Figure 3. Multiecho PFG-NMR imaging experiment after Fourier transformation of the data with respect to **k**. (a) 24 × 12 images of the packed capillary (24 **q**-steps and 12 echoes) demonstrating the modulation of the complex signals real part depending on **q** (horizontally) and echo number (vertically). (b) 24 images after zero filling in **q**-space from 24 to 72 steps and Fourier transformation with respect to **q**. The horizontal axis represents displacement space. Experimental parameters: 20 × 20 × 12 × 24 matrix; 0.8 mm field of view; 6.0 mm slice thickness; 0.8 s repetition time; $\mathbf{g}_{max}$, 0.31 T/m, $\delta = 2.3$ ms; $\Delta = 17.5$ ms; and echo time in train, 5.2 ms.

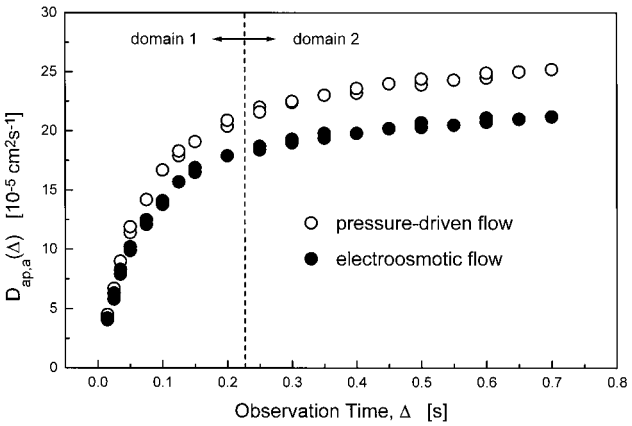

Figure 4. Observation time-dependence of the apparent axial dispersion coefficient $D_{ap,a}$ for electrokinetically and pressure-driven flows through the packed capillary at $Pe = Vd_p/D_m = 15$. $D_m = 2.25 \times 10^{-5}$ cm^2 s^{-1} (molecular diffusivity of pure water) and V is the mean velocity in the bed referring to its total porosity because the particles are porous.

Results and Discussion

The inherent length scales of axial and transverse fluid transport heterogeneities in fixed beds not only influence the asymptotic value of the axial dispersion coefficient (D_a) but also affect the time scale on which this value is approached at a given Peclet number (Pe). The ultimate goal in terms of dispersion is a rapid exchange ("equilibrium") of molecules moving in velocity extremes of the fluid flow field. It may be achieved by reducing associated correlation lengths in the bed and/or by fast lateral dispersion. In this respect, $Pe = Vd_p/D_m$ indicates the relative importance of convective and purely diffusive contributions.

Beginning with the temporal domain characterizing the transient dispersion, Figure 4 displays $D_{ap,a}$ as a function of time for electroosmotic and pressure-driven flows at $Pe = 15$, which is in a range typical for liquid chromatography ($5 < Pe < 20$). After a first, relatively steep increase up to ca. 250 ms (first domain), the curves level off and $D_{ap,a}$ seems to reach a plateau region. However, a closer look reveals that within this second domain the dispersion still increases in both types of liquid flow, i.e., $D_{ap,a}$ has not reached an asymptotic value yet and, in fact, it is not observed on the experimental time scale. In addition to this long-time tail ("disequilibrium") in the dispersion characteristics (it should be recalled that $D_{ap,a}$ itself is calculated from the NMR signal amplitude in the low-**q** limit by eq 11), Figure 5 shows corresponding, complete axial displacement probability distributions for EOF through the packed capillary. Propagator shapes for pressure-driven flow are qualitatively similar. They reveal features that have been reported earlier for nonporous particles.[88] Differences in the present work are due to the fact that the particles are totally porous, with an intraparticle porosity of about 0.65,[89] and that the aspect ratio is very low ($\psi = 5$). Thus, a contribution of wall effects (cf. Figures 1 and 2) to the studied macroscopic flow heterogeneity is aggravated.

At short times, the radially averaged axial displacement probability distribution mostly reflects the distribution of average velocity components in single pores of the porous medium (Figure 5a). It is caused by microscopic factors such as the random orientation of pores and differences in local morphology (permeability) or the electrokinetics (zeta-potential), depending on which type of flow we consider. While the diffusion length $L_D = (2D_m\Delta)^{1/2}$ in this flow regime may be sufficient to allow an exchange of velocities within the single pore, both L_D and the convective length $L_C = \bar{v}\Delta$ are typically smaller than the

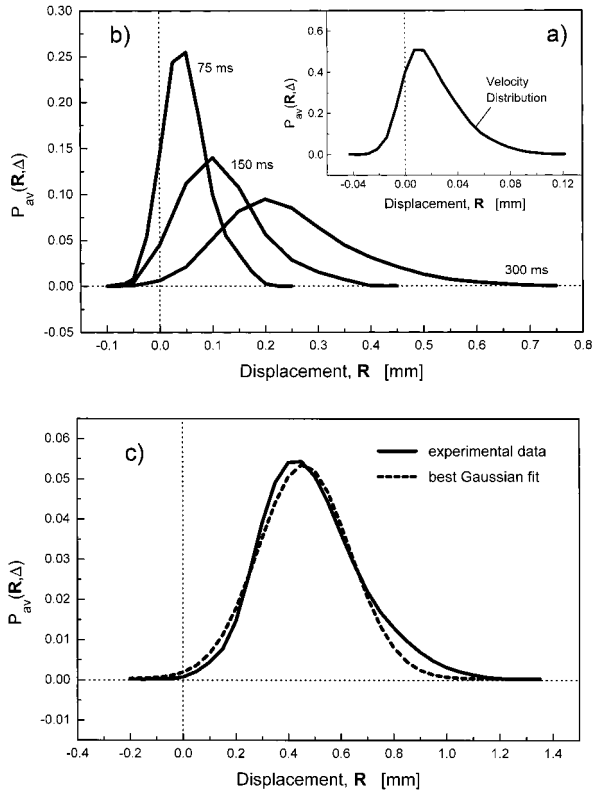

Figure 5. Radially averaged axial displacement probability distributions for EOF through the fixed bed in dependence of the observation time, $Pe = 15$. (a) $\Delta = 35$ ms, (b) Δ from 75 to 300 ms, and (c) $\Delta = 600$ ms. Electrical currents remained constant over the measurement periods within 3%.

longitudinal pore dimension, i.e., fluid molecules do not exchange between different pores ($\bar{v}$ is the average pore velocity). Concluding from this microscopic viewpoint, $P_{av}(\mathbf{R},\Delta) = P(\bar{\mathbf{v}})$ also contains the complete velocity heterogeneity underlying the macroscopic flow profile. The highest average pore velocity that we calculate with Figure 5a (neglecting the fact that lateral diffusion over an L_D of 12 μm at $\Delta = 35$ ms has already achieved some exchange between flow velocities and thus blurs the clean velocity spectrum) is about 2.95 mm/s. This is quite a high (local) value, assuming that it originates in a straight pore between charged particles. Even when we take into account that the column cross-sectional averaged EOF (as compared to the straight single-pore geometry) is reduced by the tortuosity factor of the bed (approximately 0.6), this value remains much too high for typical cation exchange resins that have been used in CEC.[90−92] It rather suggests that the high-velocity components observed in Figure 5a are associated with the fused-silica wall of the capillary. The values are, in fact, closer to those EOF velocities that have been obtained for open (fused-silica) capillaries using the same NMR approach and buffer; stronger thermal effects in the open tubular case caused by a Joule heating can explain most differences that may still exist.[51] Thus, by knowing the typical EOF velocities in open and packed capillaries at sufficiently high ψ, already the one-dimensional propagator information allows to recognize larger displacements of fluid molecules close to the column wall moving in an annular region with a lateral dimension of the order of L_D, i.e., the distance that a molecule with $\bar{v}_{max}$ at r_{eff} (eq 2) can diffuse along the radial velocity gradient.

Electrokinetic potentials at the inner wall of quartz capillaries up to −100 mV and even above are not unusual, although with the buffers and concentrations typically used in CEC the value

presents an upper limit and ζ_w usually ranges between -50 and -100 mV.[93−96] By contrast, ζ_p of many commercial strong cation exchange particles such as those used in the present work can be significantly smaller than ζ_w of the bare fused-silica capillary,[91] depending on the exact surface chemistry of the particle and associated electrokinetics. Thus, although these surfaces with sulfonic acid (cation exchange particle) and silanol groups (fused-silica capillary) both carry a negative charge density, the ratio ζ_w/ζ_p can be still substantial in current CEC practice (cf. Figure 2).[90−92] In the extreme case that the particle surface does not generate an EOF, only the capillary inner surface may contribute to a volume flow,[54] if the resistance provided by the fixed obstacles does not prevent it completely. This also depends on the ratio of involved surface areas and consequently on ψ.

Yet another remark concerning the EOF behavior in porous media should be made at this point. It has been demonstrated that the equivalent radius of interstitial channels in packed beds (r_{inter}) is 25 to 40% of the particle radius,[97] i.e., $r_{inter} \approx 8$ μm in the present work for $r_p = 25$ μm. Together with the buffer concentration (10^{-3} M), which gives κ^{-1} of the order of only 10 nm,[34] we are actually measuring in the limit of thin electrical double layers ($\kappa r_{inter} \gg 1$). In this regime, double-layer overlap in individual channels of the packed beds interstitial pore space is completely prevented (except at the contact points of particles) and the EOF should show a significantly superior performance compared to pressure-driven flows, including a relatively flat pore-level flow profile and average pore velocity that is rather independent of the pore radius (thus, also of the local packing homogeneity).[46,93] As we have already seen in Figure 4, however, the axial dispersion characteristics of the EOF at long times are only moderately better than for pressure-driven flow (about 15%) when compared to the striking difference in a straight open capillary,[50,51,98] and we demonstrate the main reason for it in due course.

By proceeding from Figure 5a, which indicates the distribution of average pore velocities via the exponential front of $P_{av}(\mathbf{R},\Delta)$,[88] to Figure 5c, the observation time Δ is increased to 600 ms. The most striking result is that (in agreement with the data shown in Figure 4) a perfect Gaussian shape has not been reached after this long time, which, on a purely diffusive basis, translates to an L_D of ca. 50 μm. It is evident that a disequilibrium in the fluid molecule axial displacement probability distribution must remain, $P_{av}(\mathbf{R},\Delta)$ shows still substantial fronting. In the literature dealing with non-Gaussian dispersion in porous media, usually two mechanisms are discussed in that context: trapping of fluid molecules in stagnant zones and macroscopic flow heterogeneity.[58,99] However, in contrast to some consolidated porous media such as rocks or sintered glass beads, the packed beds typically used in modern liquid chromatography have a relatively discete time scale and length scale characterizing transport in stagnant zones and flow heterogeneity. The particles are spherical, with narrow size distribution.[85] Thus, the interstitial pores for flow are well connected, without particle cracks and fines, while stagnant zones are limited to the intraparticle pore space and hydrodynamic boundary layer that exists on the particle's external surface.

To specifically focus on macroscopic flow heterogeneity as a cause for the observed non-Gaussian behavior, we first study the characteristic time of stagnant mobile phase mass transfer for pressure-driven flow through the packed bed. It is achieved by selecting Pe high enough that moving and stagnant fluid can be quantitatively discriminated by eq 10, i.e., that the interstitial dispersion far exceeds intraparticle diffusion (cf. Figure 6a).

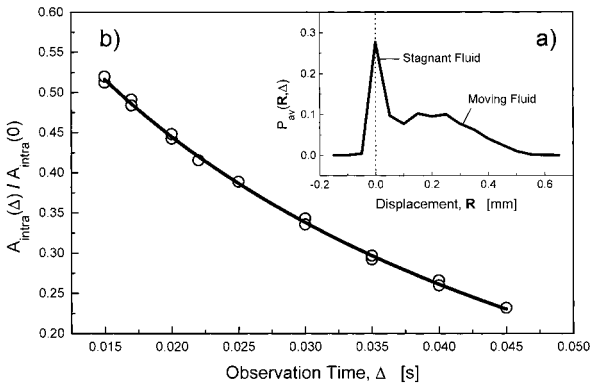

Figure 6. Stagnant mobile phase mass transfer for the 10^{-3} M sodium tetraborate buffer solution entrained in the deep pools of the cation exchange particles ($d_p = 50$ μm). (a) Averaged propagator distribution demonstrating stagnant and moving fluid fractions in the bed, $\Delta = 22$ ms. (b) Actual mass transfer kinetics and best fit of the data to eq 13 (solid line, $r^2 = 0.998$).

Then, with a series of measurements at increasing Δ, we determine $A_{intra}(\Delta)$, the amount of those fluid molecules that have remained purely diffusive inside the particles (in general, in any stagnant region of the medium as long as the characteristic dimension of that stagnant zone is much larger than L_D). By recording this fictitous emptying of the particles, we use that approach to calculate an intraparticle diffusion coefficient (D_{intra}) from the classical mass transfer rate constant[74,100]

$$\frac{A_{intra}(\Delta)}{A_{intra}(0)} = \frac{6}{\pi^2}\sum_{n=1}^{\infty}\frac{1}{n^2}\exp\left(-n^2\pi^2\frac{D_{intra}\Delta}{r_p^{\,2}}\right) \qquad (13)$$

The results of the analysis are shown in Figure 6b, and we see that the diffusion equation fits well the experimental data. Based on the intraparticle tortuosity factor (τ_{intra}), the average size and spherical shape of the particle diffusion-limited mass transfer should be finished after a characteristic exchange time (Δ_e), assuming that the molecules have to travel a net distance of $d_p/2$ to leave the porous particles completely

$$\Delta_e = \frac{\tau_{intra}}{2D_m}\left(\frac{d_p}{2}\right)^2 \text{ with } \left(\sqrt{\langle \mathbf{R}_{intra}^2 \rangle}\right)_{\Delta=\Delta_e} = \frac{d_p}{2} \qquad (14)$$

With eq 13 we find $D_{intra} = 1.34 \times 10^{-5}$ cm^2 s^{-1} ($\tau_{intra} = D_m/D_{intra} = 1.68$) and $\Delta_e = 233$ ms. Thus, the well-characterized stagnant mobile phase mass transfer in the packing (Figure 6) can be excluded as a cause for the transient dispersion behavior observed in domain 2 of Figure 4 and a corresponding non-Gaussian propagation of fluid molecules in Figure 5c. On the other hand, the temporal domain of this kinetics matches the time scale of domain 1 and, thus, may be responsible for most of the steep increase in $D_{ap,a}(\Delta)$. Actually, the dotted line in Figure 4 indicates the time when stagnant mobile phase mass transfer is complete for pressure-driven flow. This behavior is in contrast to nonporous particles for which an asymptotic dispersion, i.e., a transition from stationary random flow to pseudo-diffusion, is reached much faster than with porous ones,[64] because the holdup contribution is simply not present.[71] In this respect it has been indicated that correlation times for nonmechanical dispersion mechanisms (holdup and boundary-layer dispersion) are long diffusive times and that transient effects associated with nonmechanical dispersion are more persistent than those associated with mechanical dispersion, i.e.,

with the dispersion due to velocity fluctuations in the bulk fluid induced by the randomly distributed particles.[62]

In the present case, however, we also expect substantial macroscopic flow heterogeneity for EOF and pressure-driven flows through the bed (Figures 1 and 2). The length scales coupled to this nonuniformity of the flow pattern may spread over the whole capillary radius and by far exceed those associated with the stagnant mobile phase mass transfer (in which case it is just the particle radius). Then, the time needed to achieve an exchange of fluid molecules moving in the center of the bed and at the wall by lateral diffusion (or, more correctly, lateral dispersion at the actual Pe, because $D_t > D_m/\tau_{bed}$) can be a few seconds for $r_c = 125\ \mu$m. The situation becomes more severe for slowly diffusing biomolecules ($D_m < 10^{-7}$ cm^2 s^{-1}). It implies that through the involved transcolumn correlation length a macroscopic flow heterogeneity is responsible for the most persistent transient dispersion component (Figures 4 and 5), similar to the preasymptotic regime of Taylor−Aris dispersion in an open tube (although it shall by no means imply that the actual flow profiles are similar).[51,101] For the latter case of a transcolumn equilibration, a perfect Gaussian displacement distribution is observed only when $L_D \geq r_c$.[102] In the case of fixed beds, on the other hand, this length scale (r_c) may be covered faster due to lateral dispersion and the "diffusion" length becomes $L_D = (2D_t\Delta)^{1/2}$. By applying the magnetic field gradients perpendicular to the flow direction we can measure transverse dispersion and find $D_{ap,t} = 2.64 \times 10^{-5}$ cm^2 s^{-1} at $\Delta = 600$ ms and Pe = 15 (cf. domain 2, Figure 4). Concerning its flow rate dependence, $D_{ap,t}(\Delta)$ has just left the so-called tortuosity-limited dispersion regime characterized by $D_m/\tau_{bed} < D_t < D_m$.

The value of $D_{ap,t}(\Delta)$ is almost an order of magnitude smaller than $D_{ap,a}(\Delta)$ and translates to an L_D of only 56 μm. Although it slightly exceeds purely diffusive mass transfer, this distance is by far not enough to allow the lateral dispersion of fluid molecules over the whole column radius. Consequently, features of a macroscopic flow heterogeneity such as transient dispersion and an associated non-Gaussian distribution of the fluid-element displacements will persist at corresponding observation times (as evident in Figures 4 and 5).

Still another detail (Figure 5c) suggests that some macroscopic flow heterogeneity of a type indicated by Figures 1 and 2 is responsible for the non-Gaussian distribution of fluid-element displacements (when $L_D < r_c$). We generally observed no tailing but fronting in $P_{av}(\mathbf{R},\Delta)$, which implies the existence of a substantial region in both electroosmotic and pressure-driven flows with higher-than-average velocity (the "true" average refers to a packed segment without wall effect, i.e., to an infinite-diameter bed). By contrast, the large heterogeneities caused by low-permeability zones in which the velocity is not necessarily zero and by purely diffusive zones (especially important for porous media near the percolation threshold or very slowly diffusing solutes which strongly adsorb on the surface) usually give rise to tailing.[57,58] We now tried to spatially resolve these wall effects by dynamic NMR microimaging with in-plane resolution of 40 μm. The slice thickness was set to 6 mm because we expect the effects to be systematic along the column axis and consequently do not require a high spatial resolution in this third dimension. Thus, a reasonable signal-to-noise ratio and a sufficiently high resolution over the column cross-section (compared to the particle diameter, $d_p = 50\ \mu$m) could be achieved.

The results of this microscopic investigation are summarized in Figures 7 and 8. The single-pixel propagator distributions in

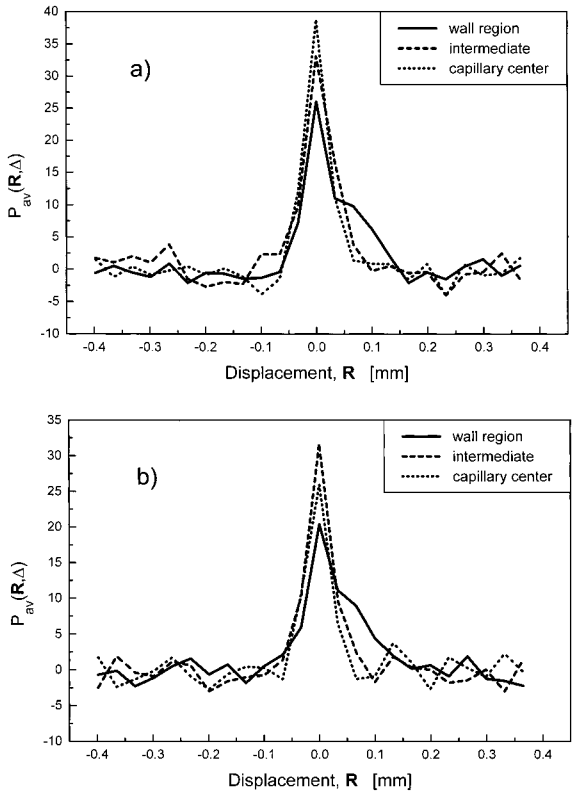

Figure 7. Axial displacement probability distribution for fluid molecules in single pixels of the image. (a) EOF and (b) pressure-driven flow through the packed capillary ($\Delta = 17.5$ ms). Pixels are taken along a straight line through the center, wall, and intermediate region of the column cross-section. For experimental parameters refer to Figure 3.

Figure 7 clearly reveal a substantial increase of fluid velocity close to the column wall as compared to the center of the bed. It seems that the macroscopic flow heterogeneities in electroosmotic and pressure-driven flows extend even further inward from the wall to pixels at intermediate positions and thus may cover length scales of the order of the column radius in the present case with $\psi = 5$. The propagators from four added pixels representative of wall and center positions are shown in Figure 8. Data were collected from opposite edges of the capillary cross-section (wall region 1 and 2), and, in contrast to $P_{av}(\mathbf{R},\Delta)$ in Figure 7, they are zero-filled and normalized. The distributions show pronounced shoulders or even separate local maxima for fluid molecules in pixels closer to the column wall and the effects scale with observation time (Figures 8a and 8b), but a lateral exchange of molecules between velocity extremes is also promoted. Thus, pore-level velocities become increasingly blurred as we approach equilibrium in the mobile phase.

In both types of flow, we observe higher velocities as we move toward the wall, although at this stage it is difficult to say whether the effects are more severe in EOF than for pressure-driven flow because the difference in $D_{ap,a}(\Delta)$ remains small at the observation times used to acquire the data shown in Figures 7 and 8 (domain 1, Figure 4). Yet, they have a completely different origin, but in both cases contribute substantially to the interstitial dispersion. At this stage, however, it is more important that the high-velocity components seen in these imaging studies close to the capillary wall compare well with top velocities in the exponential front of the 1-D propagators (Figure 5a), which a priori have been blamed on the fused-silica wall (via ξ_w). The results confirm that a first insight into the magnitude of EOF velocities in the critical wall region can

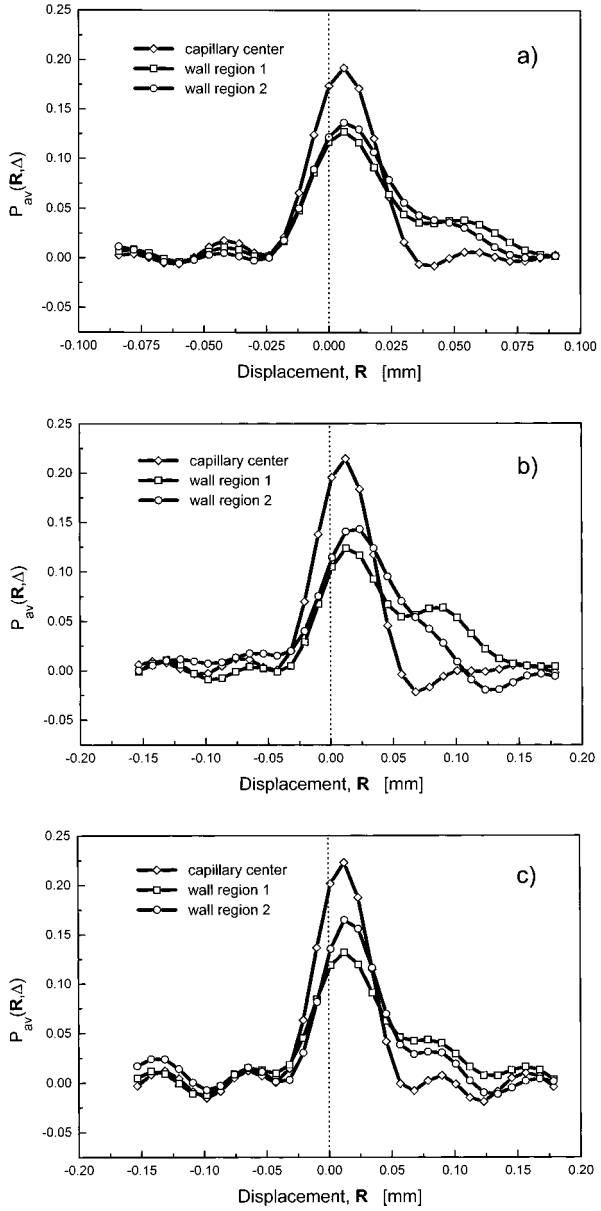

Figure 8. Added propagators comparing the fluid dynamics in wall and center positions of the capillary for EOF: (a) $\Delta = 17.5$ ms and (b) $\Delta = 35$ ms, and pressure-driven flow (c) $\Delta = 35$ ms. Displacement distributions have been normalized by their surface area. Mobile phase: 10^{-3} M sodium tetraborate buffer (pH 9.13).

already be gained from the 1-D data, with measurement times of 10 min only. Ongoing studies that could help to distinguish further between these macroscopic flow heterogeneities could employ matched surface potentials ($\zeta_w \approx \zeta_p$) while keeping ψ constant and, thus, leaving the wall effect critical for pressure-driven flow, but minimizing it with EOF.

Conclusions

Our results demonstrate that a significantly superior performance, which has been shown for EOF through packed capillaries[35−39] compared to pressure-driven flows, can be obstructed by wall effects, and it is difficult to trace back remaining differences in the asymptotic dispersion observed for these types of fluid flow to an inherent performance concerning intraparticle and film mass transfer or a macroscopic flow heterogeneity. NMR microscopy and PFG-NMR are techniques by which the physical mechanisms that contribute to dispersion in the flowing and stagnant zones of the bed may be addressed separately.

The influence of the documented electrokinetic wall effect in current CEC practice ($\psi < 50$) is two-fold. First, depending on the ratios d_c/d_p and ζ_w/ζ_p, it contributes to the long-time averaged velocity through the packed capillary. Second, it engenders additional band spreading. Even if the aspect ratio can be increased and the first consequence be neglected, systematic offsets in zeta-potential remain and sensitively influence eddy-dispersion. This particular contribution can be eliminated only when $\zeta_w \approx \zeta_p$ and is rather important to consider in CEC where particle technology has begun to focus on electrokinetics in more detail.[39]

The operation with pressure-driven flows in packed capillaries is limited by the back pressure of the beds. For this reason, aspect ratios typically used in CHPLC are below 50. Wall effects are caused by the radial distribution of porosity, which has been extensively studied for larger columns.[1−16] The problems encountered with particulate packings in CHPLC and CEC can be overcome by the use of monoliths.[103−105] They are fabricated as a continuous porous medium with small domain size of the solid or porous fractal skeleton, but relatively large flow-through pores, providing low pressure-drops and high column efficiency. In view of the zeta-potential and CEC applications, the capillary inner wall may be coated by a fluid-impervious annulus of the same material, thus reducing the excess zeta-potential between wall (usually fused-silica) and monolithic material.

Acknowledgment. We gratefully acknowledge the award of a Marie Curie Fellowship (U.T.) under the Training and Mobility of Researchers Program from the European Union (Contract ERBFMBI-CT98-3437). This research was further supported by the European Community activity Large-Scale Facility Wageningen NMR Centre (Contract ERBCHGE-CT95-0066), by the Technology Foundation STW (Project WBI.3493), Applied Science Division of the Dutch Science Foundation NWO, and the Deutsche Forschungsgemeinschaft DFG (Grant SE 586/7-1). We thank Erdmann Rapp (Otto-von-Guericke Universität Magdeburg, Germany) for preparing the packed capillary.

References and Notes

(1) Schertz, W. W.; Bischoff, K. B. *AIChE J.* **1969**, *15*, 597.
(2) Lerou, J. J.; Froment, G. F. *Chem. Eng. Sci.* **1977**, *32*, 853.
(3) Pillai, K. K. *Chem. Eng. Sci.* **1977**, *32*, 59.
(4) Schuster, J.; Vortmeyer, D. *Chem. Eng. Technol.* **1981**, *53*, 806.
(5) Vortmeyer, D.; Schuster, J. *Chem. Eng. Sci.* **1983**, *38*, 1691.
(6) Vortmeyer, D.; Michael, K. *Chem. Eng. Sci.* **1985**, *40*, 2135.
(7) Govindarao, V. M. H.; Froment, G. F. *Chem. Eng. Sci.* **1986**, *41*, 533.
(8) Ziolkowska, I.; Ziolkowski, D. *Chem. Eng. Process.* **1988**, *23*, 137.
(9) Daszkowski, T.; Eigenberger, G. *Chem. Eng. Sci.* **1992**, *47*, 2245.
(10) Legawiec, B.; Ziolkowski, D. *Chem. Eng. Sci.* **1994**, *49*, 2513.
(11) Papageorgiou, J. N.; Froment, G. F. *Chem. Eng. Sci.* **1995**, *50*, 3043.
(12) Bey, O.; Eigenberger, G. *Chem. Eng. Sci.* **1997**, *52*, 1365.
(13) Giese, M.; Rottschäfer, K.; Vortmeyer, D. *AIChE J.* **1998**, *44*, 484.
(14) Roblee, L. H. S.; Baird, R. M.; Tierney, J. W. *AIChE J.* **1958**, *4*, 460.
(15) Benenati, R. F.; Brosilow, C. B. *AIChE J.* **1962**, *8*, 359.
(16) Ridgway, K.; Tarbuck, K. J. *Chem. Eng. Sci.* **1968**, *23*, 1147.
(17) Brinkman, H. C. *Appl. Sci. Res.* **1947**, *A1*, 27.
(18) Ergun, S. *Chem. Eng. Prog.* **1952**, *48*, 89.
(19) Hsiang, T. C.; Haynes, H. W., Jr. *Chem. Eng. Sci.* **1977**, *32*, 678.
(20) Martin, H. *Chem. Eng. Sci.* **1978**, *33*, 913.
(21) Carbonell, R. G. *Chem. Eng. Sci.* **1980**, *35*, 1347.
(22) Ahn, B.-J.; Zoulalian, A.; Smith, J. M. *AIChE J.* **1986**, *32*, 170.
(23) Gunn, D. J.; Price, C. *Trans. Inst. Chem. Eng.* **1969**, *47*, 341.
(24) Guiochon, G.; Farkas, T.; Guan-Sajonz, H.; Koh, J.-H.; Sarker, M.; Stanley, B. J.; Yun, T. *J. Chromatogr. A* **1997**, *762*, 83.

(25) Guiochon, G.; Drumm, E.; Cherrak, D. *J. Chromatogr. A* **1999**, *835*, 41.
(26) Shalliker, R. A.; Broyles, B. S.; Guiochon, G. *J. Chromatogr. A* **2000**, *888*, 1.
(27) Sarker, M.; Katti, A. M.; Guiochon, G. *J. Chromatogr. A* **1996**, *719*, 275.
(28) Train, D. *Trans. Inst. Chem. Eng.* **1957**, *35*, 258.
(29) Yuan, Q. S.; Rosenfeld, A.; Root, T. W.; Klingenberg, D. J.; Lightfoot, E. N. *J. Chromatogr. A* **1999**, *831*, 149.
(30) Knox, J. H.; Laird, G. R.; Raven, P. A. *J. Chromatogr.* **1976**, *122*, 129.
(31) Eon, C. H. *J. Chromatogr.* **1978**, *149*, 29.
(32) Farkas, T.; Sepaniak, M. J.; Guiochon, G. *AIChE J.* **1997**, *43*, 1964.
(33) Probstein, R. F. *Physicochemical Hydrodynamics: An Introduction*; John Wiley & Sons: New York, 1994.
(34) Lyklema, J. *Fundamentals of Interface and Colloid Science, Vol. II: Solid−Liquid Interfaces*; Academic Press: London, 1995.
(35) Dittmann, M. M.; Wienand, K.; Bek, F.; Rozing, G. P. *LC-GC* **1995**, *13*, 800.
(36) Crego, A. L.; González, A.; Marina, M. L. *Crit. Rev. Anal. Chem.* **1996**, *26*, 261.
(37) Colón, L. A.; Reynolds, K. J.; Alicea-Maldonado, R.; Fermier, A. M. *Electrophoresis* **1997**, *18*, 2162.
(38) Fujimoto, C. *TrAC − Trends Anal. Chem.* **1999**, *18*, 291.
(39) Colón, L. A.; Burgos, G.; Maloney, T. D.; Citrón, J. M.; Rodríguez, R. L. *Electrophoresis* **2000**, *21*, 3965.
(40) Tsuda, T. *Anal. Chem.* **1987**, *59*, 521.
(41) Knox, J. H. *J. Chromatogr. A* **1994**, *680*, 3.
(42) Knox, J. H. *Chromatographia* **1988**, *26*, 329.
(43) Patankar, N. A.; Hu, H. H. *Anal. Chem.* **1998**, *70*, 1870.
(44) Rathore, R. S.; Horváth, Cs. *Anal. Chem.* **1998**, *70*, 3069.
(45) Dresner, L. *J. Phys. Chem.* **1963**, *67*, 1635.
(46) Rice, C. L.; Whitehead, R. *J. Phys. Chem.* **1965**, *69*, 4017.
(47) Gross, R. J.; Osterle, J. F. *J. Chem. Phys.* **1968**, *49*, 228.
(48) Sims, S. M.; Higuchi, W. I.; Srinivasan, V.; Peck, K. *J. Colloid Interface Sci.* **1993**, *155*, 210.
(49) Arulanandam, S.; Li, D. *Colloids Surf. A* **2000**, *161*, 89.
(50) Paul, P. H.; Garguilo, M. G.; Rakestraw, D. J. *Anal. Chem.* **1998**, *70*, 2459.
(51) Tallarek, U.; Rapp, E.; Scheenen, T.; Bayer, E.; Van As, H. *Anal. Chem.* **2000**, *72*, 2292.
(52) Knox, J. H.; Grant, I. H. *Chromatographia* **1991**, *32*, 317.
(53) Rathore, R. S.; Horváth, Cs. *J. Chromatogr. A* **1997**, *781*, 185.
(54) Liapis, A. I.; Grimes, B. A. *J. Chromatogr. A* **2000**, *877*, 181.
(55) Neale, G.; Epstein, N.; Nader, W. *Chem. Eng. Sci.* **1973**, *28*, 1865.
(56) Unger, K. K.; Lüdtke, S.; Grün, M. *LC-GC Int.* **1999**, *12*, 870.
(57) Sahimi, M. *Flow and Transport in Porous Media and Fractured Rock: From Classical Methods to Modern Approaches*; VCH: Weinheim, 1995.
(58) Salles, J.; Thovert, J.-F.; Delannay, R.; Prevors, L.; Auriault, J.-L.; Adler, P. M. *Phys. Fluids A* **1993**, *5*, 2348.
(59) Bear, J. *Dynamics of Fluids in Porous Media*; Dover Publications: New York, 1988.
(60) Koch, D. L.; Cox, R. G.; Brenner, H.; Brady, J. F. *J. Fluid Mech.* **1989**, *200*, 173.
(61) Koch, D. L.; Brady, J. F. *J. Fluid Mech.* **1987**, *180*, 387.
(62) Koch, D. L.; Brady, J. F. *Chem. Eng. Sci.* **1987**, *42*, 1377.
(63) Ding, A.; Candela, D. *Phys. Rev. E* **1996**, *54*, 656.
(64) Seymour, J. D.; Callaghan, P. T. *AIChE J.* **1997**, *43*, 2096.
(65) Amin, M. H. G.; Gibbs, S. J.; Chorley, R. J.; Richards, K. S.; Carpenter, T. A.; Hall, L. D. *Proc. R. Soc. London A* **1997**, *453*, 489.
(66) Tallarek, U.; Bayer, E.; Guiochon, G. *J. Am. Chem. Soc.* **1998**, *120*, 1494.
(67) Stapf, S.; Packer, K. J.; Graham, R. G.; Thovert, J.-F.; Adler, P. M. *Phys. Rev. E* **1998**, *58*, 6206.
(68) Stapf, S.; Packer, K. J.; Békri, S.; Adler, P. M. *Phys. Fluids* **2000**, *12*, 566.
(69) Sederman, A. J.; Johns, M. L.; Alexander, P.; Gladden, L. F. *Chem. Eng. Sci.* **1998**, *53*, 2117.
(70) Manz, B.; Alexander, P.; Gladden, L. F. *Phys. Fluids* **1999**, *11*, 259.
(71) Van As, H.; Palstra, W.; Tallarek, U.; van Dusschoten, D. *Magn. Reson. Imaging* **1998**, *16*, 569.
(72) Manz, B.; Gladden, L. F.; Warren, P. B. *AIChE J.* **1999**, *45*, 1845.
(73) Tallarek, U.; van Dusschoten, D.; Van As, H.; Guiochon, G.; Bayer, E. *Angew. Chem., Int. Ed. Engl.* **1998**, *37*, 1882; *Angew. Chem.* **1998**, *110*, 1983.
(74) Tallarek, U.; Vergeldt, F. J.; Van As, H. *J. Phys. Chem. B* **1999**, *103*, 7654.
(75) Callaghan, P. T.; MacGowan, D.; Packer, K. J.; Zelaya, F. O. *J. Magn. Reson.* **1990**, *90*, 177.
(76) Callaghan, P. T.; Coy, A.; MacGowan, D.; Packer, K. J.; Zelaya, F. O. *Nature* **1991**, *351*, 467.
(77) Cotts, R. M. *Nature* **1991**, *351*, 443.
(78) Kärger, J.; Heink, W. *J. Magn. Reson.* **1983**, *51*, 1.
(79) Kärger, J.; Pfeiffer, H.; Heink, W. *Adv. Magn. Reson.* **1988**, *12*, 1.
(80) Stejskal, E. O.; Tanner, J. E. *J. Chem. Phys.* **1965**, *42*, 288.
(81) Stejskal, E. O. *J. Chem. Phys.* **1965**, *43*, 3597.
(82) Callaghan, P. T.; Stepišnik, J. *Adv. Opt. Magn. Reson.* **1996**, *19*, 325.
(83) Callaghan, P. T.; Xia, Y. *J. Magn. Reson.* **1991**, *91*, 326.
(84) Callaghan, P. T. *Principles of Nuclear Magnetic Resonance Microscopy*; Clarendon Press: Oxford, 1993.
(85) Neue, U. D. *HPLC Columns: Theory, Technology, and Practice*; Wiley-VCH: New York, 1997.
(86) van Dusschoten, D.; Moonen, C. T. W.; de Jager, P. A.; Van As, H. *Magn. Reson. Med.* **1996**, *36*, 907.
(87) Edzes, H. T.; van Dusschoten, D.; Van As, H. *Magn. Reson. Imaging* **1998**, *16*, 185.
(88) Lebon, L.; Leblond, J.; Hulin, J. P. *Phys. Fluids* **1997**, *9*, 481.
(89) Whitney, D.; McCoy, M.; Gordon, N.; Afeyan, N. *J. Chromatogr. A* **1998**, *807*, 165.
(90) Choudhary, G.; Horváth, Cs. *J. Chromatogr. A* **1997**, *781*, 161.
(91) Rathore, A. S.; Wen, E.; Horváth, Cs. *Anal. Chem.* **1999**, *71*, 2633.
(92) Liu, Y.; Pietrzyk, D. J. *Anal. Chem.* **2000**, *72*, 5930.
(93) Overbeek, J. Th. G. Electrokinetic Phenomena. In *Colloid Science*; Kruyt, H. R., Ed.; Elsevier: Amsterdam, 1952, Chapter 5.
(94) Hunter, R. J.; Wright, H. J. L. *J. Colloid Interface Sci.* **1971**, *37*, 564.
(95) Vindevogel, J.; Sandra, P. *J. Chromatogr.* **1991**, *541*, 483.
(96) Tsuda, T. Electroosmosis and Electrochromatography. In *Electric Field Applications in Chromatography, Industrial and Chemical Processes*; Tsuda, T., Ed.; VCH: Weinheim, 1995; Chapter 3.
(97) Dullien, F. A. L. *Porous Media: Fluid Transport and Pore Structure*; Academic Press: New York, 1992.
(98) Griffiths, S. K.; Nilson, R. H. *Anal. Chem.* **1999**, *71*, 5522.
(99) Gist, G. A.; Thompson, A. H.; Katz, A. J.; Higgins, R. L. *Phys. Fluids A* **1990**, *2*, 1533.
(100) Crank, J. *The Mathematics of Diffusion*; Clarendon Press: Oxford, 1956, Chapter 6.
(101) Codd, S. L.; Manz, B.; Seymour, J. D.; Callaghan, P. T. *Phys. Rev. E* **1999**, *60*, R3491.
(102) Golay, M. J. E.; Atwood, J. G. *J. Chromatogr.* **1979**, *186*, 353.
(103) Gusev, I.; Huang, X.; Horváth, Cs. *J. Chromatogr. A* **1999**, *855*, 273.
(104) Svec, F.; Fréchet, J. M. J. *Ind. Eng. Chem. Res.* **1999**, *38*, 34.
(105) Ishizuka, N.; Minakuchi, H.; Nakanishi, K.; Soga, N.; Nagayama, H.; Hosoya, K.; Tanaka, N. *Anal. Chem.* **2000**, *72*, 1275.

Martin Pačes[1]
Juraj Kosek[1]
Miloš Marek[1]
Ulrich Tallarek[2]
Andreas Seidel-Morgenstern[2, 3]

[1]Department of Chemical Engineering and Center for Nonlinear Dynamics of Chemical and Biological Systems, Prague Institute of Chemical Technology, Prague, Czech Republic
[2]Institute of Process Engineering, Otto-von-Guericke University Magdeburg, Magdeburg, Germany
[3]Max Planck Institute for Dynamics of Complex Technical Systems, Magdeburg, Germany

Mathematical modelling of adsorption and transport processes in capillary electrochromatography: Open-tubular geometry

A mathematical modelling approach for open-tubular capillary electrochromatography is presented. The spatially one-dimensional model takes into account (i) a coupling of (non)linear adsorption of positively or negatively charged analyte molecules (at a negatively charged capillary inner surface) with the equilibrium electrokinetics at this solid-liquid interface, (ii) mobile phase transport by electroosmosis and pressure-driven flow, as well as (iii) transport of species by electrophoresis and molecular diffusion. Under these conditions the local zeta-potential and electroosmotic mobility become a function of the concentration of the charged analyte. The resulting inhomogeneity of electroosmotic flow through the capillary produces a compensating pore pressure as requirement for incompressible mobile phase flow (*i.e.*, for constant volumetric flow along the capillary). The results of the simulations are discussed in view of the surface-to-volume ratio of the capillary lumen, the analyte concentration (in combination with a Langmuir isotherm for the adsorption process), and buffer effects.

Keywords: Adsorption / Capillary electrochromatography / Coupled transports / Electrical double layer / Electroosmosis / Electrophoresis / Nonlinear effects EL 5264

1 Introduction

Capillary electrochromatography (CEC) combines the separation of analytes based on their differential partitioning between stationary and mobile phase in porous adsorbent media (microfabricated open-channel structures, particulate beds or monoliths) with electrokinetically driven transport of bulk liquid (electroosmotic flow, EOF) and additional selectivity offered by the differential migration of charged analytes in an electrical field (electrophoresis) [1–7]. Most common stationary phases in CEC are silica supports with chemically bonded surface groups [8–10], where amount and accessibility of residual silanols critically determine the surface charge density and EOF for a given set of conditions, but physically (and dynamically) adsorbed stationary phases [11], strong cation-exchange resins [12–14], and so-called mixed-mode media with both strong ion-exchange and reversed-phase chromatographic sites [15–18] have also been used. The influence of ion exchange and hydrophobic interaction on analyte retention and migration can be adjusted by organic modifier in the buffer solution and/or *via* background electrolytes (BGE) [16, 19]. In general, spatial and temporal electrokinetic properties of the surface play a key role in attaining a stable, homogeneous pore-level and macroscopic EOF through the porous medium, because surface heterogeneity results in inhomogeneous flow structures which lead to hydrodynamic dispersion and a decrease in the separation efficiency [20–23]. (NB this phenomenon, on the other hand, may be utilized to design microfluidic mixers [24, 25].) Any (un)specific adsorption of ionic species, *e.g.*, during the elution of a sample plug of finite length with a chemical composition different from that of the running mobile phase, will change (eventually significantly) the local charge equilibrium and associated interfacial electrokinetics [26–38]. This issue is further complicated when the analyte molecules and surface groups (relevant for EOF) are involved in pH-dependent equilibria.

Current interest in CEC arises because of the significantly increased separation efficiencies and peak capacities compared to capillary HPLC. This is due to the far superior flow field (hydrodynamic dispersion) characteristics of "perfusive" EOF in beds of porous particles which can be maintained over a wide range of experimental conditions [39–45]. Within suitable experimental limits concerning pore size and BGE concentration [40,

Correspondence: Martin Pačes, Department of Chemical Engineering and Center for Nonlinear Dynamics of Chemical and Biological Systems, Prague Institute of Chemical Technology, Technická 5, CZ-166 28 Prague 6, Czech Republic
E-mail: martin.paces@vscht.cz
Fax: +420-2-3333-7335

Abbreviations: EDL, electrical double layer; **OHP**, outer Helmholtz plane; **OT-CEC**, open-tubular capillary electrochromatography; **PDF**, pressure-driven flow

 0173-0835/03/0302–380 $17.50+.50/0

44] velocity extremes in the mobile phase flow pattern (on any time and length scale) may be drastically reduced compared to pressure-driven flow (PDF) for which the fluid dynamics is governed by the radial porosity distribution over the total column cross-section [46]. The spatial dimension of the electrical double layer (EDL) close to the solid-liquid interface (assumed to be locally flat) can be orders of magnitude smaller than the characteristic radial channel dimension. Thus, from a macroscopic point of view, shear and slipping planes in EOF are almost identically located at the surface [47] leading to a phenomenon observed as "apparent slip" of the velocity field at the solid-liquid interface [48, 49]. Hydrodynamic dispersion can then be ultimately limited to that by longitudinal diffusion alone. Further, as the ratio of electroosmotic to hydraulic volumetric flow rates (at a fixed potential and pressure gradient) is inversely proportional to the squared channel diameter, the EOF becomes increasingly effective in liquid transport through finer pores (*e.g.*, interstices between small porous particles in a packed bed, but here especially in the still smaller intraparticle pores; inside the skeleton of porous monolithic structures or in consolidated beds) as their size is reduced [50].

Although some of the fundamental aspects in CEC are now being evaluated [7, 39–45, 51–75] including flow heterogeneity or analyte migration (and retention) behavior, there remains a still complex interplay of many parameters affecting the efficiency and reproducibility of CEC separations which has not yet been resolved in sufficient detail. Among these influences we can name the type, pH, and concentration of the buffer solution in contact with a particular surface, electromigration dispersion, (un)specific (non)linear adsorption of charged species and its consequences for the local interfacial electrokinetics, surface (electro)diffusion, or the generated Joule heat. Our present work is concerned with a mathematical modelling approach for describing the interdependence of adsorption and electrokinetic phenomena in open-tubular (OT) CEC [76], but it can be easily extended to the macroscopic description of the dynamics in high surface area random porous media like particulate beds and monolithic structures. This approach, which extends other modelling studies [28, 51, 65, 71], is based on a combination of the following major aspects. (i) Coupling of nonlinear adsorption of charged analyte molecules with the local interfacial electrokinetics. (ii) Continuity of volumetric flow of the incompressible electrolyte solution (coupling of electroosmotic and induced PDF). (iii) Continuity of charge transport (constant net electrical current along the column). We expect that this improved modelling approach represents more realistically the dynamic behavior of analyte adsorption and migration in electrochromatographic systems for a broader range of experimental conditions and, thus, it will contribute to a validation and point towards optimization strategies in CEC.

2 Mathematical modelling approach

2.1 Introductory remarks

In this work we consider cylindrical straight capillaries with inner diameter (ID) from 100 μm down to 1 μm. The surface-to-volume ratio associated with a particular capillary of radius R is 4×10^4 m^{-1} (R = 50 μm), 4×10^5 m^{-1} (R = 5 μm), and 4×10^6 m^{-1} (R = 0.5 μm). The mobile phase is an aqueous electrolyte solution, containing either a fully dissociated inorganic salt (NaCl) or a buffer system (Tris-HCl), and it is driven electrokinetically by electroosmosis due to the externally applied electrical field. The acidic surface (*e.g.*, sulfonic acid) groups of the capillaries are assumed to be fully dissociated and the resulting negative surface charge density is unaffected by the actual changes of the mobile-phase pH. We consider a single, positively charged analyte dissolved in BGE which is injected for a fixed time interval at the capillary inlet. Consequently, in addition to its net transport by electroosmosis with the bulk mobile phase it also experiences diffusion and directed transport by electrophoresis. We then simulated the elution of the injected sample plug along the capillary. Retention takes place only at the capillary inner surface, the mobile phase contains no additive that could act as a (pseudo)stationary phase. There are no mass transfer limitations associated with the adsorption step. In general, the local EOF velocity is not bound to be constant as local changes in electrical field strength and surface charge density caused by adsorption of charged analyte molecules may occur. Then, induced PDF will necessarily arise as a compensation because of the continuity of (incompressible) mobile phase flow. The EDL and adsorption of analyte molecules at the surface are characterized by using the Stern model [77].

Our model was developed with the assumption of the following conditions: (i) The system is isothermal. (ii) We have constant physical properties of the BGE, namely the electrostatic permitivity, dynamic viscosity, and fluid density as well as constant parameters for the particular chemical species such as diffusivity, electrophoretic mobility, and dissociation constants. (iii) The BGE is a dilute symmetrical electrolyte. (iv) No other chemical reaction except dissociation is present. (v) Dissociation and adsorption equilibria, as well as a re-equilibration of the EDL are established instantaneously, in particular, with respect to the axial displacement of the analyte

molecules. (vi) The EDL field can be described by the nonlinear Poisson-Boltzmann equation and the Boltzmann distribution is undisturbed by externally forced convection which remains in the low-Reynolds number flow regime. (vii) The actual (local) PDF component of the velocity field is proportional to the local pressure gradient. (viii) The EDL thickness is negligible compared to the capillary radius and the bulk liquid is practically electroneutral. (ix) The ζ-potential, *i.e.*, the electrokinetic potential at the plane of shear, can be identified with the value of the electrostatic potential at the outer Helmholtz plane (OHP).

2.2 Notation

a	surface-to-volume ratio	(m^{-1})
A	parameter of adsorption isotherm	(m)
B	parameter of adsorption isotherm	$(m^3 mol^{-1})$
c_i	concentration of *i*-th species	$(mol \cdot m^{-3})$
c_i^s	concentration of adsorbed *i*-th species ($c_i^s = aq_i$)	$(mol \cdot m^{-3})$
c_i^t	total concentration of *i*-th species ($c_i^t = c_i + c_i^s$)	$(mol \cdot m^{-3})$
D_i	diffusivity of *i*-th species	$(m^2 s^{-1})$
F	Faraday constant	$(96487\ C \cdot mol^{-1})$
i_x	electrical current density	$(A \cdot m^{-2})$
$j_{x,i}$	mass flux density of *i*-th species	$(mol \cdot m^{-2} s^{-1})$
K_w	water dissociation constant	$(mol^2 m^6)$
$K_{i,a}$	dissociation constant of *i*-th species	$(mol \cdot m^3)$
p	hydrostatic pressure	(Pa)
q_i	surface concentration of *i*-th species	$(mol \cdot m^{-2})$
r	radial coordinate	(m)
R	capillary radius	(m)
R	universal gas constant	$(8.314\ J \cdot mol^{-1} K^{-1})$
t	time	(s)
T	thermodynamic temperature	(K)
u_i	electrophoretic mobility of *i*-th species	$(m^2 s^{-1} V^{-1})$
v_x	flow velocity	$(m \cdot s^{-1})$
x	axial coordinate	(m)
z_i	charge number of *i*-th species	$(-)$
α_i	degree of dissociation of *i*-th species	$(-)$
β	mixing ratio	$(-)$
ε_0	electrostatic permittivity of vacuum	$(8.854 \times 10^{-12}\ C^2 N^{-1} m^{-2})$
ε_r	relative electrostatic permittivity	$(-)$
η	dynamic viscosity	$(Pa \cdot s)$
κ^{-1}	Debye length	(m)
μ_{eo}	electroosmotic mobility	$(m^2 s^{-1} V^{-1})$
Π	hydraulic permeability	$(m^2 s^{-1} Pa^{-1})$
ϕ	electrostatic potential	(V)
φ	electrokinetic potential	(V)
ρ_c	volumetric charge density	$(C \cdot m^{-3})$
σ	surface charge density	$(C \cdot m^{-2})$
ξ	auxiliary spatial coordinate	$(-)$
ζ	electrokinetic potential at shear plane	(V)

2.3 Adsorption phenomenon

The (Stern layer) adsorption of charged analyte molecules A is described by means of the Langmuir isotherm [77, 78]

$$q_A = \frac{A c_A^w}{1 + B c_A^w} \tag{1}$$

where q_A is the surface concentration of (adsorbed) analyte molecules, c_A^w is their mobile phase concentration at the solid-liquid interface, while A and B are parameters of the adsorption isotherm. The actual value of c_A^w is governed by electrostatic attraction/repulsion between analyte molecules and the (originally) negatively charged capillary surface and may be calculated by using the Boltzmann equation (for a discussion of the validity of the Boltzmann distribution in the case of microchannel flow we refer to the paper of Yang *et al.* [79])

$$c_A^w = c_A \exp\left(-z_A \frac{F}{RT} \zeta\right) \tag{2}$$

where ζ is the electrokinetic potential at the (hypothetical) plane of shear which, in this work, is identified with the OHP [80], z_A is the charge number and c_A is the analyte concentration in the bulk (*i.e.*, electroneutral) solution. For the surface (Stern layer) charge density contributions we have

$$\sigma = \sigma^0 + \sigma^{ads} = \sigma^0 + F z_A q_A \tag{3}$$

where σ^0 denotes the surface charge originating only from the contact of the acidic (*e.g.*, sulfonic acid) surface groups with the electrolyte solution (without any adsorbing charged analyte) and σ^{ads} is the charge contribution due to adsorption of the analyte.

From the solution of the Poisson-Boltzmann equation for symmetrical electrolytes and a thin electrical double layer (such that the surface and EDL are locally flat) we arrive at the following relation between the total surface charge density σ and the ζ-potential [81]

$$\sigma = f(\zeta) \varepsilon_0 \varepsilon_r \kappa \zeta \tag{4}$$

where κ^{-1} is the Debye length, $\varepsilon_0\varepsilon_r$ is the electrostatic permittivity of the liquid, and $f(\zeta)$ is a correction factor taking into account higher values of ζ (*cf.* Section 6 Appendix)

$$f(\zeta) = \frac{\tanh\left(\frac{1}{4}z_A\frac{F}{RT}\zeta\right)}{\frac{1}{4}z_A\frac{F}{RT}\zeta\left[1-\tanh^2\left(\frac{1}{4}z_A\frac{F}{RT}\zeta\right)\right]} \quad (5)$$

After substitution of Eqs. (1) and (4) into Eq. (3) we obtain the following algebraic condition

$$f(\zeta)\varepsilon_0\varepsilon_r\kappa\zeta = \sigma^0 + Fz_A\frac{Ac_A\exp\left(-z_A\frac{F}{RT}\zeta\right)}{1+Bc_A\exp\left(-z_A\frac{F}{RT}\zeta\right)} \quad (6)$$

This equation describes the relation between ζ-potential and sample concentration c_A, taking into account nonlinear adsorption of charged analyte molecules and their electrostatic interaction with the charged surface.

2.4 One-dimensional model of OT-CEC

The spatially one-dimensional mathematical model of OT-CEC is based on a constant net mass flux and electrical current along the channel

$$0 = -\frac{\partial v_x}{\partial x} \quad (7)$$

$$0 = -\frac{\partial i_x}{\partial x} \quad (8)$$

and on the mass balances of particular chemical species

$$\left(1+a\frac{\partial q_i}{\partial c_i}\right)\frac{\partial c_i}{\partial t} = -\frac{\partial j_{ix}}{\partial x} \quad (9)$$

where v_x, i_x and j_{ix} are the cross-sectional averages of the flow velocity, electrical current density and mass flux density of the *i*-th species, respectively, c_i and q_i are its bulk and surface concentrations, and a is the surface-to-volume ratio of the capillary (for cylindrical geometry $a = 2/R$). Regarding species transport we consider both mobile phase EOF and PDF, as well as electrophoresis and molecular diffusion. The particular fluxes are defined as follows.

(i) Flow velocity

$$v_x = -\prod\frac{\partial p}{\partial x} - \mu_{eo}\frac{\partial\phi}{\partial x} = -\frac{R^2}{8\eta}\frac{\partial p}{\partial x} + \frac{\varepsilon_0\varepsilon_r\zeta}{\eta}\frac{\partial\phi}{\partial x} \quad (10)$$

where p is hydrostatic pressure and Π is the hydraulic permeability of a cylindrical capillary. ϕ is the electrical potential, μ_{eo} the electroosmotic mobility, and η is the dynamic viscosity of the liquid. The PDF component in the velocity field is assumed to be proportional to the pressure gradient [82]. The EDL thickness is considered negligible compared to R, the capillary radius, and the electroosmotic mobility μ_{eo} is related to the ζ-potential by the Helmholtz-Smoluchowski equation [80].

(ii) Mass flux density of the *i*-th species is given by the Nernst-Planck equation

$$j_{ix} = c_i v_x - z_i c_i\frac{F}{RT}D_i\frac{\partial\phi}{\partial x} - D_i\frac{\partial c_i}{\partial x} \quad (11)$$

where D_i, and z_i are the (free) molecular diffusivity, and the effective charge number of the *i*-th species, respectively. Additional dispersion phenomena related to (lateral) diffusion-limited mass transfer and a nonuniform flow profile (Taylor dispersion) are not considered.

(iii) Electrical current density is determined by the particular mass fluxes of the charged species

$$i_x = F\sum_{i=1}^{N} z_i j_{ix} \quad (12)$$

where N is the total number of chemical species. Neither surface conductance [83–85] (which may become important for capillaries with higher surface-to-volume ratio a or small bulk-specific conductivity), nor any other contribution to the electrical current is considered in this work.

The simulations are run under conditions of either a constant applied pressure and electrical potential difference or constant axial velocity and current density. Thus, we have the following boundary conditions.

	Inlet ($x = 0$)	Outlet ($x = L$)
Concentrations	$c_i\|_{x=0} = c_i^{inj}(t)$	$c_i\|_{x=L} = c_i^0$ = const.
Pressure	$p\|_{x=0} = p^0$	$p\|_{x=L} = (p^0 + \triangle p)$ or $v_x\|_{x=L} = v_x^0$
Electrical potential	$\phi\|_{x=0} = \phi^0$	$\phi\|_{x=L} = (\phi^0 + \triangle\phi)$ or $i_x\|_{x=L} = i_x^0$

$\triangle\phi$ and $\triangle p$ are the applied electrical potential and pressure differences, i_x^0 and v_x^0 are constant values of the electrical current density and velocity. At the beginning of the simulation the capillary is filled uniformly with pure electrolyte solution, *i.e.*, $c_i|_{x,t=0} = c_i^0$. Then, injection of sample takes place and the concentrations $c_i^{inj}(t)$, which are a function of time t, are used for simulating the injection of sample. This process is achieved by mixing pure BGE with sample (in BGE) realized by

$$c_i^{inj}(t) = 1 - (\beta(t))c_i^0 + \beta(t)c_i^1 \quad (13)$$

where the parameter $\beta(t)$ determines the actual mixing ratio and varies between 0 (pure BGE) and 1 (sample in BGE). The following equation has been used for simulating the injection process

$$\beta(t) = \frac{1}{2}\left\{\tanh\left[k_{inj}\left(t-t_{beg}\right)\right] - \tanh\left[k_{inj}\left(t-t_{end}\right)\right]\right\} \quad (14)$$

where t_{beg} and t_{end} are times denoting start and end of the injection, respectively, and k_{inj} is a factor affecting the sharpness of the injected (almost rectangular) sample plug.

2.5 Dissociation equilibria and local electroneutrality

Within the bulk aqueous electrolyte solution we consider the water dissociation equilibrium

$$K_w = c_{H^+} c_{OH^-} \tag{15}$$

where K_w is the (water) dissociation constant, c_{H^+} is the concentration of H^+ and c_{OH^-} that of OH^- ions. In addition, local electroneutrality is assumed

$$0 = \sum_{i=1}^{N} z_i c_i \tag{16}$$

Further, we consider a dissociation equilibrium of the chemical species B (*e.g.*, acidic analyte molecule or buffer component) which, in general, can be formulated as

$$B_1 \rightleftharpoons B_0 + H^+ \qquad K_{B,a} = \frac{c_{B_0} c_{H^+}}{c_{B_1}} \tag{17}$$

where $c_{B_1} = \alpha_B c_B$ and $c_{B_1} = (1 - \alpha_B) c_B$ are the concentrations of undissociated and dissociated molecules, respectively. They are related to the total concentration c_B by the extent of dissociation, expressed *via* α_B. The parameter α_B, a function of c_{H^+}, is calculated from

$$\alpha_B = \frac{K_{B,a}}{K_{B,a} + c_{H^+}} = \frac{1}{1 + 10^{(pK_{B,a} - pH)}} \tag{18}$$

2.6 Numerical implementation

The model which is described in previous sections has been solved numerically using software developed in-house. The set of partial differential and algebraic equations (Eqs. 6–9, 17, 18) was spatially discretized on an adapative nonequidistant grid using the Galerkin finite-element method (FEM) with quadratic trial/weight functions [86, 87]. The spatial domain is divided into N_e elements with constant number of grid points $N_g = 2N_e + 1$. The grid points change their positions x^j ($j = 1 \ldots N_g$) in time and their distribution is governed by the following partial differential equation:

$$K_t \frac{\partial x}{\partial t} = K_x \frac{\partial^2 x}{\partial \xi^2} + K_l \frac{\partial^2 l}{\partial \xi^2} = \frac{\partial}{\partial \xi}\left[\frac{\partial x}{\partial \xi}\left(K_x + K_l \frac{\partial l}{\partial x}\right)\right] \tag{19}$$

where $x(\xi)$ is the spatial coordinate, ξ is an auxiliary spatial coordinate, l is a function controlling the grid density, and K_l, K_x, and K_t are constants characterizing the rate of grid recombination, spatial dispersion of the grid, and the time delay of grid recombination, respectively. Equation 19 is spatially discretized using also the Galerkin FEM. Grid point coordinates of the nonequidistant grid nodes x^j ($j = 1 \ldots N_g$) were solved on an equidistant grid in ξ^j ($j = 1 \ldots N_g$) with boundary conditions $x^1 = 0$ and $x^{Ng} = L$.

The derivative $\partial l / \partial x$ is evaluated from

$$\frac{\partial l}{\partial x} = \sqrt{1 + \sum_{n=1}^{Ncv} \left(k_n \frac{\partial f_n}{\partial x}\right)^2} \tag{20}$$

where k_n is a constant weight parameter and f_n are variables controlling the grid density. The derivative $\partial l / \partial x$ forces the grid to become locally denser according to the slope of the control variables f_n, and N_{cv} is the number of control variables. We used concentrations of particular species, the pH, the ζ-potential, and magnitude of the EOF as control variables f_n, thus the slopes in c_i, pH, ζ, and $v_x^{eof} = -\mu_{eo} \frac{\partial \phi}{\partial x}$ determine the local grid density.

The resulting set of differential/algebraic equations can be formally written as

$$\boldsymbol{g}\,(t, \mathbf{u}, \mathbf{u}_t) = 0 \tag{21}$$

where t denotes time, $\boldsymbol{u}$ is a vector of independent variables, and $\boldsymbol{u}_t$ is the vector of their time derivatives. This set of equations was integrated in time by means of the DASPK software [88].

3 Results and discussion

According to the Stern model a so-called Stern layer (also known as the inner Helmholtz plane, IHP) is drawn through the center of charged analyte molecules that are assumed to be adsorbed on the charged capillary inner surface [77]. The OHP (running parallel to the IHP) touches the hydration shell of the adsorbed molecules and coincides with the shear plane. The region of the EDL extending from the OHP towards the capillary center is the diffusive part of the EDL. The Langmuir isotherm (Eq. 1), as one possible description of this adsorption phenomenon, allows for surface saturation and, thus, realizes a finite amount of the ionic species adsorbed in the Stern layer which resembles the parallel plate capacitor model for the EDL. The adsorption process itself involves contributions from both the electrical energy associated with the charged analyte being in the Stern layer (electrostatic interaction) and the specific energy associated with the adsorption (*e.g.*, due to van der Waals interaction).

Figure 1 demonstrates for a given set of adsorption isotherm parameters ($A_A = 5.0 \times 10^{-6}$ m, $B_A = 66.7$ m^3/mol), how a positive or negative elementary charge hypotheti-

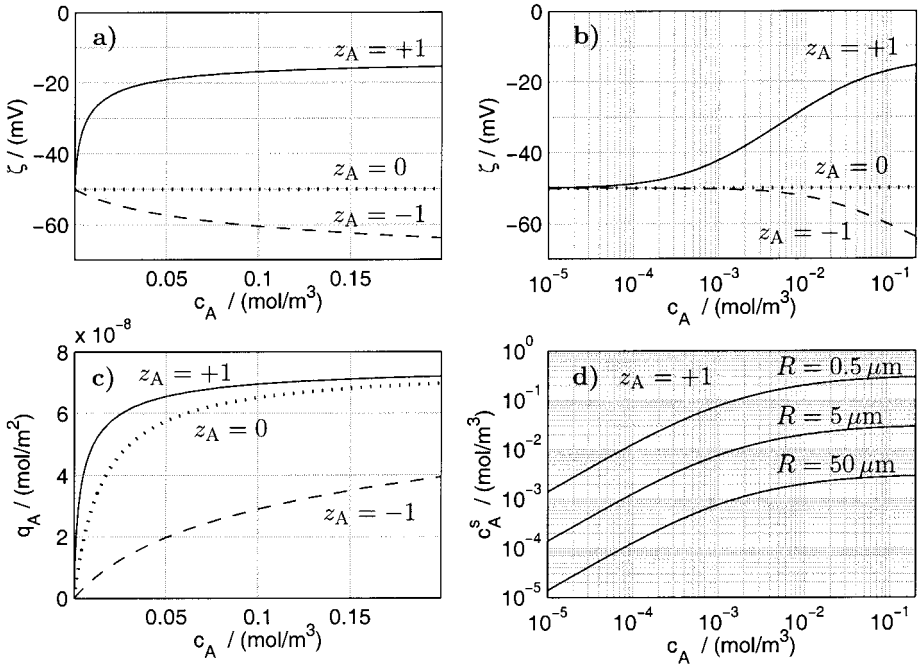

Figure 1. (a, b) Dependence of the ζ-potential on the mobile phase concentration of adsorbed analyte; (c) adsorption isotherms ($A_A = 5.0 \times 10^{-6}$ m, B_A = 66.7 m^3/mol); (d) partitioning of positively charged molecules between stationary (c_A^s) and mobile phase (c_A) for capillaries with a different inner radius. (ζ-potential, ζ° = − 50 mV; constant ionic strength, 0.01 mol/dm^3).

cally affixed to an originally electroneutral analyte molecule affects its adsorption behavior (Fig. 1c) and, as a consequence, the electrokinetic potential at the shear plane. In practice, this situation may be realized with neutral molecules involved in acid/base equilibria like an organic acid (*e.g.*, benzoic acid) or base (*e.g.*, aniline). The adsorption isotherm parameters *A* and *B* are assumed to remain unchanged by the (de)protonation of the analyte molecules. Further over the whole range of conditions in Fig. 1 the sample concentration is sufficiently smaller than the BGE concentration so that the actual EDL thickness is assumed to be unaffected by the former. Values of the ζ-potential for different mobile phase concentrations of adsorbing species (Fig. 1a, b) were calculated numerically with Eq.(6). It is obvious (Fig. 1d) that the relative amount of analyte molecules in the stationary phase increases substantially (by two decades) as the capillary radius is reduced from 50 μm *via* 5 μm to 0.5 μm.

Figure 2a shows elution profiles after 30, 60, 90, and 120 s, respectively, for an overloaded sample plug injected (for 4 s) into a 100 μm ID capillary. The sample contains positively charged analyte molecules which are, thus, electrostatically attracted by the negatively charged surface. Under the set of conditions employed for these simulation (temperature 298 K, capillary length 10 cm, sample concentration 0.1 mol/m^3, Tris-HCl buffer 10 mol/m^3, pH 8.1, sample diffusivity 10^{-9} m^2/s, externally applied electrical field 10^4 V/m with $v_x \approx 0.4$ mm/s, no externally applied pressure difference, and the same adsorption isotherm parameters as in Fig. 1), Taylor dispersion would have only a negligible influence on the shape of the elution profiles. However, the nonlinear adsorption of these charged analyte molecules has severe consequences for the distribution of electrokinetic potential, hydrostatic pressure (also reported by Ghosal [37]) and electrical potential gradients, velocity, and pH along the column.

As has been demonstrated by Fig. 1, the ζ-potential changes with the concentration of charged analyte, and the actual profiles seen in Fig. 2b are a natural result of the adsorption phenomenon. This inhomogeneous distribution of ζ-potential along the capillary axis, together with the local perturbation of the electrical potential gradient (Fig. 2c), leads to an accompanying change in EOF velocity (Fig. 2e, solid line) which necessitates a compensating PDF component (Fig. 2e, dashed line, *cf.* Fig. 2d) for conserving the volumetric flow rate (Fig. 2e, dash-dotted line). It should be noted that no pressure difference between both ends of the capillary is applied. The injection process itself causes most pronounced effects in the profiles of electrical potential and pH (Figs. 2c and f). The almost rectangular features in these distributions are due to a slightly different conductivity of the sample solution compared to pure BGE solution and are a memory effect.

Figure 3 illustrates how the replacement of an indifferent, completely dissociated BGE (NaCl, pH 7, concentration 5 mol/m^3) by a buffer system (Tris-HCl, pH 8.1, concentration 10 mol/m^3) influences the elution of charged analyte. It is demonstrated by means of the sample injection *via* frontal analysis (length of the capillary section 1 cm,

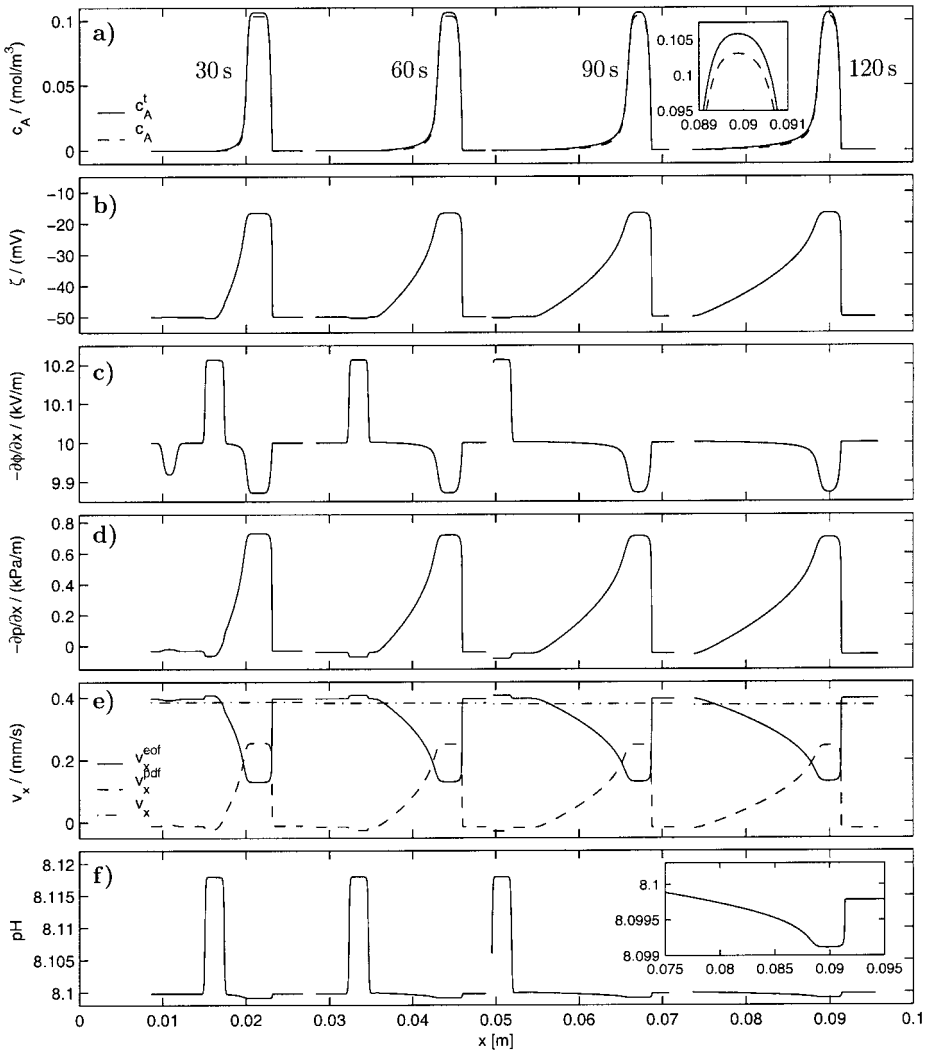

Figure 2. Elution of a sample plug containing charged molecules electrostatically attracted by and adsorbing at the capillary inner surface (Tris-HCl buffer, pH 8.1).

constant velocity $v_x = 3.96 \times 10^{-4}$ m/s, fixed electrical current density $i_x = 4.75 \times 10^2$ A/m^2 for Tris-HCl and $i_x = 6.31 \times 10^2$ A/m^2 for NaCl. These values of v_x and i_x are those which can be observed in the same capillary filled only with BGE, and in the presence of an applied electrical field of 10^4 V/m. Otherwise, the parameters are the same as in Fig. 2). At a given surface-to-volume ratio the breakthrough curves for the buffered and unbuffered mobile phases are very similar (compare Figs. 3a, b with Figs. 3g, h), except for small deviations due to an inhomogeneous distribution of the electrical field caused by different local chemical composition (and associated change in electrical conductivity) in the sample zone resulting from adsorption of the positive analyte molecules. As the result for the unbuffered system (Fig. 3i) demonstrates this adsorption, *i.e.*, the decrease of analyte concentration in the mobile phase, is compensated by a release of H^+ ions *via* water dissociation in order to satisfy local electroneutrality of the electrolyte. This effect is most pronounced at the front of the sample zone where the pH drops from 7 to less than 6.5 (Fig. 3i). Due to the high electrophoretic mobility of the small solvated H^+ ions the resulting pH front progresses into a low-pH mobile phase zone which proceeds the sample zone. This dramatic effect is demonstrated by the intermediate-profiles at times 1, 2, and 3 s after start of the injection in Fig. 3i.

It is important to note that under these conditions the physicochemical properties of the EDL at the inner wall of a capillary under some circumstances cannot be assumed to remain unaffected any longer (as done in this work). For example, with a bare fused-silica capillary (in contrast to sulfonic acid surface groups) the dissociation equilibrium of the silanol groups changes and, as a consequence, also the surface charge density, ζ-potential, local EOF, *etc*.

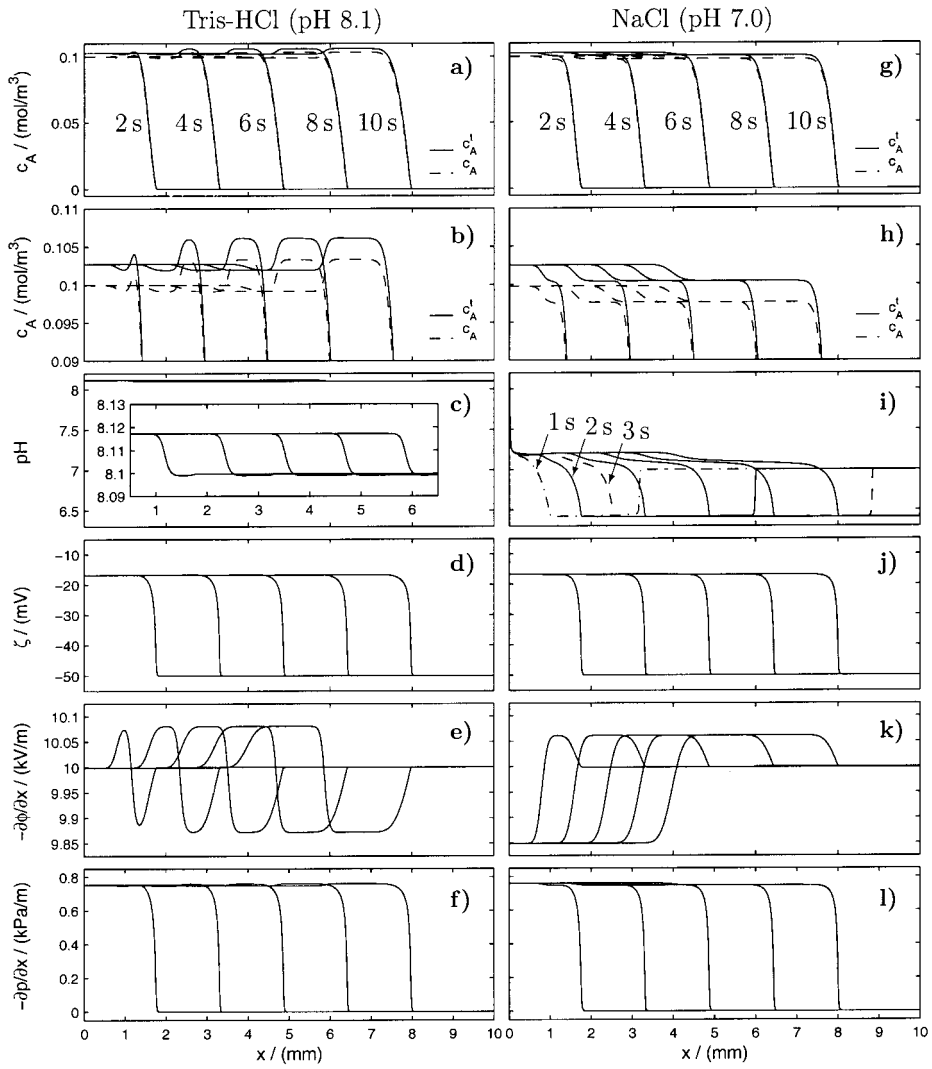

Figure 3. Injection of sample containing charged molecules electrostatically attracted by and absorbing at the capillary inner surface. The analyte is injected into capillary containing BGE solution. Filling of the capillary with sample solution continues for 10 s, with intermediate profiles recorded after 2, 4, 6, 8, and 10 s, respectively; (a)–(f) aqueous Tris-HCl solution (pH 8.1) used as BGE; (g)–(l) aqueous NaCl solution (pH 7.0) used as BGE (fixed constant velocity and electrical current density).

4 Concluding remarks

Our results demonstrate the importance and complex interplay of parameters like the ζ-potential, adsorption isotherm, surface-to-volume ratio, pH, analyte, and BGE concentrations with respect to the electrokinetically driven elution of adsorbing charged analyte molecules in porous adsorbent media. The simulations have shown that a PDF component necessarily accompanies the resulting inhomogeneous EOF (even without any externally applied pressure difference) in order to satisfy the continuity of mass within any segment of the porous medium (examplified in this work by the lumen of an OT-CEC column). Further, the continuity of charge transport is important as any local variation in electrical field and BGE composition affects the actual shape of breakthrough curves. The consequences of the latter condition become aggravated at lower buffer concentrations where accompanying changes in local pH may escalate due to insufficient buffer capacity. In contrast to the model presented by Grimes and Liapis [71], our work implies that a coupling of these phenomena is essential for an adequate description of the dynamics in CEC, especially in frontal analysis mode, but also in analytical mode when nonlinear adsorption and possible sample tailing prevail (as evidenced by Figs. 2a, b).

This work has been supported in part by the Deutsche Forschungsgemeinschaft (DFG) under grant SE-586/7-1, by the Max Planck Institute for Dynamics of Complex Technical Systems (Magdeburg, Germany), by the European Scientific. Foundation REACTOR programme, and the Grant Agency of Czech Republic under grant 104/02/0339.

Received August 26, 2002

5 References

[1] Dittmann, M. M., Wienand, K., Bek, F., Rozing, G. P., *LC-GC* 1995, *13*, 800–814.

[2] Crego, A. L., González, A., Marina, M. L., *Crit. Rev. Anal. Chem.* 1996, *26*, 261–304.

[3] Dittmann, M. M., Rozing, G. P., *J. Chromatogr. A* 1996, *744*, 63–74.

[4] Colón, L. A., Reynolds, K. J., Alicea-Maldonado, R., Fermier, A. M., *Electrophoresis* 1997, *18*, 2162–2174.

[5] Colón, L. A., Burgos, G., Maloney, T. D., Citrón, J. M., Rodriguez, R. L., *Electrophoresis* 2000, *21*, 3965–3993.

[6] Deyl, Z., Svec, F., *Capillary Electrochromatography*, Vol. 62, Elsevier, Amsterdam 2001.

[7] Xiang, R., Horváth, C., *Anal. Chem.* 2002, *74*, 762–770.

[8] Robson, M. M., Cikalo, M. G., Myers, P., Euerby, M. R., Bartle, K. D., *J. Microcol. Sep*. 1997, *9*, 357–372.

[9] Fujimoto, C., *Trends Anal. Chem.* 1999, *18*, 291–301.

[10] Matyska, M. T., Pesek, J. J., Boysen, I., Hearn, M. T. W., *Electrophoresis* 2001, *22*, 2620–2628.

[11] Zou, H. F., Ye, M. L., *Electrophoresis* 2001, *21*, 4073–4095.

[12] Cikalo, M. G.. Bartle, K. D., Myers, P., *Anal. Chem.* 1999, *71*, 1820–1825.

[13] Ye, M. L., Zou, H. F., Liu, Z., Ni, J. Y., *J. Chromatogr. A* 2000, *869*, 385–394.

[14] Liu, Y., Pietrzyk, D. J., *Anal. Chem.* 2000, *72*, 5930–5938.

[15] Smith, N., Evans, M. B., *J. Chromatogr. A* 1999, *832*, 41–54.

[16] Klampfl, C. W., Hilder, E. F., Haddad, P. R., *J. Chromatogr. A* 2000, *888*, 267–274.

[17] Scherer, B., Steiner, F., *J. Chromatogr. A* 2001, *924*, 197–209.

[18] Wu, R. A., Zou, H. F., Fu, H. J., Jin, W. H., Ye, M. L., *Electrophoresis* 2002, *23*, 1239–1245.

[19] Ståhlberg, J., Jönsson, B., Horváth, C., *Anal. Chem.* 1992, *64*, 3118–3124.

[20] Ajdari, A., *Phys. Rev. Lett.* 1995, *75*, 755–758.

[21] Long, D., Stone, H. A., Ajdari, A., *J. Colloid Interface Sci*. 1999, *212*, 338–349.

[22] Herr, A. E., Molho, J. I., Santiago, J. G., Mungal, M. G., Kenny, T. W., Garguilo, M. G., *Anal. Chem.* 2000, *72*, 1053–1057.

[23] Gillott, N. C., Euerby, M. R., Johnson, C. M., Barrett, D. A., Shaw, P. N., *Chromatographia* 2000, *51*, 167–173.

[24] Erickson, D., Li, D. Q., *Langmuir* 2002, *18*, 1883–1892.

[25] Whitesides, G. M., Stroock, A. D., *Phys. Today* 2001, *54*, 42–48.

[26] Verdegan, B. M.. Anderson, M. A., *J. Colloid Interface Sci.* 1993, *158*, 372–381.

[27] Jacobasch, H.-J., Weidenhammer, P., *Chem.-Ing.-Tech.* 1996, *68*, 1590–1594.

[28] Stålberg, O., Ståhlberg, J., *J. Chromatogr. A* 1997, *776*, 311–318.

[29] Vera, P., Gallardo, V., Salcedo, J., Ruiz, M. A., Delgado, A. V., *J. Appl. Polym. Sci.* 1997, *65*, 2721–2726.

[30] Benavente, J., Jonsson, G., *Colloids Surf. A* 1998, *138*, 255–264.

[31] Mangelsdorf, C. S., White, L. R., *J. Chem. Soc. Faraday Trans.* 1998, *94*, 2583–2593.

[32] Kovačević, D., Kallay, N., Antol, I., Pohlmeier, A., Lewandowski, H., Narres, H. D., *Colloids Surf. A* 1998, *140*, 261–267.

[33] Hayes, R. A., *Colloids Surf. A* 1999, *146*, 89–94.

[34] Löbbus, M., van Leeuwen, H. P., Lyklema, J., *Colloids Surf. A* 2000, *161*, 103–113.

[35] Dukhin, S. S., Zimmermann, R., Werner, C., *Colloids Surf. A* 2001, *195*, 103–112.

[36] Bahena, J. L.åR., Cabrera, A. R., Valdivieso, A. L., Urbina, R. H., *Sep. Sci. Technol.* 2002, *37*, 1973–1987.

[37] Ghosal, S., *Anal. Chem.* 2002, *74*, 771–775.

[38] Gunnarsson, M., Abbas, Z., Ahlberg, E., Gobom, S., Nordholm, S., *J. Colloid Interface Sci.* 2002, *249*, 52–61.

[39] Wen, E., Asiaie, R., Horváth, C., *J. Chromatogr. A* 1999, *855*, 349–366.

[40] Vallano, P. T., Remcho, V. T., *Anal. Chem.* 2000, *72*, 4255–4265.

[41] Stol, R., Poppe, H., Kok, W. T., *J. Chromatogr. A* 2000, *887*, 199–208.

[42] Tallarek, U., Rapp, E., Van As, H., Bayer, E., *Angew. Chem. Int. Ed.* 2001, *40*, 1684–1687.

[43] Vallano, P. T., Remcho, V. T., *J. Phys. Chem. B* 2001, *105*, 3223–3228.

[44] Stol, R., Poppe, H., Kok, W. T., *Anal. Chem.* 2001, *73*, 3332–3339.

[45] Dearie, H. S., Smith, N. W., Moffat, F., Wren, S. A. C., Evans, K. P., *J. Chromatogr. A* 2002, *945*, 231–238.

[46] Giddings, J. C., *Dynamics of Chromatography. Principles and Theory*, Marcel Dekker, New York 1965.

[47] Hunter, R. J., *Foundations of Colloid Science*, Oxford University Press, New York 2001.

[48] Paul, P. H., Garguilo, M. G., Rakestraw, D. J., *Anal. Chem.* 1998, *70*, 2459–2467.

[49] Tallarek, U., Rapp, E., Scheenen, T., Bayer, E., Van As, H., *Anal. Chem.* 2000, *72*, 2292–2301.

[50] Probstein, R. F., *Physicochemical Hydrodynamics*, John Wiley & Sons, New York 1994.

[51] Bello, M. S., Zhukov, M. Y., Righetti, P. G., *J. Chromatogr. A* 1995, *693*, 113–130.

[52] Coelho, D., Shapiro, M., Thovert, J. F., Adler, P. M., *J. Colloid Interface Sci.* 1996, *181*, 169–190.

[53] Rathore, A. S., Horváth, C., *J. Chromatogr. A* 1997, *781*, 185–195.

[54] Gaš, B., Štedrý, M., Kenndler, E., *Electrophoresis* 1997, *18*, 2123–2133.

[55] Wan. Q. H., *J. Chromatogr. A* 1997, *782*, 181–189.

[56] Dittmann. M. M., Rozing, G. P., J. *Microcol. Sep.* 1997, *9*, 399–408.

[57] Djordjevic, N. M., Fowler, P. W. J., Houdiere, F., Lerch, G., *J. Liq. Chromatogr. Rel. Technol.* 1998, *21*, 2219–2232.

[58] Bowser, M. T., Chen, D. D. Y., *Electrophoresis* 1998, *19*, 1452–1460.

[59] Rathore, A. S., Horváth, C., *Anal. Chem.* 1998, *70*, 3069–3077.

[60] Luo, Q. L., Andrade, J. D., *J. Microcol. Sep.* 1999, *11*, 682–687.

[61] Rathore, A. S., Wen, E., Horváth, C., *Anal. Chem.* 1999, *71*, 2633–2641.

[62] McGuffin, V. L., Krouskop, P. E., Hopkins, D. L., *ACS Symp. Ser.* 2000, *748*, 33–66.

[63] Lee, E., Lee, Y. S., Yen, F. Y., Hsu, J. P., *J. Colloid Interface Sci.* 2000, *223*, 223–228.

[64] Gaš, B., Kenndler, E., *Electrophoresis* 2000, *21*, 3888–3897.

[65] Ståhlberg, J., *J. Chromatogr. A* 2000, *887*, 187–198.

[66] Tallarek, U., Scheenen, T. W. J., Van As. H., *J. Phys. Chem. B* 2001, *105*, 8591–8599.

[67] Chaiyasut, C., Takatsu, Y., Kitagawa, S., Tsuda, T., *Electrophoresis* 2001, *22*, 1267–1272.
[68] Banholczer, A., Pyell, U., *J. Sep. Sci*. 2001, *24*, 736–742.
[69] Sounart, T. L., Baygents, J. C., *Colloids Surf. A* 2001, *195*, 59–75.
[70] Marino, S., Shapiro, M., Adier, P. M., *J. Colloid Interface Sci.* 2001, *243*, 391–419.
[71] Grimes, B. A., Liapis, A. I., *J. Colloid Interface Sci.* 2001, *234*, 223–243.
[72] Gusev, I., Horváth, C., *J. Chromatogr. A* 2002, *948*, 203–223.
[73] Jiskra, J., Claessens, H. A., Cramers, C. A., *J. Sep. Sci.* 2002, *25*, 569–576.
[74] Liu, Z., Otsuka, K., Terabe, S., *J. Chromatogr. A* 2002, *959*, 241–253.
[75] Conlisk, A. T., McFerran, J., Zheng, Z., Hansford, D., *Anal. Chem.* 2002, *74*, 2139–2150.
[76] Jinno, K., Sawada, H., *Trends Anal. Chem.* 2000, *19*, 664–675.
[77] Hiemenz, P. C., Rajagupalan, R., *Principles of Colloid and Surface Chemistry*, Marcel Dekker, New York 1997.
[78] Stern, O., *Z. Elektrochem.* 1924, *30*, 508–516.
[79] Yang, C., Li, D. Q., Masliyah, J. H., *Int. J. Heat Mass Transfer* 1998, *41*, 4229–4249.
[80] Delgado, A. V., Arroyo, F. J., in: Delgado, A. V. (Ed.), *Interfacial Electrokinetics and Electrophoresis*, Marcel Dekker, New York 2002, pp. 1–54.
[81] Dutta, P., Beskok, A., *Anal. Chem.* 2001, *73*, 1979–1986.
[82] Ghosal, S., *J. Fluid Mech.* 2002, *459*, 103–128.
[83] Lyklema, J., Minor, M., *Colloids Surf. A* 1998, *10*, 33–41.
[84] Johnson, P. R., *J. Colloid Interface Sci.* 1999, *209*, 264–267.
[85] Löbbus, M., van Leeuwen, H. P., Lyklema, J., *Colloids Surf. A* 2000, *161*, 103–113.
[86] Finlayson, B. A., *Nonlinear Analysis in Chemical Engineering*, McGraw-Hill, New York 1980.
[87] Finlayson, B. A., *Numerical Methods for Problems with Moving Fronts*, Ravenna Park Publishing, Seattle 1992.
[88] Brown, P. N., Hindmarsh, A. C., Petzold, L. R., *Siam J. Sci. Comput.* 1994, *15*, 1467–1488.

6 Appendix

6.1 Surface charge density in a cylindrical capillary

For describing the adsorption of charged solute molecules, the relation between surface charge density σ and the ζ-potential has to be known. At equilibrium and in the absence of any radial component of an externally applied electrical field, the surface charge is given by

$$\sigma = \varepsilon_0\varepsilon_r \left.\frac{\partial\varphi}{\partial r}\right|_{r=R} = -\frac{1}{R}\int_0^R \rho_c(r) r dr \qquad \text{(A-1)}$$

In the limit of thin electrical double layers ($\kappa R \gg 1$) the solution of the Poisson-Boltzmann equation for cylindrical geometry

$$\frac{1}{r}\frac{\partial}{\partial r}\left(r\frac{\partial\varphi}{\partial r}\right) = -\frac{F}{\varepsilon_0\varepsilon_r}\sum_{i=1}^{N} z_i c_i \exp\left(-z_i\frac{F}{RT}\not{\varphi}\right) \qquad \text{(A-2)}$$

subject to boundary conditons

$$\left.\frac{\partial\varphi}{\partial r}\right|_{r=0} = 0 \text{ and } \not{\varphi}|_{r=R} = \zeta \qquad \text{(A-3)}$$

becomes identical to that for a flat plane which has an analytical solution for symmetrical electrolytes [81]

$$\varphi(r) = \frac{1}{\frac{1}{4}z\frac{F}{RT}\zeta}\tanh^{-1}\left[\tanh\left(\frac{1}{4}z\frac{F}{RT}\zeta\right)\exp(\kappa r - \kappa R)\right] \qquad \text{(A-4)}$$

After analytical differentiation of Eq. (A-4) we obtain for σ

$$\sigma = \varepsilon_0\varepsilon_r\left.\frac{\partial\varphi}{\partial r}\right|_{r=R} = \varepsilon_0\varepsilon_r\kappa\zeta\frac{\tanh\left(\frac{1}{4}z\frac{F}{RT}\zeta\right)}{\frac{1}{4}z\frac{F}{RT}\zeta\left(1-\tanh^2\left(\frac{1}{4}z\frac{F}{RT}\zeta\right)\right)} \qquad \text{(A-5)}$$

For sufficiently small values of the ζ-potential this equation becomes

$$\sigma = \varepsilon_0\varepsilon_r\kappa\zeta \qquad \text{(A-6)}$$

The same relation is obtained from the solution of the Poisson-Boltzmann equation simplified by the Debye-Hückel linearization [77]. In order to estimate the limits of validity of this description, we solved numerically the Poisson-Boltzmann equation (Eq. A-2) for a range of values of the ζ-potential $(\varphi|_{r=R} = \zeta)$ and dimensionless capillary radius (κR) and these results were then compared with those of the simplified description, Eqs. (A-5) and (A-6) (Fig. A-1). From this comparison it can be seen that both equations coincide for $\kappa R > 5$ and small values of ζ, but that equation Eq. (A-5) excellently describes the relation between surface charge and ζ-potential also for higher values of ζ where Eq. (A-6) fails.

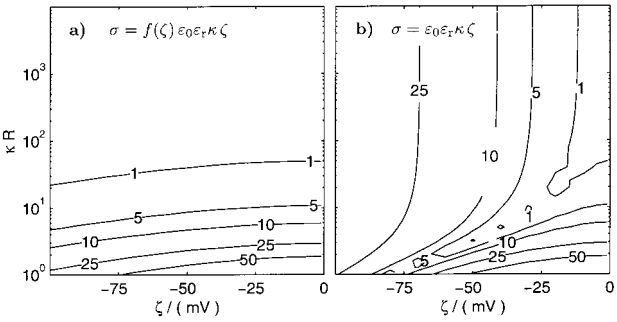

Figure A-1. Estimated relative errors (in%) for relations between surface charge density and the ζ-potential, (a) Eq. (A-5); (b) Eq. (A-6). These relations are compared with the numerical solution of the Poisson-Boltzmann equation for cylindrical geometry.

INTERNATIONAL JOURNAL FOR NUMERICAL METHODS IN FLUIDS
Int. J. Numer. Meth. Fluids 2004; **46**:507–532 (DOI: 10.1002/fld.765)

Coupled lattice-Boltzmann and finite-difference simulation of electroosmosis in microfluidic channels

Dzmitry Hlushkou[1], Drona Kandhai[2] and Ulrich Tallarek[3,*,†]

[1] *Max-Planck-Institut für Dynamik komplexer technischer Systeme, Sandtorstraße 1, 39106 Magdeburg, Germany*
[2] *Kramers Laboratorium voor Fysische Technologie, Delft University of Technology, Prins Bernhardlaan 6, 2628 BW Delft, The Netherlands*
[3] *Institut für Verfahrenstechnik, Otto-von-Guericke-Universität Magdeburg, Universitätsplatz 2, 39106 Magdeburg, Germany*

SUMMARY

In this article we are concerned with an extension of the lattice-Boltzmann method for the numerical simulation of three-dimensional electroosmotic flow problems in porous media. Our description is evaluated using simple geometries as those encountered in open-channel microfluidic devices. In particular, we consider electroosmosis in straight cylindrical capillaries with a (non)uniform zeta-potential distribution for ratios of the capillary inner radius to the thickness of the electrical double layer from 10 to 100. The general case of heterogeneous zeta-potential distributions at the surface of a capillary requires solution of the following coupled equations in three dimensions: Navier–Stokes equation for liquid flow, Poisson equation for electrical potential distribution, and the Nernst–Planck equation for distribution of ionic species. The hydrodynamic problem has been treated with high efficiency by code parallelization through the lattice-Boltzmann method. For validation velocity fields were simulated in several microcapillary systems and good agreement with results predicted either theoretically or obtained by alternative numerical methods could be established. Results are also discussed with respect to the use of a slip boundary condition for the velocity field at the surface. Copyright © 2004 John Wiley & Sons, Ltd.

KEY WORDS: lattice-Boltzmann method; finite-difference method; porous media; microfluidics; electroosmotic flow; surface charge distribution

1. INTRODUCTION

Rapid recent developments in design, patterning, and utilization of microfluidic devices (valves, pumps, mixers, reactors, sensors and actuators, or three-dimensional channel networks) have

*Correspondence to: U. Tallarek, Institut für Verfahrenstechnik, Otto-von-Guericke-Universität Magdeburg, Universitätsplatz 2, 39106 Magdeburg, Germany.
†E-mail: ulrich.tallarek@vst.uni-magdeburg.de

Published online 18 August 2004

Received 7 October 2003
Revised 30 April 2004

found many applications in the devised bulk transport and separation, identification, synthesis, and manipulation of a wide range of chemical and biological species [1–6]. It is an advancement that becomes particularly important for the lab-on-a-chip concept [7] where transport processes including the efficient mixing of micro- and nanoliter liquid volumes, the control and enhancement of reaction rates, heat and mass transfer, as well as the selectivity of chromatographic separations occur on much smaller time and length scales than traditional engineering technologies. With channel diameters from several to a few hundred micrometers (inherently placing microfluidics into the low-Reynolds number hydrodynamics regime) and channel lengths approaching centimeter dimension, these systems permit a miniaturization of chemical processes and large-scale integration of engineering principles, allowing fast response times at low operational costs [6].

Concerning the bulk transport of liquid through a microfluidic channel electroosmosis can offer distinct advantages over pressure-driven flow. Electroosmotic flow (EOF) is generated by interaction of an externally applied electrical field with that part of the electrolyte solution that has become locally charged at the interface to the stationary and oppositely charged solid surface of the confining porous medium [8, 9]. The extension into the bulk solution of the fluid-side domain of this electrical double layer can be as small as a few nanometers compared to a channel diameter of micrometer dimension, a fact that has some important consequences for the EOF dynamics under these conditions [10]. First, from a macroscopic point of view, bulk liquid moves as in plug flow, i.e. the velocity apparently slips at the wall, which is in contrast to the parabolic velocity profile typical for Poiseuille flow. Second, because the ratio of electroosmotic to hydraulic volumetric flow rates (at fixed potential and pressure gradient) is inversely proportional to the squared channel diameter, the EOF becomes increasingly effective in liquid transport through the finer channels as their size is reduced. Thus the benefit of using EOF is that chemical and biological species may be easily transported in microfluidic devices over comparatively long distances with negligible mass transfer resistance. Hydrodynamic dispersion can then be limited almost to that by longitudinal diffusion alone which has been demonstrated experimentally [11, 12].

Stimulated by the enormous potential and accompanying need for a far more detailed characterization of the electrokinetically driven mass transport in microfabricated (or microchip) devices, numerical simulation of EOF in microfluidic channels has received increased attention over the past few years [13–28]. These investigations have revealed that, in good agreement with available experimental data, the transport characteristics of the EOF in microchannels clearly depend on the properties of the working fluid and the geometrical (and physico-chemical) parameters of the surface. For example, the work of Griffiths and Nilson [16] which is based on a direct solution of the governing transport equations demonstrates that, over a wide range of conditions, the longitudinal dispersion coefficient of a neutral, non-reacting solute in EOF may be many orders of magnitude smaller than for the parabolic or nearly so velocity distribution in pressure-driven flow. Ermakov *et al.* [15] used a 2D code to address the electrokinetic species transport with respect to some basic microfluidic elements. They considered the sample focusing in a channel cross and sample mixing at a T-junction. Patankar and Hu [14] carried out 3D flow field simulations to investigate EOF behaviour at a channel cross, while Bianchi *et al.* [17] used finite element-based simulations to describe flow division at a decoupling T-junction, encountering combined electroosmotic and pressure-driven flows. Fu *et al.* [25] presented a physical model and numerical method for studying geometrical effects on the performance of electrophoresis microchips. Erickson

and Li [27] utilized 3D finite element-based numerical simulations to resolve the influence of a heterogeneous surface charge distribution on local flow circulation in the bulk liquid under the aspect of sample mixing in a T-shaped micromixer. While these numerical approaches provide valuable insight into flow behaviour in relatively simple channel geometries, traditional computational fluid dynamics can face drawbacks if higher code flexibility is required, e.g. when dealing with a more complicated pore space morphology, complex flows, or code parallelization.

Over the last decade the lattice-Boltzmann (LB) methods [29–34] have achieved great success as alternative and efficient numerical schemes in the simulation of a variety of transport phenomena in porous media, with a particular emphasis on the dynamics of pressure-driven fluid flow through complex materials [34–50]. Besides their flexibility and accuracy in dealing with the confining geometry and actual boundary conditions LB methods are inherently parallel and, thus, they are ideally suited for high-performance parallel computing. In contrast to the more conventional numerical schemes based on a discretization of macroscopic continuum equations, the LB method utilizes mesoscopic kinetic equations to recover the macroscopic Navier–Stokes equation for fluid motion in the long-time, large-scale limit [34]. Further, early systematic problems of LB methods like the existence of velocity-dependent pressures and lack of a Galilean invariance are essentially resolved, and algorithms have been simplified by the single relaxation time scheme of Bhatnagar *et al.* [51–53].

Only a few reports have been published so far in which LB simulations also consider electrokinetic phenomena. Rather recently, the LB method has been implemented to model high-Reynolds number pressure-driven flow in microfluidics, taking into account electroviscous effects that can become important due to the finite thickness of electrical double layers compared to typical channel sizes [54], and a reasonable agreement with published experimental data on the friction factor—Reynolds number relation [55] was obtained. Further, in the work by Nie *et al.* [56] an extension of the LB method was proposed based on a density-dependent viscosity model and technique for imposing a slip-velocity at the wall. It was demonstrated that this approach can capture fundamental characteristics of microchannel flow. Warren [57] analysed electrokinetic transport in a parallel-sided slit with a constant electrical charge (or potential) at this solid–liquid interface. The resulting one-dimensional problem was further restrained by assuming a thick electrical double layer compared to the width of the slit. While this work addresses cases with significant double layer overlap encountered in ultrafine capillaries [58], for many situations with technological relevance, as for the electrokinetic transport in open-channel microchip devices, a characteristic channel dimension normal to the local flow direction becomes (much) larger than the typical thickness of electrical double layers at the solid–liquid interface. It is this condition, in particular, that needs to be satisfied in order to gain full potential of the EOF (compared to pressure-driven flow) with respect to dispersion and permeability [59]. Further, most industrial and natural porous media are characterized by random or hierarchically-structured, but relatively broad pore size distributions, contrasting with the network of uniformly sized and shaped channels in microfluidic devices. In the general case, bulk transport involves conditions for which the ratio of a local pore radius to the electrical double layer thickness covers a spectrum from below unity up to several hundreds [60]. The numerical approach that we present in this work can cope with any geometry and possible surface heterogeneity and, thus, it will be particularly efficient in resolving details of the flow field that govern transport and dispersion in a transient, as well as long-time asymptotic regime.

2. ELECTROKINETICS

2.1. Electroosmotic flow in a microfluidic channel

Figure 1 illustrates, at different length scales, the basic aspects of electroosmosis in a microfluidic channel with locally flat, smooth surface. When a dielectric solid (e.g. a fused-silica capillary) is contacted with a liquid electrolyte (e.g. a dilute aqueous NaCl solution) an electrical double layer (EDL) developes at the solid–liquid interface due to ionizable groups of the material (dissociation of silanol groups in the above example: $\equiv Si-OH+H_2O \Leftrightarrow \equiv Si-O^- + H_3O^+$) or by ions adsorbing on its surface. The resulting negative charge density of the capillary (channel) inner wall affects the distribution of hydrated sodium (counter)ions in the solution: In immediate proximity to the surface there exists a layer of ions which are relatively strongly fixed by electrostatic forces. It forms the inner or compact part of the fluid-side domain of the EDL and its typical thickness is of the order of only one ion diameter (about 0.5 nm). The outer Helmholtz plane (OHP, Figure 1(c)) separates inner and diffusive layers which, together, constitute the EDL. While the ionic species in the diffusive layer undergo Brownian motion, they are also influenced by the local electrostatic potential. At equilibrium their

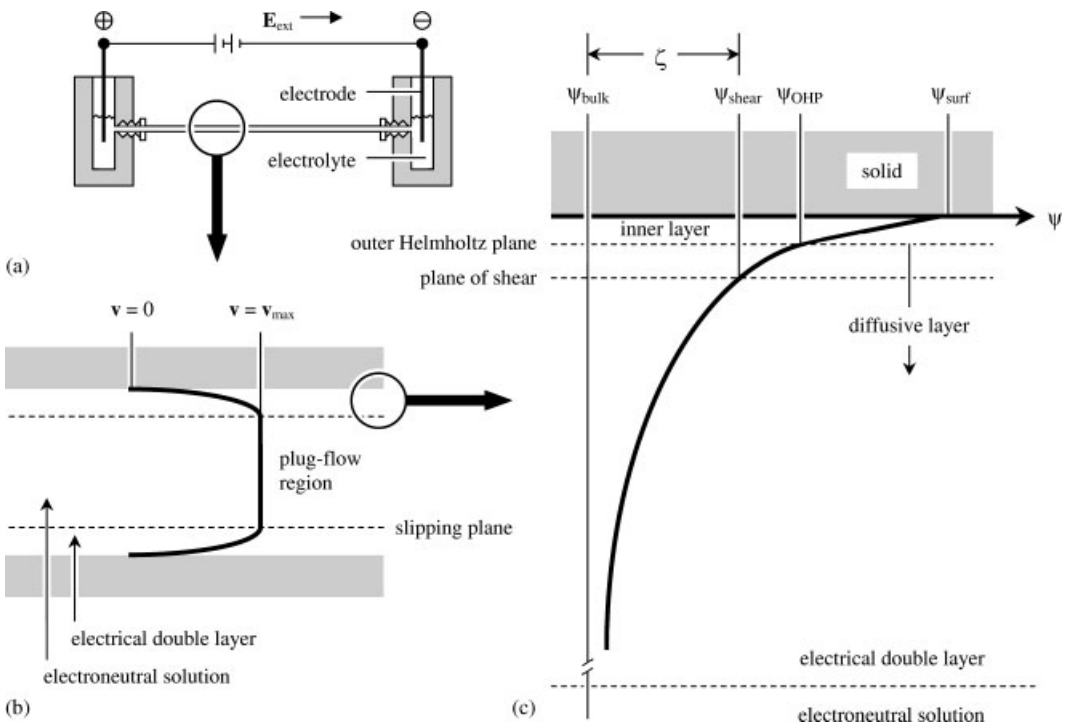

Figure 1. Illustration of electrokinetically driven flow (electroosmosis) through a straight cylindrical capillary with $\zeta < 0$: (a) Experimental set-up; (b) pore-scale velocity profile of electroosmotic flow (EOF); and (c) distribution of electrical potential in the electrical double layer (EDL).

accumulation in this region can be described by the Boltzmann equation. The spatial dimension of the diffusive layer is typically between a few and hundred nanometers.

EOF sets in when an external electrical field ($\mathbf{E}_{\text{ext}} = -\nabla\phi$) is applied. It interacts with the EDL field to create an electrokinetic body force on the liquid. Consequently, the bulk of liquid is driven by viscous drag via the shear stresses concentrated in the relatively thin EDL (compared to a capillary radius r_c of micrometer dimension). The potential (ψ) at the so-called shear plane separating mobile and immobile phases is the electrokinetic or zeta-potential (ζ). For the case considered here (smooth surface, simple ions) ζ should be close to, if not coincident with the diffusive double layer potential ψ_{OHP} (Figure 1(c)). The fluid velocity rises from zero at the shear plane to a limiting value $\mathbf{v}_{\max}$ beyond the EDL where, from a macroscopic point of view, the liquid seems to slip past the surface (Figure 1(b))

$$\mathbf{v}_{\max} = \mu_{\text{eo}}\mathbf{E}_{\text{ext}} = -\varepsilon_0\varepsilon_r\left(\frac{\zeta}{\eta_f}\right)\mathbf{E}_{\text{ext}} \tag{1}$$

μ_{eo} denotes the electroosmotic mobility and η_f is the dynamic viscosity of the fluid. ε_0 is the permittivity of vacuum and ε_r the relative permittivity of the electrolyte solution. The minus sign in Equation (1) means that $\mathbf{v}_{\max}$ and $\mathbf{E}_{\text{ext}}$ are in the same direction when ζ is negative. Without any externally applied pressure forces and uniform distribution of ζ along the channel wall the liquid moves as in plug-flow as the gradient in ψ beyond the EDL is negligible. The thickness of the EDL is characterized by

$$\lambda_D = \left(\frac{\varepsilon_0\varepsilon_r RT}{F^2\sum_i z_i^2 c_{i,\infty}}\right)^{1/2} \tag{2}$$

where R is the gas constant, T the absolute temperature and F Faraday's constant, z_i is the valency of ionic species i and $c_{i,\infty}$ its molar concentration in the electroneutral solution. λ_D is the Debye screening length and about 10 nm for a 10^{-3} M 1:1 aqueous electrolyte solution. In this case the EDL is much smaller than the radius of micrometer channels ($r_c/\lambda_D > 100$) and the volumetric EOF rate is approximately given by $Q = v_{\max}A$ (where A is the cross-sectional area of a channel). However, as the channel diameter approaches submicrometer dimension and/or as λ_D increases the EDL cannot be considered as thin any longer (e.g. $r_c/\lambda_D \approx 10$) and the plug-like velocity profile deteriorates towards a parabola, as known for Poiseuille flow ($r_c/\lambda_D = 2$), with an accompanying increase in hydrodynamic dispersion evidenced by Figure 2 [10, 61].

2.2. General mathematical formulation

The velocity field of an incompressible Newtonian electrolyte solution in low-Reynolds number flow through a microfluidic channel is governed by the Navier–Stokes equation

$$\rho_f\left(\frac{\partial\mathbf{v}}{\partial t} + (\mathbf{v}\cdot\nabla)\mathbf{v}\right) = -\nabla p + \eta_f\nabla^2\mathbf{v} + \mathbf{f} \tag{3}$$

where ρ_f is the density of the fluid, $\mathbf{v}$ represents the divergence-free velocity field ($\nabla\cdot\mathbf{v} = 0$), and p denotes hydrostatic pressure. The body force $\mathbf{f}$ is related to the volume density of

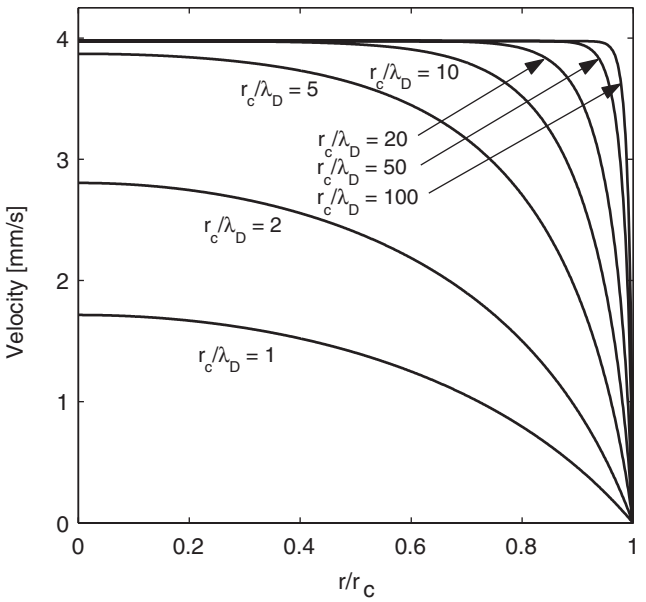

Figure 2. Velocity profiles of EOF in an open-straight, cylindrical capillary for different values of r_c/λ_D obtained by solution of the momentum balance equation [61]. Externally applied electrical field $E_{ext} = 5 \times 10^4\,\mathrm{Vm}^{-1}$, $\zeta = -0.1\,\mathrm{V}$, $\varepsilon_r = 80$; liquid density and viscosity are $10^6\,\mathrm{gm}^{-3}$ and $0.89\,\mathrm{gm}^{-1}\,\mathrm{s}^{-1}$, respectively (at $T = 298.15\,\mathrm{K}$). The Debye screening length (λ_D) is 10 nm.

charge ρ_q and the local electrical field ($\mathbf{E} = -\nabla\Phi$) by

$$\mathbf{f} = \rho_q \mathbf{E} = -q_e \nabla\Phi \sum_{i=1}^{N} z_i n_i \quad \text{for } i = 1, \ldots, N \tag{4}$$

where q_e stands for the elementary charge, n_i is the number concentration of ionic species i in the N-component electrolyte solution, and Φ denotes the local electrostatic potential governed by the Poisson equation

$$\nabla^2\Phi = -\frac{\rho_q}{\varepsilon_0 \varepsilon_r} \tag{5}$$

The flux density $\mathbf{j}_i$ (the number of ions per unit area passing through the surface of a volume element) is related to the local fluid velocity and gradients in ion density and electrical potential by the Nernst–Planck equation

$$\mathbf{j}_i = \left(\mathbf{v} - \frac{q_e z_i D_i \nabla\Phi}{k_B T} \right) n_i - D_i \nabla n_i \tag{6}$$

where D_i is the mass diffusion coefficient and k_B is the Boltzmann constant. Each ionic species satisfies the following conservation:

$$\frac{\partial n_i}{\partial t} + \nabla \cdot \mathbf{j}_i = 0 \tag{7}$$

Together with appropriate initial and boundary conditions Equations (3)–(7) describe the mass transport in systems with arbitrary geometry, distribution (and magnitude) of ζ, and aspect ratio. It is important to note that we consider here (cf. Equations (4)–(6)), without further simplification, the local electrostatic potential in the channel which, in general, includes contributions from both the EDL and $\mathbf{E}_{\text{ext}}$. Further, the presented description does not rely on the Boltzmann distribution for electrical charges in the diffusive part of the EDL applicable only at thermodynamic equilibrium. It would assume that this distribution remains undisturbed by external convective influences which is justified only under certain limiting conditions, e.g. at low Peclet number in channels of arbitrary geometry and for a uniform distribution of ζ [13].

In this work we consider fully developed, steady, isothermal EOF in the microfluidic channel. It eliminates time derivatives in Equations (3) and (7), as well as the need for initial conditions. Thus, we remain concerned with the following set of coupled equations:

$$\rho_{\text{f}}(\mathbf{v}\cdot\nabla)\mathbf{v}=-\nabla p+\eta_{\text{f}}\nabla^2\mathbf{v}-q_{\text{e}}\nabla\Phi\sum_{i=1}^{N}z_i n_i \tag{8a}$$

$$\nabla\cdot\mathbf{v}=0 \tag{8b}$$

$$\nabla^2\Phi=-q_{\text{e}}\sum_{i=1}^{N}z_i n_i/\varepsilon_0\varepsilon_{\text{r}} \tag{8c}$$

$$\mathbf{v}\nabla n_i-D_i\nabla^2 n_i-\frac{q_{\text{e}}z_i D_i}{k_{\text{B}}T}\nabla\cdot(n_i\nabla\Phi)=0 \tag{8d}$$

2.3. Boundary conditions

Because the length of a microfluidic channel is large compared to heterogeneities in the flow field and species transport on any length (and associated time) scale we assume longitudinal spatial periodicity [62]. Consequently, our description reduces to that of a representative unit (Figure 3(a)) with periodic (outer) boundary conditions

$$[|\Phi|]=C,\qquad [|n_i|]=0,\qquad [|\mathbf{v}|]=0 \tag{9}$$

where C is a constant related to the conditions of an experiment (including pH, the electrolyte concentration, $\mathbf{E}_{\text{ext}}$, surface adsorption, or temperature) and $[|\ldots|]$ denotes the difference between values of a function at opposite points lying on the corresponding unit boundaries.

The outer boundary conditions have to be complemented by inner boundary conditions which define the values of the electrical potential (or charge), flow velocity and species number concentrations at the solid–liquid interface. The common no-slip and normal-zero-flux conditions are recognized at this interface for the fluid flow velocity and number concentrations, respectively

$$\mathbf{v}=0 \tag{10a}$$

$$v\cdot\mathbf{j}_i=0 \tag{10b}$$

where v is the outer normal to the solid–liquid interface. In turn, an electrical boundary condition can be represented by either the surface charge density or zeta-potential. Since these characteristics, in particular, depend on both the nature of contacting media and the local

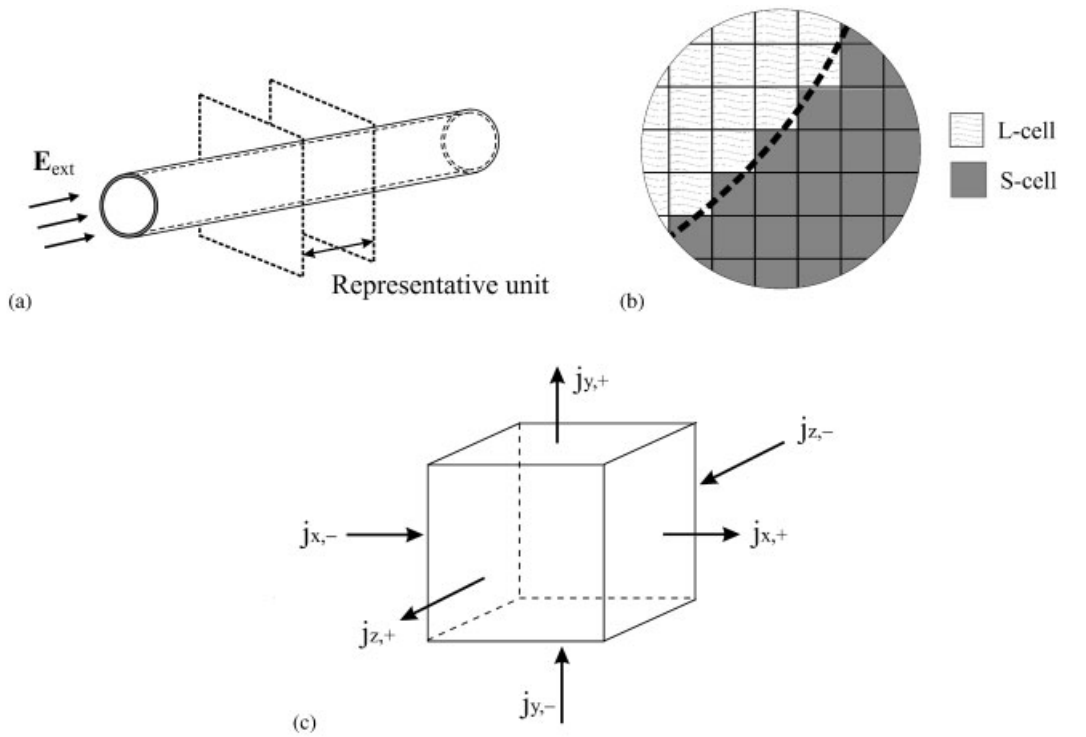

Figure 3. Discretization and approximation of the solution domain: (a) Capillary scale. Spatial periodicity reduces the description to that of a representative unit with periodic boundary conditions; (b) Solid–liquid interface. The solution domain is represented by a set of uniform cubic cells; and (c) Single L-cell. Entry and exit flux density components.

environment, e.g. the interfacial space morphology or the local pH, they can be considered, in general, as spatially variable quantities. Thus, the electrical boundary conditions at the solid–liquid interface can be imposed in two alternative ways: by given surface charge density (σ) or zeta-potential (ζ) distribution, respectively

$$v \cdot \nabla \Phi = -\frac{\sigma(\mathbf{r})}{\varepsilon_0 \varepsilon_r} \tag{11a}$$

or

$$\Phi = \zeta(\mathbf{r}) \tag{11b}$$

The former equation corresponds to the Neumann-type, the latter to the Dirichlet-type boundary condition.

This presentation of inner boundary conditions assumes that the boundary values of all quantities (flow velocity, species flux, surface charge density, zeta-potential) are related to the same location. In fact, while the no-slip and normal-zero-flux conditions, as well as the surface charge density are recognized directly at a solid–liquid interface, the zeta-potential is defined with respect to the shear plane (Figure 1(c)). However, since this plane is located in

immediate proximity ($\approx 0.5\,\mathrm{nm}$) to the solid–liquid interface, it is assumed that these surfaces coincide.

3. COMPUTATIONAL METHODS

3.1. General scheme

To solve the system of time-independent partial differential equations (Equations (8a)–(8d)) subject to inner and outer boundary conditions (Equations (9)–(11)) we implemented an iterative scheme (Figure 4). At each iteration first the coupled Nernst–Planck and Poisson equations (Equations (8c) and (8d)) were solved numerically. Then, the Navier–Stokes equation (Equation (8a)) together with the continuity equation (Equation (8b)) were solved. The iterative solution had continued until convergence of the flow field was reached. As initial guess we used zero flow field, as well as bulk number concentrations and the electrical potential distribution caused by the applied field. This contribution to the local electrical potential is assumed to be point-wise constant during iterations.

Thus, the numerical scheme requires solution of Poisson, Nernst–Planck, and Navier–Stokes equations (where the last problem is, by far, the more difficult computational task). While

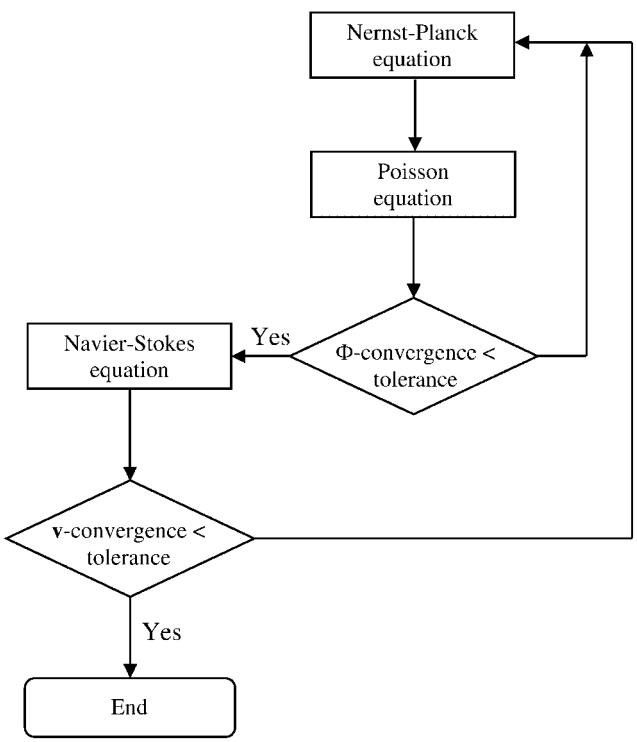

Figure 4. Flow-chart of the computational scheme employed for the PNP–LB (Poisson–Nernst–Planck coupled with lattice-Boltzmann) simulations.

we employed traditional finite-difference methods to resolve the first two problems, the lattice-Boltzmann method has been applied for solution of the Navier–Stokes problem.

3.2. Geometry and discretization of the solution domain

A uniform mesh has been utilized for numerical solution of all of the above-mentioned problems. Thus, the solution domain can be represented by a set of equal cubic cells of size h (Figure 3(b)). Cells were divided into two subsets, i.e. cells having their geometrical centre in the liquid phase (L-cells) or in the solid phase (S-cells). During a simulation the electrical potential, charge number concentration, and fluid velocity are determined at the centres of only the L-cells. S-cells adjacent to L-cells are considered as interface cells and the actual values of physical quantities at their centres are used as boundary values.

3.3. Numerical solution of the Poisson–Nernst–Planck problem

The finite-difference scheme for solution of the Nernst–Planck equation is based on the total flux density in an L-cell. For steady-state the net flux is zero. This situation can be represented by entry and exit components on each of the six cell surfaces (Figure 3(c))

$$j^{x,+}_{k,l,m} + j^{x,-}_{k,l,m} + j^{y,+}_{k,l,m} + j^{y,-}_{k,l,m} + j^{z,+}_{k,l,m} + j^{z,-}_{k,l,m} = 0 \tag{12}$$

where k, l, and m define the discrete co-ordinates of a cell. If an L-cell is not lying adjacent to the interface each of the flux density components is expressed in terms of the flow velocity, concentration, and electrical potential at the centre of a given and neighbouring points. For a particular species, for example, we have

$$j^{x,+}_{k,l,m} = \frac{v^x_{k+1,l,m} + v^x_{k,l,m}}{2}\frac{n_{k+1,l,m} + n_{k,l,m}}{2} - D\frac{n_{k+1,l,m} - n_{k,l,m}}{h} - \frac{q_e z D}{k_B T}\frac{n_{k+1,l,m} + n_{k,l,m}}{2}\frac{\Phi_{k+1,l,m} - \Phi_{k,l,m}}{h} \tag{13}$$

If an L-cell is adjacent to the interface and the normal-zero-flux boundary condition is applied, the corresponding term in Equation (12) is eliminated. By assuming that interface and boundary values lie on the border between L- and S-cells the distance $h/2$ (instead of h) should be used. This is consistent with the location of the no-slip wall in LB simulations based on the bounce-back boundary condition [63]. By using similar expressions for the other flux components, substituting into Equation (12), and solving the equation for $n_{k,l,m}$ one can obtain an explicit expression for calculation of its updated value. It is determined by the concentration values from a previous iteration, as well as with the flow velocity and electrical potential values in a given and neighbouring cells. We used an SOR scheme to get a more rapid convergence

$$\hat{n}_{k,l,m} = \omega n_{k,l,m} + (1-\omega)\check{n}_{k,l,m} \tag{14}$$

where $\hat{n}_{k,l,m}$ is updated number concentration at current iteration, $\check{n}_{k,l,m}$ is the number concentration from previous iteration, and ω is the relaxation parameter. Then, updated number concentration values for each species in all cells are used for solution of the Poisson equation.

Its finite-difference representation is

$$-\frac{\sum n_{k,l,m} z q_e}{\varepsilon_0 \varepsilon_r} = \frac{2}{h_{k+1/2}+h_{k-1/2}}\left(\frac{\Phi_{k+1,l,m}-\Phi_{k,l,m}}{h_{k+1/2}} - \frac{\Phi_{k,l,m}-\Phi_{k-1,l,m}}{h_{k-1/2}}\right) + \frac{2}{h_{l+1/2}+h_{l-1/2}}\left(\frac{\Phi_{k,l+1,m}-\Phi_{k,l,m}}{h_{l+1/2}} - \frac{\Phi_{k,l,m}-\Phi_{k,l-1,m}}{h_{l-1/2}}\right) + \frac{2}{h_{m+1/2}+h_{m-1/2}}\left(\frac{\Phi_{k,l,m+1}-\Phi_{k,l,m}}{h_{m+1/2}} - \frac{\Phi_{k,l,m}-\Phi_{k,l,m-1}}{h_{m-1/2}}\right) \tag{15}$$

where, for example, $h_{k+1/2}$ is the distance between the centres of cells $(k+1,l,m)$ and (k,l,m); the summation should be made over all ionic species. As for the Nernst–Planck equation, this expression needs to be modified if the cell is adjacent to the interface, by replacing either the corresponding distance h by $h/2$ (Dirichlet boundary condition) or the corresponding potential difference by $2\sigma/(h\varepsilon_0\varepsilon_r)$ (Neumann boundary condition). By applying the traditional Gauss–Seidel iterative procedure Equation (15) allows to obtain an explicit expression for determination of the updated value of electrical potential which, in the case of the Dirichlet boundary condition, can be written as,

$$\hat{\Phi}_{k,l,m} = \left(\frac{1}{h_{k+1/2}h_{k-1/2}} + \frac{1}{h_{l+1/2}h_{l-1/2}} + \frac{1}{h_{m+1/2}h_{m-1/2}}\right)^{-1} \times \left(\frac{\sum n_{k,l,m} z q_e}{2\varepsilon_0\varepsilon_r} + \frac{h_{k-1/2}\check{\Phi}_{k+1,l,m} + h_{k+1/2}\,\hat{\Phi}_{k-1,l,m}}{h_{k+1/2}h_{k-1/2}(h_{k+1/2}+h_{k-1/2})} + \frac{h_{l-1/2}\check{\Phi}_{k,l+1,m} + h_{l+1/2}\,\hat{\Phi}_{k,l-1,m}}{h_{l+1/2}h_{l-1/2}(h_{l+1/2}+h_{l-1/2})} + \frac{h_{m-1/2}\check{\Phi}_{k,l,m+1} + h_{m+1/2}\,\hat{\Phi}_{k,l,m-1}}{h_{m+1/2}h_{m-1/2}(h_{m+1/2}+h_{m-1/2})}\right) \tag{16}$$

The calculations of the number concentration and electrical potential stop when the convergence rate

$$\chi_{PNP} = \sqrt{\frac{\sum_{k,l,m}(\hat{\Phi}_{k,l,m} - \check{\Phi}_{k,l,m})^2}{\sum_{k,l,m}\check{\Phi}^2_{k,l,m}}} \tag{17}$$

becomes less than the predefined value δ_{PNP} (PNP $\equiv$ Poisson–Nernst–Planck), which is typically set to 10^{-6}.

3.4. The lattice-Boltzmann algorithm

The electrolyte solution as a statistical system can be described in terms of a distribution function $\mathscr{F}(\mathbf{r},\mathbf{u},t)$ defined such that $\mathscr{F}(\mathbf{r},\mathbf{u},t)\,d\mathbf{r}\,d\mathbf{u}$ gives the number of fluid molecules which, at time t, are located between $\mathbf{r}$ and $(\mathbf{r}+d\mathbf{r})$ and have velocities in a range from $\mathbf{u}$ to $(\mathbf{u}+d\mathbf{u})$.

Macroscopic quantities like the fluid density ρ_f and the velocity $\mathbf{v}$ can be determined by momentum integration of this distribution function

$$\rho_f(\mathbf{r},t) = \int M_m \mathscr{F}(\mathbf{r},\mathbf{u},t)\,d\mathbf{u} \tag{18}$$

and

$$\mathbf{v}(\mathbf{r},t) = \frac{1}{\rho_f(\mathbf{r},t)} \int M_m \mathbf{u} \mathscr{F}(\mathbf{r},\mathbf{u},t)\,d\mathbf{u} \tag{19}$$

where M_m denotes molecular mass. The evolution of the distribution function can be described by the following equation:

$$\mathscr{F}\left(\mathbf{r}+\mathbf{u}\,dt, \mathbf{u}+\frac{\mathbf{F}}{M_m}dt, t+dt\right) d\mathbf{r}\,d\mathbf{u} = \mathscr{F}(\mathbf{r},\mathbf{u},t) + \Omega(\mathscr{F})\,d\mathbf{r}\,d\mathbf{u}\,dt \tag{20}$$

where $\mathbf{F}$ is the acting external force and Ω denotes the collision operator. It is well known that the macroscopic properties are not directly dependent on the details of the microscopic behaviour, but are mainly defined through interactions between molecules expressed, for example, by an appropriate collision operator. Thus, the transition toward a simplified dynamics with discrete space, time and molecular velocities is feasible. The discrete analogy of Equation (20) is

$$\mathscr{F}_\alpha(\mathbf{r}+\mathbf{e}_\alpha \Delta t, t+\Delta t) = \mathscr{F}_\alpha(\mathbf{r},t) + \Omega_\alpha(\mathscr{F}_\alpha) + \Delta t F_\alpha \tag{21}$$

where $\mathscr{F}_\alpha$ is the distribution function for the αth discrete velocity $\mathbf{e}_\alpha$ at position $\mathbf{r}$ and time t, and Δt is the time step. In this work we are concerned with a modification of the LB approach, the so-called lattice-BGK (Bhatnagar–Gross–Krook) model [34, 52], being characterized by the discrete Boltzmann equation with a single-time relaxation collision operator

$$\mathscr{F}_\alpha(\mathbf{r}+\mathbf{e}_\alpha \Delta t, t+\Delta t) = \mathscr{F}_\alpha(\mathbf{r},t) + \frac{1}{\tau}[\mathscr{F}_\alpha^{eq}(\mathbf{r},t) - \mathscr{F}_\alpha(\mathbf{r},t) + \Delta t F_\alpha] \tag{22}$$

where $\mathscr{F}_\alpha^{eq}$ represents the equilibrium distribution function and τ is a non-dimensional relaxation time. For the D_3Q_{19} lattice-BGK model [32] $\mathscr{F}_\alpha^{eq}$ can be expressed by,

$$\mathscr{F}_\alpha^{eq} = \rho_f w_\alpha \left[1 + \frac{3}{c_s^2}\mathbf{e}_\alpha \cdot \mathbf{v} + \frac{9}{2c_s^4}(\mathbf{e}_\alpha \cdot \mathbf{v})^2 - \frac{3}{2c_s^2}\mathbf{v}\cdot\mathbf{v}\right] \tag{23}$$

where c_s is the speed of sound and w_α is a weighting factor depending on the length of the vector $\mathbf{e}_\alpha$ given by [52]

$$w_\alpha = \begin{cases} 1/3, & \alpha = 0 \text{ (rest particle)} \\ 1/18, & \alpha = 1,2,\ldots,6 \text{ (nearest neighbours)} \\ 1/36, & \alpha = 7,8,\ldots,18 \text{ (next-nearest neighbours)} \end{cases} \tag{24}$$

Incorporation of a body force term caused by the interaction of the EDL field with the externally applied electrical field into the discrete Boltzmann equation was performed using

the method described by Guo *et al.* [64]

$$F_\alpha = \left(1 - \frac{1}{2\tau}\right) w_\alpha \left[\frac{\mathbf{e}_\alpha - \mathbf{v}}{c_s^2} + \frac{(\mathbf{e}_\alpha \cdot \mathbf{v})}{c_s^4}\mathbf{e}_\alpha\right] \cdot \mathbf{F} \tag{25}$$

To satisfy the no-slip boundary condition for velocity at the solid–liquid interface, we employed the conventional bounce-back scheme, where momentum from an incoming particle is bounced back in opposite direction when it hits the wall.

After each iteration the divergence rate

$$\chi_{NS} = \sqrt{\frac{\sum_{k,l,m}(\hat{\mathbf{v}}_{k,l,m} - \check{\mathbf{v}}_{k,l,m})^2}{\sum_{k,l,m}\check{\mathbf{v}}_{k,l,m}^2}} \tag{26}$$

is calculated and compared with a predefined value of δ_{NS} (NS $\equiv$ Navier–Stokes). The simulation stops when $\chi_{NS} < \delta_{NS}$ (typically 10^{-4}) is satisfied.

Here, it should be noted that the overwhelming majority of real electrokinetic systems operates in the low-Mach number limit which is a necessary condition for application of the LB method. Typical EOF velocities are of the order of a few millimeters per second which is much less than the speed of sound in liquid media.

4. RESULTS OF SIMULATIONS

4.1. Homogeneous equilibrium double layer

Although the presented model is capable of dealing with both arbitrary distribution of ζ and geometrical configuration of the solid–liquid interface, we started to simulate EOF in relatively simple systems for which either an analytical solution to the problem exists or the results of other numerical simulations are available for comparison. Quantitative analysis of computed fields of a physical quantity Θ (e.g. species number concentration or flow velocity components) is based on the global relative error γ defined with respect to some appropriate reference value

$$\gamma = \frac{\sqrt{\sum(\Theta - \Theta_{ref})^2}}{\sqrt{\sum \Theta_{ref}^2}} \tag{27}$$

In particular, for the lattice-Boltzmann EOF velocity field in a homogeneous capillary the reference values may be obtained by numerical solution of the momentum balance equation using the Runge–Kutta method.

To test the adequacy of the model for simulating electrical charge distributions in the diffusive part of the EDL (cf. Figure 1(c)) we begin with an isolated, homogeneous solid–liquid interface for which the typical dimension of surface roughness is smaller than the EDL thickness, and simulate the ionic number concentration in the electrolyte in contact with this surface by solving the Poisson and Nernst–Planck problems. At equilibrium, without concentration gradients and any externally applied field, the electrical potential distribution can be

obtained from the Poisson–Boltzmann equation

$$\nabla^2\psi = -\frac{q_e}{\varepsilon_0\varepsilon_r}\sum_{i=1}^{N} z_i n_{i,\infty}\exp\left(-\frac{q_e z_i \psi}{k_B T}\right) \tag{28}$$

where the local concentration is determined by the Boltzmann distribution

$$n_i = n_{i,\infty}\exp\left(-\frac{q_e z_i \psi}{k_B T}\right) \tag{29}$$

The analytical solution of Equation (28) (the starting point of the Gouy–Chapman description [65] of the diffusive EDL) for a charged, flat surface, a symmetrical 1:1 electrolyte such as NaCl ($z_1 = -z_2 = z$), and an arbitrary magnitude, but uniform distribution of the zeta-potential (ζ) is [66]

$$\psi(x) = \frac{2k_B T}{q_e z}\ln\left[\frac{1 + e^{-x/\lambda_D}\tanh\left(\frac{q_e z\zeta}{4k_B T}\right)}{1 - e^{-x/\lambda_D}\tanh\left(\frac{q_e z\zeta}{4k_B T}\right)}\right] \tag{30}$$

where x is the distance from the surface. For values of ζ low enough (below ca. 25 mV) Equation (30) reduces to the so-called Debye–Hückel equation, $\psi(x) = \zeta e^{-x/\lambda_D}$. Results for the distribution of net electrical charge density based on the analytical solution (Equations (29) and (30)) and the numerical treatment outlined in Section 3.3 are shown in Figure 5. Because λ_D appears as characteristic decay length for the potential, we analysed the global relative error in dependence of the grid resolution with respect to λ_D (see inset). As electrolyte we considered an aqueous solution of NaCl at 298.15 K with concentration (9.43×10^{-4} M) adjusted

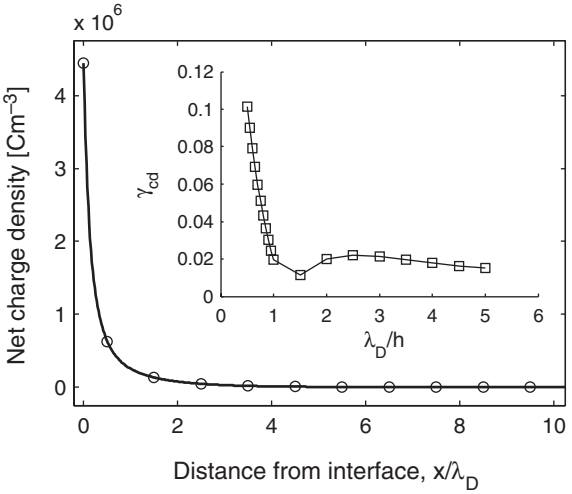

Figure 5. Distribution of net electrical charge in the EDL at a flat solid–liquid interface (the open circles are the results of the numerical solution, solid line: analytical solution) and dependence of the global relative error (γ_{cd}) on the grid resolution with respect to the double layer thickness (inset).

such that λ_D is 10 nm (Equation (2)), while the surface is characterized by $\zeta = -100$ mV. One conclusion to be drawn from Figure 5 is that the net charge density (cd) away from a charged surface can be computed with global relative errors (γ_{cd}) better than 2% for a grid resolution λ_D/h of 1 and higher ($\gamma_{cd} = 0.59\%$ for $\lambda_D/h = 30$) by using the Poisson–Nernst–Planck solver described above (in Section 3.3). It is further evident that after a distance of about $5\lambda_D$ from the surface the solution is practically electroneutral. Recalling that this distance is about 50 nm under the present set of conditions, it is only a thin liquid layer close to the interface that becomes locally charged, in general, when considering electrolytes confined by pores of micrometer dimension.

4.2. Straight, homogeneous cylindrical capillary

As a next step, we simulated EOF in a straight, homogeneous cylindrical capillary. The spatial homogeneity of this system alleviates the use of an iterative procedure for obtaining the steady-state velocity field. Ionic number concentrations are not disturbed by forced convection. Thus, the Poisson–Nernst–Planck solver and LB-code are run only once. Because there is no general analytical solution available for the EOF problem in a cylindrical capillary, the simulated velocity field was compared with one obtained by numerical solution of the one-dimensional momentum balance equation [61]

$$\frac{d^2 v_x}{dr^2} + \frac{1}{r}\frac{dv_x}{dr} = \frac{2E_{ext} q_e n_\infty}{\eta_f} \sinh\left(\frac{q_e \psi}{k_B T}\right) \tag{31}$$

The solution of this equation provides the radial distribution of axial EOF velocities in the cylindrical capillary. Equation (31) was solved with a very fine resolution (2×10^5 points per channel diameter). Further, the use of different capillary radii allowed to realize aspect ratios r_c/λ_D from 10 to 100. Figure 6 compares velocity profiles obtained by both procedures. As was already emanating from Figure 5, an applied electrical field will be interacting with the electrolyte solution only in the EDL where the liquid has acquired a net charge. Thus, the driving force for EOF is not constant over the capillary diameter: it dominates in vicinity of the capillary wall, but soon becomes zero in the central region of the capillary lumen. There, motion of bulk liquid is caused by a viscous drag force leading to the plug-like velocity distribution beyond the slipping plane (Figure 1(b)). The dependence of the global relative error γ_{vf} of the axial component in a velocity field (vf) on the spatial resolution with respect to the capillary radius is demonstrated in Figure 7 for various aspect ratios. It should be mentioned that the error associated with the spatial resolution manifests itself in an inaccuracy of both the calculated electrical charge distribution (which, in turn, is affected by the simulated electrical potential distribution) and velocity field. This can explain why the total error γ_{vf} does not exhibit the squared dependence on grid resolution which is inherent individually in the finite-difference and LB methods. Nevertheless, one can achieve higher accuracy by grid refinement, e.g. the use of 100 grid points over a capillary radius r_c resulted in γ_{vf} of less than 6% (for all aspect ratios). On the other hand, the computational time grows with the third power of the spatial resolution.

The complete simulation of EOF in a cylindrical capillary (for $r_c/h = 50$) took about 15 CPU minutes per cross-sectional layer for one computer node. In general, simulations were performed on a Hewlett-Packard Superdome at the Otto-von-Guericke-Universität Magdeburg, Germany.

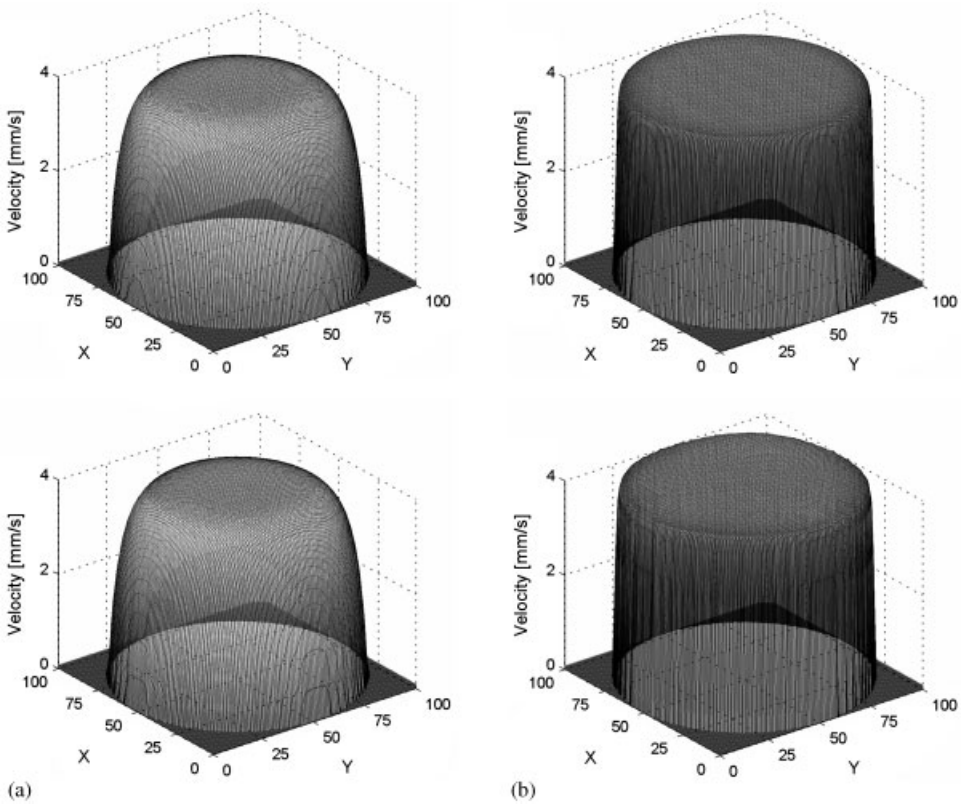

Figure 6. EOF velocity field in an open-straight, cylindrical capillary with homogeneous and smooth surface: solution of the momentum balance equation (top) vs the PNP–LB approach (bottom) for: (a) $r_c/\lambda_D = 10$; and (b) $r_c/\lambda_D = 100$. The same conditions as in Figure 2 have been used.

4.3. Straight cylindrical capillaries with axial and angular inhomogeneities in electrokinetic potential

Then, we modelled EOF in cylindrical capillaries with a destinated axial and angular distribution of the zeta-potential (Figure 8). This configuration can be considered as simplified approach for dealing with a heterogeneous surface charge distribution in porous media under more general conditions. In fact, the spatial scale of locally varying electrical potential is often significant with respect to the thickness of the EDL, and it can have a number of reasons. For example, it can already be introduced by the inherent manufacturing process of a material, specific ageing, the storage conditions, chemical reactions, or the eventually irreversible adsorption of molecular or colloidal species on the surface, with a concomitant change of local roughness and electrokinetic properties [61, 67–73]. Consequently, the favourable, i.e. plug-like EOF velocity profile becomes disturbed by induced pressure gradients resulting from an axial variation of the surface charge at the inner wall of a microfluidic channel [71–74]. In turn, this necessarily leads to additional hydrodynamic dispersion. The problem becomes especially severe for the transport of sample mixtures containing large biomolecules such as

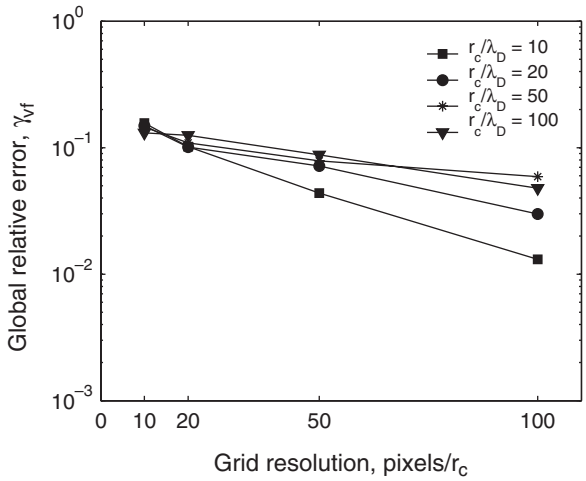

Figure 7. Global relative error of a simulated velocity field (γ_{vf}) relative to the solution of the momentum balance equation: accuracy of the followed PNP–LB approach depending on the spatial resolution with respect to a capillary radius at various aspect ratios (r_c/λ_D).

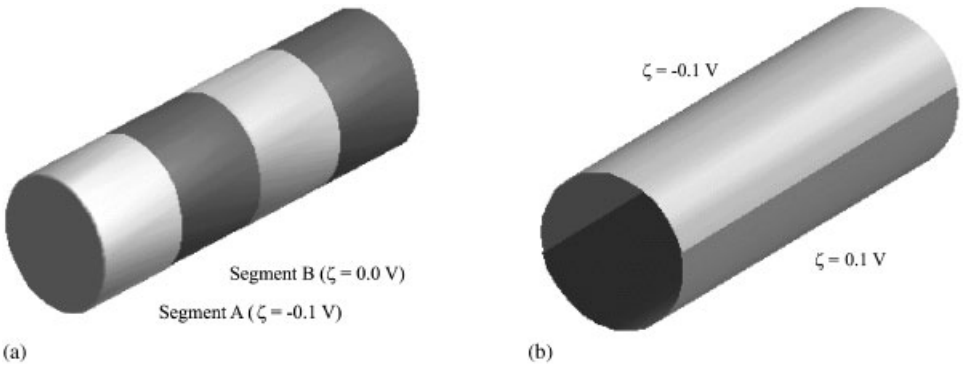

Figure 8. Inhomogeneous charge distributions (discrete patterns) at the inner wall of the cylindrical capillary: (a) Surface charge pattern 1 (P1): Step changes of ζ in the axial direction, angular uniformity; and (b) P2: Step changes of ζ in the angular direction, axial uniformity.

proteins, peptides or DNA [75] which are charged and, thus, can interact strongly with the often oppositely charged surface through hydrophobic and electrostatic mechanisms. As their adsorption progresses in time, it continues to cause unreproducible local, as well as average EOF velocities and a significant loss of resolution in the separation of individual components due to increased axial dispersion and a strong tailing in the residence-time distributions characterized by non-Gaussian shape.

In general, local variations in electrical potential produce a non-uniform electrokinetic driving force that requires local (positive or negative) pore pressure for compensating the associated momentum in an incompressible fluid [71–74]. Unfortunately, the actual spatial and

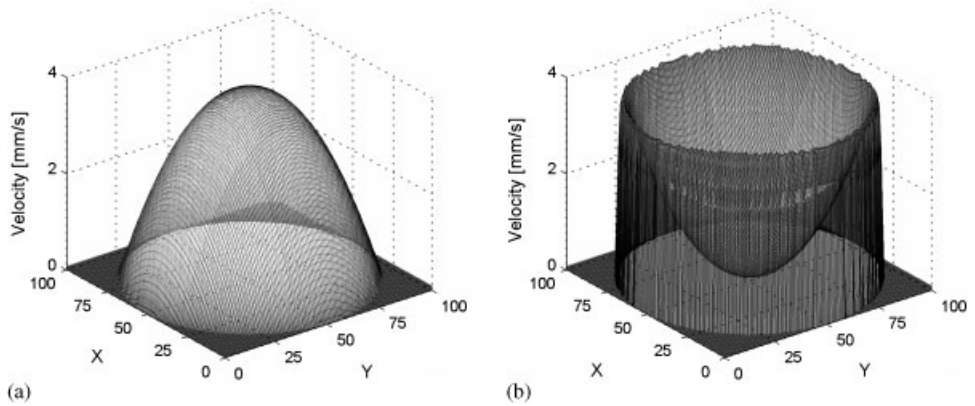

Figure 9. Local flow profiles in the capillary with surface charge pattern P1 (cf. Figure 8(a)). Velocity distributions in the central cross-section of each segment: (a) segment A ($\zeta = -100\,\mathrm{mV}$); and (b) segment B ($\zeta = 0\,\mathrm{mV}$). The Debye screening length (λ_D) is 10 nm and $r_c/\lambda_D = 100$; $E_{ext} = 5 \times 10^4\ \mathrm{V\,m^{-1}}$, liquid density and viscosity are $10^6\ \mathrm{gm^{-3}}$ and $0.89\ \mathrm{gm^{-1}\,s^{-1}}$, respectively, $\varepsilon_r = 80$, $T = 298.15\,\mathrm{K}$.

temporal distribution of electrical potential in a real porous medium usually is unknown making it difficult to study on a quantitative basis. On the other hand, this effect may be tailored, e.g. for enhanced microfluidic mixing, by employing surfaces with a patterned charge distribution [27, 76]. For example, Stroock *et al.* [76] studied EOF driven by two patterned geometries in rectangular microchannels in the limit of a thin EDL. They considered variations of surface charge both parallel and perpendicular to the applied electrical field: While a recirculating flow develops in the former case, multidirectional flow along the field and channel axis results in the latter [76]. Because these types of pattern act as a basis from which more general three-dimensional flows may be constructed and the fluid mechanical consequences of (non)intended surface charge distributions in microfluidic environments be evaluated [77], we treated similar zeta-potential distributions in cylindrical capillaries (Figure 8). The first pattern (P1) consists of cylindrical segments with spatially constant non-zero and zero zeta-potential, alternating in the axial direction and having the length $l = 2r_c$. The second pattern (P2) contains half-cylinders with zeta-potentials of opposite sign, but identical magnitude. The EOF simulations were carried out with a computational resolution of $r_c/h = 100$ ($\lambda_D/h = 2$). Characteristic local velocity distributions for steady, fully-developed flow resulting when an external electrical field is superimposed on the EDL field in a general electrolyte solution in contact with surface patterns P1 and P2 are shown in Figures 9 and 10, respectively.

The EOF in capillaries with heterogeneous distribution of surface charge (or value of ζ) has been the topic of several previous studies. Anderson and Idol [67] have developed an infinite-series analytical solution for EOF through a cylindrical capillary with zeta-potential varying periodically and solely in the axial direction. Using a similar approach Long *et al.* [74] obtained an explicit solution for specific surface charge defects. Herr *et al.* [71] considered the EOF in a cylindrical capillary with step-change in ζ in the axial direction and obtained good agreement with their experimental data. Potoček *et al.* [68] and Ren and Li [61] have numerically studied velocity distributions for EOF in circular microchannels for various non-uniform distributions of ζ. More recently, Gleeson [78] developed an analytical solution for

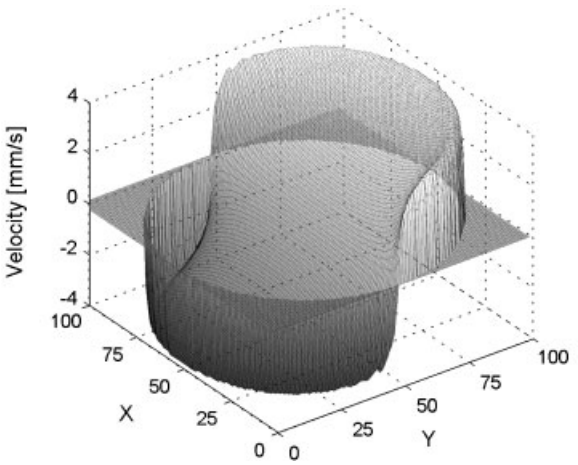

Figure 10. Simulated axial velocity distribution in a cross-section of the open cylindrical capillary with surface charge pattern P2 (cf. Figure 8(b)) for $r_c/\lambda_D = 100$ ($r_c = 1\ \mu m$) and the same conditions as in Figure 9.

the EOF problem in a cylindrical capillary with random zeta-potential distribution. It should be noted that all of the above-mentioned studies were dealing with an axisymmetrical heterogeneity only. Moreover, but except for the work of Ren and Li [61], they assumed a small EDL thickness which allowed to replace the no-slip boundary condition for the velocity at the solid–liquid interface by the Helmholtz–Smoluchowski apparent-slip velocity (Equation (1)) and simplify the analytical solution. Ghosal [72] presented a theory for EOF in channels of arbitrary cross-sectional geometry and distribution of ζ in the lubrication-limit where all axial variations exist on length scales that are large with respect to a characteristic microchannel width, but the assumption of a thin EDL also has been involved in that theory. Thus, reference values for a quantitative analysis of the accuracy with which LB flow fields were computed can be obtained only on the basis of this approximation. It should be pointed out that the slip boundary condition eliminates a fluid region close to the surface where the velocity rises from zero to the bulk value at the slipping plane. Since the thickness of this region does not depend on the channel geometry, the relative contribution of that simplification to the total error decreases with increasing channel diameter (or characteristic transverse dimension).

For a thin EDL the relation between local flow velocity and radial position in capillary segments *A* or *B* of P1 (Figure 8(a)) can be expressed by [71]

$$v_{seg}(r) = -\frac{\varepsilon_0 \varepsilon_r E_{ext}}{\eta_f}\left[\zeta_{seg} + 2(\zeta_{av} - \zeta_{seg})\left(1 - \frac{r^2}{r_c^2}\right)\right] \tag{32}$$

where ζ_{av} is the average value of ζ at the capillary inner wall (for P1 $\zeta_{av} = -50$ mV) and r_c denotes the capillary radius (the subscript 'seg' refers to $\zeta = 0$ mV or $\zeta = -100$ mV, respectively). The velocity profiles calculated by using Equation (32) and compared to those obtained from simulated LB flow fields are shown in Figure 11. The low-velocity region close to the capillary wall in the computed flow field reduces average velocity relative to the value defined by integration of Equation (32) along the radial direction. However, as mentioned

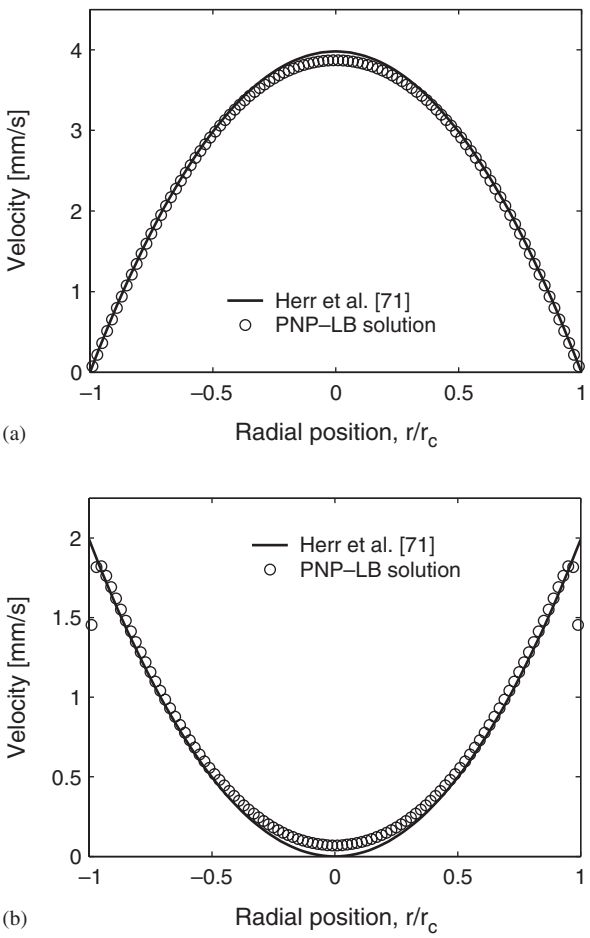

Figure 11. Capillary with pattern P1. Comparison of the simulated intrasegmental velocity profiles with the analytical solution [71]: (a) Central cross-section of segment A ($\zeta = -100$ mV); and (b) central cross-section of segment B ($\zeta = 0$ mV).

above, the discrepancy decreases with an increasing aspect ratio, e.g. the difference between simulated and calculated mean velocities for $r_c/\lambda_D = 100$ is only 0.45%, while it is 9.7% for $r_c/\lambda_D = 20$ and 16.7% for $r_c/\lambda_D = 10$.

In contrast to the discrete axial heterogeneity of P1, the second pattern (Figure 8(b)) is characterized by an azimuthal inhomogeneity. The velocity field for P2 can be obtained in the lubrication limit [72] by numerical solution of the boundary-value problem in polar co-ordinates for an effective potential $\xi(\rho, \theta)$ (ρ and θ are radial and azimuthal co-ordinates)

$$\frac{1}{\rho}\frac{\partial}{\partial\rho}\left(\rho\frac{\partial\xi}{\partial\rho}\right) + \frac{1}{\rho^2}\frac{\partial^2\xi}{\partial\theta^2} = 0, \quad \begin{matrix} \xi(r_c,\theta)|_{0\leqslant\theta<\pi} = -\zeta \\ \xi(r_c,\theta)|_{\pi\leqslant\theta<2\pi} = \zeta \end{matrix} \tag{33}$$

The flow velocity then can be determined from Equation (1) by replacing the local electrical potential ψ by the effective potential ξ, and a solution of this problem (Equation (33)) may be obtained via the following expansion [72]:

$$\xi = -\tilde{\zeta}_0 - \sum_{m=1}^{\infty} [\tilde{\zeta}_m \exp(\mathrm{i}m\theta) + \tilde{\zeta}_m^* \exp(-\mathrm{i}m\theta)]\rho^m \tag{34}$$

where $\tilde{\zeta}_m$ $(m = 0, 1, \ldots, \infty)$ is the complex Fourier transform

$$\tilde{\zeta}_m = \frac{1}{2\pi} \int_0^{2\pi} \zeta(\theta) \exp(-\mathrm{i}m\theta)\, \mathrm{d}\theta \tag{35}$$

It should be pointed out that a quantitative evaluation of the differences between the two discrete velocity fields obtained (i) by numerical solution of this problem (Equations (33)–(35)) and (ii) from computer simulation becomes difficult due to the different co-ordinate systems. While the numerical solution requires the utilization of the polar or, at least, cylindrical system, the PNP–LB computer simulations are realized in the cartesian co-ordinate system. As a result, we have two sets of points corresponding to the polar mesh and rectangular grid.

Therefore, we analysed the two velocity fields by using some of their characteristic properties. It is obvious that, due to the antisymmetry of the zeta-potential distribution in P2 with respect to a centre plane passing through the wall points where the sign of ζ changes, the velocity distribution should possess a similar antisymmetry and any net volumetric flow through the capillary should vanish. Indeed, the simulated velocity field demonstrates such 'self-compensation' (Figure 10) by a deviation of the average velocity from zero of less than 10^{-6}% as compared to the average velocity in the capillary with uniform zeta-potential ($\zeta = -100\,\mathrm{mV}$).

The velocity profiles in the plane $[\theta = \pi/2, 3\pi/2]$, which is perpendicular to the antisymmetry plane, obtained by solution of the problem in Equations (33)–(35) and by computer simulation are shown in Figure 12. Since electromotive forces are effective only in a small region

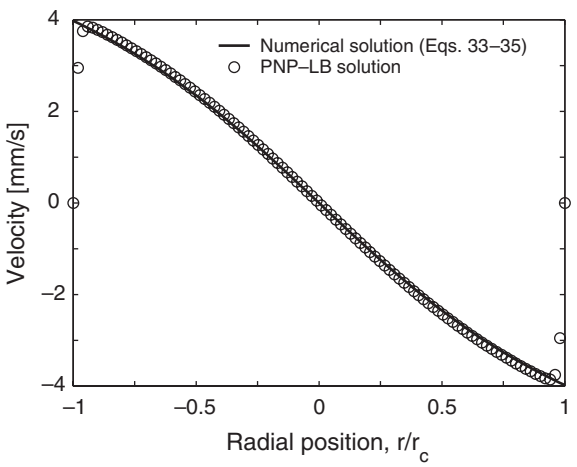

Figure 12. Comparison of velocity distributions in the plane $[\theta = \pi/2, 3\pi/2]$ for the capillary with surface charge pattern P2.

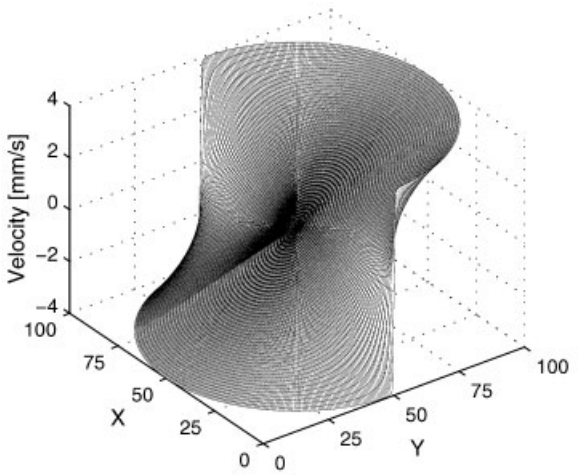

Figure 13. Velocity profile in a cross-section of the open cylindrical capillary ($r_c = 1\ \mu m$) with surface charge pattern P2 according to the approach of Ghosal [72]. The same conditions as in Figures 9 and 10 have been used.

close to the wall of the capillary, actual differences in the velocity profiles should be explainable by the respective velocity boundary conditions. While the slip-condition assumes a discontinuous change of velocity at points where ζ changes its sign (Figure 13) our simulated flow field (Figure 10) here demonstrates a more realistic, smooth transition. As already shown for the surface charge pattern P1, the global relative error in the flow field associated with the no-slip violation soon becomes significant as the aspect ratio r_c/λ_D is reduced below 50. In this region ($r_c/\lambda_D < 100$) the slip-condition should be used with care concerning a numerical investigation of the EOF and resulting hydrodynamic dispersion. Consequently, this approximation does not appear useful in simulating flow through complex porous media with broad range of aspect ratios ($1 \approx r_c/\lambda_D \gg 1$), and the more general approach described in this work could be followed.

5. CONCLUSIONS AND OUTLOOK

We have presented a numerical method for three-dimensional simulation of EOF in microfluidic channels and devices. It is applicable to structures with arbitrary pore space morphology (including their geometry, as well as topology) and an arbitrary distribution of the electrokinetic potential at the solid–liquid interface. This also covers the existence of random pore-size distributions and, as a consequence, the possibility of finding any range of aspect ratios in a particular medium. Coupled hydrodynamic, electrostatic, and mass transport problems were solved. In this work, the hydrodynamic problem has been treated with the lattice-Boltzmann method. Straight capillaries were chosen as model systems due to the possibility of comparing simulated data with the analytical solution and results of other numerical simulations for simple system configurations, in the effort to present a basis for efficient modelling of

electrokinetic phenomena in more complex porous media. Good agreement was obtained for different benchmark cases.

It should be mentioned that, in general, a further increase in the numerical accuracy of the presented approach can be achieved without additional cost of computational time by an implementation of multiscale schemes, e.g. with locally embedded grids in which the lattice spacing is refined (or coarsened) locally. This approach allows to analyse the flow problem with a finer spatial resolution in regions characterized by larger velocity gradients and define more accurately curved interfaces [79–82]. However, EOF regions which require the imposition of finer computational grids cannot always be recognized *a priori* [83], and further work is needed for devising criteria to detect such regions of interest under a given set of conditions.

A low-Reynolds number EOF dynamics on micrometer scale is not only encountered in open-channel structures of microchip devices, but also in the voids of microscopically disordered media like random particulate packings or monoliths [59]. For example, in capillary electrochromatography, as for most microchip applications, EOF is employed for achieving significantly less dispersive transport (compared to pressure-driven flow) of complex mixtures of (bio)molecular species which are separated on the high-surface area materials to become identified afterwards, preferably by on-line detection, e.g. via mass spectrometry. Our numerical approach based on the lattice-Boltzmann flow field under most general conditions can cope with any geometry and surface heterogeneity, and it will be particularly efficient in resolving details of the flow field which govern mass transport and dispersion in a transient, as well as long-time asymptotic regime. For more complex porous media and flow patterns the presented approach can contribute to a derivation of scaling laws for the EOF, involving parameters such as the Reynolds and Peclet numbers, mass diffusivity, morphology of the medium, or electrical double layer thickness. However, this also stimulates further investigation of double layer resolution effects and limits when employing a slip-velocity boundary condition, in particular with respect to the characteristic lengths in a porous medium, e.g. the sphere or intraparticle pore diameter in fixed beds of porous spherical particles, continuously changing channel dimensions and a varying shape, or the spatio-temporal heterogeneity of local surface charge distributions.

ACKNOWLEDGEMENTS

We like to thank Prof. Dr Lutz Tobiska and Dr Walfred Grambow from the ‘Interdisziplinäres Zentrum für Paralleles Rechnen’ (Fakultät für Mathematik, Otto-von-Guericke-Universität Magdeburg, Germany) for their support, and Maxim Dautau (Department of System Analysis, Belarusian State University, Minsk, Belarus) for his help in scientific computing.

REFERENCES

1. Stone HA, Kim S. Microfluidics: basic issues, applications, and challenges. *AIChE Journal* 2001; **47**: 1250–1254.
2. Jensen KF. Microreaction engineering—is small better? *Chemical Engineering Science* 2001; **56**:293–303.
3. Giordano N, Cheng JT. Microfluidic mechanics: progress and opportunities. *Journal of Physics—Condensed Matter* 2001; **13**:R271–R295.
4. Whitesides GM, Stroock AD. Flexible methods for microfluidics. *Physics Today* 2001; **54**:42–49.
5. Chovan T, Guttman A. Microfabricated devices in biotechnology and biochemical processing. *Trends in Biotechnology* 2002; **20**:116–122.

6. Hessel V, Löwe H. Microtechnology: components—plant concepts—user acceptance. *Chemie-Ingenieur-Technik* 2002; **74**:185–207.
7. Reyes DR, Iossifidis D, Auroux PA, Manz A. Micro total analysis systems, 1. Introduction, theory, and technology. *Analytical Chemistry* 2002; **74**:2623–2636.
8. Probstein RF. *Physicochemical Hydrodynamics*. Wiley: New York, 1994; 190–202.
9. Hunter RJ. *Foundations of Colloid Science*. Oxford University Press: Oxford, 2001.
10. Rice CL, Whitehead R. Electrokinetic flow in a narrow cylindrical capillary. *Journal of Physical Chemistry* 1965; **69**:4017–4024.
11. Paul PH, Garguilo MG, Rakestraw DJ. Imaging of pressure- and electrokinetically-driven flows through open capillaries. *Analytical Chemistry* 1998; **70**:2459–2467.
12. Tallarek U, Rapp E, Scheenen T, Bayer E, Van As H. Electroosmotic and pressure-driven flow in open and packed capillaries: velocity distributions and fluid dispersion. *Analytical Chemistry* 2000; **72**:2292–2301.
13. Yang C, Li D, Masliyah JH. Modeling forced liquid convection in rectangular microchannels with electrokinetic effects. *International Journal of Heat and Mass Transfer* 1998; **41**:4229–4249.
14. Patankar NA, Hu HH. Numerical simulation of electroosmotic flow. *Analytical Chemistry* 1998; **70**:1870–1881.
15. Ermakov SV, Jacobson SC, Ramsey JM. Computer simulations of electrokinetic transport in microfabricated channel structures. *Analytical Chemistry* 1998; **70**:4494–4504.
16. Griffiths SK, Nilson RH. Hydrodynamic dispersion of a neutral nonreacting solute in electroosmotic flow. *Analytical Chemistry* 1999; **71**:5522–5529.
17. Bianchi F, Ferrigno R, Girault HH. Finite element simulation of an electroosmotic-driven flow division at a T-junction of microscale dimensions. *Analytical Chemistry* 2000; **72**:1987–1993.
18. Cummings EB, Griffiths SK, Nilson RH, Paul PH. Conditions for similitude between the fluid velocity and electric field in electroosmotic flow. *Analytical Chemistry* 2000; **72**:2526–2532.
19. Arulanandam S, Li D. Liquid transport in rectangular microchannels by electroosmotic pumping. *Colloids and Surfaces A* 2000; **161**:89–102.
20. Santiago JG. Electroosmotic flows in microchannels with finite inertial and pressure forces. *Analytical Chemistry* 2001; **73**:2353–2365.
21. Dutta P, Beskok A. Analytical solution of combined electroosmotic/pressure driven flows in two-dimensional straight channels: finite Debye layer effects. *Analytical Chemistry* 2001; **73**:5097–5102.
22. Yang RJ, Fu LM, Lin YC. Electroosmotic flow in microchannels. *Journal of Colloid and Interface Science* 2001; **239**:98–105.
23. Keh HJ, Tseng HC. Transient electrokinetic flow in fine capillaries. *Journal of Colloid and Interface Science* 2001; **242**:450–459.
24. Dutta P, Beskok A, Warburton TC. Electroosmotic flow control in complex microgeometries. *Journal of Microelectromechanical Systems* 2002; **11**:36–43.
25. Fu LM, Yang RJ, Lee GB. Analysis of geometry effects on band spreading of microchip electrophoresis. *Electrophoresis* 2002; **23**:602–612.
26. Kang YJ, Yang C, Huang XY. Electroosmotic flow in a capillary annulus with high zeta-potentials. *Journal of Colloid and Interface Science* 2002; **253**:285–294.
27. Erickson D, Li D. Influence of surface heterogeneity on electrokinetically driven microfluidic mixing. *Langmuir* 2002; **18**:1883–1892.
28. Conlisk AT, McFerran J, Zheng Z, Hansford D. Mass transfer and flow in electrically charged micro- and nanochannels. *Analytical Chemistry* 2002; **74**:2139–2150.
29. Frisch U, d'Humieres D, Hasslacher B, Lallemand P, Pomeau Y, Rivet JP. Lattice gas hydrodynamics in two and three dimensions. *Complex Systems* 1987; **1**:649–707.
30. McNamara G, Zanetti G. Use of the Boltzmann equation to simulate lattice-gas automata. *Physical Review Letters* 1988; **61**:2332–2335.
31. Higuera FJ, Jiménez J. Boltzmann approach to lattice gas simulations. *Europhysics Letters* 1989; **9**:663–668.
32. Succi S, Benzi R, Higuera F. The lattice-Boltzmann equation—a new tool for computational fluid dynamics. *Physica D* 1991; **47**:219–230.
33. Benzi R, Succi S, Vergassola M. The lattice Boltzmann equation—theory and applications. *Physics Reports* 1992; **222**:145–197.
34. Chen S, Doolen GD. Lattice Boltzmann method for fluid flows. *Annual Review of Fluid Mechanics* 1998; **30**:329–364.
35. Spaid MAA, Phelan FR Jr. Lattice Boltzmann methods for modeling microscale flow in fibrous porous media. *Physics of Fluids* 1997; **9**:2468–2474.
36. Maier RS, Kroll DM, Kutsovsky YE, Davis HT, Bernard RS. Simulation of flow through bead packs using the lattice Boltzmann method. *Physics of Fluids* 1998; **10**:60–74.
37. Manz B, Gladden LF, Warren PB. Flow and dispersion in porous media: lattice-Boltzmann and NMR studies. *AIChE Journal* 1999; **45**:1845–1854.

38. Maier RS, Kroll DM, Davis HT, Bernard RS. Simulation of flow in bidisperse sphere packings. *Journal of Colloid and Interface Science* 1999; **217**:341–347.
39. Bernsdorf J, Brenner G, Durst F. Numerical analysis of the pressure drop in porous media flow with lattice Boltzmann (BGK) automata. *Computer Physics Communications* 2000; **129**:247–255.
40. Clague DS, Kandhai BD, Zhang R, Sloot PMA. Hydraulic permeability of (un)bounded fibrous media using the lattice Boltzmann method. *Physical Review E* 2000; **61**:616–625.
41. Hill RJ, Koch DL, Ladd AJC. Moderate-Reynolds-number flows in ordered and random arrays of spheres. *Journal of Fluid Mechanics* 2001; **448**:243–278.
42. Békri S, Vizika O, Thovert JF, Adler PM. Binary two-phase flow with phase change in porous media. *International Journal of Multiphase Flow* 2001; **27**:477–526.
43. Drazer G, Koplik J. Tracer dispersion in two-dimensional rough fractures. *Physical Review E* 2001; **63**:art. no. 056104.
44. Maier RS, Kroll DM, Bernard RS, Howington SE, Peters JF, Davis HT. Enhanced dispersion in cylindrical packed beds. *Philosophical Transactions of the Royal Society of London A* 2002; **360**:497–506.
45. Yoshino M, Inamuro T. Lattice Boltzmann simulations for flow and heat/mass transfer problems in a three-dimensional porous structure. *International Journal for Numerical Methods in Fluids* 2003; **43**:183–198.
46. Kandhai D, Hlushkou D, Hoekstra AG, Sloot PMA, Van As H, Tallarek U. Influence of stagnant zones on transient and asymptotic dispersion in macroscopically homogeneous porous media. *Physical Review Letters* 2002; **88**:art. no. 234501.
47. Schure MR, Maier RS, Kroll DM, Davis HT. Simulation of packed-bed chromatography utilizing high-resolution flow fields: comparison with models. *Analytical Chemistry* 2002; **74**:6006–6016.
48. Kang QH, Zhang DX, Chen SY. Unified lattice Boltzmann method for flow in multiscale porous media. *Physical Review E* 2002; **66**:art. no. 056307.
49. Zeiser T, Steven M, Freund H, Lammers P, Brenner G, Durst F, Bernsdorf J. Analysis of the flow field and pressure drop in fixed-bed reactors with the help of lattice Boltzmann simulations. *Philosophical Transactions of the Royal Society of London A* 2002; **360**:507–520.
50. Békri S, Howard J, Muller J, Adler PM. Electrical resistivity index in multiphase flow through porous media. *Transport in Porous Media* 2003; **51**:41–65.
51. Bhatnagar P, Gross E, Krook M. A model for collision processes in gases: I. small amplitude processes in charged and neutral one-component systems. *Physical Review* 1954; **94**:511–525.
52. Chen S, Chen H, Martinez D, and Matthaeus WH. Lattice Boltzmann model for simulation of magnetohydrodynamics. *Physical Review Letters* 1991; **67**:3776–3779.
53. Qian YH, d'Humieres D, Lallemand P. Lattice BGK models for the Navier–Stokes equation. *Europhysics Letters* 1992; **17**:479–484.
54. Li B, Kwok DY. Lattice Boltzmann model of microfluidics with high Reynolds numbers in the presence of external forces. *Langmuir* 2003; **19**:3041–3048.
55. Ren L, Qu W, Li D. Interfacial electrokinetic effects on liquid flow in microchannels. *International Journal of Heat and Mass Transfer* 2001; **44**:3125–3134.
56. Nie X, Doolen GD, Chen S. Lattice-Boltzmann simulations of fluid flows in MEMS. *Journal of Statistical Physics* 2002; **107**:279–289.
57. Warren PB. Electroviscous transport problems via lattice-Boltzmann. *International Journal of Modern Physics C* 1997; **8**:889–898.
58. Gross RJ, Osterle JF. Membrane transport characteristics of ultrafine capillaries. *Journal of Chemical Physics* 1968; **49**:228–234.
59. Rathore AS. Theory of electroosmotic flow, retention and separation efficiency in capillary electro-chromatography. *Electrophoresis* 2002; **23**:3827–3846.
60. Tallarek U, Rapp E, Seidel-Morgenstern A, Van As H. Electroosmotic flow phenomena in packed capillaries: from the interstitial velocities to intraparticle and boundary layer mass transfer. *Journal of Physical Chemistry B* 2002; **106**:12709–12721.
61. Ren L, Li D. Electroosmotic flow in heterogeneous microchannels. *Journal of Colloid and Interface Science* 2001; **243**:255–261.
62. Coelho D, Shapiro M, Thovert JF, Adler PM. Electroosmotic phenomena in porous media. *Journal of Colloid and Interface Science* 1996; **181**:169–190.
63. Kandhai D, Koponen A, Hoekstra AG, Kataja M, Timonen J, Sloot PMA. Implementation aspects of 3D lattice-BGK: boundaries, accuracy, and a new fast relaxation method. *Journal of Computational Physics* 1999; **150**:482–501.
64. Guo Z, Zheng C, Shi B. Discrete lattice effects on the forcing term in the lattice Boltzmann method. *Physical Review E* 2002; **65**:art. no. 046308.
65. Hiemenz PC, Rajagopalan R. *Principles of Colloid and Surface Chemistry*. Marcel Dekker: New York, 1997.
66. Delgado AV, Arroyo FJ. Electrokinetic phenomena and their experimental determination: an overview. In *Interfacial Electrokinetics and Electrophoresis*, Delgado AV (ed.). Marcel Dekker: New York, 2002.

67. Anderson JL, Idol WK. Electroosmosis through pores with nonuniformly charged walls. *Chemical Engineering Communications* 1985; **38**:93–106.
68. Potoček B, Gaš B, Kenndler E, Štědrý M. Electroosmosis in capillary zone electrophoresis with nonuniform zeta-potential. *Journal of Chromatography A* 1995; **709**:51–62.
69. Weidenhammer P, Jacobasch HJ. Investigation of adhesion properties of polymer materials by atomic force microscopy and zeta-potential measurements. *Journal of Colloid and Interface Science* 1996; **180**:232–236.
70. Hayes RA. The electrokinetic behaviour of surfaces modified by particle adsorption. *Colloids and Surfaces A* 1999; **146**:89–94.
71. Herr AE, Molho JI, Santiago JG, Mungal MG, Kenny TW, Garguilo MG. Electroosmotic capillary flow with nonuniform zeta potential. *Analytical Chemistry* 2000; **72**:1053–1057.
72. Ghosal S. Lubrication theory for electro-osmotic flow in a microfluidic channel of slowly varying cross-section and wall charge. *Journal of Fluid Mechanics* 2002; **459**:103–128.
73. Pačes M, Kosek J, Marek M, Tallarek U, Seidel-Morgenstern A. Mathematical modelling of adsorption and transport processes in capillary electrochromatography: open–tubular geometry. *Electrophoresis* 2003; **24**:380–389.
74. Long D, Stone HA, Ajdari A. Electroosmotic flows created by surface defects in capillary electrophoresis. *Journal of Colloid and Interface Science* 1999; **212**:338–349.
75. Regnier FE, Wu D. Chemical derivatization of fused silica capillaries. In *Capillary Electrophoresis Technology*, Guzman NA (ed.). Marcel Dekker: New York, 1993; 287–309.
76. Stroock AD, Weck M, Chiu DT, Huck WTS, Kenis PJA, Ismagilov RF, Whitesides GM. Patterning electroosmotic flow with patterned surface charge. *Physical Review Letters* 2000; **84**:3314–3317.
77. Ajdari A. Generation of transverse fluid currents and forces by an electric field: electro-osmosis on charge-modulated and undulated surfaces. *Physical Review E* 1996; **53**:4996–5005.
78. Gleeson JP. Electroosmotic flows with random zeta-potential. *Journal of Colloid and Interface Science* 2002; **249**:217–226.
79. Peng Y, Shu C, Chew YT, Inamuro T. Lattice kinetic scheme for the incompressible viscous thermal flows on arbitrary meshes. *Physical Review E* 2004; **69**:art. no. 016703.
80. Filippova O, Hänel D. Grid refinement for lattice-BGK models. *Journal of Computational Physics* 1998; **147**:219–228.
81. Filippova O, Schwade B, Hänel D. Multiscale lattice Boltzmann schemes for low Mach number flows. *Philosophical Transactions of the Royal Society of London A* 2002; **360**:467–476.
82. Yu D, Mei R, Luo L-S, Shyy W. Viscous flow computations with the method of lattice Boltzmann equation. *Progress in Aerospace Sciences* 2003; **39**:329–367.
83. Hlushkou D. Numerical simulation of flow and mass transport in (electro-) chromatographic systems. *Ph.D. Thesis*, Otto-von-Guericke-Universität Magdeburg, Germany, 2004.

Electrokinetics in Fixed Beds: Experimental Demonstration of Electroosmotic Perfusion**

Ulrich Tallarek,* Erdmann Rapp, Henk Van As, and Ernst Bayer

The concept of an intraparticle forced convection to reduce the resistance to mass transfer of a stagnant mobile phase in liquid chromatography has received considerable attention over the last decade, both from a theoretical and a particle engineering point of view.[1–9] By tuning the permeability of the porous particles to typical drops in column pressure, the actual pressure gradient in a fixed bed may act as a driving force for an intraparticle flow[10] so that an already small, but non-zero flow component assists or even dominates the slow diffusion of large molecules and reduces the hold-up dispersion that arises from stagnant zones. An important aspect in the design of particles has been the hierarchical architecture of the pore network to which several sets of pores may contribute.[1, 7, 9] The term perfusion chromatography differs from diffusion-limited operations in that it specifically refers to any separation process in which the intraparticle velocity is not zero.[2] However, a mobile-phase perfusion with pressure-driven flows may be operative only when relatively high drops in column pressure and particles with large pores (that have a low adsorptive capacity) are used. In any case, the intraparticle fluid velocity remains very small compared to the velocity in the interparticle pore space.

It has also been clearly demonstrated over the last decade that an electroosmotic flow field in packed capillaries can offer significantly superior dispersion characteristics relative to pressure-driven flow.[11–13] The ultimate gain in the performance of an electrokinetically driven mobile phase for capillary electrochromatography (CEC) thus currently attracts tremendous attention, because it is still unclear which factors determine the limits of such an improvement and when the limits actually appear in practice. A study of the transport phenomena must include a careful consideration of the effects of the column walls, the column-to-particle diameter ratio, flow heterogeneity on a macroscopic (column) and a microscopic (pore) level, intraparticle transport characteristics, as well as film mass transfer resistance.

Electroosmotic perfusion phenomena in combination with capillary transport models play an important role in many areas of the physical and life sciences, such as in the dewatering of waste sludge or the removal of contaminants from soil.[14] In CEC, which uses the electrokinetics to drive both the liquid and the (usually charged) solute through fixed particulate beds, an intraparticle convection mechanism for improving mass transfer is largely unexplored. Only a few studies indicate the existence of an intraparticle electroosmotic flow (EOF) and the potential that this effect, together with electrophoretic selectivity, may offer in separation science.[15–21] In simple electrokinetic terms the Helmholtz–Smoluchowski equation implies that the average EOF velocity in a pore segment of the particles is relatively independent of the pore geometry if the characteristic dimension, like the pore radius (r_{pore}), is much larger than the thickness of the electrical double layer (κ^{-1}), namely, $\kappa r_{pore} \gg 1$.[22–25] We then expect a rather flat flow profile over the cross-section of any pore and it also suggests that film mass transfer resistance is negligible in CEC over a wide range of conditions.[26] A particular feature is that average pore velocities can still be significant compared to the typical purely diffusive timescales even when $\kappa r_{pore} \rightarrow 1$ and r_{pore} is only a few nanometers.[22, 23] For thin electrical double layers, these considerations leave the intraparticle tortuosity factor (τ_{intra}) as one of the most critical parameters that determine the extent of electroosmotic perfusive solute transport. τ_{intra} also reflects the pore connectivity and consequently that fraction of the pore space which transects the particles without dead-end branching and should allow a net EOF to develop.[21]

Herein we provide clear evidence for the existence and enormous impact of an electroosmotic perfusion mechanism in porous media. We studied the performance of pressure-driven flows and EOF through a fixed bed consisting of charged porous particles packed into a capillary by using a pulsed field gradient NMR method as a noninvasive motion-encoding technique that operates (on the millisecond timescale) directly on the nuclear spin of the fluid molecules (for example, ^1H_2O).[27] Detailed descriptions of this approach concerning its implementation on the capillary dimension and the application to dispersion, flow, and mass-transfer studies in chromatographic media have recently been published.[28, 29] We start with an analysis of the axial dispersion as a function of the particle Péclet number (Pe) for both modes of fluid flow, then complement these data by the selectively measured dynamics of the intraparticle mass transfer, and also address the influence of thermal effects. Our results are finally discussed in regard to the hierarchical design of these particles and thereby achieved correlation of pore interconnectivity in a bidisperse pore network.

The effective axial dispersion coefficient (D_{ax}) is obtained from the complex NMR signal $E_{\Delta}(\boldsymbol{q})$ at an observation time (Δ) that is sufficient to allow the complete exchange of fluid molecules between intraparticle and interparticle pore spaces (steady-state) and the development of a Gaussian displacement distribution [Eq. (1)].[27]

$$E_{\Delta}(\boldsymbol{q}) = \exp(i2\pi \boldsymbol{q} \cdot \boldsymbol{u}_{av}\Delta - 4\pi^2 \boldsymbol{q}^2 D_{ax}\Delta) \quad (1)$$

$\boldsymbol{u}_{av}$ is the column cross-sectional averaged velocity and $\boldsymbol{q}$ is a wave vector that encodes fluid motion ($i^2 = -1$). Based on these dispersion coefficients, which include the intraparticle

[*] Dr. U. Tallarek, Dr. H. Van As
Laboratory of Molecular Physics and Wageningen NMR Centre
Department of Biomolecular Sciences, Wageningen University
Dreijenlaan 3, 6703 HA Wageningen (The Netherlands)
Fax: (+31) 317-48-2725
E-mail: ulrich.tallarek@water.mf.wau.nl
Dipl.-Chem. E. Rapp, Prof. Dr. E. Bayer
Forschungsstelle für Nukleinsäure- und Peptidchemie
Institut für Organische Chemie der Universität Tübingen
Auf der Morgenstelle 18, 72076 Tübingen (Germany)

[**] We acknowledge support of this work by a Marie Curie Fellowship (for U.T.) under the Training and Mobility of Researchers Program of the EU (ERBFMBI-CT98-3437) and the European Community activity Wageningen NMR Centre (ERBCHGE-CT95-0066).

  1433-7851/01/4009-1684 $ 17.50+.50/0

mass transfer kinetics, Figure 1 shows a comparison of the electroosmotic and pressure-driven flows at increasing Pe (this is better known in chromatography as the reduced velocity). The EOF shows an overwhelming enhanced performance over pressure-driven flow, and the regime in which molecular diffusion still controls the dispersion ($D_{ax}/D_m < 1$) extends to much higher Pe. This has already been shown by other research groups.[16, 17, 19] However, it is difficult to relate this improvement quantitatively to any physical mechanism because these data (as in conventional chromatography) are acquired over only a limited range of Pe. This range is hardly sufficient to separate (for example, by a power-law analysis $D_{ax} \propto Pe^{\alpha}$) adequately between dispersion processes originating in the flowing and in the stagnant zones of the packed bed.[30, 31] In pressure-driven flows stochastic velocity fluctuations in the interparticle pore space cause mechanical dispersion which grows linearly with Pe, while regions of zero velocity inside the bed particles and close to their external surface give rise to nonmechanical contributions that grow as Pe^2 and $Pe\ln(Pe)$, respectively.[32] In all cases (flow heterogeneity, film mass transfer, and intraparticle diffusion), an electrokinetically driven mobile phase may show a superior performance and D_{ax} only reflects the combined kinetics.

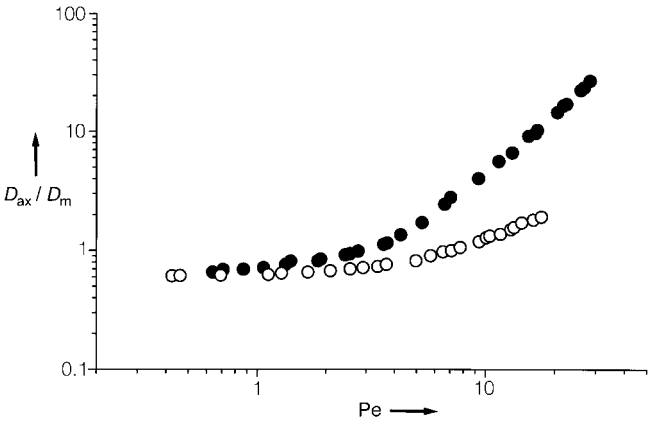

Figure 1. Axial dispersion (D_{ax}/D_m) versus the particle Péclet number ($Pe = \boldsymbol{u}_{av} d_p/D_m$) for a 1 mM sodium tetraborate buffer solution at pH 9.13 in a pressure-driven flow ( ) and EOF (○). The ^{1}H NMR measurements were performed with a special capillary-NMR set up on a 0.5 T electromagnet with open access,[28, 29] and the charged porous particles were packed in a 250 μm i.d. fused-silica capillary. The diffusion coefficient of water is $D_m(25\,^{\circ}C) = 2.25 \times 10^{-5}\ cm^2 s^{-1}$.

To obtain more direct evidence of the operation of an intraparticle EOF we made a series of NMR measurements within a temporal domain where the exchange of fluid molecules between intraparticle and interparticle pore space environments is not complete over time Δ (unsteady-state). Then, $E_{\Delta}(\boldsymbol{q})$ contains discrete contributions from both fluid fractions (stagnant and flowing). By extracting the average number of molecules $A_{intra}(\Delta)$ that are still remaining in the spherical particles at times Δ, this procedure allows a selective study of the intraparticle mass transfer kinetics [Eq. (2)].[28, 33]

$$\frac{A_{intra}(\Delta)}{A_{intra}(0)} = A_{norm}(\Delta) = \frac{6}{\pi^2}\sum_{n=1}^{\infty}\frac{1}{n^2}\exp(-4n^2 B_{intra}\Delta) \qquad (2)$$

In the case of purely diffusive mass-transfer kinetics the rate constant B_{intra} can be further analyzed to calculate the intraparticle diffusion coefficient ($B_{intra} = \pi^2 D_{intra}/d_p^2$) by using the independently measured average particle diameter (d_p). Figure 2 compares the exchange kinetics for a constant pressure gradient along the column with those acquired with an additional potential gradient. While the pressure field around the porous particles alone has hardly any measurable influence on diffusion-limited transport ($D_{intra} = 1.42 \times 10^{-5}\ cm^2 s^{-1}$), the electric field enhances significantly the exchange of fluid molecules, and hence increases the intraparticle mass transfer coefficient B_{intra}.

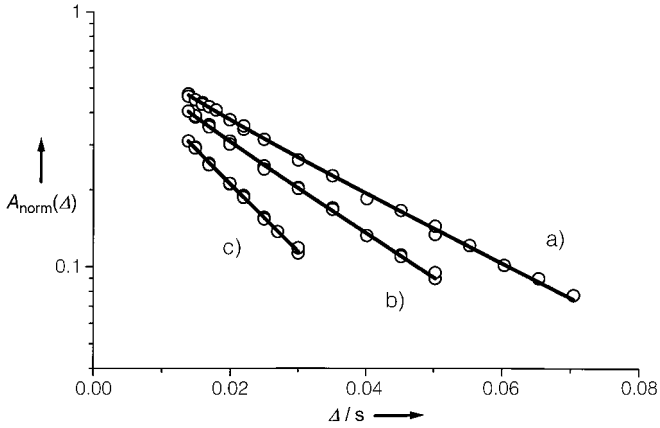

Figure 2. Influence of pressure and potential gradients on stagnant mobile phase mass transfer. The solid lines are best fits of the data to Equation (2) using the pure (a) and effective (b, c) diffusion model. a) Pressure gradient only ($D_{intra} = 1.42 \times 10^{-5}\ cm^2 s^{-1}$). b, c) Effect of a superimposed potential gradient ($E = 47.4\ kV m^{-1}$): b) $D_{ap} = 1.84 \times 10^{-5}\ cm^2 s^{-1}$ (1 mM sodium tetraborate), and c) $D_{ap} = 2.72 \times 10^{-5}\ cm^2 s^{-1}$ (3 mM sodium tetraborate) at pH 9.13.

This behavior is most probably caused by an electroosmotic perfusion mechanism (and by the existence of an intraparticle electroosmotic flow velocity), but can also be influenced by thermal effects (through the molecular diffusion coefficient D_m at the actual buffer temperature). In the case of perfusion, the apparent diffusivity D_{ap}, which is calculated with the simple diffusion model of Equation (2), in fact resembles a combination of an intraparticle EOF and molecular diffusion ($D_{ap} > D_{intra}$). This convection-augmented diffusivity[3–5] is a key parameter in characterizing the improved performance arising from mobile-phase perfusion and is based on the linear driving force approximation.[34–36] Figure 2 shows that D_{ap} even exceeds the molecular diffusivity (D_m) of the fluid at higher buffer concentration, and thus leaves the tortuosity-limited regime.

To account for the influence of thermal effects on intraparticle mass transfer we conducted a series of measurements at constant temperature within the capillary while increasing the applied potential gradient (still being the ultimate driving force for any intraparticle EOF). This effect is achieved by a variation of the buffer concentration and adjusting the potential gradient so that the product of electric field strength (E) and electric current (I) remains constant. The variation of

the buffer concentration at unchanging *EI* (and consequently at the same thermal level) results in an automatic modification of *E*. The results shown in Figure 3 demonstrate

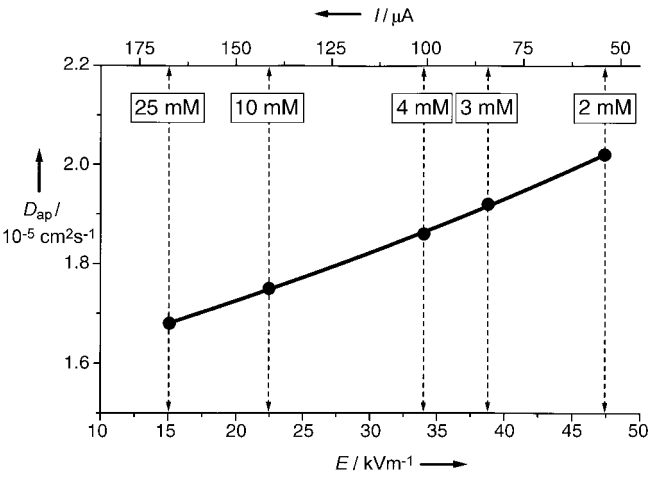

Figure 3. Dependence of the stagnant mobile phase mass transfer kinetics on the electric field strength at a constant level of heat dissipation in the capillary ($EI = 2.54\ \mathrm{W\,m^{-1}}$). While *E* increases, the buffer concentration (and the electrical current *I*) decreases from 25 to 2 mM sodium tetraborate (and *I* from 169 to 54 μA).

a clear dependence of the apparent diffusivity on the electric field strength. This systematic, almost linear, increase in D_{ap} from 1.67 to $2.02 \times 10^{-5}\ \mathrm{cm^2 s^{-1}}$ can only be explained on the basis of a convective transport mechanism. By contrast, a constant diffusivity (independent of *E*) is expected when the intraparticle mass transfer is purely diffusive, that is, only achieved by molecular diffusion at the actual (but constant) buffer temperature. The electroosmotic perfusion will be of considerable importance in the separation of slowly diffusing solutes ($D_m \ll 10^{-5}\ \mathrm{cm^2 s^{-1}}$) and promises intraparticle Péclet numbers well above unity.[21]

To correlate our results with concrete particle characteristics, we now focus on the topology of the intraparticle pore network. These hierarchically structured particles are engineered by clustering inter-adhering microspheres in several steps. The resulting particles consist of two relatively discrete sets of pores, namely, large gigapores[5] (400–600 nm, with $d_{pore}/d_p > 10^{-2}$) and macropores (50–100 nm).[37] More importantly, this hierarchical design produces an excellent correlation of the interconnectivity between these two sets of pores and minimizes dead-end branching. The gigapores transect the particle as a whole and form the primary basis for intraparticle EOF (Figure 4). The macropores are also large enough to allow an EOF by adjustment of the buffer concentration—within a convenient range—to the actual pore dimensions so that $\kappa r_p \gg 1$. Perfusive solute transport, which in addition utilizes the set of smaller pores, is impossible with pressure-driven flows! As the liquid phase is continuous and incompressible, the volume flow and the radial distribution of velocities in an interconnected pore depend on fluid body forces which originate in all neighboring pores, actually in the medium as a whole. Thus, although the microscopic

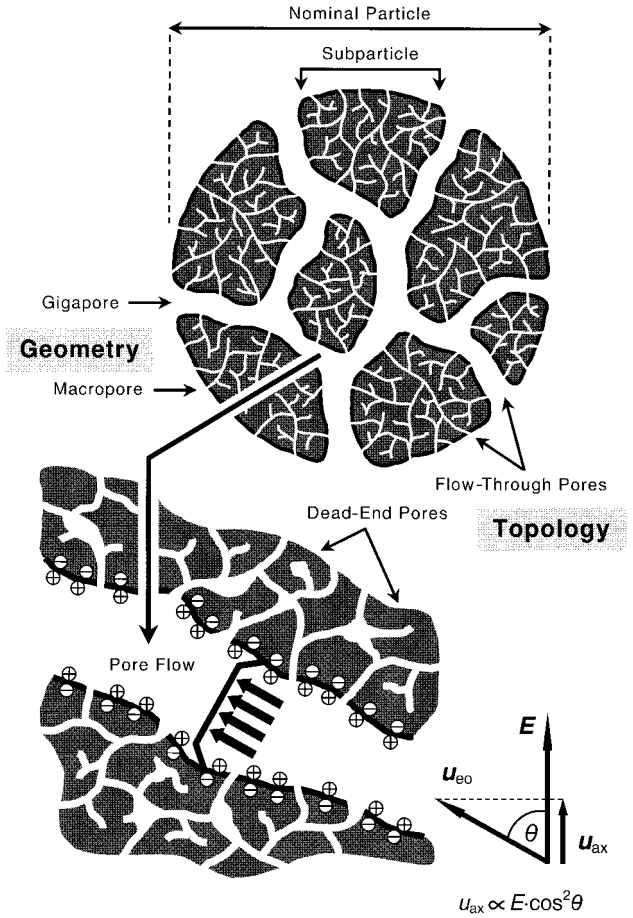

Figure 4. Pore network of a hierarchically structured particle with a bidisperse distribution of pore sizes. In general, the axis of a virtually isolated pore is at an angle θ to the electric field vector $\boldsymbol{E}$. When $\kappa r_p \gg 1$, the presence of a pluglike EOF with a linear pore velocity (u_{eo}) proportional to $E\cos\theta$ is suggested. An unfavorable orientation of pores ($0 < \theta < 90°$) reduces or even prevents ($\theta = 90°$) pore-level EOF in this decoupled single-channel view. In an unconsolidated porous medium, in contrast, all these pores are usually interconnected.

flow profiles then become convex or concave and deviate from a perfect plug-flow behavior, it also means that (viscous) flow through perpendicular pores ($\theta = 90°$) can be achieved. By contrast, no net flow exists in a dead-end pore.

Thus, a more important aspect concerning the intraparticle pore network appears to be the pore interconnectivity rather than the average diameter of the pores. Even for small pores, the buffer concentration—at least within the practical range that can be obtained, but which is still a wide range—can be matched with the pore dimensions, so that $\kappa r_p \gg 1$ (and at least $\kappa r_p > 1$) is guaranteed.

In this context, the tortuosity factor τ_{intra} relates the steady-state intraparticle diffusion coefficient to the bulk molecular diffusivity ($\tau_{intra} = D_m/D_{intra}$). By using the value for D_{intra} obtained from the diffusion-limited mass-transfer kinetics (Figure 2) we calculate a $\tau_{intra} = 1.58$, which is close to values previously measured for very similar supports.[28] This value suggests a high correlation of pore interconnectivity and the small amount of dead-end pores (see Figure 4) in hierarchically structured media, which is in good agreement with results of numerical studies (although there is no unique

  1433-7851/01/4009-1686 $ 17.50+.50/0

relation between interconnectivity in a network model and the experimental tortuosity factor).[9, 21, 38, 39]

Our data demonstrate that a significant enhancement in the performance of CEC over capillary HPLC lies in the different dimension of the perfusion mechanism. The intraparticle tortuosity factor τ_{intra} plays a key role in achieving that goal in both cases, and may also have a sensitive influence on pore migration for charged solutes. Further development in CEC particle technology should focus on the minimum pore size of the through-pore network which still allows a significant intraparticle EOF at decent buffer concentrations, while keeping the surface-to-volume ratio of the pore space attractive for the separation (gigapores, which are used in pressure-driven flows, are not required for electroosmotic perfusion). CEC is easily realized with nanoparticles using hierarchically structured media of micrometer dimension, which leaves molecular diffusion as the ultimate limitation to performance.[40, 41] Thus, the perfusive EOF field translates to an even higher separation efficiency than can currently be achieved in CEC, increased mass sensitivity in on-line coupling schemes (such as nano-ESI-MS), and the possibility of using pressurized CEC for higher analysis speed and flow stability, without significant increase in dispersion.

Received: October 30, 2000 [Z16012]

[1] N. B. Afeyan, N. F. Gordon, I. Mazsaroff, L. Varady, S. P. Fulton, Y. B. Yang, F. E. Regnier, *J. Chromatogr.* **1990**, *519*, 1 – 29.
[2] A. I. Liapis, M. A. McCoy, *J. Chromatogr.* **1992**, *599*, 87 – 104.
[3] A. E. Rodrigues, J. C. Lopes, Z. P. Lu, J. M. Loureiro, M. M. Dias, *J. Chromatogr.* **1992**, *590*, 93 – 100.
[4] G. Carta, M. E. Gregory, D. J. Kirwan, H. A. Massaldi, *Sep. Technol.* **1992**, *2*, 62 – 72.
[5] D. D. Frey, E. Schweinheim, Cs. Horváth, *Biotechnol. Prog.* **1993**, *9*, 273 – 284.
[6] R. H. Davis, H. A. Stone, *Chem. Eng. Sci.* **1993**, *48*, 3993 – 4005.
[7] D. H. Reeder, A. M. Clausen, M. J. Annen, P. W. Carr, M. C. Flickinger, A. V. McCormick, *J. Colloid Interface Sci.* **1996**, *184*, 328 – 330.
[8] P.-E. Gustavsson, P.-O. Larsson, *J. Chromatogr. A* **1996**, *734*, 231 – 240.
[9] J. J. Meyers, A. I. Liapis, *J. Chromatogr. A* **1998**, *827*, 197 – 213.
[10] J. F. Pfeiffer, J. C. Chen, J. T. Hsu, *Am. Inst. Chem. Eng. J.* **1996**, *42*, 932 – 939.
[11] M. M. Dittmann, K. Wienand, F. Bek, G. P. Rozing, *LC-GC* **1995**, *13*, 800 – 814.
[12] A. L. Crego, A. González, M. L. Marina, *Crit. Rev. Anal. Chem.* **1996**, *26*, 261 – 304.
[13] L. A. Colón, K. J. Reynolds, R. Alicea-Maldonado, A. M. Fermier, *Electrophoresis* **1997**, *18*, 2162 – 2174.
[14] R. F. Probstein, *Physicochemical Hydrodynamics: An Introduction*, Wiley, New York, **1994**.
[15] E. Venema, J. C. Kraak, H. Poppe, R. Tijssen, *J. Chromatogr. A* **1999**, *837*, 3 – 15.
[16] R. Stol, W. Th. Kok, H. Poppe, *J. Chromatogr. A* **1999**, *853*, 45 – 54.
[17] E. Wen, R. Asiaie, Cs. Horváth, *J. Chromatogr. A* **1999**, *855*, 349 – 366.
[18] A. I. Liapis, B. A. Grimes, *J. Chromatogr. A* **2000**, *877*, 181 – 215.
[19] P. T. Vallano, V. T. Remcho, *Anal. Chem.* **2000**, *72*, 4255 – 4265.
[20] R. Stol, H. Poppe, W. Th. Kok, *J. Chromatogr. A* **2000**, *887*, 199 – 208.
[21] B. A. Grimes, J. J. Meyers, A. I. Liapis, *J. Chromatogr. A* **2000**, *890*, 61 – 72.
[22] C. L. Rice, R. Whitehead, *J. Phys. Chem.* **1965**, *69*, 4017 – 4024.
[23] R. J. Gross, J. F. Osterle, *J. Chem. Phys.* **1968**, *49*, 228 – 234.
[24] Q.-H. Wan, *Anal. Chem.* **1997**, *69*, 361 – 363.
[25] S. Arulanandam, D. Li, *Colloids Surf. A* **2000**, *161*, 89 – 102.
[26] A. I. Liapis, B. A. Grimes, *J. Colloid Interface Sci.* **2000**, *229*, 540 – 543.
[27] P. T. Callaghan, J. Stepišnik, *Adv. Magn. Opt. Reson.* **1996**, *19*, 325 – 388.
[28] U. Tallarek, F. J. Vergeldt, H. Van As, *J. Phys. Chem. B* **1999**, *103*, 7654 – 7664.
[29] U. Tallarek, E. Rapp, T. Scheenen, E. Bayer, H. Van As, *Anal. Chem.* **2000**, *72*, 2292 – 2301.
[30] M. Sahimi, *Applications of Percolation Theory*, Taylor & Francis, London, **1994**.
[31] J. H. Knox, *J. Chromatogr. A* **1999**, *831*, 3 – 15.
[32] D. L. Koch, J. F. Brady, *J. Fluid Mech.* **1985**, *154*, 399 – 427.
[33] J. Crank, *The Mathematics of Diffusion*, Clarendon, Oxford, **1956**.
[34] A. E. Rodrigues, B. J. Ahn, A. Zoulalian, *Am. Inst. Chem. Eng. J.* **1982**, *28*, 541 – 546.
[35] A. Leitão, A. Rodrigues, *Chem. Eng. J.* **1995**, *60*, 81 – 87.
[36] G. Carta, *Chem. Eng. Sci.* **1995**, *50*, 887 – 889.
[37] D. Whitney, M. McCoy, N. Gordon, N. Afeyan, *J. Chromatogr. A* **1998**, *807*, 165 – 184.
[38] J. H. Petropoulos, J. K. Petrou, A. I. Liapis, *Ind. Eng. Chem. Res.* **1991**, *30*, 1281 – 1289.
[39] M. P. Hollewand, L. F. Gladden, *Chem. Eng. Sci.* **1992**, *47*, 2757 – 2762.
[40] J. H. Knox, *Chromatographia* **1988**, *26*, 329 – 337.
[41] K. K. Unger, S. Lüdtke, M. Grün, *LC-GC Int.* **1999**, *12*, 870 – 874.

First, Atropo-Enantioselective Total Synthesis of the Axially Chiral Phenylanthraquinone Natural Products Knipholone and 6′-*O*-Methylknipholone**

Gerhard Bringmann* and Dirk Menche

Dedicated to Professor Wolfgang Kiefer on the occasion of his 60th birthday

Among the more than one hundred anthraquinone natural products with biaryl axes,[1] phenylanthraquinones,[2–4] like knipholone (**1a**)[2] and 6′-*O*-methylknipholone (**1b**),[3] occupy a special position: Since they are constitutionally unsymmetric, they are most likely formed biosynthetically by a directed, enzymatic biaryl coupling and not merely by a "chemical" dimerization of the corresponding monoanthraquinones. A further hint at such an enzymatic origin of **1a** and **1b** is the fact that they are optically active and are thus axially chiral. First isolated by Dagne and Steglich in 1984,[2] knipholone (**1a**) and related phenylanthrachinones have been found in numerous African plant species of the genera *Bulbine*, *Bulbinella*, and *Kniphofia* (all Asphodelaceae),[4] which are widely used in folk medicine.[2, 5]

[*] Prof. Dr. G. Bringmann, Dipl.-Chem. D. Menche
Institut für Organische Chemie
Universität Würzburg
Am Hubland, 97074 Würzburg (Germany)
Fax: (+49) 931-888-4755
E-mail: bringman@chemie.uni-wuerzburg.de

[**] Novel Concepts in Directed Biaryl Synthesis, Part 93. This work was supported by the Deutsche Forschungsgemeinschaft (grant: SFB 347) and by the Fonds der Chemischen Industrie. We thank Prof. B. M. Abegaz und Dr. M. Bezabih for an authentic sample of 6′-*O*-methylknipholone and for valuable discussions. We thank J. Kraus for helpful suggestions and V. Barthel for technical support. Part 92: G. Bringmann, J. Hinrichs, K. Peters, E.-M. Peters, *J. Org. Chem.* **2001**, *66*, 629 – 632.

Electroosmotic Flow Phenomena in Packed Capillaries: From the Interstitial Velocities to Intraparticle and Boundary Layer Mass Transfer

U. Tallarek,*,†,‡ E. Rapp,‡ A. Seidel-Morgenstern,‡ and H. Van As†

Laboratory of Biophysics and Wageningen NMR Centre, Wageningen University, Dreijenlaan 3, 6703 HA Wageningen, The Netherlands, and Institut für Verfahrenstechnik, Otto-von-Guericke Universität Magdeburg, Universitätsplatz 2, 39106 Magdeburg, Germany

Received: March 1, 2002

Pulsed field gradient nuclear magnetic resonance studies of electrokinetic flow through a 250 μm i.d. cylindrical fused-silica capillary packed with spherical porous particles ($d_p = 41$ μm) have revealed the following phenomena and parameters: (i) An electrokinetic wall effect exists due to a mismatch of zeta-potentials associated with the capillary inner wall and the particles surface. It results in a transcolumn velocity profile which depends on the column-to-particle diameter ratio and causes additional longitudinal dispersion. (ii) Compared to the pressure-driven flow through the porous medium, the intraparticle mass transfer rate constant is significantly increased under the influence of a potential gradient. This increase also depends on the buffer concentration via electric double layer overlap. (iii) Fluid molecules in the porous particles remain diffusion-limited in the presence of a pressure gradient. By contrast, intraparticle Peclet numbers above unity have been measured for electroosmotic flow and were found to increase with the applied potential difference. (iv) Interparticle resistance to mass transfer appears to vanish on the pore scale when electric double layers are small compared to the relevant pore dimension.

Introduction

Hydrodynamic dispersion in porous media arises from the nonuniformity of the flow pattern and depends on the morphology (geometry and topology) of the pore space including stagnant and low-permeability zones, the actual flow conditions (Reynolds and Peclet numbers), interactions with the surface (adsorption and/or reaction), and the type of liquid flow. In this last respect it has been recognized that a strong, stable electroosmotic flow (EOF) can offer many advantages over pressure driven flow in bulk transport of liquid through fixed beds of fine particles and other granular or fibrous media.[1,2] The dynamics of EOF through a single straight cylindrical capillary includes the following features:

(a) For thin electric double layers, i.e., Debye lengths λ_D much smaller than the capillary radius r_c, the fluid moves as in plug flow, i.e., the velocity apparently slips at the wall.[3,4] Thus, the correlation length of velocity extremes in the flow field can be very small. Axial dispersion and boundary layer mass transfer may become negligible compared to Poiseuille flow, which has been shown theoretically[5,6] and experimentally.[7,8]

(b) The ratio of electroosmotic to hydraulic flow rates at a fixed potential and pressure gradient is proportional to r_c^{-2} which has an important implication for electroosmotic perfusive flow through porous media: Mass transfer usually covers a hierarchy of lengthscales and the EOF becomes increasingly effective in liquid transport through finer channels as their size is reduced (if $\lambda_D \ll r_c$ still holds). Thus, the spatiotemporal dimension of diffusion-limited mass transfer can be drastically reduced.

Basic applications of these EOF characteristics are mainly found in fluid and solute transport through porous media of low hydraulic conductivity, in cases where still a high volumetric throughput (not only by preferential channelling through the largest pores) and/or little flow field dispersion is mandatory. Those media often have a high electroosmotic conductivity and the EOF is insensitive to pore size and its distribution over a wide range of conditions.

Potential areas include miniaturized separation techniques such as capillary electrochromatography (CEC)[9−13] or environmental processes that use the electrokinetics for in situ remediation of fine-grained soils.[14−17] In CEC, 75−150 μm i.d. fused-silica capillaries are packed with 3−5 μm spherical, porous adsorbent particles and electric fields up to 10^5 V/m are applied to drive the liquid and solute (most often charged molecules) through the bed. This journey consists of a complex interplay between electrokinetic driving forces (electroosmosis and electrophoresis) and specific interactions with the surface (adsorption and/or reaction). The mobile phase usually is a 0.5−10 mM buffer solution which gives λ_D on the order of 1−10 nm.[18]

Although capillaries[19,20] and unit cell models[21−23] have been successful in describing the behavior of homogeneous, diluted and spatially periodic systems, modelling the electrokinetics in concentrated, disordered, and fractured media appears to be more complex.[24−26] Further, in a fixed bed of spherical porous particles, for example, which represents a porous medium with rather discrete bidisperse pore structure due to the high correlation of interconnectivity between the inter- and comparatively small intraparticle pores, fluid transport can involve conditions under which λ_D is of the same order as the intraparticle pore size, but still much smaller than interparticle channels. Theories and experimental approaches thus need to resolve the subdomain and even pore-level EOF in hierarchically

* To whom correspondence should be addressed. Address: Otto-von-Guericke Universität Magdeburg. Phone: +49 (0)391-67-18644. Fax: +49 (0)391-67-12028. E-mail: ulrich.tallarek@vst.uni-magdeburg.de.

† Laboratory of Biophysics and Wageningen NMR Centre.

‡ Institut für Verfahrenstechnik.

10.1021/jp020605c CCC: $22.00
Published on Web 11/15/2002

structured media to address the microscopic and mesoscopic details of the velocity field underlying flow and dispersion on a macroscopic scale.

Our studies were motivated by the fact that little is known about pore-level (microscopic) flow profiles, the column cross-sectional (macroscopic) velocity heterogeneity, as well as intraparticle and boundary layer mass transfer in EOF through randomly packed beds with a far more complex fluid dynamics than in a single and straight cylindrical channel. For example, in a pore network individual segments differ with respect to their orientation θ toward the electric field vector **E**, even if they are otherwise identical. This causes driving-force discontinuities from pore to pore ($\mathbf{E}_{pore} = \mathbf{E} \cdot \cos\theta$), and because the liquid phase is continuous and incompressible, it influences the actual flow profile and average velocity on a pore level. Thus, the local fluid momentum is balanced by an increase or decrease in pore pressure which may also develop as a consequence of a nonuniform local electric field intensity and surface defects, or if there exists a variation in hydraulic resistance within the medium.[27−29] On a macroscopic level a flow nonuniformity can be due to the fact that the ζ-potential associated with the capillary inner wall (ζ_w) is, in general, different from that of the particles surface (ζ_p) and so should be their EOF.[30,31] This electrokinetic wall effect further depends on the column-to-particle diameter ratio.

One particular question is related to the actual magnitude of intraparticle EOF velocities in CEC with respect to their interparticle average. Both experimental[32−39] and theoretical[31,40,41] studies have recently demonstrated that a substantial gain in performance over pressure driven flow lies in the electroosmotic perfusion mechanism, i.e., in the generation of a significant EOF through the finer intraparticle pore network which, on the other hand, has a much lower hydraulic conductivity compared to the coarser interparticle pore network. Intraparticle EOF velocities have already been calculated by the use of network modeling, but could not be deduced from experimental studies so far, although the existence of a perfusive transport was clearly shown. This phenomenon has also consequences for the electrokinetics of colloidal suspensions consisting of aggregates which themselves contain a large number of discrete particles. In contrast to the assumptions in hard sphere models, these aggregates are actually permeable and conducting.[42]

The purpose of this paper is to reveal experimentally these characteristics of the EOF in a fixed bed of permeable particles. We have used pulsed field gradient nuclear magnetic resonance (PFG-NMR)[43] to study over discrete temporal and spatial domains the dynamics of single-phase EOF through a packed capillary. Our goal was the measurement of inter- and intraparticle velocities of the perfusive flow field, as well as intraparticle and boundary layer mass transfer.

Materials and Methods

A 250 μm i.d. (365 μm o.d.) cylindrical fused-silica capillary (Polymicro Technologies, Phoenix, AZ) was packed with spherical shaped porous, hydrophilic particles (POROS 50-OH2 from PerSeptive Biosystems, Framingham, MA). The nearly Gaussian size distribution has been measured on a Coulter LS 130 (Beckman Coulter, Fullerton, CA) and is shown in Figure 1. The polystyrene−divinylbenzene matrix is coated with a graft copolymer, itself based on a copolymerization of epichlorohydrin and glycidol, to render the surface hydrophilic.[44,45] The intraparticle pore network consists of a set of gigapores (400−600 nm, $d_{pore}/d_p > 10^{-2}$) which transect the particle with

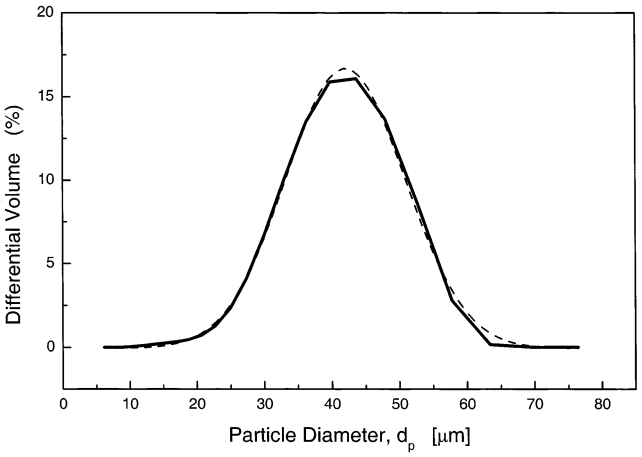

Figure 1. Size distribution of the spherical particles. Experimental data (solid line) represent an average of three independent measurements. Dashed line: Best Gaussian fit. The mean diameter is 41 μm.

relatively little branching,[46] and smaller (50−100 nm) interconnecting macropores to enhance the surface area of the support for its use in chromatography.[47] Particles were packed as aqueous slurry for ca. 30 min at 100 bar in an ultrasonic bath. This procedure gave a dense packing without crushed particles (as validated by microscopic inspection). The whole capillary setup consisting of a packed and a connecting open segment was fritless, i.e., we used fused-silica capillaries with a conus in which the particles were held by a keystone effect during packing, without blocking the orifice.[48] Afterward, the tapered end of a 150 μm i.d. open segment was fitted to the column outlet. This configuration (Figure 2) was absolutely stable over the 450 h of operation.

As the mobile phase in pressure driven flow and EOF we used thoroughly degassed sodium tetraborate buffer solutions of varying concentration without adding further electrolyte (pH 9.13, 25 °C). The Debye length is calculated according to

$$\lambda_D = \left(\frac{\epsilon_0 \epsilon_r RT}{F^2 \sum_i z_i^2 c_{i,\infty}} \right)^{1/2} \quad (1)$$

where ϵ_0 and ϵ_r denote the permittivity of vacuum and the relative permittivity of the electrolyte solution, respectively. R is the gas constant, T the absolute temperature, and F Faraday's constant; z_i is the valency of ionic species i and $c_{i,\infty}$ its concentration in electroneutral solution. At low concentrations sodium tetraborate is completely dissociated into equal amounts of boric acid and monoborate ion,[49] with an acid/base equilibrium between the two species.[50]

$$Na_2B_4O_7 + 7H_2O \rightarrow 2B(OH)_3 + 2B(OH)_4^- + 2Na^+$$

with

$$B(OH)_3 + H_2O \leftrightarrow B(OH)_4^- + H^+, \quad pK_a = 9.13$$

PFG-NMR measurements were performed on a spectrometer consisting of a 0.7 T (^{1}H 30.7 MHz) electromagnet (Bruker, Karlsruhe, Germany) and an actively shielded magnetic field gradient system from Doty Scientific (Oak Harbor, SC), interfaced with a S. M. I. S. console. The packed capillary was fixed in a home-built radio frequency (r.f.) insert based on the solenoid.[8] In contrast to a superconducting magnet where the access down its symmetry axis requires saddle or birdcage r.f.

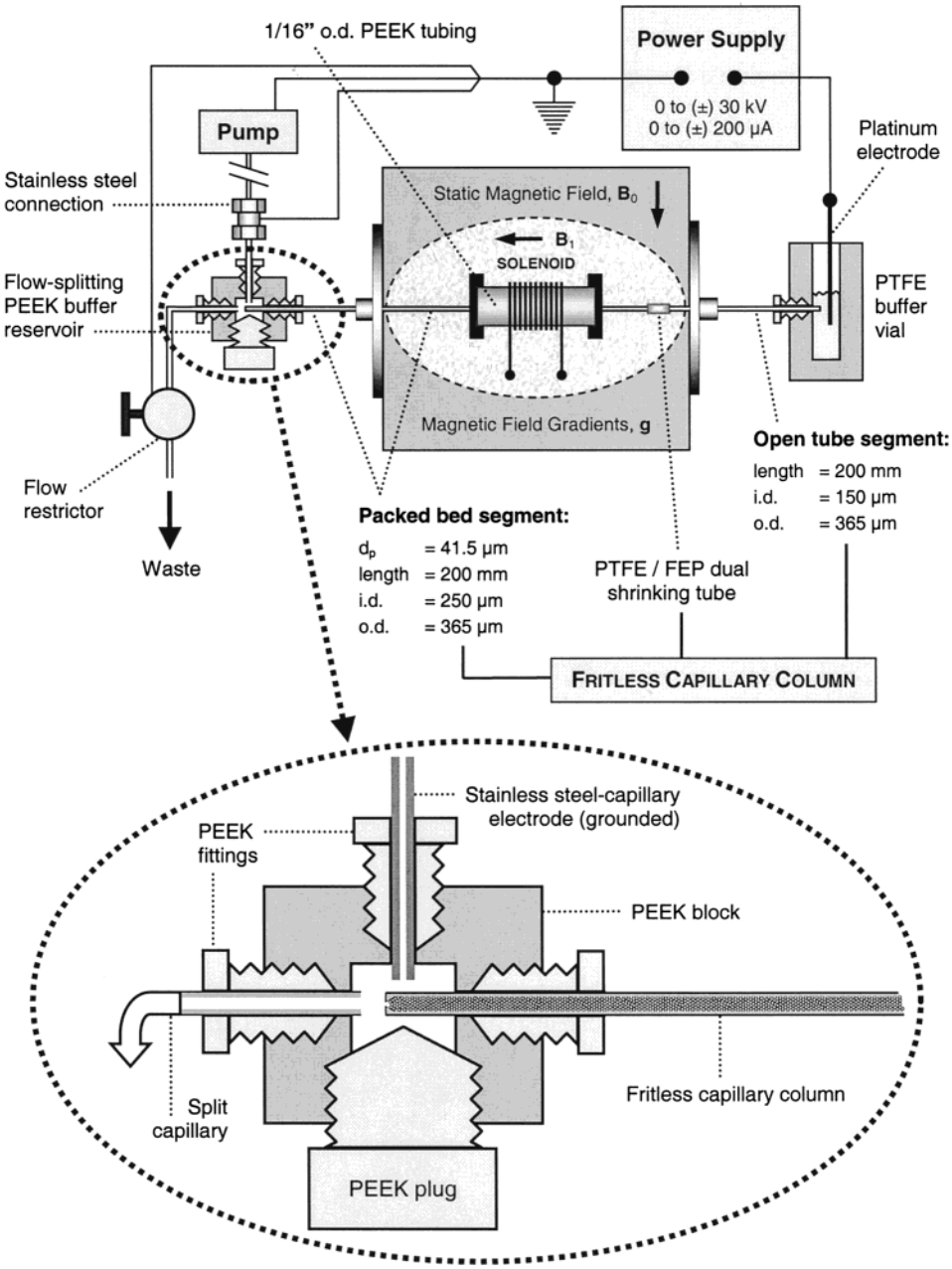

Figure 2. Experimental setup implemented for NMR measurements of fluid motion in electroosmotic and pressure driven flow through packed capillaries. The radio frequency ($\mathbf{B}_1$) field is provided by a ca. 11 mm long solenoid which is directly wound on a 35 mm long, 1.57 mm o.d. (381 μm i.d.) PEEK tubing sleeve, itself accomodating the 360 μm o.d. capillary. In pure electrokinetic flow, the split capillary is removed and the pump (at low volumetric flow rate) continuously refreshes buffer solution in the PEEK block, without inducing a measurable pressure gradient over the packed bed segment.

coil geometries[43] the electromagnet allows to use the more sensitive solenoid in a convenient axial orientation in the air gap of the magnet, facilitating the implementation and exchange of individual capillaries. For measurements involving a steady EOF through the bed the electrodes of a modular capillary electrophoresis instrument operating up to 30 kV and 200 μA (Grom, Herrenberg-Kayh, Germany) were connected to the column by a home-built PEEK block (also acting as a flow splitter) on one side and a buffer reservoir through the open capillary segment on the other (Figure 2). Thus, a conventional HPLC pump could be used in pressure-driven flow.

For our studies we implemented the stimulated echo version of the PFG-NMR methodology.[43] With this combined radio frequency and gradient pulse scheme, the motion of fluid molecules is encoded by a pair of identical magnetic field gradients of amplitude and direction $\mathbf{g}$, pulsed for a short time δ, and separated by the experimental observation time Δ. In the narrow gradient pulse limit,[51] i.e., for $\delta \ll \Delta$, the following relationship exists between the nuclear spin phase and position

$$\phi_i(\Delta) = \gamma\delta\mathbf{g} \cdot [\mathbf{r}_i(\Delta) - \mathbf{r}_i(0)] = \gamma\delta\mathbf{g} \cdot \mathbf{R}_i(\Delta) \qquad (2)$$

where γ is the magnetogyric ratio of the nucleus considered (^{1}H) and $\mathbf{R}$ is the net displacement of spin i over time Δ along the direction of $\mathbf{g}$. The total, normalized signal amplitude at the echo center is obtained by a summation over all individual spins in the measurement volume which (in propagator language) translates to

$$E(\mathbf{q},\Delta) = \int P_{av}(\mathbf{R},\Delta) \exp(i2\pi\mathbf{q} \cdot \mathbf{R})\, d\mathbf{R} \qquad (3)$$

with $\mathbf{q} = (2\pi)^{-1}\gamma\delta\mathbf{g}$. $P_{av}(\mathbf{R},\Delta)$, the average propagator, gives the probability that *any* molecule travels a net displacement $\mathbf{R}$ over time Δ.[52] It is related to the initial nuclear spin density and an equivalent to the Green function[53] by

$$P_{av}(\mathbf{R},\Delta) = \int \rho(\mathbf{r}_0)P(\mathbf{r},\Delta/\mathbf{r}_0)\,d\mathbf{r}_0 \qquad (4)$$

$P(\mathbf{r},\Delta/\mathbf{r}_0)$ is the conditional probability for finding a molecule at $\mathbf{r}$ after time Δ given that it was at $\mathbf{r}_0$. $P_{av}(\mathbf{R},\Delta)$ is reconstructed directly by Fourier transformation of $E(\mathbf{q},\Delta)$ with respect to $\mathbf{q}$. When the displacement distribution is a single Gaussian (and the exchange between velocity extremes in the flow field is complete) we obtain[54,55]

$$E(\mathbf{q},\Delta) = \exp\,(i2\pi\mathbf{q}\cdot\mathbf{u}_{av}\Delta - 4\pi^2q^2D_{a,t}\Delta_{eff}) \qquad (5)$$

where $\mathbf{u}_{av}$ is the average mobile phase velocity through the bed. D_a ($\mathbf{q} \parallel \mathbf{u}_{av}$) and D_t ($\mathbf{q} \perp \mathbf{u}_{av}$) are the long-time, asymptotic axial and transverse dispersion coefficients which (for macroscopically isotropic porous media) satisfy the following form of the convection-diffusion equation describing dispersion of a passive tracer of macroscopic mean concentration $\langle c\rangle$ in single-phase incompressible flow along the **z**-direction[56]

$$\frac{\partial\langle c\rangle}{\partial t} + \mathbf{u}_{av}\cdot\nabla\langle c\rangle = D_a\frac{\partial^2\langle c\rangle}{\partial z^2} + D_t\nabla_t^2\langle c\rangle \qquad (6)$$

When a complete exchange of fluid molecules between the intraparticle and interparticle pore space has not been achieved over time Δ, both $E(\mathbf{q},\Delta)$ and $P_{av}(\mathbf{R},\Delta)$ reveal discrete bimodal behavior. It is most pronounced at flow rates high enough that convection dominates interparticle dispersion, while (typical for pressure-driven flow) the intraparticle fluid remains purely diffusive or at least diffusion-limited[57,58]

$$E(\mathbf{q},\Delta) = \sum_{n=1}^{2}A_n(\Delta)\exp(i2\pi\mathbf{q}\cdot\mathbf{u}_n\Delta - 4\pi^2q^2D_n\Delta_{eff}) \qquad (7)$$

The fractions $A_n(\Delta)$ represent unexchanged intraparticle fluid molecules (A_{intra}) and those having experienced interparticle flow (A_{inter}). If the coefficients D_n characterizing dispersive motion are sufficiently different (usually $D_{intra} \ll D_{inter}$ because $u_{intra}/u_{inter} \rightarrow 0$), A_{intra} and the intraparticle mass transfer kinetics can be determined. By using eq 7 for that purpose we have corrected for the nuclear spin−spin and spin−lattice relaxation times, as described earlier.[58] Our ^{1}H PFG-NMR measurements were performed with 40 **q**-steps equally spaced between $\pm\mathbf{q}_{max}$ taking up to 64 averages at each value of $\mathbf{q}$ ($\delta = 2.5$ ms and $\Delta_{eff} = \Delta - \delta/3$).

Results and Discussion

As a goal of this work is to contrast between electroosmotic and pressure driven flow concerning velocity extremes of the flow field in a bed of spherical, permeable particles, Figure 3 begins to illustrate the dynamics of intraparticle diffusion and interparticle convection for laminar flow when $\Delta < r_p^2/2D_{intra}$ (r_p is the particle radius). In liquid chromatography the intraparticle pores are typically a factor 10^2-10^3 smaller than the interparticle channels.[59] By considering a particle itself as an aggregate of microparticles, a permeability estimate obtained with the Carman-Kozeny equation[60] suggests that intraparticle convection is not an important transport mechanism compared to molecular diffusion unless the pressure drop becomes exceedingly high and the solute diffusivity low or, of course, as d_{pore}/d_p increases significantly. Thus, intraparticle mass transfer is diffusive over a relatively wide range of conditions, and because the fluid molecules are small compared to the particles pore dimension (and usually nonsorbed on their surface), D_{intra} is related to the molecular diffusivity just by the tortuosity factor τ_{intra} (Figure 3). On the particle-scale (there is no need to resolve beyond this level in the present work) τ_{intra} is a parameter accounting for the *effective* pore network topology and lumps together distributions of pore size, pore shape, surface defects, and pore interconnectivity. Diffusive intraparticle liquid holdup in pressure-driven flow may constitute the most significant mechanism for transient and asymptotic axial dispersion in macroscopically homogeneous beds at flow rates where convective times ($\tau_C = u_{av}\Delta/d_p$) well exceed the dimensionless time for diffusion ($\tau_D = D_{intra}\Delta/d_p^2$).[61]

To leave a particle completely and join the interparticle streamlines a molecule that starts at the spheres center diffuses through the intraparticle pore network and a diffusive boundary layer at the particles external surface (Figure 3). This leads to a characteristic exchange time Δ_e based on r_p, D_{intra}, and, strictly, also on the thickness of the boundary layer (δ_f), which is an inverse function of the flow rate (although in most cases $\delta_f \ll r_p$). Boundary layer mass transfer manifests itself in the measurements by a distance over which diffusion normal to the solid−liquid interface remains comparable to convective transport parallel to it (Figure 3), while the velocity is zero *at* the surface due to the no-slip condition. It should be noted that D_{intra} obtained by PFG-NMR is based on a direct measurement of intraparticle displacements and, consequently, does not account for the spheres porosity (ϵ_{intra}). D_{intra} can be related to the often used effective diffusivity (as observed from "outer", i.e., the interparticle pore space) by $D_{eff} = \epsilon_{intra}D_{intra}$.

Figure 4a,b show displacement probability distributions of the fluid molecules in laminar flow through the packed capillary. While at 20 ms a substantial fluid fraction still remains unexchanged inside the particles, it becomes less than 5% after 150 ms and is only visible as the shoulder around zero displacement (Figure 4b). By recording the amount of intraparticle-only fluid as a function of Δ, a mass transfer rate constant $B_{intra} = \pi^2D_{intra}/r_p^2$ can be determined from the well-known model describing the purely diffusive emptying of spheres under the assumption of constant boundary conditions[62]

$$\frac{A_{intra}(\Delta)}{A_{intra}(0)} = \frac{6}{\pi^2}\sum_{n=1}^{\infty}\frac{1}{n^2}\exp(-n^2B_{intra}\Delta) \qquad (8)$$

The data shown in Figure 4c are well described by eq 8 and give $D_{intra} = 1.36 \times 10^{-5}$ cm^2 s^{-1}. Thus, $\tau_{intra} = D_m/D_{intra} = 1.65$, in good agreement with tortuosity factors reported recently for similar supports.[58,63,64] It should be recalled that the PFG-NMR method, in contrast to most conventional tracer techniques, detects the complete displacement spectrum of instantaneously *physically* labeled molecules (^1H_2O) residing in an equilibrium with respect to their local concentration, i.e., *chemically* the mobile phase is (and continues to be) perfectly mixed. As the pore size distribution of the particles is actually bimodal[47,65] the intraparticle mass transfer kinetics could reveal a corresponding two-component behavior, depending on the characteristic time constants for diffusion in either set of pores.[66] However, because already the shortest observation time in our work ($\Delta = 15$ ms) gives a root-mean-squared translational displacement of the order of 8 μm, which is larger than the spatial domain of both the macro- and gigaporous network,[47,65] D_{intra} in eq 8 is expected to represent effective diffusion in a

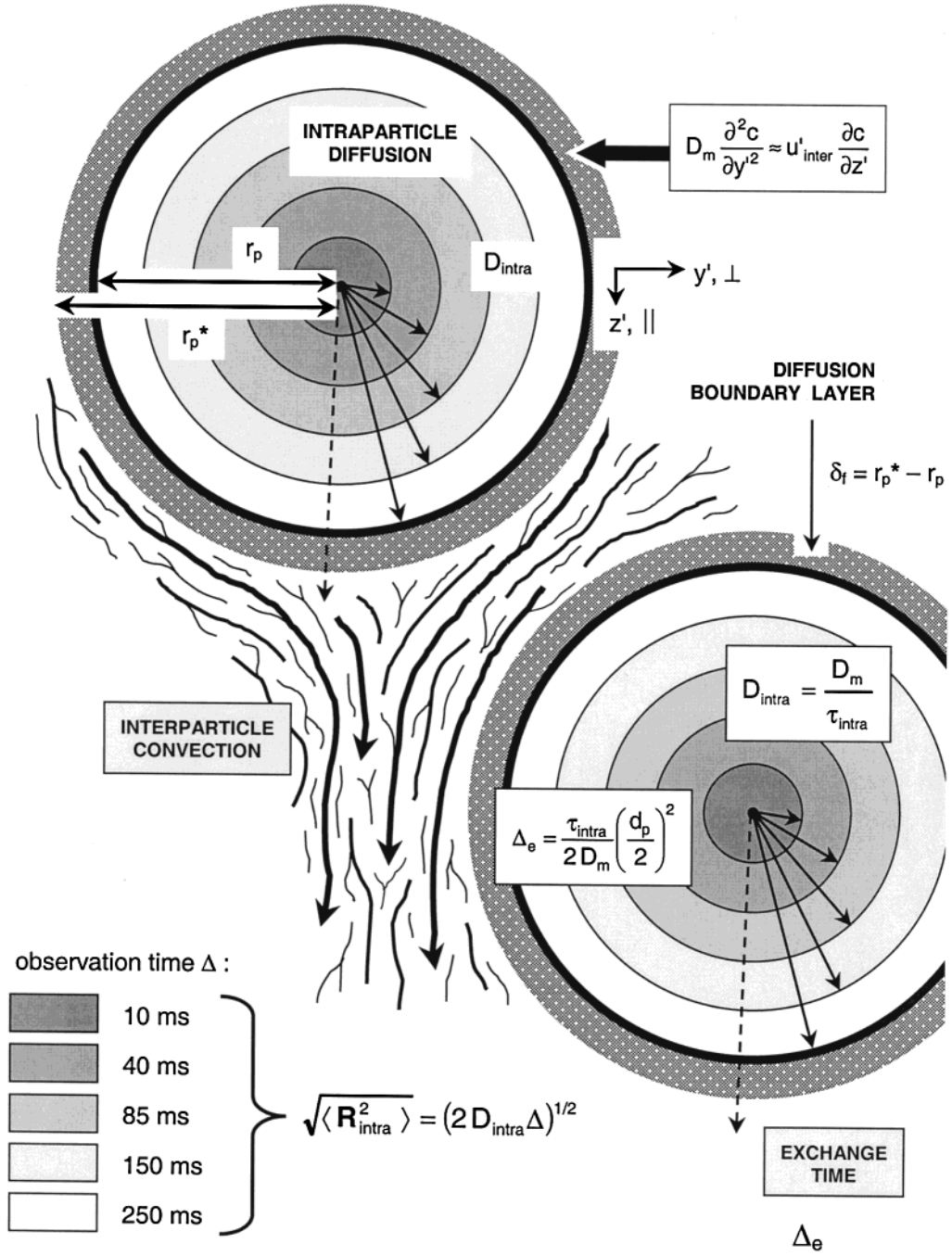

Figure 3. Dynamics of fluid in viscous flow through a fixed bed of porous spherical particles, including interparticle convection, intraparticle diffusion and boundary layer mass transfer associated with the no-slip condition at the solid−liquid interface (u'_{inter} is the local velocity component parallel to the particles external surface). Model parameters: $d_p = 50\ \mu m$, $D_m = 2.25 \times 10^{-5}\ cm^2\ s^{-1}$, $\tau_{intra} = 1.8$.

hierarchically structured intraparticle network of giga- and macropores. This is supported by earlier studies which have demonstrated that D_{intra} has indeed reached the tortuosity asymptote at this observation time,[58] in agreement with the data in Figure 4c revealing a constant value for D_{intra}.

Concerning diffusion-limited mass transfer in pressure driven flow it should be noted that if a small intraparticle velocity component indeed exists (even strong enough to dominate the transport of slowly diffusing tracers in the flow field) our measurements are relatively insensitive for its contribution to the overall kinetics as the diffusivity of flow field molecules is several orders of magnitude higher than those of large tracers such as proteins.[67] Thus, our intraparticle mass transfer data are necessarily obtained in the tortuosity-limited regime ($D_{intra} < D_m$), where transport is dominated by diffusion, but they cannot exclude the existence of a comparatively small convective driving force inside the particles.

After having started with the discrete bimodal propagator distribution in pressure driven flow (Figure 4a) which results from the large differences in hydraulic conductivity of the intra- and interparticle pore networks we turn to electrokinetically driven flow through the packing. $P_{av}(\mathbf{R},\Delta)$ in Figure 5 reveals a skewn Gaussian with significant fronting and the intraparticle fluid is not resolved as a separate peak. One reason for that observation is that the maximum driving force (electric potential gradient) now is relatively limited (30 kV) compared to the pressure gradient (≤80 bar) in the former case. Thus, even when the electroosmotic conductivities of the intra- and interparticle

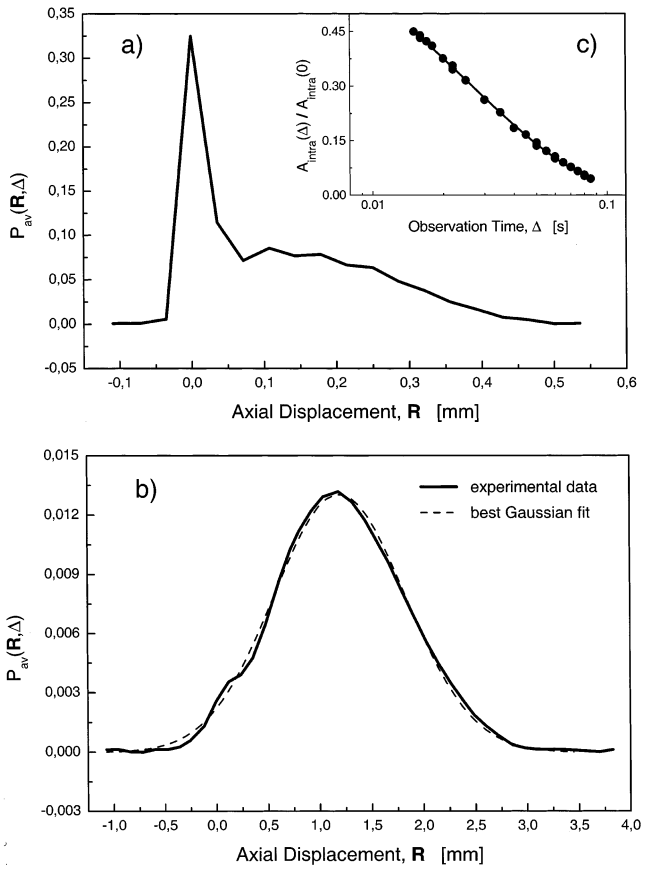

Figure 4. Pressure driven flow through the packed capillary, displacement distributions for (a) $\Delta = 20$ ms and (b) $\Delta = 150$ ms. (c) Intraparticle mass transfer kinetics (from 15 to 85 ms, upper limit given by the signal-to-noise ratio), solid line: Best fit of the data to eq 8. Pressure gradient: $\Delta P = 45$ bar, $\mathrm{Pe} = u_{av}d_p/D_m = 145$, $\mathrm{Re} = u_{av}d_p\rho/\eta = 0.36$ (kinematic viscosity: $\eta/\rho = 8.9 \times 10^{-3}$ cm^2 s^{-1} at 25 °C), $r_p = 20.5$ μm, $D_m = 2.25 \times 10^{-5}$ cm^2 s^{-1}, and $B_{intra} = \pi^2 D_{intra}/r_p^2 = 31.7$ s^{-1}.

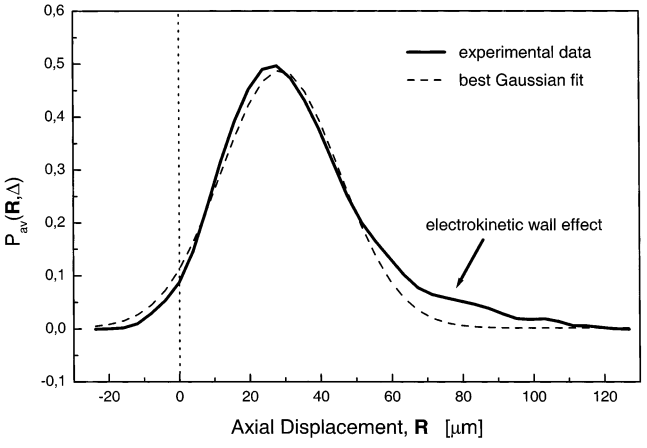

Figure 5. Electrokinetically driven flow through the packed capillary. Mobile phase: 2×10^{-3} M sodium tetraborate solution ($E = 47.4$ kV m^{-1}, $I = 53$ μA, and $\Delta = 40$ ms).

pore networks differ significantly, a corresponding displacement discrimination could probably not be achieved. However, because of the small fluid fraction that is actually left around zero displacement and the substantial character in $P_{av}(\mathbf{R},\Delta)$ of a very narrow Gaussian (Figure 5), this result rather suggests that electroosmotic conductivities of the respective pore networks are indeed similar and for that reason prevent a discrete visualization of the intraparticle fluid. Concluding already from Figure 5, it is not possible to resolve intraparticle fluid and study the associated mass transfer in *pure* electrokinetic flow. A more promising strategy for measuring the influence of a potential gradient on intraparticle mass transfer is to apply a sufficient pressure gradient, as in Figure 4a, then *add* a potential gradient and follow its effect on fluid exchange (cf. Figure 4c), using the pure hydraulic flow data as diffusive reference.

Before doing that in detail we try to understand the pronounced fronting of $P_{av}(\mathbf{R},\Delta)$ seen in Figure 5. EOF in the packed column originates in the Debye layer close to solid−liquid interfaces (where the buffer solution is locally charged) through a body force on the liquid caused by the externally applied electric field. Surfaces in contact with the liquid are those of the particles and capillary inner wall. These, however, not only differ in their chemical nature, but also concerning physical properties including the electrokinetics represented by the ζ-potential. Thus, depending on $\zeta_{ex} = (\zeta_w - \zeta_p)$ and the actual column-to-particle diameter ratio, $\psi = d_c/d_p$, the resulting macroscopic flow heterogeneity[30,31] will engender additional dispersion. Due to the low aspect ratio ($\psi \approx 6$) this effect is aggravated in the present case. Although the particles surface and capillary inner wall both carry a negative charge density, the (open) fused-silica capillaries are known to give EOF velocities which are significantly higher than those of many packing materials used in CEC, even after having corrected for the packed beds tortuosity factor.[68−70] The fronting behavior in Figure 5 is an electrokinetic phenomenon and cannot be explained by the open segment via a flow-equalizing intersegmental pressure that developes due to the conservation of volumetric flow rate for an incompressible liquid in the whole capillary setup as the hydraulic permeability of the packed segment is far too low compared to that of the open channel.[71] For our capillary configuration (Figure 2) we calculate a pressure difference between the open and packed segments of well below 1 bar,[71] insufficient to drive any measurable amount of liquid through the bed. The influence of the capillary wall on a radial distribution of EOF velocities may be estimated by[30,31]

$$\frac{u_{inter}(r)}{u_p} = 1 + \left(\frac{\zeta_w}{\zeta_p} - 1\right)\frac{I_0(\beta r/d_p)}{I_0(\beta r_{eff}/d_p)} \qquad \text{for} \quad 0 \le r \le r_c - 7\lambda_D \cong r_{eff} \quad (9)$$

I_0 is the zero-order modified Bessel function of the first kind, r_{eff} is an effective capillary radius (accounting for the no-slip condition at the inner wall of the column), and β characterizes the overall permeability of the bed.[72] Although the underlying model[30,31] may be refined by considering the actual radial porosity distribution close to the wall and its consequences for the *local* permeability in this critical region,[73,74] Figure 6 demonstrates the strong effect of ζ_w/ζ_p on transcolumn EOF profiles ($\psi = 6$). The most striking result is that ζ_w may even prevent attainment of u_p in the center of the bed.

Compared to these predictions Figure 7 illustrates the driving force dependence of the propagator shape and the consequences for axial dispersion observed in our measurements. As the electric field strength is increased (Figure 7a) the wall component becomes first visible through a decent shoulder (e.g., $E = 21.1$ kV m^{-1}), but it still leaves the average propagator substantially Gaussian. Upon further increase, however, $P_{av}(\mathbf{R},\Delta)$ deteriorates to a broad distribution (Figure 7b) and displacements of the fastest fluid molecules in the wall annulus (propagator front) are more than 3 times higher than those moving in the central core region of the bed (see arrows). The clean velocity field would probably reveal an even larger difference between

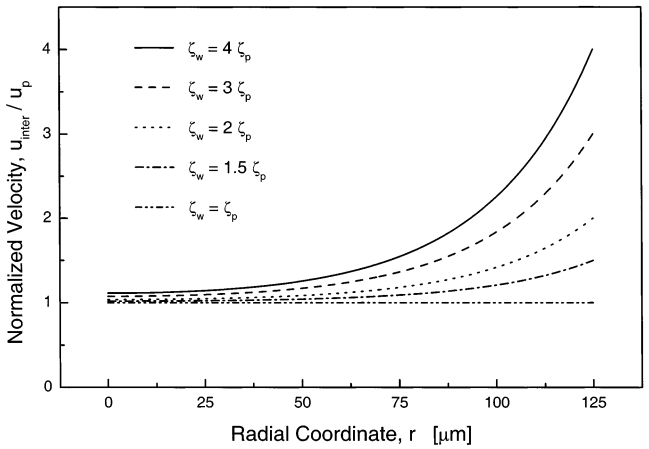

Figure 6. Column cross-sectional EOF profiles predicted by eq 9 with $r_c = 125\ \mu$m, $d_c/d_p = 6$, $\lambda_D = 3.9$ nm, and $\beta = 1.65$ (u_p is the velocity associated with the particles surface only, according to ζ_p).

wall (ζ_w) and bed (ζ_p) components because molecular diffusion tends to blur the spectrum of instantaneous velocities. The spatial dimension of the "wall annulus" is the distance from the capillary surface over which the local fluid velocity is affected by ζ_w. The resulting macroscopic flow heterogeneity needs a transcolumn equilibration of fluid molecules, i.e., exchange via lateral dispersion over the full capillary radius to approach a single, uniform Gaussian. Similar to $P_{av}(\mathbf{R},\Delta)$ in Figure 7b, the corresponding amplitude modulation of $E(\mathbf{q},\Delta)$ shown in Figure 7c reveals a bimodal behavior. Using eq 7 to calculate the apparent dispersion coefficient $D_{ap,a}(\Delta)$ of either fluid-element ensemble it becomes evident that dispersion in the wall annulus is significantly higher than in the center of the column (Figure 7c). Thus, in the limit $\Delta > r_c^2/2D_t$, the wall effect has obscured an otherwise outstanding dispersion characteristics of the EOF in the packed bed region indicated by the narrow Gaussian core of $P_{av}(\mathbf{R},\Delta)$ (Figures 7a−c).

While the bimodal behavior in pressure driven flow reflects intraparticle stagnation (Figure 4a), it addresses a macroscopic flow heterogeneity with EOF (Figure 5). Although wall effects caused by a nonuniform radial porosity distribution are well-known in the former case,[73,74] the low intraparticle velocity here dominates the appearance of $P_{av}(\mathbf{R},\Delta)$ at relatively high Pe compared to the situation with EOF where the intraparticle mass transfer is obviously faster (for reasons that we still have to demonstrate) and the wall effect becomes more pronounced and/or discrete. Recently, electrokinetic wall effects and those encountered in hydraulic flow have been spatially resolved by dynamic NMR microscopy with 40 μm in-plane resolution in a study of fluid flow through a 250 μm i.d. capillary packed with 50 μm cation exchange particles.[75] In both cases (but for different reasons) wall effects severely affected transient dispersion, causing a long-time disequilibrium in the axial displacement distribution which significantly exceeds the time scale of intraparticle mass transfer. In this context, the recent NMR imaging studies of Locke et al.[76] on spatial variations of the EOF velocity field in porous media (with a 78 × 78 μm^2 resolution in 100 μm thick slices) and of Sederman et al.[77] on the structural characterization of the interparticle void space in fixed beds should also be mentioned.

After having explained the fronting behavior of $P_{av}(\mathbf{R},\Delta)$ in EOF at low aspect ratio, we focus on the influence of a potential gradient on intraparticle fluid transport. Figure 8 compares the mass transfer kinetics obtained in pressure-driven flow with the effect of an *additional* potential gradient at increasing buffer concentration. It is evident that the electric field significantly

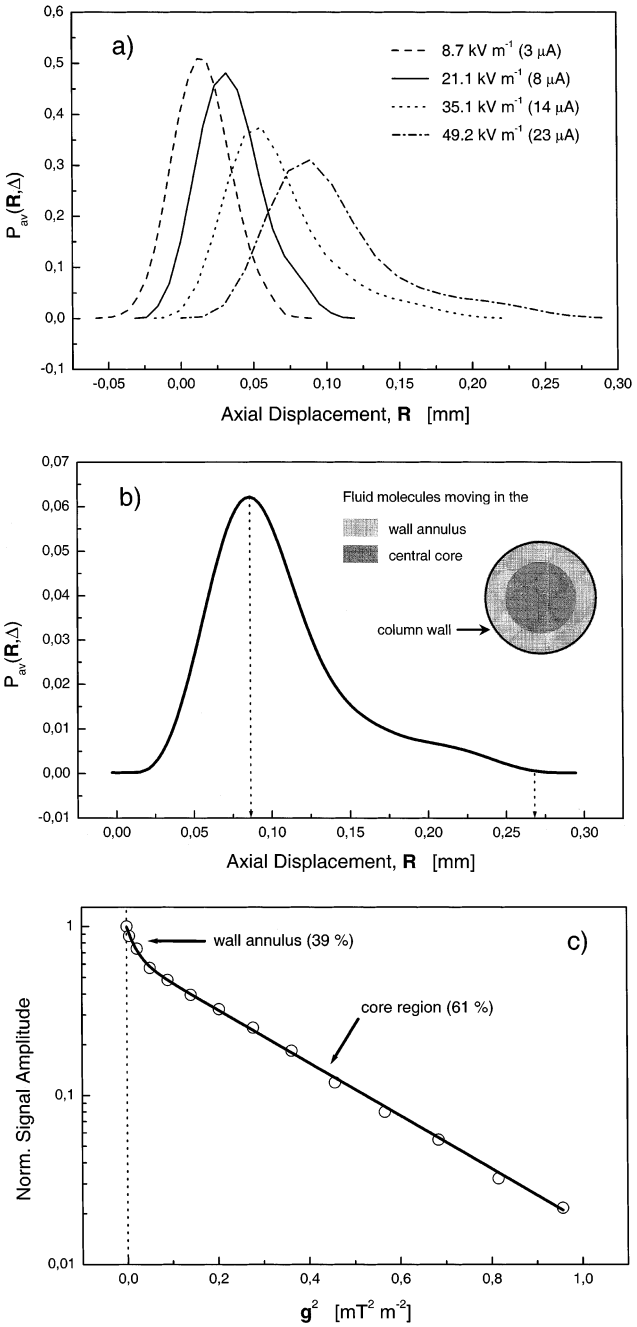

Figure 7. Electrokinetic wall effect. (a) Propagator distributions as a function of the electric field strength ($\Delta = 120$ ms, 10^{-3} M buffer), (b) last measurement (49.2 kV m^{-1}, 23 μA) with 10 times zerofilling in **q**-space prior to Fourier transformation. (c) Best fit of the normalized echo attenuation function in $E(\mathbf{q},\Delta)$ to eq 7, revealing fluid molecules in the wall annulus ($D_{ap,a} = 4.29 \times 10^{-4}$ cm^2 s^{-1}) and the beds central core ($D_{ap,a} = 3.5 \times 10^{-5}$ cm^2 s^{-1}).

enhances the exchange of fluid molecules between intra- and interparticle pore networks (even compared to diffusion on the flow field level) and that, further, the intraparticle mass transfer rate constant (still obtained from eq 8) increases with the buffer concentration. This increase can be caused by one or a combination of the following factors: (i) double-layer overlap inside the particles is reduced thereby increasing volumetric EOF, (ii) an increased amount of borate ions adsorbs on the surface and increases ζ_p, (iii) molecular diffusion is increased by thermal effects in the capillary which are aggravated by an increase of c_B (at constant E). It is important to note that, while the first two phenomena point toward an intraparticle convection,

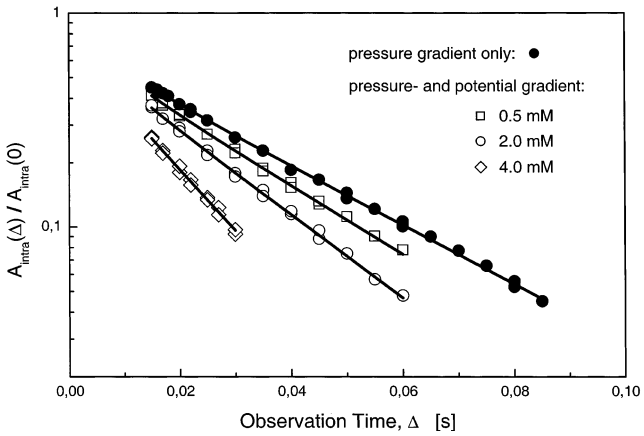

Figure 8. Intraparticle mass transfer kinetics. Influence of a pressure- and superimposed potential gradient ($E = 47.4$ kV m^{-1}) on fictitious emptying of the spherical particles. Column pressure drop, $\Delta P = 45$ bar (Pe = 145). Solid lines are best fits of the data to eq 8.

TABLE 1: Intraparticle Mass Transfer Characteristics (E = constant)[a]

c_B [10^{-3} M]	0.5	1	2	2[b]	3	4
B_{intra}^{ap} [s^{-1}], eq 8	36.9	40.3	45.2	44.3	55.9	64.6
λ_D [nm], eq 1	7.8	5.5	3.9	3.9	3.2	2.7

[a] E = 47.4 kV m^{-1}, Pe = 145 (ΔP = 45 bar), and Re = 0.36 unless stated otherwise. [b] Pe = 50 (ΔP = 15 bar) and Re = 0.12.

the last aspect leaves mass transfer purely diffusive. Most relevant parameters of this measurement series are summarized in Table 1. In general, intraparticle mass transfer may be due to a combination of diffusion *and* convection. These mechanisms are characterized by different driving forces and the concentric circles seen in Figure 3 (representing purely diffusive transport in the radial direction with a constant D_{intra}) loose their spherical symmetry, because convection in the sphere occurs along the axial direction.[78−80] For an approximate calculation of a now *apparent* mass transfer rate constant B_{intra}^{ap} based on the continued use of eq 8, our analysis neglects this geometrical aspect. It further does not realize convection as an independent transport mechanism, but relies on the simplifying concept of a convection-augmented diffusivity.[81−83] An exact, but more difficult to use analytical solution for the simultaneous transient diffusion and convection in spherical particles has been reported by Carta et al.[67] and was extended by Lu et al.[79] to include first-order reaction.

Double layer overlap inside the particles occurs mainly in the macropores (r_{pore} = 25−50 nm), to a lesser extent also in the gigapores (r_{pore} = 200−300 nm). The electric double layer is "thin" compared to the pore dimensions when $r_{pore}/\lambda_D > 100$. This ratio influences the pore-level profile in electrokinetic flow and also governs volumetric transport through a pore.[3] It ranges between 3.2 ($c_B = 5 \times 10^{-4}$ M) and 18.5 ($c_B = 4 \times 10^{-3}$ M) for the macropores and between 25.6 and 111 for the gigapores. Thus, while we expect substantial EOF in the gigaporous network, little affected by the electrolyte concentration over the range studied, volumetric EOF through the macroporous network should sensitively depend on r_{pore}/λ_D and increase significantly with c_B (cf. Table 1).[84] In the limit of a "totally perfusive regime" (which is not even reached in the present work) we have $r_{pore}/\lambda_D > 100$ for *any* set of inter- and intraparticle pores, i.e., the complete (interconnected) pore space is permeated by EOF with maximum velocities and volumetric flow rates. This, in turn, addresses the importance of a favorable network topology including high interconnectivity and a small amount of dead-end pores.[38,41]

Concluding from these considerations a suppression of double layer overlap is definitely an issue in view of the observed increase of B_{intra}^{ap} with c_B. Also mentioned in Table 1 is B_{intra}^{ap} obtained from a set of measurements ($c_B = 2 \times 10^{-3}$ M) which were conducted with a significantly reduced pressure gradient (ΔP = 15 bar), but identical potential gradient (E = 47.4 kV m^{-1}). In general, the effective Pe depends on ΔP *and* E. When comparing the data for Pe = 50 and Pe = 145 (ΔP = 15 and 45 bar) it is clear that a change in column pressure drop hardly influences the intraparticle mass transfer kinetics. On the other hand, it is well-known that the "thickness" of the boundary layer in low-Re, high-Pe (Pe > 50) pressure-driven flow through the bed (cf. Figure 3) is an inverse function of the flow rate[85] and, as such, can explain a dependence of stagnant mobile phase mass transfer on Pe in cases where intraparticle forced convection is too small to account for it.[58,86] Thus, our observation implies that boundary layer mass transfer is negligible in EOF because B_{intra}^{ap} is essentially unaffected when Pe is varied via the pressure gradient (at constant E). By returning to the ideal and comparatively simple situation encountered in a straight single capillary, this result can be understood by the spatial dimension of the velocity boundary layer in either type of liquid flow.[1] While for EOF through micrometer channels, $r_{pore}/\lambda_D >$ 100 can be easily achieved experimentally and the maximum (plug−flow) pore velocity is already reached after a few nanometers from the surface[31] ($\approx 7\lambda_D$) by lateral diffusion, the velocity (viscous) boundary layer in Poiseuille flow covers the whole radius of the capillary.[7,8] It also suggests that diffusive mass flux normal to the surface remains competitive to convective transport parallel to it over a considerably longer distance than in EOF. Concerning laminar flow through a packed bed stagnant fluid in the *inter*particle pore space may be visualized as a hydrodynamic layer around the particles with a thickness that in pressure driven flow can reach a few percent of the particle radius,[58,86] depending on Pe, Re, and the actual density of the packing. By contrast, practically all fluid molecules beyond the electric double layer move with a significant velocity in electrokinetically driven flow (at high E, ϵ_r, and ζ_p) when compared to diffusion, including those in cusp regions between particles where much of the interparticle fluid side resistance to mass transfer is located in pressure driven flow.

Returning to intraparticle mass transfer, values for B_{intra}^{ap} (Table 1) even leave the tortuosity-limited regime (for $c_B \geq 3 \times 10^{-3}$ M). It may be partly due to a reduced double layer overlap in the macropores, but because the temperature increase of the buffer solution is also most pronounced at high c_B we still need a measurement that distinguishes clearly between purely diffusive mass transfer (at any temperature) and intraparticle EOF. As the level of heat dissipation in the capillary is represented by the product of electric field strength and current, we kept EI constant in a new series of measurements at increasing buffer concentration. By adjusting E for every c_B such that EI holds the selected value (2.54 W m^{-1}), this not only ensures a constant thermal niveau in the capillary but also gives a systematic variation of E, the electrokinetic driving force, depending on c_B. The results shown in Figure 9a demonstrate that B_{intra}^{ap} increases significantly with E. Because thermal effects are now constant and do not explain this increase by the temperature dependence of D_m, only a convective transport mechanism can be responsible for the enhancement of intraparticle mass transfer (Table 2). When extrapolating these data to zero electric field strength the value for B_{intra}^{ap} (about 33.5 s^{-1}, see dotted line in Figure 9a) represents the case of pressure

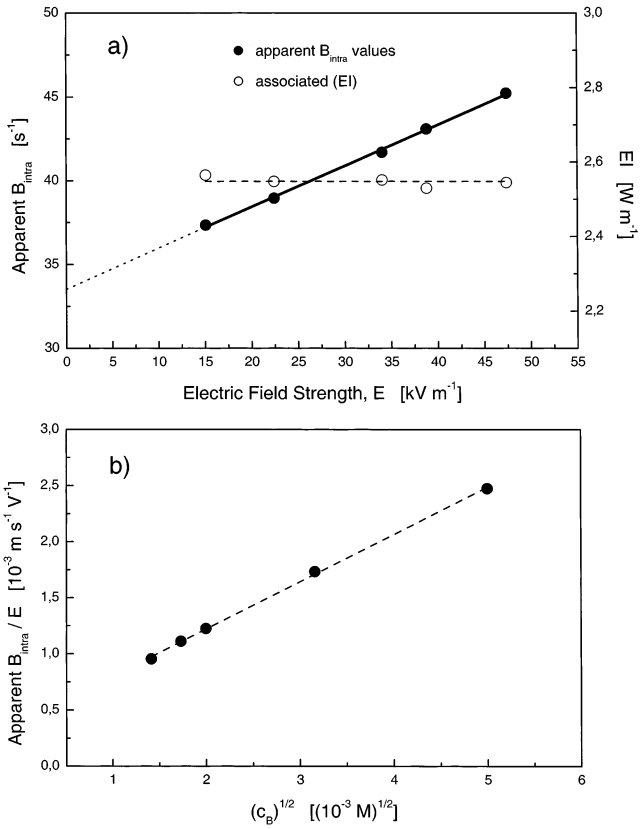

Figure 9. Intraparticle mass transfer kinetics with constant *EI* (2.54 W m^{-1}). Pressure gradient, ΔP = 45 bar (Pe = 145). (a) While the electric field strength increases from 15.1 kV m^{-1} ($c_B = 2.5 \times 10^{-2}$ M) to 47.4 kV m^{-1} ($c_B = 2 \times 10^{-3}$ M), the electric current decreases from 169 to 54 μA (cf. Table 2). (b) B^{ap}_{intra}/E vs $(c_B)^{1/2}$.

TABLE 2: Intraparticle Mass Transfer Characteristics (*EI* = constant)[a]

c_B [10^{-3} M]	2	3	4	10	25
B^{ap}_{intra} [s^{-1}], eq 8	45.2	43.1	41.7	38.9	37.3
λ_D [nm], eq 1	3.9	3.2	2.7	1.7	1.1
E [kV m^{-1}]	47.4	38.8	34.1	22.5	15.1
I [μA]	54	65	75	113	169

[a] For all measurements EI = 2.54 W m^{-1}, Pe = 145 (ΔP = 45 bar), and Re = 0.36.

driven flow alone, but it is increased by the thermal effect (*EI*). In fact, B_{intra} observed with only this pressure gradient comes close to that value (31.7 s^{-1}, Figure 4c). Thus, probably due to the substantial pressure driven flow component (ΔP = 45 bar, Pe = 150) the additional electric field causes just a small increase in B^{ap}_{intra} by a thermal effect. For example, the increase from B^{ap}_{intra} = 37.3 s^{-1} (2.5×10^{-2} M) to 45.2 s^{-1} (2×10^{-3} M) cannot be explained by diffusion, but must be due to convection (Figure 9a, Table 2). In Figure 9b the intraparticle mass transfer rate constant obtained for different c_B and E (but at a constant *EI*) is normalized with respect to E and plotted against c_B. These data reveal a linear dependence of B^{ap}_{intra}/E on $(c_B)^{1/2}$ and they now clearly demonstrate experimentally (in view of eq 1) that double layer overlap (cf. λ_D in Tables 1 and 2) is relevant and important in our studies.[84] Still, the data cannot exclude that adsorption of monoborate ions on the particles surface may also play a role in this concentration range by increasing ζ_p and the intraparticle EOF.

The results obtained so far indicate (i) negligible interparticle fluid-side resistance to mass transfer in EOF associated with the no-slip condition at the solid liquid interface (for $r_{pore}/\lambda_D \gg$ 1) and (ii) the existence of a significant intraparticle EOF. Unfortunately, the mass transfer kinetics does not directly reveal the actual velocity behind a convection-augmented B^{ap}_{intra}. To determine the value of u_{intra} from our measurements, we focus on the resolved position of stagnant fluid in pressure driven flow depending on the superimposed potential gradient. In contrast to the purely diffusive mechanism, EOF is expected to provide a *net* shift in displacement as long as formerly stagnant fluid molecules can participate in the intraparticle flow over time Δ.

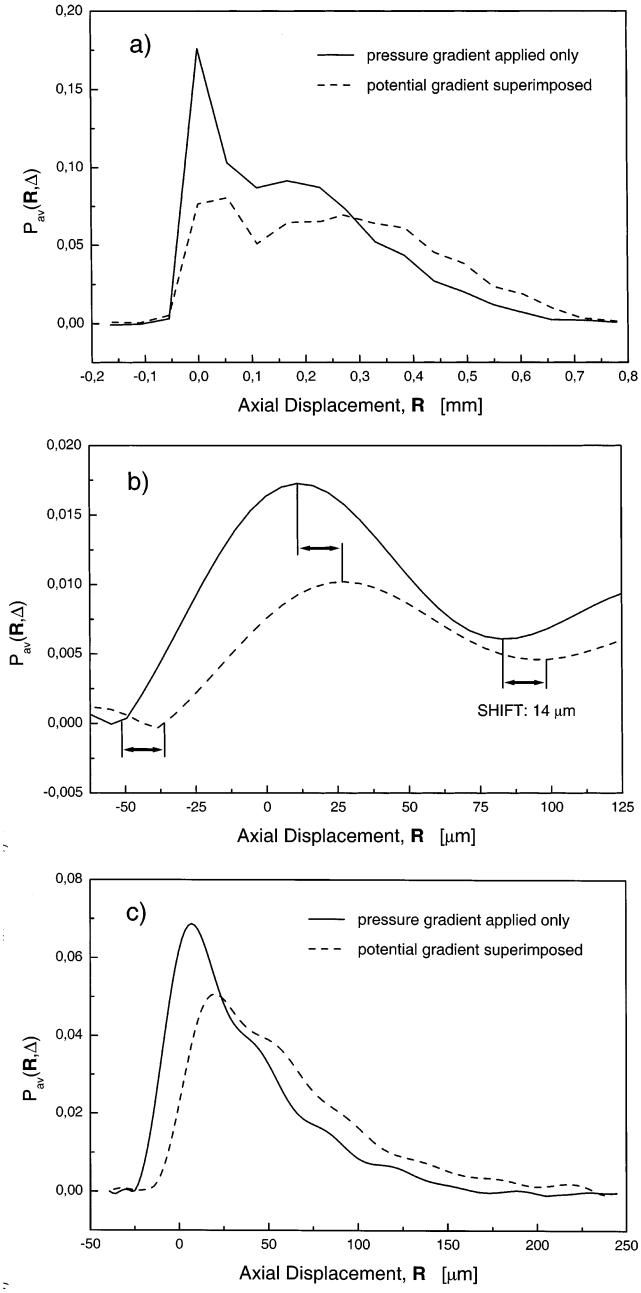

Figure 10. Effect on $P_{av}(\mathbf{R},\Delta)$ of a superimposed potential gradient (E = 47.4 kV m^{-1}) in pressure driven flow, Δ = 40 ms. Pressure drop, ΔP = 45 bar (Pe = 145): (a) Average propagator distribution obtained without zero-filling in **q**-space. (b) Focus on the region around zero displacement, raw data 10 times zero-filled. (c) ΔP = 15 bar (Pe = 50). Mobile phase: 2×10^{-3} M sodium tetraborate buffer.

Figure 10 compares displacement distributions obtained with only a pressure gradient and with an additional potential gradient. For example, Figure 10a clearly demonstrates that with the potential gradient the amount of fluid close to zero

displacement has decreased significantly and it also indicates that the distributions maximum here has shifted compared to the pressure driven flow (diffusive) reference. This is confirmed by Figure 10b which shows the region of interest after having zerofilled our raw data.[87] The peak that represents diffusion-limited fluid in hydraulic flow is indeed shifted (by ca. 14 μm) due to the additional electric field. It can only be explained by a convective electrokinetic driving force and means that, because most stagnant fluid is found *inside* the particles, the intraparticle EOF velocity seen in this shift is of the order of $u_{intra} = 0.35$ mm/s ($\Delta = 40$ ms). It is a substantial value keeping in mind that the average velocity in pure electrokinetic flow through the packed bed region "without" wall component is about $u_{eo} = 0.69$ mm/s (Figure 5). Further, this latter value is probably an overestimate due to the much stronger thermal effect in pure electrokinetic flow ($E = 47.4$ kV m^{-1}; $I = 53$ μA) and the wall effect. Thus, intraparticle and *true* interparticle EOF velocities are even closer.

As shown in Figure 10c a net shift is also visible at the lower Pe ($\Delta P = 15$ bar) where intraparticle fluid is not as clearly resolved as with the higher Pe ($\Delta P = 45$ bar). In both cases, however, the position of diffusion-limited fluid seen in the negative displacement tail of the propagator is very sensitive for a nonzero intraparticle EOF velocity. Given the fact that with the 2×10^{-3} M buffer solution we still encounter a considerable double layer overlap in the macroporous network of the particles,[84] the results shown in Figures 8−10 indicate an enormous potential for EOF in bulk transport of liquid through porous media. These data suggest that $u_{intra}/u_{inter} \rightarrow 1$ under optimized conditions, leaving molecular diffusion as the ultimate limitation to performance. In pressure driven flow, by contrast, we usually have $u_{intra}/u_{inter} \approx 0$. That the displacement shift of intraparticle fluid indeed depends on the electrokinetic driving force is demonstrated by Figure 11. While the pressure gradient alone hardly achieves measurable intraparticle forced convection (Figure 11a), the increase of an additional potential gradient clearly shifts the ensemble of intraparticle fluid molecules to higher displacements (Figure 11b). This effect is rather systematic and an intraparticle Peclet number, Pe_{intra}, may be now estimated via the time constants for diffusion ($\Delta_D = L^2/D_{intra}$) and convection ($\Delta_C = L/u_{intra}$).[88] As characteristic dimension L we used $r_p/3$, i.e., the ratio of the spheres volume to its external surface[63,82]

$$Pe_{intra} = \frac{\Delta_D}{\Delta_C} = \frac{r_p u_{intra}}{3D_{intra}} \tag{10}$$

The data in Figures 8−11 demonstrate that due to the intraparticle EOF Pe_{intra} reaches values also above unity. Thus, convection becomes comparable to the diffusive mass flux already for the flow field molecules and will clearly dominate the intraparticle transport of solute molecules with a lower diffusivity. Diffusion-limited mass transfer practically vanishes when $r_{pore}/\lambda_D \gg 1$. It also implies that the effective particle diameter, usually defined with respect to diffusion-limited mass transfer, is drastically reduced below the physical d_p (41 μm) depending on the actual perfusive regime (e.g., on double layer overlap, pore size distribution, and pore interconnectivity) and has, thus, become a dynamic parameter.

After having been able to determine experimentally the intraparticle Peclet number Pe_{intra} in EOF through the packed capillary (Figures 10 and 11), complementary to the intraparticle mass transfer kinetics (Figures 8 and 9), one question is still unanswered: Is the increase in Pe_{intra} with c_B at constant EI

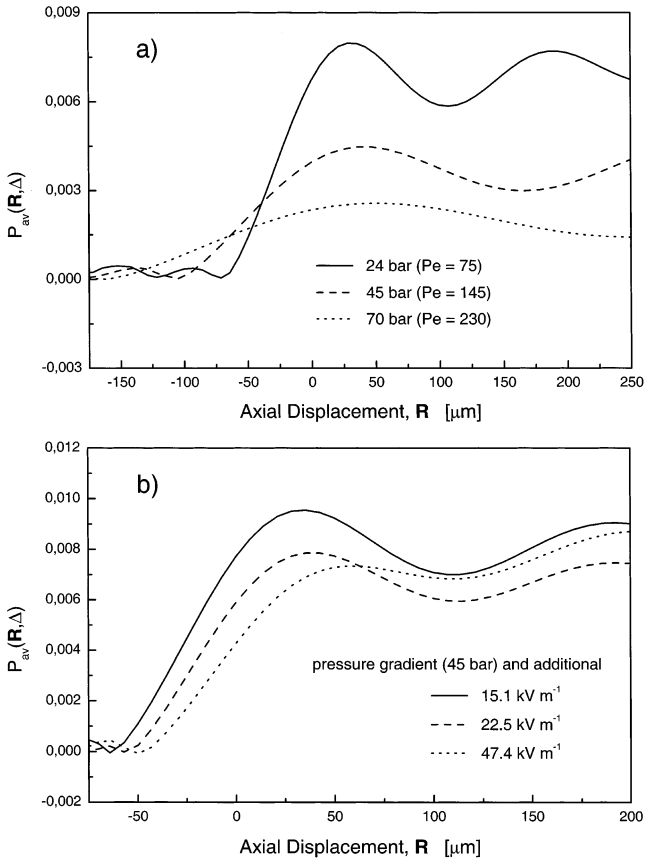

Figure 11. Net displacement of intraparticle fluid depending on the driving force. (a) Pressure gradient only with $\Delta = 60$ ms. (b) Potential gradient superimposed on a constant pressure drop ($\Delta = 50$ ms).

(Figure 9) only a consequence of suppressed double layer overlap (a mechanism that certainly contributes) or, in addition, does ζ_p increase due to adsorption of borate ions on the particles surface? Borate ions are well-known to adsorb on certain (originally uncharged) organic polyols and other surfaces carrying hydroxy groups.[89−93]

This question has been answered by studying the particles surface electrokinetics (ζ_p) in dependence of c_B. For that purpose we have measured over a concentration range from 3×10^{-5} to 4×10^{-2} M sodium tetraborate streaming potentials (Φ_{str}) of porous plugs obtained with the packing material, using the system zeta potential analyzer SZP-06 from Mütek Analytic GmbH (Herrsching, Germany). Φ_{str} can be obtained by forcing liquid through the plug with an externally applied pressure gradient and measuring the generated potential difference.[18] Results are summarized in Table 3, Γ_B is the conductivity of the plug saturated with the respective buffer solution. Because liquid flow inside the particles is negligible compared to interparticle flow, Φ_{str} characterizes the particles *external* surface. It has been shown that the mean size of interparticle voids (r_{inter}) in sphere packings is about 25−40% of the particle size (r_p).[94,95] Thus, in our case $r_{inter} \approx 7$ μm ($d_p = 41$ μm) and, together with the Debye lengths (Table 3), we are in the limit of thin electric double layers over the whole concentration range ($2 \times 10^2 < r_{inter}/\lambda_D < 8 \times 10^3$). Further, if surface conductivity of the particles is small compared to the bulk conductivity of the liquid, which is supported by a low surface-to-volume ratio of the interparticle pore space, Φ_{str} can be related to ζ_p by[96]

$$\left(\frac{\Phi_{str}}{\Delta P}\right)_{I=0} = \frac{\epsilon_0 \epsilon_r \zeta_p}{\Gamma_B \eta} \tag{11}$$

TABLE 3: Plug Streaming Potentials and Mobile Phase Conductivities[a]

c_B [10^{-3} M]	0.03	0.1	0.2	0.5	1	2	5	10	20	40
$\Phi_{str}/\Delta P$ [10^{-7} V N^{-1} m^2]	−4.1	−4.4	−4.35	−4.18	−3.49	−2.15	−1.09	−0.62	−0.26	−0.14
Γ_B [10^{-4} S/cm]	0.06	0.15	0.36	0.83	1.58	3.05	6.71	11.8	25.6	43.1
λ_D [nm], eq 1	31.9	17.5	12.4	7.8	5.5	3.9	2.5	1.7	1.2	0.9

[a] Values represent an average of two independent measurements at 25 °C.

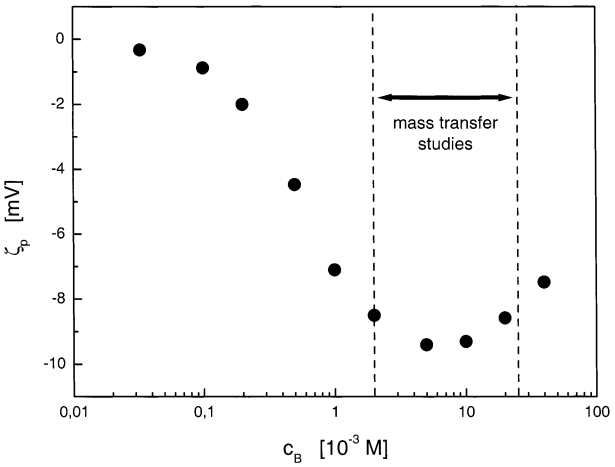

Figure 12. Elecktrokinetic characterization of the particles surface based on measurements of streaming potential factors ($\Phi_{str}/\Delta P$) and conductivities (cf. Table 3) in plugs generated in situ. ζ_p has been obtained with eq 11.

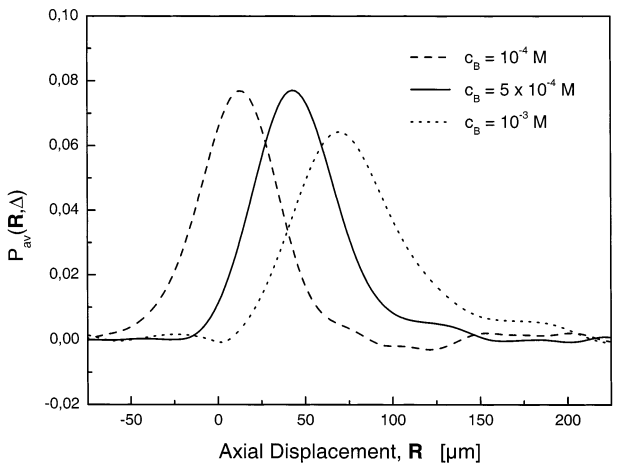

Figure 13. EOF through the packed capillary depending on the buffer concentration ($\Delta = 120$ ms, $E = 43.9$ kV m^{-1}). For $c_B = 5 \times 10^{-4}$ M and $c_B = 10^{-3}$ M the electrokinetic wall effect becomes visible again.

The result of this transformation is shown in Figure 12. The trend in these data clearly suggests that for 10^{-4} M $< c_B < 5 \times 10^{-3}$ M it is an adsorption of borate ions on the surface which substantially influences the electrokinetics. At low concentrations ζ_p approaches a value close to zero, in agreement with the particles surface chemistry[44,45] indicating that a priori no significant charge should exist on this hydrophilic support when in contact with a liquid (unless the manufacturing process gives rise to charged impurities in/on the matrix). The aliphatic surface hydroxy groups are not dissociated at pH 9.13 and interparticle double layer overlap can be excluded as seen in Table 3. Due to promoted adsorption of borate ions ζ_p increases with c_B (by a factor of almost 30!) until the adsorption capacity is approached. Then, above ca. 10^{-2} M, ζ_p begins to decrease with a further increasing c_B which represents the usual double layer behavior, i.e., addition of electrolyte compresses the double layer and therefore reduces ζ_p.[18] It should be noted that values for ζ_p in Figure 12 still include (via Γ_B) the beds *electrokinetic* porosity and tortuosity. Thus, the actual ζ_p is higher, the correction depending on contributions from inter- and intraparticle liquid.[69,97]

Complementary to this striking dependence of ζ_p on c_B, PFG-NMR measurements of EOF through the packed capillary are shown in Figure 13 for three selected buffer concentrations. At $c_B = 10^{-4}$ M, the fluid almost stands in the capillary ($u_{eo} \approx 0.1$ mm/s only), while the EOF velocity increases by a factor of 3.5 at $c_B = 5 \times 10^{-4}$ M and by a factor of 6 at $c_B = 10^{-3}$ M compared to its value at 10^{-4} M. Thus, relative velocities seen in the electroosmosis experiment (Figure 13) are in reasonable agreement with the dependence of ζ_p on c_B resulting from the streaming potential measurements (Figure 12). It should be noted that, while surface conduction is often involved to explain anomalous electrokinetic behavior of, e.g., latex plugs,[98−101] we believe that borate adsorption also contributes to the trend in Figures 12 and 13, for the following reasons: (i) the interparticle surface-to-volume ratio is relatively low in our case compared to nanoparticles used in these electrokinetic studies,[98,100,101] (ii) electroosmosis and streaming potential measurements give similar results, (iii) ζ_p increases by a large factor of 30 in the range $3 \times 10^{-5} \le c_B \le 5 \times 10^{-3}$ M, (iv) the particles surface should be originally uncharged which agrees well with $\zeta_p \rightarrow 0$ at low c_B, and (v) ζ_p values realized in our work (<10 mV, without a correction for the tortuosity and electrokinetic porosity, however) suggest that the surface charge density remains low. These arguments together indicate that conduction behind the shear plane, although possible and even probable,[99] is not necessarily the major or only contribution in the present case.

Summary

PFG-NMR studies of electrokinetic flow phenomena in a packed capillary using a home-built configuration (Figure 2) first revealed an electrokinetic wall effect (Figures 5−7) in the attempt to measure, as in pressure driven flow (Figure 4), intraparticle mass transfer in pure electrokinetic flow. For the porous medium considered ζ_w is much higher than ζ_p and this causes a pronounced fronting in $P_{av}(\mathbf{R},\Delta)$ (Figure 7). Already these measurements indicated that intraparticle mass transfer is significantly faster than in pressure driven flow where we observed discrete bimodal propagator distributions representing stagnant and flowing fluid (Figure 4). In EOF, by contrast, we were unable to resolve intraparticle fluid and instead observed an exceptionally narrow (Figure 7c) Gaussian core in $P_{av}(\mathbf{R},\Delta)$ combined with the fronting wall component (Figures 5 and 7). Studies of B_{intra}^{ap} in electrokinetically driven flow were then achieved by superimposing a potential gradient on an already existing pressure gradient. B_{intra}^{ap} increased significantly under the influence of the potential gradient (Figure 8), most probably caused by a nonzero intraparticle EOF velocity. These data also raised the question of how far thermal effects (via the dependence of the molecular diffusion coefficient on temperature) could contribute to that increase. Clear proof of the existence and actual magnitude of an intraparticle Peclet number in EOF through the bed was provided by a series of measurements at a constant thermal level in the capillary, thus, with a

constant "diffusive background" (Figures 9−11). These data have shown that $Pe_{intra} > 1$ in the present work and that $u_{intra}/u_{inter} \rightarrow 1$ under optimized conditions. By contrast, we find $u_{intra}/u_{inter} \rightarrow 0$ in pressure-driven flow (Figure 4a). Because ζ_p was relatively low throughout this study Pe_{intra} did not exceed 10 and, therefore, fluid transport due to diffusion and convection remained comparable. The increase of B^{ap}_{intra} and Pe_{intra} with c_B can be explained by a suppression of double layer overlap (Tables 1 and 2) and adsorption of monoborate ions on the particles surface (Figures 12 and 13). However, the actual increase seen in Figures 9−11 is mainly due to reduced double layer overlap as ζ_p is relatively independent of c_B in that range ($2 \times 10^{-3} \leq c_B \leq 2.5 \times 10^{-2}$ M, cf. Figure 12). Our results not only clearly demonstrate advantages of EOF in bulk transport of liquid through porous media with a distribution of pore sizes (significant perfusion and negligible boundary layer mass transfer over a wide range of conditions) but have also indicated intrinsic problems such as thermal effects and the contribution of different surfaces (with their own electrokinetics) to volumetric flow and dispersion.

Acknowledgment. This research was supported by a Marie Curie Fellowship (for U.T.) under the Training and Mobility of Researchers Program TMR from the European Union (ERBFMBI-CT98-3437), by the European Community activity Large-Scale Facility Wageningen NMR Centre (ERBCHGE-CT95-0066), and by the Deutsche Forschungsgemeinschaft DFG (SE 586/7-1). U.T. likes to thank Prof. H. Poppe, Dr. W. Th. Kok and R. Stol (Department of Chemical Engineering, University of Amsterdam), and Ab J. van der Linde (Department of Physical and Colloid Chemistry, Wageningen University) for fruitful discussions. We are indepted to Dr. R. Nitzsche (Mütek Analytic GmbH, Herrsching, Germany) for the streaming potential measurements.

References and Notes

(1) Probstein, R. F. *Physicochemical Hydrodynamics: An Introduction*; John Wiley & Sons: New York, 1994.
(2) Tsuda, T. *Electric Field Applications in Chromatography, Industrial and Chemical Processes*; VCH: Weinheim, 1995.
(3) Rice, C. L.; Whitehead, R. *J. Phys. Chem.* **1965**, *69*, 4017.
(4) Gross, R. J.; Osterle, J. F. *J. Chem. Phys.* **1968**, *49*, 228.
(5) Griffiths, S. K.; Nilson, R. H. *Anal. Chem.* **1999**, *71*, 5522.
(6) Liapis, A. I.; Grimes, B. A. *J. Colloid Interface Sci.* **2000**, *229*, 540.
(7) Paul, P. H.; Garguilo, M. G.; Rakestraw, D. J. *Anal. Chem.* **1998**, *70*, 2459.
(8) Tallarek, U.; Rapp, E.; Scheenen, T.; Bayer, E.; Van As, H. *Anal. Chem.* **2000**, *72*, 2292.
(9) Dittmann, M. M.; Wienand, K.; Bek, F.; Rozing, G. P. *LC·GC* **1995**, *13*, 800.
(10) Crego, A. L.; González, A.; Marina, M. L. *Crit. Rev. Anal. Chem.* **1996**, *26*, 261.
(11) Colón, L. A.; Reynolds, K. J.; Alicea-Maldonado, R.; Fermier, A. M. *Electrophoresis* **1997**, *18*, 2162.
(12) Fujimoto, C. *Trends Anal. Chem.* **1999**, *18*, 291.
(13) Colón, L. A.; Burgos, G.; Maloney, T. D.; Citrón, J. M.; Rodríguez, R. L. *Electrophoresis* **2000**, *21*, 3965.
(14) Shapiro, A. P.; Probstein, R. F. *Environ. Sci. Technol.* **1993**, *27*, 283.
(15) Acar, Y. B.; Alshawabkeh, A. N. *Environ. Sci. Technol.* **1993**, *27*, 2638.
(16) Acar, Y. B.; Gale, R. J.; Alshawabkeh, A. N.; Marks, R. E.; Puppala, S.; Bricka, M.; Parker, R. *J. Hazard. Mater.* **1995**, *40*, 117.
(17) Ho, S. V.; Sheridan, P. W.; Athmer, C. J.; Heitkamp, M. A.; Brackin, J. M.; Weber, D.; Brodsky, P. H. *Environ. Sci. Technol.* **1995**, *29*, 2528.
(18) Lyklema, J. *Fundamentals of Interface and Colloid Science, Vol. II: Solid−Liquid Interfaces*; Academic Press: London, 1995.
(19) Sasidhar, V.; Ruckenstein, E. *J. Colloid Interface Sci.* **1982**, *85*, 332.
(20) Hawkins-Cwirko, E.; Carbonell, R. G. *J. Colloid Interface Sci.* **1989**, *129*, 513.
(21) Levine, S.; Neale, G. H. *J. Colloid Interface Sci.* **1974**, *47*, 520.
(22) Kozak, M. W.; Davis, E. J. *J. Colloid Interface Sci.* **1986**, *112*, 403.
(23) Ohshima, H. *J. Colloid Interface Sci.* **1999**, *210*, 397.
(24) Jin, M.; Sharma, M. M. *J. Colloid Interface Sci.* **1991**, *142*, 61.
(25) Coelho, D.; Shapiro, M.; Thovert, J. F.; Adler, P. M. *J. Colloid Interface Sci.* **1999**, *181*, 169.
(26) Marino, S.; Coelho, D.; Békri, S.; Adler, P. M. *J. Colloid Interface Sci.* **2000**, *223*, 292.
(27) Eykholt, G. R. *J. Hazard. Mater.* **1997**, *55*, 171.
(28) Long, D.; Stone, H. A.; Ajdari, A. *J. Colloid Interface Sci.* **1999**, *212*, 338.
(29) Herr, A. E.; Molho, J. I.; Santiago, J. G.; Mungal, M. G.; Kenny, T. W.; Garguilo, M. G. *Anal. Chem.* **2000**, *72*, 1053.
(30) Rathore, A. S.; Horváth, Cs. *J. Chromatogr. A* **1997**, *781*, 185.
(31) Liapis, A. I.; Grimes, B. A. *J. Chromatogr. A* **2000**, *877*, 181.
(32) Li, D.; Remcho, V. T. *J. Microcolumn Sep.* **1997**, *9*, 389.
(33) Venema, E.; Kraak, J. C.; Tijssen, R.; Poppe, H. *Chromatographia* **1998**, *58*, 347.
(34) Venema, E.; Kraak, J. C.; Poppe, H.; Tijssen, R. *J. Chromatogr. A* **1999**, *837*, 3.
(35) Stol, R.; Kok, W. Th.; Poppe, H. *J. Chromatogr. A* **1999**, *853*, 45.
(36) Wen, E.; Asiaie, R.; Horváth, Cs. *J. Chromatogr. A* **1999**, *855*, 349.
(37) Vallano, P. T.; Remcho, V. T. *Anal. Chem.* **2000**, *72*, 4255.
(38) Tallarek, U.; Rapp, E.; Van As, H.; Bayer, E. *Angew. Chem. Int. Ed.* **2001**, *40*, 1684.
(39) Stol, R.; Poppe, H.; Kok, W. Th. *Anal. Chem.* **2001**, *73*, 3332.
(40) Stol, R.; Poppe, H.; Kok, W. Th. *J. Chromatogr. A* **2000**, *887*, 199.
(41) Grimes, B. A.; Meyer, J. J.; Liapis, A. I. *J. Chromatogr. A* **2000**, *890*, 61.
(42) Miller, N. P.; Berg, J. C.; O'Brien, R. W. *J. Colloid Interface Sci.* **1992**, *153*, 237.
(43) Callaghan, P. T. *Principles of Nuclear Magnetic Resonance Microscopy*; Clarendon Press: Oxford, 1993.
(44) Varady, L.; Mu, N.; Yang, Y.-B.; Cook, S. E.; Afeyan, N.; Regnier, F. E. *J. Chromatogr.* **1993**, *631*, 107.
(45) Royappa, A. T. *J. Appl. Polym. Sci.* **1997**, *65*, 1897.
(46) Frey, D. D.; Schweinheim, E.; Horváth, Cs. *Biotechnol. Prog.* **1993**, *9*, 273.
(47) Afeyan, N. B.; Gordon, N. F.; Mazsaroff, I.; Varady, L.; Fulton, S. P.; Yang, Y. B.; Regnier, F. E. *J. Chromatogr.* **1990**, *519*, 1.
(48) Rapp, E.; Bayer, E. *J. Chromatogr. A* **2000**, *887*, 367.
(49) Pezron, E.; Leibler, L.; Ricard, A.; Lafuma, F.; Audebert, R. *Macromolecules* **1988**, *21*, 1121.
(50) Ingri, N. *Acta Chem. Scand.* **1962**, *16*, 439.
(51) Stejskal, E. O.; Tanner, J. E. *J. Chem. Phys.* **1965**, *42*, 288.
(52) Kärger, J.; Heink, W. *J. Magn. Reson.* **1983**, *51*, 1.
(53) Koch, D. L.; Brady, J. F. *J. Fluid Mech.* **1987**, *180*, 387.
(54) Amin, M. H. G.; Gibbs, S. J.; Chorley, R. J.; Richards, K. S.; Carpenter, T. A.; Hall, L. D. *Proc. R. Soc. London A* **1997**, *453*, 489.
(55) Seymour, J. D.; Callaghan, P. T. *AIChE J.* **1997**, *43*, 2096.
(56) Sahimi, M. *Applications of Percolation Theory*; Taylor & Francis: London, 1994.
(57) Tallarek, U.; van Dusschoten, D.; Van As, H.; Bayer, E.; Guiochon, G. *J. Phys. Chem. B* **1998**, *102*, 3486.
(58) Tallarek, U.; Vergeldt, F. J.; Van As, H. *J. Phys. Chem. B* **1999**, *103*, 7654.
(59) Neue, U. D. *HPLC Columns: Theory, Technology, and Practice*; Wiley-VCH: New York, 1997.
(60) Bear, J. *Dynamics of Fluids in Porous Media*; Dover Publications: New York, 1988.
(61) Kandhai, D.; Hlushkou, D.; Hoekstra, A. G.; Sloot, P. M. A.; Van As, H.; Tallarek, U. *Phys. Rev. Lett.* **2002**, *88*, article no. 234501.
(62) Crank, J. *The Mathematics of Diffusion*; Clarendon Press: Oxford, 1956.
(63) McCoy, M.; Kalghatgi, K.; Regnier, F. E.; Afeyan, N. *J. Chromatogr. A* **1996**, *743*, 221.
(64) Nash, D. C.; Chase, H. A. *J. Chromatogr. A* **1998**, *807*, 185.
(65) Whitney, D.; McCoy, M.; Gordon, N.; Afeyan, N. *J. Chromatogr. A* **1998**, *807*, 165.
(66) Ruckenstein, E.; Vaidyanathan, A. S.; Youngquist, G. R. *Chem. Eng. Sci.* **1971**, *26*, 1305.
(67) Carta, G.; Gregory, M. E.; Kirwan, D. J.; Massaldi, H. A. *Sep. Technol.* **1992**, *2*, 62.
(68) Choudhary, G.; Horváth, Cs. *J. Chromatogr. A* **1997**, *781*, 161.
(69) Rathore, A. S.; Wen, E.; Horváth, Cs. *Anal. Chem.* **1999**, *71*, 2633.
(70) Liu, Y.; Pietrzyk, D. J. *Anal. Chem.* **2000**, *72*, 5930.
(71) Rathore, A. S.; Horváth, Cs. *Anal. Chem.* **1998**, *70*, 3069.
(72) Neale, G.; Epstein, N.; Nader, W. *Chem. Eng. Sci.* **1973**, *28*, 1865.

(73) Bey, O.; Eigenberger, G. *Chem. Eng. Sci.* **1997**, *52*, 1365.
(74) Giese, M.; Rottschäfer, K.; Vortmeyer, D. *AIChE J.* **1998**, *44*, 484.
(75) Tallarek, U.; Scheenen, T. W. J.; Van As, H. *J. Phys. Chem. B* **2001**, *105*, 8591.
(76) Locke, B. R.; Acton, M.; Gibbs, S. J. *Langmuir* **2001**, *17*, 6771.
(77) Sederman, A. J.; Alexander, P.; Gladden, L. F. *Powder Technol.* **2001**, *117*, 255.
(78) Stephanopoulos, G.; Tsiveriotis, K. *Chem. Eng. Sci.* **1989**, *44*, 2031.
(79) Lu, Z. P.; Dias, M. M.; Lopes, J. C. B.; Carta, G.; Rodrigues, A. E. *Ind. Eng. Chem. Res.* **1993**, *32*, 1839.
(80) Xu, Y.; Liapis, A. I. *J. Chromatogr. A* **1996**, *724*, 13.
(81) Rodrigues, A. E.; Ahn, B. J.; Zoulalian, A. *AIChE J.* **1982**, *28*, 541.
(82) Rodrigues, A. E.; Lopes, J. C.; Lu, Z. P.; Loureiro, J. M.; Dias, M. M. *J. Chromatogr.* **1992**, *590*, 93.
(83) Leitão, A.; Rodrigues, A. *Chem. Eng. J.* **1995**, *60*, 81.
(84) Wan, Q.-H. *Anal. Chem.* **1997**, *69*, 361.
(85) Happel, J.; Brenner, H. *Low Reynolds Number Hydrodynamics*; Martinus Nijhoff: The Hague, 1983.
(86) Boyd, G. E.; Adamson, A. W.; Meyers, L. S., Jr. *J. Am. Chem. Soc.* **1947**, *69*, 2836.
(87) Marshall, A. G.; Verdun, F. R. *Fourier Transforms in NMR, Optical, and Mass Spectrometry*; Elsevier: Amsterdam, 1990.
(88) Nir, A.; Pismen, L. M. *Chem. Eng. Sci.* **1977**, *32*, 35.
(89) Barrow, N. J. *J. Soil Sci.* **1989**, *40*, 427.
(90) Keren, R.; Grossl, P. R.; Sparks, D. L. *Soil Sci. Soc. Am. J.* **1994**, *58*, 1116.
(91) Sinton, S. W. *Macromolecules* **1987**, *20*, 2430.
(92) Smith, B. M.; Todd, P.; Bowman, C. N. *Sep. Sci. Technol.* **1999**, *34*, 1925.
(93) Lin, H.-L.; Yu, T. L.; Cheng, C.-H. *Colloid Polym. Sci.* **2000**, *278*, 187.
(94) Knox, J. H.; Scott, H. P. *J. Chromatogr.* **1984**, *316*, 311.
(95) Dullien, F. A. L. *Porous Media: Fluid Transport and Pore Structure*; Academic Press: San Diego, 1992.
(96) Overbeek, J. Th. G. Electrokinetic Phenomena. In *Colloid Science*; Kruyt, H. R., Ed.; Elsevier: Amsterdam, 1952.
(97) Vallano, P. T.; Remcho, V. T. *J. Phys. Chem. B* **2001**, *105*, 3223.
(98) Van der Put, A. G.; Bijsterbosch, B. H. *J. Colloid Interface Sci.* **1983**, *92*, 499.
(99) Lyklema, J.; Minor, M. *Colloids Surf. A* **1998**, *140*, 33.
(100) Folkersma, R.; van Diemen, A. J. G.; Stein, H. N. *Langmuir* **1998**, *14*, 5973.
(101) Löbbus, M.; van Leeuwen, H. P.; Lyklema, J. *Colloids Surf. A* **2000**, *161*, 103.

Effect of Intraparticle Porosity and Double Layer Overlap on Electrokinetic Mobility in Multiparticle Systems

Guofang Chen and Ulrich Tallarek*

Institut für Verfahrenstechnik, Otto-von-Guericke-Universität Magdeburg, Universitätsplatz 2, D-39106 Magdeburg, Germany

Received August 18, 2003. In Final Form: October 11, 2003

We have performed a systematic experimental study of electrokinetic mobility depending on the mobile phase ionic strength (concentration of Tris buffer) using different, well-defined porous and, for reference behavior, nonporous silica-based spherical microparticles. Effects of both an intraparticle electrical double layer overlap and the porosity on electrophoretic mobility in dilute suspensions and electroosmotic mobility in fixed beds of the devised (non)porous particles were investigated. The electrokinetically consistent results demonstrate a substantially different behavior for the porous (i.e., permeable and conducting) particles with respect to nonporous (solid) spheres. It may be related to a porous particle's dipole coefficient via the intraparticle void volume and, strongly depending on mobile phase ionic strength, to the actual magnitude of electroosmotic flow jetted through a particle's interior. In contrast to the normal electrical double layer behavior observed for the solid spheres (continuous decrease of mobility with ionic strength), these competitive contributions give rise to pronounced maxima in the mobility of the porous spheres. Our results are in qualitative agreement with the theoretical analysis of Miller et al. [*J. Colloid Interface Sci.* **1992**, *153*, 237] which, depending on the double layer interaction within a porous aggregate of solid spheres, predicts (significantly) lower or higher mobilities with respect to an impermeable and nonconducting particle.

1. Introduction

When dielectric solid particles are contacted with electrolyte solution, an electrical double layer (EDL) develops at the solid−liquid interface, for example, due to ionizable groups of the material.[1,2] Associated with the EDL, electrokinetic phenomena in dense multiparticle systems based on the tangential motion of the liquid relative to the charged surface play an important role in many processes with a technological, environmental, or analytical relevance.[3−17] Potential applications include transport of bulk liquid through fixed particulate beds in microfluidics and capillary electrochromatography, as well as water removal from concentrated particle slurries and industrial and natural porous media by electroosmosis (EO) or the enhanced settling, that is, densification of agglomerates, particle separation, and removal of colloidal contaminants from aqueous suspensions by electrophoresis (EP). Following the application of an external electrical field, a liquid, locally charged in the fluid-side domain of the EDL, begins to move relative to the stationary surface of rigid multiparticle systems in the former case (EO), while the latter involves the motion of mobile charged particles with respect to a stationary liquid (EP).

Further stimulated by the increased number and potential of applications in the physical and life sciences, a generalized and refined description of electrokinetic phenomena, particularly EO and EP, either for isolated (usually spherical and hard) particles or in multiparticle systems, has received much attention over the past decades.[18−52] Addressed issues include the magnitude and distribution of surface charge and electrokinetic potential,

* To whom correspondence should be addressed. Fax: +49 (0)-391-67-12028. E-mail: ulrich.tallarek@vst.uni-magdeburg.de.

(1) Lyklema, J. *Fundamentals of Interface and Colloid Science. Vol. II*: *Solid−Liquid Interfaces*; Academic Press: London, 1995.
(2) Delgado, A. V.; Arroyo, F. J. In *Interfacial Electrokinetics and Electrophoresis*; Delgado, A. V., Ed.; Marcel Dekker: New York, 2002; Chapter 1.
(3) Marlow, B. J.; Rowell, R. L. *Langmuir* **1991**, *7*, 2970.
(4) Mosher, R. A.; Saville, D. A.; Thormann, W. *The Dynamics of Electrophoresis*; VCH: Weinheim, 1992.
(5) Probstein, R. F.; Hicks, R. E. *Science* **1993**, *260*, 498.
(6) Sauer, J. E.; Davis, E. J. *Environ. Sci. Technol.* **1994**, *28*, 737.
(7) Ho, S. V.; Sheridan, P. W.; Athmer, C. J.; Heitkamp, M. A.; Brackin, J. M.; Weber, D.; Brodsky, P. H. *Environ. Sci. Technol.* **1995**, *29*, 2528.
(8) Dittmann, M. M.; Wienand, K.; Bek, F.; Rozing, G. P. *LC−GC* **1995**, *13*, 800.
(9) Tsuda, T., Ed. *Electric Field Applications in Chromatography, Industrial and Chemical Processes*; VCH: Weinheim, 1995.
(10) Haber, S. *J. Colloid Interface Sci.* **1996**, *179*, 380.
(11) Acar, Y. B.; Ozsu, E. E.; Alshawabkeh, A. N.; Rabbi, M. F.; Gale, R. J. *CHEMTECH* **1996**, *26*, 40.
(12) Crego, A. L.; González, A.; Marina, M. L. *Crit. Rev. Anal. Chem.* **1996**, *26*, 261.
(13) Coletta, T. F.; Brunell, C. J.; Ryan, D. K.; Inyang, H. I. *J. Environ. Eng.* **1997**, *123*, 1227.
(14) Bruin, G. J. M. *Electrophoresis* **2000**, *21*, 3931.
(15) Colón, L. A.; Burgos, G.; Maloney, T. D.; Cintrón, J. M.; Rodríguez, R. L. *Electrophoresis* **2000**, *21*, 3965.
(16) Polson, N. A.; Hayes, M. A. *Anal. Chem.* **2001**, *73*, 312A.
(17) Radko, S. P.; Chrambach, A. *Electrophoresis* **2002**, *23*, 1957.
(18) Dukhin, S. S.; Shilov, V. N. *Dielectric Phenomena and the Double Layer in Disperse Systems and Polyelectrolytes*; Wiley: New York, 1974.
(19) Levine, S.; Neale, G. H. *J. Colloid Interface Sci.* **1974**, *47*, 520.
(20) Levine, S.; Neale, G.; Epstein, N. *J. Colloid Interface Sci.* **1976**, *57*, 424.
(21) O'Brien, R. W.; White, L. R. *J. Chem. Soc., Faraday Trans. 2* **1978**, *74*, 1607.
(22) O'Brien, R. W. *J. Colloid Interface Sci.* **1983**, *92*, 204.
(23) Van der Put, A. G.; Bijsterbosch, B. H. *J. Colloid Interface Sci.* **1983**, *92*, 499.
(24) Ohshima, H.; Healy, T. W.; White, L. R. *J. Chem. Soc., Faraday Trans. 2* **1983**, *79*, 1613.
(25) O'Brien, R. W.; Perrins, W. T. *J. Colloid Interface Sci.* **1984**, *99*, 20.
(26) Anderson, J. L. *J. Colloid Interface Sci.* **1985**, *105*, 45.
(27) Zukoski, C. F.; Saville, D. A. *J. Colloid Interface Sci.* **1986**, *114*, 32.
(28) Zukoski, C. F.; Saville, D. A. *J. Colloid Interface Sci.* **1986**, *114*, 45.
(29) O'Brien, R. W. *J. Colloid Interface Sci.* **1986**, *110*, 477.
(30) Kozak, M. W.; Davis, E. J. *J. Colloid Interface Sci.* **1986**, *112*, 403.
(31) O'Brien, R. W.; Ward, D. N. *J. Colloid Interface Sci.* **1988**, *121*, 402.
(32) Kozak, M. W.; Davis, E. J. *J. Colloid Interface Sci.* **1989**, *127*, 497.
(33) Yoon, B. J. *J. Colloid Interface Sci.* **1991**, *142*, 575.

10.1021/la0355141 CCC: $25.00
Published on Web 11/20/2003

the ratio of the particle diameter to the EDL thickness, particle polydispersity, EDL polarization and surface conductivity, particle volume fraction or, vice versa, the interparticle porosity, spatial distribution of particles (periodic arrays vs random structures), Stern layer dynamics, particle−particle interaction and an EDL overlap, adsorption effects, as well as properties of the electrolyte solution like mobility, valency, and concentration of ionic species. Assumptions inherent to the popular hard-sphere models are that the particles are essentially impermeable (nonporous) and nonconducting. This often seems appropriate inasmuch as conducting particles become polarized by the applied electrical field, preventing the passage of current through the particle and causing it to behave like a nonconductor. On the other hand, to realize a significantly increased surface-to-volume ratio almost exclusively porous particles are used in the analytical and engineering sciences where packed beds are encountered as solid phase support for the devised reaction, separation, or purification of target compounds in view of high sample throughput or its complexity and where, consequently, a larger specific surface area is usually required (between 100 and 1000 $m^2 g^{-1}$, depending on application and needed pore sizes).

Apart from applications such as ion exchange and preparative liquid chromatography in which the particles' spatio-temporal surface charge pattern and EDL characteristics also become important for the retention of charged (bio)molecules,[53−57] a relatively young separation technique still more closely related to the above-mentioned electrokinetic phenomena (EO and EP) is capillary electrochromatography (CEC).[58−65] It combines the separation of molecules based on their differential partitioning between a stationary and mobile phase with the electrokinetically driven transport of liquid (EO) and an additional selectivity offered by a differential migration of charged molecules in an electrical field (EP). Typically, the 75−150 μm i.d. fused-silica capillaries are packed with 3−10 μm spherical, porous particles and fields up to 10^5 V/m are applied for moving electrolyte solution and solute through the fixed bed. Most common stationary phases in CEC are porous silica supports with chemically bonded surface groups[66−68] where the amount and accessibility of residual silanols influence the surface charge density and extent of electroosmotic flow (EOF). Compared to conventional hydraulic flow, the EOF is basically used for far superior hydrodynamic dispersion characteristics which allow more efficient separation of complex samples. A substantial fraction of the total EOF proceeds through the particles, depending on the intraparticle EDL overlap,[69−75] and further, the electrical conductivity of a column can be used to evaluate intraparticle ion transport and permeability.[76] Thus, in addition to the void space between particles, the intraparticle pore space and its relevant morphological parameters such as porosity, the shape, size distribution, and connectivity of pores play an important role in the total transport of ions and bulk liquid through a bed of porous particles. Vice versa, when an originally solid particle becomes permeable and conducting, consequences result for its electrophoretic mobility. As predicted by Miller et al.[77] and later verified to some extent experimentally by Miller and Berg,[78] the electrophoretic mobility of porous particles is expected to differ substantially from that of identical nonporous particles (being impermeable and nonconducting).

Due to the importance of porous support media with a hierarchy of length scales and resulting EDL overlap in many applications involving electrokinetic phenomena and the circumstance that the hard-sphere assumptions are violated, as well as the fact that only a very few electrokinetic data are available for porous particles, we conducted a systematic experimental study of electrophoretic and electroosmotic mobilities by using (otherwise similar) nonporous and porous silica-based, spherical particles with a different intraparticle porosity and mean pore size. This allowed us to realize a wide range of experimental conditions under which the EDL appeared either thin or thick with respect to intraparticle pore dimensions. Results obtained for the particles' electrophoretic mobility are discussed in view of the theoretical

(34) Solomentsev, Y. E.; Pawar, Y.; Anderson, J. L. *J. Colloid Interface Sci.* **1993**, *158*, 1.
(35) Dukhin, A. S.; Van de Ven, T. G. M. *J. Colloid Interface Sci.* **1994**, *165*, 9.
(36) Kang, S.-Y.; Sangani, A. S. *J. Colloid Interface Sci.* **1994**, *165*, 195.
(37) Ohshima, H. *J. Colloid Interface Sci.* **1997**, *188*, 481.
(38) Liu, Y. C.; Keh, H. J. *Langmuir* **1998**, *14*, 1560.
(39) Ennis, J.; Anderson, J. L. *J. Colloid Interface Sci.* **1997**, *185*, 497.
(40) Lee, E.; Chu, J.-W.; Hsu, J.-P. *J. Colloid Interface Sci.* **1999**, *209*, 240.
(41) Dukhin, A. S.; Shilov, V.; Borkovskaya, Y. *Langmuir* **1999**, *15*, 3452.
(42) Johnson, T. J.; Davis, E. J. *J. Colloid Interface Sci.* **1999**, *215*, 397.
(43) Ohshima, H. *J. Colloid Interface Sci.* **1999**, *210*, 397.
(44) Shugai, A. A.; Carnie, S. L. *J. Colloid Interface Sci.* **1999**, *213*, 298.
(45) Lee, E.; Lee, Y.-S.; Yen, F.-Y.; Hsu, J.-P. *J. Colloid Interface Sci.* **2000**, *223*, 223.
(46) Wei, Y. K.; Keh, H. J. *Langmuir* **2001**, *17*, 1437.
(47) Ding, J. M.; Keh, H. J. *J. Colloid Interface Sci.* **2001**, *236*, 180.
(48) Carrique, F.; Arroyo, F. J.; Delgado, A. V. *J. Colloid Interface Sci.* **2002**, *252*, 126.
(49) Chih, M.-H.; Lee, E.; Hsu, J.-P. *J. Colloid Interface Sci.* **2002**, *248*, 383.
(50) Keh, H. J.; Ding, J. M. *Langmuir* **2002**, *18*, 4572.
(51) Lin, W.-H.; Lee, E.; Hsu, J.-P. *J. Colloid Interface Sci.* **2002**, *248*, 398.
(52) Carrique, F.; Arroyo, F. J.; Jiménez, M. L.; Delgado, A. V. *J. Phys. Chem. B* **2003**, *107*, 3199.
(53) Liu, H.; Cantwell, F. F. *Anal. Chem.* **1991**, *63*, 993.
(54) Hågglund, I.; Ståhlberg, J. *J. Chromatogr., A* **1997**, *761*, 3.
(55) Okada, T. *Anal. Chem.* **1998**, *70*, 1692.
(56) Ståhlberg, J. *J. Chromatogr., A* **1999**, *855*, 3.
(57) Dziennik, S. R.; Belcher, E. B.; Barker, G. A.; DeBergalis, M. J.; Fernandez, S. E.; Lenhoff, A. M. *Proc. Natl. Acad. Sci. U.S.A.* **2003**, *100*, 420.
(58) Walhagen, K.; Unger, K. K.; Hearn, M. T. W. *J. Chromatogr., A* **2000**, *887*, 165.
(59) Pyell, U. *J. Chromatogr., A* **2000**, *892*, 257.
(60) Tang, Q. L.; Lee, M. L. *Trends Anal. Chem.* **2000**, *19*, 648.
(61) *Capillary Electrochromatography*; Deyl, Z., Svec, F., Eds.; Elsevier: Amsterdam, 2001.
(62) Bartle, K. D.; Myers, P. *J. Chromatogr., A* **2001**, *916*, 3.
(63) Rathore, A. S. *Electrophoresis* **2002**, *23*, 3827.
(64) Mistry, K.; Krull, I.; Grinberg, N. *J. Sep. Sci.* **2002**, *25*, 935.
(65) Rapp, E.; Tallarek, U. *J. Sep. Sci.* **2003**, *26*, 453.
(66) Robson, M. M.; Cikalo, M. G.; Myers, P.; Euerby, M. R.; Bartle, K. D. *J. Microcolumn Sep.* **1997**, *9*, 357.
(67) Fujimoto, C. *Trends Anal. Chem.* **1999**, *18*, 291.
(68) Matyska, M. T.; Pesek, J. J.; Boysen, I.; Hearn, M. T. W. *Electrophoresis* **2001**, *22*, 2620.
(69) Venema, E.; Kraak, J. C.; Poppe, H.; Tijssen, R. *J. Chromatogr., A* **1999**, *837*, 3.
(70) Vallano, P. T.; Remcho, V. T. *Anal. Chem.* **2000**, *72*, 4255.
(71) Stol, R.; Poppe, H.; Kok, W. Th. *Anal. Chem.* **2001**, *73*, 3332.
(72) Tallarek, U.; Rapp, E.; Seidel-Morgenstern, A.; Van As, H. *J. Phys. Chem. B* **2002**, *106*, 12709.
(73) Dearie, H. S.; Smith, N. W.; Moffat, F.; Wren, S. A. C.; Evans, K. P. *J. Chromatogr., A* **2002**, *945*, 231.
(74) Tallarek, U.; Pačes, M.; Rapp, E. *Electrophoresis* **2003**, in press. DOI 10.1002/elps.200305673.
(75) Tallarek, U.; Rapp, E.; Sann, H.; Reichl, U.; Seidel-Morgenstern, A. *Langmuir* **2003**, *19*, 4527.
(76) Vallano, P. T.; Remcho, V. T. *J. Phys. Chem. B* **2001**, *105*, 3223.
(77) Miller, N. P.; Berg, J. C.; O'Brien, R. W. *J. Colloid Interface Sci.* **1992**, *153*, 237.
(78) Miller, N. P.; Berg, J. C. *J. Colloid Interface Sci.* **1993**, *159*, 253.

work by Miller et al.,[77] and they are confirmed by electroosmotic mobility measurements in packed capillaries.

2. Theoretical Background

In their theoretical analysis of the electrophoretic mobility μ_{EP} of a permeable, conducting porous particle, Miller et al.[77] considered a model spherical porous aggregate of radius R_s consisting of numerous, much smaller discrete hard spheres of radius r_s. Fluid flow within the randomly packed matrix of dielectric spheres was modeled with the Kuwabara form[79] of the unit cell model which had been adapted by Levine and Neale[19] for EOF through a bed (or swarm) of spheres. Thus, characteristic pore dimensions inside an aggregate depend on the diameter of the impermeable and nonconducting primary particles (of uniform size and shape), as well as on the particle volume fraction φ within the aggregate. The main result of the analysis by Miller et al.[77] was to predict the dependence of μ_{EP} on zeta-potential (ζ):

$$\mu_{EP} = \left(1 + \frac{\varphi}{2}\right)\left(\frac{2\epsilon_0\epsilon_r\zeta}{3\eta} + \frac{\epsilon_0\epsilon_r\psi_a F_{EO}}{3\eta}\right) \qquad (1)$$

where ϵ_0, ϵ_r, and η are the permittivity of a vacuum and the relative permittivity and viscosity of the electrolyte solution, respectively. ζ is the shear plane potential exhibited by one of the discrete (and hard) primary particles when disconnected from the aggregate and subjected to an electrophoretic mobility measurement. ψ_a is the shear plane potential at the solid−liquid interface within a porous aggregate (which may be identified with ζ).[19]

Equation 1 results from a consideration of two phenomena.[77] First, the presence of conducting electrolyte in the aggregate introduces a normal component to the electrical field at its outer surface as field lines start bending toward the aggregate. This reduces the field's tangential component, but because the latter determines the aggregate's observable electrophoretic motion, μ_{EP} is expected to decrease compared to that of a solid particle. It becomes more pronounced as the amount of entrained conducting liquid increases. Second, the charged solid−liquid interface inside an aggregate enables the generation of internal EOF. The factor F_{EO} in eq 1 takes into account the electroosmotic mobility with respect to an aggregate frame of reference. This jetting effect tends to increase μ_{EP}. While the rather complex expression for F_{EO} derived by Levine and Neale[19] does not need to be repeated here, a dependence of F_{EO} on r_s/λ_D at different porosities is shown in Figure 1 because of its importance for the upcoming discussion in view of intraparticle EDL overlap. The EDL thickness is characterized via the Debye screening length (λ_D):[1,2]

$$\lambda_D = \left(\frac{\epsilon_0\epsilon_r RT}{F^2\sum_i z_i^2 c_{i,\infty}}\right)^{1/2} \qquad (2)$$

where R is the gas constant, T is absolute temperature, F is Faraday's constant, z_i is the valency of ionic species i, and $c_{i,\infty}$ is its concentration in electroneutral solution. Depending on the EDL overlap (represented by r_s/λ_D) and internal void space or porosity (with $\epsilon_{intra} = 1 - \varphi$), F_{EO}

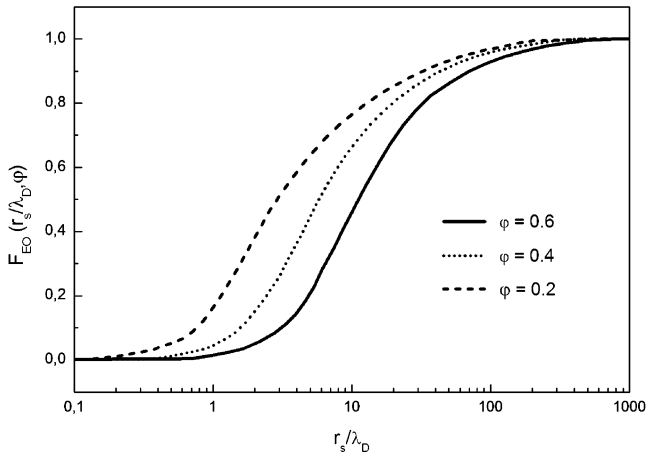

Figure 1. Electroosmotic flow factor F_{EO} vs r_s/λ_D for different void fractions $\epsilon_{intra} = 1 - \varphi$ in a spherical aggregate consisting of much smaller hard spheres with radius r_s and total solid volume fraction φ (adapted from Levine and Neale, ref 19).

gives the actual amount of EOF through an aggregate:[77]

$$\mathbf{u}_{EO} = -\frac{\epsilon_0\epsilon_r\psi_a\mathbf{E}}{\eta}F_{EO}(r_s/\lambda_D,\varphi) \qquad (3)$$

where $\mathbf{u}_{EO}$ and $\mathbf{E}$ are the volume-averaged fluid velocity and electrical field within the aggregate. Any pressure-driven flow through the porous aggregate is neglected. As demonstrated by Figure 1, F_{EO} for $0 < \varphi < 1$ asymptotically approaches zero and unity in the limits of $r_s/\lambda_D \to 0$ and $r_s/\lambda_D \to \infty$, respectively. While the lower limit corresponds to complete EDL overlap between neighboring unit cells of the model[77] or in the void space of a single porous particle, in general, the upper limit ($F_{EO} = 1$) is consistent with Smoluchowski's classical result for EOF within a porous medium of arbitrary pore geometry (when surface conductance is negligible) including porosity and pore size and shape.[80] Thus, $\mathbf{u}_{EO}$ decreases sharply as the EDL interaction in the porous aggregate increases. A similar behavior is recognized for EOF through open capillaries and the void space of random sphere packings.[81−85]

3. Experimental Section

Physical data of the (non)porous, spherical-shaped C18-silica particles relevant to the present study are summarized in Table 1. As can be seen, while these particles have an almost identical averaged diameter, the intraparticle porosity and mean pore sizes are systematically varied which allowed us to address the influence of an intraparticle EDL overlap (r_{pore}/λ_D) and solid volume fraction (φ or $\epsilon_{intra} = 1 - \varphi$) in our measurements of electrophoretic and electroosmotic mobility. Silica-based particles were received as research samples from Merck KGaA (Darmstadt, Germany), together with mercury intrusion and nitrogen adsorption data needed for determining intraparticle pore volume and surface area, respectively. As the mean pore diameter increases, the surface-to-volume ratio decreases significantly, and it is expectedly least for nonporous particles. The size distributions were characterized on a CILAS 1180 laser particle size analyzer (CILAS, Marcoussis, France) using dilute suspensions in 2-propanol. All particles used in our work show the same surface chemistry. Part of the activated silanol groups of the original native silica material are covalently bonded to C18-chains by reaction with suitable silanes. They are responsible

(79) Kuwabara, S. *J. Phys. Soc. Jpn.* **1959**, *14*, 527.

(80) Smoluchowski, M. *Z. Phys. Chem.* **1918**, *93*, 123.
(81) Rice, C. L.; Whitehead, R. *J. Phys. Chem.* **1965**, *69*, 4017.
(82) Knox, J. H.; Grant, I. H. *Chromatographia* **1991**, *32*, 317.
(83) Wan, Q.-H. *Anal. Chem.* **1997**, *69*, 361.
(84) Cikalo, M. G.; Bartle, K. D.; Myers, P. *J. Chromatogr., A* **1999**, *836*, 35.
(85) Arulanandam, S.; Li, D. Q. *Colloids Surf., A* **2000**, *161*, 89.

Table 1. Physical Data for the (Non)Porous Silica-Based Particles

particles	d_p [μm][a]	V_{pore} [mL/g]	d_{pore} [nm][b]	ϵ_{intra}[c]	r_{pore}/λ_D[d]	A_s [m^2/g][e]
porous spheres	2.45	0.88	41	0.66	0.6−12.8	64.7
	2.46	0.65	105	0.59	1.6−32.8	21.1
	2.42	0.34	232	0.43	3.6−72.5	7.5
nonporous	2.45					ca. 1[f]

[a] Refers to the external surface-averaged value ($d_p = 2R_s$). [b] Mean intraparticle pore diameter based on mercury porosimetry ($d_{pore} = 2r_{pore}$). [c] Intraparticle porosity calculated according to $\epsilon_{intra} = (1 + (1/\rho_{SiO}V_{pore}))^{-1}$, with ρ_{SiO} (density of the silica skeleton) taken as 2.24 g/mL. [d] For the range of buffer concentrations encountered in this work (1×10^{-4} to 4×10^{-2} M Tris). [e] Specific surface area based on the nitrogen adsorption data. [f] Finite, albeit small, because of the solid particles' external surface area.

for the hydrophobic nature of these surfaces, while residual silanol groups provide the surface charge. For modern particle and bonding technologies, it is possible to reproduce both the surface coverage of the bonded phase and residual silanol activity within 3%.[86]

Electrophoretic mobilities were measured at 298 K on a Zetasizer 3000 (Malvern Instruments Ltd., Worcestershire, U.K.) based on standard operation. The reported values for μ_{EP} (simply the ratio of particle velocity to the applied electrical field) represent an average of five independent runs. For the acquisition of electroosmotic mobilities, the ratio of the EOF velocity to the applied electrical field, stationary sphere packings (i.e., fixed beds) had to be prepared. For this purpose, 100 μm i.d., 360 μm o.d. fused-silica capillaries (Polymicro Technologies, Phoenix, AZ) were packed according to the slurry technique[86] using a WellChrom K-1900 pneumatic pump (Knauer GmbH, Berlin, Germany). Slurries were made from 10 mg of dry material and 100 μL of ethanol under gentle ultrasonication for 10 min. Glass-lined metal tubing (500 μm i.d.) was used as a reservoir into which the slurries were injected for the packing process. The pressure then was adjusted between 150 and 350 bar with respect to mean intraparticle pore sizes to avoid particle damage during further compaction of the beds toward random close sphere packings. Temporary outlet frits for the packing were provided by prepunched glass-fiber filters fixed in the zero-dead-volume unions (Upchurch Scientific, Oak Harbor, WA) to which all open-tubular capillaries were first connected. After having forced water as the pushing liquid for about 20 min at selected pressure through the packed capillaries, desired bed lengths of between 30 and 40 cm were reached. The permanent inlet and outlet frits were prepared by controlled particle sintering via heating with an arc fusion splicer FSM-05S (Fujikura, Tokyo, Japan) in its prefusion mode. Finally, the remainder of the particles was washed out and the union was removed.

The packed capillary columns were assembled in a HP^{3D}CE capillary electrophoresis instrument (Hewlett-Packard, Waldbronn, Germany) which allowed us to generate gradients in electrical potential from 0 to 30 kV between both ends of a capillary column. Measurements were made at a controlled temperature of 298 K. Electroosmotic mobilities μ_{EO} were calculated using the actual potential drop over a bed and residence time distributions of an unretained, uncharged flow field marker (which provides the mobile phase linear velocity) transported through the column by molecular diffusion and EOF. Thiourea was used for that purpose, and the standard photodiode array detector of the instrument was used to monitor its absorbance at 235 nm. Thiourea samples prepared in running mobile phase were injected electrokinetically (+5 kV for 3 s). An external helium pressure of 10 bar was exerted on both inlet and outlet mobile phase vials for minimizing bubble formation. EOF velocities were measured at typically 10 different field strengths, with μ_{EO} calculated as the slope of a linear dependence. Development of Joule heat was negligible in these experiments.

Tris(hydroxymethyl)aminomethane (Tris) buffer solutions in 80:20 acetonitrile/water (v/v) were used as the liquid electrolyte.

(86) Neue, U. D. *HPLC Columns*: *Theory, Technology, and Practice*; Wiley-VCH: New York, 1997.

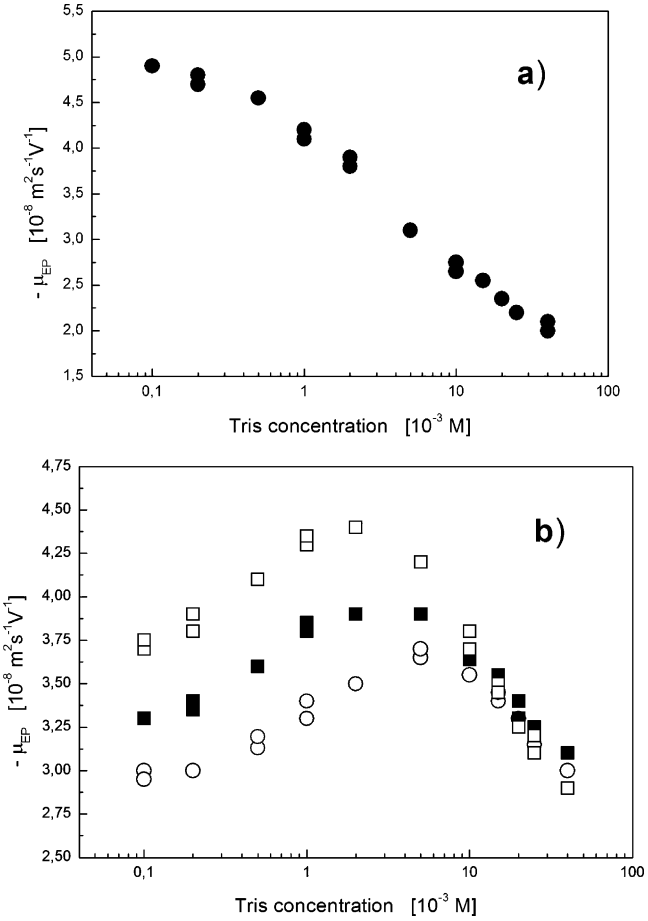

Figure 2. Electrophoretic mobility of the spherical-shaped, silica-based particles (Table 1) depending on the mobile phase concentration of Tris buffer: (a) nonporous particles (●); (b) porous particles with a mean intraparticle pore diameter (d_{pore}) of 41 nm (○), 105 nm (■), and 232 nm (□), respectively. The mobile phase ionic strength is half of the Tris concentration.

Mobile phases were filtered over a 0.45 μm nylon membrane filter and degassed by ultrasonication. An aqueous stock solution of 0.2 M Tris (the base form) was prepared using water purified on a Milli-Q-Gradient (Millipore GmbH, Eschborn, Germany), and the pH was adjusted to 8.3 by titration with concentrated hydrochloric acid. Appropriate volumes of this stock solution, MilliQ water, and HPLC grade acetonitrile were mixed to yield the Tris buffer solutions of desired ionic strength in 80:20 acetonitrile/water (v/v) covering the range from 1×10^{-4} to 4×10^{-2} M effective Tris concentration; for example, 2×10^{-3} M Tris in the final mobile phase corresponds to 0.01 M Tris in the aqueous part. The concentration of protonated Tris (acid form) needed for estimating the EDL thickness by means of λ_D (eq 2) was calculated from the Henderson−Hasselbalch equation with pH ≈ pK_a. For measurement of μ_{EO}, packed capillaries were preconditioned electrokinetically (using separate mobile phase vials) by applying a voltage of 5 kV for 10 min and then a voltage ramp up to 20 kV in 15 min and holding this final voltage over another 10 min. For measurement of μ_{EP}, 5 mg of the particles were suspended in 20 mL of degassed buffer under gentle ultrasonication, followed by overnight stirring in a rotary shaker. The relative permittivity (ϵ_r) and viscosity (η) at 298 K of the final 80:20 acetonitrile/water (v/v) electrolyte solutions were taken as 44.53 and 5.03×10^{-4} kg/(m·s), respectively.[87]

4. Results and Discussion

We first present results for electrophoretic mobilities and analyze individual contributions. Figure 2 demonstrates the influence of mobile phase Tris concentration

(87) Banholczer, A.; Pyell, U. *J. Chromatogr., A* **2000**, *869*, 363.

on μ_{EP} of the nonporous and porous silica-based particles (cf. Table 1 for particle characteristics). The dependence for nonporous spheres seen in Figure 2a reveals normal electrokinetic behavior in the sense that as the ionic strength of the liquid increases, the EDL is compressed, resulting in a reduced shear plane potential at the solid−liquid interface.[1] The thickness of the EDL remained small with respect to the particle radius over the whole range of buffer concentrations, that is, $38 < R_s/\lambda_D < 766$ (R_s denotes the radius of a macroscopic particle). Thus, the assumption of a thin EDL is valid on the particle scale ($R_s/\lambda_D \gg 1$) throughout the present study including all media. The continuously decreasing values of μ_{EP} at increasing Tris concentration (Figure 2a) then represent an electrokinetic behavior that is expected, at least qualitatively, for solid dielectric spheres with less significant contribution from surface conductance (over a range of mobile phase ionic strengths encountered in our work). It is noteworthy because conduction behind the shear plane may strongly influence and sometimes even overshadow usual EDL behavior, in particular at low electrolyte concentrations and higher values of ζ, leading to an increase of the electrokinetic mobility with ionic strength toward an intermediate, often just spurious maximum.[88−95] The magnitude of this effect further depends on the base material (although it has been predominantly investigated for polymer latices), surface modification, and post-treatments.

In striking contrast to the more or less familiar behavior of the hard spheres, the trend in μ_{EP} for the porous particles (Figure 2b) reveals distinct differences which obviously depend on the intraparticle porosity and actual extent of the EDL overlap and, thus, on the ratio r_{pore}/λ_D (the thin EDL assumption cannot be made inside these particles). With increasing concentration of Tris buffer from 1×10^{-4} M, the particle mobilities first increase and then move through a maximum at some particle-specific concentration between 1×10^{-3} and 1×10^{-2} M, followed by a decrease toward relatively common curves (above ca. 1×10^{-2} M Tris). Because all particles originated from the same base material, differences among porous spheres, as well as between the nonporous and porous spheres, in general, most probably can be related to the fact that porous particles are permeable for EOF and conducting depending on intraparticle porosity and pore sizes. To clarify the observed differences in view of these aspects, Figure 3 contrasts the typical behaviors. Here, the gray area separates regimes in which the mobility of either the nonporous or porous particles dominates over the other. At lower buffer concentrations, μ_{EP} for the solid spheres significantly exceeds that of any porous spheres encountered in this work (for clarity in a general comparison only the representative results for porous particles with $d_{pore} = 105$ nm are included in Figure 3). As indicated earlier, when an originally solid dielectric sphere is made permeable and conducting, the ratio of specific conductivities within the now-porous particle and bulk liquid

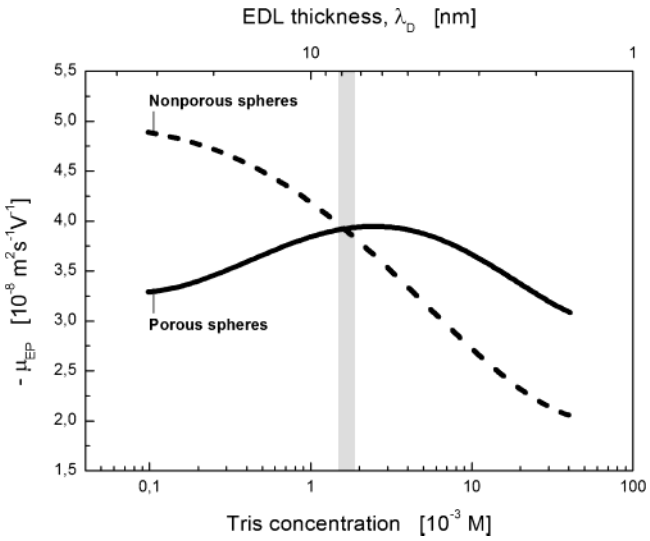

Figure 3. Comparison of spherical nonporous and porous (d_{pore} = 105 nm) silica-based particles in view of the electrophoretic mobilities depending on mobile phase ionic strength (which corresponds to half of the actual Tris concentration).

will increase from zero, bending electrical field lines toward the particle interior which reduces the tangential field component at a particle's external surface. Consequently, this contribution from the porosity effect reduces electrophoretic slip velocities associated with shear stress concentrated in the relatively thin EDL at the external solid−liquid interface, and it can explain the decreased values of μ_{EP} with respect to nonporous, dielectric spheres at lower buffer concentrations (Figure 3, between 1×10^{-4} and about 2×10^{-3} M Tris) where strong intraparticle EDL overlap prevails.

However, this contribution to μ_{EP} of the porous particles is more than compensated at increasing buffer concentration by the jetting effect due to intraparticle-forced EOF (relative to the solid skeleton of a particle and opposite to its electrophoretic motion). In contrast to the first effect, this phenomenon strongly depends on the buffer concentration and will begin to dominate μ_{EP} only when intraparticle EDL overlap is substantially reduced, enabling a significant amount of volumetric EOF through the particles (cf. F_{EO} in eq 1 and its dependence on r_s/λ_D in Figure 1). As evidenced by Figure 3, the jetting effect is responsible for an increasing mobility of permeable spheres between 1×10^{-4} and 2×10^{-3} M Tris (with $1.6 < r_{pore}/\lambda_D < 7.3$). The maximum in μ_{EP} then is a consequence of competitive contributions from this intraparticle EOF (increasing jetting effect) and the normal EDL behavior at the particles' external surface. The latter effect which ultimately dominates (leading to the decrease of μ_{EP} above 2×10^{-3} M Tris although EDL overlap continues to be further reduced) has already been recognized as the origin of a continuous mobility decrease at increasing buffer concentration for the nonporous spheres (Figure 2a). The presence of the jetting effect nevertheless can explain the finally higher values of μ_{EP} for these porous particles compared to the nonporous ones (see Figure 3 between 2×10^{-3} and 4×10^{-2} M Tris, with $7.3 < r_{pore}/\lambda_D < 32.8$).

To summarize, the unique dependence of electrophoretic mobilities of porous particles used in this work on ionic strength (Figure 2b) is a consequence of basically three contributions: (i) usual EDL behavior at the external particle surface leading to a decrease of mobility at increasing ionic strength, (ii) generation of intraparticle volumetric EOF (the jetting effect increases mobility at increasing ionic strength), and (iii) the dipole coefficient

(88) Van der Put, A. G.; Bijsterbosch, B. H. *J. Colloid Interface Sci.* **1983**, *92*, 499.
(89) Hidalgo-Álvarez, R.; Martín, A.; Fernández, A.; Bastos, D.; Martínez, F.; de las Nieves, F. J. *Adv. Colloid Interface Sci.* **1996**, *67*, 1.
(90) Lyklema, J.; Minor, M. *Colloids Surf., A* **1998**, *140*, 33.
(91) Folkersma, R.; van Diemen, A. J. G.; Stein, H. N. *Langmuir* **1998**, *14*, 5973.
(92) Johnson, P. R. *J. Colloid Interface Sci.* **1999**, *209*, 264.
(93) Löbbus, M.; van Leeuwen, H. P.; Lyklema, J. *Colloids Surf., A* **2000**, *161*, 103.
(94) Moncho, A.; Martínez-Lopez, F.; Hidalgo-Álvarez, R. *Colloids Surf., A* **2001**, *192*, 215.
(95) Hunter, R. *Adv. Colloid Interface Sci.* **2003**, *100*, 153.

of a porous particle which depends on its porosity but not on ionic strength. While the first contribution dominates overall mobility at higher ionic strengths (above 1×10^{-2} M Tris in Figure 2b) where, independent of actual intraparticle EDL overlap, mobilities for all porous particles are very similar and decreasing, the jetting effect, together with a different mean intraparticle pore size, is responsible for the increasing mobilities at lower ionic strengths and the different position of the maximum for μ_{EP} which shifts to higher ionic strength as the mean intraparticle pore size (and r_{pore}/λ_D) becomes smaller.

Based on the data in Figure 2b and Table 1, the actual porosity difference between particles, thereby referring to the last of the above-mentioned contributions, could also contribute to a shift of μ_{EP} to higher values at the increasing pore size because ϵ_{intra} concomitantly decreases. This would agree qualitatively with the theoretical analysis of Miller et al.[77] (eq 1), although the porosity, in addition, influences μ_{EP} oppositely via the jetting effect (Figure 1). In an intermediate regime of EDL interaction, both effects of a porosity difference (on the dipole coefficients and intraparticle EOF) may compensate each other or nearly so, while for sufficiently small and large values of r_{pore}/λ_D the former (conductivity) effect is expected to dominate.[77]

Before discussing these experimental results that have been obtained for the different particle porosities and systematic variation of intraparticle EDL overlap further in view of the work of Miller et al.,[77] we compare the dependence of μ_{EP} on ionic strength with the corresponding result for μ_{EO} summarized in Figure 4. These data confirm the substantially different electrokinetic behavior of porous versus nonporous spherical particles consisting of the same base material which has already been observed for μ_{EP} (Figure 2). In particular, we find again a continuous decrease of μ_{EO} with increasing Tris concentration for nonporous particles characterizing normal EDL behavior (Figure 4a), while the mobility for porous particles displays pronounced maxima which depend, because of the different intraparticle pore sizes, on mobile phase ionic strength in a particular case (Figure 4b). If we normalize the mobility data for porous particles with respect to the intraparticle EDL overlap (magnitude of the jetting effect) and plot μ_{EO} against r_{pore}/λ_D (Figure 5), we locate the mobility maxima at a similar r_{pore}/λ_D ratio of approximately 10, demonstrating a rather unique dependence of the jetting effect on intraparticle EDL overlap. The slight but systematic shift of this maximum toward lower values of r_{pore}/λ_D at a decreasing pore size (also evidenced by the data for μ_{EP} in Figure 2b) can be explained by the actual differences in R_s/λ_D at a given r_{pore}/λ_D ratio (because of a different λ_D but an almost identical R_s). This reflects the influence of the normal EDL behavior associated with the particles' external surface (cf. Figure 4a) and leads to the relatively stronger decrease in mobility as r_{pore} and λ_D become smaller at constant r_{pore}/λ_D for different particles (Figure 5). Partly in combination with a decreasing ϵ_{intra} (Table 1), that is, the same effect discussed earlier for μ_{EP} (porosity dependence of a particle's dipole coefficient), it is also responsible for the fact that this figure generally reveals higher values of μ_{EO} for particles with larger pore size.

Not unexpectedly, results for μ_{EO} based on the measurement of $\mathbf{u}_{EO}$ in random close packings of the employed spherical particles (fixed beds) did not reveal different electrokinetic behavior than observed by monitoring μ_{EP} for dilute suspensions of the same particles. This is related to the fact that relevant contributions to the overall mobility (jetting effect, dipole coefficient, normal EDL behavior) are similarly influenced by the particles' porosity and intraparticle EDL overlap in either type of experiment. However, one systematic difference is obvious and should be noted. While displaying a very similar behavior, the values for μ_{EO} are generally smaller than those for μ_{EP}. The offset may be largely removed by taking into account the tortuous nature of the pore space between particles in the random close sphere packings, a purely geometrical effect which reduces the macroscopically measured μ_{EO} in

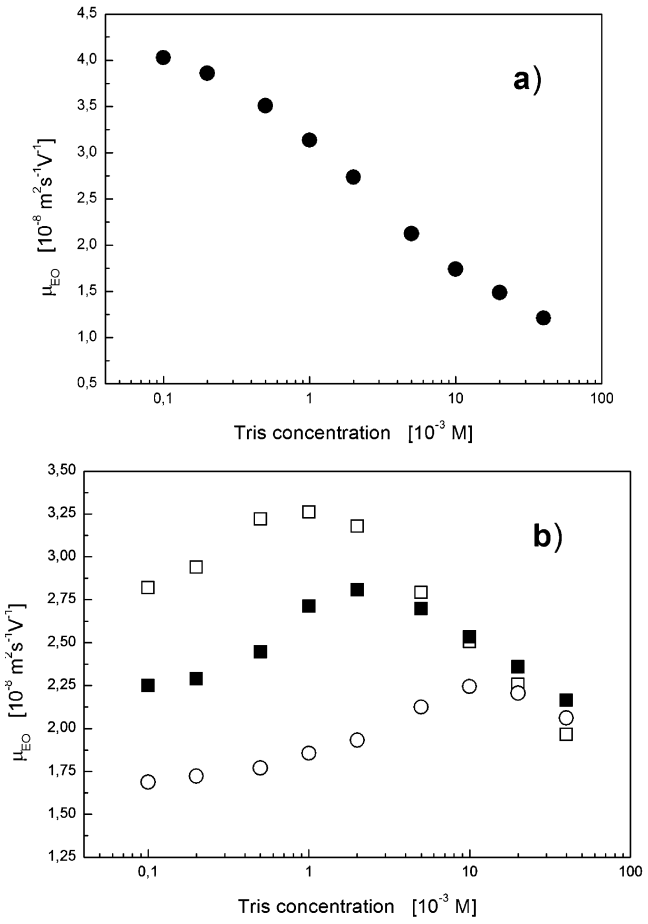

Figure 4. Electroosmotic mobility in fixed beds (packed capillary columns) of the spherical particles depending on the mobile phase Tris concentration: (a) nonporous particles (●); (b) porous particles with a mean intraparticle pore diameter (d_{pore}) of 41 nm (○), 105 nm (■), and 232 nm (□), respectively.

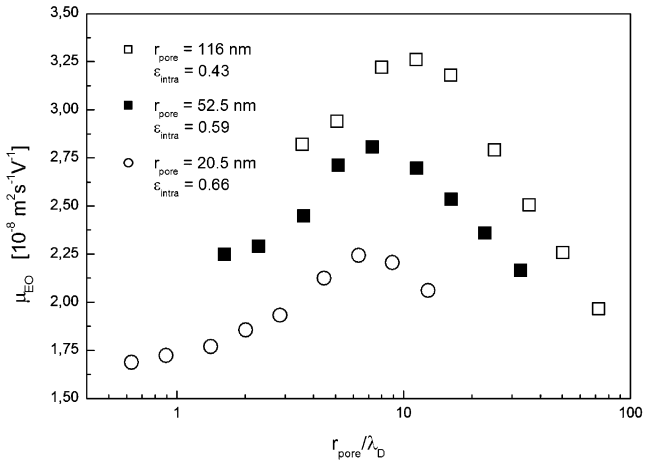

Figure 5. Electroosmotic mobility vs r_{pore}/λ_D for spherical porous particles with a different intraparticle mean pore size and porosity (cf. Table 1).

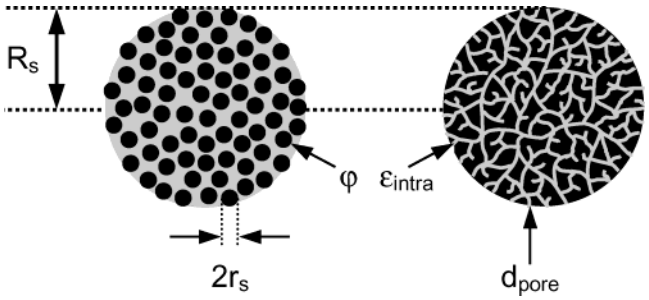

Figure 6. Representation of an aggregated spherical porous particle of radius R_s (with solid volume fraction φ and uniform subparticle diameter d_s) and the particles used in this work (with void fraction ϵ_{intra} and mean pore diameter d_{pore}). In both cases, the pore space morphology and surface chemistry are assumed to be effectively isotropic on the particle scale.

such dense particle systems relative to μ_{EP} for the dilute suspension of an electrophoresis experiment.[96−98]

The consistent dependencies of μ_{EP} and μ_{EO} on both intraparticle porosity and EDL overlap demonstrate a substantially different electrokinetic behavior for porous compared to nonporous particles which has been predicted by Miller et al.[77] However, the final comparison of our data with their theoretical description becomes somehow difficult by a different generation of the pore space morphology within an aggregate or a particle. While porosity and pore size distribution are easily introduced and become adjustable via the diameter and arrangement of much smaller primary particles for a hierarchically structured spherical aggregate,[77,99] porous particles used in this work do not resemble that design. They have been prepared according to the sol−gel process which results in a different microstructure schematically shown in Figure 6. It does not appear straightforward to translate the pore space morphology imposed by the diameter, spatial distribution, and final volume fraction of solid spheres within the aggregate to another particle architecture (e.g., in view of r_s/λ_D vs r_{pore}/λ_D), even though for some special cases the mean size of voids between particles may be estimated based on a touching sphere model.

Consequently, we will compare our results only qualitatively with implications originating from the theoretical work of Miller et al.[77] Based on their analysis, Figure 7 illustrates the dependence of μ_{EP} of a spherical aggregate on EDL overlap (r_s/λ_D) and void volume fraction ($\epsilon_{intra} = 1 - \varphi$) within the aggregate (cf. Figure 6) assuming that the shear plane potential for EOF remains constant and, thus, could be taken as the usual zeta-potential defined for an isolated, discrete solid particle (constant potential assumption concerning EDL overlap in the pores of the aggregate, $\psi_a \equiv \zeta$ in eq 1).[19,77] Figure 7 includes, as a baseline for a better comparison, the mobility of a solid dielectric sphere with $\zeta = 25$ mV and $R_s/\lambda_D \gg 1$. While μ_{EP} decreases with φ at r_s/λ_D below unity due to the normal field component introduced at the outer surface of an aggregate by its conducting interior, this decrease is soon overcompensated with respect to the solid sphere behavior by the jetting effect ($r_s/\lambda_D \geq 7$). As φ is decreasing, the magnitude of this contribution to μ_{EP} can increase significantly in an intermediate r_s/λ_D range (cf. Figure 1)

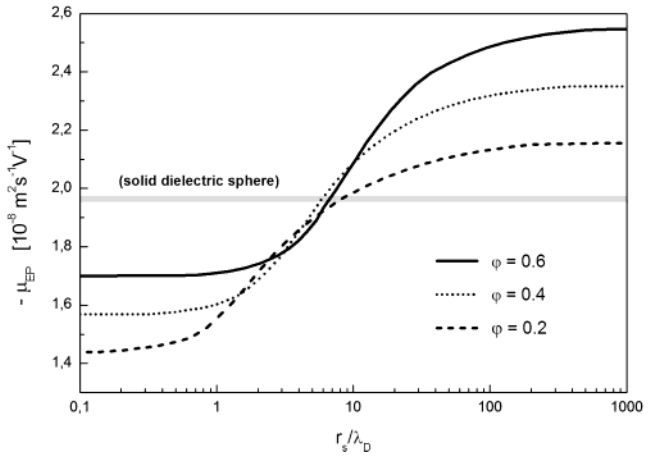

Figure 7. Electrophoretic mobility predicted for a spherical-shaped porous aggregate comprised of solid spheres with $\zeta = 25$ mV and $r_s \ll R_s$ based on the theoretical analysis of Miller et al. (ref 77) (eq 1). The mobile phase is assumed to consist of 80:20 acetonitrile/water (v/v) electrolyte solutions, with $\epsilon_r = 44.53$ and $\eta = 5.03 \times 10^{-4}$ kg/(m·s) at 298 K. F_{EO} at a given r_s/λ_D and φ is obtained from Figure 1.

and, together with the influence of φ on the aggregate's dipole coefficient, porosity differences do not have a strong impact on the net mobility in this regime (Figure 7).

Predictions in Figure 7 indicate that the mobility of a porous aggregate will be significantly less than that of a solid sphere for $r_s/\lambda_D \leq 1$ and significantly greater for $r_s/\lambda_D \geq 20$.[77] They are in qualitative agreement with our experimentally observed dependence of electrokinetic mobility on intraparticle EDL overlap (r_{pore}/λ_D) and porosity (ϵ_{intra}). For example, the data in Figures 2−5 indicate mobility maxima for both μ_{EP} and μ_{EO} of the porous particles in a range $5 < r_{pore}/\lambda_D < 10$. This, in turn, compares favorably with predictions concerning dominating contributions to mobility (with respect to the behavior of a solid sphere) from either a particle's dipole coefficient or the jetting effect, but for obvious reasons (Figure 6) r_s/λ_D is used to characterize EDL interaction in a porous aggregate with known r_s, while it seems straightforward to use r_{pore}/λ_D when the pore size distribution and r_{pore} are available. Apart from the two operative effects (i.e., conducting particle interior and intraparticle EOF) which were shown to cancel each other at specific ionic strengths, another phenomenon relevant to our study is the normal EDL behavior at a particle's external surface. This modifies the reference behavior of the solid, dielectric sphere and asymptotic trends for μ_{EP} of a porous aggregate at low and high r_s/λ_D (Figure 7) accordingly.[78]

5. Conclusions

The experimentally observed dependence on mobile phase ionic strength of electrophoretic and electroosmotic mobilities has revealed substantially different behavior for porous (permeable and conducting) as compared to similar but nonporous (impermeable and nonconducting) spherical particles. While R_s/λ_D remains almost identical for all particles encountered in this work (depending only on ionic strength), r_{pore}/λ_D is further determined by a particular type of porous spheres (Table 1). In addition to the influence of the intraparticle porosity on both μ_{EP} and μ_{EO}, the contribution from the intraparticle EOF has been studied systematically in view of EDL overlap covering the range $0.6 \leq r_{pore}/\lambda_D \leq 72.5$. This, in turn, has allowed us to discriminate between competitive contributions to mobility from a particle's dipole coefficient (intraparticle conductivity) and the jetting effect (intraparticle perme-

(96) Rathore, A. S.; Horváth, Cs. *Anal. Chem.* **1998**, *70*, 3069.
(97) Rathore, A. S.; Wen, E.; Horváth, Cs. *Anal. Chem.* **1999**, *71*, 2633.
(98) Sánchez Muñoz, O. L.; Pérez Hernández, E.; Lämmerhofer, M.; Lindner, W.; Kenndler, E. *Electrophoresis* **2003**, *24*, 390.
(99) Reeder, D. H.; Clausen, A. M.; Annen, M. J.; Carr, P. W.; Flickinger, M. C.; McCormick, A. V. *J. Colloid Interface Sci.* **1996**, *184*, 328.

ability), consistently demonstrated for μ_{EP} (Figures 2 and 3) and μ_{EO} (Figures 4 and 5) with respect to the normal EDL behavior characterizing the nonporous particles. Because most technological and analytical processes involving electrokinetic transport phenomena in porous media like particulate beds use permeable and conducting base material, our results strengthen the importance of the resolved phenomena which can so markedly change electrokinetic behavior compared to solid supports.[77,78] Further, the dependence of macroscopic electrokinetic transport coefficients on the actual pore space morphology, the nature of the surface, and electrolyte properties is of fundamental relevance because it critically guides performance and the design strategies of a particular electrokinetic process with respect to alternative diffusive−convective transport schemes.

Acknowledgment. We are grateful to Dieter Lubda from Merck KGaA (Darmstadt, Germany) for the preparation and characterization of the particle research samples. We further acknowledge financial support by the Landesgraduiertenförderung Sachsen-Anhalt. The authors thank Bernd Ebenau and Dr. Werner Hintz (Institut für Verfahrenstechnik, Otto-von-Guericke-Universität Magdeburg, Germany) for their help with the electrophoretic mobility measurements.

LA0355141

Quantitative Study of Electrokinetic Transport in Porous Media by Confocal Laser Scanning Microscopy

Ulrich Tallarek,*,† Erdmann Rapp,† Heiner Sann,‡ Udo Reichl,†,‡ and Andreas Seidel-Morgenstern†,‡

Institut für Verfahrenstechnik, Otto-von-Guericke-Universität Magdeburg, Universitätsplatz 2, D-39106 Magdeburg, Germany, and Max-Planck-Institut für Dynamik komplexer technischer Systeme, Sandtorstraβe 1, D-39106 Magdeburg, Germany

Received February 3, 2003. In Final Form: March 26, 2003

Refractive index matching of liquid and solid phases in a bed of porous spherical glass beads allowed the use of confocal laser scanning microscopy for a quantitative study of intraparticle electrokinetic transport phenomena. By recording transient profiles of fluorescent, charged, and uncharged tracers, a significantly faster mass transfer was demonstrated for the electrokinetically enhanced transport as compared to a diffusion-limited process. Intraparticle electroosmotic and electrophoretic migration velocities were found to produce nonsymmetric distributions of tracer inside a sphere, contrasting with the symmetric profiles observed for diffusive transport.

Mass transport in porous media induced by an external electrical field which is superimposed on internal fields plays a central role in a variety of analytical, technological and environmental processes, including the dewatering of waste sludge, soil remediation, capillary electrophoresis, or chromatographic separations on microfluidic devices.[1−8] One of the key problems is a still deficient mechanistic understanding of the interrelation between external control variables and electrokinetic transport coefficients which depends on the surface's physicochemical nature, the pore space morphology, and properties of the saturating liquid. The characterization of these parameters is of fundamental relevance, as it critically guides the performance and compelling advantages, as well as design strategies of a particular electrokinetic process with respect to alternative diffusive−convective transport schemes.

We have implemented confocal laser scanning microscopy for a study of electrokinetic transport phenomena in a bed of spherical, porous particles. Optical transparency is a prerequisite for analyzing quantitatively at any depth inside particles the distribution profile of (un)charged fluorescent molecules during their uptake in (or release from) single beads in view of the mass transfer mechanisms operating under the influence of an externally applied electrical field. For this purpose we used a dynamic, widely applicable approach for matching the refractive index of the liquid to that of the solid skeleton of the particles. For the first time we have visualized that electrokinetic species transport through a fixed bed of spheres produces, in striking contrast to the symmetric-spherical distributions observed for diffusion-limited operations, pronounced asymmetric concentration profiles inside the particles. We could demonstrate that this behavior is caused by the unidirectional character of electroosmosis and electrophoresis, contrasting with the stochastic nature of Brownian motion, and that it forms the basis for a significantly faster intraparticle mass transfer compared to the diffusion-limited kinetics. Further, quantitative image analysis permitted a direct determination of the velocities of the underlying intraparticle-forced electroosmotic convection and electrophoretic migration. Obtained with a unique device, these important results are seen as the first in an upcoming series of studies using confocal laser scanning microscopy for characterizing salient features of electrokinetic transport in originally opaque particulate and monolithic structures. The flexible experimental configuration devised for that purpose is described in Figure 1.

Proposed by Minsky,[9] confocal microscopy has been intensively used in biology over the past decades.[10] It was only recently that its potential has been explored and utilized for applications in chemistry and physics,[11−21] particularly (in view of the present work) with respect to the mass transfer characteristics in porous beads used for a variety of applications, including ion exchange

* To whom correspondence should be addressed. Fax: +49 (0)-391-67-12028. E-mail: ulrich.tallarek@vst.uni-magdeburg.de.

† Otto-von-Guericke-Universität.

‡ Max-Planck-Institut.

(1) Ho, S. V.; Sheridan, P. W.; Athmer, C. J.; Heitkamp, M. A.; Brackin, J. M.; Weber, D.; Brodsky, P. H. *Environ. Sci. Technol.* **1995**, *29*, 2528.

(2) Tsuda, T., Ed. *Electric Field Applications in Chromatography, Industrial and Chemical Processes*; VCH: Weinheim, 1995.

(3) Acar, Y. B.; Ozsu, E. E.; Alshawabkeh, A. N.; Rabbi, M. F.; Gale, R. J. *CHEMTECH* **1996**, *26*, 40.

(4) Jennings, A. A.; Mansharamani, P. *Environ. Modell. Software* **1999**, *14*, 624.

(5) Bruin, G. J. M. *Electrophoresis* **2000**, *21*, 3931.

(6) Colón, L. A.; Burgos, G.; Maloney, T. D.; Cintrón, J. M.; Rodríguez, R. L. *Electrophoresis* **2000**, *21*, 3965.

(7) Polson, N. A.; Hayes, M. A. *Anal. Chem.* **2001**, 312A.

(8) Delgado, A. V., Ed. *Interfacial Electrokinetics and Electrophoresis*; Marcel Dekker: New York, 2002.

(9) Minsky, M. U.S. Patent 3,013,467 (Dec. 19, 1961); *Scanning* **1988**, *10*, 128.

(10) Pawley, J. B., Ed. *Handbook of Biological Confocal Microscopy*; Plenum: New York, 1995.

(11) Malmsten, M.; Xing, K.; Ljunglöf, A. *J. Colloid Interface Sci.* **1999**, *220*, 436.

(12) Whipple, W. L.; Maltesh, C. *Langmuir* **2000**, *16*, 3124.

(13) Barone, J. R.; Wang, S. Q.; Farinha, J. P. S.; Winnik, M. A. *Langmuir* **2000**, *16*, 7038.

(14) Song, Y.; Srinivasarao, M.; Tonelli, A.; Balik, C. M.; McGregor, R. *Macromolecules* **2000**, *33*, 4478.

(15) Velev, O. D.; Kaler, E. W.; Lenhoff, A. M. *J. Phys. Chem. B* **2000**, *104*, 9267.

(16) Hoheisel, W.; Jacobsen, W.; Lüttge, B.; Weiner, W. *Macromol. Mater. Eng.* **2001**, *286*, 663.

(17) Spiess, A.; Kasche, V. *Biotechnol. Prog.* **2001**, *17*, 294.

(18) Fergg, F.; Keil, F. J.; Quader, H. *Colloid Polym. Sci.* **2001**, *279*, 61.

(19) Reichert, U.; Linden, T.; Belfort, G.; Kula, M.-R.; Thömmes, J. *J. Membr. Sci.* **2002**, *199*, 161.

(20) Bromley, E. H. C.; Hopkinson, I. *J. Colloid Interface Sci.* **2002**, *245*, 75.

(21) Lowry, M.; He, Y.; Geng, L. *Anal. Chem.* **2002**, *74*, 1811.

10.1021/la034183p CCC: $25.00
Published on Web 04/25/2003

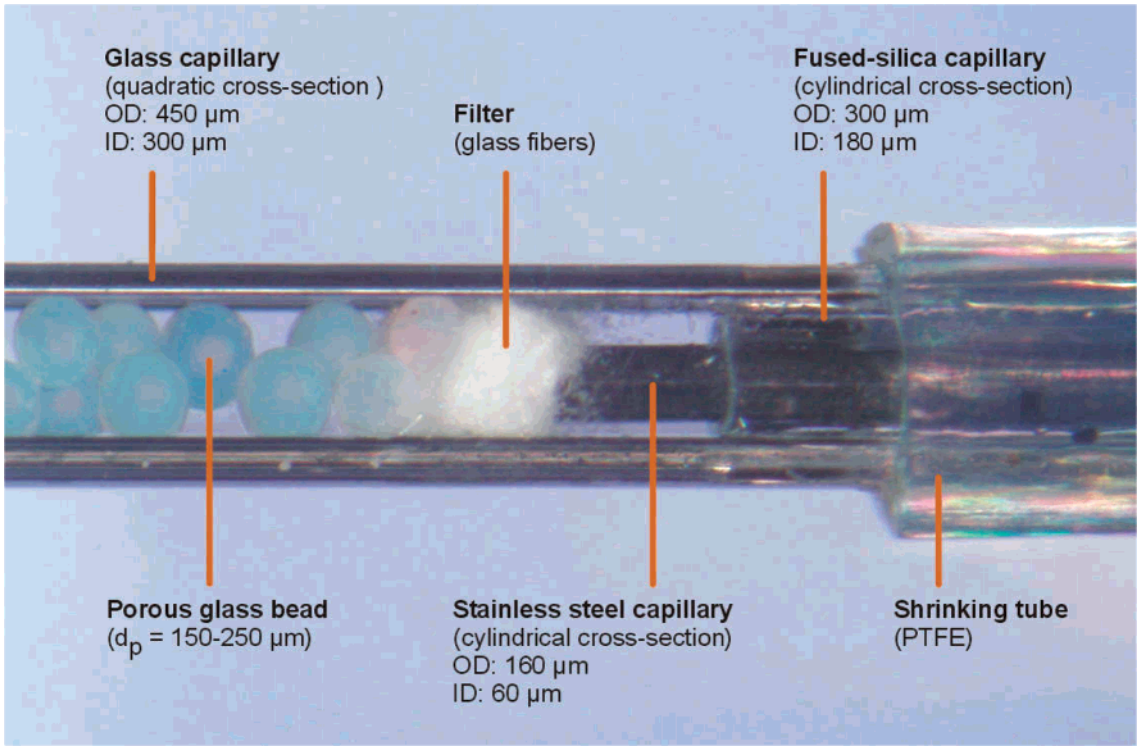

Figure 1. Inlet section of the packed capillary configuration used for studying electrokinetic transport phenomena in single porous particles. Spherical native glass beads have an average intraparticle pore size of 120 nm (Schuller, Steinach, Germany). Stainless steel capillaries at both ends of the setup (close to the packing) are used as electrodes.

chromatography, solid-phase synthesis, or controlled drug delivery.[22−26] To our knowledge, electrokinetic transport processes have not been investigated so far by quantitative confocal microscopy. On the other hand, miniaturization demands for electrokinetically controlled mass flux in capillary columns, as well as in microfluidic devices, are excellently suited for implementation with a confocal microscope. A key feature of this instrument is a pinhole (confocal aperture) in the detection optics which excludes light from all but that location in the focal plane where the laser beam is focused (confocal spot).[27] Two-dimensional images can be generated by sweeping the specimen, for example, a single porous particle (cf. Figure 1), with the light beam at the focal plane of interest.[28]

While the advantages of a confocal laser scanning microscope include its high spatial resolution and sensitivity, as well as short acquisition times,[28] one of the main disadvantages is the requirement for a uniform refractive index over the optical path length (Figure 2a),[29−31] including refractive index matching between the capillary and the immersion medium, but especially—in view of a quantitative single-bead analysis—between the randomly distributed solid in porous particles and the saturating liquid.[32−34] Concerning our experimental device, the glass bead skeleton has a refractive index (RI) of 1.465, a value that is indeed representative for many solid-phase support materials (with an RI between 1.4 and 1.5) based on, for example, porous silica, methacrylates, or polyesters. By contrast, the solvents typically encountered in (electro)chromatography and other applications have a refractive index significantly below that value, notably water (RI = 1.333), methanol (RI = 1.329), and acetonitrile (RI = 1.344). Thus, for any of these liquids saturating the intraparticle pore space of glass beads (or that of similar materials), the resulting refractive index mismatch (Figure 2a) leads to inevitable loss in fluorescence intensity depending on the actual penetration depth and, thus, on radial position.[32] To eliminate artifacts relating to abberation caused by absorption and scattering of both the excitation and fluorescence light, we used a dynamic procedure for approaching a quantitative match between the refractive indices of liquid and solid.[11,35] We selected dimethylsulfoxide (DMSO), a versatile dipolar aprotic solvent with RI of 1.479, and systematically varied its mole fraction in water until the glass beads appeared optically transparent (Figure 2b). The final refractive index mismatch over the whole experimental setup could be adjusted to below 0.5% (Figure 2a), and it was less than only 0.1% inside the beads (Figure 2b).

With the device shown in Figure 1 and an optimized refractive index distribution over the whole sample (Figure 2), we conducted a series of experiments for a variety of conditions with respect to an electrokinetic intraparticle mass transport. For this purpose, we injected a slug of (un)charged fluorescent molecules into the packed capillary and basically used pressure-driven flow to achieve

(22) Kim, H.-B.; Hayashi, M.; Nakatani, K.; Kitamura, N.; Sasaki, K.; Hotta, J.; Masuhara, H. *Anal. Chem.* **1996**, *68*, 409.
(23) Ljunglöf, A.; Thömmes, J. *J. Chromatogr., A* **1998**, *813*, 387.
(24) Bouillot, P.; Ubrich, N.; Sommer, F.; Minh Duc, T.; Loeffler, J.-P.; Dellacherie, E. *Int. J. Pharm.* **1999**, *181*, 159.
(25) Linden, T.; Ljunglöf, A.; Kula, M.-R.; Thömmes, J. *Biotechnol. Bioeng.* **1999**, *65*, 622.
(26) Rademann, J.; Barth, M.; Brock, R.; Egelhaaf, H.-J.; Jung, G. *Chem. Eur. J.* **2001**, *7*, 3884.
(27) Webb, R. H. *Rep. Prog. Phys.* **1996**, *59*, 427.
(28) Wilson, T., Ed. *Confocal Microscopy*; Academic Press: London, 1990.
(29) Visser, T. D.; Groen, F. C. A.; Brakenhoff, G. J. *J. Microsc.* **1991**, *163*, 189.
(30) Sheppard, C. J. R.; Török, P. *J. Microsc.* **1997**, *185*, 366.
(31) Booth, M. J.; Neil, M. A. A.; Wilson, T. *J. Microsc.* **1998**, *192*, 90.
(32) Liljeborg, A. *Proc. SPIE* **1996**, *2655*, 11.
(33) Booth, M. J.; Wilson, T. *J. Biomed. Opt.* **2001**, *6*, 266.
(34) Diaspro, A.; Federici, F.; Robello, M. *Appl. Opt.* **2002**, *41*, 685.
(35) Kluijtmans, S. G. J. M.; de Hoog, E. H. A.; Philipse, A. P. *J. Chem. Phys.* **1998**, *108*, 7469.

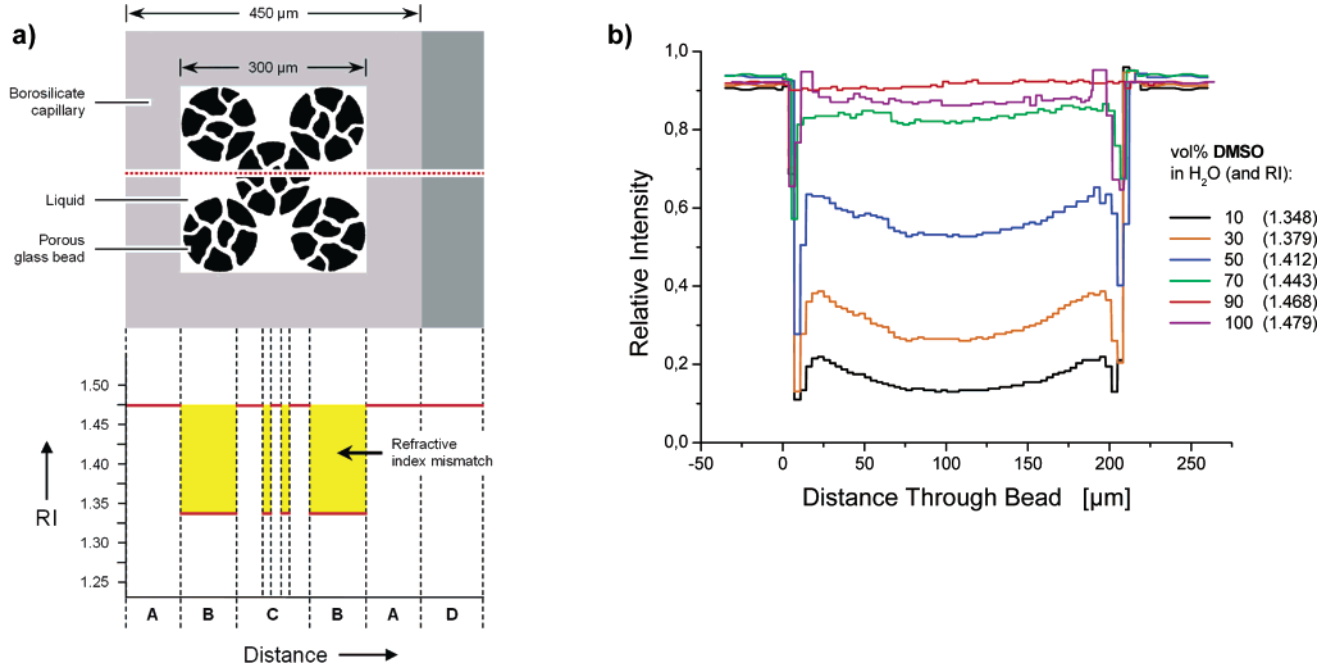

Figure 2. (a) Refractive index distribution over the experimental setup: (A) capillary wall (here borosilicate; RI = 1.474); (B) liquid (RI between 1.329 and 1.334 for water, methanol, or acetonitrile); (C) glass bead skeleton (RI = 1.465) and saturating liquid; (D) immersion medium (here glycerol; RI = 1.472). (b) Refractive index matching on a particle-scale. At 90:10 vol % DMSO−H_2O (RI = 1.468) the intensity profile of light transmitted through a single bead and the interface to external, particle-surrounding liquid becomes a straight line. Attenuation artifacts at lower DMSO mole fractions (depending on radial position due to the spherical geometry) are eliminated.

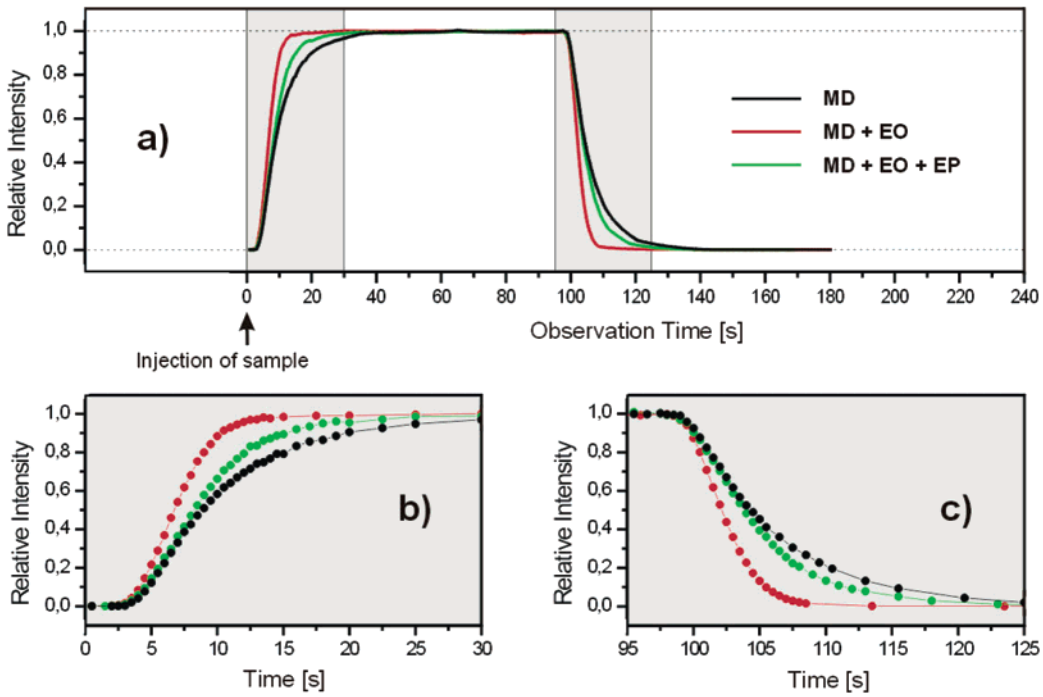

Figure 3. Mass transfer kinetics (tracer uptake and release dynamics) observed in a 12.4 μm thick center slice within a glass bead, itself located on top of the packing, during elution of (un)charged fluorescent molecules. The mobile phase is a 90:10 vol % DMSO−H_2O mixture (cf. Figure 2), containing 10^{-5} M BODIPY 493/503 or BODIPY 492/515-disulfonate (Molecular Probes Europe, Leiden, The Netherlands) as uncharged or charged tracer, respectively. The effective ionic strength of the liquid was 10^{-3} M (NaCl). Beads were analyzed by section scanning, using a Zeiss LSM 510 laser scanning microscope with excitation at 488 nm and an Ar laser power of 0.06 mW. Two-dimensional single-scan confocal (x−y) images were obtained with a 40× oil immersion lense (NA = 1.3) every 0.5 s. For studying electrokinetic transport of fluorescent tracer, a difference in electrical potential of −100 V (E = 6.7 × 10^3 V/m) was generated between the electrodes. The first bead behind the inlet filter (cf. Figure 1) has been used to avoid a tracer re-entry from upstream spheres during the release dynamics.

fast interparticle convection of the mobile phase and an initially uniform distribution of tracer around a particle. Thus, the spherical glass beads were first loaded, saturated, and then emptied by the unretained fluorescent tracer, depending on a carefully adjusted combination of driving forces (Figure 3). As the tracer, we separately employed negatively charged and uncharged molecules which chemically differed only with respect to the group

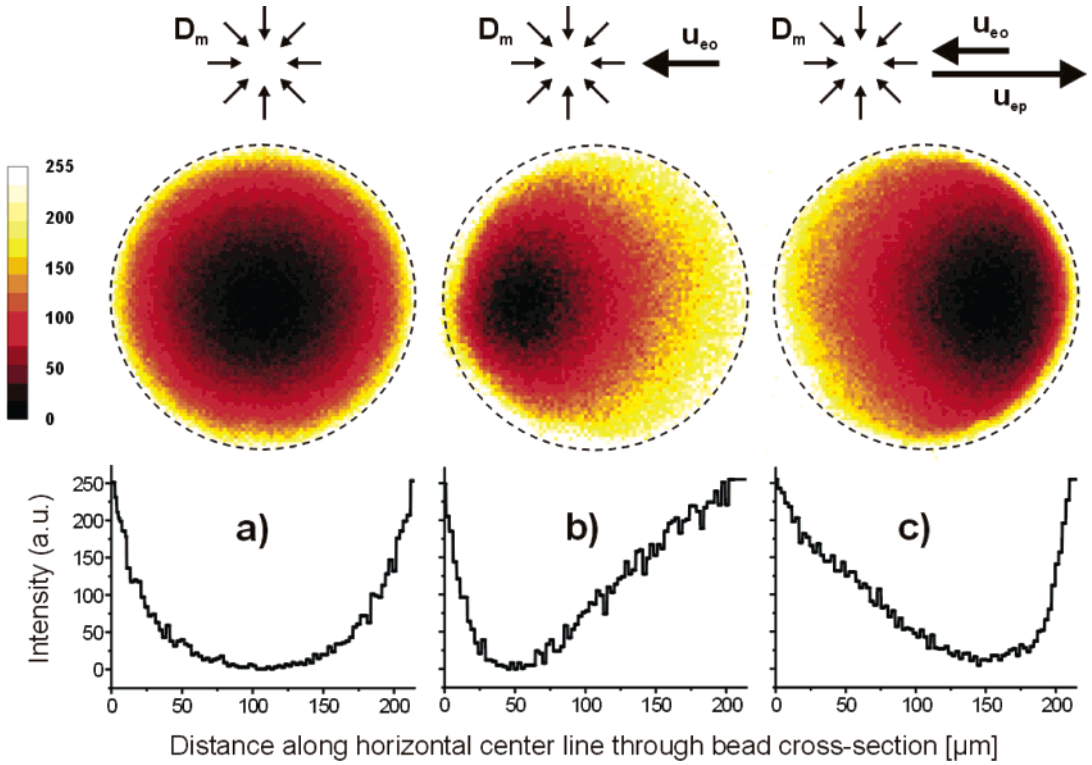

Figure 4. Quantitative distribution of (un)charged fluorescent molecules in a 12.4 μm thick ($x-y$) slice parallel to the column axis moving through the center of a porous glass bead ($d_p = 211$ μm), and intensity profiles recorded along the horizontal center line through this slice. (a) Uncharged tracer, intraparticle mass transport by molecular diffusion only (no electrical field applied). (b) Still uncharged tracer, but additional transport by electroosmotic flow ($\mathbf{E} = 6.7 \times 10^3$ V/m and $\mathbf{u}_{eo} = 21$ μm/s). (c) Charged tracer ($\mathbf{E}$ as before), transport now governed by a combination of electrophoretic migration ($\mathbf{u}_{ep} = -32$ μm/s), electroosmosis, and molecular diffusion. Mobile-phase composition and other conditions as in Figure 2; the pixel size is 2.54 μm. Images were selected on the basis that the fractional attainment of intraparticle equilibrium is similar in each case.

providing a net charge to the molecule. Consequently, in the presence of an externally applied electrical field (cf. Figure 1), the neutral fluorescent tracer molecules are expected to be transported inside the particles by electroosmosis (EO) of the bulk mobile phase, in addition to molecular diffusion (MD), while for the charged molecules we also expect electrophoretic migration (EP), in addition to the electroosmotic flow and molecular diffusion along the concentration gradient. In the absence of an externally applied electrical field, intraparticle transport remains diffusion-limited.[36] Thus, by a directed choice of experimental conditions and adjusted properties of the saturating liquid, fluorescent tracer, and particle surface, a clean and stepwise analysis of the complex interplay between diffusive, electrophoretic, and electroosmotic driving forces is possible. Figure 3 compares the intraparticle mass transfer kinetics obtained from a quantitative single-bead analysis in the presence and absence of an externally applied electrical field (superimposed on a pressure gradient). Data are recorded both for the charged and uncharged tracers. These results clearly demonstrate that electrokinetic transport mechanisms involved in either case (electroosmosis and/or electrophoresis) can significantly accelerate intraparticle transport. Even more important for a practical implication, the increase of associated mass transfer rate constants occurs already under relatively modest conditions concerning electrical field strength, background salt concentration, and the average pore size (in view of Joule heating effects, double-layer overlap inside the pores, or the adsorptive capacity of a particle).[37] While the thickness of the electrical double layer is about 10 nm, the average diameter of intraparticle pores is 120 nm. Thus, a significant double-layer overlap occurs on this pore scale, reducing the achievable volumetric electroosmotic flow.[38] Nevertheless, compared to the case of the purely diffusive mass transfer, the data in Figure 3 indicate the existence of substantial intraparticle velocities for electroosmotic flow and electrophoretic migration. Because the glass beads' surface carries a negative charge density, the also negatively charged fluorescent molecules experience an electrophoretic migration in the direction opposite to that of the forced electroosmotic flow. As evidenced by Figure 3, these opposing driving forces still result in a faster intraparticle mass transfer (MD + EO + EP) compared to the diffusion-limited kinetics (MD), but it is slower than that with electroosmotic flow alone (MD + EO).

To provide a quantitative analysis not only with respect to the mean tracer concentration in a spherical particle (at any time and depth) but also concerning the individual transport mechanisms, we finally determined the velocities underlying electrokinetically enhanced mass transfer in the intraparticle pore space. To our knowledge, direct measurement of nonzero velocities inside single porous beads has not been reported before, but it has always remained a challenging task, especially the characterization of experimental conditions that could form the basis for mass transfer enhanced and finally dominated by intraparticle convection. This is particularly important for porous media with a low (average and local) hydraulic

(36) Tallarek, U.; Vergeldt, F. J.; Van As, H. *J. Phys. Chem. B* **1999**, *103*, 7654.

(37) Rathore, A. S. *Electrophoresis* **2002**, *23*, 3827.

(38) Probstein, R. F. *Physicochemical Hydrodynamics*; Wiley: New York, 1994.

permeability that adversely affects volumetric throughput of liquid and the separation or reaction efficiency. For example, with hydraulic flow the permeability of porous particles may be tuned to typical column pressure drops under the aspect that the pressure fields prevailing in fixed bed adsorbers or catalysts act as driving force for relevant intraparticle flow.[39] A small, but nonzero, velocity could assist the diffusion of large molecules and reduce hold-up dispersion originating in stagnant zones.[40−43] However, the mobile-phase perfusion in pressure-driven flow will be operating only if relatively high column pressure drops and particles with large pores (having low adsorptive capacity) are used. Thus, for most processes employing hydrostatic flow through a packed bed, the intraparticle mass transfer remains diffusion-limited (if not purely diffusive) and the distribution profiles during an uptake of tracer by a porous particle reveal spherical symmetry, as seen in Figure 4a.[32] In contrast to this well-known behavior,[22,23] Figure 4b and c demonstrates the effect of nonzero electroosmotic and electrophoretic velocities inside a particle, and an examination of concentration profiles reveals a distinct deviation from spherical symmetry. Both charged and uncharged fluorescent tracer molecules respond to the applied electrical field (unidirectional driving force) by producing nonsymmetric distribution profiles parallel to it, but in opposite directions.

In particular, for intraparticle electroosmotic flow (MD + EO, Figure 4b), the concentration minimum moves downstream compared to pure molecular diffusion (MD, Figure 4a), resulting in a higher concentration in the upstream half of the sphere than the downstream half. This is due to the electroosmotic convection mechanism operating in the same direction as molecular diffusion in the upstream part of the particle but opposite to diffusion downstream. The results become even more compelling when both electroosmosis and electrophoresis are present (MD + EO + EP, Figure 4c). In this case, because the intraparticle electrophoretic migration velocity ($\mathbf{u}_{ep}$) is sufficiently higher than the electroosmotic flow velocity ($\mathbf{u}_{eo}$) and in the opposite direction, the sphere is effectively loaded from the (former) downstream side, with an accompanying shift of the concentration minimum into the opposite half of the particle. Even under these conditions where the (fictitiously decoupled) electrokinetic transport mechanisms lead to countercurrent mass transport, the tracer uptake and release kinetics are faster than those for the purely diffusive case (see Figure 3). By analyzing the time-evolution of tracer fronts in a particle and also accounting for the effect of molecular diffusion, we could calculate the mean intraparticle electroosmotic and electrophoretic velocities. Their values are given in Figure 4, and they exactly fit into the time scales of the mass transfer kinetics in Figure 3, providing direct validation of the convection-augmented transport mechanisms.

Thus, we were able to conduct a quantitative sound analysis of electrokinetic transport in a bed of porous spherical particles. Relevant transport parameters were obtained for well defined, easily variable experimental conditions. The device (Figure 1), procedures (Figure 2), and results (Figures 3 and 4) are unique by combining miniaturization aspects of microfluidics and capillary separation techniques with advanced electrokinetic transport schemes and the inherent potential of confocal laser scanning microscopy. This approach and its straightforward implementation allow us to resolve spatio-temporal details of fundamental mechanisms involved in the electrical field-assisted transport of species through porous media, including an interplay between adsorption and a local electrokinetics, double-layer overlap effects, nonlinear electrokinetic phenomena, or the mobility of large (bio)molecules in confining geometries, also in view of a single-molecule dynamics at complex interfaces studied by fluorescence microscopy.[44−55]

LA034183P

(39) Pfeiffer, J. F.; Chen, J. C.; Hsu, J. T. *AIChE J.* **1996**, *42*, 932.
(40) Stephanopoulos, G.; Tsiveriotis, K. *Chem. Eng. Sci.* **1989**, *44*, 2031.
(41) Carta, G.; Gregory, M. E.; Kirwan, D. J.; Massaldi, H. A. *Sep. Technol.* **1992**, *2*, 62.
(42) Lu, Z. P.; Dias, M. M.; Lopes, J. C. B.; Carta, G.; Rodrigues, A. E. *Ind. Eng. Chem. Res.* **1993**, *32*, 1839.
(43) Frey, D. D.; Schweinheim, E.; Horváth, Cs. *Biotechnol. Prog.* **1993**, *9*, 273.
(44) Dukhin, S. S. *Adv. Colloid Interface Sci.* **1991**, *35*, 173.
(45) Lee, E.; Chu, J. W.; Hsu, J. P. *J. Colloid Interface Sci.* **1998**, *205*, 65.
(46) Hernandez, A.; Lopez, R.; Calvo, J. I.; Pradanos, P. *Colloids Surf., A* **1998**, *145*, 11.
(47) Xu, X. H. N.; Yeung, E. S. *Science* **1998**, *281*, 1650.
(48) Kemery, P. J.; Steehler, J. K.; Bohn, P. W. *Langmuir* **1998**, *14*, 2884.
(49) Rubinstein, I.; Zaltzman, B. In *Surface Chemistry and Electrochemistry of Membranes*; Sørensen, T. S., Ed.; Marcel Dekker: New York, 1999; Chapter 17.
(50) Wirth, M. J.; Swinton, D. J. *J. Phys. Chem. B* **2001**, *105*, 1472.
(51) Marino, S.; Shapiro, M.; Adler, P. M. *J. Colloid Interface Sci.* **2001**, *243*, 391.
(52) Hanley, D. C.; Harris, J. M. *Anal. Chem.* **2001**, *73*, 5030.
(53) Tallarek, U.; Rapp, E.; Seidel-Morgenstern, A.; Van As, H. *J. Phys. Chem. B* **2002**, *106*, 12709.
(54) Locke, B. R. *Electrophoresis* **2002**, *23*, 2745.
(55) Pačes, M.; Kosek, J.; Marek, M.; Tallarek, U.; Seidel-Morgenstern, A. *Electrophoresis* **2003**, *24*, 380.

Ulrich Tallarek[1]
Martin Pačes[2, 3]
Erdmann Rapp[2]

[1]Institut für Verfahrenstechnik, Otto-von-Guericke-Universität, Magdeburg, Germany
[2]Max-Planck-Institut für Dynamik komplexer technischer Systeme, Magdeburg, Germany
[3]Department of Chemical Engineering and Center for Nonlinear Dynamics of Chemical and Biological Systems, Prague Institute of Chemical Technology, Prague, Czech Republic

Perfusive flow and intraparticle distribution of a neutral analyte in capillary electrochromatography

The relevance and magnitude of an electroosmotic perfusion mechanism in electrochromatography is analyzed. To systemize our studies we first considered the transport of an electroneutral and nonadsorbing tracer. Based on the refractive index matching in a microfluidic setup containing fixed spherical porous particles, we conducted a quantitative analysis in real time of the spatio-temporal distribution of fluorescent tracer molecules during their uptake by (and a release from) single particles using confocal laser scanning microscopy. Even under conditions of a significant electrical double layer overlap the intraparticle electroosmotic flow produces due to its unidirectional nature and in striking contrast to the symmetric (spherical) distributions typical for purely diffusive transport strongly asymmetric concentration profiles inside spherical particles as the locally charged pore liquid begins to respond to the externally applied electrical field. The profiles retain an axisymmetric nature, *i.e.*, rotational symmetry with respect to the field direction. Results of our measurements could be successfully interpreted and further analyzed by a compact mathematical model. Intraparticle Peclet numbers of up to 150 have been realized and found to significantly enhance the mass transport on particle scale towards the convection-dominated regime when compared to a conventional (diffusion-limited) kinetics.

Keywords: Concentration profile / Confocal laser scanning microscopy / Electrical double layer / Electrochromatography / Electroosmotic flow / Intraparticle transport / Neutral analyte / Refractive index
DOI 10.1002/elps.200305673

1 Introduction

The theoretical concept and experimental utilization of an intraparticle-forced convection in classical solid-liquid chromatography for reducing mobile-phase mass transfer resistance originating in the (intraparticle) stagnant zone of packed beds has received a significant attention over the last decade [1–14] although consequences of this phenomenon were recognized already earlier, *e.g.*, in size-exclusion chromatography [15] and catalyst design [16, 17], or for the nutrient transport in biological pellets [18]. By using porous particles with a tailored hydraulic permeability such that the pressure drops typically encountered in packed columns act as a decent driving force for an intraparticle flow [8, 19] the non-zero velocity component can assist (or even dominate – depending on its magnitude relative to time scales of analyte diffusion and adsorption-desorption processes) conventional, *i.e.*, diffusion-limited intraparticle transport. It reduces hold-up dispersion due to stagnant zones, a contribution that begins to dominate the longitudinal dispersion in packed beds of porous particles at reduced velocities (or Peclet numbers, *Pe*) above 25 [20]. The result of these studies [20] which have combined advanced numerical and experimental methods for differentiating between dispersion mechanisms that originate in stagnant and flowing regions of random sphere packings of nonporous and completely porous particles suggests that the hold-up dispersion is more important than often assumed [21]. By contrast, the term perfusion chromatography refers to separation processes with a non-zero intraparticle velocity.

However, mobile-phase perfusion in beds of permeable spherical-shaped particles is realized with hydraulic flow to any significant amount only when relatively high column pressure drops and particles having large pores are encountered. This, in turn, limits the intraparticle surface-to-volume ratio in view of the mechanical strength or adsorption capacity of a particle. Even then, the intraparticle fluid velocity remains small compared to velocities in the interparticle pore space and becomes relevant

Correspondence: Dr. Ulrich Tallarek, Institut für Verfahrenstechnik, Otto-von-Guericke-Universität Magdeburg, Universitätsplatz 2, D-39106 Magdeburg, Germany
E-mail: ulrich.tallarek@vst.uni-magdeburg.de
Fax: +49-391-67-12028

Abbreviations: CLSM, confocal laser scanning microscopy; **EDL**, electrical double layer; **RI**, refractive index

only for the transport of very slowly diffusing molecules with a comparatively fast adsorption-desorption kinetics [11, 22].

Electroosmotic perfusion through fixed beds of porous particles proceeds with a significantly higher intraparticle (electroosmotic) permeability [23–25]. It is in striking contrast to both the intensity of efforts and prerequisites concerning an optimized particle technology, as well as the realized magnitude of any perfusive, but hydraulic flow and the (still) remaining velocity inequalities between the inter- and intraparticle flow patterns. Indeed, similar behavior has already been recognized earlier by selective applications in the physical and life sciences, including electrokinetic dewatering of waste sludge or the removal of contaminants from soil [26]. Concerning the permeability of packed capillaries electroosmotic flow (EOF) has shown to offer a far superior dispersion characteristics (compared to pressure-driven flow) which accompanies a reduction of velocity extremes in the mobile phase flow pattern on any time and length scale [27–31]. In particular, plate heights and dispersion coefficients reduced by up to a decade with respect to those normally observed in pressure-driven flow have been reported, especially for weakly and unretained solutes [25, 27, 29]. Based on measured porosimetry data for porous particles already simple (cylindrical) capillary models of a packed bed, together with the approximate expressions after Rice and Whitehead [32] for pore-level EOF, could successfully explain relative magnitudes of intraparticle-to-interparticle EOF depending on electrical double layer (EDL) overlap inside the particles [29, 33].

On the other hand, it becomes difficult to relate this improvement quantitatively to an electroosmotic perfusion mechanism because – due to the relatively small particle diameters (d_p = 3–5 μm) and limitations in maximum electrical field strength and currents resulting from Joule heating [34] – plate height data in capillary electrochromatography (CEC) are inherently acquired over only a limited range of *Pe*, with average EOF velocities typically not exceeding 2–3 mm/s. This appears insufficient for the adequate separation between dispersion processes originating in the flowing and (remaining) stagnant zones of a packed bed [21, 35–37]. For example, it is well known that for pressure-driven flow stochastic velocity fluctuations in the interstitial pore space cause mechanical dispersion which grows linearly with *Pe*, while regions of zero velocity inside the particles and close to their external surface give rise to nonmechanical contributions growing as Pe^2 (hold-up dispersion) and $Pe \cdot \ln(Pe)$ (boundary-layer dispersion), respectively [36]. How these contributions coexist in CEC to determine the plate height dependence on *Pe* under a set of conditions, including the distribution of pore sizes and EDL thickness, pore geometry and interconnectivity, the fractal nature and possible chemical heterogeneity of the surface, dissociation equilibria of both the analyte and surface groups, type of buffer, charge of analyte, retention mechanism, or a coupling of nonlinear adsorption with the local electrokinetics [38] is a yet unresolved issue, although recently reported plate height expressions for uncharged analytes may be initial steps [39, 40].

This situation underlines the need for experimental techniques that allow to capture directly and quantitatively individual transport phenomena in CEC. In this work, we examine how the intraparticle EOF influences in contrast to conventional (*i.e.*, diffusion-limited) operation the intraparticle mass transfer and, in particular, the resulting spatio-temporal distribution of a neutral, nonadsorbing analyte in single porous particles of a packed capillary. By employing refractive index (RI) matching we could implement confocal laser scanning microscopy (CLSM) for this purpose and measure quantitatively at any depth inside particles local concentration profiles of fluorescent flow field tracer molecules, EOF velocities and the associated mass transport relevant on particle scale. A simple, compact mathematical model could successfully interpret and help in further analyzing the observed behavior. Although CLSM has found increased potential over the last years for studying the analyte distribution and adsorption processes in single chromatographic particles [41–46] its application to electrokinetic transport phenomena in packed capillaries has been demonstrated only most recently [47, 48].

2 Materials and methods

2.1 Materials

Borosilicate glass capillaries (RI = 1.474) with quadratic cross section (300 μm inner, 450 μm outer edge) were purchased from Hilgenberg GmbH (Malsfeld, Germany), while cylindrical fused-silica and stainless-steel capillaries were obtained from Polymicro Technologies (Phoenix, AZ, USA) and Hamilton (Bonaduz, Switzerland), respectively. Macroporous native glass beads (RI = 1.465) from Schuller (Steinach, Germany) had a particle size distribution between 150 and 250 μm and mean intraparticle pore size of 122 nm. Dimethyl sulfoxide (DMSO) in Uvasol® quality (RI = 1.479) was purchased from Merck (Darmstadt, Germany), hydrochloric acid and anhydrous glycerol (MicroSelect quality, RI = 1.472) were obtained from Fluka (Sigma-Aldrich Chemie, Taufkirchen, Ger-

many). Aqueous solutions were prepared using water (RI = 1.333) purified on a Milli-Q-system (model Milli-Q-Gradient; Millipore, Eschborn, Germany). As fluorescent dye in the CLSM studies we used BODIPY® 493/503 (4,4-difluoro-1,3,5,7,8-pentamethyl-4-bora-3a,4a-diaza-*s*-indacene) which has been received as a neat compound from Molecular Probes Europe BV (Leiden, The Netherlands).

2.2 Setup and procedures

Dry spherical glass beads were packed by sufficient vacuum (suction) into the glass capillary with quadratic cross section. Particles were fixed between two prepunched glass-fiber filter plugs prepared to fit exactly into the inner cross sectional area of this capillary (300 μm × 300 μm). These filters were held in place at both ends by cylindrical fused-silica capillaries (180 μm ID, with an OD smaller than 300 μm after removal of polyimide coating) acting as stabilizing inlet and outlet pistons. Afterwards, stainless-steel capillaries (60 μm ID, 160 μm OD) were carefully moved into the two 180 μm ID fused-silica capillaries until they touched the glass-fiber filters. This alignment was fixed with PTFE shrinking tubes (types Dual-SS IL065 and UTW 34; IFK-Isofluor, Neuss, Germany). Finally, the stainless-steel inlet and outlet capillaries later used as the electrodes were connected to polyimide-coated cylindrical fused-silica capillaries with 75 μm ID at the inlet side of the setup and 150 μm ID at its outlet *via* zero-dead-volume microtight unions from Upchurch Scientific (Oak Harbor, WA, USA).

The capillary system was assembled in a home-built alignment interface to allow *xyz*-positioning for the CLSM studies. The inlet fused-silica capillary was coupled to syringe pumps *via* a low-dead-volume two-position valve (Valco International, Schenkon, Switzerland) and stainless-steel capillary electrodes were connected to the power supply. Pressure-driven flow through the setup was achieved by high-pressure PHD 4400 syringe pumps (Harvard Apparatus, Holliston, MA, USA) giving flow rates down to the submicroliter range without pulsation. For electrokinetically driven flow we used a DC power supply (model HCN 6M-30000) from F.u.G. Elektronik (Rosenheim, Germany). For this mode, the outlet stainless-steel capillary served as high-voltage electrode, while the inlet stainless-steel capillary was connected to the ground. In general, we injected a slug of BODIPY® 493/503 (10^{-5} M in a refractive index-tuned mobile phase described in Section 3.1) which was transported through the microfluidic device containing the porous particles. Thus, during a complete cycle, a single glass bead became loaded, saturated and emptied again by the fluorescent tracer, thereby revealing (*via* the quantitative CLSM studies) an influence of particular driving forces, *i.e.*, gradients in concentration, pressure, and electrical potential on the intraparticle tracer uptake and release dynamics (mass transfer kinetics), as well as on the local distribution of tracer.

2.3 Confocal laser scanning microscopy

2.3.1 Refractive index matching

While definite advantages of CLSM include a high spatial resolution and sensitivity, as well as short acquisition time [49, 50], a major disadvantage is the requirement for uniform RI distribution over the whole optical path length [51–55]. In our case, because we attempted a quantitative single-bead analysis RI matching between the solid skeleton of a porous particle and its saturating liquid appears most important [48, 56–58]. Any RI mismatch inside particles will lead to inevitable intensity loss in BODIPY® fluorescence depending on the actual penetration depth, thus, on radial position. For eliminating artifacts related to abberation caused by absorption and scattering of both the excitation and fluorescence light, we used DMSO and systematically varied its mole fraction in water until the glass beads became optically transparent [48] (*cf.* Fig. 1). This was achieved at 90:10 vol% DMSO-H_2O (RI = 1.468). In addition, the capillary was immersed in anhydrous glycerol for minimizing refraction and scattering of light at the interface between capillary and surrounding medium. The final RI mismatch over the whole setup could be adjusted to below 0.5%, and it was less than only 0.1% inside the beads [48]. The 90:10 vol% DMSO-H_2O mixture was used as a basic mobile phase composition in subsequent experiments. While the high DMSO content may not be suitable for certain stationary phases it provides a convenient intraparticle RI match for the glass beads. This, in turn, is the prerequisite for analyzing on quantitative basis at any depth inside the particles distribution profiles of fluorescent tracer during its uptake in (or release from) single beads in view of the transport processes operating under the influence of both internal and externally applied electrical fields. Further, DMSO offers a reasonably high dielectric constant compared to other organic solvents making it suitable for these investigations. Finally, we added NaCl to this mobile phase (10^{-3} M effective ionic strength) resulting in a controlled EDL thickness.

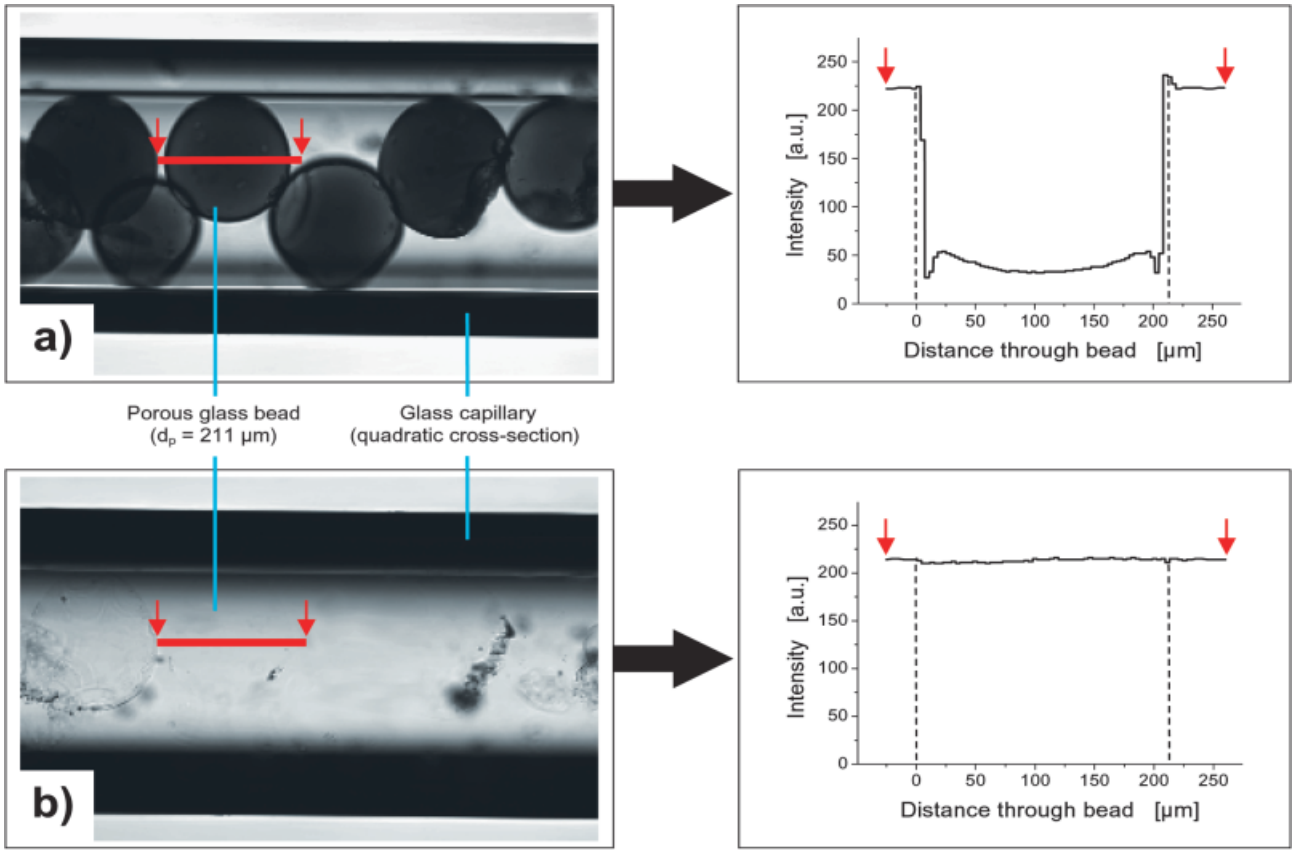

Figure 1. Transmission light contrast in the microfluidic device and intensity profile through a single porous particle including the interface to external liquid (red bar and arrows). Dashed lines indicate the particle boundaries. (a) Significant RI mismatch between the intraparticle liquid (10:90 vol% DMSO-H_2O, RI = 1.348) and glass bead skeleton (RI = 1.465) resulting in attenuation artifacts which, due to the spherical geometry, depend on radial position. (b) Intraparticle RI matching with 90:10 vol% DMSO-H_2O (RI = 1.468). The glass beads appear optically transparent and spherical abberation is minimized.

2.3.2 Image acquisition

Measurements were made on a confocal laser scanning microscope Axiovert 100 with LSM 510 scan module from Carl Zeiss (Jena, Germany) equipped with an argon ion laser and Zeiss LSM 2.8 software. The quadratic capillary segment containing glass beads over a length of 15 mm was mounted on the objective such that one of its plane faces was perpendicular to the light path. Acousto-optical tuneable filters regulated the power of the argon ion laser used for excitation at 488 nm. Key feature of the confocal microscope is a pinhole (confocal aperture) in the detection optics which excludes light from all but that location within the focal plane where the laser beam was focused (confocal spot) [59]. Fluorescence light from BODIPY molecules was directed through the adjustable pinhole and detected by a photomultiplier tube. The spectral range of fluorescence emission was selected by an appropriate long-pass filter (LP 505).

Two-dimensional single-scan confocal images were obtained with a 40× oil immersion objective (NA = 1.3) by sweeping the porous particles with the light beam at the focal plane of interest. Beads were analyzed in the section-scanning mode, *i.e.*, in the *xy*-plane which is perpendicular to the optical axis, but parallel to the column axis. Based on a careful adjustment in the *z*-direction with the alignment interface this scanning technique was used for generating two-dimensional images of fluorescence intensity distribution in the equatorial section of a single glass bead with *xy*-layer thickness of 12.4 µm. The pixel size was 2.54 µm × 2.54 µm. Images were recorded every 0.5 s as time series and built by means of a single *xy*-scan in 393.2 ms. Prior to measurement series we verified that the detection range exhibited a linear relation between BODIPY concentration and the detected fluorescence signal.

2.4 Mathematical model

A compact mathematical model is presented and used for analyzing the effect of intraparticle EOF on the mass transfer kinetics and spatio-temporal distribution of an uncharged, nonadsorbing analyte in a single porous spherical particle. The particle morphology including geometrical aspects like pore shape, orientation or size and its distribution functions, as well as topological parameters (*e.g.*, pore interconnectivity) is assumed to be isotropic with respect to typical time and length scales encountered in the measurements. Further, subpore level heterogeneities including surface fractality and other defects which can lead to an inhomogeneous pattern of surface charge and local flow are considered to be uniformly distributed within pores. Thus, transport properties like the effective intraparticle diffusivity (D_{intra}) are constant on observation scale. In the model, the spherical support particle is hypothetically fixed in space. Mobile phase containing tracer at low concentration (10^{-5} M in the experiments) is streaming by a combination of strong pressure-driven flow and much weaker EOF mainly around, but partly also through this permeable particle. Since its hydraulic permeability is assumed to be small enough that intraparticle convection due to the surrounding pressure field can be neglected as transport mechanism compared to intraparticle diffusion, the perfusion is only caused by EOF. Perfusive flow is assumed to be uniform [39, 60], *i.e.*, flow velocity has the same direction and magnitude inside a particle. This direction coincides with that of the (externally applied) electrical field. Based on the results of a recent pulsed field gradient nuclear magnetic resonance study [61] we neglect extraparticle fluid-side domain (boundary-layer) mass transfer resistance for uncharged tracer toward the intraparticle pore fluid. It should be noted, however, that diffusion-limited transport close to the particles external surface may become quite important for charged analytes [62, 63]. We further assume that pressure-driven convection which only operates outside the particle is strong enough that extraparticle axial displacements of the tracer are (much) larger than those inside a particle due to any intraparticle transport mechanism. Thus, the mobile phase concentration at the particles external surface can be considered as uniform and any (uniform) changes as occuring relatively fast with respect to the time scale of intraparticle mass transport. For this type of experiment, it is the only reason for using a significant pressure-driven flow component in extraparticle space: This allows to establish a uniform distribution of tracer around the particle, but it leaves intraparticle transport governed by the EOF and diffusion. We have observed that under the actual experimental conditions EOF alone is insufficient for that purpose due to its inherently perfusive nature. With the set of the aforementioned assumptions and conditions the transport of a nonadsorbing and electroneutral single analyte in the particle can be described by the following differential mass balance equation which accounts for molecular diffusion in a direction of decreasing concentration and electroosmotic convection in the direction of a unidirectional DC field (perfusive flow)

$$\frac{\partial c}{\partial t} = D_{intra}\nabla^2 c - \boldsymbol{v}_{intra}\nabla c \tag{1}$$

where c is the local concentration of analyte in the sphere (at any time) and $\boldsymbol{v}_{intra}$ is the intraparticle flow velocity. If only diffusive mass transport were considered it would be straightforward to formulate the analysis in spherical coordinates since spherical symmetry would reduce the problem to a one-dimensional model. However, with intraparticle EOF the analyte begins to respond to a unidirectional electrical field applied in one of the Cartesian space dimensions (eliminating spherical symmetry) but we still can simplify the problem by expressing Eq. (1) in cylindrical coordinates [64] and aligning the flow direction with the axial coordinate [65]. Then, this assumed symmetry reduces the problem to a two-dimensional model, and after expansion of the Laplace operator and transformation into dimensionless form we obtain

$$\frac{\partial \tilde{c}}{\partial \tau} = \frac{1}{\rho}\frac{\partial \tilde{c}}{\partial \rho} + \frac{\partial^2 \tilde{c}}{\partial \rho^2} + \frac{\partial^2 \tilde{c}}{\partial \xi^2} - Pe_{intra}\frac{\partial \tilde{c}}{\partial \xi} \tag{2}$$

where $\tilde{c}$ is the dimensionless tracer concentration, τ is the dimensionless time, ξ and ρ are the dimensionless central axial and radial coordinates, respectively (*cf.* Fig. 2), and Pe_{intra} is the intraparticle Peclet number. These parameters are given by

$$\tilde{c} = \frac{c}{c_0} \tag{3}$$

$$\tau = \frac{t}{t_0} \tag{4}$$

$$\xi = \frac{x - x_0}{d_p} \tag{5}$$

$$\rho = \frac{r}{d_p} = \frac{|y - y_0|}{d_p} \tag{6}$$

$$Pe_{intra} = \frac{v_{intra} d_p}{D_{intra}} \tag{7}$$

with c_0, the characteristic concentration of the tracer, d_p as characteristic length, and $t_0 = d_p^2/D_{intra}$ as the characteristic diffusion time. Equation (2) was subject to a Dirichlet boundary condition for analyte concentration at the external surface of the particle and symmetry boundary condition at the particle center (Fig. 2). The

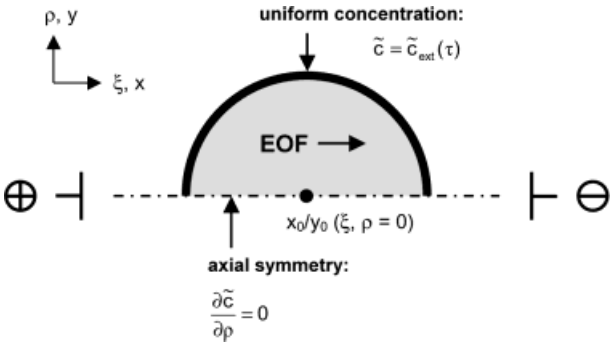

Figure 2. Definition of the two-dimensional coordinate system and boundary conditions making use of the (three-dimensional) lateral rotational symmetry in the model. For a surface with negative charge density (as for the glass beads under the set of experimental conditions) positive EDL counterions move toward the cathode. Thus, the direction of intraparticle flow ($\boldsymbol{v}_{intra}$) is parallel to the applied field ($\boldsymbol{E}$) coinciding with the axial direction.

parabolic partial differential equation in the two-dimensional domain was spatially discretized (quadrilateral grid) by using the Galerkin finite-element method with linear base functions [66]. The set of linear (ordinary) differential equations was integrated in time. The whole program was implemented in Matlab (The MathWorks, Natick, MA, USA).

2.5 Processing of experimental data

From the two-dimensional fluorescence intensity profiles in the 12.4 μm thick equatorial *xy*-slice of a glass bead the center of that particle (located at x_0/y_0 where ξ and ρ are zero) and its diameter (d_p) were determined. Intensities $I_i(t)$ obtained during a measurement series in this slice at positions x_i/y_i ($i = 1, \ldots, N$) were distinguished according to their location inside or outside the particle. These data then were used to calculate mean internal and external intensities

$$\langle I^{int}\rangle(t) = \frac{\sum_{i=1}^{N} |y_i - y_0| I_i^{int}(t)}{\sum_{i=1}^{N} |y_i - y_0|} \tag{8}$$

$$\langle I^{ext}\rangle(t) = \frac{\sum_{i=1}^{N} I_i^{ext}(t)}{N} \tag{9}$$

Axial symmetry of intraparticle analyte profiles in the presence of a unidirectional pore flow required the use of weighted average values for the internal intensity. Maximum and minimum values of average intensities were used to normalize the experimental intraparticle data

$$\tilde{c}_{exp}(x/y,t) = \frac{I^{int}(x/y,t) - \langle I^{int}\rangle_{min}}{\langle I^{int}\rangle_{max} - \langle I^{int}\rangle_{min}} \tag{10}$$

where $\tilde{c}_{exp}$ (x/y, t) is the normalized intensity (dimensionless concentration) and $I^{int}(x/y,t)$ is the measured intensity. Experimental data were then transformed into the coordinate system ($\xi/\rho,\tau$) of the model. Intraparticle profiles at different times were compared with data bilinearly interpolated from the numerical results (utilizing a quadrilateral grid). Model parameters t_0 and Pe_{intra} were determined by minimizing the sum of squares of the differences between experimental $\tilde{c}>_{exp}(\xi/\rho,\tau)$ and the calculated $\tilde{c}(\xi/\rho,\tau)$ data. The mean external concentration (normalized intensity) was used in the model for the boundary condition at the particles external surface (*cf.* Fig. 2)

$$\tilde{c}_{ext}(t) = \frac{\langle I^{ext}\rangle(t) - \langle I^{ext}\rangle_{min}}{\langle I^{ext}\rangle_{max} - \langle I^{ext}\rangle_{min}} \tag{11}$$

Initially, we considered a uniform intraparticle distribution of the analyte molecules with zero or unity dimensionless concentration depending on whether the particle is filled or emptied by tracer.

3 Results and discussion

Figures 3–5 show the results of our CLSM measurements and comparison with the mathematical model concerning the intraparticle transport of a dilute electroneutral, unretained tracer over discrete temporal and spatial domains, as well as for a combination of mass transport driving forces (electroosmosis and molecular diffusion) inside the particle. While Fig. 3 demonstrates the influence of an externally applied electrical field on the spatially averaged mass transfer kinetics for particle filling and emptying processes, Figs. 4 and 5 reveal details of the associated intraparticle tracer distribution profiles.

As pointed out earlier, we in general employed a relatively strong and constant pressure-driven flow in the interparticle pore space of the packed bed and the extraparticle space of the model for assuming a uniform tracer distribution at the particles external surface (Fig. 2). As evidenced by Figs. 3a and c for the external concentration during the particle filling and emptying processes, the resulting interparticle convection becomes so dominant that it is hardly affected by EOF due to a gradient in electrical potential superimposed on the constant pressure gradient. Thus, attainment of a steady-state tracer distribution outside the spherical porous particle (including its external surface) is determined by the interparticle pressure-driven flow and remains constant throughout the different measurement series (*cf.* Figs. 3a and c). In other words, the applied electrical field has only a negligible influence on the transport of tracer in the interparticle pore space. By contrast, it has a strong impact on the mass transfer

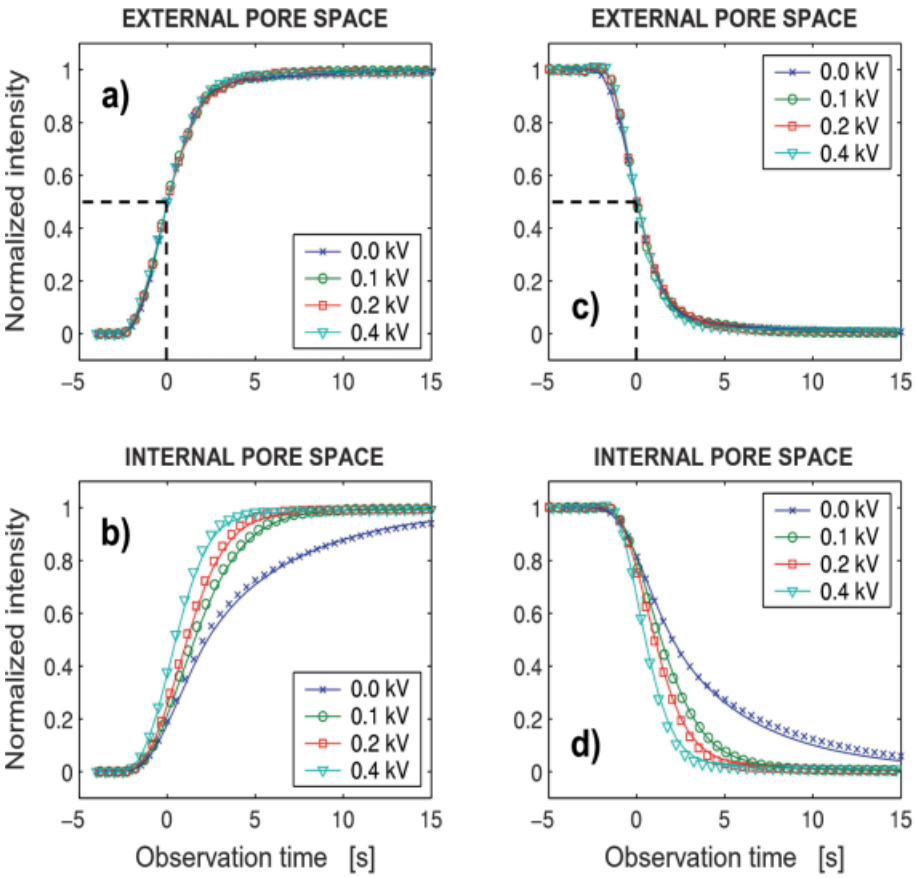

Figure 3. Dynamics of tracer transport in the microfluidic device. The mobile phase is a 90:10 vol% DMSO-H_2O mixture with an effective ionic strength of 10^{-3} M (NaCl). For device and particle filling it also contains the fluorescent flow field marker (10^{-5} M BODIPY 493/503). (a), (c) Interparticle tracer concentration close to a spheres external surface during filling (left) and emptying (right) procedures. (b), (d) The corresponding intraparticle mass transfer kinetics (tracer uptake and release dynamics, respectively). For studying perfusive EOF a difference in electrical potential (U as indicated) was superimposed on the pressure gradient, the distance between electrodes (also the bed length) was 15 mm. Experiments were run at a controlled temperature of 298 ± 1 K. Solid lines represent best fits of the mathematical model to our data. For convenience, time zero has been set with respect to half saturation level in the external pore space (dashed lines).

inside a particle (see Figs. 3b and d for the particle-filling and emptying processes, respectively) where, *vice versa*, the pressure field around a particle seems to have no significant effect on tracer transport which is consequently diffusion-limited in the absence of an external electrical field (Table 1).

It should be noted that after a comparison of Figs. 3a and c with Figs. 3b and d, respectively, it is clear that the attainment of a steady-state concentration at the particles external surface is not instantaneous with respect to the intraparticle mass transfer kinetics, even though it remains always faster in the extraparticle than in the intra-

Table 1. Analysis of purely diffusive transport (U = 0.0 kV)

	Cycle No. 1		Cycle No. 2	
	Particle filling	Particle emptying	Particle filling	Particle emptying
t_0 (s)	215.4	190.7	215.8	186.2
D_{intra} (m^2/s)	1.79×10^{-10}	2.02×10^{-10}	1.74×10^{-10}	2.02×10^{-10}
d_p (m)	1.96×10^{-4}	1.96×10^{-4}	1.94×10^{-4}	1.94×10^{-4}

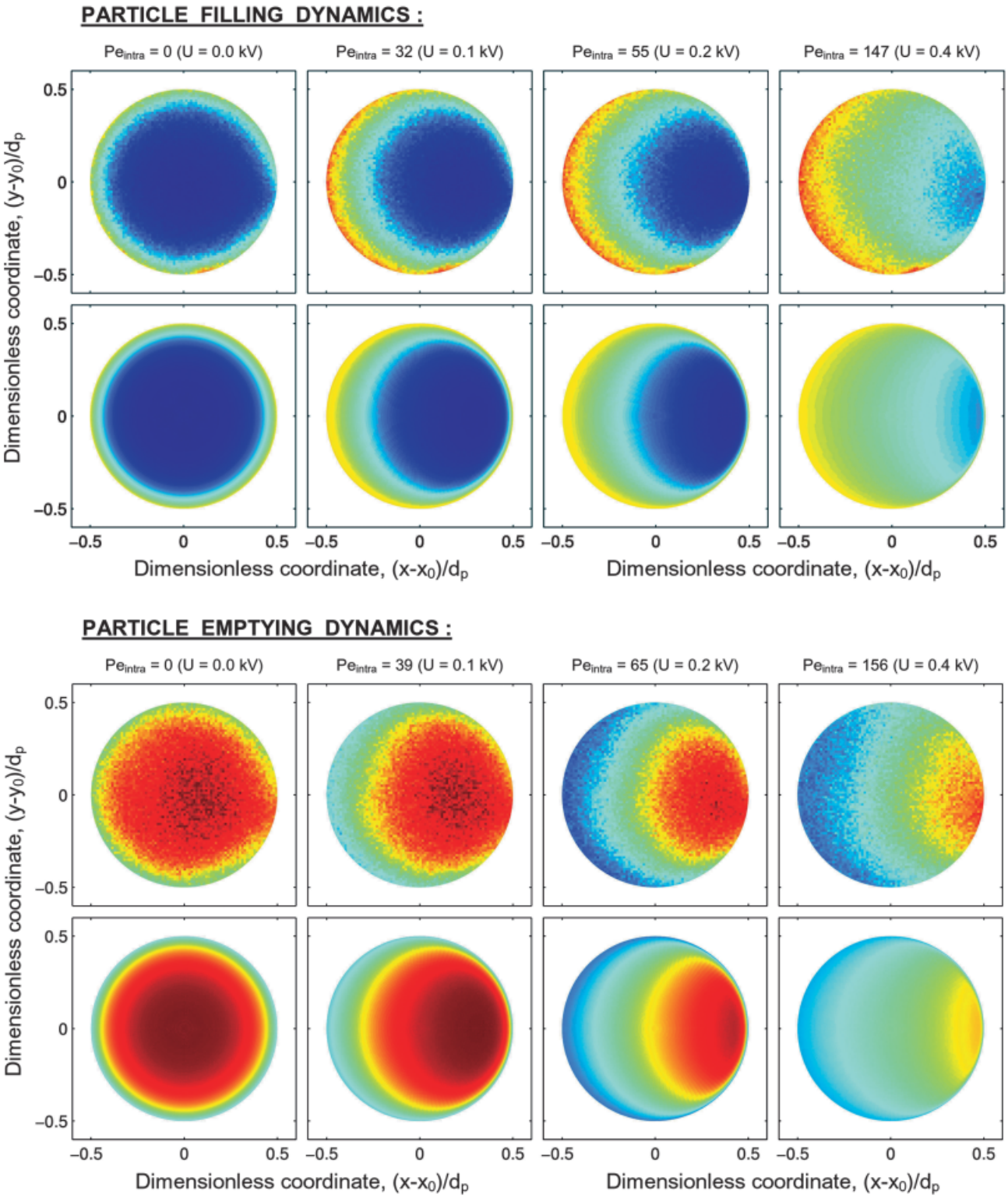

Figure 4. Intraparticle two-dimensional profiles of normalized concentration for electroneutral tracer molecules in a 12.4 μm thick *xy*-slice parallel to the column axis (and through the center of a single particle) during filling and emptying processes under various conditions. Experimental results (top rows) are compared with best fits of the mathematical model (bottom rows). The applied electrical field created electroosmotic mobility from left to right in the two-dimensional profiles which, in general, correspond to observation times of about 0.5 s (*cf.* Fig. 3). During a measurement electrical currents were constant and on a decent level (*e.g.*, 6 μA for $U = 0.4$ kV which translates to $E = 26.7$ kV/m).

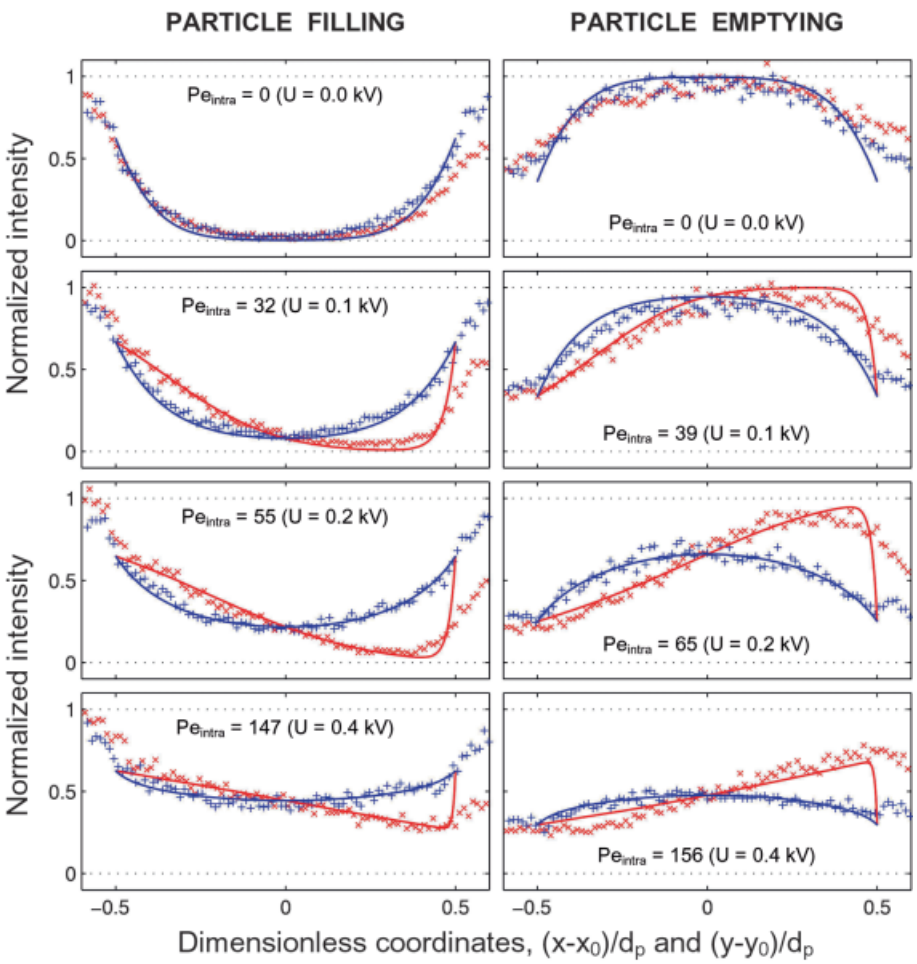

Figure 5. Tracer distribution profiles recorded along horizontal (red) and vertical (blue) center lines through the 12.4 μm thick *xy*-slice of a single spherical particle during its filling (left column) and emptying (right column). The data refer to the two-dimensional profiles seen in Fig. 4 and solid lines are best fits of the mathematical model to these data. The applied electrical field created electroosmotic mobility from left to right in the tracer distribution profiles and running mobile phase was a 90:10 vol% DMSO-H_2O mixture containing NaCl with an effective ionic strength of 10^{-3} M. For the purely diffusive filling and emptying processes ($E = 0$ kV/m) the fitting results coincide for both profile directions, indicating an isotropic and symmetrical behavior.

particle space. Thus, this finite response at the particles external surface (still assumed as occuring uniformly) must be incorporated in the respective boundary condition as explained in Fig. 2, *i.e.*, $\tilde{c} = \tilde{c}_{ext}(\tau)$. The influence of an electrical field on the intraparticle mass transfer kinetics during particle filling and emptying manifests itself in a much faster attainment of equilibrium (Figs. 3b and d) compared with the diffusion-limited operation as a "reference dynamics" for which $Pe_{intra} = 0$ (because $E = 0$ kV/m). Results of these systematic studies in view of the obtained parameters t_0, D_{intra}, v_{intra}, and Pe_{intra} are summarized in Tables 1 and 2. The single-bead CLSM analysis on which our experimental data are based has focused on a particle immediately behind the glass fiber inlet filter to avoid re-entry of tracer molecules during the emptying process originating in their release from the intraparticle pore space of glass beads located upstream. As seen in Table 1 for two representative subsequent (filling-emptying) cycles, the reproducibility of data acquired with the device and technique is good.

Table 2. Analysis of perfusive transport (U as indicated)

	$U = 0.1$ kV		$U = 0.2$ kV		$U = 0.4$ kV	
	Filling	Emptying	Filling	Emptying	Filling	Emptying
v_{intra} (m/s)	3.18×10^{-5}	3.87×10^{-5}	5.36×10^{-5}	6.34×10^{-5}	1.43×10^{-4}	1.52×10^{-4}
Pe_{intra}	32.4	39.5	54.8	64.7	146.6	155.7
d_p (m)	1.93×10^{-4}	1.93×10^{-4}	1.93×10^{-4}	1.93×10^{-4}	1.94×10^{-4}	1.94×10^{-4}

The data in Tables 1 and 2 demonstrate that the tracer transport kinetics for a porous glass bead with d_p = 194 μm (fitted average value) is significantly increased beyond the diffusion-limited regime by application of an electrical field. It is dominated by intraparticle EOF which, under the actual conditions and assumptions (*e.g.*, uncharged tracer and isothermal flow), is the only explanation for this massive transport enhancement. For example, with the highest potential gradient of only 0.4 kV $Pe_{intra} \approx 150$. Keeping in mind that Pe_{intra} (Eq. 7) represents the actual ratio of characteristic dimensionless times for convection ($v_{intra}t/d_p$) and diffusion ($D_{intra}t/d_p^2$) it is straightforward to see that the convection clearly dominates over diffusion in mass transport on a particle scale. Two aspects are worth mentioning in a discussion of Pe_{intra} (Table 2) with respect to the purely diffusive intraparticle transport kinetics (Table 1). First, the high values for Pe_{intra} in the present case are only realized because of a rather large d_p compared to current CEC practice (d_p = 3–10 μm). Second, significant EDL overlap exists inside the glass beads because of a modest electrolyte concentration in the mobile phase (*cf.* Fig. 3). It leads to an estimate of the Debye screening length (λ_D) of approximately 10 nm [67], while the average intraparticle pore size (d_{pore}) is 120 nm. Consequently, $r_{pore}/\lambda_D = 6$ only which means that strong EDL overlap contributes to limit the attainable velocities inside a particle. Although this problem could be partly resolved by using a higher electrolyte concentration to compress the EDL further (and increase pore flow), the maximum electrical field strength and current, together with the ionic strength are limited by Joule heat that is generated in a packed capillary [34, 68].

Returning to the first aspect, as d_p is reduced toward the submicrometer dimension, purely diffusive intraparticle mass transfer becomes increasingly competitive with respect to perfusive transport. Plate height data for columns packed with nanoparticles then anyway cannot be recorded sufficiently far beyond that regime ($Pe = v_{av}d_p/D_m < 5$; v_{av} is the average velocity through a column and D_m is the analytes mobile-phase diffusivity) in which molecular diffusion dominates overall dispersion, presenting the ultimate limitation to performance [69, 70]. As demonstrated recently, the hold-up contribution to dispersion originating in the intraparticle stagnant zone begins to dominate the longitudinal dispersion in beds of porous particles only if $Pe > 25$ [20]. The ratio of characteristic interparticle convective to intraparticle diffusive times becomes more sensitive again for an electroosmotic perfusion mechanism (as d_p is reduced) when the diffusivity of analyte molecules decreases concomitantly and/or additional pressure-driven flow is used for accelerating transport in the interparticle pore space to reduce the analysis time of electrochromatographic separations when needed. Because of hardware aspects related to the generation of stable liquid flow hydraulic assistance in CEC requires beds having a decent hydraulic permeability [71] that cannot be realized with nanoparticles. The mechanical strength of fused-silica capillaries and efficient packing of nanoparticles as sufficiently extended fixed beds present further limitations [72, 73]. Thus, it appears advantageous to employ larger particles (d_p = 5–10 μm) for achieving a higher interparticle hydraulic permeability and then utilize the electroosmotic perfusion mechanism in (pressurized) CEC for an independent optimization of separation efficiency and adsorption capacity by adjustment of the EDL thickness and surface-to-volume ratio of the intraparticle pore space. An alternative to this procedure is the use of pressure-assisted electroosmotic perfusive flow through a comparatively permeable and mechanically stable high-surface-area continuous structure like the silica-based monolith with its tailored bimodal pore size distribution [74].

In the next step (Figs. 4 and 5), we analyzed the distribution profiles of the uncharged tracer inside a particle associated with the augmented mass transfer kinetics (Fig. 3, Tables 1 and 2) due to an intraparticle-forced electroosmotic convection. As seen in Fig. 4, diffusion-limited transport (resulting when only a pressure gradient is used for moving liquid through the device, *i.e.*, E = 0 kV/m) produces distribution profiles during an uptake of tracer by the empty particle or its release from the saturated bead which reveal spherical symmetry. This is a well-known and anticipated behavior with respect to the initial and boundary conditions [41–43, 56, 75]. According to the spherical symmetry, intraparticle tracer profiles recorded along the axial and radial direction (*cf.* Fig. 2) during the particle filling and emptying processes (Fig. 5, top left and right, respectively) were coinciding reasonably. This observation, in turn, validates to a fair degree the initial assumption that the concentration of tracer at the particles external surface may be considered as uniform, even though Fig. 5 for the axial profiles (in the direction of pressure-driven interparticle convection) reveals a slightly lower (or higher, depending on a particular process) tracer concentration at the downstream than the upstream side of the particle.

By contrast, an examination of the concentration profiles observed in the presence of an (externally applied) electrical field reveals distinct deviations from the spherical symmetry under identical boundary conditions for the tracer concentration at a particles external surface (*cf.* Figs. 3a and c). The uncharged fluorescent molecules responded to the unidirectional driving force by producing nonsymmetric distribution profiles parallel to it (Figs. 4 and 5), but perpendicular to the applied field the profiles

retained their symmetric nature (see Fig. 5 for details). The applied field yielded an electroosmotic mobility from left to right across the contour plot (Fig. 4). For a slice parallel to the flow direction the results show that during an uptake (release) of tracer the intraparticle EOF moves the concentration minimum (maximum) downstream as compared to pure molecular diffusion, resulting in higher (lower) concentrations in the upstream half of the sphere than the downstream. It is caused by the fact that convection operates in the same (opposite) direction as diffusion in the upstream half of a bead, but opposite (parallel) to diffusion downstream [18]. Thus, for nearly half of the molecules intraparticle convection occurs in the direction opposite to their diffusive mass transfer and, consequently, situations should be avoided where these opposing transports would be of similar magnitude. As expected (and demonstrated by Figs. 4 and 5) departure from spherical symmetry becomes more pronounced as Pe_{intra} increases.

If the tracer molecules were charged (but, to keep this analysis systematic, still nonadsorbing at the particles surface) they would possess an additional intraparticle electrophoretic mobility, being either parallel or opposite to the unidirectional motion caused by intraparticle EOF. This depends on the relative sign of tracer charges with respect to the net surface charge. As was demonstrated recently [48], compared to the situation for an uncharged tracer, the particles then can become filled from the downstream side (concerning the direction of net flow through a porous medium due to the applied gradients in pressure and electrical potential) if the electrophoretic mobility of charged tracer is higher than the EOF field mobility and points in opposite direction. While this counteraction still resulted in a faster intraparticle mass transfer compared to the purely diffusive kinetics (for identical initial and boundary conditions), it may adversely affect the overall performance in pure CEC (*i.e.*, without the pressure-driven flow component), as it prevents charged analytes from being transported down the column by the EOF alone. Thus, also those situations should be avoided where (opposite) electroosmotic and electrophoretic mobilities become of similar magnitude. Further complexity in the analysis involving charged tracers may arise due to the permselectivity of a particle and (concentration) boundary-layer mass transfer resistance [62, 63].

4 Concluding remarks

Quantitative CLSM studies of intraparticle purely diffusive and combined diffusive-convective mass transfer (the latter due to flow induced by an externally applied electrical field) have revealed the following behavior for the spatio-temporal dynamics of electroneutral unretained fluorescent tracer in spherical-shaped porous particles under a set of well-defined boundary conditions. First, the unidirectional character of intraparticle EOF which is in contrast to the stochastic nature of diffusion reduces spherical to an axial symmetry (with respect to the direction of the applied field) of the distribution profiles observed during tracer uptake by an empty particle or its release from saturated beads (Figs. 4 and 5). However, the symmetry aspect is not the only characteristics in the tracer distribution profile that changed as a consequence of increasing Pe_{intra}. As already demonstrated by the mass transfer kinetics in Figs. 3b and d, the average concentration of tracer in a particle increases (decreases) with respect to the diffusion-limited process during the particles response to changes in the external tracer concentration. A range was covered from diffusion-limited ($Pe_{intra} = 0$) to convection-dominated ($Pe_{intra} = 150$) intraparticle transport. Thus, the EOF drastically reduced overall intraparticle mass transfer resistance and the electroosmotic perfusion provides one mechanism by which a significantly improved separation performance may be achieved [25, 28–30].

It should be emphasized that a convection-dominated transport in our device is already approached at relatively moderate field strengths. For example, the voltage of 0.1 kV (leading to $Pe_{intra} \approx 35$) translates to $E = 6.7$ kV/m. Due to the dielectric constant and viscosity of DMSO a measured intraparticle electroosmotic mobility of about 5×10^{-9} $m^2s^{-1}V^{-1}$ is expectedly lower than with a purely aqueous electrolyte solution having the same ionic strength or for one containing (an in this view) more favorable organic modifier like acetonitrile, methanol, or acetone [76]. However, the resulting mobile-phase compositions are not suitable for quantitative CLSM studies based on liquid-solid phase RI matching and the use of DMSO is a compromise [48].

By providing complementary information, Figs. 3–5 reveal experimentally and, in good agreement with the CLSM data, also describe *via* our presented mathematical model (Section 2.4) the basic effects of an intraparticle velocity during electroosmotic perfusion through particulate beds. Both the average temporal concentration and spatial distribution of tracer were significantly affected depending on Pe_{intra}. Based on the conditions encountered in our work, this parameter needs to be carefully considered and scaled to the actual dimensions of a particular system when estimating the benefits of electroosmotic perfusion. In general, flow inside particles, the classical stagnant zone [77], is advantageous for dispersion because it reduces (in a global sense) the velocity inequality of the flow pattern through the porous medium. However,

it becomes less effective compared to intraparticle diffusion ($Pe_{intra} = v_{intra}d_p/D_m$) as the particle diameter is reduced. On the other hand, the diffusivities of typically relevant analytes span a range from 10^{-9} to 10^{-12} m^2/s and, thus, they also determine inherently the relative importance of an electroosmotic perfusion. Concerning the remaining parameter in Eq. (7) (v_{intra}) our results clearly demonstrate that the substantial EDL overlap ($r_{pore}/\lambda_D = 6$) presents no limitation to an already significantly increased intraparticle mass transfer rate constant, and that the resulting average pore velocity can be still significant compared to purely diffusive time scales, even when r_{pore}/λ_D approaches unity and r_{pore} is only a few nanometers. Nevertheless, the intraparticle flow can be increased by applying higher fields (and/or mobile-phase ionic strengths leading to further suppression of EDL overlap). However, at least with the present device limitations then may arise from Joule heating.

Closely related to a dependence of intraparticle EDL overlap on ionic strength is the corresponding behavior in the interparticle pore space where the average channel size or a characteristic dimension normal to the local surface is much larger than for the intraparticle pore space. While the suppression of EDL overlap may dominate the effect of an increasing ionic strength on volumetric EOF inside a particle (leading to flow enhancement), it is the usual electrokinetic behavior beyond EDL overlap [67] which dominates between particles. The latter predicts a decrease of EOF upon further compaction of the EDL. Because the general dependence of EOF on ionic strength is supposed to have a similar form for both (fictitiously decoupled) pore spaces, but with only the characteristic features translated to the different r_{pore}/λ_D ratios it may provide a mechanism by which intra- and interparticle velocities can be aligned *via* the controlled increase of EOF inside and its concomitant decrease between the particles. For that purpose, both the ratio of inter- to intraparticle pore dimensions (through d_p/d_{pore}) and λ_D need to be adjusted.

The actual value of Pe_{intra} results from a complex interplay between pore space morphology and topology (including the pore size distribution and pore interconnectivity), properties of the saturating liquid (like ionic strength and dielectric constant), electrical field strength, the origin, stability, and spatial homogeneity of chemical surface modifications, as well as the molecular diffusion coefficient of tracer molecules in the pore liquid. Our experimental approach and derived data are a useful basis for detailed further studies of more complex electrokinetic phenomena, *e.g.*, the transport of charged molecules in hierarchically structured media containing fine pores (particulate beds, monoliths, membranes) with a substantial EDL overlap in part of the pores and strong adsorption at the surface. In these cases, a similar complementary information as provided by Figs. 3–5 helps to resolve transport mechanisms (surface *vs.* pore diffusion, electroosmotic *vs.* electrophoretic motion), determine relevant parameters (ion mobilities, fluid velocities), or analyze peculiar features of concentration polarization in strong electrical fields and nonlinear phenomena which reflect the performance of a particular electrokinetic process.

Received May 25, 2003

5 References

[1] Afeyan, N. B., Gordon, N. F., Mazsaroff, I., Varady, L., Fulton, S. P., Yang, Y. B., Regnier, F. E., *J. Chromatogr.* 1990, *519*, 1–29.

[2] Rodrigues, A. E., Lu, Z. P., Loureiro, J. M., *Chem. Eng. Sci.* 1991, *46*, 2765–2773.

[3] Liapis, A. I., McCoy, M. A., *J. Chromatogr.* 1992, *599*, 87–104.

[4] Rodrigues, A. E., Lopes, J. C., Lu, Z. P., Loureiro, J. M., Dias, M. M., *J. Chromatogr.* 1992, *590*, 93–100.

[5] Carta, G., Gregory, M. E., Kirwan, D. J., Massaldi, H. A., *Sep. Technol.* 1992, *2*, 62–72.

[6] Frey, D. D., Schweinheim, E., Horváth, Cs., *Biotechnol. Prog.* 1993, *9*, 273–284.

[7] Carta, G., Rodrigues, A. E., *Chem. Eng. Sci.* 1993, *48*, 3927–3935.

[8] Davis, R. H., Stone, H. A., *Chem. Eng. Sci.* 1993, *48*, 3993–4005.

[9] Reeder, D. H., Clausen, A. M., Annen, M. J., Carr, P. W., Flickinger, M. C., McCormick, A. V., *J. Colloid Interface Sci.* 1996, *184*, 328–330.

[10] Gustavsson, P.-E., Larsson, P.-O., *J. Chromatogr. A* 1996, *734*, 231–240.

[11] McCoy, M., Kalghatgi, K., Regnier, F. E., Afeyan, N., *J. Chromatogr. A* 1996, *743*, 221–229.

[12] Nash, D. C., Chase, H. A., *J. Chromatogr. A* 1998, *807*, 185–207.

[13] Meyers, J. J., Liapis, A. I., *J. Chromatogr. A* 1998, *827*, 197–213.

[14] Li, Q. L., Grandmaison, E. W., Goosen, M. F. A., Taylor, D., *AIChE J.* 2000, *46*, 1927–1936.

[15] Van Kreveld, M. E., Van den Hoed, N., *J. Chromatogr.* 1978, *149*, 71–91.

[16] Nir, A., Pismen, L. M., *Chem. Eng. Sci.* 1977, *32*, 35–41.

[17] Rodrigues, A. E., Ahn, B. J., Zoulalian, A., *AIChE J.* 1982, *28*, 541–546.

[18] Stephanopoulos, G., Tsiveriotis, K., *Chem. Eng. Sci.* 1989, *44*, 2031–2039.

[19] Pfeiffer, J. F., Chen, J. C., Hsu, J. T., *AIChE J.* 1996, *42*, 932–939.

[20] Kandhai, D., Hlushkou, D., Hoekstra, A. G., Sloot, P. M. A., Van As, H., Tallarek, U., *Phys. Rev. Lett.* 2002, *88*, article no. 234501.

[21] Knox, J. H., *J. Chromatogr. A* 1999, *831*, 3–15.

[22] Tallarek, U., Vergeldt, F. J., Van As, H., *J. Phys. Chem. B* 1999, *103*, 7654–7664.

[23] Venema, E., Kraak, J. C., Poppe, H., Tijssen, R., *J. Chromatogr. A* 1999, *837*, 3–15.

[24] Vallano, P. T., Remcho, V. T., *J. Phys. Chem. B* 2001, *105*, 3223–3228.

[25] Tallarek, U., Rapp, E., Van As, H., Bayer, E., *Angew. Chem. Int. Ed.* 2001, *40*, 1684–1687.

[26] Probstein, R. F., *Physicochemical Hydrodynamics*, John Wiley & Sons, New York 1994, Chapter 6.

[27] Stol, R., Kok, W. Th., Poppe, H., *J. Chromatogr. A* 1999, *853*, 45–54.

[28] Wen, E., Asiaie, R., Horváth, Cs., *J. Chromatogr. A* 1999, *855*, 349–366.

[29] Vallano, P. T., Remcho, V. T., *Anal. Chem.* 2000, *72*, 4255–4265.

[30] Stol, R., Poppe, H., Kok, W. T., *Anal. Chem.* 2001, *73*, 3332–3339.

[31] Dearie, H. S., Smith, N. W., Moffat, F., Wren, S. A. C., Evans, K. P., *J. Chromatogr. A* 2002, *945*, 231–238.

[32] Rice, C. L., Whitehead, R., *J. Phys. Chem.* 1965, *69*, 4017–4024.

[33] Stol, R., Poppe, H., Kok, W. T., *J. Chromatogr. A* 2000, *887*, 199–208.

[34] Crego, A. L., González, A., Marina, M. L., *Crit. Rev. Anal. Chem.* 1996, *26*, 261–304.

[35] Koch, D. L., Brady, J. F., *J. Fluid Mech.* 1985, *154*, 399–427.

[36] Sahimi, M., *Flow and Transport in Porous Media and Fractured Rock*, VCH, Weinheim 1995, Chapter 9.

[37] Tallarek, U., Bayer, E., Guiochon, G., *J. Am. Chem. Soc.* 1998, *120*, 1494–1505.

[38] Pačes, M., Kosek, J., Marek, M., Tallarek, U., Seidel-Morgenstern, A., *Electrophoresis* 2003, *24*, 380–389.

[39] Poppe, H., Stol, R., Kok, W. T., *J. Chromatogr. A* 2002, *965*, 75–82.

[40] Grimes, B. A., Lüdtke, S., Unger, K. K., Liapis, A. I., *J. Chromatogr. A* 2002, *979*, 447–466.

[41] Kim, H.-B., Hayashi, M., Nakatani, K., Kitamura, N., Sasaki, K., Hotta, J., Masuhara, H., *Anal. Chem.* 1996, *68*, 409–414.

[42] Ljunglöf, A., Hjorth, R., *J. Chromatogr. A* 1996, *743*, 75–83.

[43] Ljunglöf, A., Thömmes, J., *J. Chromatogr. A* 1998, *813*, 387–395.

[44] Linden, T., Ljunglöf, A., Kula, M.-R., Thömmes, J., *Biotechnol. Bioeng.* 1999, *65*, 622–630.

[45] Rademann, J., Barth, M., Brock, R., Egelhaaf, H.-J., Jung, G., *Chem. Eur. J.* 2001, *7*, 3884–3889.

[46] Hubbuch, J., Linden, T., Knieps, E., Thömmes, J., Kula, M.-R., *Biotechnol. Bioeng.* 2002, *80*, 359–368.

[47] Lowry, M., He, Y., Geng, L., *Anal. Chem.* 2002, *74*, 1811–1818.

[48] Tallarek, U., Rapp, E., Sann, H., Reichl, U., Seidel-Morgenstern, A., *Langmuir* 2003, *19*, 4527–4531.

[49] Wilson, T., *Confocal Microscopy*, Academic Press, London 1990.

[50] Pawley, J. B., *Handbook of Biological Confocal Microscopy*, Plenum, New York 1995.

[51] Visser, T. D., Groen, F. C. A., Brakenhoff, G. J., *J. Microsc.* 1991, *163*, 189–200.

[52] Sheppard, C. J. R., Török, P., *J. Microsc.* 1997, *185*, 366–374.

[53] Booth, M. J., Neil, M. A. A., Wilson, T., *J. Microsc.* 1998, *192*, 90–98.

[54] Booth, M. J., Wilson, T., *J. Biomed. Opt.* 2001, *6*, 266–272.

[55] Diaspro, A., Federici, F., Robello, M., *Appl. Opt.* 2002, *41*, 685–690.

[56] Liljeborg, A., *Proc. SPIE* 1996, *2655*, 11–17.

[57] Kluijtmans, S. G. J. M., de Hoog, E. H. A., Philipse, A. P., *J. Chem. Phys.* 1998, *108*, 7469–7477.

[58] Malmsten, M., Xing, K., Ljunglöf, A., *J. Colloid Interface Sci.* 1999, *220*, 436–442.

[59] Webb, R. H., *Rep. Prog. Phys.* 1996, *59*, 427–471.

[60] Grimes, B. A., Liapis, A. I., *J. Sep. Sci.* 2002, *25*, 1202–1214.

[61] Tallarek, U., Rapp, E., Seidel-Morgenstern, A., Van As, H., *J. Phys. Chem. B* 2002, *106*, 12709–12721.

[62] Mishchuk, N. A., Takhistov, P. V., *Colloids Surf. A* 1995, *95*, 119–131.

[63] Rubinstein, I., Zaltzman, B., in: Sørensen, T. S. (Ed.), *Surface Chemistry and Electrochemistry of Membranes*, Marcel Dekker, New York 1999, pp. 591–621.

[64] Lu, Z. P., Dias, M. M., Lopes, J. C. B., Carta, G., Rodrigues, A. E., *Ind. Eng. Chem. Res.* 1993, *32*, 1839–1852.

[65] Jennings, A. A., Mansharamani, P., *Environ. Modell. Software* 1999, *14*, 624–635.

[66] Finlayson, B. A., *Nonlinear Analysis in Chemical Engineering*, McGraw-Hill, New York 1980.

[67] Lyklema, J., *Fundamentals of Interface and Colloid Science. Vol. II: Solid-Liquid Interfaces*, Academic Press, London 1995.

[68] Rathore, A. S., Reynolds, K. J., Colón, L. A., *Electrophoresis* 2002, *23*, 2918–2928.

[69] Knox, J. H., *Chromatographia* 1988, *26*, 329–337.

[70] Unger, K. K., Lüdtke, S., Grün, M., *LC·GC Int.* 1999, *12*, 870–874.

[71] Rapp, E., Tallarek, U., *J. Sep. Sci.* 2003, *26*, 453–470.

[72] Engelhardt, H., Hafner, F.-T., *Chromatographia* 2000, *52*, 769–776.

[73] Colón, L. A., Maloney, T. D., Fermier, A. M., *J. Chromatogr. A* 2000, *887*, 43–53.

[74] Leinweber, F. C., Tallarek, U., *J. Chromatogr. A* 2003, *1006*, 207–228.

[75] Crank, J., *The Mathematics of Diffusion*, Clarendon Press, Oxford 1956.

[76] Banholczer, A., Pyell, U., *J. Chromatogr. A* 2000, *869*, 363–374.

[77] Giddings, J. C., *Dynamics of Chromatography. Part I: Principles and Theory*, Marcel Dekker, New York 1965.

Nonequilibrium Electrokinetic Effects in Beds of Ion-Permselective Particles

Felix C. Leinweber and Ulrich Tallarek*

Institut für Verfahrenstechnik, Otto-von-Guericke-Universität Magdeburg, Universitätsplatz 2, 39106 Magdeburg, Germany

Received June 28, 2004. In Final Form: September 22, 2004

Electrokinetic transport of fluorescent tracer molecules in a bed of porous glass beads was investigated by confocal laser scanning microscopy. Refractive index matching between beads and the saturating fluid enabled a quantitative analysis of intraparticle and extraparticle fluid-side concentration profiles. Kinetic data were acquired for the uptake and release of electroneutral and counterionic tracer under devised conditions with respect to constant pressure-driven flow through the device and the effect of superimposed electrical fields. Transport of neutral tracer is controlled by intraparticle mass transfer resistance which can be strongly reduced by electroosmotic flow, while steady-state distributions and bead-averaged concentrations are unaffected by the externally applied fields. Electrolytes of low ionic strength caused the transport through the charged (mesoporous) beads to become highly ion-permselective, and concentration polarization is induced in the bulk solution due to the superimposed fields. The depleted concentration polarization zone comprises extraparticle fluid-side mass transfer resistance. Ionic concentrations in this diffusion boundary layer decrease at increasing field strength, and the flux densities approach an upper limit. Meanwhile, intraparticle transport of counterions by electromigration and electroosmosis continues to increase and finally exceeds the transport from bulk solution into the beads. A nonequilibrium electrical double layer is induced which consists of mobile and immobile space charge regions in the extraparticle bulk solution and inside a bead, respectively. These electrical field-induced space charges form the basis for nonequilibrium electrokinetic phenomena. Caused by the underlying transport discrimination (intraparticle electrokinetic vs extraparticle boundary-layer mass transfer), the dynamic adsorption capacity for counterions can be drastically reduced. Further, the extraparticle mobile space charge region leads to nonlinear electroosmosis. Flow patterns can become highly chaotic, and electrokinetic instability mixing is shown to increase lateral dispersion. Under these conditions, the overall axial dispersion of counterionic tracer can be reduced by more than 2 orders of magnitude, as demonstrated by pulse injections.

Introduction

Classical electrokinetic phenomena are usually treated in textbooks as operating in a single macroporous compartment confined by a locally flat, charged solid−liquid interface which itself is characterized by moderate values of the ζ-potential and a thin (compared to the macropore dimensions) fluid-side electrical double layer (EDL).[1−4] These electrolytes are considered as quasi-equilibrium systems in which the diffuse counterionic space charge responsible for electroosmotic flow (EOF) by interaction with an external electrical field is located directly at this interface. The quasi-equilibrium (primary) EDL is assumed as stable and unaffected by the external fields concerning its charge density and dimension. Therefore, the properties of this space charge layer only depend on static electrolyte and material characteristics, for example, ionic strength and surface charge density, but not on the fluid dynamics. Consequently, the EOF velocity follows a linear relationship with respect to the applied field strength, as described by the Helmholtz−Smoluchowski equation.[1−4] Many experimental studies support the assumption that the average EOF velocity in fixed beds of porous (permeable and conducting) particles depends linearly on the field strength.[5−11] Any influence of intraparticle meso- and/or microporous compartments on charge transport, the ionic concentration distributions, and bulk flow is usually neglected.

However, the transport of charged species such as simple ions, analyte molecules, or globular particles is actually much more complex in such porous media with a hierarchically structured pore space characterized by a high degree of interconnectivity between the different sets of pores. In addition to the bulk electrolyte in the macroporous compartment with equivalent ionic concentrations and balanced ionic fluxes, at least another meso- and/or microporous compartment has to be taken into account. For example, the mean size of mesopores is of the order of a typical EDL thickness or even smaller. Then, the diffuse space charge region at the solid−liquid interface extends over the whole cross section of a pore. This EDL overlap leads to an enrichment of counterions in the mesoporous domain but exclusion of co-ions. At electrochemical equilibrium, the Donnan potential balances the concentration gradient of ions between macro- and mesoporous domains.[2,12,13]

The distribution of ionic concentrations under these conditions is shown in Figure 1a. Strong EDL overlap and

* To whom correspondence should be addressed. Fax: +49 (0)-391-67-12028. E-mail: ulrich.tallarek@vst.uni-magdeburg.de.

(1) Overbeek, J. Th. G. In *Colloid Science*; Kruyt, H. R., Ed.; Elsevier: Amsterdam, The Netherlands, 1952; Vol. 1, pp 194−244.
(2) Helfferich, F. *Ion Exchange*; McGraw-Hill: New York, 1962.
(3) Lyklema, J. *Fundamentals of Interface and Colloid Science, Vol. I: Fundamentals*; Academic Press: San Diego, CA, 1991.
(4) Probstein, R. F. *Physicochemical Hydrodynamics*; John Wiley & Sons: New York, 1994.
(5) Pretorius, V.; Hopkins, B. J.; Schieke, J. D. *J. Chromatogr.* **1974**, *99*, 23.
(6) Jorgenson, J. W.; Lukacs, K. D. *J. Chromatogr.* **1981**, *218*, 209.
(7) Knox, J. H.; Grant, I. H. *Chromatographia* **1987**, *24*, 135.
(8) Knox, J. H.; Grant, I. H. *Chromatographia* **1991**, *32*, 317.
(9) Dittmann, M. M.; Wienand, K.; Bek, F.; Rozing, G. P. *LC-GC* **1995**, *13*, 800.
(10) Crego, A. L.; González, A.; Marina, M. L. *Crit. Rev. Anal. Chem.* **1996**, *26*, 261.
(11) Deyl, Z., Svec, F., Eds. *Capillary Electrochromatography*; Elsevier: Amsterdam, The Netherlands, 2001.

10.1021/la048408n CCC: $27.50
Published on Web 11/16/2004

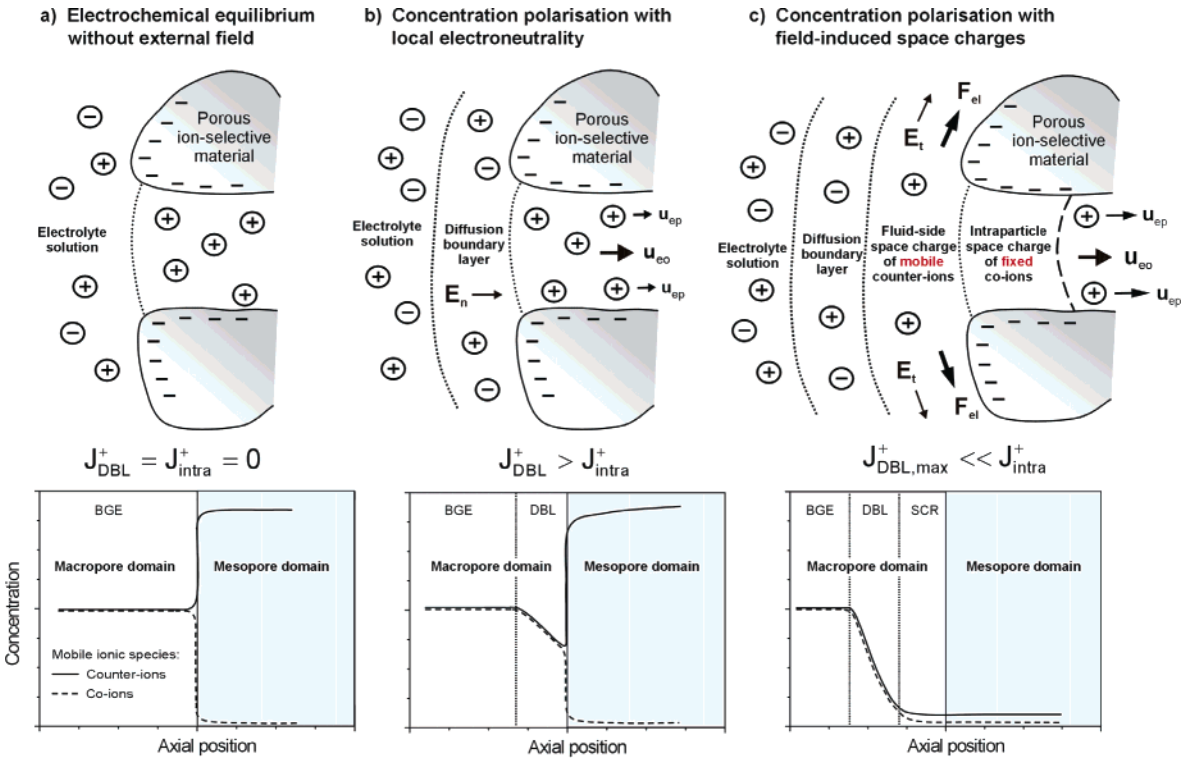

Figure 1. Schematic view on the concentration distributions and transport properties of ionic species in a mesoporous, ion-permselective support particle and the adjacent electrolyte solution (here, at the anodic pole of the material with negative surface charge density). The normalized concentration profiles for mobile counterions and co-ions reflect (a) Donnan equilibrium without an applied field and (b and c) different stages of the concentration polarization induced locally by the normal field component ($\mathbf{E}_n$). BGE, background electrolyte (electroneutral); DBL, diffusion boundary layer (electroneutral); SCR, fluid-side space charge region of a secondary EDL induced under nonequilibrium conditions (containing an excess of mobile counterions). $\mathbf{F}_{el}$ denotes the interaction of the mobile SCR with the tangential component of the applied field ($\mathbf{E}_t$) leading to electroconvection in the macropore space outside a particle. $\mathbf{J}^+_{intra}$ is the intraparticle counterion flux density due to electrophoretic and electroosmotic velocities ($\mathbf{u}_{ep}$ and $\mathbf{u}_{eo}$), and $\mathbf{J}^+_{DBL}$ is the diffusive flux density through the DBL.

the resulting equilibrium concentrations of mobile co-ions and counterions within the mesopores cause a highly ion-permselective mass transport as driving forces are superimposed. The interior of the mesoporous particles shows ion-exchange properties which become aggravated by an increasing EDL overlap. Favored permeation of counterions is the main transport characteristic of ion-exchange materials, and ion-permselective transport is the basis for various electrochemical and electrokinetic processes including electrode reactions and electrodialysis.[14,15] A theoretical treatment of coupled mass and charge transport in fixed beds of porous particles thus may be improved by models developed for transport through ion-exchange membranes.[15–24] The main implication of coupled transport is that under the influence of either chemical or electrical potential gradients concentration polarization develops.[25–33] As a consequence, zones of increased and decreased ionic concentrations occur in the bulk fluid at the cathodic and anodic interfaces of a (cation-selective) porous bead, respectively. Concentration distributions at the anodic pole are illustrated in Figure 1b. Under these conditions, the electrical current through an ion-permselective particle in a fixed bed remains in the Ohmic region. Local electroneutrality is preserved in the depleted concentration polarization zone of the macropore space between the particles, as well as in the intraparticle mesopore space.

Concentration polarization plays a central role in many electrokinetic processes because it affects both local ionic concentrations and mass transport in order to preserve the continuity of mass and charge fluxes. Especially the zone of decreased ionic concentration at the frontal (here, anodic) pole of a porous particle in a fixed bed is of importance because the ionic flux through this region is diffusion-limited due to the electrokinetically induced concentration gradient (Figure 1b).[14,15] This concentration polarization zone is a diffusion boundary layer which

(12) Donnan, F. G. *Z. Elektrochem.* **1911**, *17*, 572.
(13) Donnan, F. G.; Guggenheim, E. A. *Z. Phys. Chem.* **1932**, *162*, 346.
(14) Rubinstein, I. *Physical Electrochemistry*; Marcel Dekker: New York, 1995.
(15) Sørensen, T. S., Ed. *Surface Chemistry and Electrochemistry of Membranes*; Marcel Dekker: New York, 1999.
(16) Spiegler, K. S.; Yoest, R. L.; Wyllie, M. R. J. *Discuss. Faraday Soc.* **1956**, 174.
(17) Morrison, F. A.; Osterle, J. F. *J. Chem. Phys.* **1965**, *43*, 2111.
(18) Gross, R. J.; Osterle, J. F. *J. Chem. Phys.* **1968**, *49*, 228.
(19) Fair, J. C.; Osterle, J. F. *J. Chem. Phys.* **1971**, *54*, 3307.
(20) Saracco, G. *Chem. Eng. Sci.* **1997**, *52*, 3019.
(21) Sen, P. N. *Phys. Rev. B* **1989**, *39*, 9508.
(22) Révil, A.; Glover, P. W. J. *Phys. Rev. B* **1997**, *55*, 1757.
(23) Révil, A. *J. Colloid Interface Sci.* **1999**, *212*, 503.
(24) Basu, S.; Sharma, M. M. *J. Membr. Sci.* **1997**, *124*, 77.
(25) Mandersloot, W.; Hicks, R. E. *Ind. Eng. Chem. Process Des. Dev.* **1965**, *4*, 304.
(26) Khedr, G.; Varoqui, R. *Ber. Bunsen-Ges. Phys. Chem.* **1981**, *85*, 116.
(27) Rubinstein, I. *J. Chem. Soc., Faraday Trans. 2* **1990**, *86*, 1857.
(28) Koter, S.; Hamann, C. H. *J. Non-Equilib. Thermodyn.* **1990**, *15*, 315.
(29) Tanaka, Y. *J. Membr. Sci.* **1991**, *57*, 217.
(30) Manzanares, J. A.; Kontturi, K.; Mafé, S.; Aguilella, V. M.; Pellicer, J. *Acta Chem. Scand.* **1991**, *45*, 115.
(31) Manzanares, J. A.; Murphy, W. D.; Mafé, S.; Reiss, H. *J. Phys. Chem.* **1993**, *97*, 8524.
(32) Shaposhnik, V. A.; Vasil'eva, V. I.; Reshetnikova, E. V. *Russ. J. Electrochem.* **2000**, *36*, 773.
(33) Choi, J. H.; Park, J. S.; Moon, S. H. *J. Colloid Interface Sci.* **2002**, *251*, 311.

engenders a significant extraparticle fluid-side mass transfer resistance to the counterionic flux from bulk solution toward an ion-exchange material's external surface and, therefore, into the ion-permselective, mesoporous compartment. At sufficiently low field strength, the resulting voltage−current curves on the single-particle scale are expected to follow Ohm's law. It should be realized that, in contrast to the membrane geometry, a bed of particles with large extraparticle voids remains charge-nonselective on the macroscopic scale. With increasing field strength, the concentration of ions in the depleted zone is reduced toward zero. Diffusion-limited transport through this boundary layer approaches a maximum value which, in the classical description of concentration polarization, particularly in the context of electrodialysis, is known as limiting current density.[25,26,34−38] On the other hand, classical models of concentration polarization consider transport properties as constant on temporal and spatial scales. Bulk and surface heterogeneities of the material as well as random fluctuations of fluid phase properties are not considered. Thus, static models are deficient of dynamic aspects and cannot explain overlimiting electrical current densities through a membrane.[39]

The potential of overcoming the limiting current densities has stimulated much research on concentration polarization and its effects in electrodialysis.[25,26,29−31] One possibility is to convectively reduce the thickness of the depleted polarization zone, for example, by vigorously stirring the fluid.[30] However, overlimiting current densities through an ion-exchange membrane have also been realized in macroscopically quiescent electrolyte solutions, by increasing electrical field strengths just further beyond values characterizing the plateau region.[40] Since that behavior cannot be described by the classical theory of electrodialysis,[38] dynamic mechanisms may account for overlimiting current densities. Detailed studies of this nonlinear regime have revealed periodically varying transmembrane currents which, at still higher field strengths, become oscillating at high frequencies.[39,40] A visualization of the hydrodynamics directly in the depleted concentration polarization zone has revealed strong fluctuations in the fluid phase, suggesting the existence of convection in close vicinity to the membrane surface.[41] Nonequilibrium electroosmotic slip has been proposed as the mechanism for hydrodynamic convection at the solid−liquid interface.[42] At higher field strengths, a nonequilibrium (secondary) EDL, in contrast to the quasi-equilibrium (primary) EDL, can be electrokinetically induced. It is located in the bulk fluid phase between the depleted concentration polarization zone and the pore fluid inside the solid (see Figure 1c, where the concentration profiles of ionic species are depicted—in the macroporous domain according to ref 43 and for the mesoporous domain as derived from experiments reported in this work). The nonequilibrium space charges are induced locally by the normal component of the applied electrical field and disturb the local electroneutrality of the system over a much larger region than the primary EDL. By body-force interaction of the bulk fluid-side space charge region with the tangential field component, the nonequilibrium electroosmotic slip results between the membrane surface and the diffusion boundary layer (as indicated in Figure 1c). Therefore, the originally quiescent concentration polarization zone is convectively disturbed and the resulting convective instability tends to destroy the diffusion boundary layer locally. Then, the diffusion limitation to the mass transport is removed in this region and overlimiting current densities through a membrane can be realized.[40,42,44−47]

Compared to the ion-exchange membranes, systems of a single ion-permselective particle (and multiparticle systems) locally show a similar transport behavior. Thus, due to an externally applied electrical field, concentration polarization is expected to develop as well, but in the granular systems, anodic and cathodic compartments around ion-exchange beads are actually connected via bulk solution. Even though the electrical currents through an ion-permselective bead can become overlimiting (which is quite difficult to verify experimentally in a bed of many spheres), the current density through the bed is determined by transport in the charge-nonselective macroporous compartment. Due to the thin-EDL approximation being valid on the macropore scale, a linear dependence of electrical current on applied field strength should be observed for any local intensity of concentration polarization under isothermal conditions. In contrast to extended vortices near the surface of a single sphere observed in closed electrolysis cells,[43,48] the extraparticle macropore space in fixed beds of such ion-permselective spheres allows a net nonequilibrium EOF based on the secondary EDL. Electrokinetics originating in these field-induced space charges is also referred to as nonequilibrium (or nonlinear) electrokinetics, or electrokinetics of the second kind.[43,49−52]

This nonequilibrium electrokinetics has a number of implications which, in the past, have been intensively investigated for systems containing isolated particles, either as a fixed single sphere or in the form of a dilute suspension. For freely dispersed spheres which are ionic or electrical conductors, a strong nonlinear dependence of electrophoretic velocity on the applied field strength could be measured, especially in low-ionic-strength electrolytes (electrophoresis of the second kind).[53−56] On the other hand, in devices containing a fixed single sphere, nonlinear dependence of EOF slip velocities around the curved

(34) Seno, M.; Yamagata, K.; Shinoda, J.; Yamabe, T. *J. Electrochem. Soc. Jpn.* **1966**, *34*, 232.
(35) Sata, T.; Yamane, R.; Mizutani, Y. *Bull. Chem. Soc. Jpn.* **1969**, *42*, 279.
(36) Yamane, R.; Sata, T.; Mizutani, Y.; Onoue, Y. *Bull. Chem. Soc. Jpn.* **1969**, *42*, 2741.
(37) Metayer, M.; Bourdille, C.; Selegny, E. *Desalination* **1973**, *13*, 129.
(38) Forgacs, C.; Ishibashi, N.; Leibovitz, J.; Sinkovic, J.; Spiegler, K. S. *Desalination* **1972**, *10*, 181.
(39) Rubinshtein, I.; Zaltzman, B.; Pretz, J.; Linder, C. *Russ. J. Electrochem.* **2002**, *38*, 956.
(40) Rubinstein, I.; Shtilman, L. *J. Chem. Soc.* **1972**, *75*, 231.
(41) Li, Q.; Fang, Y.; Green, M. E. *J. Colloid Interface Sci.* **1983**, *91*, 412.
(42) Rubinstein, I.; Zaltzman, B. *Phys. Rev. E* **2000**, *62*, 2238.
(43) Mishchuk, N. A.; Takhistov, P. V. *Colloids Surf., A* **1995**, *95*, 119.
(44) Rubinstein, I.; Maletzki, F. *J. Chem. Soc., Faraday Trans. 2* **1991**, *87*, 2079.
(45) Rubinstein, I. *Phys. Fluids A* **1991**, *3*, 2301.
(46) Zholkovskij, E. K.; Vorotyntsev, M. A.; Staude, E. *J. Colloid Interface Sci.* **1996**, *181*, 28.
(47) Vasil'eva, V. I.; Shaposhnik, V. A.; Grigorchuk, O. V.; Malykhin, M. D. *Russ. J. Electrochem.* **2002**, *38*, 846.
(48) Ben, Y.; Chang, H.-C. *J. Fluid Mech.* **2002**, *461*, 229.
(49) Dukhin, S. S. *Adv. Colloid Interface Sci.* **1991**, *35*, 173.
(50) Rastogi, R. P.; Srivastava, R. C.; Singh, S. N. *Chem. Rev.* **1993**, *93*, 1945.
(51) Barany, S. *Adv. Colloid Interface Sci.* **1998**, *75*, 45.
(52) Ben, Y.; Demekhin, E. A.; Chang, H.-C. *J. Colloid Interface Sci.* **2004**, *276*, 483.
(53) Dukhin, S. S.; Mishchuk, N. A.; Tarovskii, A. A.; Baran, A. A. *Colloid J. USSR* **1987**, *49*, 544.
(54) Mishchuk, N. A.; Barany, S.; Tarovsky, A. A.; Madai, F. *Colloids Surf., A* **1998**, *140*, 43.
(55) Barany, S.; Mishchuk, N. A.; Prieve, D. C. *J. Colloid Interface Sci.* **1998**, *207*, 240.
(56) Mishchuk, N.; Gonzalez-Gaballero, F.; Takhistov, P. *Colloids Surf., A* **2001**, *181*, 131.

surface of the sphere on the field strength was revealed (electroosmosis of the second kind).[43,57−61] Since most investigations of electroosmosis of the second kind were made in a closed electrolysis cell, no net flow through the cell from the anode to the cathode was possible. Then, to preserve mass continuity, extended vortices stationary for several minutes could be visualized in the bulk solution around the ion-permselective particles.[48]

To summarize the existing literature on the nonequilibrium space charge effects in ion-exchange materials and the consequences for the local and bulk fluid dynamics, most articles are concerned with primarily basic research, either in electrodialysis which employs flat membranes or in single-particle and dispersed systems, and only quite recently with microfluidic applications.[62] Concentration polarization, boundary-layer mass transfer resistance, and the induction of nonequilibrium space charges can be expected to affect the fluid dynamics also in dense multiparticle systems such as a random-close packing (fixed bed) of spheres. These effects are then relevant in several analytical, technological, and environmental processes including dewatering and remediation technologies and electrical field-assisted chromatographic separations.

This work is concerned with the visualization and analysis of the impact of electrical fields on the general (electro)hydrodynamics and, in particular, on the elution and desorption behavior of counterionic tracer in porous media containing discrete, ion-permselective domains. For a quantitative analysis of the applied electrical potential and pressure gradients, a model system consisting of a fixed bed of ion-permselective glass beads was implemented in a microfluidic device. This allowed us to study concentration distributions by confocal laser scanning microscopy at high temporal and spatial resolution in the packing and thereby gain profound insight into the dynamics of the coupled mass and charge transport. Central to the present work is an identification of the origin of nonequilibrium electrokinetic effects based on field-induced space charges which result from concentration polarization and nonlinear transport. First, the intraparticle and extraparticle fluid-side flow fields were investigated using electroneutral tracer. Then, the transport of a counterionic tracer was studied on the particle scale. Strong extraparticle mass transfer resistance could be revealed arising from a convective-diffusion boundary layer which itself results directly from concentration polarization around the glass beads, a behavior which could not be observed for the transport of electroneutral tracer. This phenomenon is of key importance for the loading and stationary concentration distribution and can be used to decouple electrokinetically the intraparticle counterionic concentrations from those in the extraparticle fluid. The data indicate that with sufficiently strong fields nonequilibrium space charges are induced on the (mobile) bulk fluid and (fixed) particle sides and that these space charges are responsible for a number of widely unknown phenomena in porous media. The resulting nonequilibrium electrokinetics includes a dynamically reduced adsorption capacity for counterionic tracer and the generation of nonlinear electroosmotic slip which can result in electrokinetic instability over the complete macropore dimension. The effects point toward new, tailored mechanisms for electrical field-assisted processes in a variety of applications.

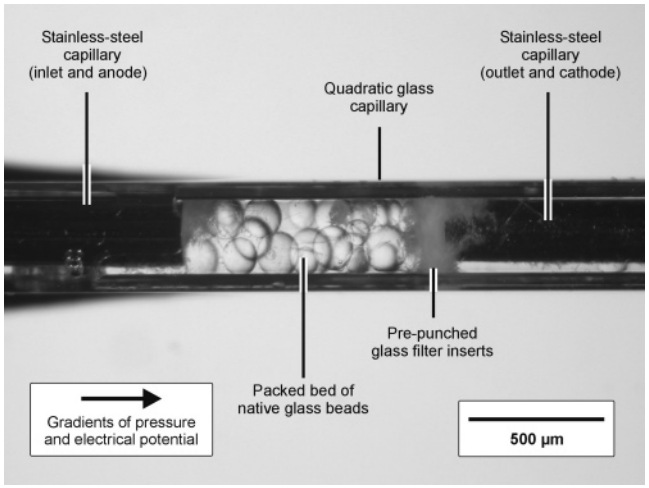

Figure 2. Details of the experimental setup. The spherical-shaped glass beads have an average intraparticle mesopore diameter of 20 nm and a mean particle diameter of 175 μm. Stainless steel capillaries are introduced from both ends of the device; they terminate the packing and serve as electrodes, as well as connect the tubing for mobile phase delivery.

Experimental Section

Microfluidic Device and Sphere Packing. To acquire reproducible kinetic data during in situ investigation of electrokinetic transport in porous media, a configuration was implemented meeting the following requirements: (i) fast and reversible variation of the mobile phase composition during tracer uptake and release experiments, (ii) application of electrical fields up to 10^5 V/m without complex safety precautions, (iii) efficient dissipation of Joule heat, and (iv) use of strong pressure gradients over the bed. For this purpose, a stainless steel capillary with a 50 μm i.d. and a 250 μm o.d. (Harry Rieck Edelstahl GmbH, Hilden, Germany) was inserted into a glass capillary with a 300 μm × 300 μm quadratic cross section (Hilgenberg GmbH, Malsfeld, Germany) and fixed with a commercial two-component epoxide glue. Spherical-shaped glass beads with an average mesopore diameter of 20 nm (Schuller GmbH, Steinach, Germany) were vacuum-sucked into the capillary until a bed length of ∼2 mm was reached. The packing was terminated by prepunched glass-fiber filter plugs serving as inlet and outlet frits. Final consolidation of the bed was realized by inserting a second stainless steel capillary. The distance between electrodes was determined microscopically. This setup (Figure 2) was fixed with epoxide glue on a conventional microscope slide.

Refractive index mismatch between the porous glass beads (RI = 1.474) and the saturating fluid causes significant loss of fluorescence light intensity at increasing penetration depth due to optical aberration.[63] This was avoided by using a fluid phase which, in all experiments, consisted of a 90:10 mixture of dimethyl sulfoxide (DMSO; RI = 1.479) and aqueous sodium acetate buffer (pH 5.0; 0.01 mol/L), resulting in an effective buffer concentration of 10^{-3} mol/L. This background solution contained 10^{-5} mol/L of either of the following fluorescent dyes: BODIPY 493/503 (neutral tracer) and BODIPY disulfonate (twice negatively charged tracer) from Molecular Probes (Leiden, The Netherlands) or positively charged rhodamine 6G (Fluka, Taufkirchen, Germany). The fluid phase delivery was achieved by a dual syringe pump (Harvard Apparatus, Holliston, MA) at a constant volumetric flow rate of 6.0 μL/min. Pulse injections were made by switching for a constant period of 2 s between pure and dyed solutions realized by an

(57) Dukhin, S. S. *Adv. Colloid Interface Sci.* **1991**, *36*, 219.
(58) Baran, A. A.; Babich, Y. A.; Tarovsky, A. A.; Mishchuk, N. A. *Colloids Surf.* **1992**, *68*, 141.
(59) Mishchuk, N. A.; Takhistov, P. V. *Colloid J. Russ. Acad. Sci.* **1993**, *55*, 244.
(60) Mishchuk, N. A. *Colloids Surf., A* **1998**, *140*, 75.
(61) Rubinstein, I.; Zaltzman, B. *Math. Models Methods Appl. Sci.* **2001**, *11*, 263.
(62) Wang, S. C.; Lai, Y. W.; Ben, Y.; Chang, H.-C. *Ind. Eng. Chem. Res.* **2004**, *43*, 2902.
(63) Tallarek, U.; Rapp, E.; Sann, H.; Reichl, U.; Seidel-Morgenstern, A. *Langmuir* **2003**, *19*, 4527.

electrically actuated six-port valve (VICI Valco, Schenkon, Switzerland). Precolumn band dispersion was minimized with low dead-volume units and small-diameter capillaries for connecting the microfluidic device with the mobile phase delivery system. The electrical potential gradients were applied by a medium direct current (dc) power supply with a 1.25 kV maximum (F.u.G. Elektronik GmbH, Rosenheim, Germany), while the stainless steel capillaries served as anode on the inlet side and as cathode on the outlet side of the packing.

Confocal Laser Scanning Microscopy (CLSM). Due to the high lateral resolution and fast data acquisition,[64] CLSM has been used to study the tracer dynamics in adsorbent particles concerning diffusive[65−77] and possible electrokinetic[63,78−80] transport mechanisms. Our experiments were conducted on an Axiovert 100 confocal laser scanning microscope (Carl Zeiss, Jena, Germany) equipped with two continuous noble gas lasers (argon ion laser, 488 nm and 25 mW maximum output power; helium−neon ion laser, 543 nm and 1 mW) and a 40× oil immersion objective (1.3 NA). Prior to each measurement series, fine-tuning of the maximum laser power was done for each dye to gain a high signal-to-noise ratio but avoid photobleaching (Ar laser, 6.25 mW; He−Ne laser, 1 mW). CLSM images were acquired in the section-scanning mode (the *xy*-section), generating vertical slices of 230.4 μm × 230.4 μm, with voxels of 1.80 μm in the *xy*-directions and 3.2 μm in the *z*-direction (128 × 128 pixels). The geometry of the microfluidic device allowed it to be inserted like a conventional microscopy slide into the frame and adjust the *xy*-plane perpendicular to the optical light path but parallel to the direction of the hydrodynamic and electrokinetic driving forces. Time series experiments were run with an image-sampling rate of 4 scans/s and a 12-bit data depth.

Processing and Analysis of Data. The CLSM data stored as TIF files were exported and further processed by the software package ScionImage for Windows (Scion Corporation, Frederick, MD). Quantitative data evaluation was accomplished using macros written in-house to define regions of interest with arbitrary shape and size and to derive the average fluorescence intensities in these regions as a function of time. The intraparticle diffusion coefficients and EOF velocities were extracted with least-squares fitting procedures by applying the convective-diffusion model implemented in Matlab (The MathWorks GmbH, Aachen, Germany) to the kinetic data.[79]

Results and Discussion

Intraparticle Flow Field. The uptake and release kinetics of a nonadsorbing, electroneutral tracer representing the intraparticle fluid dynamics was recorded for purely diffusive transport, as well as for a combination of driving forces, that is, concentration and electrical potential gradients, to derive complementary results on intraparticle transport behavior. Data recorded in the midplane through a particle and in the direction of the applied field are displayed as particle-averaged concentration profiles in Figure 3. Already qualitative data inspection reveals a significant acceleration of the intraparticle mass transfer by electrical fields due to intraparticle-forced EOF.[81−83] This perfusive electroosmosis based on intraparticle pore flow allows the steady-state loading to be reached much faster than with purely diffusive transport. For quantitative assessment of relevant intraparticle parameters (diffusion coefficient and EOF velocities), these kinetics were further analyzed with a convection-diffusion model.[4,79,84] The differential mass balance for diffusive and convective fluxes in a porous bead reads

$$\frac{\partial c_{\text{intra}}}{\partial t} = D_{\text{intra}} \nabla^2 c_{\text{intra}} - \mathbf{u}_{\text{intra}} \nabla c_{\text{intra}} \qquad (1)$$

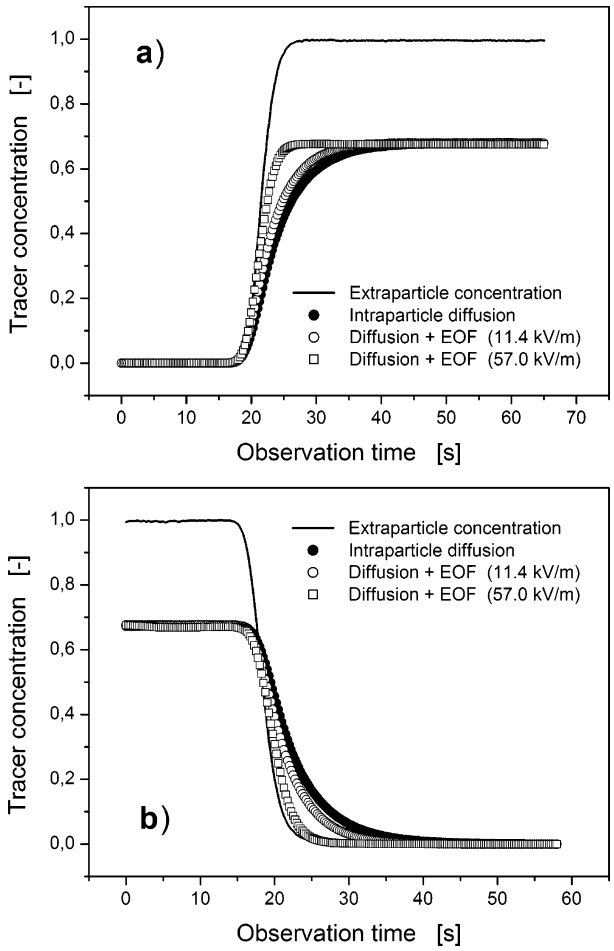

Figure 3. Tracer uptake and release by purely diffusive and electrokinetically enhanced transport of nonadsorbing, electroneutral tracer. The extraparticle pressure-driven flow (PDF) results in intraparticle diffusion only, while superimposed electrical fields increase mass transfer due to forced intraparticle EOF. The data were normalized with respect to the extraparticle tracer concentration.

(64) Sheppard, C. J. R.; Shotton, D. M. *Confocal Laser Scanning Microscopy*; BIOS Scientific Publishers: Oxford, U.K., 1997.
(65) Ljunglöf, A.; Hjorth, R. *J. Chromatogr., A* **1996**, *743*, 75.
(66) Kim, H. B.; Hayashi, M.; Nakatani, K.; Kitamura, N.; Sasaki, K.; Hotta, J. I.; Masuhara, H. *Anal. Chem.* **1996**, *68*, 409.
(67) Ljunglöf, A.; Thömmes, J. *J. Chromatogr., A* **1998**, *813*, 387.
(68) Malmsten, M.; Xing, K. Z.; Ljunglöf, A. *J. Colloid Interface Sci.* **1999**, *220*, 436.
(69) Linden, T.; Ljunglöf, A.; Kula, M.-R.; Thömmes, J. *Biotechnol. Bioeng.* **1999**, *65*, 622.
(70) Ljunglöf, A.; Larsson, M.; Knuuttila, K. G.; Lindgren, J. *J. Chromatogr., A* **2000**, *893*, 235.
(71) Velev, O. D.; Kaler, E. W.; Lenhoff, A. M. *J. Phys. Chem. B* **2000**, *104*, 9267.
(72) Song, Y.; Srinivasarao, M.; Tonelli, A.; Balik, C. M.; McGregor, R. *Macromolecules* **2000**, *33*, 4478.
(73) Heinemann, M.; Wagner, T.; Doumeche, B.; Ansorge-Schumacher, M.; Büchs, J. *Biotechnol. Lett.* **2002**, *24*, 845.
(74) Linden, T.; Ljunglöf, A.; Hagel, L.; Kula, M.-R.; Thömmes, J. *Sep. Sci. Technol.* **2002**, *37*, 1.
(75) Kasche, V.; de Boer, M.; Lazo, C.; Gad, M. *J. Chromatogr., B* **2003**, *790*, 115.
(76) Hubbuch, J.; Linden, T.; Knieps, E.; Thömmes, J.; Kula, M.-R. *Biotechnol. Bioeng.* **2002**, *80*, 359.
(77) Yuan, Y. H.; Velev, O. D.; Lenhoff, A. M. *Langmuir* **2003**, *19*, 3705.
(78) Lowry, M.; He, Y.; Geng, L. *Anal. Chem.* **2002**, *74*, 1811.
(79) Tallarek, U.; Pačes, M.; Rapp, E. *Electrophoresis* **2003**, *24*, 4241.
(80) Dziennik, S. R.; Belcher, E. B.; Barker, G. A.; DeBergalis, M. J.; Fernandez, S. E.; Lenhoff, A. M. *Proc. Natl. Acad. Sci. U.S.A.* **2003**, *100*, 420.
(81) Li, D.; Remcho, V. T. *J. Microcolumn Sep.* **1997**, *9*, 389.
(82) Stol, R.; Poppe, H.; Kok, W. Th. *J. Chromatogr., A* **2000**, *887*, 199.
(83) Tallarek, U.; Rapp, E.; Van As, H.; Bayer, E. *Angew. Chem., Int. Ed.* **2001**, *40*, 1684.

Table 1. Intraparticle Diffusivity (for Nonadsorbing Electroneutral Tracer) and Fluid Velocities[a]

operational modes	intraparticle diffusion only	intraparticle diffusion and convection			
E (kV/m)	0	5.7	11.5	28.7	57.4
D_{intra} (10^{-10} m^2/s)	2.04	2.04	2.04	2.04	2.04
u_{intra} (10^{-6} m/s)	0	5.1	11.5	39.6	86.8
$Pe_{intra} = u_{intra}d_p/D_{intra}$	0	4.4	9.9	33.9	74.5

[a] The average value of $D_{intra} = 2.04 \times 10^{-10}$ m^2/s obtained from the purely diffusive intraparticle mass transfer kinetics (PDF only) has been used as a fixed value during the subsequent parameter fitting procedure to extract u_{intra} by means of eq 1.

where c_{intra} is the local concentration of electroneutral tracer in a spherical particle at any time, D_{intra} is the intraparticle diffusion coefficient, and $\mathbf{u}_{intra}$ is the average intraparticle EOF velocity in the direction of the unidirectional dc field. All details concerning the numerical implementation of the model based on eq 1 can be found in ref 79. A characteristic of this particle macroscopic model is the use of lumped, isotropic parameters (assumed as constant on the observation time scale) which summarize the microscopic physicochemical properties of a glass bead. Under the present conditions, significant intraparticle fluid velocities can be caused only by forced electroosmosis because, compared to the extraparticle void space dimensions, the intraparticle mesopores are far too small to allow any measurable hydrodynamic perfusive flow.[85]

Results of the quantitative CLSM studies with electroneutral tracer can be summarized as follows: (i) Within resolution limits, we do not observe diffusion boundary-layer mass transfer resistance close to the particle's external surface,[2] (ii) steady-state distributions are uniform over the complete particle, (iii) loading capacities are unaffected by superimposed electrical fields, as demonstrated by Figure 3, and (iv) evaluation of intraparticle transport reveals substantial enhancement of mass transfer by intraparticle EOF (see Table 1).

At the highest field strength of 60 kV/m, the mean intraparticle EOF velocity is ~0.1 mm/s. As a consequence, the intraparticle Peclet numbers $Pe_{intra} = u_{intra}d_p/D_{intra}$ which represent the ratio of dimensionless times for convection ($u_{intra}t/d_p$) and diffusion ($D_{intra}t/d_p^2$) increase up to $Pe_{intra} \approx 100$ for the selected bead with a diameter (d_p) of 175 μm. This demonstrates that electroosmotic perfusion promotes the intraparticle hydrodynamics far beyond the diffusion-limited regime, even under the actual conditions with significant EDL overlap on the intraparticle mesopore scale. These flow field data serve as the basis for the analysis of intraparticle transport of a counterionic analyte discussed below.

Intraparticle Counterion Transport. Uptake and release experiments with counterionic tracer were carried out following an experimental protocol similar to that for the electroneutral tracer. Data acquired with purely diffusive mass transfer as reference kinetics, but identical laser and detector settings, reveal, besides a global electrokinetically induced enhancement of intraparticle transport also for the counterion, a strong dependence of the steady-state loading capacity on applied field strength. Stationary, particle-averaged concentrations of the counterionic tracer decrease sharply at the increasing field strength, rather than approach the same saturation capacity observed for the diffusion-limited kinetics without a superimposed field (Figure 4). Further, a spatially resolved investigation of counterionic tracer distributions

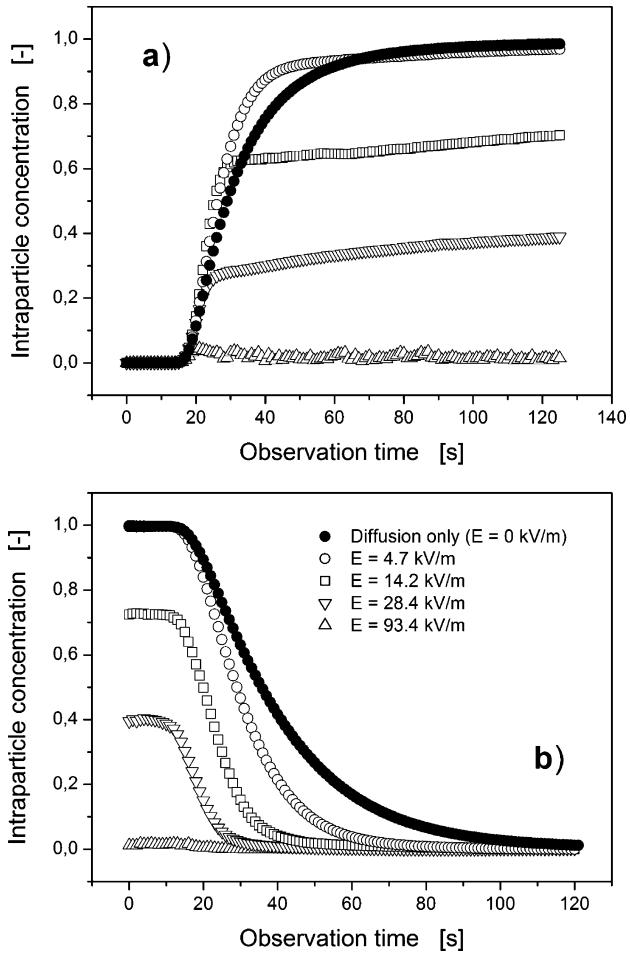

Figure 4. Uptake and release of positively charged counterionic fluoresent tracer by purely diffusive transport (PDF in the extraparticle domain) and electrokinetic effects realized by superimposing electrical fields, as indicated. The data were normalized with respect to the maximum loading at electrochemical equilibrium (E = 0 kV/m).

inside the ion-exchange beads at the encountered field strengths reveals very unusual patterns (Figure 5). This quantitative CLSM visualization proves the existence of extended intraparticle zones of reduced counterionic concentration. These depleted zones begin at the surface of the anodic bead hemisphere and increase until, with a sufficiently strong field, they extend over the whole bead which remains effectively emptied.

An explanation for this unexpected behavior can be found in the ion-permselective behavior of ion-exchange beads and concentration polarization characterized by the formation of ionic concentration gradients in bulk electrolyte solution adjacent to an ion-permselective interface upon the passage of electrical current normal to that interface. Due to the concentration gradient in the depleted concentration polarization zone (Figure 1b), transport through this boundary layer becomes diffusion-limited. On the other hand, the concentration increases at the opposite side of the ion-exchange bead because of the large number of counterions that leave it at the interface of the cathodic hemisphere. This creates an enriched concentration polarization zone. In other words, the concentration polarization induced close to the external surface of a single, negatively charged bead is characterized by an antisymmetrical nature, with a depleted zone along the anodic bead hemisphere and an enriched zone along the cathodic hemisphere. The continued increase of applied field strength is most important for electrokinetically

(84) Jennings, A. A.; Mansharamani, P. *Environ. Modell. Software* **1999**, *14*, 625.
(85) Pfeiffer, J. F.; Chen, J. C.; Hsu, J. T. *AIChE J.* **1996**, *42*, 932.

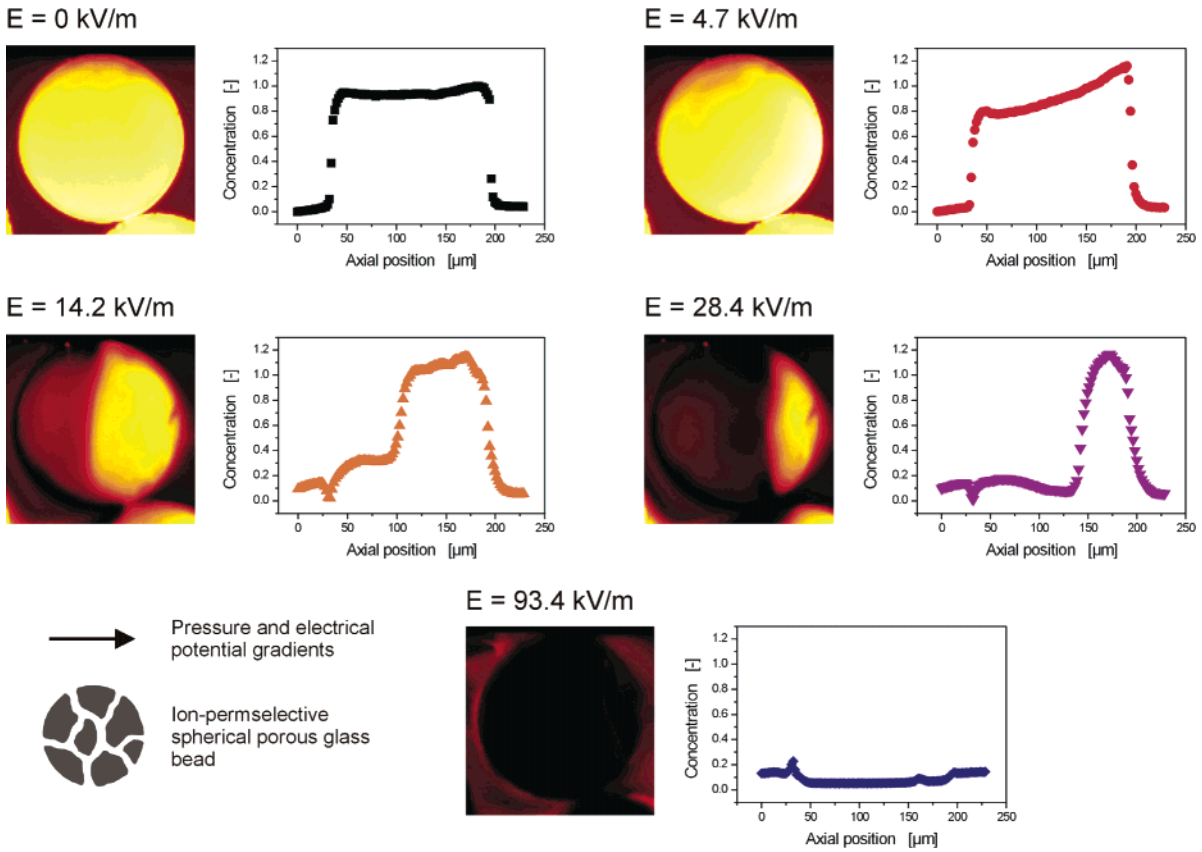

Figure 5. Representative CLSM images and corresponding normalized concentration profiles for steady-state centerline distributions of the strongly adsorbing counterionic tracer. The profiles were recorded in the direction of applied pressure and electrical potential gradients and normalized with respect to the maximum loading at electrochemical equilibrium (observed for the purely diffusive transport, $E = 0$ kV/m). The laser and detector settings remained unchanged over the complete imaging series. In all measurements, a constant pressure gradient was applied over the sphere packing and electrical fields were then superimposed, as indicated.

induced mass transfer resistance in the depleted zone because ionic concentrations approach zero (Figure 1b). Therefore, the diffusive molar flux density of counterions through this boundary layer ($\mathbf{J}^+_{DBL}$) for a single bead with ideal ion-permselectivity reaches a maximum value of[2]

$$J^+_{DBL,max} = -D^+_m \frac{c^+}{\delta_{DBL}} \tag{2}$$

where D^+_m and c^+ denote respectively the molecular diffusivity and concentration of counterionic tracer in the bulk fluid and δ_{DBL} is the thickness of the diffusion boundary layer.

While the maximum concentration gradient in eq 2 is straightforward to analyze, the resulting flow regime needs a closer examination for estimating δ_{DBL}. Under the present conditions, convection between the beads is dominated by strong pressure-driven flow (PDF). A contribution to the average interstitial velocities (u_{inter}) by EOF is assumed negligible because the EOF at maximum reaches only a tenth of the PDF velocity. The actual high-Peclet, low-Reynolds number regime with $Pe = u_{inter}d_p/D_m = 193$ and $Re = u_{inter}d_p/\nu = 0.12$ represents convection-dominated interparticle transport in laminar flow. Then, transport through the convective-diffusion layer can be expressed by the following relationship between the Sherwood number (Sh) and Pe[86]

$$Sh \equiv \frac{k_{film}d_p}{D_m} = \Omega Pe^{1/3} \tag{3}$$

where the value of Ω is a function of the interstitial porosity (ϵ_{inter}) only and ~2.2 for $\epsilon_{inter} \approx 0.5$ used to represent our experiments at low column-to-particle diameter ratios.[87] δ_{DBL} can be estimated by relating D_m to the film mass transfer coefficient (k_{film})[88,89]

$$\delta_{DBL} = \frac{D_m}{k_{film}} = \frac{d_p}{\Omega Pe^{1/3}} \tag{4}$$

Since volumetric flow through the microfluidic device is dominated by the strong and constant PDF, δ_{DBL} is assumed to vary only insignificantly with the field strength. Thus, maximum extraparticle fluid-side counterionic transport to a bead's external surface ($\mathbf{J}^+_{DBL,max}$) is practically unaffected by superimposed electrical fields. In contrast, the overall flux density of the positively charged counterion ($\mathbf{J}^+_{intra}$) in the intraparticle pore space is determined by (i) diffusive flux ($\mathbf{J}^+_{diff}$) arising from chemical potential gradients, (ii) electrical transference ($\mathbf{J}^+_{el}$) due to electrical potential gradients, and (iii) convective transfer ($\mathbf{J}^+_{con}$)[2]

$$\begin{aligned}\mathbf{J}^+_{intra} &= \mathbf{J}^+_{diff} + \mathbf{J}^+_{el} + \mathbf{J}^+_{con} \\ &= -D^+_{intra}\left(\nabla c^+_{intra} + c^+_{intra}\nabla(\ln \beta^+) + z^+ c^+_{intra}\frac{F}{RT}\nabla\phi\right) + c^+_{intra}\mathbf{u}_{intra}\end{aligned} \tag{5}$$

where D^+_{intra} is the intraparticle diffusion coefficient of

(86) Pfeffer, R. *Ind. Eng. Chem. Fundam.* **1964**, *3*, 380.

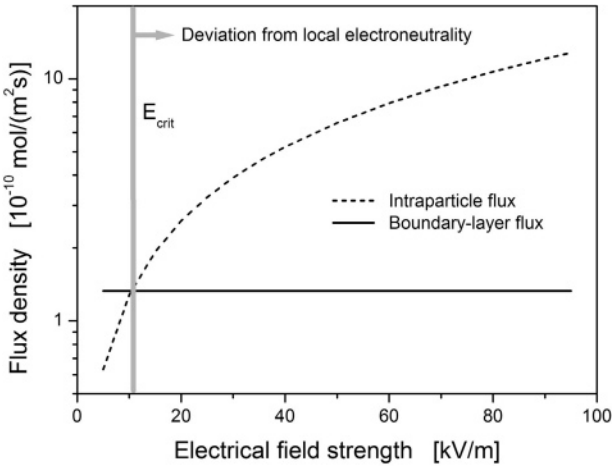

Figure 6. Analysis of the molar flux densities of the counterionic tracer. Beyond $E_{crit} = 10.4$ kV/m, tracer transport from bulk solution through the diffusion boundary layer cannot balance any longer intraparticle electrokinetic flux densities; a field-induced (nonequilibrium) EDL is created. Intraparticle flux densities were calculated using eq 6, while boundary-layer transport was approximated on the basis of eqs 2 and 4. The existence and value of E_{crit} explains the behavior seen in Figures 4 and 5.

positively charged tracer molecules, c^+_{intra} is their molar concentration and β^+ is the respective activity coefficient, z^+ is their charge number, and ϕ denotes the electrical potential. By rewriting eq 5 in the absence of concentration gradients and assuming an ideal solution behavior, the intraparticle flux densities of the counterions reduce to the electrophoretic and electroconvective transfer rates

$$\mathbf{J}^+_{intra} = -z^+ c^+_{intra} D^+_{intra} \frac{F}{RT} \nabla\phi + c^+_{intra} \mathbf{u}_{intra} \qquad (6)$$

It is evident that the transport inside a particle correlates well with the applied field strength, as both intraparticle EOF and electrophoresis depend linearly (in a first approximation) on the electrical potential gradient. An analysis of the external and internal molar flux densities of the positively charged counterionic tracer under the present set of conditions using eqs 2, 4, and 6 allows us to derive a critical field strength of $E_{crit} = 10.4$ kV/m at which intraparticle electrokinetic mass transfer begins to exceed transport through the diffusion boundary layer (Figure 6). Because inside a bead more counterions are removed at the surface of the anodic hemisphere than can be supplied from bulk solution via the diffusion boundary layer, deviations from local electroneutrality may occur. This will lead to the induction of mobile fluid-side (see space charge region in Figure 1c) and immobile particle-side (see depleted zones in Figure 5) space charge regions which, together, comprise a nonequilibrium or secondary EDL.

With the estimated E_{crit} value, also an explanation for the different kinetics and stationary concentration profiles of the counterionic tracer (Figures 4 and 5) becomes possible: For $E < E_{crit} = 10.4$ kV/m, its transport is limited by intraparticle contributions, mainly electroosmosis and electrophoresis, and particle-averaged concentrations reach a value similar to that obtained without an electrical field because there is no limitation for tracer supply from bulk solution toward a particle. Due to concentration polarization of bulk solution around the beads, the resulting steady-state concentration profiles are slightly tilted in the field direction (see Figure 5 for $E = 4.7$ kV/m). When $E > E_{crit}$, electrokinetic intraparticle flux in the axial direction exceeds counterionic mass transfer toward the surface, through the diffusion boundary layer. Since intraparticle fluxes cannot be balanced any longer by supply from bulk solution, zones of reduced counterionic concentration develop in the beads representing local space charge in the form of unscreened, fixed co-ionic surface charge (Figure 1c).

On the basis of eqs 2 and 6, the beads should become completely emptied at field strengths above the critical value. In practice, however, concentration gradients exist between the intraparticle pore space and the enriched concentration polarization zone at the cathodic hemisphere. Consequently, the extension of the intraparticle zones of reduced counterionic concentration is determined by relative contributions from electrokinetic intraparticle flux and counterdirectional diffusive flux into a particle. As demonstrated by the quantitative CLSM data (Figures 4 and 5), the area of the depleted intraparticle regions increases and, on the other hand, particle-averaged loading capacities decrease with the field strength until the beads are empty. The concentration of counterionic tracer in the depleted intraparticle zones is reduced far below the value at electrochemical equilibrium (see Figure 5 for $E = 0$ and 93.4 kV/m). This implies that these zones represent an immobile region (because they are located inside the fixed particles) of field-induced space charge, also referred to as nonequilibrium space charge.[43,49−52] It is the immobile intraparticle counterpart to the mobile, fluid-side space charge region that is responsible for electrokinetic phenomena of the second kind. Thus, as ion-permselective beads are subjected to conditions favoring nonequilibrium concentration polarization, a space charge region of mobile counterions in the bulk electrolyte solution close to a bead's external surface and an immobile space charge region of fixed co-ions at the inner surface of the bead are created. While electroneutrality on the scale of a single bead is disturbed, the overall electroneutrality of the bed remains preserved.

Extraparticle Fluid Dynamics. For the PDF under the present conditions, the flow regime in the sphere packing is laminar and Reynolds numbers are well below unity. However, when an electrical field with $E > E_{crit}$ is superimposed, the flow characteristics change drastically. Spatiotemporally strongly fluctuating concentration patterns are observed, as demonstrated by snapshots of the local tracer distribution and variations monitored at a fixed position in the extraparticle pore space (Figure 7). These observations are unexpected for a laminar flow regime based on PDF alone. In addition, real-time CLSM imaging series of the concentration distributions for co-ionic and counterionic tracer also provide clear evidence for an existence of strong, random fluctuations in the flow path between particles (available as Supporting Information on the Web). Under conditions of strong concentration polarization, the flow field locally behaves chaotic and shows significant lateral velocity components.

A possible explanation for this behavior is found in the characteristics of the field-induced space charge regions. As described earlier, for field strengths beyond E_{crit}, a diffuse space charge of mobile counterions is induced locally in the macroporous (extraparticle) compartment. In contrast to the quasi-equilibrium EDL which is relatively unaffected by the hydrodynamics concerning its charge density and dimension, the field-induced

(87) Wilson, E. J.; Geankoplis, C. J. *Ind. Eng. Chem. Fundam.* **1966**, *5*, 9.
(88) Horváth, Cs.; Lin, H.-J. *J. Chromatogr.* **1976**, *126*, 401.
(89) Tallarek, U.; Vergeldt, F. J.; Van As, H. *J. Phys. Chem. B* **1999**, *103*, 7654.

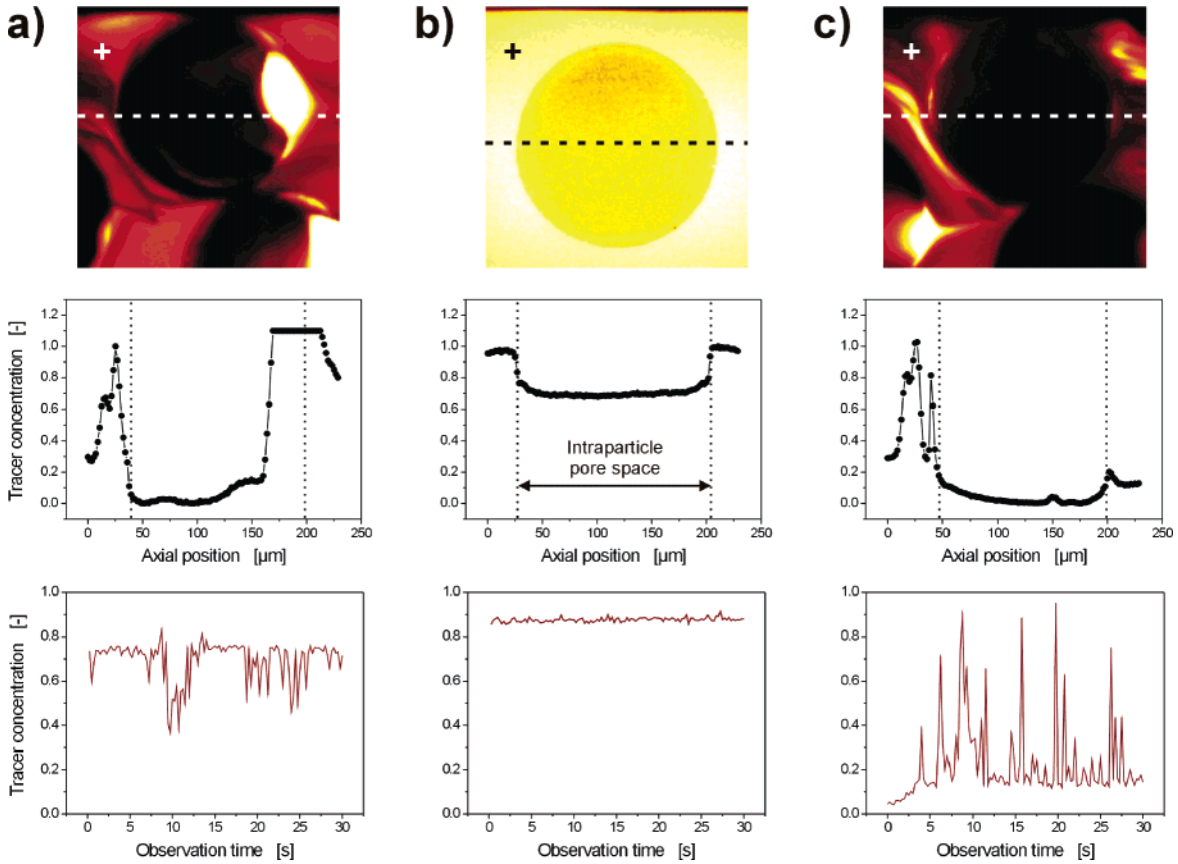

Figure 7. Representative images, axial centerline concentration profiles, and time-resolved fluid-side tracer concentrations recorded at the position indicated by the plus sign for (a) counterionic, (b) electroneutral, and (c) co-ionic tracer molecules at field strengths beyond E_{crit}. The PDF remained constant (6 μL/min), and applied electrical field strengths were adjusted to 93.4 kV/m for co-ionic and counterionic tracer molecules and to 118.2 kV/m for electroneutral tracer. Electronic signal amplification was tuned for optimum intensity in the extraparticle pore space; enriched concentration polarization zones then were out of the linear range. Profiles were normalized with respect to maximum interstitial intensity. The same color code was used for all images. Pressure and electrical potential gradients were applied from left to right. Real-time imaging data (in video format) are available as Supporting Information on the Web.

(nonequilibrium) space charge of mobile counterions close to the surface of the anodic bead hemisphere extends much further into bulk fluid. Thus, a major difference between nonequilibrium and quasi-equilibrium electrokinetics is that with the secondary EDL the origin of electroconvection (the interaction between the applied field and fluid-side space charge) is located directly in the bulk electrolyte solution rather than being confined to a relatively thin layer very close to the surface. Due to this peculiarity and tortuous flow paths in the material, manifold and mutual interactions between flow-inducing mobile space charge and convective flow arise, leading to a complex and random flow behavior. Although the strong PDF provides bulk convective transport through the bed, the (electro)-hydrodynamics resulting from combined PDF and the induced-charge electroosmosis actually reveals highly chaotic patterns and shows turbulent flow characteristics.[41]

Consequently, the local velocity field is characterized by strong lateral fluctuations and instationary vortices, as demonstrated by the real-time CLSM imaging series. In contrast to the experiments in a closed electrolysis cell where comparatively large and stationary vortices have been observed,[43,48] the vorticity found in the present work has a random nature and significantly smaller spatial dimensions. This is caused by the fact that in a random-close sphere packing the vortex generation can occur only in the extraparticle void space which is far more confining. Further, because of the open system used in the present work, nonequilibrium electroosmosis induces net flow through the material instead of large recirculation zones. Due to the enhanced generation of vortices, also referred to as electroosmotic whirlwinds in closed systems,[43] the resulting flow field contains strong lateral velocity components which increase radial dispersion. In combination with the random nature of these flow paths, strong electrokinetic instability mixing then prevails in the material on a macropore scale.

Pulse Injection of Counterionic Tracer. The influence of this nonequilibrium electrokinetics (for electrical field strengths beyond E_{crit}) on hydrodynamic dispersion was evaluated by analyzing the elution profiles of counterionic tracer following pulse injection. Fluorescence intensity distributions are shown in Figure 8. They were subjected to an exponentially modified Gauss function for further analysis, and Table 2 summarizes most relevant data.[90−92] At field strengths below E_{crit}, only a slight decrease of the signal variances is discernible and peak shapes still show a high degree of asymmetry (peak tailing). Obviously, a significant improvement of the overall elution dynamics is possible only with electrical fields above E_{crit}. Then, particle-averaged pulse variances are indeed improved by more than two decades, signal asymmetry is dramatically reduced, differences between the centers of gravity for intra- and extraparticle concentration profiles almost vanish, and the extraparticle

(90) Foley, J. P.; Dorsey, J. G. *J. Chromatogr. Sci.* **1984**, *22*, 40.
(91) Jeansonne, M. S.; Foley, J. P. *J. Chromatogr. Sci.* **1991**, *29*, 258.
(92) Marco, V. B. D.; Bombi, G. G. *J. Chromatogr., A* **2001**, *931*, 1.

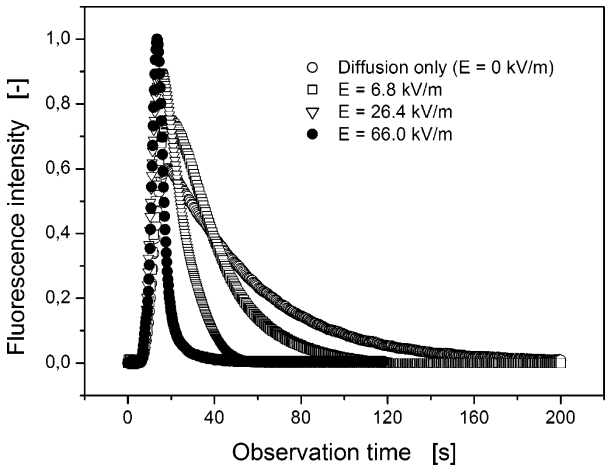

Figure 8. Particle-averaged fluorescence signals following pulse injection of the counterionic tracer for purely diffusive and electrokinetically enhanced intraparticle transport.

Table 2. Analysis of Pulse Injections for Strongly Adsorbing Counterionic Tracer[a]

E (kV/m)	$\sigma^2_{solution}$ (s^2)	Δt_R (s)	$\sigma^2_{particle}$ (s^2)	τ/w	improvement factor: extraparticle	improvement factor: intraparticle
0	338.2	29.1	2083.0	14.2	1.0	1.0
6.8	103.0	20.4	848.6	5.9	3.3	2.5
26.4	59.9	8.5	199.9	3.8	5.6	9.3
66.0	21.2	0.6	19.5	1.4	16.0	106.9

[a] σ^2, variance of elution signals; Δt_R, difference between the centers of gravity for extraparticle fluid-side and particle-based elution signals; τ/w, ratio of the first-order decay time constant and width of the exponentially modified Gaussian (characterizing peak asymmetry). The improvement factor is the ratio of signal variances for transport without and with the electrokinetic effects.

fluid-side axial dispersion is further reduced by more than a decade (Table 2). An explanation for this massive improvement in the tracer elution dynamics based only on the enhancement of the intraparticle transport by electromigration and electroconvection estimated with the Nernst−Planck equation (see Figure 6) is insufficient because the intraparticle molar flux density is increased by just one decade, rather than by more than two. Thus, additional phenomena need to account for this axial dispersion characteristics of a counterionic tracer.

Under nonequilibrium electrokinetic conditions, the intraparticle mass transfer exceeds significantly transport through the diffusion boundary layer into a bead. Thus, the counterion adsorption occurs effectively in a reduced area of a bead which decreases further as the field strength continues to increase (illustrated in Figure 5). This means that the surface area available for adsorption of counterionic tracer is dynamically reduced toward a small fraction of physically large particles. As a result of this electrokinetically induced stationary state, the large-diameter spheres demonstrate elution efficiencies typical for a bed of much smaller particles due to the significantly reduced effective surface area; signal variances of the elution data refer to this dynamically reduced sphere diameter (Table 2). To summarize, intraparticle mass transfer resistances are removed almost completely under nonequilibrium conditions; first, by an enhanced intraparticle transport (Figure 6), and second, by a dynamic reduction of the surface area available for adsorption (Figure 5).

In addition, not only is the particle-averaged mass transfer resistance substantially reduced under conditions of strong concentration polarization, but also the variances of extraparticle fluid-side concentration profiles are improved by more than one decade (Table 2). This aspect is particularly important, since, due to strong PDF in the interstitial void space of the bed, extraparticle axial dispersion may be considered as remaining unaffected by superimposed electrical fields. However, a locally enhanced radial convective transport due to electrokinetic instability mixing reduces the extraparticle fluid-side variance of the elution signals. In this respect, increased lateral mixing helps to decrease axial dispersion.

The combination of these two consequences of local, electrical field-induced space charges in a bed of ion-permselective particles, that is, the dynamically reduced intraparticle adsorption area (effective particle diameter) and increased extraparticle lateral dispersion (chaotic mixing), has a strong impact on the elution behavior in liquid phase separation techniques relying on the devised application of external electrical fields, which includes electrochromatography, field-assisted preparative chromatography, and counteracting chromatographic electrophoresis.[5−11,93−95] While the first effect results in a substantially reduced intraparticle mass transfer resistance, the second effect accelerates lateral equilibration between particles. Thus, all relevant contributions to the axial dispersion of a counterionic analyte can become very small, while the transport of electroneutral analytes still may benefit from the extraparticle (electro)hydrodynamic effects.

Desorption of Counterionic Tracer. In contrast to purely diffusive tracer uptake and release, the interplay between extraparticle fluid-side diffusive transport through the induced boundary layer (Figure 1) and the intraparticle electrokinetic flux has unique consequences for a particle emptying kinetics of counterionic analytes, as now illustrated. In the first series of experiments, the complete bed of porous beads was initially equilibrated with an electrolyte solution containing counterionic tracer. After reaching saturation at electrochemical equilibrium, the mobile phase was switched to pure (undyed) buffer solution. Thus, tracer release from the beads started immediately due to a steep concentration gradient between the intraparticle pore space and the bulk fluid phase. The complete series of the experiments is shown in Figure 9, where the electrokinetically enhanced tracer release from a bead is compared with purely diffusive transport. As expected, superimposed electrical fields cause a substantial acceleration of particle emptying until, with nonequilibrium electrokinetic conditions, this takes place almost instantaneously.

As discussed earlier, for field strengths beyond E_{crit}, counterionic flux out of a particle exceeds transport through the diffusion boundary layer into the support (Figure 6); that is, the tracer molecules are released much faster from the bead than they enter it from bulk solution. As demonstrated by experiments in Figure 9, this offers the possibility to release target molecules efficiently from saturated adsorbents because all beads are emptied electrokinetically just after the electrical field is switched on. Since this process occurs simultaneously in the whole bed, there is hardly any readsorption of tracer molecules released upstream into beads further downstream. Counterion desorption becomes independent from the actual tracer concentration in the extraparticle pore space. This means that a particle emptying without significant reentry of analyte molecules can be induced electrokineti-

(93) Ivory, C. F.; Gobie, W. A. *Biotechnol. Prog.* **1990**, *6*, 21.
(94) Rudge, S. R.; Basak, S. K.; Ladisch, M. R. *AIChE J.* **1993**, *39*, 797.
(95) Keim, C.; Ladisch, M. *Biotechnol. Bioeng.* **2000**, *70*, 72.

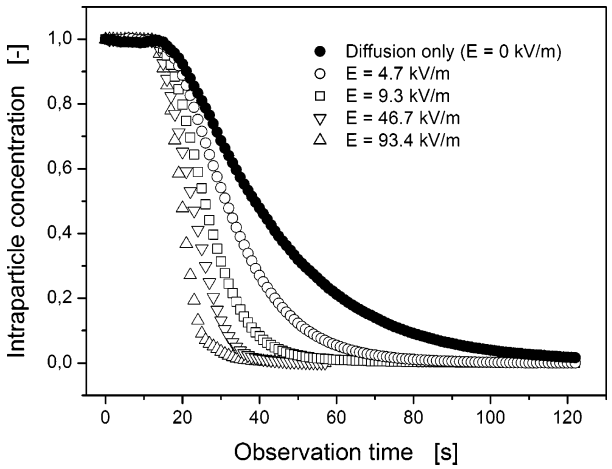

Figure 9. Purely diffusive and electrokinetically enhanced release of strongly adsorbing (counterionic) fluorescent tracer from a saturated particle. For the field-assisted transport, electrical fields were superimposed (as indicated) on a resulting concentration gradient as undyed electrolyte solution reached the selected bead (after 17 s).

cally due to the combination of strong intraparticle electrokinetic flux and extraparticle fluid-side mass transfer resistance offered by the diffusion boundary layer as a result of concentration polarization (see Figure 1c).

This strategy is illustrated in a second experiment which also employs initially saturated beads. In this case, however, instead of inducing concentration gradients between the intra- and extraparticle pore space by switching to undyed solution, the same electrolyte composition was used in the whole experiment. Then, an electrical field with $E > E_{crit}$ was applied and the beads indeed started to become immediately emptied electrokinetically, irrespective of the resulting concentration gradient between the electrolyte solutions in the extraparticle and intraparticle pore spaces (see Figure 10 for representative concentration profiles and CLSM images). The real-time CLSM imaging of the process provides clear evidence for this profound effect of the superimposed electrical fields on the dynamic concentration distribution of a counterionic tracer in the fixed bed of ion-permselective particles. Recalling that these data are obtained with the same solution used for loading the beads, it is evident that the effective adsorption capacity, not only of a single bead but of the whole packing, becomes decoupled electrokinetically from the extraparticle concentration. This offers new opportunities for an application of these nonequilibrium electrokinetic effects, for example, in large-scale processes employing fixed bed adsorbers, in view of selectivity, efficiency, and throughput.

Conclusions

Concentration polarization of the electrolyte solution in a fixed bed of ion-permselective adsorbent particles strongly affects mass transport on a particle scale, as highlighted by the electrokinetic induction of space charges. These are localized in a region of unscreened co-ionic surface charge inside the porous particles and a mobile region of counterionic space charge in the bulk extraparticle fluid. Physical properties of the electrical field-induced nonequilibrium EDL contrast with behavior known from the quasi-equilibrium (or primary) EDL. The dimension of this nonequilibrium (or secondary) EDL strongly depends on the applied field strength, and the mobile counterionic space charge region is located in bulk solution rather than adhering closely to the confining

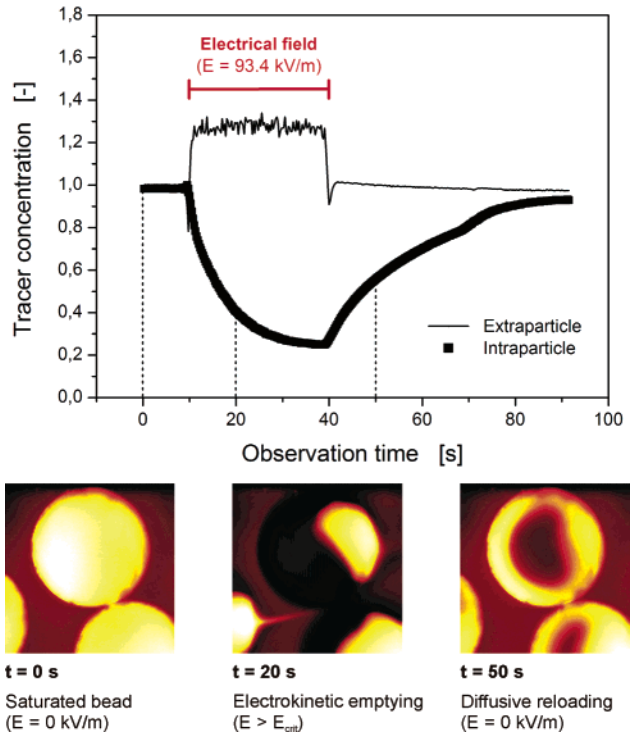

Figure 10. Extraparticle fluid-side and averaged intraparticle concentrations, together with CLSM images at selected times (indicated by the dotted lines) for an electrokinetic induction of counterionic tracer release from a saturated bead. The mobile phase composition already used for the particle saturation remained constant during the whole experiment. An electrical field with $E = 93.4$ kV/m was superimposed (on a constant pressure gradient) between $t = 10$ s and $t = 40$ s. Pressure and electrical potential gradients were applied from left to right. Real-time CLSM imaging of the desorption dynamics is also available as Supporting Information on the Web.

solid−liquid interface. These characteristics have unique consequences for the hydrodynamics and transport of charged species through hierarchically structured adsorbents. Due to the mutual, complex interactions between the field-induced mobile space charge region with the bulk convection, highly chaotic flow patterns result which lead to increased lateral mixing in the extraparticle void space (electrokinetic instability mixing). In addition, the immobile space charge region of unscreened surface charge is an intraparticle zone with reduced counterionic concentrations reflecting a decreased adsorption capacity of the material. At high field strength, this region covers the whole bead and its dynamic adsorption capacity is electrokinetically reduced to practically zero. As a result of these effects, transport of counterionic analytes can be substantially manipulated. Axial dispersion is strongly reduced and a release from saturated beads tuned without influence of the extraparticle fluid-side concentration. The documented phenomena offer new opportunities for the application of nonequilibrium electrokinetic effects, for example, in microfluidic pumping and mixing, for speed and separation efficiency in capillary electrochromatography, or the process intensification in electrical field-assisted chromatography, as well as sample purification.

Acknowledgment. We thank Matthias Pfafferodt (Institut für Verfahrenstechnik, Otto-von-Guericke-Universität Magdeburg, Germany) for his help with the numerical implementation of the model. This work was supported by the Deutsche Forschungsgemeinschaft (under grants SE 586/7-2 and TA 268/1-1) and Fonds der Chemischen Industrie.

Supporting Information Available: Real-time imaging by confocal laser scanning microscopy of the dynamic processes behind part a of Figure 7, part c of Figure 7, and Figure 10; the video clips are in AVI format. This material is available free of charge via the Internet at http://pubs.acs.org.

LA048408N

Ivo Nischang
Ulrich Tallarek

Institut für Verfahrenstechnik,
Otto-von-Guericke-Universität,
Magdeburg, Germany

Nonlinear electroosmosis in hierarchical monolithic structures

We studied the dependence of electroosmotic flow (EOF) velocity and separation efficiency for neutral analytes in 100 μm ID capillary monoliths on a variation of the mobile phase ionic strength and applied electrical field strength, *i.e.*, we covered a range for the concentration of Tris buffer from 10^{-5} to 10^{-2} M and applied electrical field strengths up to 10^5 V/m. The silica-based monoliths are hierarchically structured having intraskeleton mesopores and interskeleton macropores. While a linear dependence of the average EOF velocity on applied field strength could be observed with 5×10^{-3} M Tris (turning slightly nonlinear at a higher concentration due to thermal effects), this dependence becomes systematically nonlinear as the Tris concentration is reduced towards 10^{-4} M. Increased velocities by more than 50% compared to those expected from linear behavior are realized at 10^5 V/m. Concomitantly, as the Tris concentration is reduced from 10^{-3} to 10^{-4} M, we notice an improvement in plate heights by a factor of more than 2 (they approach 2 μm for ethylbenzoate). We complementary analyzed the onset of the nonlinear EOF dynamics in a hierarchical monolith and the significantly reduced axial dispersion in view of nonequilibrium electrokinetic effects which may develop in porous media due to the presence of ion-permselective regions, *e.g.*, the mesoporous monolith skeleton. In this respect, a decreasing mobile phase ionic strength favors the formation of nonequilibrium concentration polarization in strong electrical fields, and a coupling of the electrostatics and hydrodynamics then may explain nonlinear EOF velocities and increasing separation efficiencies depending on the Tris concentration and applied field strength.

Keywords: Capillary electrochromatography / Electroosmotic flow velocity / Hierarchical monolithic structures / Nonlinear electroosmosis DOI 10.1002/elps.200405990

1 Introduction

The devised transport of mobile phase and complex sample mixtures through high- and low-surface area materials induced by an externally applied electrical field plays a central role in many analytical, technological, and environmental processes. This includes dewatering of waste sludge and soil remediation, capillary electrophoresis, or electrochromatographic separations in particulate and monolithic fixed beds, as well as microchip devices [1–34]. Transport is primarily achieved *via* electromigration of ions (background electrolyte), electrophoresis (charged analyte molecules or particles), and electroosmosis (bulk liquid) driven by the shear stress concentrated in the electrical double layer (EDL) at solid-liquid interfaces [35]. Both the local and macroscopic transient behavior and long-time average magnitude, stability, and uniformity of electroosmotic flow (EOF) in porous media are inherently related to the physicochemical nature of the surface and its dynamics, the pore space morphology, and properties of the liquid electrolyte [36–47]. A detailed analysis of these parameters on the relevant spatio-temporal scales has a fundamental importance as it critically guides performance and design strategies of an electrokinetic process with respect to competitive (diffusive-convective) transport schemes. This becomes amplified by the significant role of noncontinuum effects, interfacial contributions, and surface forces, as well as multiscale and multiphysics effects in a low-Reynolds number fluid dynamics on micro- and nanometer dimensions [48–60].

Concerning fluid flow through random sphere packings in capillary columns with a relatively low hydraulic permeability EOF has demonstrated superior conductivity and dispersion behavior as compared to pressure-driven flow, accompanying a reduction of velocity extremes in the mobile-phase flow pattern [61–69]. Axial plate heights and dispersion coefficients reduced by more than a dec-

Correspondence: Dr. Ulrich Tallarek, Institut für Verfahrenstechnik, Otto-von-Guericke-Universität Magdeburg, Universitätsplatz 2, D-39106 Magdeburg, Germany
E-mail: ulrich.tallarek@vst.uni-magdeburg.de
Fax: +49-(0)391-67-12028

Abbreviations: CP, concentration polarization; **EDL**, electrical double layer; **EO**, electroosmosis

ade with respect to those typically found in capillary HPLC have been reported for capillary electrochromatography (CEC) [70–72]. This massive improvement is mainly caused by a strong electrokinetic flow field perfusion in the beds of porous particles, which operates with substantial intraparticle EOF velocities even under conditions favoring strong EDL overlap on intraparticle pore level [69, 73, 74]. The effect of intraparticle EOF on mass transfer of electroneutral analyte has been visualized and analyzed recently with quantitative confocal laser scanning microscopy studies [75, 76]. These results are in a contrast to both the intensity of efforts (and prerequisites) concerning optimized particle technology, as well as the magnitude of a perfusive, but hydraulic flow and remaining velocity inequalities between inter- and intraparticle flow patterns [77–88]. In this respect, it has been shown that hydraulic flow usually leaves the intraparticle fluid practically stagnant (purely diffusive or diffusion-limited) [89], unless relatively high column pressure drops, particles with large pores and transport of slowly diffusing analyte molecules are involved, which is manifested in a hold-up contribution that begins to dominate axial hydrodynamic dispersion in packed beds of porous particles at Peclet numbers above *ca.* 25 [90]. The permeability criterion and a straightforward implementation also make electroosmosis very attractive for electrokinetic micropumping technology in a miniaturization of HPLC systems and the actuation of microscale mechanical components [91–96].

While the characterization and adjustment of an electroosmotic perfusive flow field and optimum particle dimensions in CEC have received much attention for improving the separation efficiency of mainly electroneutral analytes [97], a particularly important aspect which has largely escaped the research focus in the context of CEC is the role played for simple ions and charged analytes by the meso- and microporous spatial domains often, if not in general, contained in the (typically hierarchically structured) materials. For example, random packings of porous spherical particles or monoliths are frequently characterized by rather discrete bimodal pore size distributions, with macropores in the interparticle or interskeleton pore space, and mesopores inside the particle or monolith skeleton [98–101]; micropores can also be present, but it is principally irrelevant for our upcoming discussion. This creates the unique situation that common EDL dimensions which are estimated with the Debye screening length (λ_D) are much less than the mean macropore radius ($r_{macro}/\lambda_D \gg 1$), while a substantial EDL interaction prevails on mesopore scale ($r_{meso}/\lambda_D \approx 1$). As a consequence, most particulate and also monolithic stationary phase materials employed in CEC contain spatial domains which develop an ion-permselective behavior, they exlude co-ions and enrich the counter-ions [102–104].

Together with the electrical field strengths used in CEC (up to 100 kV/m) this may lead to strong concentration polarization (CP). It is a phenomenon or better, a complex of effects related to the formation of concentration gradients in the electrolyte solution adjacent to an ion-permselective (*i.e.*, charge selective) solid-liquid interface upon the passage of electrical current normal to that interface. For porous media containing ideally ion-permselective regions the charge transport in these domains is exclusively achieved by the counter-ions. When the electrical current becomes strong bulk charge is induced in the CP zones [105, 106]. For curved interfaces, it is determined by the normal component of the external field, while the tangential component exerts a force on this charge leading to fluid motion along the interface. These consequences and also conditions favoring a strong CP become quite important for the spatio-temporal dynamics of EOF in many materials with ion-permselective properties. It is a topic that has received considerable attention in the past, both from a theoretical and experimental point of view [107–113].

It should be mentioned that, in contrast to classical electroosmosis of the first kind (EO-1) which results from an interaction between the tangential electrical field and space charge of the usual, quasi-equilibrium (primary) EDL, electroosmosis of the second kind (EO-2) developing in strong electrical fields is caused by a force of the tangential field component on the induced, extended space charge of the nonequilibrium (secondary) double layer [112]. While the EOF velocity in a sphere packing responds linearly to the applied field strength concerning EO-1, it is expected to show nonlinear dependence for EO-2 [114]. To our knowledge, electrokinetic phenomena of the second kind [106], especially EO-2 have hardly been investigated in a context of CEC, although potential benefits of this phenomenon (EO-2) can be readily anticipated [114]. First, it provides a unique scheme towards increased EOF velocities compared to current CEC practice dominated by the EO-1 dynamics. Second, electroosmotic whirlwinds associated with EO-2 around a single (isolated) spherical particle [107, 113] also have implications for an accelerated, primarily lateral mixing in sphere packings which may reduce the time scale for transverse analyte equilibration. However, the operational domain of this effect, resulting flow patterns, and its influence on axial dispersion in fixed particulate and monolithic beds so far have not been studied.

In this work, we examine electrochromatographic separation efficiencies for neutral analytes and the behavior of EOF in C18-silica capillary monoliths with bimodal pore size distribution over a wide range of mobile phase Tris concentrations. The observed dependence of plate heights and fluid dynamics on applied electrical field and

mobile phase ionic strengths is discussed in view of the salient features of EO-2 indicating a unique, yet unexplored potential of this electrokinetic transport mechanism in separation science.

2 Materials and methods

In our CEC investigations we used C18-silica monoliths fixed in 100 μm ID and typically *ca.* 50 cm long cylindrical fused-silica capillaries. They were received as research samples from Merck (Darmstadt, Germany). The morphology of this monolithic material is characterized by bimodal pore size distributions due to intraskeleton mesopores and interskeleton macropores [115]. The C18-silica surface was not endcapped to provide a stronger silanol activity. Monoliths were cut to desired lengths and then assembled directly, *i.e.*, without needing any open-tubular segment, in the HP^{3D}CE capillary electrophoresis instrument (Agilent Technologies, Waldbronn, Germany). This allows to generate gradients in electrical potential from 0 to 30 kV between both ends of a monolith. Measurements were run at controlled temperature of 298 K. Both vials were pressurized for minimizing bubble formation, and detection was performed in-column at 230 nm. Tris, hydrochloric acid, and acetonitrile of HPLC-grade were purchased from Fluka (Sigma-Aldrich Chemie, Taufkirchen, Germany), while the alkylbenzoates came from Merck. Tris buffer solutions in acetonitrile/water 80:20 v/v were used as the electrolyte. Mobile phases were filtered over 0.45 μm nylon membrane filters and degassed by ultrasonication. An aqueous stock solution of 0.1 M Tris (base form) was prepared using water purified on a Milli-Q-Gradient (Millipore, Eschborn, Germany); the pH was adjusted to 8.3 by titration with concentrated hydrochloric acid. Appropriate volumes of this stock solution, Milli-Q water, and acetonitrile were then mixed to yield Tris buffer solutions of the desired ionic strengths in acetonitrile/water 80:20 v/v. In our studies we covered the overall range from 10^{-5} to 10^{-2} M effective Tris concentration (*e.g.*, 1×10^{-3} M Tris in the final electrolyte corresponded to 5×10^{-3} M Tris in the aqueous part). The concentration of protonated Tris (acid form) needed to estimate the thickness of the primary (quasi-equilibrium) EDL *via* λ_D was determined using the Henderson-Hasselbalch equation, with pH $\approx$ pK_a. Fresh samples were prepared on a daily basis by dissolving test compounds directly in running mobile phase (5×10^{-2} g/L). Alkylbenzoates were used as slightly retained, electroneutral analytes and thiourea as the flow field (average velocity) marker.

Figure 1 shows a typical electrochromatogram. All samples were injected electrokinetically (5 kV for 3 s). Analyte peaks always showed a high symmetry (effectively that of a Gaussian) and they were consequently analyzed by Gaussian fitting based on macros written in-house. To verify the robustness of the whole setup, ten independent injections were made at five selected separation voltages. The reproducibility in mobile phase velocity was generally better than 1.5% (*e.g.*, 0.9% under conditions mentioned in Fig. 1). For all buffer concentrations used in this work retention factors remained practically unchanged concerning a constant, basic composition of the running mobile phase (acetonitrile/water 80:20 v/v).

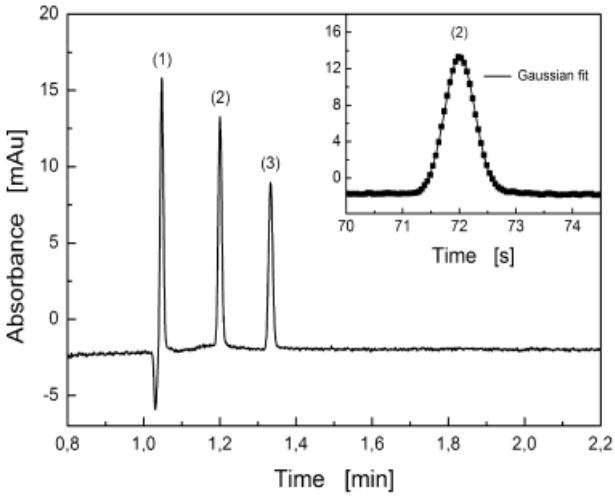

Figure 1. Typical electrochromatogram obtained with the silica-based capillary monolith. (1) Thiourea, (2) ethylbenzoate, and (3) butylbenzoate. Mobile phase, acetonitrile/water 80:20 v/v with 0.1 mM effective Tris concentration; applied field strength, 102 kV/m resulting in u_{eo} = 3.4 mm/s; separation efficiency for the ethylbenzoate, 4.75×10^5 N/m.

In view of the upcoming analysis and discussion of our experimental results (with an eye on the ion-permselectivity in materials characterized by bimodal pore size distributions), it will be helpful to realize *a priori* the pore-scale interactions of the primary EDL in the investigated monoliths as function of the mobile phase ionic strength. For this purpose, Fig. 2 illustrates the dependence of r_{pore}/λ_D on the effective Tris concentration. λ_D is calculated by

$$\lambda_D = \left(\frac{\varepsilon_0 \varepsilon_r RT}{F^2 \sum_i z_i^2 c_{i,\infty}} \right)^{1/2} \quad (1)$$

where ε_0 and ε_r are the permittivity of vacuum and relative permittivity of the electrolyte solution, respectively, R is the gas constant, T is the absolute temperature, and F is the Faraday constant; z_i is the valency of ionic species i and $c_{i,\infty}$ its concentration in the electroneutral solution (that is, beyond the primary EDL). The relative permittivity and viscosity at 298 K of the final mobile phases were taken as 44.53 and 5.03×10^{-4} kg/(m·s), respectively [43].

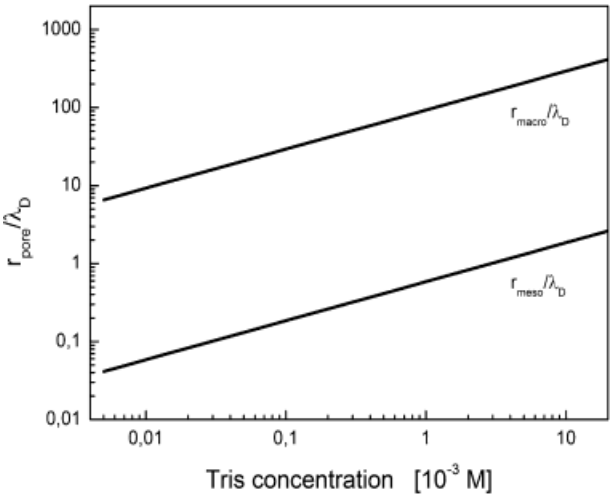

Figure 2. Aspect ratio r_{pore}/λ_D against the effective mobile phase concentration of Tris buffer for mesopores and macropores of the silica-based monolith. In this illustration we assumed r_{meso} = 6 nm and r_{macro} = 950 nm as typical dimensions [115]. The given Tris concentrations (× M) in general correspond to effective concentrations in final mobile phase which consists of acetonitrile/water (5× M Tris) 80:20 v/v.

As seen in Fig. 2, r_{pore}/λ_D for the meso- and macropores increases, as expected, at increasing mobile phase ionic strength (corresponding to half of its Tris concentration). For the macropores the ratio increases from *ca.* 10 to nearly 300 at 10 mM Tris. For the mesopores it remains below unity over almost the whole range of Tris concentrations indicating what is referred to as "strong EDL overlap" in the double-layer model. Alternatively, this situation may be analyzed in terms of Donnan exclusion [102]. At electrochemical equilibrium between the electrolyte solutions in both compartments, the counter-ion concentration in the intraskeleton mesopore space is higher and the co-ion concentration lower than in the interskeleton macropore space. The Donnan potential (Φ_{Don}) balances a tendency of ions to level out existing concentration differences: it pulls cations back into the (negatively charged) intraskeleton pore space and anions back into the (positively charged) interskeleton compartment [103]. For ideal solutions we have

$$\Phi_{Don} \equiv \phi_{meso} - \phi_{macro} = -\frac{RT}{z_i F} \ln \frac{c_{i,meso}}{c_{i,macro}} \quad (2)$$

with i = $TrisH^+$, H_3O^+, Cl^-, and OH^-. The distribution coefficient $c_{i,meso}/c_{i,macro}$ which represents the ion-permselectivity, depends on ionic strength of the mobile phase, surface charge density in the mesopores, as well as on valencies of co- and counter-ionic species. Actually, these parameters similarly influence EDL overlap and resulting ion-exclusion in a double-layer model. To conclude for now, an ion-permselectivity in the investigated monoliths should be recognized which can be illustrated by either approach.

3 Results and discussion

We present our experimental results in view of closely related phenomena which provide complementary insight: the flow field dynamics of electroosmosis and hydrodynamic dispersion in a silica-based capillary monolith with bimodal pore size distribution. The revealed peculiarities are then analyzed in view of CP and EO-2 to provide possible explanation for the nonlinear EOF behavior and the significantly improved separation efficiencies which sensitively depend on the applied electrical field and mobile phase ionic strengths.

3.1 EOF behavior

Figure 3 shows a basic set of results demonstrating the dependence of average EOF velocity in the monolith on the applied electrical field strength (up to 102 kV/m), covering a range of mobile phase Tris concentrations from 5×10^{-5} to 1×10^{-2} M. While for the 5 mM solution we observe a practically linear behavior (see linear fit to the data in Fig. 3), it becomes slightly nonlinear at 10 mM Tris. The deviation can be easily explained by development of Joule heat in the monolith as a plot of the EOF velocity against the electrical current verifies a linear dependence (data not shown). This origin of nonlinear EOF velocities is not surprising and well-known [116]. However, at Tris concentrations below 5 mM where the thermal effects appear insignificant we witness the development of yet another nonlinear dependence of the average EOF velocity on field strength which is very systematic and becomes more pronounced as the Tris concentration is decreased further towards 5×10^{-5} M. It is evidenced by the excellent second-order polynomial fit to the 0.1 mM Tris data (see Fig. 3). Also caused by this developing nonlinearity, velocities up to almost 3.5 mm/s are finally reached around 10^5 V/m with the lower mobile phase ionic strengths (which exceed those expected from linear dependence by more than 50%).

Figure 4 demonstrates that dissipation of Joule heat in the monolith indeed cannot explain the nonlinear flow field dynamics at decreasing ionic strength, because electrical current through the hierarchical porous structure depends practically linearly on applied field strength, as expected according to Ohm's law, while the velocities display a clearly nonlinear behavior. This finding also indicates that a contribution from the EOF to the overall electrical cur-

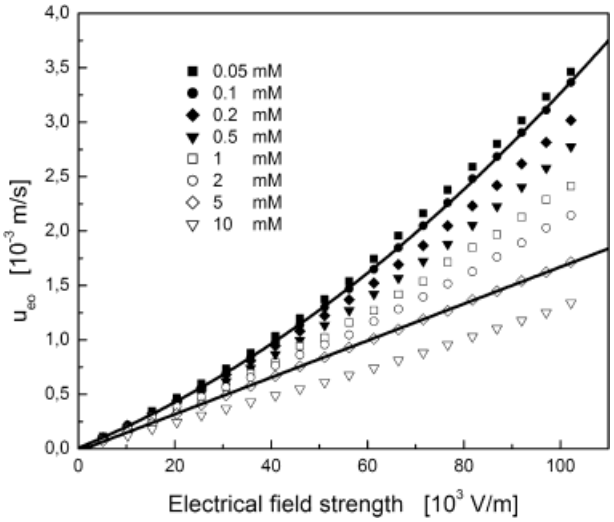

Figure 3. Average EOF velocity in the capillary monolith *vs.* applied electrical field strength for different Tris concentrations, as indicated. Second-order polynomial and linear fits for 0.1 and 5 mM effective Tris, respectively, are a guide to the eye; the length of the monolith bed is 29.4 cm.

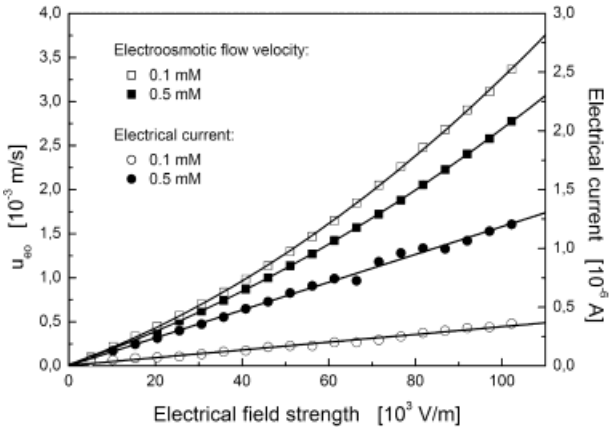

Figure 4. EOF velocity and electrical current *vs.* applied electrical field strength for selected Tris concentrations. Second-order polynomial and linear fits for EOF velocity and electrical current, respectively, are a guide to the eye.

rent is negligible with respect to the bulk conductivity of these electrolyte solutions [117]. It can be related to the actual EDL thickness which remains too small compared to macropore dimensions ($r_{macro}/\lambda_D \gg 1$, see Fig. 2) and too large with respect to the mesopore size ($r_{meso}/\lambda_D < 1$). As a consequence, the EOF in the interskeleton macropores mostly carries liquid close to local electroneutrality and intraskeleton EOF is remaining relatively unimportant [67]. In contrast to the 10 mM Tris solution and associated Joule heating, the plot of EOF velocity against electrical current then is nonlinear for the lower Tris concentrations, and an effect other than heat dissipation in the monolith must be responsible for the nonlinear dynamics of the velocity field (Figs. 3 and 4).

Figure 5 shows the variation of electroosmotic mobility in the silica-based capillary monolith with mobile phase Tris concentration (covering the range from 1×10^{-5} to 3×10^{-3} M Tris) for selected field strengths. First, we can observe a relatively common trend insofar as the mobility increases at decreasing ionic strength of the solution to approach a maximum at about 5×10^{-5} M Tris and decrease below this concentration. While the decrease in mobility with increasing ionic strength above 5×10^{-5} M Tris represents normal double-layer behavior in the interskeleton macropores when EDL overlap is negligible, *i.e.*, the EDL continues to be compressed resulting in a reduced shear plane potential, the increase in mobility from below that concentration towards a spurious maximum can have several origins [118, 119]. These include the role of surface conductance or ion adsorption, but a simple and straightforward reason is EDL interaction in our monolith which is becoming relevant also in the macropores under these conditions (*cf.* Fig. 2). A much more intriguing conclusion emanating from the data in Fig. 5 is that the mobility depends on applied field strength at a constant mobile phase composition under conditions that may be assumed as isothermal. Further, the increase in mobility with electrical field strength is getting stronger when the Tris concentration is reduced between 3×10^{-3} M and 5×10^{-5} M (seen in the different slopes of these curves, Fig. 5). However, this observation resembles nothing else than a developing, clearly nonlinear EOF dynamics demonstrated already in the systematic u_{eo}-E-plots (Fig. 3) at Tris concentrations below 5×10^{-3} M. Before analyzing further this (at a first glance

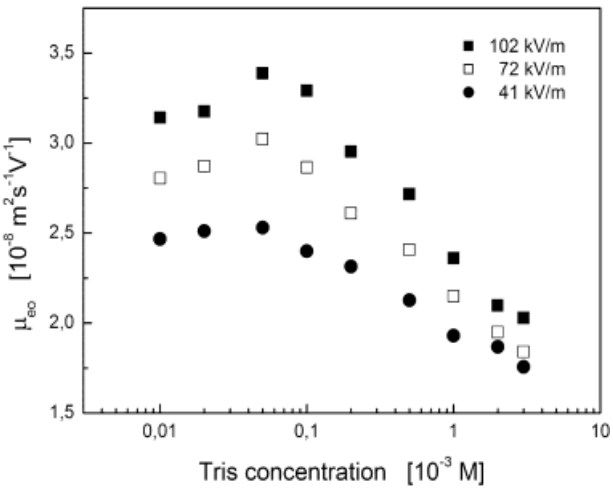

Figure 5. Electroosmotic mobility in the capillary monolith *vs.* the effective Tris concentration at selected field strengths, as indicated.

less familiar) behavior, we present axial plate height data which have been recorded over the whole range of electrical field and mobile phase ionic strengths.

3.2 Separation efficiencies

The onset of a significantly nonlinear EOF dynamics is observed at 2×10^{-3} M Tris concentration (Fig. 3). In order to retrieve a possible effect accompanying this nonlinear electrokinetics also in the achieved separation efficiency, corresponding trends in the axial plate height curves were screened. Figure 6 shows data for ethylbenzoate as slightly retained analyte. They demonstrate a clear and systematic behavior. Plate height curves (Fig. 6a) as expected coincide at lower velocities where molecular diffusion naturally dominates the overall dispersion. Further, for all of the encountered ionic strengths the plate heights approach an increasingly extending plateau at higher velocities which (for the 1×10^{-4} M Tris solution) reaches from about $u_{eo} = 1.5$ mm/s up to the highest velocity realized with the commercial equipment. It indicates a negligible contribution from nonmechanical and mechanical dispersion mechanisms which are most generally involved in the scaling of band spreading with increasing velocity. Still, this finding is not really a surprise because the discretely bimodal pore size distribution of this type of monolith is known to provide large macropores and a thin, mechanically relatively stable, highly porous skeleton [120]. These characteristics, together with the possibility to create the hierarchically structured pore space *via* independent adjustment of relevant skeleton parameters, form the basis for unique combination of macropore hydraulic permeability, characteristic path lengths in the mesoporous skeleton and adsorption capacity [101]. Band-broadening in CEC due to Taylor dispersion on macopore-scale should be substantially reduced compared to that with hydraulic flow in capillary HPLC, resulting in relatively flat plate height curves at increasing EOF velocities as observed in this work (Fig. 6a). That behavior, as well as the realized EOF velocities at higher mobile phase ionic strength ($u_{eo} \approx 1.3$ mm/s with 1×10^{-2} M Tris at 10^5 V/m, *cf.* Fig. 3) and the then achieved plate heights of *ca.* 5 μm for a slightly retained analyte agree well with already published work in which similar capillary monoliths have been investigated [24, 115].

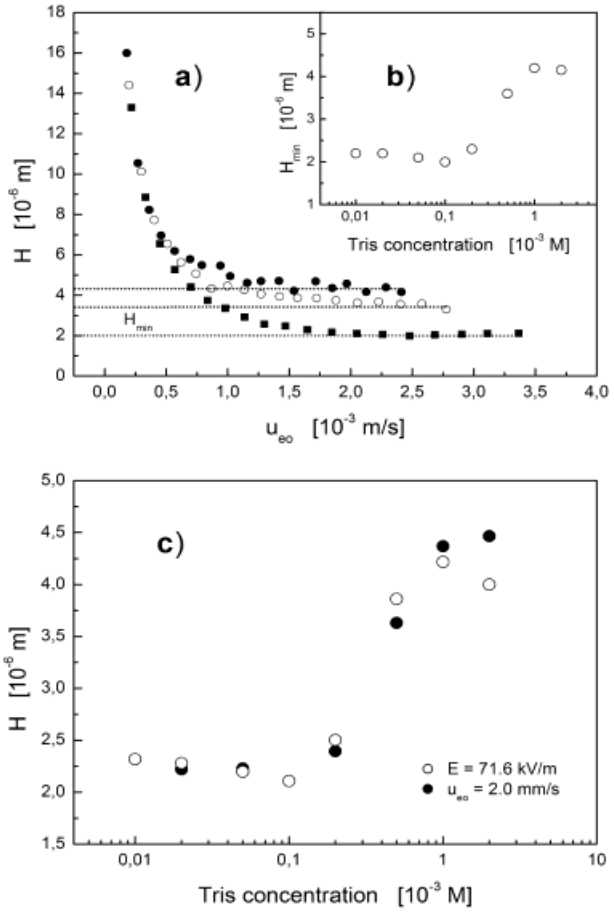

Figure 6. Separation efficiencies for ethylbenzoate. (a) Plate height curves at varying mobile phase Tris concentration: (●) 1 mM, (○) 0.5 mM, (■) 0.1 mM. (b) Minimum plate height, and (c) plate height at constant applied field strength or velocity (in plateau regions) against the effective Tris concentration.

While this is familiar, actually the most striking result of our electrochromatographic plate height studies with the silica-based monolith is a further significant decrease in the plateau value (H_{min}) as Tris concentrations are reduced towards 5×10^{-5} M (Fig. 6b), *i.e.*, an improvement in plate height by a factor of more than two occurs while moving from 1 mM to 0.1 mM Tris. Usually, this range of mobile phase ionic strength for several reasons is rarely encountered in CEC, including needs for a minimum buffer capacity or certain EDL dimensions. Figure 6c clearly demonstrates that the increase in separation efficiencies monitored at a constant field strength or EOF velocity systematically depends on the Tris concentration, as long as the plate height data are evaluated in their plateau region. The improving axial dispersion at decreasing ionic strength is remarkable indeed from the standpoint of an electroosmotic perfusion mechanism. A growing EDL thickness reduces EOF in the mesoporous skeleton due to EDL overlap (*cf.* Fig. 2) which, together with the normal EDL behavior dominating in the macropores (Figs. 2 and 5), increases the global velocity heterogeneity over the cross-section of the hierarchical monolithic column. On this basis, we generally would expect rather an adverse effect by a decreasing ionic strength on separation efficiency [61, 69–71], in contradiction with our experimental results (Fig. 6).

Consequently, the perfusion mechanism must be of only limited relevance over this whole range of Tris concentrations, *e.g.*, mesopore-level EDL overlap is not sufficiently suppressed in view of Fig. 2 and diffusive mass transfer that remains in the mesopores cannot become limiting then because of the thin monolith skeleton which translates to small porous particles [101]. However, still another transport mechanism must be operative and so strong that it can easily compensate this tendency. An important observation in this direction is that the plate height improvement (as seen in Figs. 6b and c) at decreasing ionic strength coincides with the onset of the nonlinear EOF dynamics in Fig. 3. Obviously, both phenomena appear to be correlated, *e.g.*, below 0.1 mM Tris we can neither witness a further increase in the separation efficiencies (Fig. 6), nor a significant change in the nonlinearity of electroosmosis (Figs. 3 and 5). Whatever the reasons for this behavior are, they open the possibility for highly efficient and fast separations based on a significantly increased EOF. The minimum plate height is easily reached and separations can be run at a high velocity due to the plateau in plate height curves. This potential is demonstrated in Fig. 7 using a 16-component mix of (electroneutral) polynuclear aromatic hydrocarbons. As evident a good resolution can be achieved for most components under isocratic conditions in an elution of less than only 5 min.

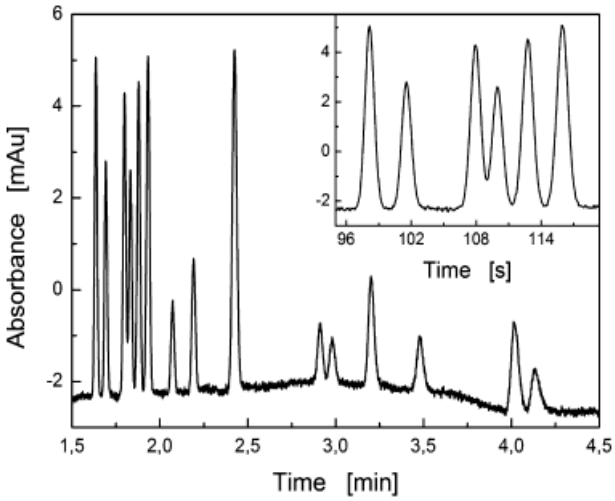

Figure 7. Elution of polynuclear aromatic hydrocarbons mix (Supelco, Bellefonte, PA, USA) using acetonitrile/water 80:20 v/v containing 0.1 mM Tris, and an applied field strength of 95 kV/m. The bed length of this C18-silica monolith is 31.6 cm.

3.3 Electroosmosis of the second kind

In an attempt to explain complementary the nonlinear EOF dynamics (Fig. 3) and plate height improvement (Fig. 6), we focus our attention on the ion-permselective properties arising in the monolithic structure at a decreasing mobile phase ionic strength due to its mesoporous skeleton and discuss the possible consequences of CP in a strong external electrical field [106, 107]. It is in this respect that the creation of bulk electrical charge close to the ion-permselective interface induced by the applied field plays a crucial role because the induced-charge electroosmosis can explain both a nonlinear flow behavior and improved axial dispersion characteristics. Thus, we try to illustrate this process.

For that purpose, we consider in Fig. 8 the locally flat interface between a bulk, macroporous domain and an ideally ion-permselective region (meaning that the permeability for co-ions in the latter becomes negligible compared to that of counter-ions) with a negative internal and external surface charge. This is assumed to represent the local interfaces in monoliths with bimodal pore size distribution or beds of porous particles (Fig. 8). As a consequence, the molar flux density of a negatively charged co-ion in the intraskeleton (or intraparticle) pores is zero. In contrast to complete exclusion of mobile co-ions ($\mathbf{J}^-_{intra} = 0$), the overall flux density of a positively charged coun-

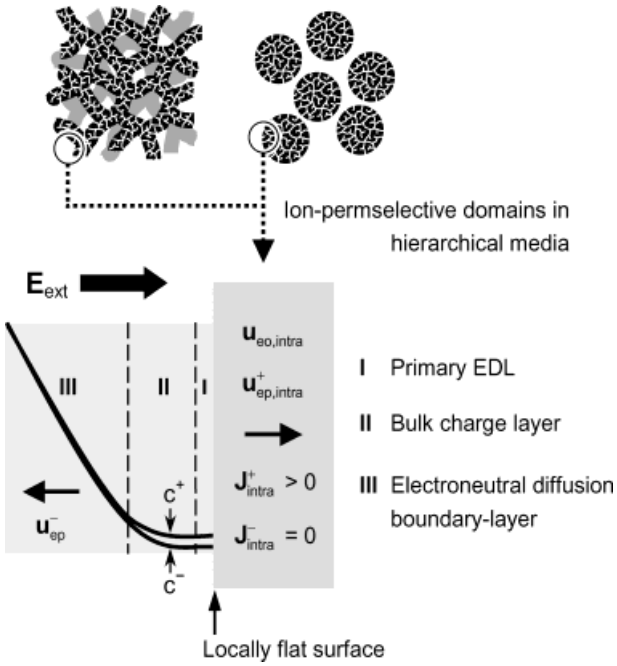

Figure 8. Illustration of nonequilibrium CP in a strong electrical field close to the interface of a bulk macroporous compartment and an (ideally) ion-permselective mesoporous domain. As shown, such interfaces naturally occur in beds of porous particles and monoliths with meso- and/or microporous skeleton. Close to that interface, in the macroporous compartment, a mobile space charge (here, $c^+ > c^-$) can be induced under conditions favoring strong CP. Concerning development of nonequilibrium electrokinetic effects the discrete particle diameter is replaced by a (yet unknown) characteristic length of the monolith skeleton.

ter-ion in the ion-permselective domain ($\mathbf{J}^+_{\text{intra}}$) consists of diffusive flux ($\mathbf{J}^+_{\text{diff}}$) and electrical transference ($\mathbf{J}^+_{\text{el}}$), as well as convective transfer ($\mathbf{J}^+_{\text{con}}$) *via* electrokinetic flow associated with a quasi-equilibrium EDL at the internal surface [102]:

$$\begin{aligned}\mathbf{J}^+_{\text{intra}} &= \mathbf{J}^+_{\text{diff}} + \mathbf{J}^+_{\text{el}} + \mathbf{J}^+_{\text{con}} \\ &= -D^+_{\text{intra}}\left(\nabla c^+_{\text{intra}} + z^+ c^+_{\text{intra}}\frac{F}{RT}\nabla\phi\right) + c^+_{\text{intra}}\mathbf{u}_{\text{eo,intra}} \\ &= -D^+_{\text{intra}}\nabla c^+_{\text{intra}} + c^+_{\text{intra}}(\mathbf{u}^+_{\text{ep,intra}} + \mathbf{u}_{\text{eo,intra}}) \qquad (3)\end{aligned}$$

where D^+_{intra} is the intraskeleton (or intraparticle) diffusion coefficient of the counter-ion (*e.g.*, the protonated Tris molecule in the context of the present work), c^+_{intra} is its molar concentration and z^+ is the charge number, and ϕ denotes the electrical potential. This equation underlines a strong dependence of intraskeleton (or intraparticle) molar flux densities of a counter-ion on the applied field strength as the electrophoresis and electroosmosis velocities ($\mathbf{u}^+_{\text{ep,intra}}$ and $\mathbf{u}_{\text{eo,intra}}$ in Fig. 8) are pointing in the same direction (Leinweber and Tallarek, submitted).

Due to the external field the electrolyte concentration is induced to decrease where counter-ions enter the ion-permselective domain from the bulk solution. Co-ions migrate in opposite direction, away from the interface ($\mathbf{u}^-_{\text{ep}}$ in Fig. 8), and because this withdrawal cannot be compensated by supply from the intraskeleton (or intraparticle) pores the co-ion concentration decreases. The interplay of the ion-permselectivity, electromigration, and diffusive flux leads to the formation of a diffusion boundary-layer. In sufficiently strong fields which can force the concentration of co-ions in this CP zone towards zero close to the interface, while that of the counter-ions remains finite, a space charge can be induced in the interskeleton (or interparticle) fluid-side [106, 107] (Fig. 8). The counterpart of this mobile positive space charge is probably inside the ion-permselective region as immobile (fixed) negative surface charge (Leinweber and Tallarek, submitted). The induced space charge represents a nonequilibrium charge layer (or secondary double layer) which can interact with the tangential component of the electrical field to generate EO-2 along curved interfaces like that of a monolith skeleton or spherical particle. The CP zone reaching towards the primary, *i.e.*, quasi-equilibrium EDL may be pictured as covering (i) an induced space charge region where the concentration of counter-ions significantly exceeds that of the co-ions, absent at lower voltages with established equilibrium CP, and (ii) the diffusion boundary-layer with linear variation of the ion concentrations and local electroneutrality in the sense that $c^+ - c^- \ll c^+ + c^-$ [112, 121] (Fig. 8).

The local deviation from electroneutrality in the bulk fluid-side induced by the normal component of the electrical field under conditions of nonequilibrium CP close to a curved, ion-permselective interface has unique consequences. First, and in contrast to a linear EOF dynamics known from EO-1, the resulting EO-2 naturally shows a nonlinear behavior because it depends on both the normal and tangential components of the applied field *via* creation of a space charge (induction step) and force exerted on the mobile part of this secondary EDL (interaction step), respectively. Further, because normal and tangential field components vary locally along the curved surfaces in monoliths or sphere packings, also the intensity of nonequilibrium CP and EO-2 velocities are expected to change accordingly. Then, local back pressures must generate based on continuity, and complex coupling between the electrostatics and hydrodynamics may lead to a formation of microvortices. Although resulting patterns certainly depend on the pore space morphology, any potential operation of this phenomenon in porous media having technical or analytical relevance is a challenging task. For example, to which extent can large recirculation zones that have been visualized for a spherical, isolated particle [107, 113] develop in random-close packings of these particles or in monolithic structures? If vortices develop locally, can they interact cooperatively to create even lateral mixing bands? – Accelerated column cross-sectional equilibration of analyte (here caused by an electrokinetic chaotic mixing) would be very beneficial as it may reduce axial dispersion further by orders of magnitude (Leinweber and Tallarek, submitted).

In view of the foregoing discussion our experimental findings now appear in a different light: The nonlinear EOF dynamics developing with decreasing mobile phase ionic strength (Fig. 3) and complementary trend in plate height data (Fig. 6) can be analyzed and consistently explained by nonequilibrium electrokinetic effects. Due to a decreasing concentration of Tris buffer (Fig. 3) the mesopore space in the monolith skeleton is adjusted towards ideal ion-permselectivity (*cf.* Fig. 8). Its permeability for the co-ions decreases, and a critical field strength above which the nonequilibrium CP starts to contribute significantly to a global electrokinetics in the monolith also decreases. In other words, the lower the co-ion permeability of the mesopore domain the easier it is for electrical fields realized in our work to decrease the co-ion concentration in the CP zones towards nonequilibrium conditions and induce space charge. We then observe a systematically developing nonlinear EOF behavior at decreasing ionic strength due to an increased relevance of EO-2 in the macropore space of the monolith, being most pronounced between 1 and 0.1 mM Tris (Figs. 3 and 5). This is exactly the range in which we observe the substantial plate height improvement (Fig. 6). It may be caused by induced local pressure components and formation of patterns which help to equilibrate analytes in the macropore

domain and thereby reduce axial dispersion, as observed with fixed beds of particles (Leinweber and Tallarek, submitted). Even though geometrical restraints in most porous media probably hinder a formation of extending recirculation zones visualized for a single sphere [107, 113], the remaining patterns still may be able to enhance significantly lateral mixing (at least on the pore scale). In this respect, differences in morphology of sphere packings and monolithic structures should be remembered [101] as they will influence the development of nonequilibrium electrokinetic effects. One of the goals is to characterize (and tailor) such effects in hierarchical porous media concerning the ion-permselectivity, pore space morphology, mobile phase composition, and applied field strength.

4 Concluding remarks

The nonlinear EOF behavior revealed in our work using silica-based capillary monoliths with a bimodal pore size distribution indicates an existence and importance of EO-2 also in CEC practice. It is a nonequilibrium electrokinetic phenomenon relating to ion-permselective domains and developing CP in a material and, thus, has a general rather than special significance for the global electrokinetics in hierarchically structured porous media like random sphere packings and monoliths. EO-2 does not appear on an exclusive basis, but acts together with the more familiar EO-1. This may be a reason why it is usually not clearly manifested in CEC, because the typical particle diameter in fixed beds (3–10 μm), the mesopore size (10–30 nm) and mobile phase ionic strength (1–10 mM) do not promote EO-2 intensively, leaving EO-1 as a dominant contribution to the overall EOF under most conditions. In this direction, the monolithic structures appear unique as the thin, continuous skeleton may provide length scales which favor significant development of EO-2 in CEC as alternative to a use of larger, but discrete particles. Then, ion-permselectivity can be adjusted with the ionic strength, providing one route to significantly higher EOF velocities than those in an EO-1 regime. Strong electrical fields could be applied under these conditions in capillary and chip devices containing tailored hierarchical material for electrokinetic separations or pumping technology, without significant thermal effects, but with a full high-speed potential of the EO-2 dynamics (which is inherently nonlinear).

Another beneficial effect accompanying the EO-2 dynamics is the development of pore pressure based on continuity arguments. Although the details of a microscopic operation in porous media and potential use of this effect for enhanced lateral fluid mixing need more resolving studies, our present and earlier results (Leinweber and Tallarek, submitted) indicate that it can be tuned to largely overcome a bottleneck in liquid-phase separations, namely analyte equilibration over the whole column cross-section. It is a slow process governed by the actual transverse dispersion coefficient which is a much weaker function of the average velocity than dispersion in the axial direction [122]. Consequently, lateral equilibration of analyte usually is diffusion-limited and the electrokinetically promoted convective (chaotic) mixing becomes of an outstanding importance.

Compared to the electroosmotic perfusion mechanism [61–76], electrokinetic phenomena based on a nonequilibrium EDL develop in a different operational domain. While substantially perfusive EOF in particulate or monolithic beds require a quasi-equilibrium EDL thickness (much) smaller than typical macro- and mesopore sizes, the nonequilibrium CP underlying EO-2 requires strong ion-permselectivity within a porous medium, meaning that the EDL dimension is large compared to pore sizes in the ion-permselective regions. Further, while electroosmotic perfusion effectively removes stagnant zones which dramatically reduces velocity extremes in the mobile phase flow pattern in view of improved dispersion and increased average velocities, the conditions for EO-2 develop ion-permselectivity to leave these zones practically stagnant. In this case, the mesopore space is used for indirect manipulation of EOF velocities in the macropore space where possible lateral mixing associated with the hydrodynamic pattern of EO-2 reduces axial dispersion. Thus, *via* the EDL interaction both phenomena (the perfusive electroosmosis and EO-2) may be tuned towards high-speed, high-efficiency electrokinetic transport mechanisms in porous media simply by adjusting the mobile phase ionic strength.

We are grateful to Dieter Lubda from Merck KGaA (Darmstadt, Germany) for capillary monoliths used in our work and to Dr. Gerard Rozing from Agilent Technologies (Waldbronn, Germany) for the loan of the HP^{3D}CE instrument. We further acknowledge financial support from the Deutsche Forschungsgemeinschaft (DFG) and Fonds der Chemischen Industrie (FCI).

Received February 1, 2004

5 References

[1] Probstein, R. F., Hicks, R. E., *Science* 1993, *260*, 498–503.
[2] Sauer, J. E., Davis, E. J., *Environ. Sci. Technol.* 1994, *28*, 737–745.
[3] Yeung, A. T., *Adv. Porous Media* 1994, *2*, 309–395.
[4] Dittmann, M. M., Wienand, K., Bek, F., Rozing, G. P., *LC·GC* 1995, *13*, 800–814.

[5] Ho, S. V., Sheridan, P. W., Athmer, C. J., Heitkamp, M. A., Brackin, J. M., Weber, D., Brodsky, P. H., *Environ. Sci. Technol.* 1995, *29*, 2528–2534.

[6] Tsuda, T. (Ed.), *Electric Field Applications in Chromatography, Industrial and Chemical Processes*, VCH, Weinheim 1995.

[7] Acar, Y. B., Ozsu, E. E., Alshawabkeh, A. N., Rabbi, M. F., Gale, R. J., *CHEMTECH* 1996, *26*, 40–44.

[8] Crego, A. L., González, A., Marina, M. L., *Crit. Rev. Anal. Chem.* 1996, *26*, 261–304.

[9] Coletta, T. F., Brunell, C. J., Ryan, D. K., Inyang, H. I., *J. Environ. Eng.* 1997, *123*, 1227–1233.

[10] Fujimoto, C., *Trends Anal. Chem.* 1999, *18*, 291–301.

[11] Colón, L. A., Burgos, G., Maloney, T. D., Cintrón, J. M., Rodríguez, R. L., *Electrophoresis* 2000, *21*, 3965–3993.

[12] Pyell, U., *J. Chromatogr. A* 2000, *892*, 257–278.

[13] Ericson, C., Holm, J., Ericson, T., Hjertén, S., *Anal. Chem.* 2000, *72*, 81–87.

[14] Yu, C., Svec, F., Fréchet, J. M. J., *Electrophoresis* 2000, *21*, 120–127.

[15] Hayes, J. D., Malik, A., *Anal. Chem.* 2000, *72*, 4090–4099.

[16] Bousse, L., Cohen, C., Nikiforov, T., Chow, A., Kopf-Sill, A. R., Dubrow, R., Parce, J. W., *Annu. Rev. Biophys. Biomol. Struct.* 2000, *29*, 155–181.

[17] Tang, Q. L., Lee, M. L., *Trends Anal. Chem.* 2000, *19*, 648–663.

[18] Bruin, G. J. M., *Electrophoresis* 2000, *21*, 3931–3951.

[19] Deyl, Z., Svec, F. (Eds.), *Capillary Electrochromatography*, Journal of Chromatography Library, Vol. 62, Elsevier, Amsterdam 2001.

[20] Whitesides, G. M., Stroock, A. D., *Phys. Today* 2001, *54*, 42–48.

[21] Tanaka, N., Kobayashi, H., Nakanishi, K., Minakuchi, H., Ishizuka, N., *Anal. Chem.* 2001, *73*, 420A–429A.

[22] Stone, H. A., Kim, S., *AIChE J.* 2001, *47*, 1250–1254.

[23] Polson, N. A., Hayes, M. A., *Anal. Chem.* 2001, *73*, 312A–319A.

[24] Kobayashi, H., Smith, C., Hosoya, K., Ikegami, T., Tanaka, N., *Anal. Sci.* 2002, *18*, 89–92.

[25] Rathore, A. S., *Electrophoresis* 2002, *23*, 3827–3846.

[26] Minerick, A. R., Ostafin, A. E., Chang, H.-C., *Electrophoresis* 2002, *23*, 2165–2173.

[27] Mistry, K., Krull, I., Grinberg, N., *J. Sep. Sci.* 2002, *25*, 935–958.

[28] Delgado, A. V. (Ed.), *Interfacial Electrokinetics and Electrophoresis*, Marcel Dekker, New York 2002.

[29] Throckmorton, D. J., Shepodd, T. J., Singh, A. K., *Anal. Chem.* 2002, *74*, 784–789.

[30] Ceriotti, L., de Rooij, N. F., Verpoorte, E., *Anal. Chem.* 2002, *74*, 639–647.

[31] Legido-Quigley, C., Marlin, N. D., Melin, V., Manz, A., Smith, N. W., *Electrophoresis* 2003, *24*, 917–944.

[32] Peric, I., Kenndler, E., *Electrophoresis* 2003, *24*, 2924–2934.

[33] Jemere, A. B., Oleschuk, R. D., Harrison, D. J., *Electrophoresis* 2003, *24*, 3018–3025.

[34] Broyles, B. S., Jacobson, S. C., Ramsey, J. M., *Anal. Chem.* 2003, *75*, 2761–2767.

[35] Probstein, R. F., *Physicochemical Hydrodynamics*, John Wiley & Sons, New York 1994.

[36] Saksena, S., Zydney, A. L., *J. Membr. Sci.* 1995, *105*, 203–215.

[37] Eykholt, G. R., *J. Hazard. Mater.* 1997, *55*, 171–186.

[38] Dittmann, M. M., Rozing, G. P., *J. Microcol. Sep.* 1997, *9*, 399–408.

[39] Choudhary, G., Horváth, Cs., *J. Chromatogr. A* 1997, *781*, 161–183.

[40] Erickson, D., Li, D., *Langmuir* 2002, *18*, 1883–1892.

[41] Jiskra, J., Jiang, T., Claessens, H. A., Cramers, C. A., *J. Microcol. Sep.* 2000, *12*, 530–540.

[42] Gaš, B., Kenndler, E., *Electrophoresis* 2000, *21*, 3888–3897.

[43] Banholczer, A., Pyell, U., *J. Chromatogr. A* 2000, *869*, 363–374.

[44] Tanigawa, T., Nakagawa, T., Kimata, K., Nagayama, H., Hosoya, K., Tanaka, N., *J. Chromatogr. A* 2000, *887*, 299–305.

[45] Bohinc, K., Kralj-Iglič, V., Iglič, A., *Electrochim. Acta* 2001, *46*, 3033–3040.

[46] Sounart, T. L., Baygents, J. C., *Colloids Surf. A* 2001, *195*, 59–75.

[47] Pačes, M., Kosek, J., Marek, M., Tallarek, U., Seidel-Morgenstern, A., *Electrophoresis* 2003, *24*, 380–389.

[48] Bath, B. D., White, H. S., Scott, E. R., *Anal. Chem.* 2000, *72*, 433–442.

[49] Moy, G., Corry, B., Kuyucak, S., Chung, S.-H., *Biophys. J.* 2000, *78*, 2349–2363.

[50] Corry, B., Kuyucak, S., Chung, S.-H., *Biophys. J.* 2000, *78*, 2364–2381.

[51] Kuo, T. C., Sloan, L. A., Sveedler, J. V., Bohn, P. W., *Langmuir* 2001, *17*, 6298–6303.

[52] Zhao, B., Moore, J. S., Beebe, D. J., *Science* 2001, *291*, 1023–1026.

[53] Karniadakis, G. E., Beskok, A., *Micro Flows – Fundamentals and Simulation*, Springer-Verlag, New York 2002.

[54] Vainshtein, P., Gutfinger, C., *J. Micromech. Microeng.* 2002, *12*, 252–256.

[55] Conlisk, A. T., McFerran, J., Zheng, Z., Hansford, D., *Anal. Chem.* 2002, *74*, 2139–2150.

[56] Uitto, O. D., White, H. S., Aoki, K., *Anal. Chem.* 2002, *74*, 4577–4582.

[57] Qiao, R., Aluru, N. R., *Nano Lett.* 2003, *3*, 1013–1017.

[58] Bau, H. H., Zhu, J. Z., Qian, S. Z., Xiang, Y., *Sens. Actuators B* 2003, *88*, 207–218.

[59] Stroock, A. D., Whitesides, G. M., *Acc. Chem. Res.* 2003, *36*, 597–604.

[60] Hau, W. L. W., Trau, D. W., Sucher, N. J., Wong. M., Zohar, Y., *J. Micromech. Microeng.* 2003, *13*, 272–278.

[61] Li, D., Remcho, V. T., *J. Microcol. Sep.* 1997, *9*, 389–397.

[62] Wen, E., Asiaie, R., Horváth, Cs., *J. Chromatogr. A* 1999, *855*, 349–366.

[63] Venema, E., Kraak, J. C., Poppe, H., Tijssen, R., *J. Chromatogr. A* 1999, *837*, 3–15.

[64] Tallarek, U., Rapp, E., Scheenen, T., Bayer, E., Van As, H., *Anal. Chem.* 2000, *72*, 2292–2301.

[65] Stol, R., Poppe, H., Kok, W. Th., *Anal. Chem.* 2001, *73*, 3332–3339.

[66] Tallarek, U., Scheenen, T. W. J., Van As, H., *J. Phys. Chem. B* 2001, *105*, 8591–8599.

[67] Vallano, P. T., Remcho, V. T., *J. Phys. Chem. B* 2001, *105*, 3223–3228.

[68] Dearie, H. S., Smith, N. W., Moffat, F., Wren, S. A. C., Evans, K. P., *J. Chromatogr. A* 2002, *945*, 231–238.

[69] Tallarek, U., Rapp, E., Seidel-Morgenstern, A., Van As, H., *J. Phys. Chem. B* 2002, *106*, 12709–12721.

[70] Stol, R., Kok, W. Th., Poppe, H., *J. Chromatogr. A* 1999, *853*, 45–54.

[71] Vallano, P. T., Remcho, V. T., *Anal. Chem.* 2000, *72*, 4255–4265.

[72] Tallarek, U., Rapp, E., Van As, H., Bayer, E., *Angew. Chem. Int. Ed.* 2001, *40*, 1684–1687.

[73] Stol, R., Kok, W. Th., Poppe, H., *J. Chromatogr. A* 2001, *914*, 201–209.

[74] Chen, G., Tallarek, U., *Langmuir* 2003, *19*, 10901–10908.

[75] Tallarek, U., Rapp, E., Sann, H., Reichl, U., Seidel-Morgenstern, A., *Langmuir* 2003, *19*, 4527–4531.

[76] Tallarek, U., Pačes, M., Rapp, E., *Electrophoresis* 2003, *24*, 4241–4253.

[77] Afeyan, N. B., Gordon, N. F., Mazsaroff, I., Varady, L., Fulton, S. P., Yang, Y. B., Regnier, F. E., *J. Chromatogr.* 1990, *519*, 1–29.

[78] Rodrigues, A. E., Lu, Z. P., Loureiro, J. M., *Chem. Eng. Sci.* 1991, *46*, 2765–2773.

[79] Liapis, A. I., McCoy, M. A., *J. Chromatogr.* 1992, *599*, 87–104.

[80] Rodrigues, A. E., Lopes, J. C., Lu, Z. P., Loureiro, J. M., Dias, M. M., *J. Chromatogr.* 1992, *590*, 93–100.

[81] Carta, G., Gregory, M. E., Kirwan, D. J., Massaldi, H. A., *Sep. Technol.* 1992, *2*, 62–72.

[82] Frey, D. D., Schweinheim, E., Horváth, Cs., *Biotechnol. Prog.* 1993, *9*, 273–284.

[83] Boschetti, E., *J. Chromatogr. A* 1994, *658*, 207–236.

[84] Pfeiffer, J. F., Chen, J. C., Hsu, J. T., *AIChE J.* 1996, *42*, 932–939.

[85] Rodrigues, A. E., *J. Chromatogr. B* 1997, *699*, 47–61.

[86] Reeder, D. H., Clausen, A. M., Annen, M. J., Carr, P. W., Flickinger, M. C., McCormick, A. V., *J. Colloid Interface Sci.* 1996, *184*, 328–330.

[87] Nash, D. C., Chase, H. A., *J. Chromatogr. A* 1998, *807*, 185–207.

[88] Majors, R. E., *LC·GC Europe* 2003, *16*, 8–13.

[89] Tallarek, U., Vergeldt, F. J., Van As, H., *J. Phys. Chem. B* 1999, *103*, 7654–7664.

[90] Kandhai, D., Hlushkou, D., Hoekstra, A. G., Sloot, P. M. A., Van As, H., Tallarek, U., *Phys. Rev. Lett.* 2002, *88*, art. No. 234501.

[91] Paul, P. H., Arnold, D. W., Rakestraw, D. J., in:*Micro Total Analysis Systems '98*, Harrison, D. J., Van den Berg, A. (Eds.), Kluwer, Dordrecht 1998, pp. 49–52.

[92] Paul, P. H., Arnold, D. W., Neyer, D. W., Smith, K. B., in:*Micro Total Analysis Systems 2000*, Van den Berg, A., Olthuis, W., Bergveld, P. (Eds.), Kluwer, Dordrecht 2000, pp. 583–590.

[93] Zeng, S., Chen, C.-H., Mikkelsen, J. C., Santiago, J. G., *Sens. Actuators B* 2001, *79*, 107–114.

[94] Kirby, B. J., Shepodd, T. J., Hasselbrink, E. F., *J. Chromatogr. A* 2002, *979*, 147–154.

[95] Reichmuth, D. S., Kirby, B. J., *J. Chromatogr. A* 2003, *1013*, 93–101.

[96] Chen, L., Ma, J., Tan, F., Guan, Y., *Sens. Actuators B* 2003, *88*, 260–265.

[97] Stol, R., Poppe, H., Kok, W. Th., *Anal. Chem.* 2003, *75*, 5246–5253.

[98] Minakuchi, H., Nakanishi, K., Soga, N., Tanaka, N., *Anal. Chem.* 1996, *68*, 3498–3501.

[99] Nakanishi, K., *J. Porous Mater.* 1997, *4*, 67–112.

[100] Tallarek, U., Leinweber, F. C., Seidel-Morgenstern, A., *Chem. Eng. Technol.* 2002, *25*, 1177–1181.

[101] Leinweber, F. C., Tallarek, U., *J. Chromatogr. A* 2003, *1006*, 207–228.

[102] Helfferich, F., *Ion Exchange*, Dover, New York 1995.

[103] Ståhlberg, J., *J. Chromatogr. A* 1999, *855*, 3–55.

[104] Yaroshchuk, A. E., *Sep. Purif. Technol.* 2001, *22–23*, 143–158.

[105] Rubinstein, I., *J. Chem. Soc. Faraday Trans. II* 1981, *77*, 1595–1609.

[106] Dukhin, S. S., *Adv. Colloid Interface Sci.* 1991, *35*, 173–196.

[107] Mishchuk, N. A., Takhistov, P. V., *Colloids Surf. A* 1995, *95*, 119–131.

[108] Mishchuk, N. A., *Colloids Surf. A* 1998, *140*, 75–89.

[109] Rubinstein, I., Zaltzman, B., in: *Surface Chemistry and Electrochemistry of Membranes*, Sørensen, T. S. (Ed.), Marcel Dekker, New York 1999, pp. 591–621.

[110] Rubinstein, I., Zaltzmann, B., *Phys. Rev. E* 2000, *62*, 2238–2251.

[111] Mishchuk, N., Gonzalez-Caballero, F., Takhistov, P., *Colloids Surf. A* 2001, *181*, 131–144.

[112] Rubinstein, I., Zaltzmann, B., *Math. Models Methods Appl. Sci.* 2001, *11*, 263–300.

[113] Ben, Y., Chang, H.-C., *J. Fluid Mech.* 2002, *461*, 229–238.

[114] Rathore, A. S., Horváth, Cs., *J. Chromatogr. A* 1997, *781*, 185–195.

[115] Ishizuka, N., Minakuchi, H., Nakanishi, K., Soga, N., Nagayama, H., Hosoya, K., Tanaka, N., *Anal. Chem.* 2000, *72*, 1275–1280.

[116] Rathore, A. S., Reynolds, K. J., Colón, L. A., *Electrophoresis* 2002, *23*, 2918–2928.

[117] Wan, Q.-H., *J. Phys. Chem. B* 1997, *101*, 4860–4862.

[118] Lyklema, J., *Fundamentals of Interface and Colloid Science. Vol. 2: Solid-Liquid Interfaces*, Academic Press, London 1995.

[119] Hidalgo-Álvarez, R., Martín, A., Fernández, A., Bastos, D., Martínez, F., de las Nieves, F. J., *Adv. Colloid Interface Sci.* 1996, *67*, 1–118.

[120] Nakanishi, K., Minakuchi, H., Soga, N., Tanaka, N., *J. Sol-Gel Sci. Technol.* 1998, *13*, 163–169.

[121] Manzanares, J. A., Murphy, W. D., Mafé, S., Reiss, H., *J. Phys. Chem.* 1993, *97*, 8524–8530.

[122] Tallarek, U., Albert, K., Bayer, E., Guiochon, G., *AIChE J.* 1996, *42*, 3041–3054.